

Thermal Hydrocarbon Chemistry

Thermal Hydrocarbon Chemistry

Alex G. Oblad, EDITOR

University of Utah

Hubert G. Davis, EDITOR

Union Carbide Corporation

R. Tracy Eddinger, EDITOR

Cogas Development Company

Based on a symposium

jointly sponsored by

the ACS Divisions of

Petroleum Chemistry and

Fuel Chemistry at the

175th National Meeting of the

American Chemical Society,

Anaheim, California,

March 15–16, 1978.

ADVANCES IN CHEMISTRY SERIES

183

AMERICAN CHEMICAL SOCIETY
WASHINGTON, D. C. 1979



Library of Congress Data

Thermal hydrocarbon chemistry.

(Advances in chemistry series; 183 ISSN 0065-2393)

Includes bibliographies and index.

1. Hydrocarbons—Congresses. 2. Pyrolysis—Congresses.

I. Oblad, Alex Golden, 1909— . II. Davis, Hugh G., 1915— . III. Eddinger, R. Tracy, 1922— . IV. American Chemical Society. Division of Petroleum Chemistry. V. American Chemical Society. Division of Fuel Chemistry. VI. American Chemical Society. VII. Series.

QD1.A355 no. 183 [QD305.H5] 540'.8s [661'.81]
ISBN 0-8412-0468-3 ADCSAJ 183 1-364-1979
79-22817

Copyright © 1979

American Chemical Society

All Rights Reserved. The appearance of the code at the bottom of the first page of each article in this volume indicates the copyright owner's consent that reprographic copies of the article may be made for personal or internal use or for the personal or internal use of specific clients. This consent is given on the condition, however, that the copier pay the stated per copy fee through the Copyright Clearance Center, Inc. for copying beyond that permitted by Sections 107 or 108 of the U.S. Copyright Law. This consent does not extend to copying or transmission by any means—graphic or electronic—for any other purpose, such as for general distribution, for advertising or promotional purposes, for creating new collective works, for resale, or for information storage and retrieval systems.

The citation of trade names and/or names of manufacturers in this publication is not to be construed as an endorsement or as approval by ACS of the commercial products or services referenced herein; nor should the mere reference herein to any drawing, specification, chemical process, or other data be regarded as a license or as a conveyance of any right or permission, to the holder, reader, or any other person or corporation, to manufacture, reproduce, use, or sell any patented invention or copyrighted work that may in any way be related thereto.

PRINTED IN THE UNITED STATES OF AMERICA

**American Chemical
Society Library**
1155 16th St. N. W.
Washington, D. C. 20036

Advances in Chemistry Series

M. Joan Comstock, *Series Editor*

Advisory Board

Kenneth B. Bischoff

Donald G. Crosby

Robert E. Feeney

Jeremiah P. Freeman

E. Desmond Goddard

Jack Halpern

Robert A. Hofstader

James D. Idol, Jr.

James P. Lodge

John L. Margrave

Leon Petrakis

F. Sherwood Rowland

Alan C. Sartorelli

Raymond B. Seymour

Aaron Wold

Gunter Zweig

FOREWORD

ADVANCES IN CHEMISTRY SERIES was founded in 1949 by the American Chemical Society as an outlet for symposia and collections of data in special areas of topical interest that could not be accommodated in the Society's journals. It provides a medium for symposia that would otherwise be fragmented, their papers distributed among several journals or not published at all. Papers are reviewed critically according to ACS editorial standards and receive the careful attention and processing characteristic of ACS publications. Volumes in the **ADVANCES IN CHEMISTRY SERIES** maintain the integrity of the symposia on which they are based; however, verbatim reproductions of previously published papers are not accepted. Papers may include reports of research as well as reviews since symposia may embrace both types of presentation.

PREFACE

Thermal reactions of hydrocarbons have been of great interest to chemists even before the petroleum industry began. Thermal cracking and reforming processes primarily for gasoline production dominated the industry through World War II, but have been replaced by catalytic processes in the ensuing years with the dominance of high octane gasoline and the high compression engine. The industry of producing chemicals from petroleum began when chemists in the 1920's produced alcohols from the ethylene and propylene formed in thermal cracking. From this start, thermal processes for making the main chemical building blocks: ethene, propene, butenes, butadiene, and aromatics (epbba) have grown in importance. Now a vast industry exists in many parts of the world based upon olefins and aromatics produced by thermal reactions of hydrocarbons. An array of other products, such as cokes and carbons, pitches and asphalts, are available as commercial items and all are produced by thermal means. Thermal reactions will play an important role in the production of hydrocarbons from shale, tar sands, coal, and lignite.

Interest in the chemistry of thermal reactions of hydrocarbons has persisted. The size of the U.S. manufacturing industry in chemicals from petroleum and the dollar volume of the products are enormous. It has recently been reported that the petrochemical output comprised nearly 23% of all manufacturing sales in the U.S. in 1976 and required over 16% of the total capital investment for that year. The Division of Petroleum Chemistry of the American Chemical Society, in its programs, has continued over the years to bring advances in this field to the attention of chemists, chemical engineers, and others interested in petroleum processing. This book contains papers from two division programs held at Anaheim, California in March, 1978: "Thermal Hydrocarbon Chemistry" and "Recent Advances in the Production and Utilization of Light Olefins."

Previous "Advances in Chemistry Series" have dealt with aspects of thermal hydrocarbon chemistry. Volume 97, "Refining Petroleum for Chemicals," edited by Leo J. Spillane was published in 1970. Symposium Series 32, "Industrial and Laboratory Pyrolyses," edited by Lyle F. Albright and Billy L. Crynes, was published in 1976.

The chapters in this volume are grouped in several sequences as follows: Chapters 1-6 relate to epbba production directly. Specific subjects covered are pyrolysis of alpha-olefins, butenes, paraffins, unsubsti-

tuted mono-, di-, and tricycloalkanes, virgin and hydrogenated gas oils, and feedstocks from processed shale oils.

Chapters 7–9 deal with the process aspects of pyrolysis to produce epbba. The first discusses the use of aerospace technology to simulate an unconventional process. The second discusses the results of recent attempts to develop computer models for large scale pyrolysis of hydrocarbons and the third discusses recent process and furnace design advances.

Chapters 10–12 cover important aspects of coke formation in metal tubular reactors during pyrolysis of hydrocarbons. Chapters 13 and 14 are concerned with coal and lignite pyrolysis. Chapters 15 and 16 deal with pitch formation from, respectively, heavy petroleum fraction and tar sand bitumen. Chapters 17 and 18 cover studies on the mechanisms of thermal alkylation and hydrolysis. Chapters 19 and 20 on oil shale deal with the properties of oil shale and shale oil as developed by techniques of microwave heating and thermal analysis.

This volume, although it covers a wide range of subjects in the general area of thermal hydrocarbon chemistry, contains the latest information on subject areas important to the petrochemical industry and to the science of pyrolysis. It is hoped that it will be a useful addition to this important area of science and technology. We want to thank all those who helped in arranging these symposia, and participated in them. Particular thanks go to J. W. Bunger for his help.

University of Utah
Salt Lake City, Utah

ALEX G. OBLAD

Union Carbide Corp.
South Charleston, West Virginia

HUGH G. DAVIS

Cogas Development Co.
Princeton, New Jersey
April 24, 1979

R. TRACY EDDINGER

Pyrolysis of Alpha-Olefins—A Mechanistic Study

CHARLES REBICK

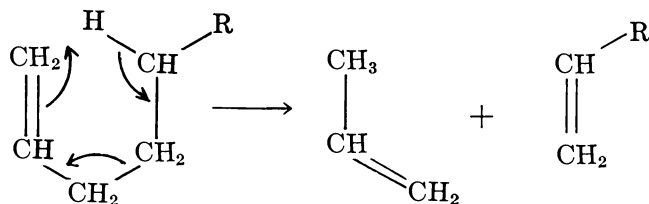
Exxon Research and Engineering Company, P.O. Box 45, Linden, NJ 07036

The products from the pyrolyses of four higher alpha-olefins have been accounted for by an empirical model involving three competing decomposition pathways: a molecular decomposition involving a six-membered ring transition state (which yields both propylene and an alpha-olefin with three less carbon atoms than the reactant) and two free radical chain pathways. One free radical channel involves hydrogen abstraction from, the second radical addition to the reactant olefin. The relative contributions of these three paths have been estimated from experimental data from the laboratory pyrolysis of higher alpha-olefins. The pyrolyses were carried out at low conversions in a quartz flow reactor at 475°–550°C.

The expansion of the petrochemical industry and the accompanying increase in the demand for ethylene, propylene, and butadiene has resulted in renewed interest and research into the pyrolytic reactions of hydrocarbons. Much of this activity has involved paraffin pyrolysis for two reasons: saturates make up most of any steam cracker feed and since the pioneering work of Rice 40 years ago, the basic features of paraffin cracking mechanisms have been known (1). The emergence of gas chromatography as a major analytical tool in the past 15 years has made it possible to confirm the basic utility of Rice's hypotheses (*see*, for example, Ref. 2).

By contrast, few studies have been made of the pyrolysis of alpha-olefins. The large number of apparent primary reaction products and the complexity of the mechanism as well as the absence of olefins in cracking feedstocks all have inhibited research. Yet, it is well known that alpha-

olefins are major primary products of paraffin cracking, and secondary reactions of alkenes must be important in moderate-to-high severity steam cracking to ethylene and in thermal cracking processes such as coking and visbreaking. Most of the prior olefin studies have involved propylene or butene cracking since these are the major primary olefinic products besides ethylene from gaseous and naphtha feedstocks (3, 4). However, longer chain olefins play an important role in the cracking of gas oils, residual stocks, and whole crudes. Previous studies of higher alpha-olefins have included octadecene (5), heptene, dodecene, and tetradecene (6), and various isomers of tetradecene (7). These compounds crack to form shorter alpha-olefins, diolefins, methane, ethane, and hydrogen. Also, all of these researchers reported a surprisingly high yield of $C_{n-3}H_{2n-6}$ from the cracking of C_nH_{2n} . A concerted molecular mechanism was proposed by Miller (5) to account for this product:



This retro-ene reaction is accepted as the primary mode of ester decomposition. For olefins, it has been investigated both directly (8) and via the reverse reaction, the ene reaction (9). The best estimates for 1-hexene and 1-heptene are that the reaction proceeds with an activation energy of about 54 kcal/mol and a preexponential factor of 10^{12} sec^{-1} .

It has been assumed that the remaining products are formed by some sort of free radical chain mechanism, but no generalized mechanism like that of Rice's for paraffin pyrolysis has been proposed. Tanaka et al. have been able to simulate product distributions for shorter olefins—up to hexene (10). We shall describe a model for higher alpha-olefin pyrolysis and use it to account for the products from the cracking of several olefins.

Experimental

All experiments were carried out in a simple flow system. A schematic diagram of the apparatus is shown in Figure 1. The quartz reactor (10 mm i.d.) was heated in a three-zone electric furnace which gave a flat ($\pm 2^\circ\text{C}$) temperature profile over about 45 cm. Reactor temperatures were measured by a thermocouple which could be moved in a sheath attached to the outside of the reactor. Initially, the sheath was placed inside the reactor, but the inside temperatures agreed so closely with the reactor wall temperatures that the inner thermocouple was removed to minimize catalytic effects.

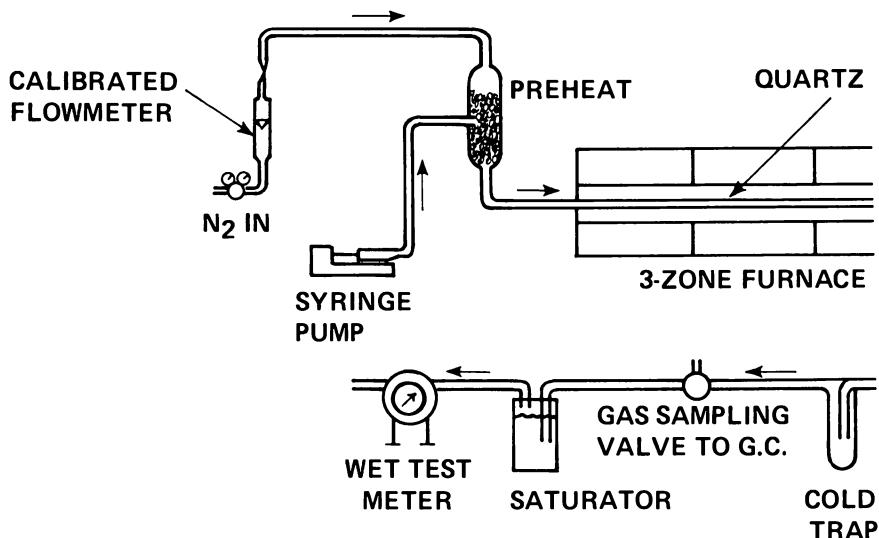


Figure 1. Diagram of flow apparatus

N_2 diluent was metered into the system through a calibrated flowmeter. Olefins were fed by a syringe pump to a preheater where they were vaporized and mixed with the diluent gas. The mixture flowed through the reactor tube, and unreacted hydrocarbon and liquid products condensed in two traps, one at room temperature and one at approximately -50°C . Gaseous products were sampled on-line and were analyzed by using gas chromatography. Total gas flow was measured by using a wet test meter. At the conclusion of an experiment, the liquid products were collected and analyzed by using gas chromatography. Initial product identification was made with gas chromatography-mass spectroscopy. The gas chromatography and programming rates used are summarized on Table I. Commercially available alpha-olefins were used

Table I. Gas Chromatographic Analysis

| Analysis | Column | Detector | Temperature Program |
|----------------------------|---|----------------------|---|
| H_2 | molecular sieve 5A 6 ft \times 1/8 in. | thermal conductivity | 100°C isothermal |
| C_1 - C_5 hydrocarbons | 0.19% picric acid on 80/100 mesh carbopack C 3 m \times 1/8 in. | flame ionization | 4 min at 30°C 30° - 100°C @ $4^\circ/\text{min}$ |
| Hydrocarbon liquids | 20% SP2100 on 80/100 mesh chromosorb W AW-DMCS 10 ft \times 1/8 in. | flame ionization | 4 min at 60°C 60° - 300°C @ $4^\circ/\text{min}$ |

without further purification. Four olefins were studied: 1-nonene, 1-dodecene, 1-tetradecene, and 1-hexadecene. Gas chromatographic analysis showed the purity of all reagents to be at least 99%.

Results

Typical product distributions for the four olefins studied are shown in Table II. The major products are ethylene, propylene, methane, and ethane. Lesser amounts of higher alpha-olefin products also are observed. In these respects the product distribution from the cracking of an alpha-olefin resembles that of the corresponding *n*-paraffin. However, there are several differences between olefin and paraffin cracking. The first is the presence of butadiene and smaller amounts of higher diolefins (mostly alpha-omega dienes) and cyclic olefins as primary products of olefin cracking. These products are not primary cracking products of paraffins. A second difference is the surprisingly large yield of $C_{n-3}H_{2n-6}$ from the cracking of C_nH_{2n} . This effect is most visible if we compare the olefin product yields from the cracking of an alpha-olefin and the corresponding paraffin. Figure 2 does this for hexadecene and hexadecane. The fluctuations in product olefin levels with carbon number are real and reproducible, reflecting mechanistic features and not experimental scatter. Figure 3 indicates this by comparing olefin product yields from the different compounds pyrolyzed.

Another difference between olefin and paraffin pyrolysis is the reaction order. Typically, higher *n*-paraffins crack according to first-order kinetics. Alpha-olefin pyrolysis is somewhat higher order. Figure 4 is a log-log plot of average dodecene cracking rate vs. average $C_{12}C_{24}$ pressure at 525°C. The decomposition is 1.33 order in dodecene. Table III gives the reaction orders (in $C_{12}H_{24}$) for the formation of individual products. Reaction order measurements for C_4 - C_6 products have been omitted because of small partial-pressure-dependent errors in the detection of these products, which make order measurements impossible. Note that ethylene, propylene, and nonene formation are of significantly lower order than those of the other products. Reasons for this will be discussed in the next section.

The rates of alpha-olefin decomposition measured in our laboratory are only slightly higher than those for corresponding paraffins. For example, at 500°C, hydrocarbon partial pressure of 0.18 atm, and approximately 20 seconds residence time, 6.2% hexadecene is cracked compared with 4.5% hexadecane. Figure 5 shows average rate constants for alpha-olefin cracking plotted vs. the size of the olefin being cracked, indicating only a slight increase in cracking rate with increasing molecular weight.

Table II. Product Distributions from Alpha-Olefin Pyrolysis

| | Reactant | | | |
|--|-------------|----------------|----------------|----------------|
| | C_9H_{18} | $C_{12}H_{24}$ | $C_{14}H_{28}$ | $C_{16}H_{32}$ |
| Temperature ($^{\circ}C$) | 500 | 500 | 500 | 500 |
| Initial hydrocarbon partial pressure (atm) | 0.26 | 0.22 | 0.19 | 0.18 |
| Space time (sec) | 18.0 | 9.7 | 19.8 | 9.2 |
| Conversion (wt %) | 6.4 | 2.8 | 5.8 | 3.1 |
| Products (mol/100 mol cracked) | | | | |
| H_2 | 1.9 | — | — | — |
| CH_4 | 23.6 | 27.8 | 27.7 | 28.2 |
| C_2H_4 | 53.8 | 63.1 | 60.9 | 60.4 |
| C_2H_6 | 14.5 | 19.8 | 19.7 | 18.6 |
| C_3H_6 | 46.0 | 49.7 | 47.0 | 46.2 |
| C_3H_8 | 2.9 | 3.7 | 3.5 | 3.7 |
| 1- C_4H_8 | 12.3 | 16.4 | 15.4 | 16.3 |
| 1,3- C_4H_6 | 8.6 | 9.3 | 7.6 | 8.7 |
| C_5H_{10} | 13.3 | 15.4 | 8.3 | 11.9 |
| C_5H_8 | 8.1 | 1.7 | 2.2 | 1.1 |
| C_6H_{12} | 22.4 | 11.3 | 12.1 | 13.3 |
| C_6H_{10} { $C_6 = =$ | 5.6 | 1.2 | 1.3 | 1.2 |
| { MCP = + CH = ^a | 5.3 | 3.8 | 4.3 | 3.9 |
| C_7H_{14} | 5.8 | 6.7 | 12.3 | 9.6 |
| C_7H_{12} | 6.4 | 3.3 | 4.9 | 3.0 |
| C_8H_{16} | 5.8 | 8.5 | 9.0 | 8.0 |
| C_8H_{14} | 4.3 | 3.1 | 0.7 | 2.7 |
| C_9H_{18} | — | 20.8 | 6.3 | 11.6 |
| C_9H_{16} | — | 1.5 | 1.7 | 1.9 |
| $C_{10}H_{20}$ | — | 4.4 | 9.3 | 10.2 |
| $C_{10}H_{18}$ | — | 0.9 | 1.3 | 1.3 |
| $C_{11}H_{22}$ ^b | — | 2.7 | 24.3 | 4.9 |
| $C_{12}H_{24}$ | — | — | 4.7 | 8.0 |
| $C_{13}H_{26}$ | — | — | 2.5 | 24.6 |
| $C_{14}H_{28}$ | — | — | — | 3.5 |
| $C_{15}H_{30}$ | — | — | — | 1.5 |

^a Methylcyclopentene and cyclohexene.

^b C_{11}^+ diolefins were not separated from C_{11}^+ olefins.

An Arrhenius plot of log rate constant vs. reciprocal temperature (Figure 6) indicates an activation energy of 61.9 ± 1.3 kcal/mol for dodecene cracking. This is similar to the activation energies measured for *n*-paraffin cracking and is somewhat higher than previously measured values for alpha-olefins (6).

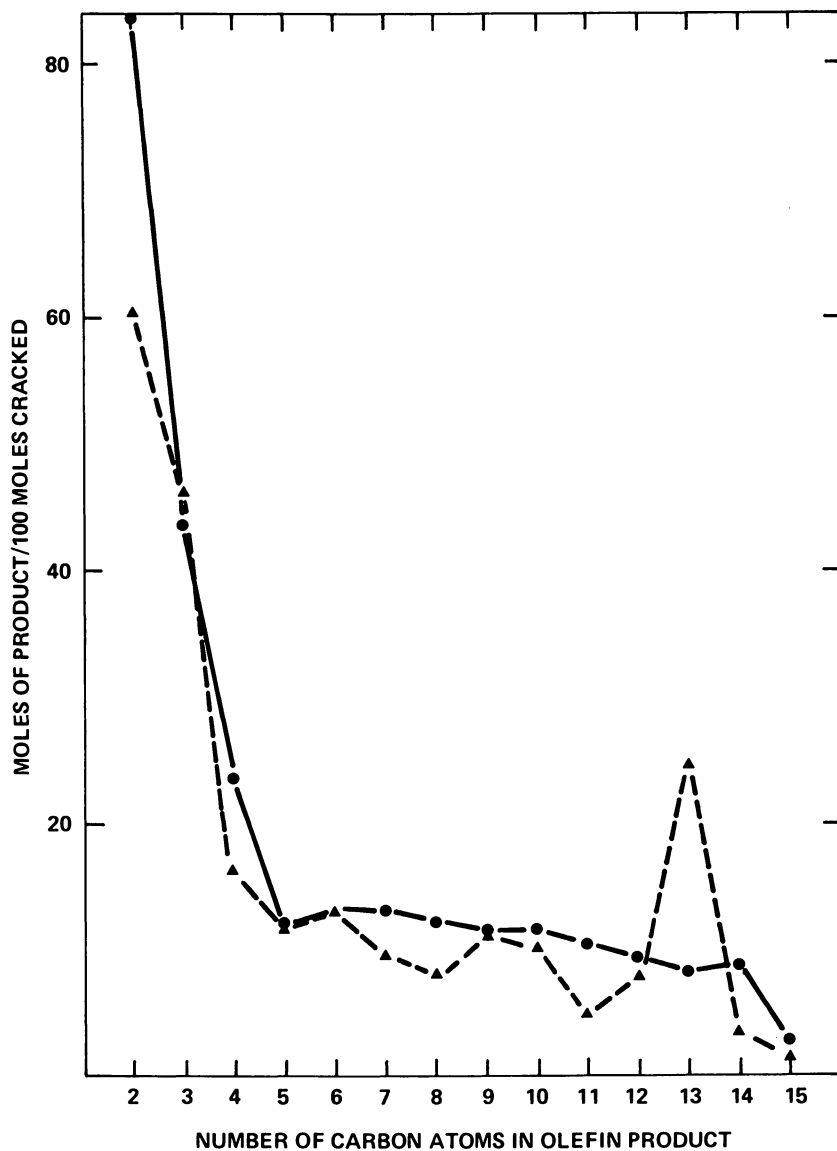


Figure 2. A comparison of the yields of alpha-olefin products from the pyrolysis of hexadecane and hexadecene at 500°C. (●) From $C_{16}H_{34}$, (▲) from $C_{16}H_{32}$.

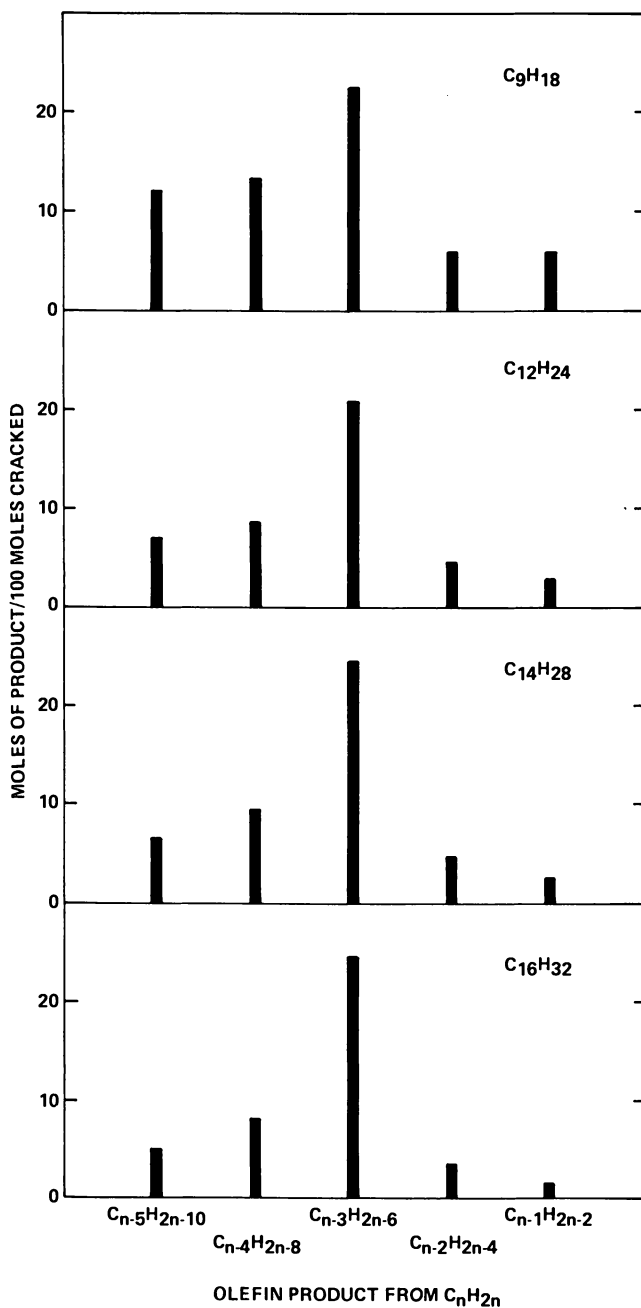


Figure 3. A comparison of the α -olefin product yields from the pyrolysis of four higher α -olefins at 500°C

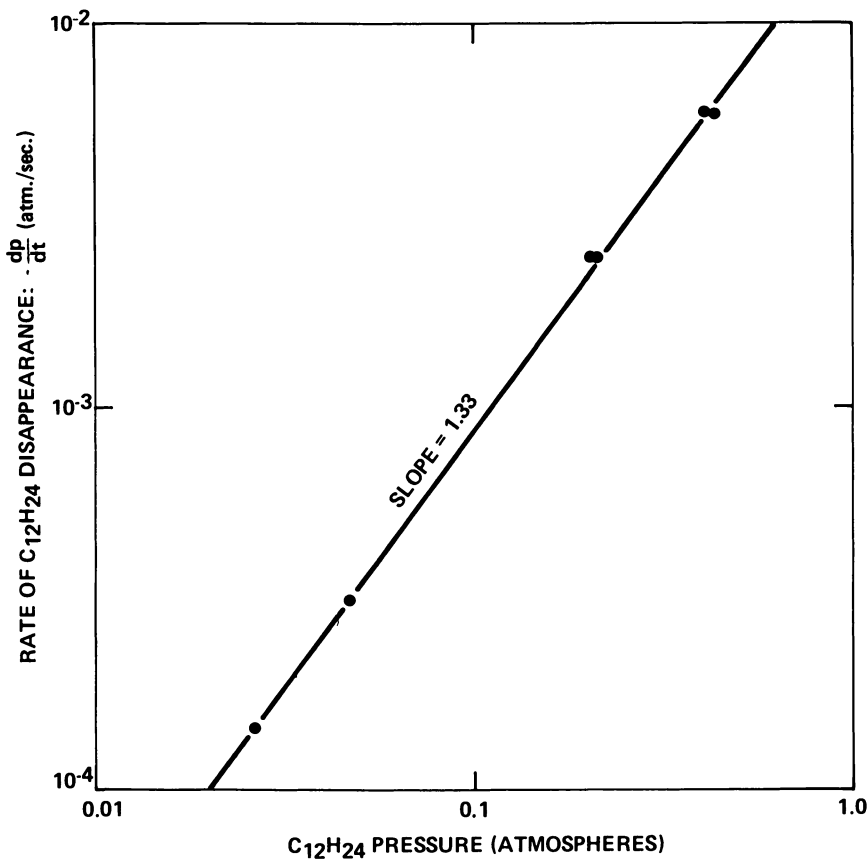


Figure 4. Determination of the overall reaction order for 1-dodecene pyrolysis at 525°C

Table III. Reaction Orders for Product Formation in Dodecene Pyrolysis at 525°C

| Product | Order of Reaction with Respect to Dodecene |
|-----------|--|
| Methane | 1.25 |
| Ethylene | 1.17 |
| Ethane | 1.40 |
| Propylene | 1.10 |
| Propane | 1.37 |
| 1-Heptene | 1.62 |
| 1-Octene | 1.43 |
| 1-Nonene | 1.16 |
| Overall | 1.33 |

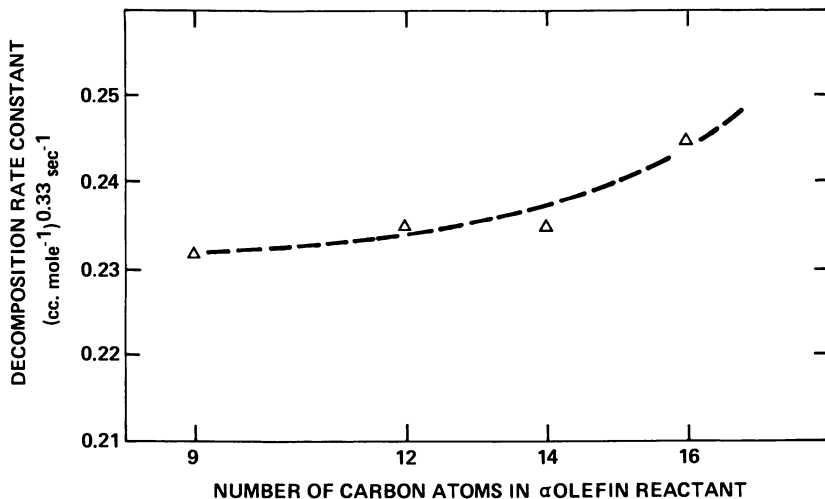


Figure 5. Variation in decomposition rate constants for alpha-olefins with molecular weight at 500°C

Discussion

Any attempt to rationalize the product distribution from alpha-olefin cracking must start with the large $C_{n-3}H_{2n-6}$ yield. This product has not been accounted for by any reasonable free radical mechanism. Rather, the retro-ene pathway described in the introduction has been postulated. Rumyantsev et al. (6) support this hypothesis by showing that in 1-heptene cracking, the addition of NO (a known free radical inhibitor) increases the amounts of 1-butene and propylene relative to the other products. The overall level of inhibition and the partial pressures of reactant and NO were not reported. Girard-Horvilleur also reports attempts to prove the molecular hypothesis in tetradecene pyrolysis by inhibition with propylene and NO (7). Addition of either increases the relative yield of undecane. However, this is not a conclusive proof that the undecane comes from a molecular mechanism since neither C_3H_6 nor NO reduces the cracking rate significantly, i.e., there is no proof of inhibition of the free radical part of the mechanism. In our laboratory, no inhibition was observed at NO partial pressures up to 36 mm Hg. Nonetheless, this molecular pathway appears reasonable from the point of view of orbital symmetry (11).

The remaining products can be accounted for by free radical mechanisms. There appear to be two main pathways involved. The propagation steps of the first are shown in Equations 1 and 2. The

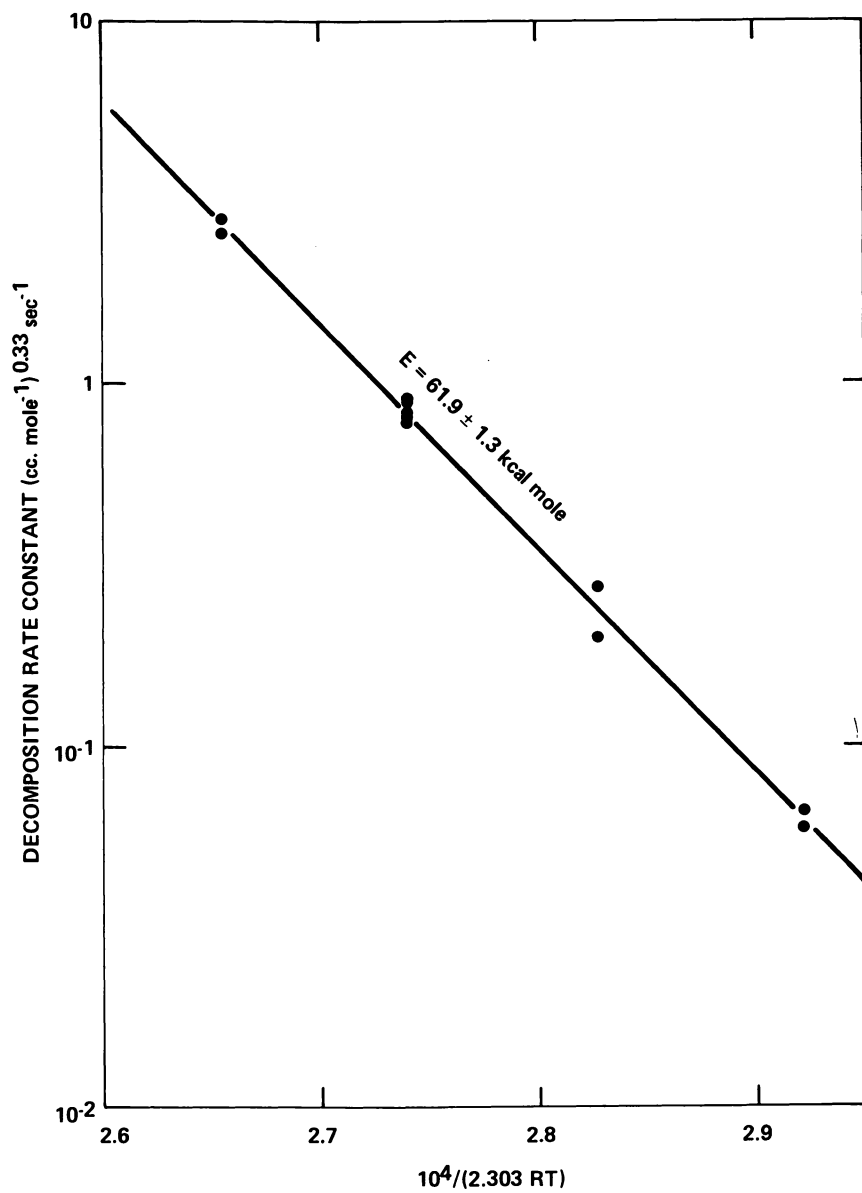
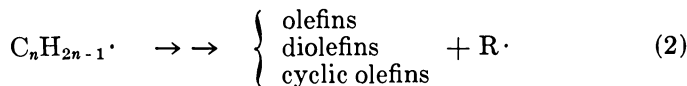
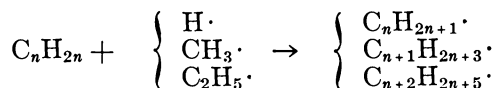


Figure 6. Determination of the activation energy for dodecene cracking in the range 475°C – 550°C



mechanism is analogous to paraffin decomposition in that small radicals abstract hydrogen from the olefin reactant to form what we shall call parent radicals. These large radicals isomerize rapidly to equilibrium. The parent radicals decompose via β -scission or $H\cdot$ elimination until a radical which cannot readily decompose is formed. This radical abstracts hydrogen from the reactant olefin to form a new parent radical and continues the chain. The chain carriers in this mechanism are most likely $CH_3\cdot$ and $C_2H_5\cdot$ and, to a lesser extent, $H\cdot$ and $C_3H_5\cdot$.

This mechanism qualitatively accounts for all products except the $C_{n-1}H_{2n-2}$ and $C_{n-2}H_{2n-4}$ olefins. These olefins cannot be formed from a $C_nH_{2n-1}\cdot$ parent radical by any reasonable bond cleavage; an alternate pathway also must be available. The most likely possibility is that these olefins come from heavier (than $C_nH_{2n-1}\cdot$) parent radicals formed by the addition of chain carriers to the reactant olefins, followed by decomposition. The presence of small amounts of $C_{n+1}H_{2n+2}$ and $C_{n+2}H_{2n+4}$ olefins as primary products supports this hypothesis. Typical addition reactions follow.



There is little rate data available for addition and abstraction reactions involving higher α -olefins. Where such data are available, they have usually been obtained from lower temperature studies (12, 13, 14). However, the available information indicates that addition should be competitive with abstraction in the temperature range of this study. For example, Steacie's data for ethyl radical reactions with 1-hexene and 1-heptene indicate that at 525°C, the addition rate would be about seven-tenths of the abstraction rate. For dodecene, one would expect this ratio to decrease because of the increase in abstractable hydrogen, but addition should still be a significant pathway. For methyl radicals and $H\cdot$ atoms, available data (13, 14) indicate that addition is somewhat faster relative to abstraction.

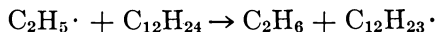
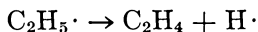
The three parent radicals mentioned earlier would decompose to form the same product distributions as the corresponding C_n , C_{n+1} , and C_{n+2} n -paraffins; namely, the whole range of smaller olefins, methane, and ethane. It is doubtful that any other addition reactions are significant.

The overall mechanism, then, is the sum of the contributions of three paths:

- (A) A molecular decomposition into C_3H_6 and $C_{n-3}H_{2n-6}$;
- (B) A free radical chain mechanism with parent radical $C_nH_{2n-1}\cdot$;
- (C) A free radical chain mechanism with parent radicals $C_nH_{2n+1}\cdot$, $C_{n+1}H_{2n+3}\cdot$, and $C_{n+2}H_{2n+5}\cdot$.

The measured reaction orders support the proposed mechanism. Path A is certainly first order in reactant. Paths B and C may be 1/2, first, or 3/2 order, depending on the termination reaction (15). Most likely, termination involves combination or disproportionation of small chain carrying radicals ($CH_3\cdot$, $C_2H_5\cdot$). With first-order initiation, this would result in 3/2-order kinetics. The overall reaction order would then be somewhere between first (Mechanism A) and 3/2 (Mechanisms B and C). The measured order of 1.33 for dodecene agrees with this prediction. The fact that propylene and nonene are formed with reaction orders of 1.10 and 1.16 with respect to dodecene (Table III) supports the hypothesis that they are formed largely by a first-order decomposition.

Ethylene also is formed with a reaction order in dodecene significantly closer to first order than is the overall reaction (1.17 vs. 1.33). This most likely is because of the competitive reactions of ethyl radicals,



with ethylene formation being relatively more favorable at lower dodecene partial pressures. Figure 7 illustrates this. Analogous arguments account for the relatively higher orders for ethane and propane formation.

The relative contributions of the three proposed reaction paths remain to be determined. The products from both the retro-ene and the addition reactions can be predicted with some quantitative certainty. For dodecene, the former produces only 1-nonene and propylene. The product distributions from the addition paths should be identical to those from the cracking of the corresponding paraffins. These product distributions can be predicted using the method of Rice and Kossiakoff (16). This approach parallels excellently with experiments (16, 17). (From available data we estimate its accuracy as $\pm 10\%$.) For dodecene, the addition of hydrogen atoms, methyl radicals, and ethyl radicals will produce $C_{12}H_{25}\cdot$, $C_{13}H_{27}\cdot$, and $C_{14}H_{29}\cdot$ parent radicals. The product distributions predicted by the Rice-Kossiakoff method for the decomposition of these radicals at 525°C are shown in Table IV.

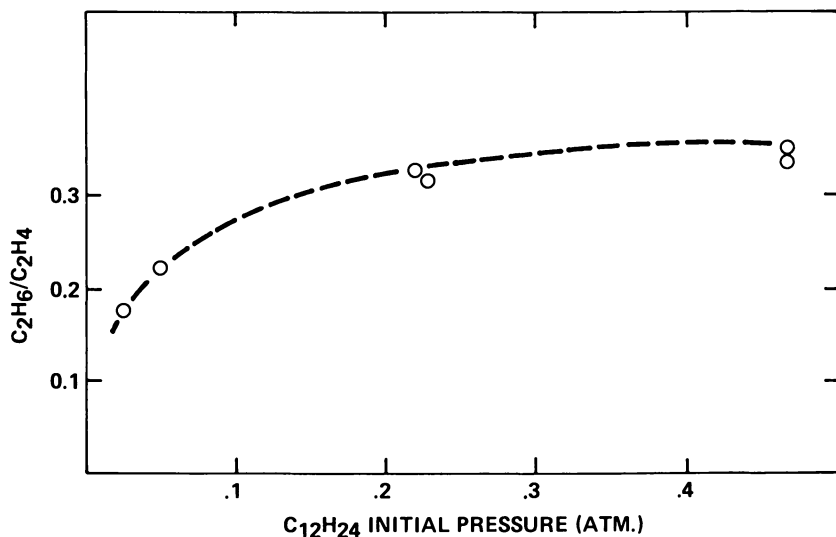


Figure 7. Variation in the molar ratio of ethane to ethylene produced from dodecene cracking at 525°C with initial dodecene partial pressure

Table IV. Calculated Product Distributions for Radical Addition to Dodecene at 525°C

| Product (mol/100 mol cracked) | Radical Added | | |
|----------------------------------|---------------|-------------------|---------------------------------|
| | H· | CH ₃ · | C ₂ H ₅ · |
| C ₂ H ₄ | 100 | 103 | 107 |
| C ₃ H ₆ | 49 | 53 | 54 |
| C ₄ H ₈ | 26 | 27 | 28 |
| C ₅ H ₁₀ | 17 | 18 | 19 |
| C ₆ H ₁₂ | 16 | 17 | 17 |
| C ₇ H ₁₄ | 14 | 15 | 16 |
| C ₈ H ₁₆ | 11.5 | 13 | 14 |
| C ₉ H ₁₈ | 9.9 | 10.6 | 12 |
| C ₁₀ H ₂₀ | 9.8 | 9.4 | 10.3 |
| C ₁₁ H ₂₂ | 4.9 | 9.3 | 9.0 |
| C ₁₃ H ₂₆ | — | — | 4.4 |
| H ₂ | -100 | — | — |
| CH ₄ | 61 | -41.2 | 65.9 |
| C ₂ H ₆ | 39 | 41.2 | -65.9 |

Unfortunately, the product distribution from the decomposition of olefinic radicals cannot be predicted with any quantitative certainty. When a hydrogen atom is abstracted from an olefin, three types of radicals can be formed: primary, secondary, and allylic radicals. The

relative rates of isomerization and decomposition of these large olefinic radicals are unknown. However, we can make some simple assumptions that will allow us to estimate the relative contributions of the three reaction paths. The procedure used for dodecene is outlined in Appendix A. A similar approach can be used for other olefins.

The estimated relative contributions of the three paths for dodecene cracking under a variety of conditions are shown in Table V. Two trends are visible in the data. First, at constant temperature and increasing dodecene partial pressure, the relative importance of the retro-ene path decreases while that of the abstraction path increases. The contribution of the addition path remains constant. The average estimated relative contributions of the retro-ene reaction at 525°C taken from Table V correspond to a reaction order of 0.95 ± 0.4 in dodecene; this satisfies the requirement that retro-ene reaction be first order.

The reason for the increase in the importance of the H· abstraction path with increasing pressure is more subtle. While the reaction order for the radical addition path is 1.33 (the same as the overall reaction), the abstraction path is 1.40 order in dodecene (from the data in Table V). This may be attributable to a decrease in $[H\cdot]$ with increasing pressure because more ethyl radicals are stabilized to ethane and fewer are decomposed to ethylene and H· as the pressure is increased (*see* Figure 7). If H· atoms are the most efficient addition species, a decrease in their relative concentration would result in a relative decrease in the contribution of the addition path and a corresponding increase in the role of the H· abstraction route.

The second trend is that at constant dodecene partial pressure as the temperature is increased, the relative importance of the retro-ene reaction decreases slightly, while the H· abstraction path and the radical addition path show much more marked temperature dependences. The former increases while the latter decreases in relative importance. This suggests that the activation energy for hydrogen abstraction is significantly higher

Table V. Relative Contributions of Reaction Paths in Dodecene Cracking

| T (°C) | Dodecene Partial P (atm) | Fraction of Product Yield | | |
|--------|--------------------------------|------------------------------|-------------------------|----------------------------|
| | | (A) Retro-ene Reaction | (B) H Abstraction | (C) Radical Addition |
| 475 | 0.22 | 0.14–0.15 | 0.14–0.15 | 0.71 |
| 500 | 0.22 | 0.10–0.13 | 0.42–0.45 | 0.45 |
| 525 | 0.027 | 0.18–0.22 | 0.43–0.47 | 0.35 |
| | 0.049 | 0.17–0.20 | 0.44–0.47 | 0.36 |
| | 0.22 | 0.08–0.13 | 0.50–0.55 | 0.37 |
| | 0.46 | 0.05–0.10 | 0.54–0.59 | 0.36 |
| 550 | 0.22 | 0.06–0.11 | 0.59–0.64 | 0.30 |

than that for addition. This is in qualitative agreement with Steacie's studies of ethyl radical reactions with heptene and octene (12). However, the temperature dependence here is much larger than that expected from the activation energy difference of 1.3 kcal/mol determined by Steacie. It is perhaps attributable to a temperature-dependent change in the decomposition routes of the alkyl radical formed by the addition reaction. As the temperature is raised, the rates of the reverse reaction (hydrogen elimination) and the direct alkyl radical decomposition will increase faster than that for radical isomerization. Since the Rice-Kossiakoff mechanism assumes isomerization to equilibrium before decomposition, temperature-dependent deviations attributable to reverse reaction or to direct decomposition will alter the apparent radical addition contribution. Then the calculated ratio of abstraction to addition will increase more rapidly with temperature than the difference in their activation energies would lead one to expect.

An Arrhenius plot of the retro-ene contribution is shown in Figure 8.

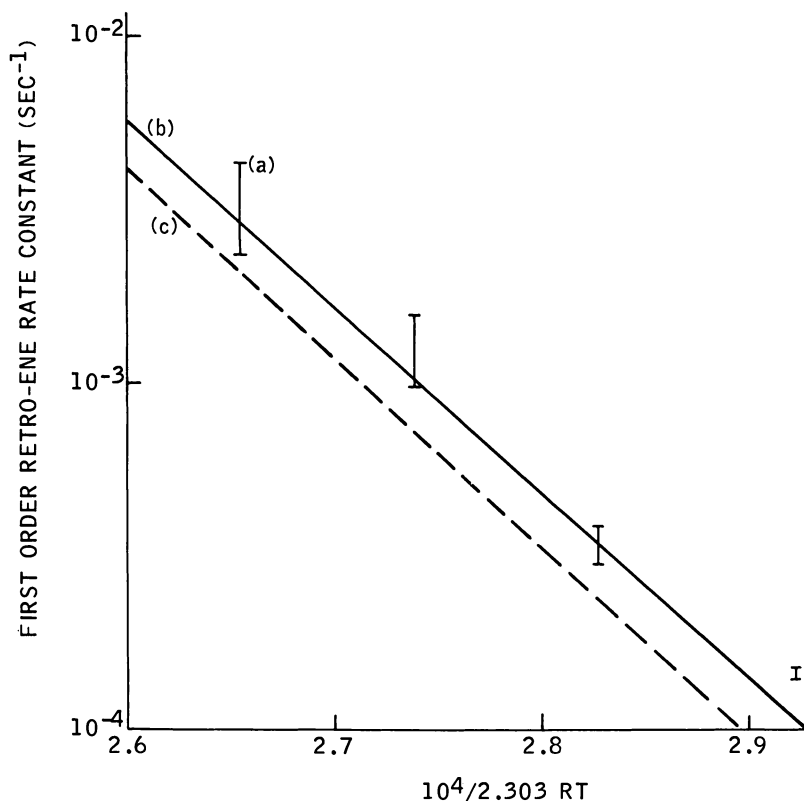


Figure 8. Arrhenius plot for the retro-ene reaction: (a) this work, 1-dodecene; (b) Blades and Sandhu, 1-heptene (8); (c) Richard and Back, 1-hexene (9).

The solid and dotted lines on the figure are calculated from the Arrhenius parameters determined by Blades and Sandhu for 1-heptene (9) and Back and Richard for 1-hexene (10), respectively. Within the error inherent in our method, the results for dodecene are in agreement.

This work represents a first attempt to assess the relative rates of the competing reaction paths in higher alpha-olefin pyrolysis. Ideally, one would like to write down all the possible reactions in the system, estimate rate constants, and solve the resulting coupled differential equations on a computer. However, for molecules of the size discussed here, or even for higher paraffins, such an undertaking would prove too time-consuming to be justifiable. Hence, we believe that the empirical approach presented here represents a useful first step in developing a model for predicting pyrolysis yields.

Acknowledgment

The author would like to thank W. H. Davis, Jr., and R. K. Lyon for helpful discussions. The excellent technical assistance of J. C. Dowling is also gratefully acknowledged. Thanks also to T. R. Ashe and C. S. Hsu for performing the gas chromatography/mass spectroscopy analyses to identify the products.

Literature Cited

1. Rice, F. O. *J. Am. Chem. Soc.* **1933**, *55*, 3035.
2. Doue, F.; Guiochon, J. *J. Chim. Phys.* **1969**, *64*, 395.
3. Powers, D. R.; Corcoran, W. H. In "Industrial and Laboratory Pyrolyses"; *ACS Symp. Ser.* **1976**, *32*, 117-130.
4. Crynes, B. L.; Ghaly, M. A. In "Industrial and Laboratory Pyrolyses"; *ACS Symp. Ser.* **1976**, *32*, 218-240.
5. Miller, D. B. *Ind. Eng. Chem. Prod. Res. Dev.* **1963**, *2*, 221.
6. Rummyantsev, A. N.; Nametkin, N. S.; Lavrovsky, K. P.; Sanin, P. I.; Musaev, I. A.; Vinnitsky, O. M.; Kurashava, E. Kh. *Proc. World Pet. Congr., 9th* **1975**, *5*, 155.
7. Giraud-Horvilleur, F.; Bluori, B. *Inf. Chim.* **1977**, *164*, 113.
8. Blades, A. T.; Sandhu, H. S. *Int. J. Chem. Kinet.* **1971**, *3*, 187.
9. Richard, C.; Back, M. H. *Int. J. Chem. Kinet.* **1978**, *10*, 389.
10. Tanaka, S.; Arai, Y.; Saito, S. *J. Chem. Eng., Jpn.* **1976**, *9*, 504.
11. Woodward, R. B.; Hoffman, R. *Angew. Chem., Int. Ed. Engl.* **1969**, *8*, 781.
12. James, D. G. L.; Steacie, E. W. R. *Proc. R. Soc.* **1958**, *A244*, 297.
13. Kondratiev, V. N. "Rate Constants of Gas Phase Reactions," *U.S. Dept. of Commerce*, **1972**, NSRDS-COM-72-10014.
14. Kerr, J. A.; Parsonage, M. J. "Evaluated Kinetic Data on Gas Phase Hydrogen Transfer Reactions of Methyl Radicals"; Butterworths: London, **1976**.
15. Laidler, K. J. "Chemical Kinetics"; McGraw-Hill, New York, **1965**; p. 390-393.
16. Kossiakoff, A.; Rice, F. O. *J. Am. Chem. Soc.* **1943**, *65*, 590.
17. Voge, H. H.; Good, G. M. *J. Am. Chem. Soc.* **1949**, *71*, 593.

RECEIVED July 5, 1978.

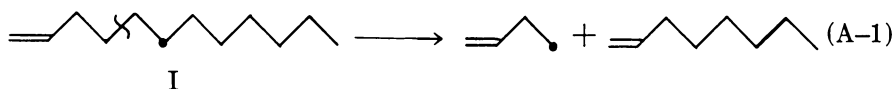
Appendix A. Method of Determining Relative Contributions of Reaction Paths in Dodecene Cracking

We wish to determine the relative importance of the three reaction paths: retro-ene, radical addition, and $H\cdot$ abstraction. The product distributions from the first two are known with some confidence, but little is known about the third. To start, two simple assumptions about the hydrogen abstraction path can be made. First, it is assumed that all secondary $C_{12}H_{23}\cdot$ radicals are present in equal concentrations. The second assumption is that dodecyl radicals decompose, if possible, by scission of the C-C bond β to the radical site. If two β -scission paths are available that produce products of equivalent stability, then both paths are equally likely to occur. If the products have different heats of formation, then the scission leading to more stable products should be favored, but the actual rates will be unknown. These assumptions are reasonable given our present understanding of paraffin cracking. They are all that is needed to estimate the relative contributions of the three paths. The procedure is as follows.

Given the β -scission hypothesis, an examination of possible dodecyl radicals indicates no reasonable mechanism of formation of $C_{10}H_{20}$ or $C_{11}H_{22}$. These products are formed only from the radical addition path. They can be used then to predict the relative importance of this path, X_A . Decene is used to do this since it is better separated by GC from the corresponding diolefin than is undecene. X_A is given by the ratio of the predicted value for decene from Table IV to the actual experimental yield. (Values for hydrogen atom addition are used here; they are fairly close to those for $CH_3\cdot$ and $C_2H_5\cdot$ addition, and available rate data (13, 14) indicate that $H\cdot$ atoms are the most likely radicals to add to dodecene.)

X_A is then used to correct the yields of all other products; by subtracting X_A times the $H\cdot$ -addition yields in Table IV from the experimental yields, one obtains an estimate of the combined product distribution from the retro-ene and abstraction paths. In this product distribution, nonene and propylene came from both paths; all other compounds are produced only by the $H\cdot$ -abstraction path. If the rate of formation of either nonene or propylene can be estimated in the abstraction path relative to one of the other products, the relative contributions of the two paths can be determined. As the following discussion indicates, nonene and octene meet this requirement.

Octene can be produced from only one $C_{12}H_{23}\cdot$ radical via Reaction A-1:

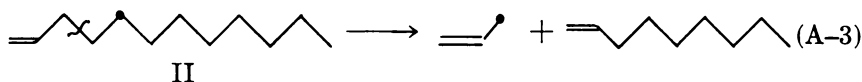


Radical I also can decompose via Reaction A-2:

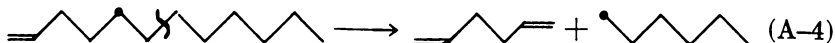


The endothermicities of Reactions A-1 and A-2 are roughly equal and one therefore might expect about half of radical I to decompose to 1-octene.

Nonene is formed uniquely from another $\text{C}_{12}\text{H}_{23}\cdot$ radical:



Radical II also decomposes via Reaction A-4:



In this case, the endothermicities of Reactions A-3 and A-4 are not equal since Reaction A-3 produces an allyl radical. Therefore, one would expect Reaction A-3 to be somewhat faster than Reaction A-4. If Radicals I and II are present in equal concentrations, then the yield of nonene from the hydrogen-abstraction path is between one and two times the yield of octene. The nonene in excess of this is formed by the retro-ene reaction. This defines a range of importance for the molecular path and by difference the contribution of the hydrogen abstraction path. This procedure is illustrated for the dodecene cracking yields from column two of Table II.

A. Calculation of X_A . Predicted yield of decene from Table IV, 9.8. (These yields are independent of temperature over the range studied here.) Experimental yield of decene, 4.4.

$$X_A = 4.4/9.8 = 0.45$$

B. Correction of Octene and Nonene Yields

| | <i>Experimental Yield</i> | $X_A \times$ <i>Predicted Yield</i> | <i>Corrected Yield</i> |
|---------------------------|---------------------------|-------------------------------------|------------------------|
| C_8H_{16} | 8.5 | 5.1 | 3.4 |
| C_9H_{18} | 20.8 | 4.4 | 16.4 |

C. Estimation of Ranges of Retro-ene Contribution. C_9H_{18} from abstraction path is 1-2 times C_8H_{16} or 3.4-6.8. By difference, C_9H_{18} from retro-ene reaction is 9.6-13.0. To convert this yield (mol/100 mol cracked) to the retro-ene relative contribution X_{RE} , we divide by 100.

Then the relative importance of the abstraction path is $1 - X_A - X_{RE}$. The relative contributions of the three paths then are:

| | |
|-------------|-----------|
| Retro-ene | 0.10–0.13 |
| Abstraction | 0.42–0.45 |
| Addition | 0.45 |

The sensitivity of this procedure to errors in the predicted yields of Table IV was checked. An overestimation of all three (C_8H_{16} , C_9H_{18} , and $C_{10}H_{20}$) yields from the prediction would have no effect on the estimated retro-ene contribution, and any changes in the free radical path contributions would be equal and opposite and proportional to the size of the error in prediction. An error in decene alone would affect all three. For example, a 10% overestimate of decene in Table IV changes the relative importances of the retro-ene, abstraction, and addition paths by + 0.004 (3.5%), - 0.05 (10%), and + 0.05 (10%), respectively. Thus, the predicted contribution of the retro-ene path is relatively insensitive to errors in the Rice-Kossiakoff predictions.

The estimation method described above has the following additional advantages: the products used are determined by analysis of only one phase in our experiments, and their relative magnitudes should be reasonably accurate; and, they are all alpha-olefins, and secondary reactions involving these products should be no faster than the reactant decomposition rate. Therefore, at low conversions (< 10%), secondary reactions can be neglected.

Steam Pyrolysis of Normal Butenes

HARRY P. LEFTIN

Pullman Kellogg, Research & Development Center, Houston, TX 77084

The normal butenes were pyrolyzed in the presence of steam in a nonisothermal flow reactor at 730°–980°C and contact times between 0.04 and 0.15 sec to obtain conversion covering the range between 3% and 99%. Isomerization reactions accompanied the decomposition of these olefins; however, the decomposition was the dominant reaction under these conditions. Pyrolysis of 1-butene is faster than that of either cis- or trans-2-butene. Methane, propylene, and butadiene are initial as well as major products from the pyrolysis of the n-butenes. Hydrogen is an initial product only from the 2-butenes. Ethylene appears to be an initial product only from 1-butene; it becomes the most prominent product at high conversions. Over the range of conditions of potential practical interest, the experimental rate expressions for the disappearance of the respective butene isomers, have been derived.

Pyrolysis of heavier hydrocarbons (such as gas oils) results in the production of a broad range of coproducts in very substantial quantities. While significant variations in product yield distributions are possible, depending on feed composition and pyrolysis process conditions, localized and wide ranging swings in market demand for specific coproducts can have a major impact on the economics of ethylene production. Consequently, the ability to increase or decrease the yields of specific coproducts in accordance with market fluctuations can provide an increased margin of profit for the plant operator. This may be achieved by separate cracking of selected secondary products or by cocracking of such products in admixture with fresh feedstocks. Design of units to obtain the highest selectivity in such operations requires extensive and precise kinetic equations and detailed product distributions for the thermal decomposition of the feedstocks, the initial and secondary olefinic products, and the mixtures of these.

While literature dealing with the cracking of paraffinic hydrocarbons is extensive, that concerning olefins, diolefins, and naphthenes is scarce and generally does not extend into the range of residence times, temperatures, and pressures that are characteristic of industrial process conditions.

This chapter comprises part of an experimental program undertaken to provide precise kinetic and product distribution data for the steam pyrolysis of a number of pure olefins, diolefins, and naphthenes over a wide range of temperatures and residence times, including those encountered in industrial practice. Runs were carried out in the bench-scale flow reactor (1), which has been shown (2) to provide yield and conversions data that are in excellent agreement with pilot plant and commercial data.

Results from this laboratory for steam pyrolysis of isobutene were reported earlier (1), and this chapter describes the pyrolysis of the three normal butene isomers: 1-butene, *cis*-2-butene, and *trans*-2-butene. Reaction schemes are derived from the product distributions, and kinetic parameters are established.

Thermal decomposition of 1-butene provides a more complex product spectrum than is obtained from either *cis*- or *trans*-2-butenes. Between 550° and 760°C in a flow system with nitrogen dilution (3), methane, propylene, butadiene, and ethylene were major products as well as hydrogen, ethane, 1-pentene, 2-pentene, 3-methyl-1-butene, and 1,5-hexadiene. In studies in a static system (4), cyclohexadienes, benzene, cyclopentene, cyclopentadiene, toluene, orthoxylene, and cyclohexene were observed among the liquid products of the reaction over the temperature range 490°–560°C.

In contrast, only methane, propylene, butadiene (all three in approximately equal quantities), and hydrogen comprise the major products obtained from decomposition of either *cis*- or *trans*-2-butenes under a variety of conditions (5). While isomerization occurred in all cases, equilibrium isomer distribution was never achieved. Ethylene was observed among the products at high temperatures and high conversion levels. Skeletal isomerization has not been observed; however, at low temperatures (6, 7) substantial conversion to 1-butene has been reported.

There is no general agreement on the kinetics or mechanism of pyrolysis of 1-butene. Activation energies are reported in the range between 59.1 kcal/mol (8) and 71.5 kcal/mol (9), and reaction order (with respect to 1-butene) is reported to be 0.7 (8), 1.0 (9–12), approaching 2.0 at low pressures (13), and different than 1.0 at temperatures below 540°C (4).

In this work, all of the major products and many minor ones have been identified and their dependence on conversion established. Over

the temperature range of this investigation, the calculated first-order rate constants for decomposition of 1-butene decreased with increasing conversion while calculated second-order rate constants were substantially invariant over the range of conversions from 3% to 99%.

Experimental

The reactor and flow system, as well as the general procedures used in the present study have been described in detail previously (1). The experimental arrangement was comprised of a feed system, vaporizer preheater, an electrically heated furnace, and a product recovery section. Liquid butenes were metered from pressurized feed tanks into the vaporizer, where they were mixed with superheated steam before passing through the preheater and into the reactor. The reaction zone was an annulus between the reactor and a coaxial thermocouple, both of 347 stainless steel. Temperature profiles were measured with a calibrated Chromel-Alumel thermocouple, manually driven along the length of the reactor. On leaving the reaction zone, the process stream was rapidly cooled by admixture with a recycled stream of cooled product gas. In this way, a rapid quench was achieved. The quenched products were further cooled against chilled water in an indirect heat exchanger, and the water condensate plus any liquid products were separated by means of a small cyclone separator that was an integral part of the product gas, recycle-quench system. To avoid formation of carbon oxides through steam reforming reactions, the walls of the stainless steel reactor were maintained in an inactive form by sulfiding, and the pyrolysis experiments were performed in the presence of 50 ppm sulfur, which was introduced to the system as ethyl mercaptan contained in the process feed water.

Phillips Petroleum Co., research grade, 1-butene (0.2 mol % *n*-butane) and a mixture of 71.2% *trans*-2-butene and 28.8% *cis*-2-butenes were used. Distilled water, used for generation of reaction steam, was degassed and freed of carbon dioxide prior to use. Runs were normally carried out for 1–3 hr as required (depending on feed rate) to establish reliable material balance. Two gas samples were taken at about 25% and 75% into the run for analysis by mass spectroscopy (MS) and a third sample at midrun for analysis by gas chromatography (GC). Calculations of yield and conversions at conversions below 20% are based on GC, except for hydrogen yields, which are from MS. At greater conversions, data from MS are used except for determination of isomer distributions, which are determined by GC. Results of the duplicate MS determinations usually fell within the established limits of this analytical method, and the averaged values were then used. When, on occasion, the deviations were greater, the particular experiment was repeated until good agreement was obtained.

The mass spectrometer used for these studies was a Type 21-103-C (Consolidated Electrodynamics Corp.) operated with a 250°C Isotron and 70-V ionization potential. Results were derived by using a computerized matrix developed for pyrolysis product gas mixtures.

A F&M Model 609 gas chromatograph with flame ionization detector was used. A 40-ft, 1/8 in. o.d. stainless steel column packed with 20 wt % dimethylsulfolane on 40–60 mesh Chromasorb W was followed by a 6-in. column packed with 10 wt % squalene on the same support. Analysis was carried out at ambient temperature, using helium carrier gas flowing at 25 mL/min.

Data and Discussion

Experiments were carried out between 720° and 985°C with 1-butene and between 760° and 925°C with the mixed isomers of 2-butene, using steam dilution corresponding to a steam:hydrocarbon weight ratio of between 0.17 and 1.2 g/g. All runs were isobaric at total pressure of 1.0 psig. Material balances generally fell within $\pm 2\%$ for all of the experiments. Tables I and II summarize the individual run conditions, the observed yields and conversions, and the calculated rate constants for pyrolysis of 1-butene and the 2-butenes, respectively.

Over the range of conditions, 1-butene decomposes more rapidly than either of the 2-butene isomers. Double-bond shift and geometrical isomerization accompany the decomposition of the *n*-butenes; however, skeletal isomerization does not occur, as isobutene is not found among the products of the pyrolysis. Isomerization reactions apparently are kinetically controlled, as equilibrium distributions are not generally observed. Trans:cis ratios in the products do not correspond to equilibrium at either the maximum or the average reactor temperatures, and in some cases the ratio falls below equilibrium values based on American Petroleum Institute (API) data (14). However, none of these data exceed the equilibrium values based on more recent thermodynamic data (15).

Butadiene, propylene, and methane are major products as well as initial products in the decomposition of both 1- and 2-butene. Ethylene is not an initial product for 2-butene but does become a major product at high conversion levels. For 1-butene, ethylene becomes the most prominent product at high conversions. Hydrogen yield behavior is also different for the butene isomers. It is an initial product only in decomposition of 2-butene and its yield is largely independent of conversion level. For 1-butene decomposition, the hydrogen yield becomes significant only at high conversions.

Decomposition of 1-butene is more complex than that for the 2-butene isomers. Double-bond migration is rapid at the lower end of the temperature range of these experiments and becomes a minor reaction path as the temperature increases. At all temperatures and conversions, products heavier than the feed are produced; these make only a minor contribution to the products from the 2-butenes. While some carbon is formed under all of the experimental conditions, significant amounts are not observed below about 50% conversion with either of the isomers.

Earlier workers have identified some of the products of 1-butene pyrolysis (3, 4). In this work, several previously unreported products were found along with many of those previously noted. Acetylene was observed among the products from 1-butene as well as 2-butene in yields that paralleled the formation of ethylene. Yields varied from a trace at low temperatures to between 5%–10% of the total C₂ product at the highest temperatures. Methylacetylene + propadiene (MAP) yield varied in a similar manner for 1-butene pyrolysis ranging between 2% and 20% of the C₃ product. In 2-butene pyrolysis, the MAP yield comprised approximately 10% of the C₃ product in all of the runs.

Hydrogen becomes a significant product only at high conversion of 1-butene, but its yield ranges between 20 and 25 mol per 100 mol of 2-butene cracked over the entire range of conversions. This observation is in contrast to the work of Jeffers and Bauer (5), who, although they were not able to determine hydrogen by their analytical method, concluded that it was not a significant product for the pyrolysis of the 2-butenes in their shock tube.

Tabulations of yields of all identified products from runs in the 80-wt % conversion range are given in Tables III and IV for 1-butene and mixed 2-butene pyrolysis, respectively. These product distributions are typical of those observed in all of the high conversion runs.

Product Distribution

Dependence on Experimental Variables. Correlation of product yields (wt %) against conversion of 1-butene and of the mixed-2-butenes are shown in Figures 1 and 2, respectively. Yields of major products are determined largely by the conversion level and are substantially independent of the temperature and contact time required to attain the observed conversion.

For both feeds, propylene and butadiene are the major products obtained. The order of their production, however, appears to depend on the structure of the feed olefin. Thus, butadiene is the single, most prevalent product from the 2-butenes while propylene is predominant from 1-butene. A similar reversal in relative yield can be noted for the C₁/C₂ products. Over the entire conversion range, the combined yields of butadiene and ethylene are approximately equal to the combined yields of propylene and methane for both starting olefins.

At high conversions, initial products undergo secondary decomposition. This is most noticeable for 1-butene data, where very high conversions were examined. Thus the yields of C₃ products (mainly propylene), butadienes, and the C₅ products pass through a broad maximum in the region of 80%–90% conversion.

Table I. Run Condition and Major Product

| Run No. | T_{Max} ($^{\circ}C$) | H_2O/C_4H_8 (g/g) | V/F ^a (sec) | Press. C_4H_8 Inlet (atm) | Conversion $\Delta P/P_0$ (%) | Moles Product per 100 Moles Converted | | | |
|---------|---------------------------|---------------------|------------------------|-----------------------------|-------------------------------|---------------------------------------|--------|---------|---------|
| | | | | | | H_2 | CH_4 | $C_2's$ | $C_3's$ |
| 1 | 871 | 0.524 | 0.137 | 0.380 | 95.8 | 33.5 | 55.2 | 46.0 | 28.7 |
| 2 | 872 | 0.506 | 0.052 | 0.388 | 82.6 | 13.7 | 41.3 | 39.1 | 34.0 |
| 3 | 927 | 0.510 | 0.134 | 0.387 | 99.6 | 27.3 | 62.7 | 57.0 | 18.4 |
| 4 | 926 | 0.520 | 0.050 | 0.382 | 97.7 | 24.1 | 58.9 | 51.8 | 25.8 |
| 5 | 986 | 0.524 | 0.043 | 0.381 | 99.7 | 32.6 | 63.4 | 60.2 | 15.3 |
| 6 | 760 | 0.491 | 0.071 | 0.395 | 23.8 | 6.9 | 31.7 | 16.0 | 40.1 |
| 7 | 760 | 0.524 | 0.143 | 0.380 | 39.5 | 7.1 | 32.1 | 27.9 | 34.8 |
| 8 | 817 | 0.498 | 0.070 | 0.390 | 63.0 | 11.4 | 41.0 | 30.6 | 40.1 |
| 9 | 819 | 0.508 | 0.141 | 0.387 | 78.3 | 13.9 | 48.4 | 37.4 | 38.1 |
| 10 | 760.5 | 0.495 | 0.050 | 0.394 | 17.3 | 6.5 | 30.5 | 12.2 | 33.0 |
| 11 | 818 | 0.489 | 0.048 | 0.397 | 49.2 | 9.9 | 36.7 | 27.3 | 38.2 |
| 12 | 871 | 0.489 | 0.047 | 0.397 | 78.1 | 14.5 | 43.8 | 38.7 | 35.5 |
| 13 | 731 | 0.586 | 0.037 | 0.378 | 7.9 | 6.0 | 26.1 | 6.5 | 33.5 |
| 14 | 722 | 0.595 | 0.090 | 0.374 | 13.2 | 7.2 | 23.5 | 7.8 | 28.9 |
| 15 | 754 | 0.508 | 0.029 | 0.414 | 9.7 | 5.6 | 26.8 | 5.0 | 34.3 |
| 16 | 758 | 0.171 | 0.162 | 0.696 | 40.1 | 6.2 | 29.0 | 25.1 | 34.8 |
| 17 | 767 | 0.656 | 0.158 | 0.351 | 47.1 | 6.4 | 28.8 | 27.5 | 34.1 |
| 18 | 757 | 1.24 | 0.180 | 0.220 | 38.3 | 6.4 | 27.3 | 27.0 | 34.8 |

^a Based on reactor volume at temperatures above 600°C and average of inlet and outlet flow rates.

Table II. Run Conditions and Major Product

| Run No. | T_{Max} ($^{\circ}C$) | V/F ^b (sec) | H_2O/C_4H_8 (g/g) | Inlet 2-Butene Partial Press. (atm) | Conversion $\Delta P/P$ (%) | Moles Product/100 Moles Converted | | | |
|---------|---------------------------|------------------------|---------------------|-------------------------------------|-----------------------------|-----------------------------------|--------|---------|---------|
| | | | | | | H_2 | CH_4 | $C_2's$ | $C_3's$ |
| 1 | 761 | 0.066 | 0.509 | 0.387 | 4.16 | 20.8 | 46.8 | — | 39.3 |
| 2 | 766 | 0.147 | 0.494 | 0.394 | 10.8 | 18.6 | 43.1 | 6.4 | 40.2 |
| 3 | 817 | 0.072 | 0.487 | 0.398 | 19.2 | 17.1 | 42.5 | 6.6 | 42.2 |
| 4 | 818 | 0.133 | 0.509 | 0.387 | 37.2 | 18.5 | 46.0 | 10.1 | 41.6 |
| 5 | 871 | 0.050 | 0.489 | 0.397 | 47.1 | 19.8 | 43.8 | 12.3 | 41.1 |
| 6 | 871 | 0.095 | 0.489 | 0.397 | 67.9 | 21.2 | 51.7 | 19.7 | 39.5 |
| 7 | 925 | 0.043 | 0.499 | 0.392 | 85.0 | 25.5 | 52.1 | 29.6 | 36.4 |
| 8 | 759 | 0.067 | 0.555 | 0.367 | 3.63 | 17.2 | 44.9 | 1.4 | 38.3 |
| 9 | 760 | 0.127 | 0.537 | 0.374 | 8.28 | 18.0 | 43.3 | 3.5 | 36.8 |

^a 71.2% *trans*-, 28.8% *cis*-2-butene.

^b Based on reactor volume at temperatures above 600°C and average of inlet and outlet flow rates.

Yields; Steam Pyrolysis of 1-Butene

| <i>Moles Product per 100 Moles Converted</i> | | | | <i>Car- bon^b (wt %)</i> | <i>Trans: Cis</i> | <i>k_s (atm⁻¹ sec⁻¹)</i> | <i>H. C. Bal (wt %)</i> | <i>H₂O Bal (wt %)</i> |
|--|------------------|------------------------|------------------------|--|-----------------------|--|---------------------------------|--|
| <i>C₄H₆</i> | <i>2-Butenes</i> | <i>C₃'s</i> | <i>C₂'s</i> | | | | | |
| 16.2 | 2.7 | 4.1 | 6.0 | 7.0 | 1.35 | 365 | 103.0 | 100 |
| 23.1 | 4.0 | 5.8 | 8.2 | 2.4 | 1.50 | 235 | 97.3 | 98.9 |
| 9.5 | — | 3.2 | 13.8 | 6.2 | — | 2390 | 100.5 | 97.7 |
| 14.6 | 1.0 | 4.0 | 7.7 | 7.1 | 1.67 | 2220 | 99.2 | 99.9 |
| 7.7 | — | 2.8 | 16.3 | 6.2 | — | 8680 | 98.5 | 100.9 |
| 26.7 | 13.4 | 8.0 | 1.1 | 2.0 | 1.60 | 11.2 | 99.0 | 101.7 |
| 27.0 | 9.2 | 10.6 | 0.7 | 1.2 | — | 12.1 | 101.6 | 99.4 |
| 26.2 | 6.0 | 8.5 | 1.0 | 1.3 | — | 62.0 | 98.3 | 103 |
| 21.7 | 2.0 | 6.0 | 1.4 | 5.6 | — | 66.2 | 97.1 | 102 |
| 27.8 | 16.6 | 12.4 | 1.7 | 0.0 | 2.00 | 10.6 | 100.1 | 99.0 |
| 27.7 | 5.8 | 9.9 | 1.4 | 0.9 | 1.78 | 50.8 | 96.1 | 101.8 |
| 24.3 | 4.3 | 6.6 | 2.3 | 3.0 | 1.40 | 192 | 98.1 | 102.8 |
| 23.9 | 18.1 | 15.2 | 1.5 | 0.0 | 1.75 | 8.80 | 98.2 | 100.9 |
| 25.4 | 22.5 | 14.7 | 0.4 | 0.8 | 1.32 | 5.55 | 101.2 | 98.0 |
| 24.9 | 17.2 | 12.1 | 0.6 | 0.0 | 1.73 | 8.80 | 99.9 | 99.7 |
| 25.5 | 6.5 | 11.3 | 1.1 | 0.4 | 1.37 | 9.03 | 100.2 | 102 |
| 21.9 | 13.8 | 11.2 | 1.0 | 0.5 | 1.41 | 16.0 | 100 | 96.9 |
| 26.5 | 6.9 | 11.2 | 0.7 | 0.2 | 1.40 | 15.6 | 101.3 | 96.4 |

^b Calculated value basis C/H ratio of product.^c Calculated second order rate constants for disappearance of 1-butene.**Yields; Steam Pyrolysis of Mixed 2-Butenes^a**

| <i>Moles Product/100 Moles Converted</i> | | | | <i>Car- bon^c (wt %)</i> | <i>k₁ (sec⁻¹)^d</i> | <i>Trans/ Cis (Prod- ucts)</i> | <i>H. C. Bal- ance (wt %)</i> | <i>H₂O Bal- ance (wt %)</i> |
|--|-------------------------------------|------------------------|------------------------|--|---|--|---|--|
| <i>C₄H₆</i> | <i>i-C₄H₈</i> | <i>C₃'s</i> | <i>C₂'s</i> | | | | | |
| 55.0 | — | 3.1 | — | 0.05 | 0.65 | — | 97.9 | 99.9 |
| 49.2 | 7.7 | 3.4 | 1.6 | 0.05 | 0.78 | 1.66 | 101.4 | 102.9 |
| 49.5 | 3.8 | 4.0 | 0.3 | 0.03 | 2.97 | 1.58 | 101.7 | 96.7 |
| 45.6 | 5.1 | 4.4 | 0.7 | 0.15 | 3.50 | 1.32 | 103.7 | 96.1 |
| 45.6 | 5.0 | 4.2 | 0.7 | 0.79 | 12.8 | 1.26 | 99.4 | 100.7 |
| 39.4 | 4.3 | 4.6 | 1.5 | 2.4 | 12.0 | 1.23 | 102.0 | 99.9 |
| 34.4 | 2.5 | 4.8 | 2.2 | 4.2 | 44.1 | 1.39 | 98.0 | 106.0 |
| 56.2 | 7.0 | 2.5 | — | 0.02 | 0.55 | 1.89 | 100.0 | 104.6 |
| 51.6 | 8.0 | 4.3 | 1.7 | 0.05 | 0.68 | 1.71 | 100.9 | 103.2 |

^a Calculated value basis C:H ratio of products.^d Calculated first-order rate constant for disappearance of *cis*- and *trans*-2-butenes.

Table III. Typical Product Yields from Steam Pyrolysis of 1-Butene^a

| <i>Yield (wt % basis feed)</i> | | | |
|--------------------------------|------|----------------------------|-------------------|
| Hydrogen | 0.38 | <i>cis</i> -1,3-Pentadiene | 0.60 |
| Methane | 9.08 | 3-Methyl-1-butene | 0.50 |
| Acetylene | 0.81 | 1-Pentene | 0.44 |
| Ethylene | 12.5 | 2-Methyl-1-butene | 0.78 |
| Ethane | 0.6 | <i>trans</i> -2-Pentene | 0.56 |
| Propadiene | 0.84 | <i>cis</i> -2-Pentene | 0.16 |
| Methylacetylene | 0.20 | <i>n</i> -Pentane | 0.15 |
| Propylene | 18.1 | C ₆ olefins | 0.33 ^b |
| Propane | 0.1 | C ₆ paraffins | 0.05 |
| 1,3-Butadiene | 17.0 | Benzene | 2.62 |
| 1-Butene (feed) | 22.3 | Toluene | 0.68 |
| <i>trans</i> -2-Butene | 1.32 | Ethylbenzene | 0.10 |
| <i>cis</i> -2-Butene | 0.95 | <i>p</i> -Xylene | 0.01 |
| <i>n</i> -Butane | 0.1 | <i>m</i> -Xylene | 0.03 |
| Cyclopentadiene | 1.56 | <i>o</i> -Xylene | 0.02 |
| Isoprene | 0.36 | Styrene | 0.22 |
| Cyclopentene | 0.30 | C ₉ & heavier | 0.25 ^b |
| <i>trans</i> -1,3-Pentadiene | 1.06 | Carbon | 3.04 ^c |

^a 871°C; 78.7 wt % conversion.

^b Isomers not identified.

^c Calculated from H/C balance.

Table IV. Typical Product Yields from Steam Pyrolysis of Mixed 2-Butenes^a

| <i>Yield (wt % basis feed)</i> | | | |
|--------------------------------|-------|------------------------------|------|
| Hydrogen | 0.75 | <i>cis</i> -2-Butene | 7.2 |
| Methane | 12.2 | Cyclopentadiene ^b | 1.6 |
| Acetylene | 1.47 | Cyclopentene | 0.27 |
| Ethylene | 9.78 | 1,3-Pentadiene ^b | 1.00 |
| Methylacetylene | 1.36 | Isoprene | 0.50 |
| Propadiene | 1.16 | 1-Pentene | 0.20 |
| Propylene | 18.3 | 2-Pentene ^b | 0.17 |
| Propane | trace | Benzene | 2.30 |
| 1,3-Butadiene | 24.4 | Toluene | 0.23 |
| 1-Butene | 1.18 | Carbon ^c | 4.23 |
| <i>trans</i> -2-Butene | 10.0 | | |

^a 925°C; 82.8 wt % conversion.

^b Isomers not identified.

^c Calculated from H/C balance.

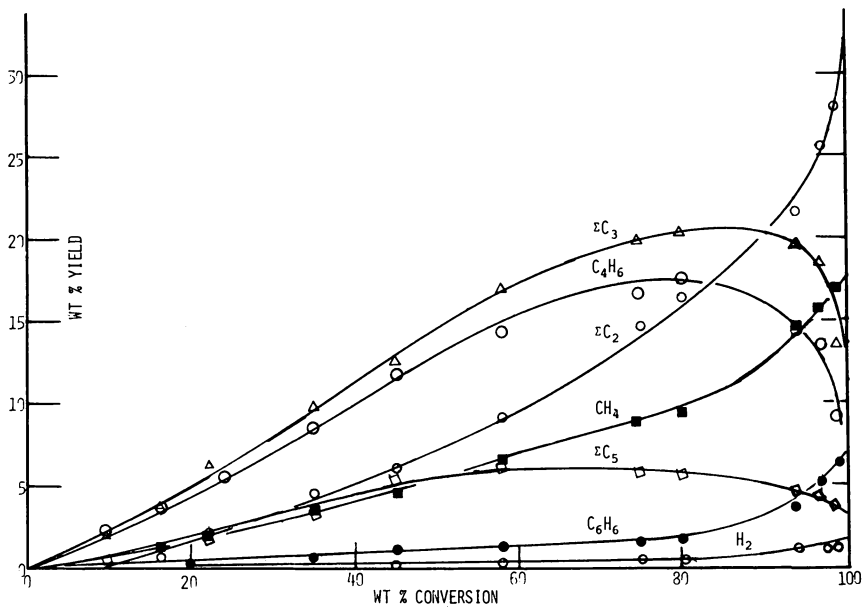


Figure 1. Product distribution for 1-butene pyrolysis

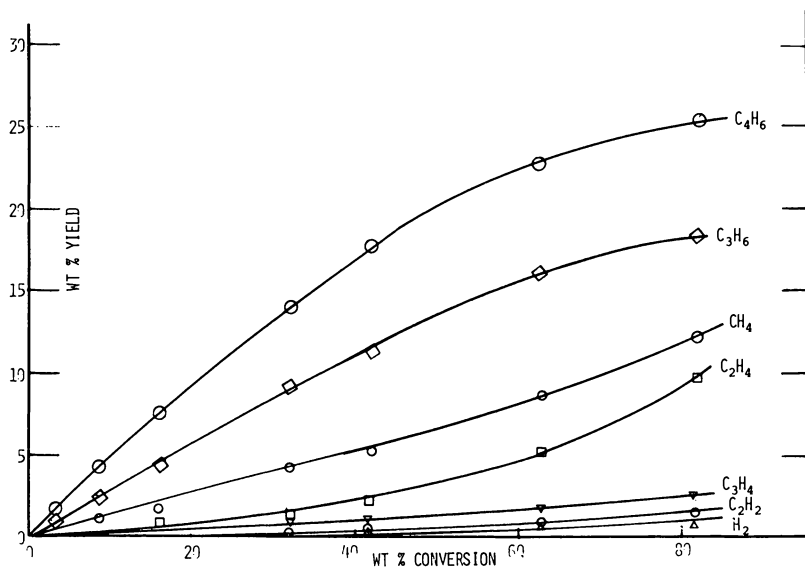


Figure 2. Product distribution for 2-butene pyrolysis

Significant yields of products heavier than the starting olefin are observed only for 1-butene. Traces of C_5^+ are observed from 2-butenes at the highest conversion levels. While the total yields of the C_5 products correlate satisfactorily with feed conversion, distribution of the components within this fraction is strongly influenced by both temperature and contact time in a manner that suggests that the initially formed C_5 products undergo sequential dehydrogenation reactions.

Primary Products

Primary products of a complex reaction can be inferred from zero conversion extrapolation of selectivity diagrams, as first described by Schneider and Frolich (16). According to this method, the molar selectivity of each product (mol product formed per 100 mol of reactant decomposed) is plotted against the percent conversion. The validity of this method has been seriously questioned (17). In principle, this method suffers from the fact that at the very low conversions required for reliable extrapolation to zero conversion, data on yields of individual products are subject to substantial analytical uncertainty. Consequently, the calculated conversion is subject to the summation of all of the errors in the yields of all of the products, and the calculated selectivities are increasingly unreliable as the conversion decreases. However, because of the vastly improved accuracy available through the use of modern analytical techniques, the criticism of the use of this method is far less valid, and significant insight into initial product distribution can be derived.

Figure 3 shows the selectivity diagram for the major products from 1-butene pyrolysis. This shows that molecular hydrogen is not an initial product of decomposition. Initial products appear to be (in mol/100 mol): butadiene, 25; methane, 30; ethylene, 15; propylene, 40; C_5 products, 10; and isomerization products as *cis*- and *trans*-2-butene, 25.

A selectivity diagram for 2-butene decomposition (Figure 4) shows that the initial products include (in mol/100 mol): butadiene, 50; methane, 40; propylene + MAP, 40; and hydrogen, 20. In contrast to decomposition of 1-butene, ethylene is not an initial product from 2-butene decomposition.

Further insight into the reaction mechanism can be obtained from consideration of the conversion dependence of product ratios. These can provide more reliable information than normal selectivity plots since, although these ratios are subject to the uncertainties in the individual product yields, their accuracy is not affected by the larger uncertainty in the calculated conversion levels. Moreover, the variation in product yield ratios with conversion can provide a clearer insight into the course of secondary reactions.

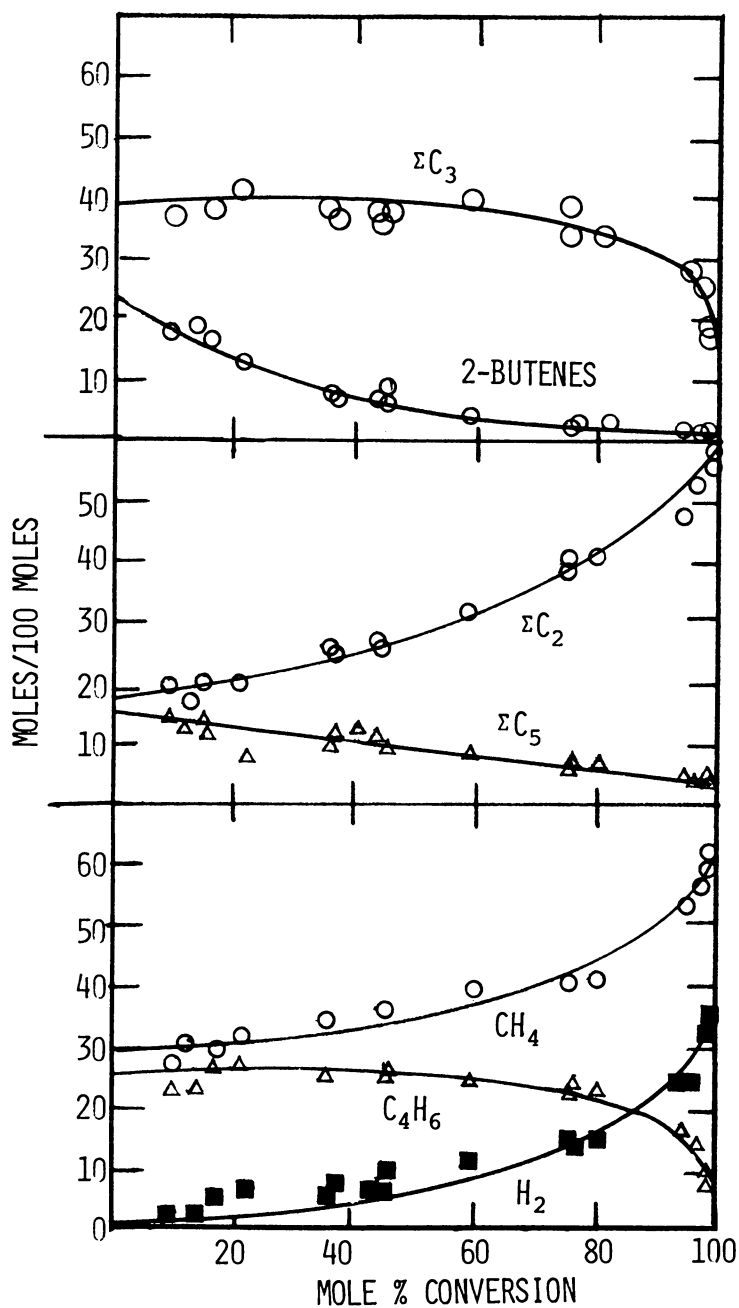


Figure 3. Selectivity diagrams for 1-butene pyrolysis

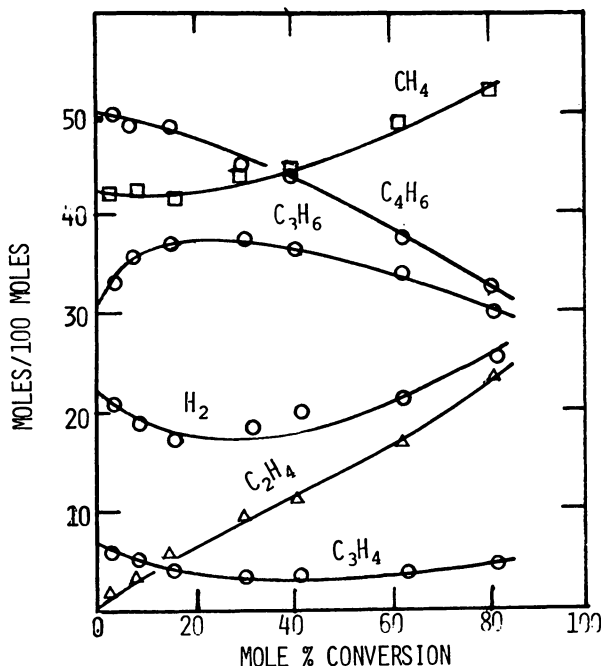
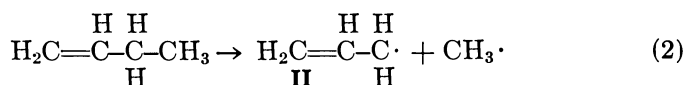
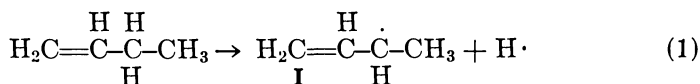


Figure 4. Selectivity plot for 2-butenes pyrolysis

Figure 5 shows in the decomposition of 1-butene that butadiene, methane, and C₃ products (C₃H₄ + C₃H₆) are produced in essentially equal amounts at low conversion. A decrease in the CH₄:C₃H₆ ratio parallels the formation of C₅ products. As conversion increases, the C₅ products decompose to C₂ and C₃ products, and finally at the higher conversions all products appear to decompose to methane and ethylene.

A free-radical reaction scheme to account for these observations must include at least two primary reaction paths (*see* Reactions 1 and 2).



Each of these reactions involve the initial cleavage of a bond that is alpha to the olefinic unsaturation and produces an allylic radical. Although the energy requirement for cleavage of a C-H bond (Reaction 1) is slightly greater than that for a C-C bond (Reaction 2), both

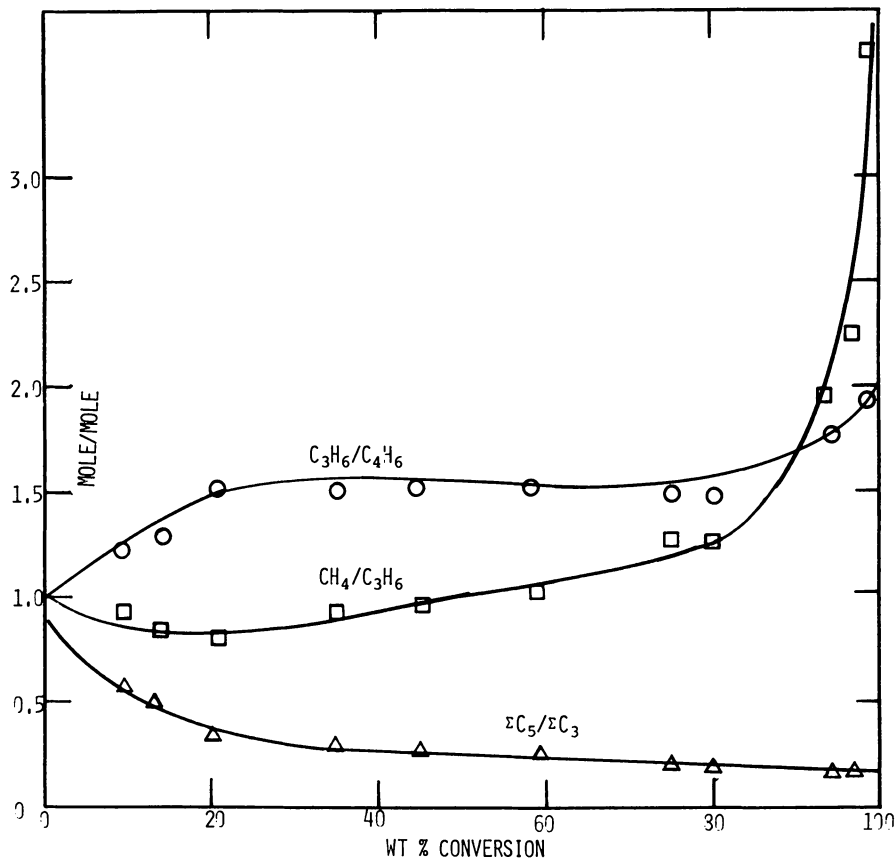
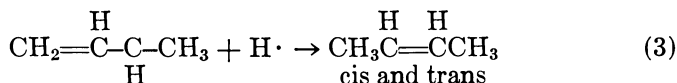
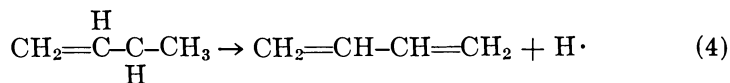


Figure 5. Variation of some product ratios with 1-butene conversion

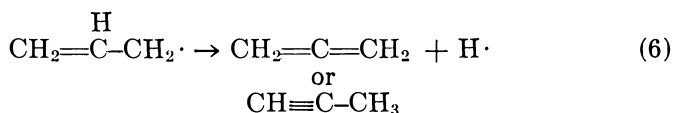
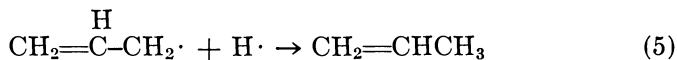
reaction paths appear to have similar probabilities in the temperature range of our investigation. Consequently, the energy difference of the C-H and C-C bonds appears to be largely compensated by the more favorable statistical factor (two C-H bonds vs. one C-C bond) associated with Reaction 1.

The methyl allyl radical (I) can decompose by either addition of a hydrogen atom to give 2-butene isomers or by loss of a hydrogen atom (abstraction by another radical) to give butadiene (*see* Reactions 3 and 4). Reaction 3 would be favored at lower temperatures, while Reaction 4 would predominate at higher temperatures. This is supported

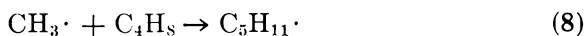
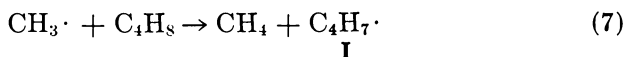




by the experimental data recognizing that the low conversion data are also those obtained at the lowest temperatures examined. The allyl radical (II) can decompose along similar lines to give allene (or methylacetylene) and propylene (*see* Reactions 5 and 6).

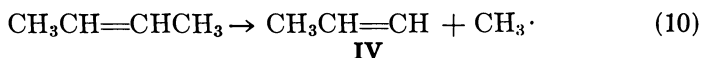
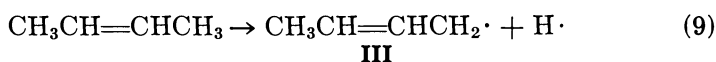


The methyl radical produced in primary Reaction 2 can abstract a hydrogen atom from an unreacted butene molecule in a chain propagation step or it can add to a butene molecule to provide a pentyl radical, which is the precursor for the observed C₅ products (*see* Reactions 7 and 8). Methyl radical addition (Reaction 8) is favored at low conversion



levels where the 1-butene concentration is large and also at low temperatures since the activation energy for methyl radical addition to 1-butene is 3–6 kcal/mol lower than that for hydrogen abstraction (18). At higher temperatures, the pentenyl radical becomes increasingly unstable and decomposes to C₂ and C₃ products.

Two primary reaction steps also must be considered to account for the decomposition of 2-butene (*see* Reactions 9 and 10). In this case, however, Reaction 9 is clearly the predominant reaction path at the lower end of the temperature range since the dissociation of a vinylic C–C



bond (Reaction 10) requires 10 kcal/mol more energy than is required for the rupture of an allylic C–H bond (Reaction 9) (19). The observed decreased selectivity to propylene at low (temperatures) conversions of 2-butene and the observation that C₃H₄(MAP) is an initial product are in agreement with these requirements.

Since the 1-but-2-enyl radical (III) can be an intermediate to geometrical isomerization, this reaction path will play a major role in the low temperature region. It has been reported that the rate of isomerization of *cis*- or *trans*-2-butene exceeds the rate of cracking (5). An alternate path for decomposition of the radical III is by loss of a hydrogen atom to give butadiene as a product.

The methylvinyl radical (IV) can abstract a hydrogen atom from a feed or product molecule to form propylene or it can lose a hydrogen atom to form allene or propadiene as products. For the 2-butenes, steric factors inhibit methyl radical addition; thus C₅ products are formed to a far lesser extent than from 1-butene. While ethylene may be formed by a sequential decomposition of propylene, this cannot be the only path for its formation, as the yield of ethylene in the high conversion region increases about twice as rapidly as does the methane yield. An additional source of ethylene is the symmetrical cleavage of butadiene to vinyl radicals.

In the foregoing reaction schemes, only the formation of the observed initial products has been considered. Coke as well as aromatics also are observed as minor products (particularly for 1-butene) at high conversion levels. A multitude of reaction sequences can be considered and, indeed, several have been proposed (4, 11). However, further mechanistic considerations are not warranted for the limited data that are available.

Kinetics

Evaluation of Rate Constants. Reaction rate constants were evaluated by using the integrated form of the first-order rate law:

$$\ln \frac{p}{p_0} = k_1(V/F)$$

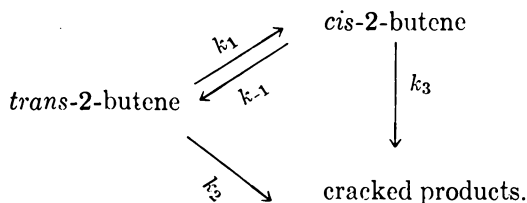
where, V/F is the nominal contact time based on reactor volume at temperatures above 600°C and F is the mean flow rate through the reactor. The calculated first-order rate constants for the mixture of 2-butenes were found to be constant with conversion at each temperature, indicating that 2-butene pyrolysis can be described adequately by a first-order rate law in agreement with published data (11, 13).

For 1-butene pyrolysis, the calculated first-order rate constants decreased significantly with increasing conversion at each temperature. Reduction of the data by using the integrated form of the second-order rate law provided specific rate constants that were satisfactorily independent of conversion.

$$\frac{1}{p} - \frac{1}{p_0} = kt$$

where p = partial pressure of 1-butene in atmospheres. Such deviation from first-order kinetics has been previously reported for pyrolysis of 1-butene (8,9). Reaction order at the high pressure limit is unity, and the reaction becomes second-order at low pressures. Extrapolation of observed first-order rate constants to zero conversion can provide an approximation to the limiting high pressure rate constants. This approach was not considered to be justified for the present investigation since the conditions studied are those of potential industrial practice (i.e., high conversions), and therefore only the actual kinetic behavior should be considered. In the range of present interest, the decomposition of 1-butene is best represented by a second-order rate law; the reaction is in the "fall off" region of unimolecular kinetics at the experimental pressures.

The pyrolysis of the 2-butenes was studied by using a mixture of the *trans* and *cis* isomers that was far from the equilibrium composition at reaction temperatures. The rate of disappearance of 2-butenes comprises the summation of the rates of disappearance of the individual isomers, and each isomer decomposes by cracking and also by conversion to the other isomer. Thus, the rate of disappearance of *trans*-2-butene in the mixture is a composite of the rate of cracking and of isomerization, viz:



In the low temperature region (low conversions in the present study), the rate of isomerization is a significant part of the overall rate of disappearance of *trans*-2-butene. Consequently, although *cis*-2-butene is undergoing cracking, the overall result is a net formation of the *cis* isomer. Figure 6 illustrates this observation as a plot of the fraction of

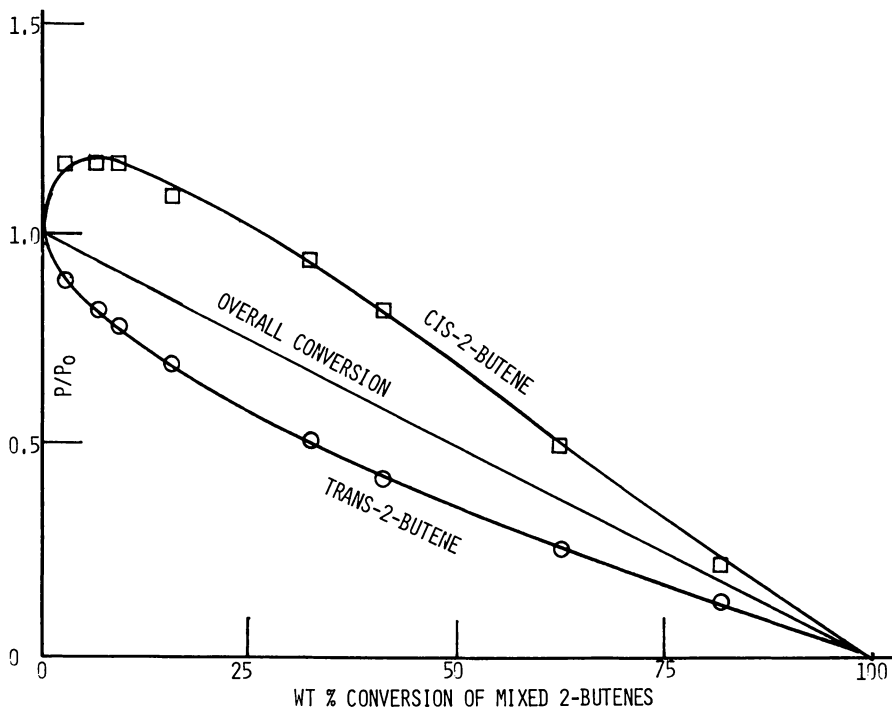


Figure 6. Fraction of isomers remaining vs. 2-butenes conversion

each isomer remaining as a function of disappearance (conversion) of total 2-butenes. It is evident that up to the first 25% of overall conversion there is no apparent net conversion of *cis*-2-butenes; there is a net production. Thus the data of this investigation do not lend themselves to a separate determination of the kinetics of thermal decomposition of the individual isomers of 2-butenes. Literature data indicate that the rates of pyrolysis of *cis*- and *trans*-2-butenes differ only slightly with a difference in activation energy of the order of 1–2 kcal/mol (13). Relevant calculated rate constants are summarized in Tables I and II.

Activation Energies

Figures 7 and 8 show the Arrhenius plots for pyrolysis of 1-butene and 2-butene, respectively. An apparent activation energy of 57.2 kcal/mol is indicated for 1-butene pyrolysis. This compares favorably with values reported by Kerr, Spencer, and Trotman-Dickenson (8) and by Shibatani (3) but differs from those reported by Molera and Stubbs (13), by Kunugi (12), by Sehon and Swarc (10), and by Bryce and Kebarle

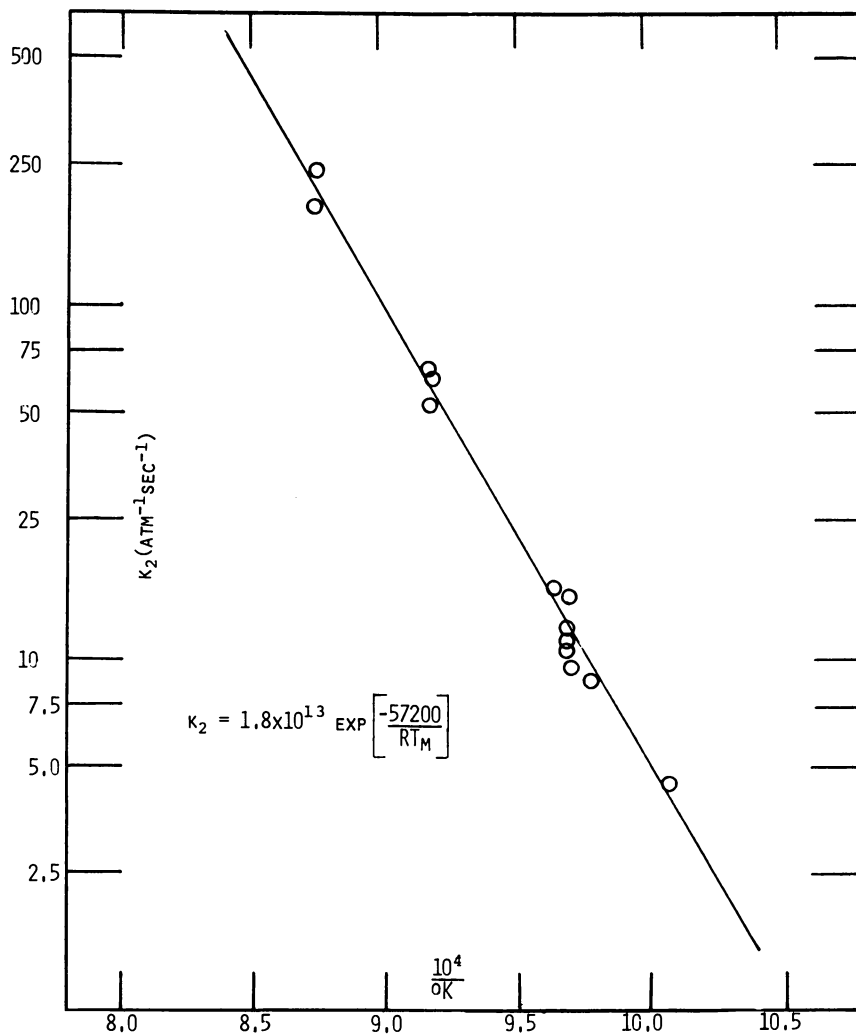


Figure 7. Temperature dependence of the rate for 1-butene pyrolysis

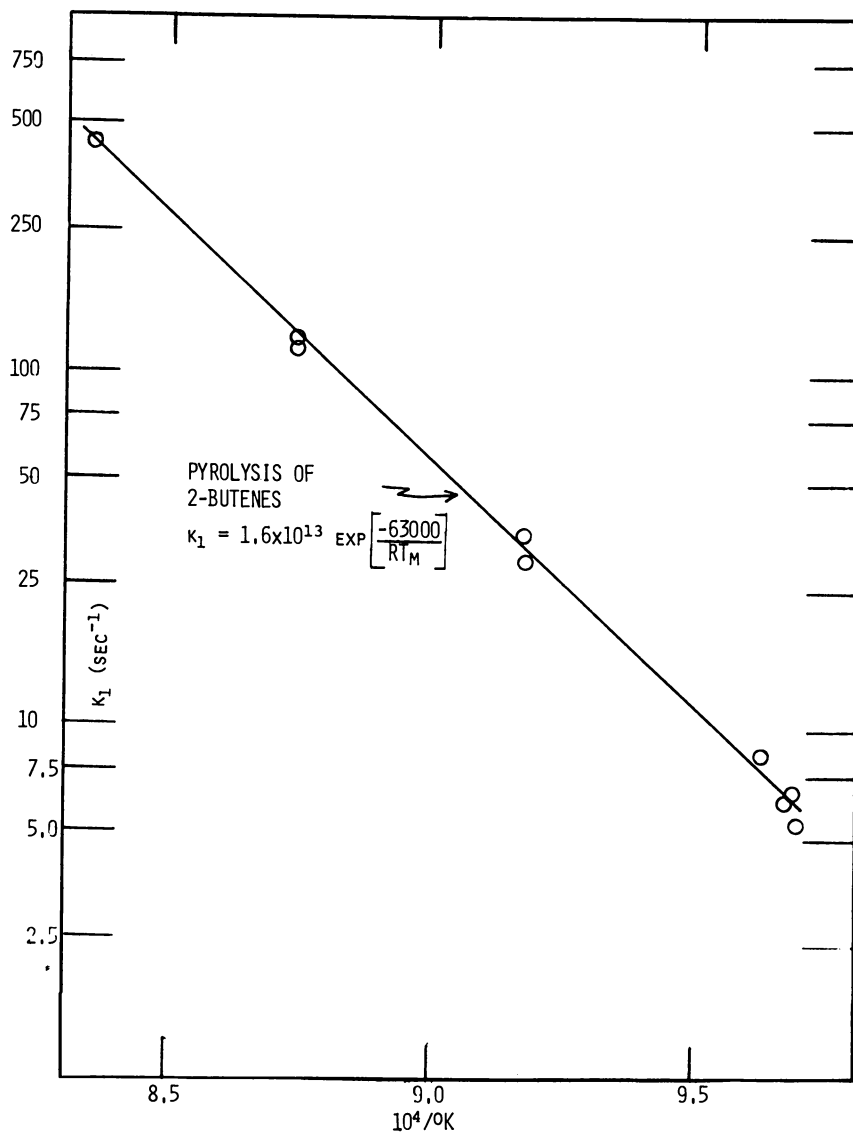


Figure 8. Temperature dependence of the rate of conversion of 2-butenes

(4). Based on these data, the pyrolysis of 1-butene over the range of conditions studied can be described by:

$$k (\text{atm}^{-1} \text{sec}^{-1}) = 1.8 \times 10^{13} \exp \left[\frac{-57,200}{RT_m} \right]$$

The activation energy for thermal cracking of 2-butenes is found to be 63.3 kcal/mol. This agrees favorably with that reported by Powers and Corcoran (11) but differs from that reported by Molera and Stubbs (13) and by Jeffers and Bauer (5). The rate of thermal cracking of 2-butenes can be described by:

$$k (\text{sec}^{-1}) = 1.6 \times 10^{13} \exp \left[\frac{-63,300}{RT_m} \right]$$

Acknowledgment

The author acknowledges the valuable assistance of Antonio Cortes and Albert Loguidice in obtaining the experimental data.

Literature Cited

1. Leftin, H. P.; Cortes, A. *Ind. Eng. Chem., Proc. Des. Dev.* **1972**, *11*, 613.
2. Leftin, H. P.; Newsome, D. S.; Wolff, T. J.; Yarze, J. C. In "Industrial and Laboratory Pyrolyses," *ACS Symp. Ser.* **1976**, *32*, 373.
3. Shibatani, H.; Kinoshita, H. *Nippon Kagaku Kaishi* **1973**, 1005.
4. Bryce, W. A.; Kebarle, P. *Trans. Faraday Soc.* **1958**, *54*, 1660.
5. Jeffers, P. J.; Bauer, S. H. *Int. J. Chem. Kinet.* **1974**, *VI*, 771.
6. Hurd, C. D.; Goldsby, A. R. *J. Am. Chem. Soc.* **1934**, *56*, 1812.
7. Richard, D.; Martin, R. *J. Chim. Phys.* **1976**, *73*, 745.
8. Kerr, J. A.; Spencer, R.; Trotman-Dickenson, A. F. *J. Chem. Soc.* **1965**, 6652.
9. Trenwith, A. B. *Trans. Faraday Soc.* **1970**, *66*, 2805.
10. Sehon, A. H.; Szwarc, M. *Proc. R. Soc. London, Ser. A* **1950**, *202*, 263.
11. Powers, D. R.; Corcoran, W. H. In "Industrial and Laboratory Pyrolyses", *ACS Symp. Ser.* **1976**, *32*, 117.
12. Kunugi, T.; Tominaga, H.; Abiko, S.; Uehara, K.; Ohno, T. *Kogyo Kagaku Zasshi*, **1967**, 1477.
13. Molera, M. J.; Stubbs, F. *J. Chem. Soc.* **1952**, 381.
14. American Petroleum Institute; "Selected Values of Physical and Thermodynamic Properties of Hydrocarbons and Related Compounds"; Carnegie Press: Pittsburgh, 1953.
15. Meyer, E. F.; Stroz, D. G. *J. Am. Chem. Soc.* **1972**, *94*, 6344.
16. Schneider, J.; Frolich, P. K. *Ind. Eng. Chem.* **1931**, *23*, 1405.
17. Hurd, C. D.; Eilers, L. K. *Ind. Eng. Chem.* **1934**, *26*, 776.
18. Lossing, F. P.; Henderson, I. H. S.; Farmer, J. B. *Can. J. Chem.* **1956**, *34*, 345.
19. Simons, J. W.; Rabinovitch, B. S.; Dorer, F. H. *J. Phys. Chem.* **1966**, *70*, 1976.

RECEIVED June 5, 1978.

Product Inhibition in the Pyrolysis of Paraffinic Hydrocarbons

H. G. DAVIS and K. D. WILLIAMSON

Union Carbide Corp., Chemicals and Plastics, P.O. Box 8361,
South Charleston, WV 25303

Results of pyrolysis of propane, n-butane, and n-hexane at a wide range of temperatures and conversions, including the range of commercial operation, are presented. Extensive product inhibition is evident in all cases. The rates of decomposition can be characterized by two pseudo energies of activation: E, calculated by comparing data at constant decomposition, variable time and temperature, and E' (always less than E) at constant time, variable decomposition and temperature. Both E and E' are relatively constant over the conversion range studied. Near atmospheric pressure data fit the equation: $X = \exp \{-a_0 [1 + 1.3 (N_c - 2)] t^{1/r} \cdot -E'/RT\}$ where X = fraction feed paraffin undecomposed, N_c = carbon number of feed paraffin, $r = E/E' = 1.68$, t = reaction time (seconds), T = reaction temperature (K), $a_0 = 2.85 \cdot 10^9$ (from propane data) or $2.66 \cdot 10^9$ (better to n-butane and n-hexane data), and $E' = 46.0$ kcal/mol.

The literature on pyrolysis of paraffin hydrocarbons is extensive. A recent review (1) of propane pyrolysis lists 103 references covering a period from 1928 to 1976. The study indicates a remarkable lack of quantitative agreement on energies of activation and on the effect of product inhibition on rate of decomposition. Energies of activation, from reputable experimental efforts, cover a range from 40 to 80 kcal/mol.

The qualitative features of paraffin pyrolysis, on the other hand, are reasonably well understood. The decomposition is, in general, initiated by rupture of C-C bonds, carried by chains of hydrogen atoms, methyl radicals, and to some extent ethyl radicals, and terminated by assorted radical recombinations. Product inhibition occurs through the reaction

of these chain carriers with product species to form less reactive radicals. For example, reaction of hydrogen atom with propylene results in formation of the less reactive propyl, methyl, and allyl radicals. Propylene, along with nitric oxide, is the standard classical inhibitor of these free radical reactions. However, ethylene and other olefin, diolefin, and aromatic products are also inhibitors.

The difficulty of attaching a single value of energy of activation to the decomposition of propane is related to the problem of product inhibition. This is pointed out in Ref. 1 and has been discussed previously by others, including one author of this chapter (2, 3).

The only experimental number which is properly referred to as the activation energy is that obtained from rate constants extrapolated to zero conversion. However, a reasonable approximation to this value can be obtained by comparing integral rate constants at constant conversion, variable temperature and residence time. Values of E_{act} so determined tend to be in the high range (65–80 kcal/mol).

If integral rate constants are compared at constant reaction time, variable temperature and conversion, a different, much lower value of E_{act} is calculated. This tends to be in the range of 40–50 kcal/mol. The low value results from the fact that product inhibition is an increasing function of conversion and therefore of temperature. At the highest experimental temperature the overall rate is most depressed from the zero time uninhibited rate. This low value of E_{act} has otherwise no particular theoretical significance. However, it may, under controlled conditions, be used for practical modeling (3).

In this chapter we propose to show that a practical and useful model of paraffin cracking can be obtained by combining these two experimentally definable activation energies in a fairly simple mathematical expression. Since E (constant conversion) approximates the zero conversion E_{act} , we call it simply, E . E (constant time) we term E' , and the model we term the double energy of activation, or EE' model.

As several workers have shown (for example, Ref. 6), it is possible to avoid any explicit rate expression for the overall decomposition of a paraffin. One defines all the larger number of free radical and molecular equations of significance, develops an appropriate computer program and adjusts, within credible limits, Arrhenius parameters of the various rate expressions to fit an available body of rate and yield data.

In principle, this form of modeling based directly on established or postulated mechanisms, appears to be the most desirable. With one recent apparent exception (The Spyro program described in Ref. 7, which appeared while this paper was in review, appears to meet the criteria of broad, reliable data base and applicability to both single feeds and mixtures.) the approach has generally left something to be desired:

(1) The rate and yield data available must be of truly excellent quality in the whole range of times and temperatures of interest.

(2) The number of adjustable parameters is great or, alternately, literature values of A_s and E_s must be used which are often only one order of magnitude accurate; these modeling exercises, while useful in a predictive mode, therefore leave much to be desired in demonstrating a mechanism.

(3) A model which fits excellently specific data for single feeds may not work at all well for mixtures (5).

A practical approach we have used in the past is to define a simple empirical model for the decomposition of feedstock (single or mixed feeds). Then yields, product gas composition, expansion on cracking, partial pressure, and so forth, are all calculated by using a back-up program which relates yields to decomposition or other internal measures of severity and to the other conditions of cracking (reaction time, average partial pressure).

The object of the present work is to show that the double activation energy or EE' model is a suitable approximation to the decomposition rate equation for propane, *n*-butane, and *n*-hexane and, by extension, other paraffins and isoparaffins. Ethane is a somewhat special case and is excluded for the present.

Experimental

The basic conversion rate data for the present study are from experiments on propane cracking made several years ago by one of the authors (K. D. Williamson). The conversion/time/temperature data have been published in graphical form (2). We believe these to be superior to any high-temperature cracking rate data available. The range of decompositions covered (0–80%) is extended by recourse to some older propane data available to us but not previously published. These latter data are of somewhat poorer quality. Previously unpublished data on *n*-butane and *n*-hexane conversion (0–99% decomposition) from the Williamson study are used to verify the model.

Feedstocks. Propane and *n*-butane, 99.9+ % (Matheson Co., E. Rutherford, NY), were used without further purification. Impurities included very small amounts of methane, ethane, isobutane, and traces of higher paraffins. *n*-Hexane (Phillips) was 99+ %.

Apparatus

The reactors for the basic propane and *n*-butane pyrolysis were of monolithic annular quartz construction (Type I reactor). The reaction space was kept virtually isothermal by a surrounding bath of Ottawa sand fluidized vigorously by a stream of nitrogen. Temperature profiles were measured by calibrated Pt–Rh couples in a central thermowell. A description of this type of reactor has been given elsewhere (6).

The older and less reliable high-conversion propane data were obtained in a small fluidized bed reactor (Type II) directly over coarse-sized Ottawa sand. Despite the presence of the sand, the surface:volume ratio in this reactor was not greatly different from that in the annular reactors. In any case, all quartz or sand surfaces were rapidly coated with carbon during the initiation of pyrolysis. Thus it is not believed that surface effects were significant to the experimental results.

A typical Type II reactor was 4½ in. high by 1 in. i.d. wound with platinum resistance wire and heavily insulated. Above 4½ inches, the reactor tapered into a 2-in. i.d. expanded head, but product samples were taken at the 4½-in. level by suction through a capillary tap. Temperature was controlled and vertical gradient measured by means of a central well containing a calibrated Pt-Rh couple. Except at very high thermal loadings, no significant radial gradient could be detected, and the vertical temperature, as measured, was flat from about ½ in. above the quartz frit used as a bottom diffuser plate. Several checks, such as determination of the H₂:C₂H₄:C₂H₆ equilibrium at about 850°C, indicated measured temperature approximated true temperature within about ±5°C or better. Sieved Ottawa sand (for example, 40–60 mesh) was used with the average particle size about at the free-fall velocity in the reactor. This ensured a vigorously-stirred, essentially turbulent fluid bed.

Material balances in the experiments in Type I reactors were excellent, typically 100.0% ± about 0.3%. There was no evidence of the relatively major carbon formation or the excess hydrogen formation which have characterized small metal-walled laboratory reactors (4, 5). With the Type II reactors, C₅⁺ yields were calculated to give 100% hydrogen and carbon atom balance.

Scope of Data

In the annular reactors, propane pyrolysis was studied at atmospheric pressure and at 775°, 800°, 825°, and 850°C, with reaction times of 0.005–0.113 sec and conversions from 10 to 82%. Percent conversion as a function of time and temperature is shown in Table I.

From simple plots of fraction unreacted vs. time (Figure 1), it was clear that this was an unusually self-consistent set of kinetic data. We therefore have taken it as the basis for our kinetic modeling and used additional data available to confirm and extend. Experiments in the same equipment also were carried out at 2 atm pressure, at 0.13 atm, and, with helium dilution, at 1 atm total pressure and about 0.13 atm initial partial pressure of propane. The effects of pressure and partial pressure observed are discussed briefly.

n-Butane and *n*-hexane also were cracked in the annular reactors. The range of conditions used with butane was particularly wide. Temperature was varied from 725° to 900°C, reaction time from 0.065 to 1.35 sec and butane conversion from 24 to 98%. The data are therefore very useful for validating and extending the proposed model. The *n*-hexane data are not extensive, but are of interest in checking the model.

Table I. Rate of Decomposition of Propane—Calculated and Observed Rates in Isothermal Annual Reactor at Atmospheric Pressure

| <i>T</i> (°C) | Fraction Unre- acted, <i>X</i> (Obs.) | Reaction Time (sec) | | | First-Order Integral Rate Constant (<i>k</i> , sec ⁻¹) | | |
|------------------|--|---------------------|---------|-----------|--|---------|-------|
| | | (Obs.) | (Calc.) | (Δ, msec) | (Obs.) | (Calc.) | (Δ%) |
| 775 | 0.9085 | 0.011 | 0.0086 | -2.4 | 8.72 | 11.16 | +27.9 |
| | 0.8510 | 0.020 | 0.0201 | +0.1 | 8.07 | 8.03 | -0.5 |
| | 0.7576 | 0.049 | 0.0484 | -0.6 | 5.67 | 5.74 | +1.3 |
| | 0.6281 | 0.113 | 0.1119 | -1.1 | 4.12 | 4.16 | +1.0 |
| 800 | 0.8492 | 0.008 | 0.0091 | +1.1 | 20.43 | 17.97 | -12.0 |
| | 0.7707 | 0.018 | 0.0193 | +1.3 | 14.47 | 13.50 | -6.7 |
| | 0.6405 | 0.044 | 0.0461 | +2.1 | 10.13 | 9.66 | -4.6 |
| | 0.5057 | 0.095 | 0.0920 | -3.0 | 7.18 | 7.41 | +3.2 |
| 825 | 0.8059 | 0.006 | 0.0065 | +0.5 | 36.0 | 33.2 | -7.7 |
| | 0.7521 | 0.009 | 0.0102 | +1.2 | 31.7 | 27.9 | -12.0 |
| | 0.6319 | 0.019 | 0.0222 | +3.2 | 24.2 | 20.7 | -14.5 |
| | 0.4879 | 0.046 | 0.0458 | -0.2 | 15.6 | 15.6 | +0.6 |
| | 0.3178 | 0.096 | 0.0980 | +2.0 | 11.9 | 11.7 | -2.0 |
| 850 | 0.7143 | 0.005 | 0.0064 | +1.4 | 67.3 | 52.6 | -21.8 |
| | 0.6572 | 0.008 | 0.0091 | +1.1 | 52.5 | 46.1 | -12.0 |
| | 0.5058 | 0.018 | 0.0091 | +2.0 | 37.9 | 34.1 | -10.0 |
| | 0.3468 | 0.041 | 0.0409 | -0.1 | 25.8 | 25.9 | +0.3 |
| | 0.1762 | 0.094 | 0.0912 | -2.8 | 18.5 | 19.0 | +2.7 |
| | | Mean | +0.2 | | Mean | -3.8 | |
| | | Ave. | | | Ave. | | |
| | | Dev. | ±1.3 | | Dev. | ±7.8 | |

Temperature and Time Dependence of Conversion

From Figure 1 it is possible to pick values of fraction propane unconverted (*X*) at various reaction times and at the four experimental temperatures, and to calculate an integral specific rate, $k = -\ln X/t$. In Figure 2, net values of *k* are plotted against $1/T$ on semilog paper with either residence time or decomposition held constant. The constant decomposition *k*'s give steep linear plots, corresponding to E_{act} values of about 75 kcal/mol, while the constant time plots (also linear) give E_{act} values of about 46 kcal/mol. A plot of $\ln k(t = 0)$, based on initial slopes of *X* vs. *t*, is parallel to the constant decomposition plots.

Visual inspection of Figure 1 indicates that the curves drawn are all of the same general shape. Thus, by using a reduced time scale, it should be possible to fit all of the data to a single curve. Figure 3 shows that

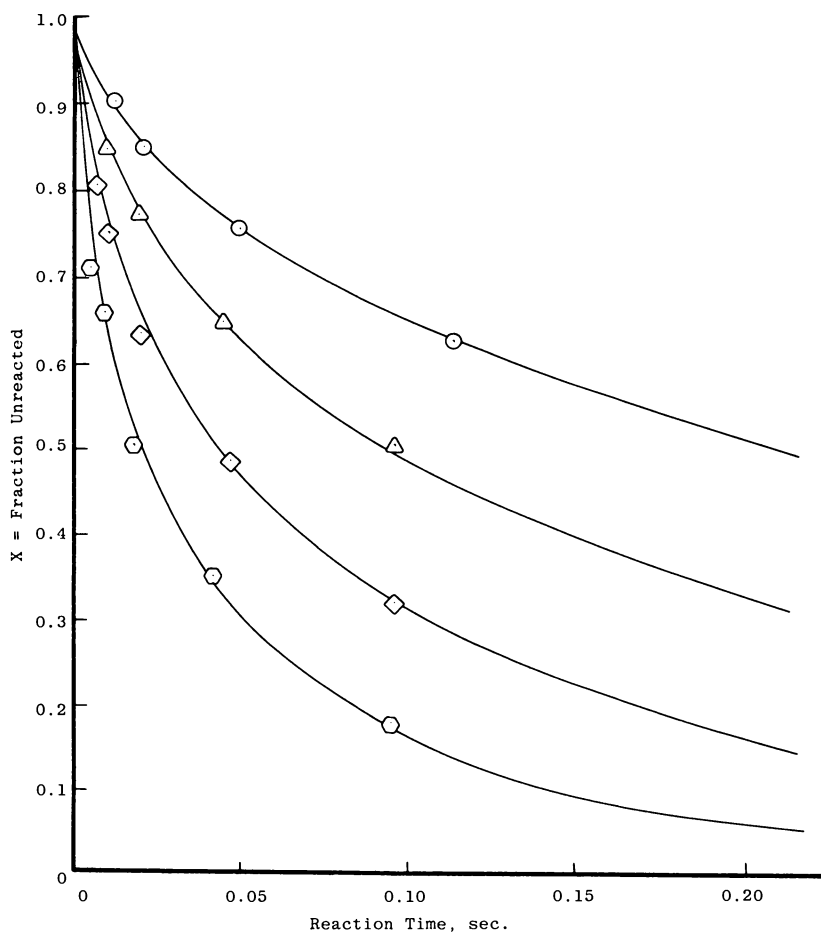


Figure 1. Calculated curves and experimental data. Mole fraction propane unreacted vs. reaction time. (○) 775°C; (△) 800°C; (◇) 825°C; (⊙) 850°C; P = 1 atm.

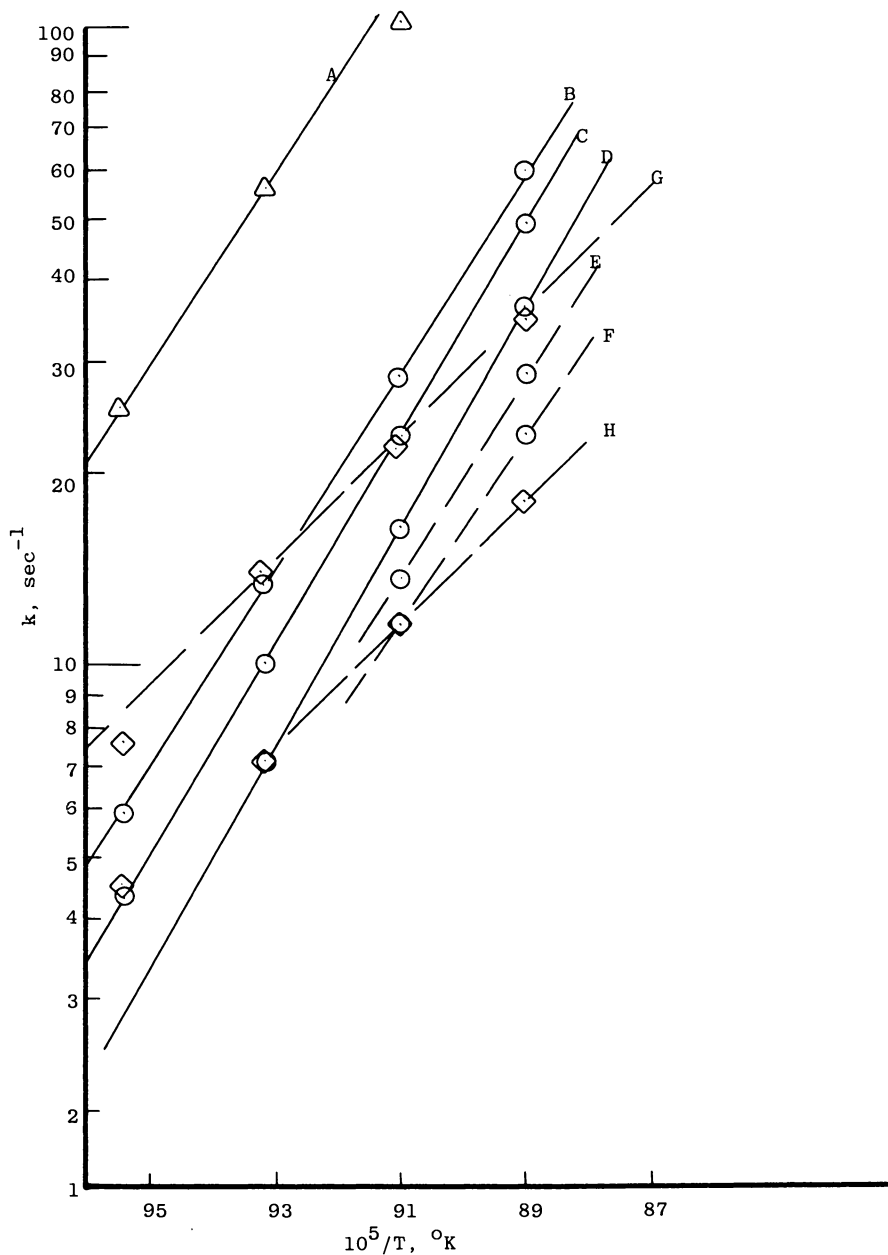


Figure 2. Overall first-order constant vs. reciprocal temperature at constant decomposition and constant time. (A) $X = 1.00$ (zero decomp.); (B) $X = 0.75$; (C) $X = 0.65$; (D) $X = 0.50$; (E) $X = 0.40$; (F) $X = 0.30$; (G) $t = 0.02$ sec; (H) $t = 0.10$ sec; $P = 1$ atm.

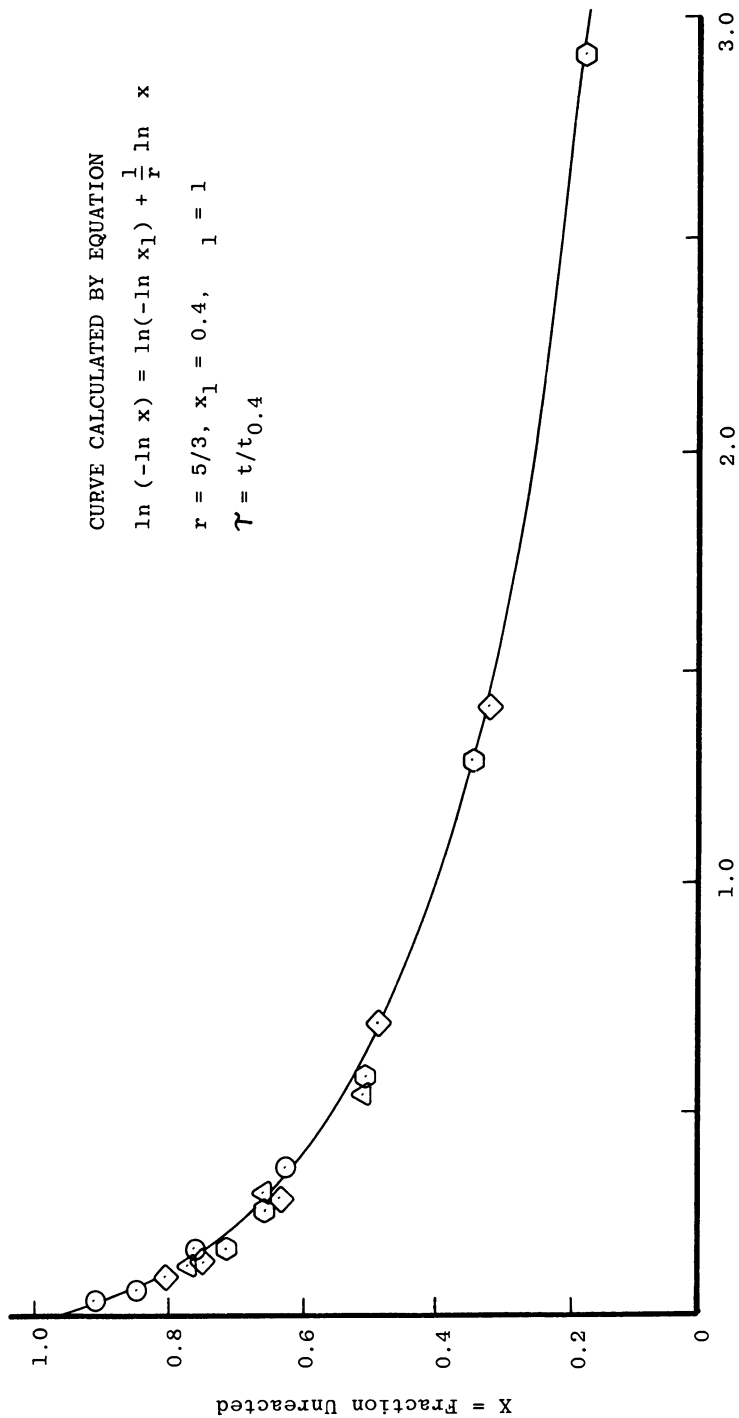


Figure 3. Reduced time curve; propane decomposition at one atmosphere fraction unreacted vs. τ
 (○) 775°C; (△) 800°C; (◇) 825°C; (◇) 850°C.

this is actually true. The reduced time variable τ is equal to actual reaction time divided by the time to reach $X = 0.4$, $\tau = t/t_{0.4}$. The equation of the curve drawn is derived from the EE' model, as will be shown later.

Models for Propane Cracking

First efforts to take into account the effects of product inhibition resulted in a fairly simple equation (termed the product inhibition or "PI" model).

$$-\frac{d \ln x}{dt} = \frac{A_0 e^{-E/RT}}{1 + (1 - X) B e^{-H/RT}} \quad (1)$$

Here the term $1 - X$, the fraction of feed propane decomposed, is a measure of the gross amount of product which has been formed. A least squares fit of the data of Table I gave: $A_0 = 2.761 \times 10^{17} \text{ sec}^{-1}$; $B = 40.886$; $E = 77.910 \text{ kcal/mol}$; $H = 2170$; with $R^2 \sim 0.99$. This gives X as a function of t to about ± 0.013 , and must be considered an excellent fit. It should be noted that Saito and co-workers (8-13) have used essentially the same equation to fit their rate data for a number of paraffins. Saito's equation does not contain an exponential in the product inhibition term of the denominator. However, it is doubtful whether any available data justify calculating such a term (assumption that $H = 0$ makes the fit trivially worse).

Equation 1 has certain desirable features. Apart from fitting the present data, it behaves well mathematically at $X = 1$ and thus is valuable for extrapolation to low and even zero conversions. Further, the value of E_{act} obtained is satisfyingly high (78 kcal/mol). The generally accepted, free radical mechanism requires a value of E_{act} equal to the C-C bond energy in propane (85 kcal), less a number related to one or more of the chain-carrying reactions (5-10 kcal), hence in the range of 75-80 kcal.

The PI model does not extrapolate in simple fashion from a paraffin of one carbon number to other carbon numbers, nor is it easily applicable to mixtures. Saito, et al. (8-13) also have observed this. We found evidence that the model did not fit actual data very well at the high conversions (90-99%) used in commercial steam cracking. (These factors are discussed further in the following section.)

Hence, it seemed worthwhile to pursue another, possibly better, kinetic model based on algebraic consequences of the observation that both E (constant decomposition) and E' (constant time) were constant over considerable ranges of conversion and reaction time. The EE' model is the result of this effort.

Development of EE' Model

We assume that a decomposition reaction exhibiting product inhibition depends upon temperature and reaction time in such a way that two energies of activation, E and E' , can be defined, both constant from some very low conversion to the highest conversion of interest. E = energy of activation calculated from values of fraction unconverted (X) at constant conversion and variable time and temperature. E' is calculated at constant reaction time and variable conversion and temperature. Also we define $r = EE'$ and X_1 = fraction unconverted at $T = T_1$ and $t = t_1$, where t_1 and T_1 are reaction times and temperatures conveniently chosen in the range of the known data.

At any other fraction unconverted (X), we can calculate the reaction time (t) in two steps. First we calculate, using E' , the temperature (T_2) at which we would obtain X at constant reaction time t_1 , then apply the constant decomposition energy of activation (E). Working through the algebra we have:

$$T_2^{-1} = \frac{R}{E'} [\ln(-\ln X_1) - \ln(-\ln X)] + T_1^{-1} \quad (2)$$

$$\ln(-\ln X) = \ln t + \ln A - \frac{E T_1^{-1}}{R} \quad (3)$$

$$\ln(-\ln X) = \ln t_1 + \ln A - \frac{E T_2^{-1}}{R} \quad (4)$$

Substituting from Equation 2 in Equation 4, we get:

$$\ln(-\ln X) = \ln t_1 + \ln A - r \ln(-\ln X_1) - \frac{E T_1^{-1}}{R} + r \ln(-\ln X) \quad (5)$$

and solving Equations 3 and 5 we find:

$$\ln(-\ln X) = \ln(-\ln X_1) + \frac{1}{r} \ln(t/t_1) \quad (6)$$

Defining $t/t_1 = \tau$ we obtain:

$$\ln(-\ln X) = \ln(-\ln X_1) + \frac{1}{r} \ln \tau \quad (7)$$

Equation 7 is shown as the curve drawn in Figure 3. The existence of a unique reduced curve for X vs. τ is a direct result of the constancy of E and E' .

The value of t at $X = X_1$ for any value of T can, of course, be obtained from the Arrhenius parameters. This was done when drawing Figure 3. The equation is:

$$\ln(-\ln X) = \frac{\ln t}{r} + \frac{r-1}{r} (\ln t_1) + \ln A_1' - E'/RT$$

which can be represented as Equation 8 where $\ln a = \ln A_1' + (r-1)/r (\ln t_1)$.

$$\ln(-\ln X) = \frac{\ln t}{r} + \ln a = \frac{E'}{RT} \quad (8)$$

or
$$-\ln X = at^{1/r} \exp(-E'/RT) \quad (8a)$$

$$X = \exp[-at^{1/r} \exp(-E'/RT)] \quad (8b)$$

While A_1' is a function of reaction time, a is a constant within the assumptions of this development (E and E' independent of t and T). If t_1 is any chosen fixed reaction time in the range of applicability of the assumptions, the relation is

$$A' = at_1 \frac{1-r}{r} \quad (9)$$

Equation 8 is the preferred integrated form of the EE' model. It can be readily used with linear regression analysis to fit the three parameters (a , E , or r) to experimental X vs. τ data from an isothermal reactor (see for example, Table I and Figure 1).

Differentiation of Equation 8a and back substitution for t from Equation 8a gives a differential form suitable for use with isothermal or nonisothermal reactors:

$$-\frac{dt}{d \ln X} = k_{\text{diff}} = \frac{a^r}{r} (-\ln X)^{(1-r)} e^{-E'/RT} \quad (10)$$

While Equations 8a and 8b correctly give $X = 1$ at $t = 0$, it is clear from Equation 10 that the model does not really behave properly at very low conversion or low times. The value of k_{diff} becomes infinite at $X = 1$ and $t = 0$. At very high conversion the EE' model predicts that k_{diff} will continue to fall off rapidly with decreasing X . In contrast, the PI model (Equation 1) predicts that at low X ($1 - X$ approaches 1) the reaction will become first order with a high energy of activation approaching E (or $E - H$).

Evaluation of Parameters for Propane Cracking

The propane conversion data of Table I have been used to evaluate a , E , and r through both Equations 8 and 10. Fits were equally excellent ($R^2 > .99$). These values: $\ln a = 22.604$, $a = 6.558 \times 10^9$, $E = 77.28$ kcal/mol, $r = 1.68$, and $E' = E/r = 46.0$ kcal/mol, can be used to predict X from t to ± 0.009 (σ), slightly better than with the PI model.

The curves drawn for Figure 1, while originally "eyeballed" through the data, are indistinguishable from curves calculated by Equation 8 when using the above parameters. Evidently, the fit is satisfactory even for reaction times less than 0.020 sec. At longer reaction times it is excellent.

Extension to High Propane Conversions

In commercial practice, propane is often cracked at percent decompositions above 90%. C_4^+ paraffins are commonly cracked at 90% to nearly 100% decomposition. A kinetic model fitting decomposition data in the 90+% range should, therefore, be valuable.

The data given in Table I stop well short of 90% conversion. The older data obtained with the Type II reactors, described in the experimental section above, are less self-consistent and are systematically inconsistent with Table I. The inconsistency could conceivably be identified as a substantial error in temperature. In Figure 4, we have plotted results obtained in the second reactor at nominal temperatures from 825° to 900°C and residence times from 0.07 to 0.18 sec. The curves drawn are calculated with Equation 8 and the values of parameters given above, but with the temperatures shown in parentheses. If a temperature error is the cause of the inconsistency and the temperatures of Table I are as accurate, as we believe, then the temperature measurements in the second reactor were high by about 20°C.

The shape of the EE' curves is verified to the extent possible with the obviously not too self-consistent data. The amount of falling-off of the specific rate with increasing conversion appears to be great even above 85% decomposition.

This is shown more clearly in Figure 5, where we have plotted the nominal 900°C points, at 93% to 98% decomposition, against time on an expanded scale. If anything, the fall-off in rate at 98% conversion is even greater than predicted by the EE' model fit. For comparison, curves drawn based on the PI model and a straight first-order model are shown. Both predict a much higher conversion at 0.16 sec than was observed. (At 98% conversion at 878°C the pressure ratio, $H_2 \cdot C_3H_6 : C_3H_8$, is 0.69, compared with an equilibrium value of 23; overall backreaction cannot, therefore, be significant.)

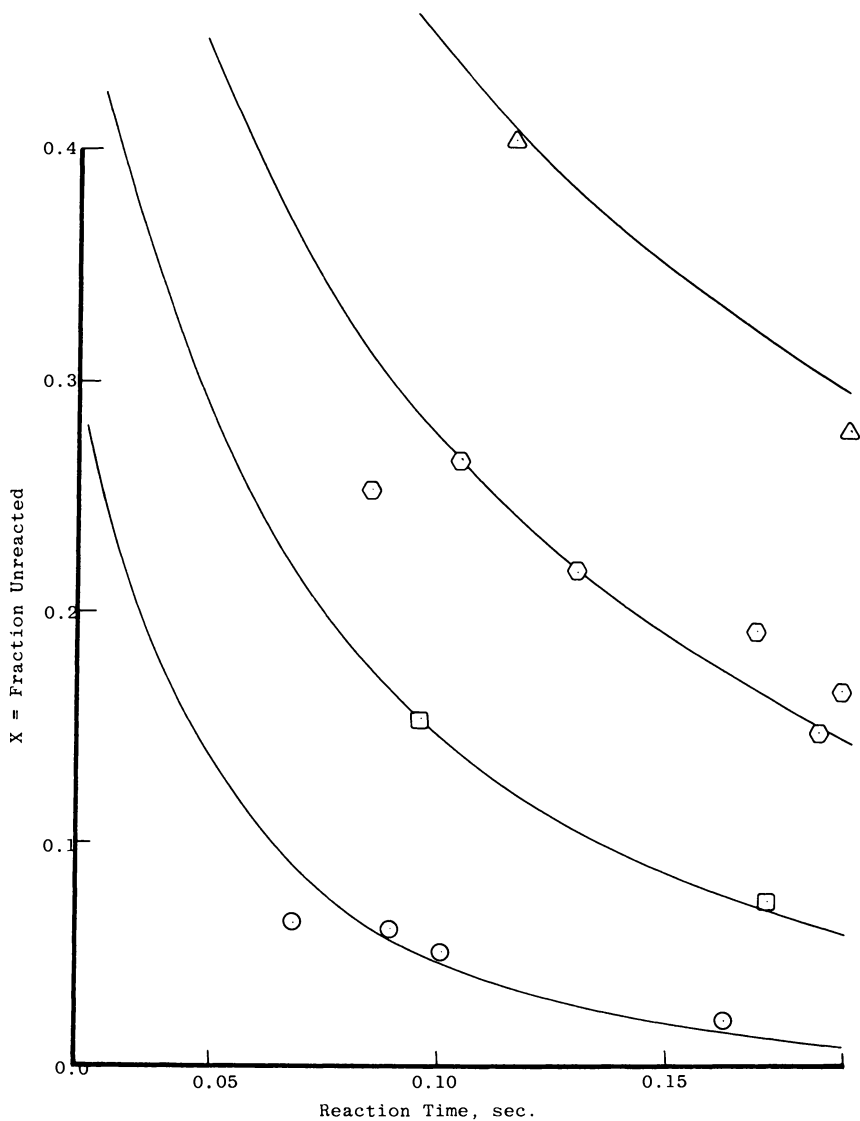


Figure 4. Calculated curves and experimental data. Mole fraction propane unreacted vs. reaction time at high conversions. (Δ) 825°C (807.5); (\odot) 850°C (830); (\square) 875°C (852); (\circ) 900°C (878).

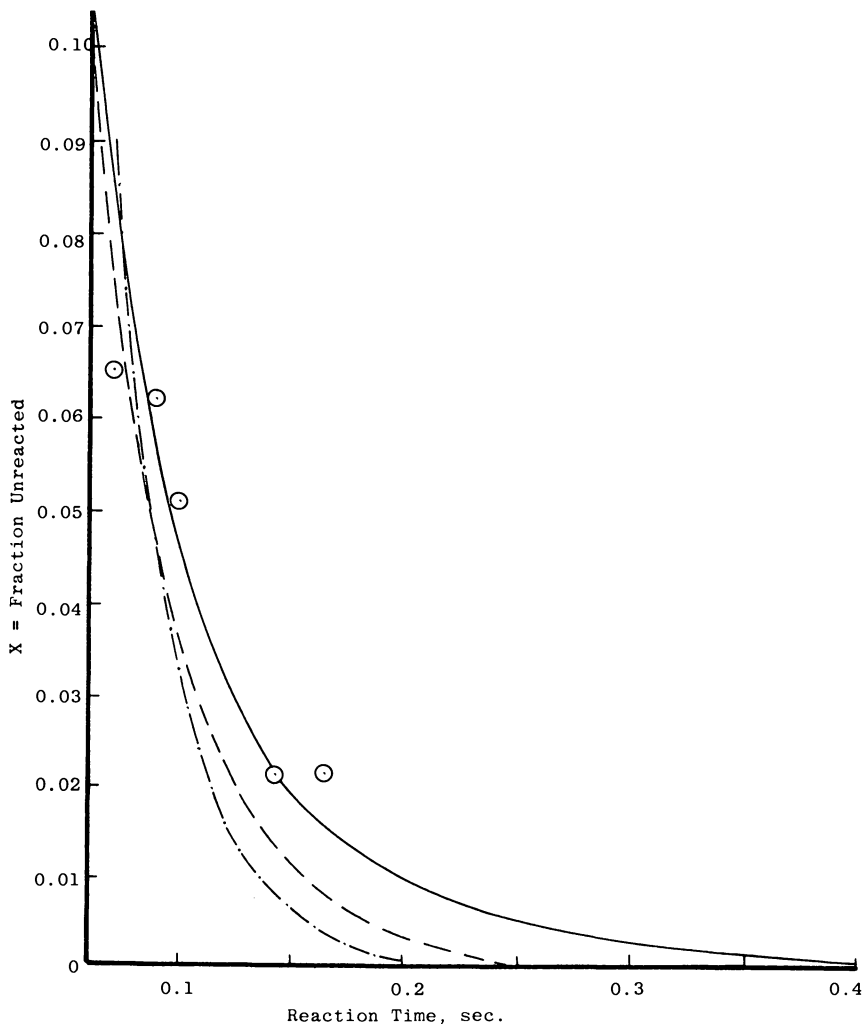


Figure 5. Comparison of kinetic models at high conversion. (\odot) Experimental propane data: (—) EE' model ($T = 878^{\circ}\text{C}$); (---) PI model ($T = 875^{\circ}\text{C}$); (- · -) first-order curve.

Points corrected to $t = 0.16$ sec were estimated from the data points plotted in Figure 4. If the basic EE' assumptions are valid, these should give an activation energy (E') of about 46 kcal/mol. Figure 6 shows that they give 41 kcal/mol if the nominal reactor temperatures are used, 46 kcal/mol if the temperatures needed to fit the EE' model curves to the data are used. If the PI models were valid, a nonlinear plot with a much steeper slope, especially at the high temperature end, would be expected.

Thus the high conversion data indicate, at least conditionally, that the EE' model is useful even beyond the maximum decompositions used in commercial propane cracking.

Two observations can be made about the disparity between the two reactors. The ratio of integral first-order rate constants (extrapolated from the Type I reactor data) to those calculated from the data of Figure 4 is about 1.4. This is a magnitude of difference frequently

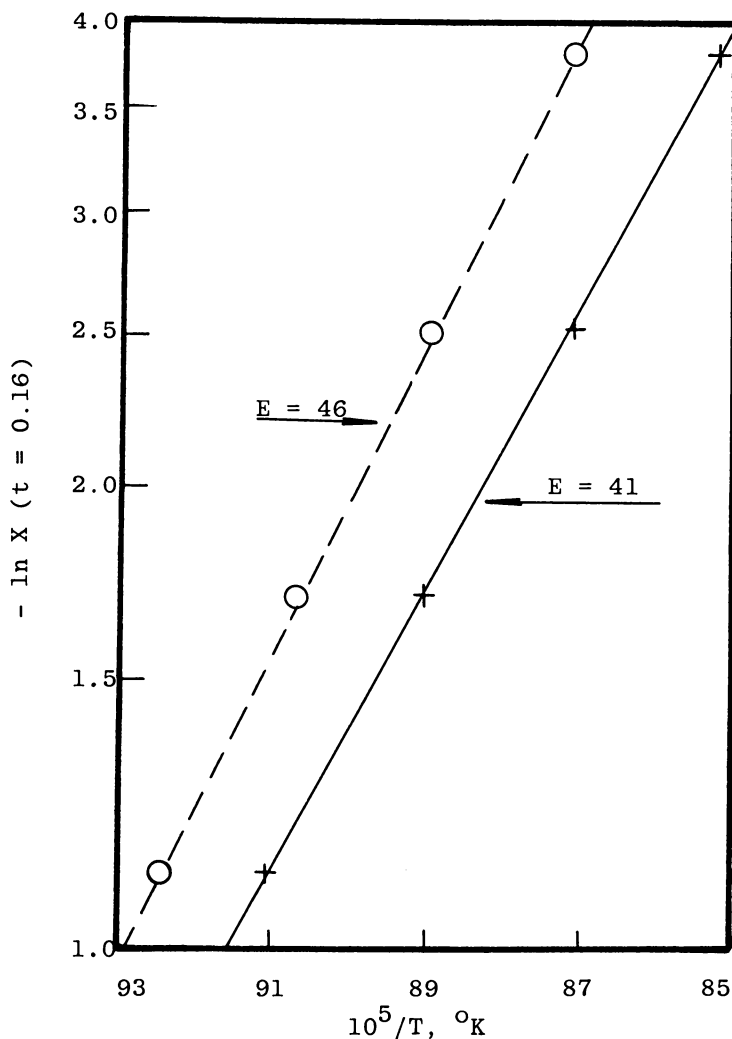


Figure 6. Propane at high decompositions. Dependence of fraction undecomposed (X) on temperature at constant reaction time. (+) Experimental temperature; (O) Calculated temperature.

observed in comparisons of rate data from various sources in this relatively high-temperature range. While some of the discrepancies can be blamed on analysis or on faulty estimation of residence time, they are commonly attributed to errors in temperature.

Actually, we are quite confident that the temperatures in the older reactor were accurate, at least to about $\pm 5^\circ\text{C}$, and probably as accurate as those in the annular reactor. A more likely source of the discrepancy lies in the undoubted existence of some back-mixing or partial gas bypassing in the older, fluid-bed reactor. Although, the a priori applicability of the model seemed doubtful, we have attempted to estimate the magnitude of this back-mixing effect by using the dispersion model described by Levenspiel (14).

Levenspiel defines the dispersion criterion D/uL , where D is an axial diffusion coefficient, u is velocity, and L is length of a reactor. D/uL is 0 for plug flow and infinite for back-mixed flow. For the annular reactors as well as for typical plant reactors, D/uL is on the order of 10^{-3} , substantially plug flow. Levenspiel presents graphs (Chapter 9, Figures 22 and 23) relating fraction unconverted (X) in first- and second-order reactions, respectively. Uninhibited first order is a very poor model for propane cracking, and Figure 22 proved inapplicable. However, in the range of conversions of interest, second order is a fairly good approximation to either the EE' or PI models of propane cracking, so Figure 23 was tested as follows.

With the EE' parameters evaluated above, values of X were calculated for $t = 0.1$ and $T = 825^\circ, 850^\circ, 875^\circ,$ and 900°C . These values, taken as the plug-flow base, were then compared with X for these conditions based on the data near $t = 0.1$ for the fluid-bed reactor, extrapolated to precisely 0.1 with the aid of Figure 4. At all four temperatures, the experimental values of X were transformed to X_p (plug flow) with D/uL equal to about 1.0. Assuming D/uL was always 1.0, we then calculated X_p —that is, the fraction unconverted which would have been reached had there been no back-mixing—for all data points obtained with propane at atmospheric pressure in the fluid reactor.

The raw and the plug-flow corrected data are given in Table II. Fraction unconverted X_1 and plug-flow corrected X_p are compared with X calculated from the Type I reactor data by Equation 8. The comparison also can be made through the integral specific rate k , and the table shows $k_p = (-\ln X_p)/t$ and $k_{\text{calc}} = (-\ln X_{\text{calc}})/t$. X_p also is plotted against x_{calc} in Figure 7.

Of 21 points in the data set, 18 show X_p agreeing with X_{calc} better than does the actual experimental value of X (X_{exp}). One point (850°C , 0.041 sec) is worse and one is no better. The four shortest time points (not counting the 950°C point where any agreement is surprising) are

Table II. Values of X_p and Integral k_p from Fluid-Bed Reactor Data Compared with EE' Model Predictions^a

| T (°C) | Time (sec) | X | X_p | X_{calc} | k_p | k_{calc} |
|--------|------------|-------|--------|------------|-------|------------|
| 800 | 0.045 | 0.689 | 0.615 | 0.641 | 10.8 | 9.9 |
| | 0.105 | 0.570 | 0.470 | 0.479 | 7.2 | 7.0 |
| | 0.20 | 0.460 | 0.33 | 0.339 | 5.5 | 5.4 |
| | 0.33 | 0.328 | 0.212 | 0.234 | 4.7 | 4.4 |
| | 0.61 | 0.216 | 0.104 | 0.123 | 3.7 | 3.4 |
| 825 | 0.115 | 0.405 | 0.277 | 0.281 | 11.2 | 11.0 |
| | 0.20 | 0.263 | 0.143 | 0.172 | 9.7 | 8.8 |
| 850 | 0.041 | 0.350 | 0.224 | 0.334 | 36.5 | 26.7 |
| | 0.084 | 0.252 | 0.133 | 0.186 | 24.0 | 20.0 |
| | 0.104 | 0.268 | 0.145 | 0.148 | 18.6 | 18.4 |
| | 0.13 | 0.217 | 0.105 | 0.112 | 17.3 | 16.8 |
| | 0.17 | 0.217 | 0.105 | 0.077 | 14.5 | 15.1 |
| | 0.184 | 0.146 | 0.057 | 0.068 | 15.6 | 14.6 |
| | 0.19 | 0.166 | 0.069 | 0.065 | 14.1 | 14.4 |
| 875 | 0.096 | 0.152 | 0.061 | 0.058 | 29.1 | 29.7 |
| | 0.173 | 0.073 | 0.021 | 0.017 | 22.3 | 23.6 |
| 900 | 0.068 | 0.065 | 0.018 | 0.028 | 59.1 | 52.6 |
| | 0.089 | 0.062 | 0.016 | 0.015 | 46.5 | 47.2 |
| | 0.10 | 0.051 | 0.012 | 0.011 | 44.2 | 45.1 |
| | 0.163 | 0.021 | 0.0035 | 0.0025 | 35.0 | 36.8 |
| 950 | 0.062 | 0.013 | 0.002 | 0.005 | 100.0 | 123.0 |

^a X = Fraction unconverted, experimental; X_p = X (plug flow), calculated with $D/uL = 1$; X_{calc} = X from EE' model based on annular reactor data; k_p = integral specific rate = $-\ln X_p/t$; k_{calc} = $-\ln X_{calc}/t$.

overcorrected. After eliminating these and the 950°C point, X_p agrees with X_{calc} to ± 0.013 standard deviation. More significantly, the corrected integral specific rate constants agree well with those calculated from the Type I reactor data. Before the plug flow correction, $k/k_{calc} = 0.72 \pm 0.086$; after correction, $k_p/k_{calc} = 1.035 \pm 0.099$. With the five shortest time runs eliminated, $k/k_{calc} = 0.70 \pm 0.046$ and $k_p/k_{calc} = 1.014 \pm 0.048$.

We concluded that the fluid-bed reactor was indeed partly back-mixed; also, that the assumption, $D/uL = 1$, allows a satisfactorily quantitative correction to plug-flow conditions. The EE' kinetic model gives an excellent fit to these corrected data. We therefore conclude that the model can be used for rather high conversions—in the 90–99% range.

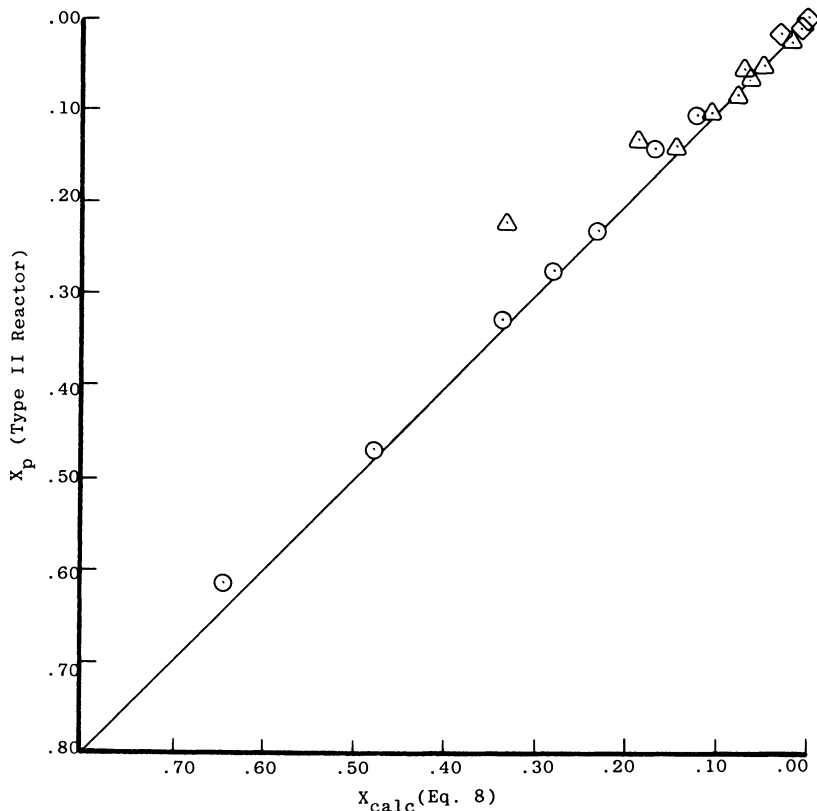


Figure 7. Propane pyrolysis in Type II reactor. Fraction unconverted corrected to plug flow vs. value calculated by Equation 8 (X_p vs. X_{calc}). (○) 800°C, 825°C; (△) 850°C, 875°C; (◇) 900°C.

It is interesting to compare the deviations from plug flow in our fluid bed with the much larger deviations shown in Levenspiel (14), Figures 14–28. With our very high ratio of velocity to minimum fluidization velocity (u_o/u_{mv}), there must be little or no bypassing, but the reactor evidences a modest degree of back-mixing.

Extension to Higher Paraffins

Extension of the propane model to *n*-butane and to C_4+ paraffins and isoparaffins in general is a complicated subject. Details should be covered in a separate paper. At this point, we wish to probe the area only to establish two points:

(1) The *EE'* model apparently does fit *n*-butane and probably *n*-hexane reasonably well. It is possible therefore to look for applicability to other C_4+ paraffins.

(2) The *n*-butane conversion rate data can be calculated fairly accurately from the propane data and the carbon number relation previously described (3).

Based on relative rates of decomposition determined in mixtures plus conversion rates of pure ethane, propane, and *n*-butane determined in the fluid-bed type of reactor, the following relation was determined (3):

$$k_{\text{int}} = k_0 [1 + 1.3(Nc - 2)] \quad (11)$$

where k_0 is a parameter depending on time, temperature, and perhaps other reaction conditions but not on carbon number (Nc). This relation appeared to work well for C_3 to C_8 normal and isoparaffins. Its applicability to ethane is less precise, partly because back hydrogenation of ethylene must be accounted for. In mixtures, the constant 1.3 can be related to the number and relative reactivities to hydrogen abstraction of the C-H bonds in the paraffin molecules. However, limited data indicated that the equation applied, somewhat surprisingly, to pure propane and *n*-butane, and (with reservations) ethane cracked separately.

For any specified reaction time (t) we write Equation 12. We can now incorporate Equation 12 with Equation 8 and obtain a generalized expression which can be tested against hydrocarbons other than propane

$$k_t = -\frac{\ln x}{t} A_t e^{-E'/RT} [1 + 1.3(Nc - 2)] \quad (12)$$

(see Equations 13 and 13a). From the propane data $\ln a_0 = 21.7711$, while E' and r remain as before (46,000 and 1.68, respectively). This equation can be tested against *n*-butane data collected using the annular reactor.

$$\ln(-\ln X) = \frac{\ln t}{r} + \ln a_0 + \ln [1 + 1.3(Nc - 2)] - \frac{E}{RT} \quad (13)$$

or

$$X = \exp\{-a_0[1 + 1.3(Nc - 2)] t^{1/r} e^{-E'/RT}\} \quad (13a)$$

Figure 8 shows a comparison of experimental fraction of *n*-butane undecomposed (X) vs. X_{calc} from Equation 13. While the four sets of data show some systematic differences, it is clear that Equation 13 represents the rate of conversion of *n*-butane nearly as well as it does for propane. (Set 4, variable time at 750°C, gives mainly higher conversions than predicted; Sets 1, 2, and 3 about as predicted or a little lower.) Experimental X varies from calculated X by an average of $-.023 \pm .03$.

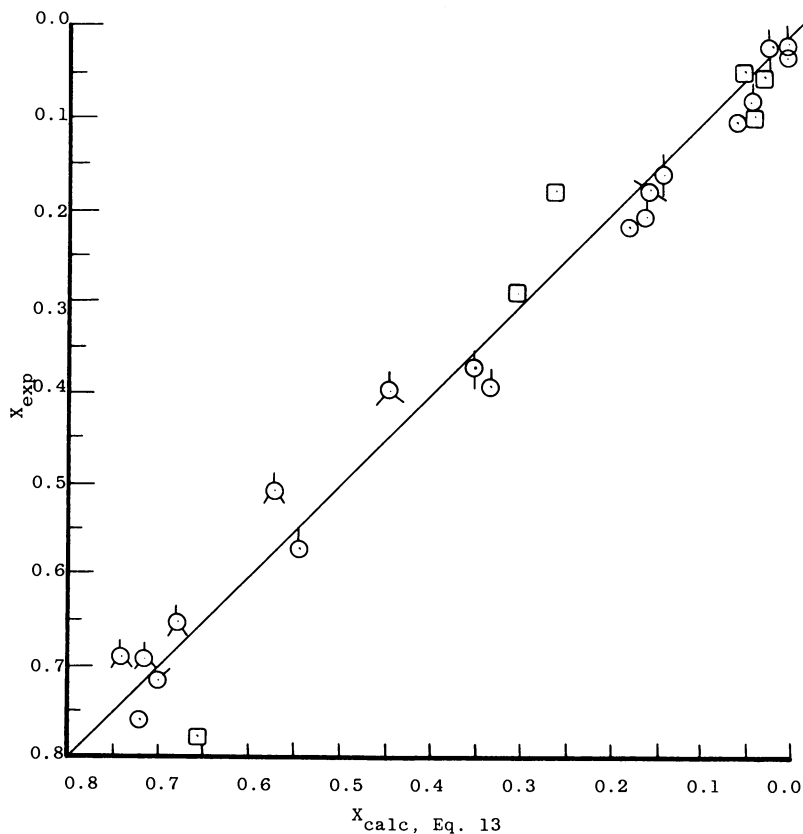


Figure 8. Experimental and calculated conversion. *n*-Butane and *n*-hexane at 1 atm pressure. (○) *n*-Butane, set 1, $t = 0.2$, $T = 725^{\circ}\text{--}850^{\circ}\text{C}$; (○) *n*-butane, set 2, $t = 0.22$, $T = 725^{\circ}\text{--}830^{\circ}\text{C}$; (○) *n*-butane, set 3, miscellaneous; (○) *n*-butane, set 4, $T = 725^{\circ}\text{C}$, $t = .065\text{--}.178$; (□) *n*-hexane.

By extension, if we accept the conclusions of Ref. 3, which are based on more tenuous kinetic evidence, Equation 13 also is applicable to $\text{C}_4\text{--}\text{C}_8$ normal and isoparaffins, at least in mixtures. Unfortunately, we have very little data of good kinetic quality on other paraffins. A few runs obtained with pure *n*-hexane in the annular reactor exist. Conversions obtained are compared with calculated conversions in Figure 8. The agreement is fairly good.

One way to check the applicability of Equation 13 is to plot X vs. τ , the reduced time used in Figure 3. Figures 9, 10, and 11 show that when τ is calculated as t/t_1 with t_1 calculated from Equation 13 with $X_1 = 0.4$ and the parameters estimated from the propane atmospheric pressure data, both butane and hexane points lie a little above the atmospheric pressure propane curve. The higher paraffins decompose a little less

rapidly than predicted. The fit can be improved by dropping a_0 from 2.851×10^9 to 2.666×10^9 . It should be noted that dilution with nitrogen appears to drop the observed rate a little, while raising the pressure to 1.65 atm has little effect.

Saito and co-workers have published extensively in recent years on the pyrolysis rates of several paraffins and on the interactions of mixtures. The temperature range covered (~ 650 – 700°C) and the degrees of decomposition are lower than those in our work. Also, the experiments were generally carried out in the presence of nitrogen diluent, which affects the rate of conversion somewhat (*see above*). These conditions are compatible with Saito et al.'s objectives, which involve elucidating the free radical mechanisms and their interaction rather than determining gross kinetic effects in the practical conversion range. In the studies where highest conversions were attained (10, 12, 13), quite high nitrogen dilutions (in the range of 5–10/1) were used.

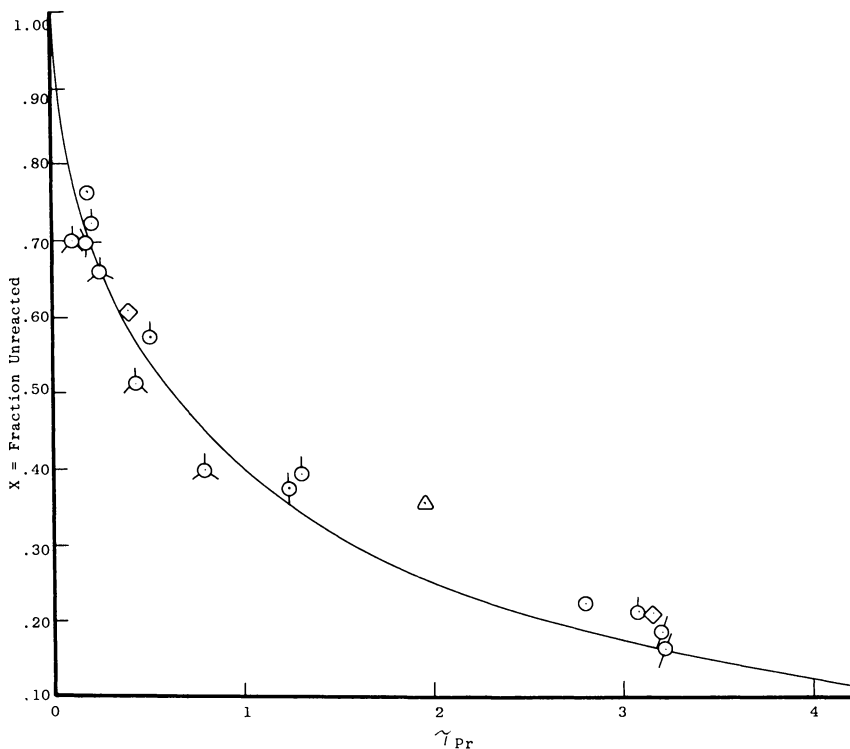


Figure 9. Fraction of n-butane unconverted vs. reduced time, τ_{Pr} . (○) Atmospheric pressure, set 1; (⊙) atmospheric pressure, set 2; (⊖) atmospheric pressure, set 3; (⊕) atmospheric pressure, set 4; (△) 2/1 dilution nitrogen; (◇) 1.65 atm; $\tau_{Pr} = t/t_{0.4}$. $t_{0.4}$ calculated by Equation 13 with parameters derived from propane data.

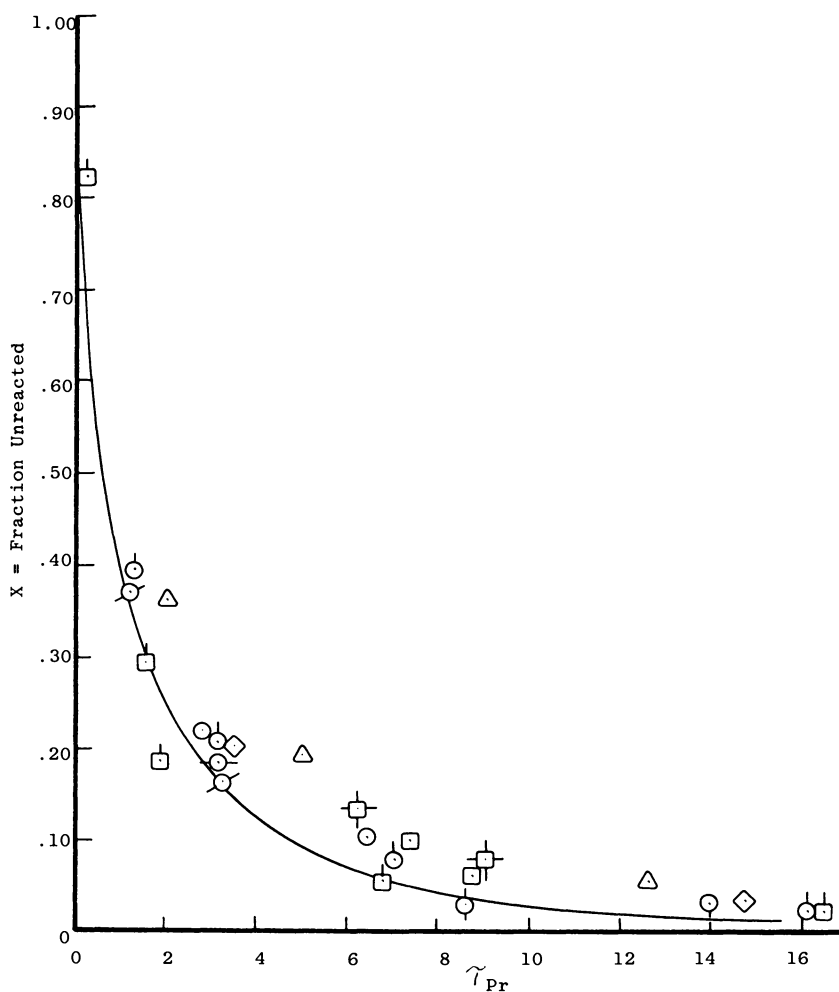


Figure 10. Fraction of n-butane or n-hexane unconverted vs. reduced time (τ_{Pr}). (\odot) n-Butane, 1 atm, set 1; (\odot) n-butane, 1 atm, set 2; (\odot) n-butane, 1 atm, set 3; (\odot) n-butane, 1 atm, set 4; (\triangle) n-butane, 1 atm, 2/1 dil. (N_2); (\diamond) n-butane, 1.65 atm; (\square) n-hexane, 1 atm, set 1; (\square) n-hexane, 1 atm, set 2; (\square) n-hexane, 1 atm, 4:1 dilution nitrogen, $\tau_{Pr} = t/t_{0.4}$, calculated by Equation 13 with parameters derived from propane data.

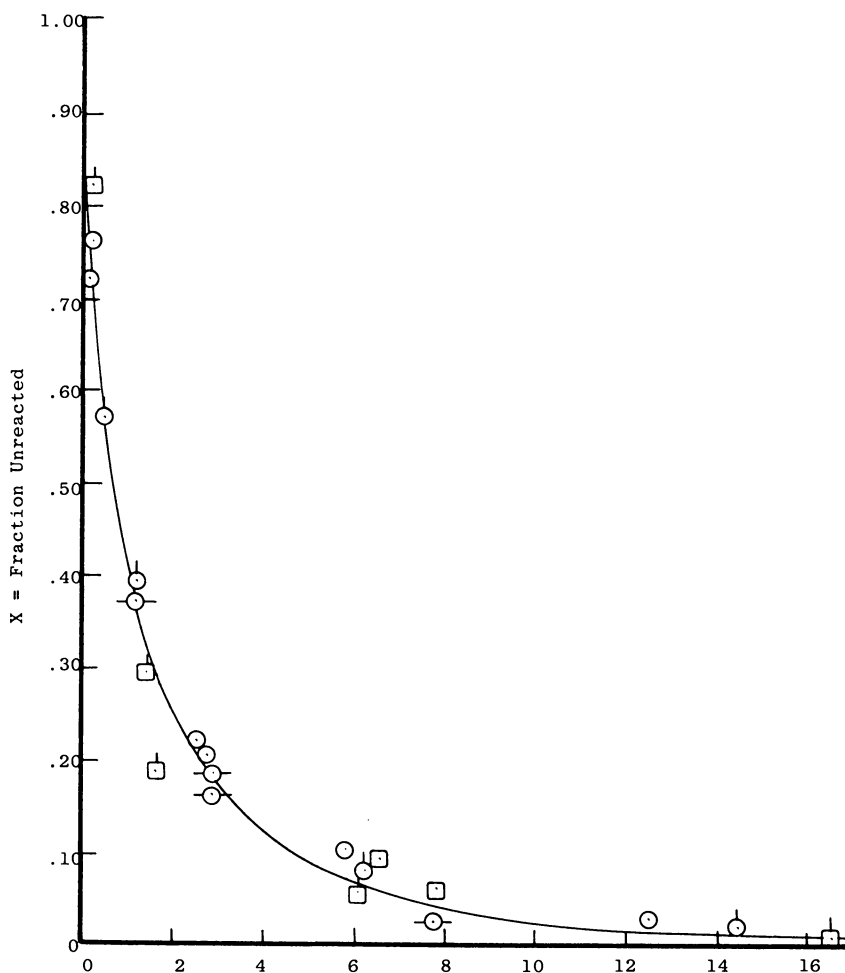


Figure 11. Fraction of n-butane or n-hexane converted vs. $\tau = t/t_1$ (1 atm data only, t_1 calc for best fit to butane:hexane data). (\odot) n-butane, 1 atm, set 1; (\ominus) n-butane, 1 atm, set 2; (\circ) n-butane, 1 atm, set 3; (\odot) n-butane, 1 atm, set 4; (\square) n-hexane, 1 atm, set 1; (\square) n-hexane, 1 atm, set 2; $\tau = t/t_{0.4}$, $t_{0.4}$ calculated by Equation 13 fitted to n-butane and n-hexane data.

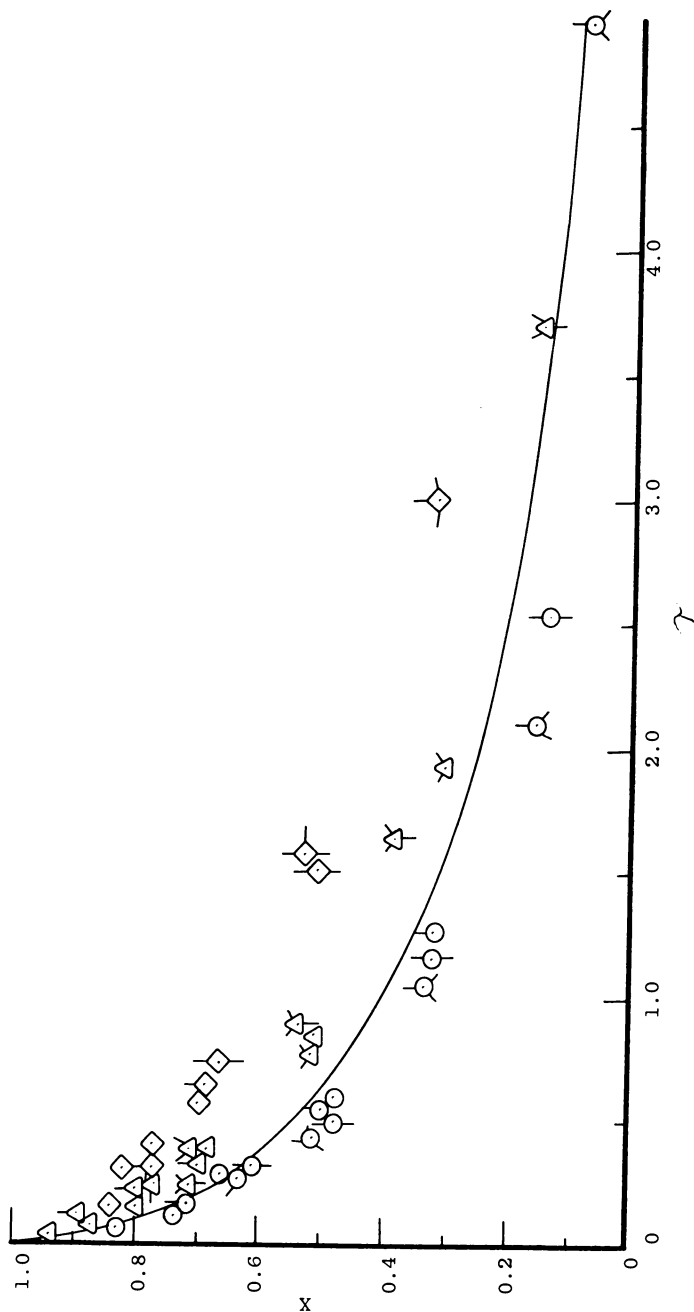


Figure 12. Effect of pressure and dilution on rate of propane conversion, fraction unreacted (X) vs. reduced time (τ). (○) 2 atm; (△) .13 atm; (◇) 7/1 helium dilution, .125 initial partial pressure; (⊙) 825°, 800°, 775°, 800°, 825°, 850°C, respectively; (—) curve from Figure 3 (1 atm data); $\tau \equiv t/t_{0.4}$, $t_{0.4}$ calculated from 1 atm data.

Still, some conclusions can be drawn. In the mixtures, specific rate of reaction is more a function of carbon number than of degree of branching, and the effect of carbon number in mixtures is not greatly at variance with the conclusions of Ref. 3. Specific rates of individual compounds in the mixtures appear to be somewhat lower than we would predict from Equation 13. This can perhaps be partially attributed to the effects of nitrogen diluent.

Saito et al. used an overall kinetic model for their pyrolyses equivalent to our PI equation. See Equation 14 where α was termed the self-inhibition constant. As we also found, they observed that α was not a predictable function of carbon number; it had to be adjusted rather arbitrarily to fit mixtures.

$$k_1 = \frac{k_1^0}{1 + \alpha(1 - X)} \quad (14)$$

Effects of Pressure and Partial Pressure

Total pressure and partial pressure (by means of helium, nitrogen or water dilution) were varied, especially with propane. At low total pressure (for example, 0.13 atm), rates of conversion fell drastically. They also fell somewhat when partial pressure of paraffin was reduced by dilution.

Some typical effects of pressure and partial pressure on propane conversion are shown in Figure 12. Between 1 and 2 atm, the increasing effects of pressure on specific rate can be represented as proportional to $P^{0.2}$. Between 0.13 and 1 atm, the power of P is somewhat higher. Since commercial reactors operate at slightly superatmospheric pressure (a typical case might be 3 atm at the radiant zone inlet and 1.5 atm at the outlet), the rate equations should probably incorporate a $P^{0.2}$ term, where P is total pressure in atmospheres. At one atmosphere, helium dilution slightly reduces the specific rates. This probably indicates that the effect is a total pressure rather than a partial pressure effect but that helium is a poorer third body than propane and its products. Dilution of *n*-butane and *n*-hexane with nitrogen, as seen above, also reduces the specific rate of decomposition a little, although increasing the *n*-butane or *n*-hexane pressure above atmospheric pressure showed no significant effect on the specific rate.

Overall Conclusions

1. The generalized EE' model fits conversion rate data for propane, *n*-butane, and *n*-hexane within the reproducibility of separate sets of data. The conversion range covered is from 10% or less to 99% or more.

2. Near atmospheric pressure, propane decomposition rate increases slightly with increasing total pressure. *n*-Butane is probably not sensitive to pressure.

3. Dilution with inert gas, at constant total pressure, reduces the specific rate for propane, *n*-butane, and *n*-hexane.

4. Rate data, obtained in a bed fluidized with inert, sized sand at approximately free-fall velocity, can be reconciled with plug-flow data by assuming a modest amount of back-mixing.

Acknowledgment

The authors thank Union Carbide for permission to publish this work.

Literature Cited


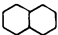
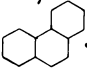
1. Volkan, A. G.; April, G. C. *Ind. Eng. Chem., Process Des. Dev.* **1977**, *16*, 429.
2. Davis, H. G.; Keister, R. G. "Industrial and Laboratory Pyrolyses," *ACS Symp. Ser.* **1976**, *32*, 392-411.
3. Davis, H. G.; Farrell, T. J. *Ind. Eng. Chem., Process Des. Dev.* **1973**, *12*, 171-181.
4. Dunkelman, J. J.; Albright, L. F. "Industrial and Laboratory Pyrolyses," *ACS Symp. Ser.* **1976**, *32*, 241-260.
5. *Ibid.*, 261-273.
6. Williamson, K. D.; Davis, H. G. "Industrial and Laboratory Pyrolyses," *ACS Symp. Ser.* **1973**, *32*, 51-71.
7. Goosens, A. G.; Dente, M.; Ranzi, E. *Hydrocarbon Process.*, **1978**, September, 227-236.
8. Murata, M.; Saito, S.; Amano, A.; Maeda, S. *J. Chem. Eng. Jpn.* **1973**, *6*, 252.
9. Murata, M.; Takeda, N.; Saito, S. *J. Chem. Eng. Jpn.* **1974**, *7*, 286.
10. Murata, M.; Saito, S. *J. Chem. Eng. Jpn.* **1975**, *8*, 39.
11. Utsagi, H.; Arai, Y.; Arai, K.; Saito, S. *J. Chem. Eng. Jpn.* **1976**, *9*, 58.
12. Tanaka, S.; Arai, Y.; Saito, S. *J. Chem. Eng. Jpn.* **1976**, *9*, 504.
13. Arai, Y.; Murata, M.; Tanaka, S.; Saito, S. *J. Chem. Eng. Jpn.* **1977**, *10*, 303.
14. Levenspiel, O. "Chemical Reaction Engineering," 2nd ed.; Wiley: New York, 1972; pp 282-289, 519.

RECEIVED June 29, 1978.

Pyrolysis of Unsubstituted Mono-, Di-, and Tricycloalkanes

P. S. VIRK,¹ A. KOROSI, and H. N. WOEBCKE


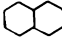
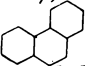
Stone and Webster Engineering Corp., Box 2325, Boston, MA 02107

Experimental data are presented to show the yield of unsaturated chemicals available from pyrolysis of unsubstituted cycloalkanes, respectively , , and . Such compounds are of interest because analogous alicyclic rings occur in virgin gas oils and are abundant in feedstocks upgraded by catalytic hydrogenation. Pyrolysis experiments were conducted at commercial steam-cracking conditions in a tubular flow reactor. Product-yield spectra obtained from the di- and tricyclic compounds closely resembled each other while differing greatly from cyclohexane; e.g., the methane, ethylene, and butadiene yields from cyclohexane were respectively one-half, twice, and five times those obtained from decalin and perhydrophenanthrene. These results can be partially interpreted as reflecting the effect of substrate-bond topology on the pyrolysis pathway." data-bbox="187 337 809 642"/>

The present work forms part of a research and development effort by Stone and Webster aimed at understanding the production of olefins from naphthenic feedstocks. Such feedstocks are currently of great commercial interest for three reasons. First, olefin feedstocks derived from certain petroleum deposits, e.g., in Nigeria and Venezuela, can be highly naphthenic, containing large amounts of cyclic relative to linear alkanes, which significantly affects the proportions of olefinic products available upon pyrolysis. Second, catalytic hydrogenation processes are under

¹ Also Department of Chemical Engineering, Massachusetts Institute of Technology, Cambridge, MA 02139.

active consideration as a means of upgrading olefin feedstocks of high aromatic content; such hydrogenation tends to saturate the aromatic molecules originally present without much ring rupture, yielding a high proportion of alicyclic compounds in the upgraded feedstock that is eventually pyrolyzed. Third, current coal liquefaction processes yield highly aromatic products which are noteworthy in containing relatively unsubstituted polynuclear aromatic compounds; deep hydrogenation of these coal liquids (*see, e.g., Ref. 1*) produces a coal-derived olefin feedstock that is almost entirely naphthenic.

The three model compounds chosen for the present study, namely cyclohexane  (CYH), decahydronaphthalene  (DHN), and perhydrophenanthrene  (PHP), respectively, simulate unsubstituted cycloalkanes in the naphtha, kerosene, and atmospheric gas-oil boiling ranges. Of the model compounds used, cyclohexane has previously been pyrolyzed (2, 3 and references therein); the literature also contains some information about decahydronaphthalene pyrolysis (1, 3), including a detailed report by the present authors (1). To the best of our knowledge there has been no previous work on perhydrophenanthrene pyrolysis.

In what follows, we will focus on experimental results concerning the characterization and pyrolysis of the model substrates; the pyrolysis data also will be interpreted in terms of likely reaction mechanisms. Related work in progress includes further theoretical and experimental study of alicyclic pyrolysis pathways, with special attention to substituted substrates.

Substrate Sample Characterization

The cyclohexane (CYH) sample was a commercial grade of nominal purity 97%; analysis by GCMS showed its actual purity to be 98.5 wt % cyclohexane with 1.5 wt % methyl cyclohexane as the main contaminant.

The decahydronaphthalene (DHN) sample was a high-purity commercial grade and analysis showed it to contain 99.9 wt % decahydronaphthalene with 0.1 wt % naphthalene as the main impurity. Density and refractive index measurements on the DHN sample suggested cis-trans isomer percentages of 47–53, respectively.

The perhydrophenanthrene (PHP) sample was specially prepared for the present tests by two-stage catalytic hydrogenation of pure phenanthrene in a proprietary process. Analysis of the PHP sample showed it to contain 95.7 wt % perhydrophenanthrene with 4.3 wt % octahydrophenanthrene the main impurity; no residual phenanthrene could be detected. The measured hydrogen content of the PHP sample, 12.54 wt % H, accorded closely with the value independently estimated from the foregoing sample composition. The isomer distribution within the PHP

sample was uncertain; knowledge (4) of phenanthrene hydrogenation pathways would suggest that the *cis-syn-cis* stereoisomer of perhydrophenanthrene should predominate while the octahydrophenanthrene should be exclusively the symmetrical isomer.

Pyrolysis Experiments

The pyrolysis experiments were conducted in an electrically heated, once-through tubular flow reactor, designed to simulate the time-temperature history experienced in commercial steam-cracking operations. Reactor effluent compositions were ascertained by gas chromatograph and mass spectrometer analyses. Material and hydrogen balances could always be effected, with typical closures of 98 ± 2 wt %.

Pyrolysis results are summarized in Table I, parts a, b, and c of which respectively concern substrate characterization, pyrolysis conditions, and product yields.

Part a of Table I has been considered in the preceding section. Table Ib, pertaining to pyrolysis conditions, shows that all three feedstocks were pyrolyzed under substantially identical steam-to-hydrocarbon weight ratios of unity, identical residence times of 0.3 sec, and the same reactor exit pressures of 1.8 bar abs. The DHN and PHP samples were pyrolyzed to the same reactor exit temperature of 820°C, under which conditions the respective substrate conversions were 88 and 95%. The CYH was appreciably more refractory than either DHN or PHP, and a reactor exit temperature of 900°C was used to obtain a substrate conversion of 91%, comparable with that of the other two samples.

Pyrolysis product spectra, shown in Table Ic, merit comparisons first between the DHN and PHP substrates and then between DHN and CYH. In the former comparison it is immediately apparent that product yields from DHN and PHP show striking similarities, the yields of compounds from hydrogen through to the C₉* to 205°C fraction being virtually identical. The C₉* to 205°C fraction yields appear to differ greatly in the table (DHN, PHP) = (19.02, 6.82) wt %, but for DHN the reported yield includes about 12 wt % unconverted substrate (boiling range 187–196°C), and correction for this makes the actual yields (DHN, PHP) = (7.02, 6.82). Finally, the pyrolysis fuel oil ($\geq 205^\circ\text{C}$ boiling range) yield for PHP required adjustments for both unconverted substrate (5 wt %) and impurities (4.3 wt %) so that the correct comparison reads (DHN, PHP) = (7.2, 13.7), with PHP yielding appreciably more fuel oil. While the congruence between the DHN and PHP product spectra is much the most striking feature of any comparison, the data in Table Ic are precise enough to show certain small, but nevertheless significant, yield differences as well. Thus the PHP yields somewhat less 1,3-buta-

Table I. Summary of Pyrolysis Experiments

| <i>(a) Substrate Characterization</i> | | | |
|---------------------------------------|--------------------------------|---------------------------------|---------------------------------|
| Sample ^a | CYH | DHN | PHP |
| Formula | C ₆ H ₁₂ | C ₁₀ H ₁₈ | C ₁₄ H ₂₄ |
| Hydrogen content (wt %) | 14.37 | 13.12 | 12.54 |
| Specific gravity 15/15 C | 0.779 | 0.883 | 0.938 |
| Purity (wt %) | 98.5 | 99.9 | 95.7 |
| <i>(b) Pyrolysis Conditions</i> | | | |
| Steam/hydrocarbon weight ratio | 1.0 | 1.0 | 1.0 |
| Residence time (sec) | 0.3 | 0.3 | 0.3 |
| Reactor exit pressure (bar abs) | 1.8 | 1.8 | 1.8 |
| Reactor exit temperature (°C) | 900 | 820 | 820 |
| Substrate conversion (%) | 91 | 88 | 95 |
| <i>(c) Product Yields (wt %)</i> | | | |
| Hydrogen | 1.50 | 0.99 | 0.99 |
| Methane | 5.62 | 6.74 | 6.96 |
| Acetylene | 1.17 | 0.25 | 0.30 |
| Ethylene | 32.39 | 17.13 | 16.56 |
| Ethane | 2.64 | 1.91 | 2.09 |
| Propadiene, propyne | 0.50 | 0.29 | 0.17 |
| Propylene | 6.65 | 6.08 | 5.99 |
| Propane | 0.13 | 0.18 | 0.19 |
| 1,3-Butadiene | 18.83 | 5.79 | 4.86 |
| Butenes | 1.83 | 2.10 | 2.29 |
| C5 olefins, diolefins | 4.15 | 4.04 | 5.03 |
| Benzene | 7.61 | 11.62 | 9.37 |
| Toluene | 1.53 | 7.70 | 6.67 |
| C8 Aromatics | 0.62 | 3.34 | 4.51 |
| Other C6, C7, C8 | 9.12 | 5.62 | 4.23 |
| C9+ to 205°C | 4.80 | 19.02 | 6.82 |
| Pyrolysis fuel oil (≥ 205°C) | 0.92 | 7.20 | 22.97 |
| Total | 100.00 | 100.00 | 100.00 |

^a Abbreviations as follows: (CYH) cyclohexane, (DHN) decahydronaphthalene (mixture of two isomers, approx 53% trans), (PHP) perhydrophenanthrene (mixture of isomers, distribution unknown).

diene and somewhat more C5 diolefins than DHN; and in the aromatic 'BTX' fraction, PHP yields less benzene and toluene but more C8 aromatics than DHN with different ratios of B:T:X, namely DHN (1.00:0.66:0.29) vs. PHP (1.00:0.71:0.48).

The second comparison, between CYH and DHN product spectra in Table Ic, shows profound differences in the yields of essentially all components. Thus, relative to DHN, the CYH yields one and a half times the hydrogen, twice the ethylene, and three times as much 1,3-butadiene but makes only two-thirds as much benzene, one-fifth the toluene, and

one-seventh the pyrolysis fuel oil. The absolute yields of methane, propylene, and C5s are roughly equal for both substrates. It also should be noticed that yields of acetylene and of propadiene plus propyne from CYH are respectively about five times and twice those from DHN; these observations for the minor acetylenic compounds are most likely a consequence of the CYH pyrolysis having been conducted at a significantly higher temperature than the DHN pyrolysis.

Discussion

Hydrocarbon pyrolysis involves mainly free radical and pericyclic types of reactions, the principles of which are known well enough (5, 6) to permit inference of likely pyrolysis pathways for any given molecule. Some examples pertinent to the present experiments are presented next to provide a framework for discussion of the data.

Figure 1 shows a pathway for CYH pyrolysis. In this case it is evident that a cyclohexyl radical must be involved in the propagation sequence which then leads, by β scission and ring opening, to the isomeric hex-1-ene-6-yl radical, with decomposition continuing as shown to yield ethylene, 1,3-butadiene, and a hydrogen atom that is the chain carrier. This is the rather well-established primary pathway for CYH decomposition (2) and properly accounts for the three dominant products. However, the pathway is subject to branching by way of stable intermediates such as but-1-ene and hex-1-ene, which result from H-abstraction reactions of the primary intermediate radicals; these stable molecules then undergo further pyrolysis reactions to yield a spectrum of pyrolysis products, e.g., methane and propylene, which are seen in smaller amounts during CYH pyrolysis.

Figure 2 shows a pathway for DHN pyrolysis. In this case there is appreciably greater complexity than for CYH because all three types of decalyl radicals shown are possible and each admits of a variety of decomposition routes. We show one particular pathway leading from the

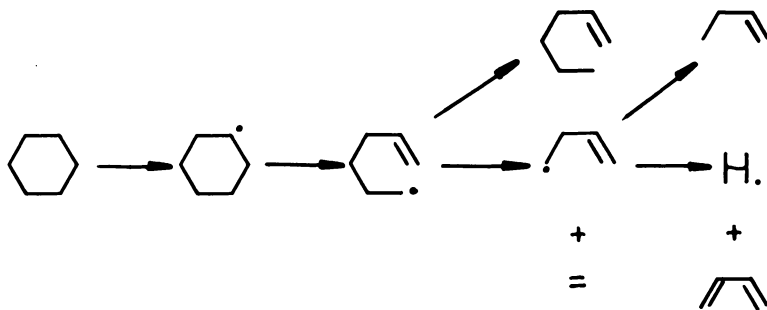


Figure 1. Cyclohexane pyrolysis pathways

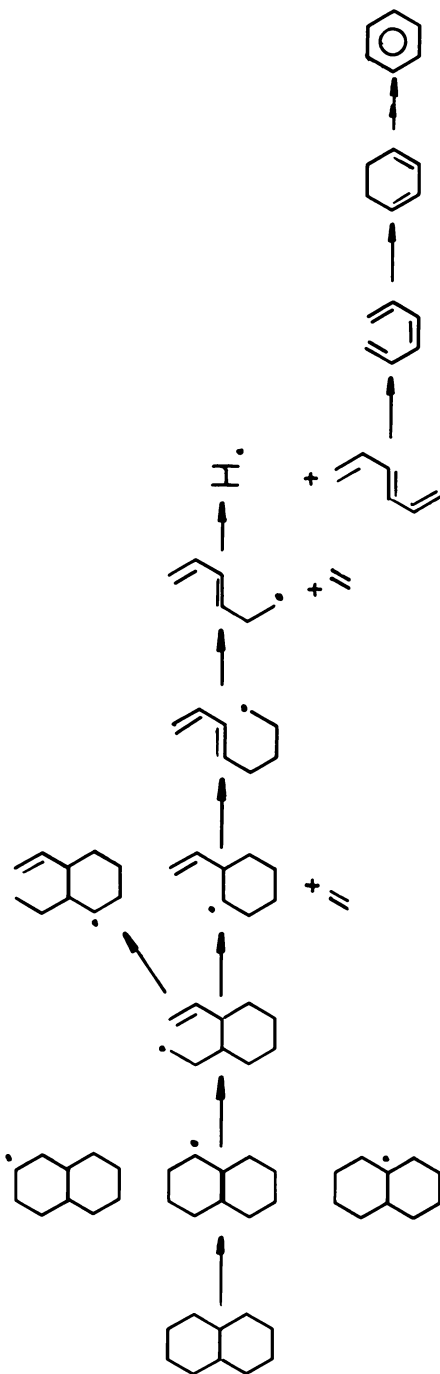


Figure 2. Decahydronaphthalene pyrolysis pathways

2-decalyl radical to products. It should be noted that with these relatively larger radicals, the classical β -scission reaction must compete with others such as Rice-Kossiakoff isomerizations, which are capable of switching the pathway along alternate branches; this has the effect of widening the product spectrum compared with that which a primary decomposition scheme would predict. Despite such difficulties, pyrolysis pathways inferred for each of the decalyl radicals derived from DHN are in accord with the main features of the observed DHN product spectra, giving the order of the yields of ethylene, butadiene, and benzene, and the ratios of methane/ethylene and propylene/ethylene.

Finally, Figure 3 shows pathways for PHP pyrolysis in two parts: (a) for perhydrophenanthrene, the main constituent, and (b) for octahydrophenanthrene, the main impurity. The pathway in Figure 3a commences in classical Rice-Herzfeld fashion, with hydrogen abstraction from the 10 position (this is one of seven possible abstraction positions); the resulting radical undergoes three successive beta C-C bond scissions and a final hydrogen atom elimination, leading to the 'primary' unsaturated products of ethylene, 1,3-butadiene, and 1,3,5-hexatriene. The hexatriene is unstable relative to its 1,3-cyclohexadiene isomer, the pericyclic pathway shown proceeding through electrocyclic ring closure of a butadiene moiety to cyclobutene, followed by a 1,3-sigmatropic-alkyl migration (alternately, the hexatriene could isomerize to the all-cis form which undergoes electrocyclic ring closure). Finally, 1,3-hexadiene pyrolysis leads to benzene in high yields (7) by a radical mechanism. The pathway in Figure 3b, with an aromatic substrate, starts with hydrogen abstraction from the 2 position; this leads to a radical in which β scission either requires rupture of the strong 1-11 bond or forms a nonpropagating benzylic radical at the 4 position, making hydrogen-atom elimination a likely alternative. The molecule produced now contains a 1,4-dihydronaphthalene moiety, which is prone to pericyclic group transfer (1,4 elimination) with formation of the corresponding naphthalene moiety. This type of pathway will evidently cause any originally hydroaromatic substrate to revert to its fully aromatic analog.

The preceding pathways can be applied to the observed pyrolysis yield patterns using elementary graph theory which makes use of substrate topology. As seen in Figure 4, the graph of each substrate is simply its chemical structure; cyclohexane and all monoalicyclic compounds contain only methylene-carbon atoms, C-(C)₂(H)₂, whereas DHN and PHP and fused-ring alicyclic compounds in general contain, in addition, branching carbon atoms of the type C-(C)₃(H). This substrate topology is compactly summarized by means of the Adjacency (or 'A') Matrix in which an element $a_{ij} = 1$ if i and j are bonded and 0 otherwise; the sum of any row i , called the 'degree' of vertex i , is evidently the number of

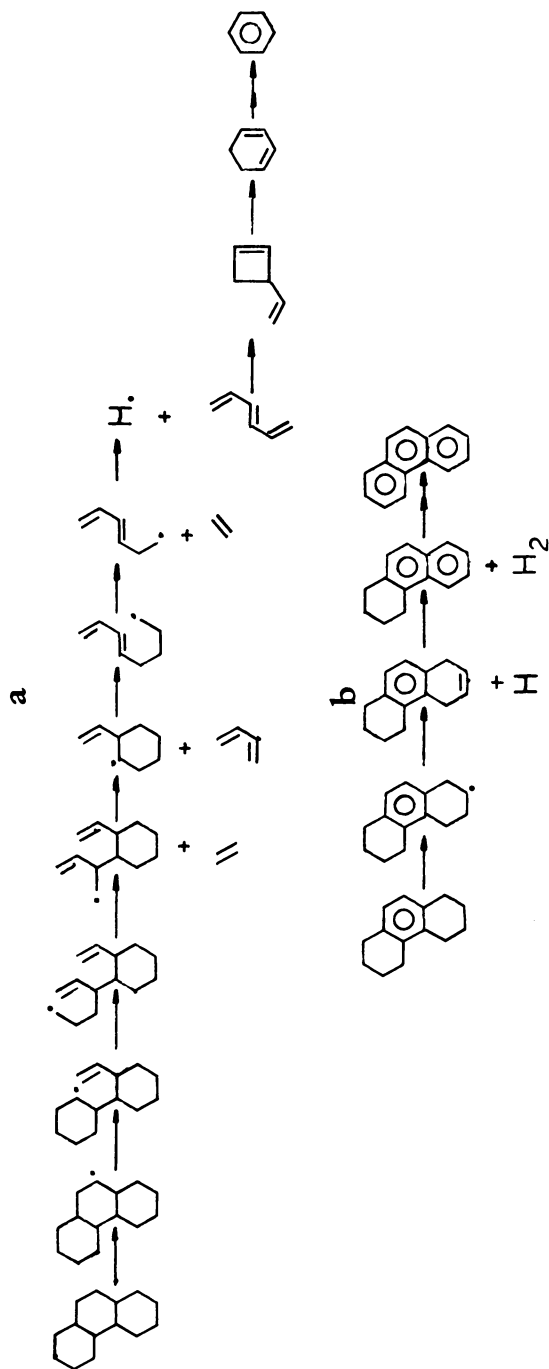


Figure 3. Pyrolysis pathways for perhydrophenanthrene sample (PHP). (a) Perhydrophenanthrene, (b) *sym*-octahydrophenanthrene.

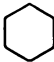
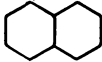
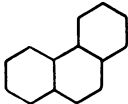
| Substrate | <i>CYH</i> | <i>DHN</i> | <i>PHP</i> |
|----------------|---|--|--|
| Structure |  |  |  |
| A Matrix | 010001 101000 010100 001010 000101 100010 | 0100000001 1010000000 0101000000 0010100010 0001010000 0000101000 0000010100 0000001010 0001000101 1000000010 | 01000000000001 10100000000000 01010000000000 00101000000010 00010100010000 00001010000000 00000101000000 00000010100000 00000001010000 00001000101000 0000000010100 0000000001010 0001000000101 1000000000010 |
| Vertices | | | |
| Degree 2 | 6 | 8 | 10 |
| Degree 3 | 0 | 2 | 4 |
| Cycles | 1 | 3 | 6 |
| Girth | 6 | 6 | 6 |
| Circumference | 6 | 10 | 14 |
| Diameter | 3 | 5 | 7 |
| Longest 2-path | 6 | 3 | 3 |

Figure 4. Substrate graphs

C–C bonds to atom i . Now since pyrolysis by free-radical paths essentially involves β -scission reactions that break C–C bonds, it would appear that all possible reaction pathways available to a substrate exist on its A matrix, which becomes progressively sparser as reaction proceeds. Inspection of the respective A matrices of CYH and DHN show them to possess an essentially different structure; thus A (CYH) possesses only vertices of degree 2 whereas A (DHN) has vertices of degree 2 and 3, the latter branch points increasing the multiplicity of pathways and thus smearing out the product distribution for DHN relative to the rather sharp distribution for CYH. On the other hand, the A matrices of DHN and PHP show remarkable similarity: they possess the same types of vertices, of degrees 2 and 3; they have many cyclic paths, with appreciable disparity between the shortest (girth) and the longest (circumference), which

leads to broad product distributions. Lastly, it should be noted that β -scission reactions can yield ethylene only when the α bond is between methylene carbons, otherwise a substituted olefin will result. In graph-theoretic terms, therefore, ethylene production should depend primarily on the longest path available among vertices of degree 2 (and only 2) in the substrate. From Figure 4 it is seen that in CYH the longest 2-path has length six whereas in each of DHN and PHP the longest 2-path length is only three, with two such paths available. Graph theory thus suggests that ethylene yields from each of DHN and PHP should be approximately equal and appreciably lower than from CYH, which accords with the experimental results.

Two consequences of the present data for practical pyrolyses are worth mentioning in conclusion. First, virgin feedstocks rarely contain appreciable quantities of unsubstituted alicyclic compounds, and therefore DHN and PHP, which possesses branched carbon atoms, should be much better analogs of the naphthenic fractions than is CYH. Equivalently, we should expect pyrolysis patterns of CYH to be greatly altered by substitution, although in all cases branching (vertices of degree > 2) should decrease ethylene yields. Second, in regard to upgrading petrochemical feedstocks and coal liquids by catalytic hydrogenation, the example in Figures 3a and 3b is instructive. It shows that the polynuclear aromatic molecules contained in the original feedstock must be hydrogenated to their fully alicyclic analogs to provide desirable pyrolysis products; partial hydrogenation leads to hydroaromatic molecules which tend to revert to their fully aromatic form upon pyrolysis, contributing mainly to the relatively undesirable fuel-oil fraction. Put another way, the incremental yield of desirable olefinic products increases most strongly as the feedstock aromatics content approaches zero.

Literature Cited

1. Korosi, A.; Woebecke, H. N.; Virk, P. S. *Am. Chem. Soc., Div. Fuel Chem., Prepr.* **1976**, *21*, 190.
2. Zdonik, S. B.; Green, E. J.; Hallee, L. P. *Oil Gas J.* **1967**, *64*.
3. Fabuss, B. M.; Kafesjian, R.; Smith, J. O.; Satterfield, C. N. *Ind. Eng. Chem., Process Des. Dev.* **1964**, *3*, 248.
4. Linstead, R. P. *J. Am. Chem. Soc.* **1942**, *64*, 1985.
5. Kochi, J. K. 'Free Radicals'; John Wiley & Sons: 1973.
6. Woodward, R. B.; Hoffman, R. "The Conservation of Orbital Symmetry"; Verlag Chemie GmbH Weinheim; 1970.
7. Benson, S. W.; Shaw, R. *J. Am. Chem. Soc.* **1967**, *89*, 5351.

RECEIVED September 28, 1978.

Pyrolysis of Virgin and Hydrogenated Gas Oils

P. S. VIRK¹, A. KOROSI, and H. N. WOEBCKE

Stone & Webster Engineering Corp., P.O. Box 2325, Boston, MA 02107

Experimental data are presented to show how feedstock hydrogenation alters the yields of chemicals available from pyrolysis of a kerosene and of an atmospheric gas oil, both originating from the same crude. Hydrogenated feedstocks were derived from each of the virgin feedstocks by catalysis, with hydrogen uptake 500 ± 50 scf/bbl. Pyrolysis experiments were conducted at commercial steam-cracking conditions in a tubular flow reactor. The two virgin feedstocks yielded product spectra which were quite similar for compounds with less than eight carbon atoms but which differed greatly in total gasoline and fuel oil. Corresponding component yields from the hydrogenated kerosene and hydrogenated gas oil indicated, in each case, an increased production of olefins and an appreciable reduction in fuel oil relative to the virgin feedstocks.

The objective of the present work was to determine quantitatively the influence of feedstock hydrogenation upon the yields of petrochemicals available from pyrolysis of petroleum distillates. This subject is currently of considerable commercial significance (particularly in regard to gas oil feedstocks) because feed hydrogenation offers the potential for increased light olefin yields, decreased pyrolysis fuel oil yields, and possible operating benefits, such as longer cracking furnace runs.

¹ Also, Department of Chemical Engineering, Massachusetts Institute of Technology, Cambridge, MA 02139.

Previous literature contains very little information concerning the effect of feedstock hydrogenation (1, 2) on pyrolysis yields, and previously published works provide virtually no quantitative information. In this work, two virgin feedstocks were used, a kerosene of boiling range 177°–266°C and an atmospheric gas oil of boiling range 248°–336°C, both originating from the same South American crude. Hydrogenated feedstocks were derived from each of the virgin feedstocks by catalytic hydrogenation, with a hydrogen uptake of about 500 scf/bbl in each case. Both sets of virgin and hydrogenated feedstocks were then pyrolyzed at commercial steam-cracking conditions. Their detailed product yield patterns provide a quantitative basis for assessment of the effect of hydrogenation; these product yield data can further be related to chemical composition changes, available from feedstock analyses before and after hydrogenation.

Sample Characterization

Both the virgin kerosene and gas oil samples were obtained directly (by distillation) from a South American crude oil and were used in the present experiments without any further treatment. Characterization of these feedstocks is attempted in Table I (Virgin column), which contains information regarding specific gravity, elemental analyses, distillation data, and hydrocarbon group types. Further details are provided for some of the hydrocarbon groups, namely normal paraffin average carbon numbers, alicyclics breakdown by rings, and aromatics analyses both by mass spectrometry and proton nuclear magnetic resonance (NMR) spectroscopy. The NMR analyses, which were obtained by a modified Brown–Ladner treatment (3, 4) of the data, provide the following information for the average molecule in the aromatic fraction: the number of aromatic carbons (C_a), the number of substituents (C_s), the average chain length per substituent (n_s), and the aromaticity ($f_a = C_a/[C_a + n_s C_s]$). Comparison of the characterization data for the virgin feedstocks reveals that between the kerosene (KE) and gas oil (GO) samples, the latter has the higher specific gravity, lower hydrogen content, and higher boiling point, all of which are the expected results. In regard to hydrocarbon group types, both feedstocks are highly naphthenic, the alicyclic fraction being the largest in each case; both samples contain about 35 wt % paraffins, with the absolute amount of normal paraffins and also the normal-to-isoparaffin ratio rather higher in the GO. The average carbon number for the *n*-paraffin fraction, 11 and 16 carbons for the KE and GO, respectively, essentially follow the boiling ranges of these samples. Alicyclic ring breakdowns show that single-ring alicyclics are dominant in

Table I. Feedstock Characterization

| Type | Feedstock | | | |
|---|-----------------------------|--------------------------|-----------------------------|--------------------------|
| | Virgin | | Hydrogenated | |
| | <i>Kero-</i> <i>sene</i> | <i>Gas</i> <i>Oil</i> | <i>Kero-</i> <i>sene</i> | <i>Gas</i> <i>Oil</i> |
| Sample Code | <i>KE</i> | <i>GO</i> | <i>HKE</i> | <i>HGO</i> |
| Specific gravity 15/15 C | 0.822 | 0.861 | 0.810 | 0.843 |
| Elemental analysis (wt %) | | | | |
| carbon | 86.53 | 86.97 | 85.83 | 86.20 |
| hydrogen | 13.42 | 12.90 | 14.17 | 13.76 |
| sulfur | 0.05 | 0.13 | 0.04 | 0.04 |
| Distillation ASTM D86 (vol % vs. °C) | | | | |
| 0 (IBP) | 177 | 248 | 174 | 212 |
| 10 | 188 | 257 | 186 | 250 |
| 30 | 196 | 268 | 195 | 266 |
| 50 | 202 | 281 | 202 | 279 |
| 70 | 209 | 300 | 211 | 300 |
| 90 | 219 | 326 | 226 | 331 |
| 100 (EP) | 226 | 336 | 244 | 343 |
| Hydrocarbon group types (wt %) | | | | |
| <i>n</i> -paraffins | 11.5 | 14.9 | 11.9 | 10.0 |
| <i>i</i> -paraffins | 22.2 | 23.3 | 22.8 | 29.4 |
| alicyclics | 47.4 | 31.0 | 62.5 | 48.7 |
| aromatics | 18.9 | 30.8 | 2.8 | 11.9 |
| <i>n</i> -Paraffin average carbon number | 11 | 16 | 11 | 16 |
| Alicyclic ring breakdown (wt %) | | | | |
| 1 | 34.0 | 13.9 | 46.6 | 22.0 |
| 2 | 11.4 | 12.4 | 13.4 | 19.2 |
| 3 | 2.0 | 4.7 | 2.5 | 7.5 |
| Aromatic analysis MS (wt %) | | | | |
| alkyl benzenes | 9.4 | 4.8 | 2.6 | 3.8 |
| indanes, indenes, tetralins | 4.6 | 8.0 | 0.0 | 5.6 |
| alkylnaphthalenes | 3.8 | 10.0 | 0.0 | 0.7 |
| triaromatics | 0.0 | 2.2 | 0.0 | 0.4 |
| Aromatic analysis NMR (per aver- age molecule in aromatic fraction) | | | | |
| aromatic carbons C_a | 8.0 | 8.4 | 7.2 | 7.9 |
| substituents C_s | 2.8 | 2.2 | 3.0 | 3.1 |
| substituent chain length n_s | 2.0 | 7.7 | 2.0 | 3.8 |
| aromaticity f_a | 0.59 | 0.33 | 0.55 | 0.40 |

each case. Aromatic fraction analysis by mass spectrometry (MS) shows that alkylbenzenes predominate in the KE sample with some alkylnaphthalenes and no triaromatics whereas in the GO, alkylnaphthalenes are the major aromatic component with some alkylbenzenes and a trace of triaromatics. The NMR analyses are especially interesting because they reveal an essential difference between the aromatic fractions; thus the average aromatic molecule in the KE sample contains many short-chain substituents whereas in the GO sample, it contains relatively fewer substituents with appreciably longer chain lengths.

The hydrogenated feedstocks were prepared from the virgin samples by catalytic hydrogenation under typical commercial conditions. Characterization of the hydrogenated samples, HKE and HGO, respectively, is reported in Table I (Hydrogenated column), with a format identical to that of the Virgin column of the same table. Comparison of the virgin and hydrogenated samples shows that for both the kerosene and gas oil, the specific gravity decreased slightly, the hydrogen content increased appreciably, and the distillation data were virtually unchanged. It is worth noting that the hydrogen uptake of sample HKE relative to KE corresponds to 470 scf/bbl of the virgin sample while that of sample HGO relative to GO corresponds to 560 scf/bbl. Data of the hydrocarbon group type show that between each of KE and HKE and of GO and HGO the total paraffins remain essentially constant within experimental error while the decrease in aromatics is approximately matched by the increase in alicyclics. Average carbon numbers for the *n*-paraffin fraction were unchanged by hydrogenation. Among alicyclic ring compounds, monoalicyclics increased the most in both cases; there was also a substantial increase in the dialicyclic fraction in HGO relative to GO. In the aromatic fractions, the MS data show a similar pattern in both cases; following hydrogenation, the absolute aromatics content decreases and the remaining aromatic fraction contains a greater proportion of monoaromatic compounds. Thus, only alkylbenzenes remain in HKE whereas the original KE contained alkylnaphthalenes as well; similarly, the residual aromatics in HGO contain just a trace of alkylnaphthalenes and triaromatics whereas the original GO had alkylnaphthalenes as the major aromatic type as well as some triaromatics. This suggests that the main chemical transformation involved in the present hydrogenations was the progressive conversion of aromatic molecules to their alicyclic analogs. Some ring opening also appears to have occurred in both cases since the increase in dialicyclic and trialicyclic compounds was somewhat less than the reduction in multiple-ring aromatic compounds; ring opening also is suggested by the NMR data, which show that the average number of substituents increased while their average chain length decreased in HGO relative to GO.

Pyrolysis Experiments

The pyrolysis experiments were conducted in an electrically heated once-through tubular flow reactor designed to simulate the time-temperature history experienced in commercial steam-cracking operations. Reactor effluent compositions were ascertained by gas chromatograph and mass spectrometer analyses of each of five fractions obtained in a downstream separation train. Overall material and hydrogen balances always could be effected, with typical closures of 98 ± 2 wt %.

Detailed pyrolysis results for each of the virgin and hydrogenated feedstocks at comparable conditions are presented in Table II under pyrolysis conditions and product yields.

Table II. Summary of Pyrolysis Experiments

| | <i>Sample*</i> | | | |
|------------------------------------|----------------|-----------|------------|------------|
| | <i>KE</i> | <i>GO</i> | <i>HKE</i> | <i>HGO</i> |
| <i>Pyrolysis Conditions</i> | | | | |
| Steam/hydrocarbon weight ratio | 0.8 | 1.0 | 0.8 | 1.0 |
| Residence time (sec) | 0.3 | 0.3 | 0.3 | 0.3 |
| Reactor exit pressure (bar abs) | 2.0 | 2.1 | 2.0 | 2.0 |
| Reactor exit temperature (°C) | 835 | 835 | 835 | 835 |
| <i>Product Yields (wt %)</i> | | | | |
| Hydrogen | 0.55 | 0.54 | 0.69 | 0.64 |
| Methane | 9.11 | 9.19 | 10.75 | 10.28 |
| Acetylene | 0.10 | 0.27 | 0.31 | 0.30 |
| Ethylene | 17.36 | 18.55 | 19.83 | 21.00 |
| Ethane | 2.87 | 2.93 | 3.31 | 3.16 |
| Propadiene, propyne | 0.29 | 0.31 | 0.53 | 0.52 |
| Propylene | 12.04 | 13.09 | 13.89 | 13.67 |
| Propane | 0.47 | 0.38 | 0.54 | 0.42 |
| 1,3-Butadiene | 4.07 | 4.59 | 5.30 | 5.17 |
| Butenes | 5.53 | 5.48 | 6.12 | 5.77 |
| C4 and lighter | 52.39 | 55.33 | 61.27 | 60.93 |
| C5 olefins, diolefins | 1.76 | 2.18 | 3.04 | 2.51 |
| Benzene | 4.77 | 4.50 | 6.03 | 6.22 |
| Toluene | 4.19 | 3.30 | 5.21 | 4.76 |
| C8 Aromatics | 4.20 | 2.20 | 3.23 | 2.97 |
| C9+ to 205 C | 16.03 | 6.60 | 12.96 | 8.23 |
| C5 to 205 C | 30.95 | 18.78 | 30.47 | 24.69 |
| Pyrolysis fuel oil (≥ 205 C) | 16.66 | 25.89 | 8.26 | 14.38 |

* Feedstock sample abbreviations are as follows: KE, virgin kerosene; GO, virgin gas oil; HKE, hydrogenated kerosene; and HGO, hydrogenated gas oil.

The data in Table II pertaining to pyrolysis conditions shows that all four feedstocks were pyrolyzed under substantially similar conditions, namely steam-to-hydrocarbon weight ratios of 0.9 ± 0.1 , residence times of 0.3 sec, reactor exit pressures of 2.0 bar absolute, and reactor exit temperatures of 835°C. Care also was taken to maintain identical axial temperature profiles in the reactor for each of these runs. No unambiguous measure of substrate conversion during pyrolysis is possible for distillate feedstocks of the type used in the present experiments; in terms of the empirical kinetic severity function of Zdonik et al. (5), all of the present experiments were conducted at a severity of about 2.

Pyrolysis product spectra are shown in Table II and merit a comparative description. Considering first the virgin feedstocks KE and GO, it is apparent that these provided very similar quantities of low molecular weight products from hydrogen to C5s, while the KE sample yielded more benzene, toluene, and xylene (BTX fraction) and appreciably less pyrolysis fuel oil (boiling range $\geq 205^\circ\text{C}$) than did the GO sample. Closer scrutiny of the data shows that both the hydrogen and methane yields from the virgin feedstocks were essentially identical, the ethylene and propylene yields obtained were each about 1 wt % greater from the GO than from the KE, with the ratio of propylene: ethylene 0.70 ± 0.01 in each case; and the proportion of BTX components differed somewhat, being B:T:X::1:0.75:0.5 for the GO and B:T:X::1:1:1 for KE. Overall, the virgin feedstocks yielded product spectra which were quite similar for compounds with less than eight carbon atoms but which differed considerably in total gasoline and fuel oil, the gasoline yield being about 10 wt % greater and that of fuel oil about 10 wt % smaller from the KE compared with GO. Considering next the hydrogenated feedstocks HKE and HGO, it can be seen that these two also gave virtually identical yields of all components from hydrogen to the C8 aromatics, with HKE yielding about 6 wt % more pyrolysis gasoline and about 6 wt % less pyrolysis fuel oil than did the HGO. Finally, a comparison of the hydrogenated with the virgin feedstocks reveals, in both cases, an increase in the olefins yields and an appreciable reduction in the pyrolysis fuel oil yields. Thus the yields (ethylene, propylene, butadiene, benzene, gasoline, fuel oil) in weight percent of feed for the kerosene samples were, respectively, HKE (20, 14, 5, 6, 31, 8) vs. KE (17, 12, 4, 5, 31, 17) while the corresponding yields for the gas oil samples were, respectively, HGO (21, 14, 5, 6, 25, 14) vs. GO (18, 13, 5, 5, 19, 26). It should be noted that the reduction in fuel oil yield was rather greater for the gas oil than for the kerosene, but the corresponding improvement in light olefin yields was comparable in both cases, with pyrolysis gasoline yield increasing for the gas oil while remaining constant for the kerosene.

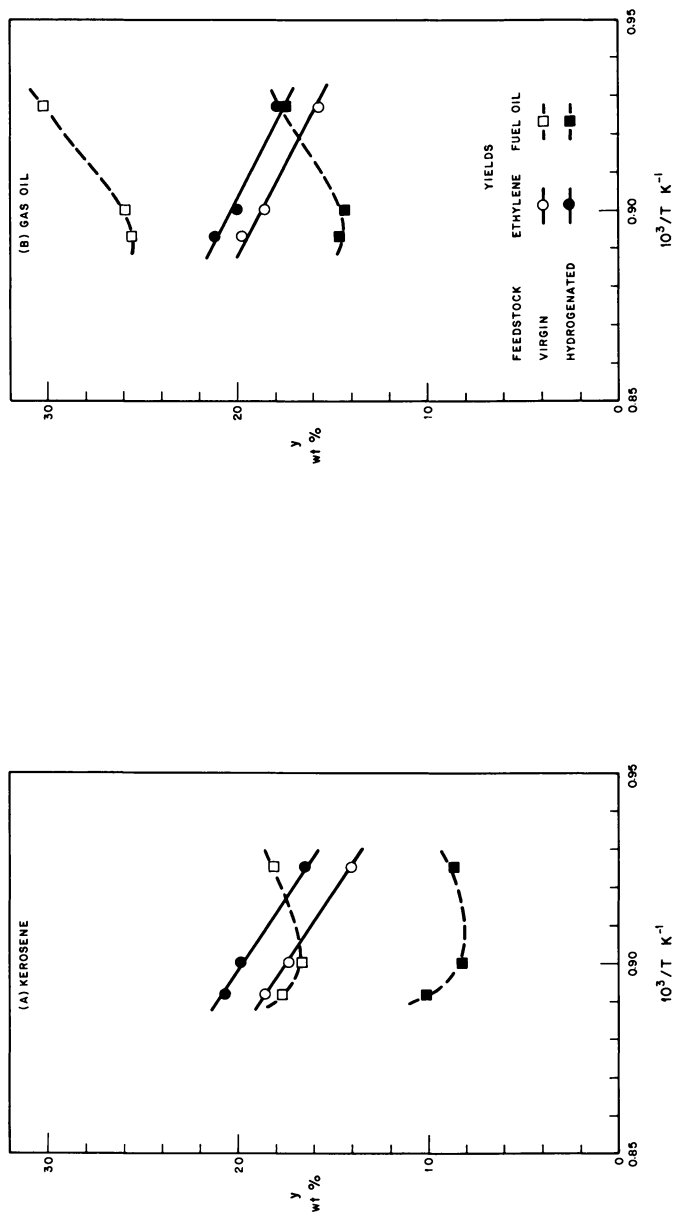


Figure 1. Effect of pyrolysis severity on ethylene and fuel oil yields for virgin and hydrogenated feedstocks. (A) Kerosene and (B) gas oil.

The effect of pyrolysis severity upon the yield spectra for both virgin and hydrogenated feedstocks was obtained from additional experiments in which all conditions were maintained essentially as given in Table I except that reactor exit temperatures were varied from 810° to 850°C. The corresponding variation of ethylene and fuel oil yields (in wt %) with the reciprocal of the reactor exit temperature (in K⁻¹) for each of the kerosene and gas oil feedstocks is indicated in Figures 1a and 1b, respectively; it should be noted that the abscissae of Figure 1 are inversely proportional to the pyrolysis severity function of Zdonik, et al. (5). In Figure 1 it can be seen that the ethylene yield increased monotonically with increasing severity for all feedstocks, with the hydrogenated samples producing on the average about 2 wt % more ethylene than did their virgin precursors at all severities. Also, the fuel oil yield can be seen to decline somewhat with increasing severity in all cases, with the hydrogenated feedstocks yielding appreciably less fuel oil than did their virgin feedstocks; on the average, HKE yielded about 8.5 wt % less fuel oil than did KE while HGO yielded about 12.0 wt % less fuel oil than did GO. Results similar to those shown in Figure 1 could be obtained for all pyrolysis products. From these it could be concluded that whereas the absolute yields of all products were a function of pyrolysis severity, the difference between the yield of a given product obtained from a hydrogenated feedstock and the yield of that product obtained from the virgin feedstock was relatively insensitive to pyrolysis severity over the range of the present experiments.

Discussion

Results obtained with the virgin feedstocks require only brief discussion. Thus the gas (C4 and lighter), pyrolysis gasoline (C5 to 205 C), and pyrolysis fuel oil (> 205 C) yields obtained from the KE sample were, respectively, about equal, appreciably greater than, and much less than those obtained from the GO sample. The observed trends in the gasoline and fuel oil fractions are to be expected since the KE is a lower-boiling distillate than is GO. However, the close equality of the gas yields merits some discussion. Inspection of Table II reveals that the yields of each of ethylene and propylene obtained from GO and from KE were closely comparable (indeed yields from GO exceeded those from KE by about 1 wt %) despite the GO sample having an appreciably higher aromatics content than did the KE sample (*see* Table I), namely 31 vs. 19 wt %. A possible explanation for this apparent anomaly is provided by the respective sample NMR analyses in Table I which suggest that the aromatics in GO possessed relatively longer aliphatic side chains than did those in KE and were therefore able to contribute more effec-

tively to olefins production. Quantitatively, within the aromatic fraction of a feedstock, aromatic carbons and aliphatic carbons alpha to an aromatic ring are incapable of yielding olefins upon pyrolysis so that, in the terminology of Table I, the fraction of these ineffective carbons is $\phi_i = [(C_a + C_s)/(C_a + n_s C_s)]$. For the aromatic fractions of the KE and GO feedstocks, ϕ_i is 0.79 and 0.42, respectively; when these values are multiplied by the respective amounts of the aromatic fractions, the ineffective carbons in the total samples are 14.9 and 12.9 wt % for KE and GO, respectively, which are closely comparable (and, interestingly, differ in the same sense as the observed ethylene and propylene yields).

The gross effect of feedstock hydrogenation was evident from the data contained in Table II and in Figure 1, which showed that for both the kerosene and gas oil feedstocks, hydrogenation increased the yield of the gas fraction (C4 and lighter) and reduced the fuel oil yield. However, the data in Table II are unsuited to direct comparisons between hydrogenated and virgin feedstocks because of the inherently small differences involved. Since the principal effect of hydrogenation is to reduce the aromatics content of the feedstock, it is appropriate to consider all yield differences per unit of aromatics content reduction. Thus, for any pyrolysis product, say j , we define a differential yield D_j as follows:

$$D_j = \frac{(y_j^h - y_j^v) 100}{(w_A^v - w_A^h)}$$

where: D = differential yield of product (wt %), y = yield of product (wt %), w_A = aromatic content in feed (wt %), j = product, h = hydrogenated feedstock, v = virgin feedstock. From the foregoing definition it follows that the differential yields of all products must sum to zero: $\sum_{\text{all } j} D_j = 0$. Pyrolysis data for each pair of feedstocks (HKE, KE) and (HGO, GO) were translated to differential yields as defined above, and the results are presented in Table III. The first two rows of Table III show the aromatics content reduction ($w_A^v - w_A^h$) and the corresponding hydrogen uptake in scf/bbl for each pair of feedstocks. While both these quantities are somewhat higher for the gas oil than for the kerosene, the aromatic content reduction per unit of hydrogen uptake is essentially the same for both feedstocks. Turning to the differential product yields in Table III, we consider first the broad results in terms of the gas, gasoline, and fuel oil fractions; it can be seen that D_{gas} , D_{gasoline} , and $D_{\text{fuel oil}}$ are respectively 55, -3, and -52 for the kerosene and 30, 31, and -61 for the gas oil. Thus, hydrogenation caused similar reductions in the fuel oil yield obtained from both feedstocks; this fuel oil reduction was offset by a quantitatively equal increase in gaseous products in the case of kerosene but was equally distributed among gas and gasoline products in the case

Table III. Differential Yield Spectra per Unit of Aromatics Reduction

| | <i>Feedstock</i> | |
|---|-----------------------------|----------------------------|
| | <i>Kerosene</i> (HKE-KE) | <i>Gas Oil</i> (HGO-GO) |
| Aromatics Reduction (wt %) | 16.1 | 18.9 |
| Hydrogen Uptake (scf/bbl) | 470 | 560 |
| <i>Differential Product Yields (wt %)</i> | | |
| Hydrogen | 0.87 | 0.53 |
| Methane | 10.19 | 5.77 |
| Acetylene | 1.30 | 0.16 |
| Ethylene | 15.34 | 12.96 |
| Ethane | 2.73 | 1.22 |
| Propadiene, propyne | 1.49 | 1.11 |
| Propylene | 11.49 | 3.07 |
| Propane | 0.43 | 0.21 |
| 1,3-Butadiene | 7.64 | 3.07 |
| Butenes | 3.66 | 1.54 |
| C4 and lighter | 55.16 | 29.63 |
| C5 olefins, diolefins | 7.89 | 1.74 |
| Benzene | 7.83 | 9.10 |
| Toluene | 6.34 | 7.72 |
| C8 Aromatics | -6.02 | 4.07 |
| C9+ to 205 C | -19.07 | 8.64 |
| C5 to 205 C | -2.98 | 31.27 |
| Pyrolysis fuel oil (≥ 205 C) | -52.17 | -60.90 |

of the gas oil. Considering the gaseous components in more detail, Table III shows that for both feedstocks, all products within the gas fraction have positive differential yields, i.e., are increased by hydrogenation, with ethylene having the highest magnitude and methane, propylene, and butadiene being the other major components. The values of absolute D_j for all gaseous components are higher for the kerosene than for the gas oil, and their relative proportions also appear to differ somewhat; for example, the ratio $D_{\text{ethylene}}:D_{\text{gas}} = 0.28$ for kerosene and 0.44 for gas oil while the ratios $D_{\text{methane}}:D_{\text{ethylene}}$, $D_{\text{propylene}}:D_{\text{ethylene}}$, and $D_{\text{butadiene}}:D_{\text{ethylene}} = 0.66, 0.75,$ and $0.50,$ for kerosene and 0.45, 0.24, and 0.24 for gas oil, respectively. In regard to the gasoline fraction, for the kerosene feedstocks the relatively larger positive D_j values for the C5 to C7 components were offset by equally large negative D_j values for the C8 and C9 to 205 C components to provide a negligible net differential yield $D_{\text{gasoline}} = -3$. For the gas oil, all the gasoline components from C5 to C8 possess positive D_j while $D_{\text{C9 to 205}} \sim 0$, giving an appreciably positive net differential yield $D_{\text{gasoline}} = 31$.

Chemical interpretation of the differential yield data requires the recognition (from Table I) that feedstock hydrogenation essentially converted aromatic molecules to their alicyclic analogs. Therefore the observed differential yield for any component j is in the nature of a difference between the yield of j obtained from pyrolysis of an alicyclic molecule and that obtained from pyrolysis of its aromatic precursor, averaged over the species present in the original feedstock, which were hydrogenated. As discussed earlier, the aromatic species contained in the virgin kerosene were predominantly alkyl benzenes and naphthalenes with two or three short-chain substituents ($n_s = 2.0$) while those in the gas oil were mainly alkyl naphthalenes with two relatively long-chain substituents ($n_s = 7.7$). In regard to fuel oil yields, pyrolysis of dialicyclic compounds under the present conditions provides, typically (6), $y_{\text{fuel oil}} \sim 15$ while their diaromatic precursors are expected to yield mainly fuel oil, say $y_{\text{fuel oil}} \sim 85$, so that we may expect that the differential fuel oil yield will be a large negative number, $D_{\text{fuel oil}} \sim -70$. The experimentally observed $D_{\text{fuel oil}}$ is indeed approximately of this magnitude in both cases. In regard to the gasoline fraction yield, dialicyclic compounds might typically provide $y_{\text{gasoline}} \sim 30$ while the yield from diaromatics is virtually zero, leading to an expected $D_{\text{gasoline}} \sim 30$. The observed D_{gasoline} for the gas oil feedstocks is of this expected magnitude. In the kerosene case, however, the above simple picture is complicated because appreciable amounts of the virgin feedstock itself boil in the gasoline range, specifically among the C8 and C9 to 205 C components (see Table I). The gasoline yield from pyrolysis of the virgin feedstock therefore includes some residual aromatic feed materials among the C8 and C9+ to 205 C components; feed hydrogenation converts these C8 to 205 C aromatic materials to alicyclic compounds which pyrolyze to lower molecular weight products. There is thus a trade-off between the increase in lighter components (C5 to C7) vs. a reduction in the heavier components (C8, C9 to 205 C), and we should therefore expect that for the kerosene feedstocks, D_{gasoline} should be of rather small magnitude with either positive or negative sign. This accords with the experimentally observed $D_{\text{gasoline}} = -3$. Finally, in regard to differential gas yields, we had earlier noted that in any aromatic molecule, the aromatic and alpha carbon atoms are incapable of yielding gas upon pyrolysis, and the fraction of such ineffective carbons was derived to be $\phi_i = 0.79$ and 0.41 , respectively, for the aromatic portions of the virgin kerosene and gas oil. Following feedstock hydrogenation, the previously ineffective carbons are now no longer so, and we should therefore expect the differential gas yield to be proportional to $100 \phi_i$, with the proportionality constant close to unity; i.e., $D_{\text{gas}} \sim 100 \phi_i$. The experimentally observed D_{gas} for both feedstocks are lower than that of the respective $100 \phi_i$, with the proportionality constants

($D_{\text{gas}}/100 \phi_i$) about 0.70 in each case; from the latter it is seen that very nearly ($D_{\text{gas, kerosene}}/D_{\text{gas, gas oil}} = (\phi_{i, \text{kerosene}}/\phi_{i, \text{gas oil}})$). Among individual gas components, only the ethylene yields merit comment. Since the aromatics in kerosene were more heavily substituted than those in the gas oil ($C_s/C_a = 0.35$ and 0.26 , respectively), the hydrogenated kerosene should possess, correspondingly, more heavily substituted alicyclic compounds than should the hydrogenated gas oil. Inasmuch as substitution tends to decrease ethylene yields, we should expect that the proportion of ethylene in the differential gas should be lower for kerosene than for gas oil, and this was seen to be the case earlier during the discussion of Table III.

In conclusion, it is worth considering some practical implications of the present results. First it should be noted that we have focused exclusively on product yields whereas in practical operations, the effect of feed hydrogenation upon pyrolysis furnace operations is also of great importance. Since the fouling propensity of a given feedstock is known (7) to be related to its enthalpy of formation and since hydrogenation, which is exothermic, lowers the enthalpy of formation, we should theoretically expect the hydrogenated feedstocks to be superior to the virgin feedstocks in regard to furnace operation; however, this remains to be experimentally tested. Second, the present results were obtained at one level of hydrogenation for each feedstock, and it would be cogent to ascertain the effect of hydrogenation depth upon differential yields. In principle, for a given feedstock, all D_j should be a function of hydrogenation depth, say $h = (w_A^v - w_A^h)/w_A^v$, which varies from zero to unity. Experimental work is in progress to determine the precise variation of D_{gas} vs. h for representative feedstocks. Finally, the data in Table III are of commercial significance in the following way. Since hydrogen uptake per unit of aromatic reduction was equal for both feedstocks, the differential yield spectra provide a direct comparison of how effectively the hydrogen was used. For increasing olefins production (i.e., D_{gas}), it is clear that hydrogenation of the kerosene feedstock was almost twice as effective as hydrogenation of the gas oil. A more complete economic assessment requires appropriate unit prices p_j for all components in Table III, the net product value enhancement being given by the summation $\sum_{\text{all } j} D_j p_j$. Use of representative unit prices suggest that in the present case, net product value enhancement for the kerosene was about 1.25 times that for the gas oil. The conclusion to be drawn is that, in regard to olefins production, catalytic hydrogenation was more effective in upgrading the lighter of two feedstocks. Further experiments using alternate catalytic hydrogenation procedures and still lighter feedstocks (e.g., aromatic naphthas) are in progress to indicate how broadly the preceding conclusion applies.

Literature Cited

1. Nowak, S.; Keil, G.; Gunschel, H.; Pechstein, G. *Proc. World Pet. Cong, 9th, 1975*, Paper 19 (4).
2. Sze, M. C.; Kales, N. C. U.S. Patent 3 720 729, 1973.
3. Brown, J. K.; Ladner, W. R. *Fuel* **1960**, *39*, 87.
4. Clutter, D. R.; Petrakis, L.; Stenger, R. L.; Jensen, R. K. *Anal. Chem.* **1972**, *44*, 1395.
5. Zdonik, S. B.; Green, E. J.; Hallee, L. P. *Oil Gas J.* **1969**, *66*(7), 192.
6. Wuebcke, H. N.; Korosi, A.; Virk, P. S. *Am. Chem. Soc., Div. Pet. Chem., Prepr.* **1978**, *23*, 1159.
7. Keep, C. W.; Baker, R. T. K.; France, J. A. *J. Catal.* **1977**, *47*, 232.

RECEIVED September 5, 1978.

Feedstocks from Paraho Shale Oil

C. G. RUDERSHAUSEN and J. B. THOMPSON

Experimental Station, E. I. du Pont de Nemours & Co., Inc.,
Wilmington, DE 19898

Shale oil from internally fired retorting to 482°C was converted in 36% yield to BTX and C₂-C₄ olefins. In a scouting program with bench-scale equipment and without recycle, the process entailed (1) distillation, (2) hydrocracking, (3) hydrotreating to further reduce heteroatoms, (4) reforming, and (5) steam pyrolysis. Established and readily available catalysts were used for steps 2, 3, and 4. The yield to chemical feedstocks could probably be improved significantly by using state-of-the-art catalysts with well-optimized process conditions, by reducing nitrogen in reformer feed, and by increasing severity in steam pyrolysis to favor olefins.

For about 50 years, petroleum and natural gas have replaced conventional coal tar derivatives as the essential sources of large-scale organic chemicals in the United States. The present petrochemical industry has evolved to convert these raw materials to commodity-scale products such as benzene, toluene, ethylene, butadiene, and propylene, together with methane-based ammonia and methanol. A large and diverse chemical industry has grown up relying on these petrochemicals as feedstocks.

More recently, the chemical industry has seen the need to look beyond petroleum to processes for converting nonpetroleum materials to feedstocks (1, 15). These processes, all fuel-oriented but having feedstock potential in varying degrees, usually deal with coal-derived liquids, shale oil, and biomass.

Shale oil is of special interest here because of its comparatively high hydrogen content, similar to that for petroleum and about twice that in coal. This feature is especially attractive for conversion to fuels and feedstocks. A short but comprehensive review of the huge oil shale potential in the United States is given in Ref. 1; it notes some of the

processes recently under development for oil recovery. Oil shale was studied in the fifties as a source of chemicals; in a review article by Thorne (2), by-product chemicals and liquid fuels potential were specifically noted. High temperature retorting—actually a steam cracking operation—yielded up to 90 pounds of C_2 – C_4 olefins per ton of high quality shale (30 gal oil/ton). But conventional retorting gave a heavy oil very high in nitrogen and therefore undesirable for a petroleum refiner. A recent view on oil shale development is presented comprehensively in Ref. 3 which notes that widely ranging uncertainties (especially concerning mining techniques, environmental problems, and water supplies) continue to restrain the pace of oil shale development despite the abundance of high quality shale in the United States. Nevertheless, some predictions suggest the availability of as much shale oil as 0.8 million bbl/day by 1990 (17); mostly, if not all, would be from the Green River formation. During a recent three-year test program funded by private companies, 10,000 bbl of shale oil was refined into fuels for specific testing (18).

Objectives

The potential for converting synthetic crudes to chemical feedstocks has been judged in a manner roughly analogous to that tried by the Bureau of Mines (4) and others for refining shale oil to fuels, including gasoline. One of our long-term goals was to find correlations between process results and simple analytical tests of the raw crude. For petroleum, much progress has been made, and refiners can predict rather closely the value of a given crude for a given product mix from analytical tests alone.

In this chapter we will describe some of our initial evaluation work on Paraho shale oil. This initial evaluation was not performed in depth; rather, this first step consisted of chemical characterizations and high-spot, bench-scale processing of oil shale and several other syncrudes for direct comparisons of chemical feedstocks potential. Conventional analytical and petroleum processing techniques were used in the expectation that these would provide reference data on which to base specifically adapted techniques for evaluations of individual syncrudes. The results represent only our first attempts and except for occasional comparisons, are only for Paraho shale oil.

Analytical Characterization

The sample used for the present work was produced by Paraho on October 23, 1975 by using the direct mode (Figure 1), that is, by internal firing using the heat of combustion from coke formed on the rock in a

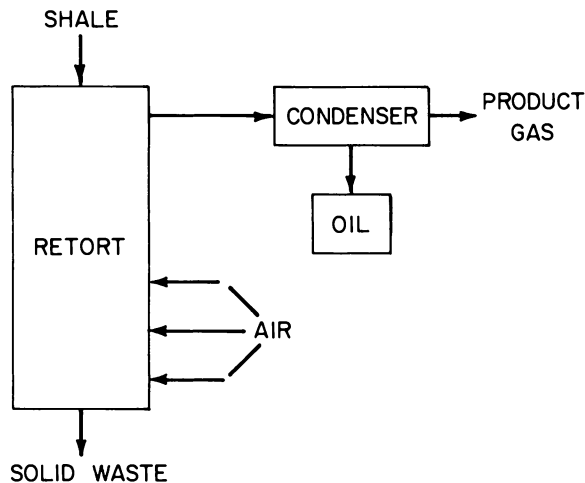
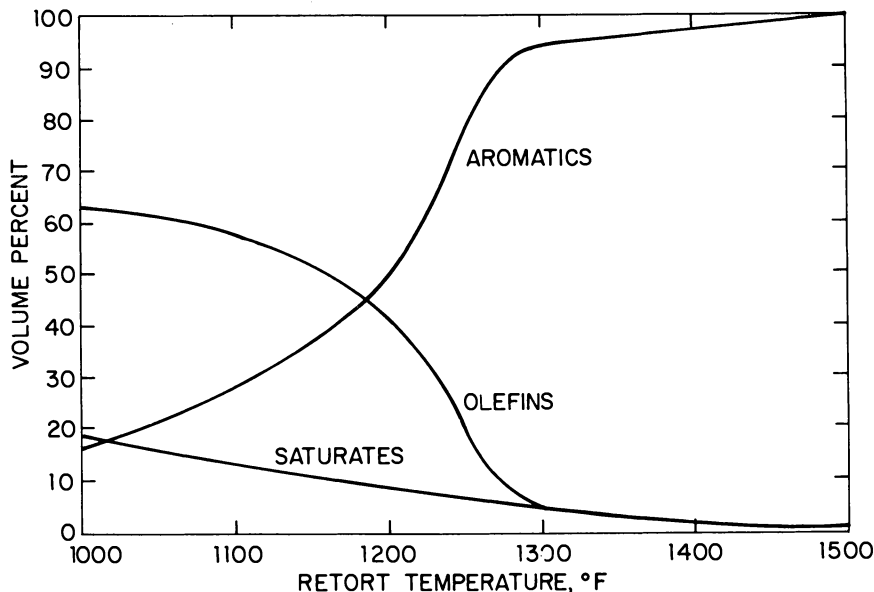


Figure 1. Paraho Process (gas combustion mode)

retort whose temperature profile was 318°–482°C. The Green River shale (Rifle, Colorado) contained 28 gal oil/ton. Some further background on the Paraho and other shale oil processes is given in Ref. 5. The importance of specific retorting temperature is emphasized in Figure 2 by Thorne (2), showing a sharp increase in aromatics as retorting temperature is



Hydrocarbon Process. Pet. Refiner

Figure 2. Hydrocarbon type distribution in naphthas from entrained-solids retort crudes (19)

increased to 650°C. Another qualification of the present shale oil is that indirect retorting (external firing) may produce a higher-quality oil. The whole crude as well as the fractions used for subsequent processing studies were analyzed, as summarized in Table I.

Table I. Paraho Shale Oil

| | Whole Crude | < 175°C 5.1 (wt %) | 175°–345°C 31.0 (wt %) | 345°–460°C 37.6 (wt %) |
|--------------------------|----------------|--------------------------|------------------------------|------------------------------|
| C (%) | 84.34 | 82.56 | 83.53 | 84.85 |
| H (%) | 11.32 | 12.37 | 11.76 | 10.20 |
| N (%) | 2.35 | 1.30 | 1.86 | 1.87 |
| O (%) | 1.21 | 1.51 | 1.54 | 1.15 |
| S (%) | 0.58 | 0.73 | 0.69 | 0.57 |
| Total | 99.80 | 98.47 | 99.38 | 98.64 |
| Sediment ^a | 0.2 | — | — | — |
| Mol wt | 265 | 149 | 215 | 336 |
| C/H | 0.621 | 0.556 | 0.592 | 0.693 |
| API gravity ^a | 21.3 | — | — | — |
| Ref. index, 20° | | 1.4637 | 1.4965 | 1.5291 |
| Density | | | | |
| 20° | — | — | — | — |
| 30° | — | 0.8273 | 0.8872 | 0.8931 |
| 90° | 0.8895 | 0.7803 | 0.8467 | 0.8830 |
| 110° | 0.8712 | — | — | — |
| Viscosity (CS) | | | | |
| 30° | — | 1.914 | 9.457 | — |
| 90° | 6.61 | 0.842 | 2.20 | 9.55 |
| 110° | 4.18 | — | — | 5.70 |
| NMR, % Ar. C | | | | |
| NMR, % Ar. H | | | | |
| Aliphatic, LC (%) | 7.6 | 30 | 13 | 10 |
| SARA Nonpolar | 68 | | 68 | 60 |
| aromatics (%) | 74 | | 54 | 44 |
| saturates (%) | 26 | | 46 | 56 |
| Polar | | | | |
| 1 | — | | 9 | 15 |
| 2 | — | | 4 | 6 |
| 3 | — | | 19 | 19 |
| Asphaltenes | 3 | | 0 | 0 |
| Benzene insol. | 0.01 | | 0 | 0 |

^a Data furnished by Paraho.

Important analyses for the whole crude are as follows, including a liquid chromatographic separation adapted from the published SARA procedure (Saturates–Aromatics–Resins–Asphaltenes) for isolation of seven classes of compounds from mid-distillate (9).

| | |
|----------------|-------|
| N | 2.35% |
| O | 1.21% |
| S | 0.58% |
| C/H | 0.621 |
| Mol wt equiv. | 265 |
| Density @ 90°C | 0.890 |
| SARA, nonpolar | 68% |
| aromatics | 74% |
| saturates | 26% |

Distillation

| <i>Fraction</i> | <i>bp Range</i> (@ 1 atm; °C) | <i>Each Fraction</i> (wt %) |
|----------------------|----------------------------------|--------------------------------|
| Naptha | < 175 | 5.1 |
| Light gas oil (LGO) | 175–345 | 31.0 |
| Medium gas oil (MGO) | 345–460 | 37.6 |
| Heavy gas oil (HGO) | > 460 | 26.6 |
| and residuum | | (balance) |

For three narrow fractions with midcut boiling points of 235°–325°C, the Bureau of Mines Correlation Index (BMCI) is 42–45, respectively.

Processing

Conventional refinery techniques, supplemented with steam pyrolysis, were used in bench-scale continuous flow equipment which, however, was not integrated. Important liquid recycles were simulated; gases were not recycled. The processing sequence is depicted in Figure 3 and is summarized as: (1) distillation of crude into four fractions, (2) hydrocracking of gas oils to naphtha, (3) naphtha hydrotreating for further heteroatom removal, (4) naphtha reforming to aromatics, and (5) steam pyrolysis of gas oils to olefins. Conventional and readily obtainable petroleum refinery catalysts were used (Table II). This includes a simple and earlier form of reforming catalyst (platinum only) in deference to its apparently greater resistance to sulfur and nitrogen poisoning.

Distillation of crude provided the gas oils that were used in subsequent processing and also that are described in Table I. Note that the total that was distilled-off represents 73.7 wt %. Less effort was applied to the heavy gas oil (>460°C) and to the residuum, and none to the coking where this fraction might be directed for recovery of coke and lighter gas oils.

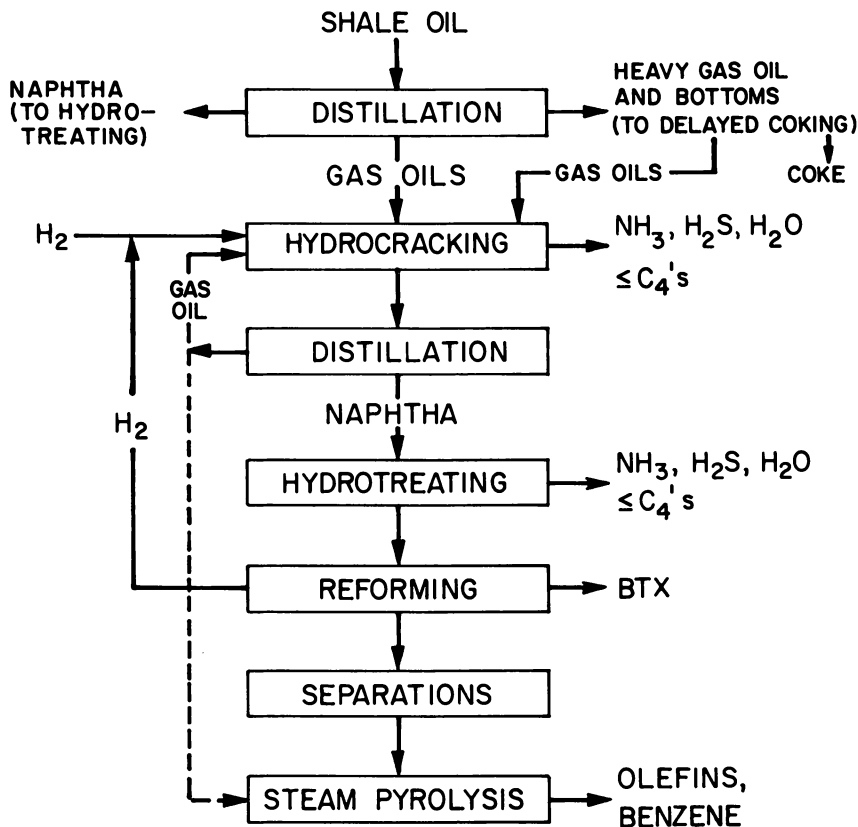


Figure 3. Conversion to chemical feedstocks—processing scheme

Table II. Catalysts Used in This Program^a

| | Description | Mfr./Designation | Remarks |
|---------------|---|-------------------|-------------------|
| Hydrocracking | Ni/W/SiO ₂ -Al ₂ O ₃ | Ketjen/HC-5; 1.5E | 0.06-in. diameter |
| Hydrotreating | Ni/Mo/Al ₂ O ₃ | AmCy/Aero HDS-3A | 0.07-in. diameter |
| Reforming | 0.6% Pt/Al ₂ O ₃ | — | Pretreated |

^a Each with ca. 200 m²/g and 0.6–0.7 mL/g PV.

Hydrocracking

Hydrocracking is commonly used to convert heavier oils while both cracking and hydrogenating are used to produce essentially saturated products. Because of the high sulfur and nitrogen content of shale oil and of the desire to emphasize chemical feedstocks production (11–14),

this process was applied to the shale gas oils that were initially distilled off. The gas oils were hydrocracked over Ni/W on $\text{SiO}_2\text{-Al}_2\text{O}_3$ catalyst (Table II) under the following conditions (10) in a 1-in. nominal diameter trickle bed reactor. For the comparisons shown later, specific departures were made from these conditions: 1500 psig, 450°C , 2.4 liquid hourly space velocity (LHSV), 11 M scf H_2/bbl . Results were interpreted by gas chromatographic analyses of the off-gas from a 0°C condenser used at the nominal reactor pressure and by simulated distillation analyses (SDA) of the condensate (9).

Conversions to naphtha are shown in Figures 4 and 5 from both light and medium gas oils (LGO and MGO, respectively) and in Figure

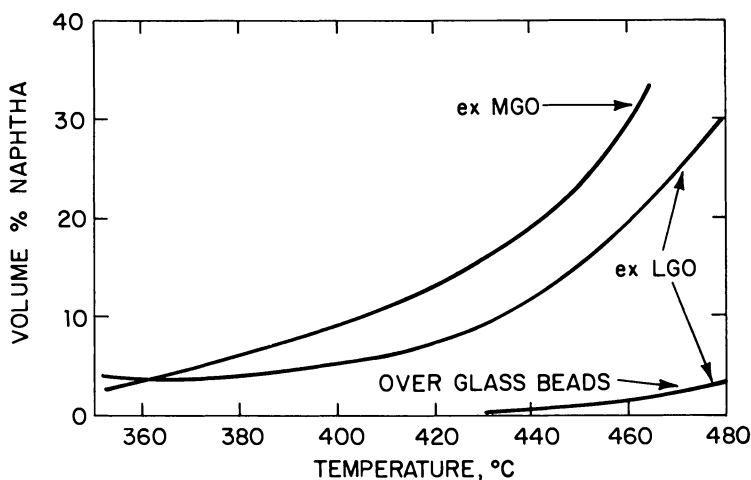


Figure 4. Hydrocracking of Paraho shale oil light and medium gas oils

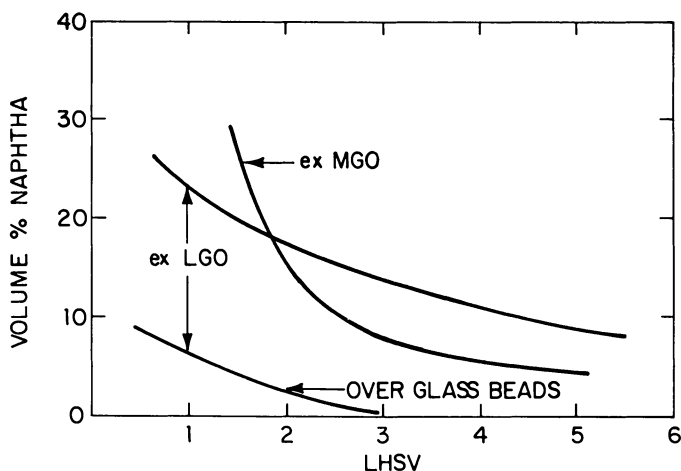


Figure 5. Hydrocracking of Paraho shale oil light and medium gas oils

6 from LGO. Conversion to nearly 20 vol % of the condensate are obtainable from LGO at conditions tabulated earlier, although somewhat lower LHSV and higher temperature and pressure might have been preferable for producing more naphtha. For comparison, the modest conversions obtained merely over glass beads also are shown. At higher temperature, thermal hydrocracking can be expected to become an increasingly significant route to less desirable methane with increasing hydrogen demand.

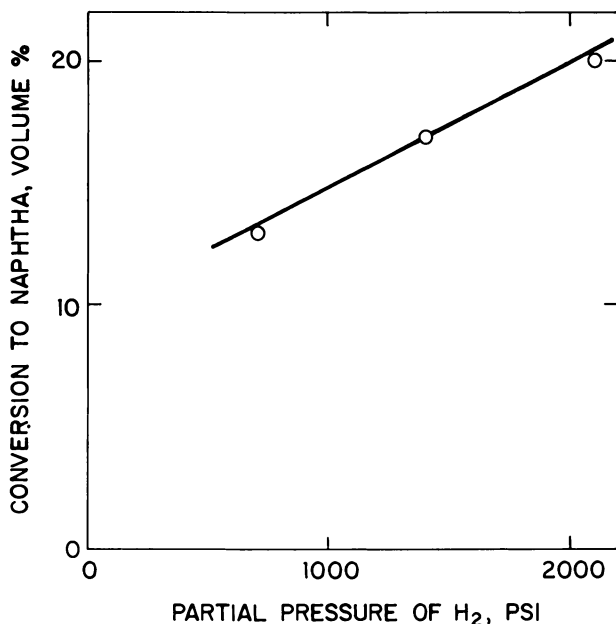


Figure 6. Hydrocracking shale-derived LGO effect of hydrogen pressure

Conversion of higher boiling fractions is illustrated in Table III. Heavy gas oil (HGO) is reduced from 72 to 5 vol %. At very high temperature (545°C), dewaxed MGO (wax removed: 8 wt % of the straight-run MGO) was largely converted to naphtha and LGO (56 and 35 vol %, respectively). However, a large loss to C₁-C₄ off-gas (5.5 wt %) occurred.

Limited naphtha in the crude (5 wt %) plus that obtainable from single-pass hydrocracking appear insufficient for economical derivation of chemical feedstocks. Therefore, simulated recycle was attempted. After

Table III. Hydrocracking of Heavy Gas Oils*

| | <i>Simulated Distillation Analyses (vol %)</i> | | | | | <i>Off-Gas (wt %) to ≤ C₄'s</i> |
|-------------------------|--|----------------------|------------|------------|------------|--|
| | <i>Lt. Ends</i> | <i>Naph- tha</i> | <i>LGO</i> | <i>MGO</i> | <i>HGO</i> | |
| Feed (HGO/MGO) | 0 | 0 | 0 | 22 | 72 | — |
| 454°C | 3 | 19 | 40 | 35 | 5 | 0.3 |
| 515°C | 4 | 22 | 46 | 28 | 1 | 0.7 |
| Feed (MGO) (dewaxed) | 0 | — | — | 91 | 3 | — |
| 545°C | 0 | 56 | 35 | 9 | 1 | 5.5 |
| Feed (175°C) | 0 | 0 | 52 | 35 | 14 | — |
| 450°C | 0 | 19 | 58 | 19 | 5 | — |
| Feed (LGO) | 0 | 1 | 82 | 18 | 0 | — |
| 450°C | 0 | 19 | 74 | 8 | 0 | 0.9 |

* Conditions: 1500 psig, 2.4 LHSV over Ketjen HC-5 Ni/W on SiO₂-Al₂O₃, with ca. 11 M scf H₂/bbl.

each hydrocracking pass, naphtha was topped off and the remainder was recycled. Conversions decreased significantly, as shown below for identical hydrocracking conditions:

| <i>Pass</i> | <i>Vol % in Hydrocrackate</i> | |
|-------------|-------------------------------|-------------------------|
| | <i>Naphtha from LGO</i> | <i>LGO from MGO/HGO</i> |
| First | 16 | 22 |
| Second | 5 | 17 |
| Third | 3 | — |

Increased severity was not tested as a means of mitigating the decreases. But for the same catalyst batch, the same pattern of declining conversion was observed, suggesting that permanent poisoning did not occur.

Shale oil contains significant concentrations of oxygen, sulfur, and especially nitrogen. Fortunately, much is removed during hydrocracking, as illustrated in Table IV for successive recycles (no makeup). Conversion occurs to water, ammonia, and hydrogen sulfide, thereby adding to the hydrogen consumption already required for hydrocracking. From analysis of the off-gas and comparative elemental analyses of the liquids, the following hydrogen consumptions were estimated. However, these estimates are believed too low, based on comparison with commercial practice for petroleum-derived gas oils. A significant fraction of these gross requirements is provided by subsequent reforming.

Table IV. Heteroatom Removal During
LGO Elemental Analysis

| <i>Gas Oil</i> | <i>H (%)</i> | <i>O (%)</i> | <i>N (ppm)</i> | <i>S (ppm)</i> |
|----------------|--------------|--------------|----------------|----------------|
| Light (LGO) | 11.76 | 1.54 | 18600 | 6880 |
| HC 1X | 12.34 | 0.28 | 5000 | 718 |
| HC 2X | 12.06 | 0.24 | 1148 | 102 |
| HC 3X | 12.43 | 0.22 | 490 | 79 |
| Medium (MGO) | 11.05 | 1.27 | 23200 | 5784 |
| HC 1X* | 11.83 | 0.22 | — | — |
| HC 2X* | 11.01 | 0.22 | 471 | 607 |

* Naphthas topped off hydrocrackates, remainder recycled; hydrocracking at 1500 psig, 450°C, but for recycle, at 4.8 LHSV and 22 scf H₂/bbl feed rate.

| <i>Fraction Hydrocracked</i> | <i>scf H₂/bby</i> |
|------------------------------|------------------------------|
| LGO | 1160 |
| > 175°C | 1120 |
| MGO | 1110 |

Hydrotreating

Two stages of hydrotreatment were used to reduce further oxygen and especially nitrogen and sulfur contents in the naphtha from hydrocracking LGO. A catalyst of Ni/Mo on Al₂O₃ (Table II) was used in a 1-in. diameter trickle bed reactor at 400°C, 1500 psig, 5 M scf H₂/bbl, and 4.8 LHSV in the first pass and at 450°C and 1.5 LHSV for recycle of the naphtha successively distilled off.

| <i>Feed</i> | <i>g/mL</i> | <i>Elemental Analyses</i> | | | |
|----------------|-------------|---------------------------|--------------|----------------|----------------|
| | | <i>H (%)</i> | <i>O (%)</i> | <i>N (ppm)</i> | <i>S (ppm)</i> |
| Straight run | 0.827 | 12.37 | 1.51 | 13,000 | 7270 |
| Second recycle | 0.746 | 15.92 | 0.3 | 28 | 18 |

Still further reductions in heteroatom content would have been preferred but for present purposes, this naphtha was passed to reforming.

Reforming

Hydrotreated naphthas (combined) were then reformed over a 0.6% Pt on Al₂O₃ catalyst at 500°C, 500 psig, 3 LHSV, and 5 M scf H₂/bbl. This simple catalyst was chosen in preference to the more advanced bi- and trimetallic catalysts because of its probably lower sensitivity to heteroatom poisoning. The reformates were analyzed by gas chromatography

Hydrocracking—Simulated Recycle^a

| <i>Naphtha Elemental Analysis</i> | | | | <i>Conversion (vol % to naphtha)</i> |
|-----------------------------------|--------------|----------------|----------------|--|
| <i>H (%)</i> | <i>O (%)</i> | <i>N (ppm)</i> | <i>S (ppm)</i> | |
| — | — | — | — | — |
| 13.81 | 0.00 | — | 232 | 38 |
| 13.31 | 0.00 | 360 | 27 | 5 |
| 10.76 | 0.00 | 230 | 41 | 3 |
| — | — | — | — | — |
| 11.71 | 0.60 | 15000 | 685 | 7% and to 25% LGO |
| 11.78 | 0.63 | 293 | 322 | 7% and to 23% LGO |

with a column providing resolution up through the C₉ range. Table V describes product content in more detail.

| <i>Origin of Hydrotreated Naphtha</i> | <i>Product (wt %)</i> | | |
|---|---------------------------------|------------|-----------------------------|
| | <i>Monocyclic Aromatics</i> | <i>BTX</i> | <i>Cyclo- paraffins</i> |
| Hydrocracking of LGO | 57.9 | 41.5 | 9.7 |
| Straight run | 48.7 | 39.5 | 10.4 |

Modifications of the conditions listed above were tried within the ranges given above but these resulted in lower conversions (35%–53% monocyclic aromatics). More severe hydrocracking (higher conversion to naphthenes) and more effective nitrogen removal would almost surely have yielded more aromatics from reforming.

The compositions of progressively processed naphtha were also determined by mass spectrographic analysis and are summarized in Table VI. These show the expected shifts from paraffins in the straight-run naphtha as well as naphtha from hydrocracking LGO to aromatics, especially benzenes in the reformat.

Steam Pyrolysis

Steam pyrolysis was conducted on the following components to determine their potential for conversion to C₂–C₄ olefins: naphtha (straight run), LGO (straight run), MGO (straight run), LGO (after four successive passes through hydrocracking), and MGO (after three successive passes through hydrocracking). Reaction conditions were: 790°–865°C, 8–10 psig, 1–5 sec contact time, and 0.6–3 H₂O:oil weight ratio. Background that prompted the selection of these conditions is from industrial steam pyrolysis processes, described in Ref. 5, 6, 7, and 16.

Table V. Reformer*Products as Wt % of Hydrotreated Naptha Fed^b*

| <i>Naptha Feed</i> | <i>Aromatics</i> | | | | <i>Other Mono-cyclics</i> |
|--------------------|------------------|----------------|------------|----------|---------------------------|
| | <i>Benzene</i> | <i>Toluene</i> | <i>EtB</i> | <i>X</i> | |
| Hydrocracking | 8.1 | 20.2 | 0.8 | 16.3 | 12.5 |
| Straight Run | 8.6 | 18.1 | 0.8 | 12.8 | 8.4 |

^a 0.6% Pt on Al₂O₃; 3 LHSV; 500°C, 500 psig, 5 M scf H₂/bbl.

Table VI. Compositions of*Mass Spectrometry Analyses^a (vol %)*

| | <i>Paraffins</i> | | <i>MCP</i> |
|---|------------------|-------------------|------------|
| | <i>Paraffins</i> | <i>MCP</i> | |
| Straight run | 33.7 | 26.1 ^b | |
| Hydrocracking of LGO | 51.8 | 18.7 | |
| After hydrotreating naphtha ex hydrocracking | 38.9 | 45.9 | |
| Reformate (from naphtha ex hydrocracking LGO) | 34.8 | 8.9 | |

^a MCP, monocyclic paraffins; DCP, dicycloparraffins; PCP, polycyclic paraffins; MCA, monocyclic aromatics excluding benzenes; DCA, dicyclic aromatics; and PCA, polycyclic aromatics.

Table VII.

| <i>Feed</i> | <i>Conditions</i> | | |
|----------------------------|-------------------|------------|--------------------------|
| | <i>°C</i> | <i>sec</i> | <i>H₂O/HC</i> |
| Naptha (straight run) | 790 | 2.6 | 1.6 |
| LGO (straight run) | 809 | 2.2 | 1.4 |
| MGO (dewaxed straight run) | 808 | 2.2 | 1.1 |
| Crude (whole) | 815 | 1.4 | 0.9 |
| LGO (straight run) | 865 | 1.1 | 0.6 |
| LGO (after 4X recycled) | 793 | 4.7 | 3.0 |
| Cyclohexane | 817 | 2.4 | 1.5 |
| Benzene | 785 | 2.5 | 1.2 |

Product Distribution^a*Products as Wt % of Hydrotreated Naphtha Fed^b*

| <i>Cycloparaffins</i> | | | <i>Aliphatics</i> | | <i>Total MC Aromatics (wt %)</i> | <i>Total BTX (wt %)</i> |
|-----------------------|-------------|---------------|------------------------------------|------------------------------------|--|---------------------------------|
| <i>MCP</i> | <i>CHex</i> | <i>Others</i> | <i>C₁-C₄</i> | <i>C₅-C₇</i> | | |
| 3.9 | 4.0 | 1.8 | 4.4 | 16.9 | 57.9 | 41.5 |
| 4.1 | 5.3 | 1.0 | 4.5 | 18.5 | 48.7 | 39.5 |

^b EtB, ethylbenzene; X, xylenes; MCP, methylcyclopentane; CHex, cyclohexane; MC, monocyclic; and BTX, benzene, toluene, xylenes.

Progressively Processed Naphthas*Mass Spectrometry Analyses^a (vol %)*

| <i>DCP</i> | <i>PCP</i> | <i>Benzenes</i> | <i>MCA</i> | <i>DCA</i> | <i>PCA</i> |
|------------------|-------------------|-----------------|------------|------------|------------|
| 7.7 ^b | 12.5 ^b | 11.1 | 6.7 | 2.1 | 0.1 |
| 2.5 | 2.2 | 21.2 | 3.2 | 0.5 | < 0.1 |
| < 0.1 | 0.1 | 12.9 | 1.8 | 0.3 | < 0.1 |
| < 0.1 | < 0.1 | 53.5 | 2.5 | 0.4 | < 0.1 |

^b Olefin content and other interferences probably cause errors which would change these figures.

Steam Pyrolysis*Apparent Conversions (wt %)*

| <i>CH₄</i> | <i>C₂⁼</i> | <i>C₃⁼</i> | <i>BD</i> | <i>Benzene</i> |
|-----------------------|----------------------------------|----------------------------------|-----------|----------------|
| 8.4 | 12.6 | 2.1 | 3.4 | 8.0 |
| 11.3 | 17.5 | 1.8 | 2.6 | 3.3 |
| 11.1 | 18.4 | 2.3 | 3.0 | 4.5 |
| 9.7 | 16.2 | 3.5 | 3.8 | 2.2 |
| 14.0 | 11.4 | 0.3 | 0.1 | 2.9 |
| 6.5 | 18.5 | 5.8 | 7.3 | 5.2 |
| 4.9 | 16.2 | 0.7 | 3.5 | 4.4 |
| 8.8 | 11.2 | 2.5 | 1.6 | 3.3 |

The data of Table VII suggest that under the nearly constant conditions tested, conversion to ethylene increases with boiling range of the straight run fraction:

| <i>Fraction</i> | <i>Conversion to Olefins (wt %)</i> | | |
|------------------|-------------------------------------|------------------|------------------|
| | <i>Ethylene</i> | <i>Propylene</i> | <i>Butadiene</i> |
| Naphtha | 12.6 | 2.1 | 3.4 |
| LGO | 17.5 | 1.8 | 2.6 |
| MGO | 18.5 | 2.3 | 3.0 |
| Crude (whole) | 16.2 | 3.5 | 3.8 |

In hydrocracking, yields to lower boiling fractions were shown to diminish rapidly with progressive recycling. However, the following results show significant potential for conversion to olefins:

| <i>Feed</i> | <i>Recycled Through Hydro- cracking</i> | <i>RT (sec)</i> | <i>Conversion to Olefins (wt %)</i> | | |
|-------------|---|---------------------|-------------------------------------|------------------|------------------|
| | | | <i>Ethylene</i> | <i>Propylene</i> | <i>Butadiene</i> |
| LGO | 4X | 4.7 | 18.5 | 5.8 | 7.3 |
| MGO | 3X | 1.2 | 13.8 | 0.4 | 1.2 |

Yield of Chemical Feedstocks

Yields of hydrocarbon feedstocks were estimated from the process data described in preceding sections, based on the integrated process of Figure 3 for which results are shown in Table VIII. Many assumptions and approximations were made, particularly with respect to recycle. Furthermore, the estimate reflects no economic constraints imposed by these recycle burdens, particularly hydrocracking. Finally, material not

Table VIII. Estimated Gross Overall Yields of Hydrocarbon Feedstocks (wt %)

| | |
|----------------------------|------|
| Ethylene | 9.4 |
| Propylene | 1.7 |
| Butadiene | 1.1 |
| Benzene | 7.9 |
| Toluene | 8.6 |
| Xylenes | 7.0 |
| Other monocyclic aromatics | 18.3 |
| Coke and other byproducts | 5.7 |
| Fuels (byproduct) | 33.4 |
| Methane | 6.4 |
| Hydrogen consumption (net) | 0.9 |

identified in the gas collected from pyrolysis was assumed to be converted to fuels except for methane which, although a fuel, was readily detected and is explicitly identified in Table VIII.

The following summarizes the yields estimated in this way for Paraho shale oil (in wt %): olefins (ethylene, propylene, butadiene, 12.2; BTX, 23.5; fuels (including methane), 39.8; coke, 18.3; and hydrogen consumption (net), 0.9. No internal fuel requirements are reflected in these yields. The 36% yield to olefins and BTX could probably be increased significantly by further work, especially on steam pyrolysis to olefins. A bench mark is given in Ref. 8 for a hypothetical "petrochemical refinery" operated to obtain a 60% yield of BTX and olefins from petroleum.

Literature Cited

1. Anonymous; "Oil Shale: A Huge Resource of Low-Grade Fuel," *Science* June 24, 1974, 184.
2. Thorne, H. M. "Retort Oil Shale for Chemicals," *Pet. Refiner* 1956, 35(7).
3. White, Philip; "Statement on ERDA's R&D Program in Oil Shale" (to Senate Committee on Interior and Insular Affairs); ERDA Weekly Announcements, Week ending 12/24/76.
4. Frost, C. M.; Cottingham, P. L. "Methods for Refining Crude Shale Oil Produced by In-Situ Retorting," *U.S. Bur. Mines* RR-7844, 1974.
5. Schoro, F. C.; Tarman, P. B.; Feldkirchner, H. L. "State-of-the-Art—Above Ground Shale Processing," *Hydrocarbon Process., February 1977*.
6. Zdonik, S. G.; Hayward, G. L. "Olefins Production by Gas Oil Cracking," *Hydrocarbon Process., August 1975*.
7. Offen, M. J. "Which Route to Olefins from VGO?" *Hydrocarbon Process., October 1976*.
8. Stewart, M. F.; Jensen, J. T. In "Refining Petroleum for Chemicals," *Adv. Chem. Ser.* 1970, 97, 123.
9. Standard Method of Test for Boiling Range Distribution of Petroleum Fractions by Gas Chromatography, American Society for Testing and Materials, ASTM Designation D 2887-73.
10. Thomas, C. L. "Catalytic Processes and Proven Catalysts"; Academic: New York, 1970.
11. Anonymous; "1978 Refining Process Handbook," *Hydrocarbon Process., September 1978*.
12. Ward, J. W. "The Varieties of Hydrocracking," *Hydrocarbon Process., September 1975*.
13. Langlois, G. E.; Sullivan, R. F. In "Refining Petroleum for Chemicals," *Adv. Chem. Ser.* 1970, 97, 38.
14. Billon, A.; Franck, J. P.; Peries, J. P.; Fehr, E.; Gallei, E.; Lorenz, E. "More Ways to Use Hydrocracking," *Hydrocarbon Process., May 1978*.
15. Peters, B. C. "Chemicals from Coal," National Technical Information Service, October 25, 1977, FE-1534-50.
16. Ishikawa, T.; Keister, R. G. "A Petrochemical Alternative—ACR," *Hydrocarbon Process., December 1978*.
17. Shell Oil Co. "The National Energy Outlook, 1980-1990," September, 1976.
18. Anonymous; "Paraho: Put Oil Shale Development on Crash Basis," *Oil Gas J., January 22, 1979*.
19. Thorne, H. M. *Hydrocarbon Process. Pet. Refiner* 1956, 7.

RECEIVED September 28, 1978.

Development of Scaling Methods for a Crude Oil Cracking Reactor by Using Short Duration Test Techniques

J. D. KEARNS, D. MILKS, and G. R. KAMM

Union Carbide Corporation, South Charleston, WV 25303

Union Carbide's codevelopment with Kureha and Chiyoda has resulted in an Advanced Cracking Reactor (ACR) technology primarily for ethylene production. In the ACR process, unique reactor conditions produce high value chemicals directly from the world's limited oil resources. Process similarity concepts have been investigated to scale-up pilot data. Testing of these concepts has been accomplished using short duration testing during which steady-state fluid dynamics and chemical performance are reached in a matter of seconds. Injected liquid particle sizes and trajectories have been measured during cold-flow simulation studies. Full-scale reactor tests at commercial process conditions were conducted in rocket test cells. The tests, described in this chapter, verified commercial ACR scale criteria and gas yield cracking patterns.

Union Carbide Corp., Kureha Chemical Industry Co., Ltd., and Chiyoda Chemical Engineering and Construction Co., Ltd., entered into a codevelopment program in 1973 to commercialize a new ethylene technology based on flame cracking of crude oil and crude oil fractions. This unique Advanced Cracking Reactor (ACR) technology results in producing 60–70% high value chemical products (1), including more than 30% ethylene from selected crude oils or a wide range of distillate feedstocks (see Table I). This process offers a step change in the yields of nonfuel products from the world's valuable and limited resources of crude oil.

Table I. Ethylene from Crude Oil Yields in the Advanced Cracking Reactor

| | <i>Pennsyl- vania Crude</i> | <i>Arabian Light Distil- late</i> | <i>Light Naphtha</i> | <i>Light Gas Oil</i> | <i>Vac- uum Gas Oil</i> |
|---|-------------------------------------|---|---------------------------------------|------------------------------|-------------------------------------|
| Ethylene/acetylene wt ratio | 15.0 | 8.0 | 9.99 | 7.45 | 6.48 |
| Residence time (msec) | 30 | 15 | 16 | 15 | 16 |
| Hydrogen/methane | 11.29 | 10.05 | 16.70 (<i>lb/100 lb oil</i>) | 11.65 | 10.45 |
| C ₂ H ₂ | 2.26 | 4.01 | 4.34 | 4.49 | 4.34 |
| C ₂ H ₄ | 34.00 | 32.11 | 43.62 | 33.55 | 28.14 |
| C ₂ H ₆ | 2.44 | 1.99 | 3.14 | 1.83 | 1.57 |
| C ₃ H ₄ | 1.32 | 1.98 | 1.79 | 1.83 | 2.10 |
| C ₃ H ₆ | 12.00 | 8.39 | 11.47 | 7.04 | 5.62 |
| C ₃ H ₈ | 0.51 | 0.25 | 0.37 | 0.16 | 0.07 |
| C ₄ H ₄ | 0.65 | 0.48 | 0.19 | 0.32 | 0.72 |
| C ₄ H ₆ | 5.50 | 3.78 | 3.43 | 3.29 | 3.08 |
| C ₄ H ₈ | 2.40 | 0.83 | 1.65 | 0.64 | 0.36 |
| C as CO, CO ₂ , and H ₂ S | 1.5 | 1.70 | 1.97 | 1.58 | 3.14 |
| C ₅ s—160°F | 3.93 | 2.21 | 1.52 | 0.94 | 1.14 |
| Pyrolysis gasoline fraction | 9.56 | 9.31 | } 9.81 | } 32.68 | } 39.27 |
| C ₉ —430°F | 0.63 | 3.34 | | | |
| 430—650°F | 3.06 | 15.12 | | | |
| 650°F+ | 8.95 | 4.45 | | | |

Chemical Engineering Progress

In this process (*see* Figure 1), crude oil or distillate is injected into high temperature gases ($\sim 2000^{\circ}\text{C}$) somewhat less than twice its weight, which are generated by pure oxygen combustion with an excess of fuel. The vaporized feedstock and combustion gases ("steam") are accelerated through a venturi nozzle reaction chamber where an adiabatic cracking reaction occurs at pressures significantly higher than those commonly used. The reaction products are quenched rapidly at about 20 msec residence time by a unique heat recovery system (2). After gas-liquid phase separation and fractionation, the product gas is compressed and processed in a specially developed acid-gas absorption system for the removal of H₂S and CO₂. The sweet gas is processed through somewhat conventional separation devices for the recovery of ethylene, propylene, acetylene, and other cracking by-products. The extreme flexibility with regard to feedstocks and product yields, combined with the intrinsically high chemical yields, results in a decided economic advantage over

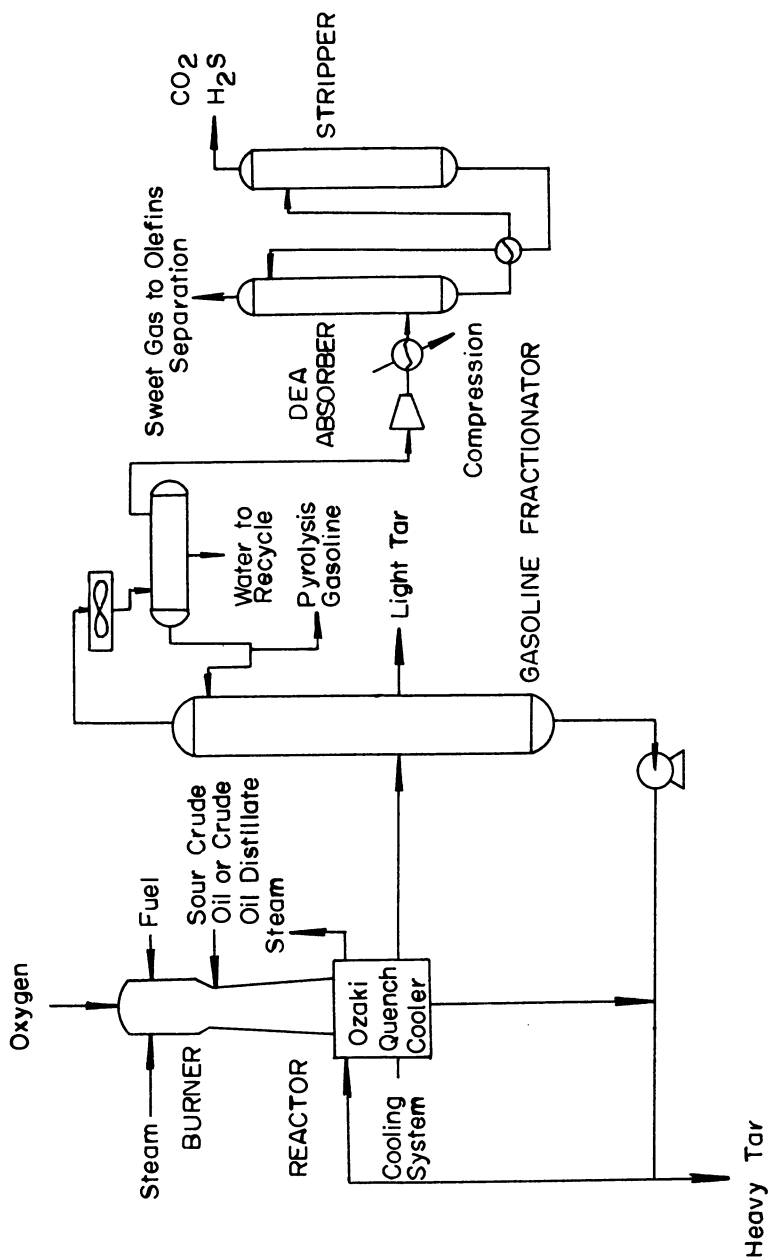


Figure 1. Schematic of ACR process

conventionally produced ethylene. Also, this process offers to chemical companies a greater independence on their raw material supply from oil companies with whom they must compete in petrochemical markets.

Development Effort

The ACR technology has been investigated extensively during the past four years through a series of research and development programs. Six major test facilities have been operated at Carbide's Technical Center in South Charleston, WV, and at Kureha's facilities in Nishiki, Japan. These tests led to an extended pilot-plant run demonstrating all of the key elements of the process including acid gas removal.

Also, geometric, kinematic, and dynamic process similarity concepts have been investigated to scale-up typical ACR pilot data to a commercial reactor basis. Selected fundamental experiments were performed in which the scale-up criteria were refined. These tests included heat transfer studies as well as wind tunnel studies and other fluid dynamic tests that used three-dimensional imagery (holography), laser shadow photography, spark shadow photography, ultra-high speed motion pictures, along with conventional photography. Several of these tests and techniques used the facilities of aerospace contractors. The data obtained from this work were used to mathematically correlate and estimate the position, size, slip velocity, and vaporization time of the injected oil droplets as a function of the characteristics of the injector, reactor geometry, and operating conditions.

This technology led to testing of a full scale, 100 million lb-per-year ethylene reactor. The full-scale tests have verified scale criteria and gas yield cracking patterns. To further minimize the technical risk and complete the development effort, Union Carbide is constructing a \$15 MM ACR prototype unit at Seadrift, TX, primarily to prove long-term equipment operability. This demonstration unit will be completed in 1979 and can lead to the construction of a world-scale ethylene unit by the mid-1980s.

Similarity in Scale-Up

Scale-up implies a change from a small configuration to a larger one. To successfully perform the scale-up of a chemical process, one must first establish the categories for which similarity must be ensured. The difficulty that arises is that techniques based on the governing differential equations or dimensional analysis provide only a means for identifying pertinent dimensionless groups. Their absolute relationships in complex processes must be developed from small-scale experiments which usually

cannot provide complete similarity. Ideal similarity is often unattainable because it requires the ratio of corresponding measurements in both the small-and-large-scale process to be identical. It then becomes economical to isolate and examine only those conditions critical to the scale-up of the process. Given the known desirable performance of the small reactor system, variables important in scale-up can be studied in terms of the following similarity categories from Johnstone and Thring (3): geometric, mechanical (static, kinematic, dynamic), thermal, and chemical.

Critical Scale-Up Conditions

In an effort to maintain equivalent chemical performance or product yields in the ACR, we are, in effect, attempting to develop chemically similar reactor systems. Because of the two-phase flow in the reaction section of the ACR process, it is important to note that there are two principal chemical reaction subdivisions. The first is controlled by mass action (homogeneous) while the second depends upon the surface or interface between the phases (heterogeneous).

By 1975, pilot-plant development studies of the ACR process had proceeded to the stage where the associated potential scale effects were being investigated. Computer simulation of the ACR reaction system revealed that: (1) the initial vapor phase cracking reactions were extremely fast compared with the vaporization of sprayed feedstock particles, and (2) vaporization was essentially complete by the end of the reactor throat. This meant that although the scaling situation would be complicated by having a so-called "mixed regime," the difficulty pertained mainly to the reactor throat section and was not a problem in the diffuser section of the reactor venturi.

The rate of chemical pyrolysis in the ACR to a large extent depends upon the temperature profile while the rate of bulk flow depends upon the flow pattern. Hence, ACR chemical similarity requires both thermal and kinematic similarity. Damköhler (*see* Ref. 3) proposed a set of dimensionless similarity groups which apply to continuous reacting systems. Assuming that the ratio of liberated heat to transported heat will be similar because thermal similarity is maintained, most of the Damköhler numbers have little bearing on the ACR process. This is attributable to the essentially adiabatic ACR cracking process for which molecular diffusion can be neglected compared with bulk flow. The Reynolds number should be kept constant during scale-up, but the ACR flow is well into the turbulent range so that viscous forces are relatively unimportant.

Chemical similarity in the diffuser section of the ACR can thus be defined in terms of the remaining (first) Damköhler number, $D_{aI} =$

rL/uC , which depends upon reaction rate (r), reaction time (L/u), and initial concentration (C). In terms of the ACR process this becomes:

$$D_{ar} = \frac{\text{Rate of chemical formation}}{\text{Rate of bulk flow}} = \frac{P}{T} = \frac{P}{F(1 + S/F)} = \frac{Y}{1 + S/F} \quad (1)$$

where P = production rate (lb/hr), T = reactor throughput (lb/hr), F = feed (cracking stock) rate (lb/hr), S = heat carrier (cracking medium) rate (lb/hr), and Y = yield (lb product/lb feed). The similarity criteria which applies to this section (controlled by mass action) ultimately requires equal residence time (or space velocity) when scaled.

Since particle vaporization is the controlling factor in the reactor throat, the reaction rate depends upon the fluid dynamics. Chemical similarity in this region is therefore subject mainly to a dynamic regime rather than a chemical one. Thus, dynamic similarity applies for the detailed scale-up of the reactor throat section.

Dynamic similarity requires that the ratio of corresponding forces is equal in geometrically similar systems. The principal force ratio operating in the ACR venturi throat section is the dynamic pressure ratio (q):

$$\bar{q} = \frac{q_1}{q_g} = \frac{(\rho V^2)_1}{(\rho V^2)_g} \quad (2)$$

where ρ = density (lb/ft³), and V = velocity (ft/sec). When scaling the injection system it is more effective to accommodate the desired higher oil flow rates by increasing nozzle capacity than by increasing the number of nozzles. However, to satisfy kinematic similarity, the relative position of particles or trajectory should correspond in geometrically similar ACR throat sections. It turns out that q is not particularly useful as a similarity criteria but can be used to predict conditions required for kinematic similarity of the sprayed particles. For example, the radial position of a particle is a function of q , injector capacity, and of downstream distance from injection. Thus, kinematic similarity of the particle trajectory, when constrained by the required change in injector capacity, can only be achieved by varying q during scale-up. In this instance, kinematic similarity becomes the desired objective.

Some of the heterogeneous flow difficulties in the throat section can be avoided if the particle surface per unit volume is maintained constant. If the Sauter mean diameter of sprayed particles could be held constant during scale-up, the surface area per unit volume (or mass for constant density) of feed would be fixed. Because the ratio of heat carrier to feed

will have to be fixed to obtain consistent yields (*see* Equation 1), the constant surface area per unit mass of heat carrier would imply that the oil droplet surface per unit volume also would be constant. This is analogous to the situation described by Walas (4) of equal activity (vaporization rate) in heterogeneous catalysis when the specific surface per unit volume is constant; the scale equations then revert to a homogeneous reaction form where equality of residence time (or space velocity) again becomes the important similarity criteria.

Thermal similarity is achieved in the ACR by providing a temperature profile which can be held geometrically similar when scaled. The temperature profile drives the ACR chemical kinetics and is a combined result of the heat transfer attributable to cracking and the heat effects caused by the bulk fluid movement. Thus, true thermal similarity in the ACR can only be achieved in conjunction with chemical and kinematic similarity. Kinematic similarity in the ACR is made possible during scale-up by forcing geometrically similar velocity profiles. The ACR temperature, pressure, and velocity profiles are governed by compressible gas dynamics so that an additional key scale parameter is the Mach number.

The method for achieving kinematic similarity in the ACR when scaling from a known pilot scale reactor to a commercial scale reactor includes Mach number matching. Equation 3 from Shapiro (5) can be used in the Mach number scaling technique to obtain estimates of the diameters in each of the reactor sections.

$$\frac{W}{A} = \sqrt{\frac{k}{R}} \frac{P_o}{\sqrt{T_o}} \frac{M}{\left(1 + \frac{k-1}{2} M^2\right)^{\frac{k+1}{2(k-1)}}} \quad (3)$$

where W = mass flow rate through a given cross section; A = area of cross section; k = specific heat ratio; R = specific gas constant = R_u/MW ; R_u = universal gas constant; MW = molecular weight of the gas; P_o = stagnation pressure of the gas flow; T_o = stagnation temperature of the gas flow; M = Mach number at the given cross section.

Applying Equation 3 with the assumption of Mach number matching between a desired commercial scale (subscript c) and a known pilot scale (subscript p) leads to Equation 4,

$$\frac{D_c}{D_p} = \sqrt{\frac{\left(\frac{W}{P_o} \frac{\sqrt{T_o}}{\sqrt{MW}}\right)_c}{\left(\frac{W}{P_o} \frac{\sqrt{T_o}}{\sqrt{MW}}\right)_p}} \quad (4)$$

where D 's are diameters; the effect of small changes in k has been neglected. Equation 4 can be used to determine the commercial diameters from the known pilot data and the desired commercial flow conditions. Equation 3 also can be used directly to estimate the required diameters, provided Mach number information is available.

To satisfy physical limitations, modifications to the diameters are made depending upon the magnitude of the compressible flow effects in each of the reactor sections. Lengths are geometrically scaled in the reactor throat. However, the diffuser angle is forced below a maximum angle of 6° to avoid flow separation. Residence times are controlled by appropriate variation of the length of the reactor's cylindrical section.

Consistent performance of the ACR during scale-up depends upon thermal and kinematic similarity throughout, but with a dynamic influence on kinematic similarity in the throat and chemical similarity in the diffuser. As a result of the above considerations, it was felt that the ACR process could be scaled in a geometrically similar reactor based on matching Mach numbers, S:F ratio, and residence time in the reaction section, provided two critical conditions could be met. When scaled, the sprayed particle size distributions would have to be approximately equal (i.e., equality of Sauter mean diameter) while a kinematically similar oil-particle trajectory also would be required.

Droplet-Size Experiments

The hydrocarbon feedstock is injected into the ACR's high temperature carrier gas from a circular array of nozzles. The atomized spray emitted from these injector nozzles is comprised of many droplets of varying size. Both small-scale and commercial capacity spray nozzles were extensively studied during the ACR development.

The conditions necessary for equality of particle size distribution were determined under ambient conditions. The nozzles used in the investigation can be classified as swirl-spray pressure nozzles. They accommodate a swirl insert which imparts a tangential velocity to the exiting fluid and results in a conical spray pattern. These nozzles were sufficiently different from conventional swirl nozzles (*see* Putnam et al., Ref. 6) to require an experimental study of particle size distribution.

Particle size measurements were made using an UV-laser, shadow photographic technique. The particle sizing system displayed real-time droplet images onto a television monitor. The images (shadows) were obtained when a pulsed (30 times per second) UV-laser beam was directed through a spray scene onto a synchronized UV-sensitive vidicon camera/recorder. The narrow depth of field used by this system can record shadows from 300 in-focus droplets per second with a resolution down to approximately $0.3 \mu\text{m}$ in diameter.

The actual size measurements were taken from the stored videotaped data. Typically, droplets were observed up to 600 μm in diameter, with the major portion occurring in the 0–100 μm range. A count of the number of particles per size interval was made by grouping the data into one of 16 size intervals. Histograms, number distributions, and number frequency distributions were generated from this information. Mean diameters, calculated according to the equations developed by Mugele and Evans (7), also were used to evaluate the nozzles. During this test program we were able to vary the nozzle diameter, injection pressure, fluid surface tension, and location in the spray pattern where size measurements were recorded.

The data indicated that droplet-size changes are primarily influenced by injection pressure and orifice size while secondary changes can be attributed to fluid properties, orifice shape, and the nozzle's internal length:diameter ratio. This last point was not observed by Dombrowski and Wolfsohn (8) for more conventional swirl spray nozzles. Nevertheless, they present a useful correlation between Sauter mean diameter and operating conditions.

During an earlier test program, a limited number of observations were made on the maximum drop size generated by a commercial scale nozzle under conditions present in an ACR reactor. The tests were conducted at a production unit operated by Kureha. A nondestructive recording of the spray was obtained with the aid of a pulsed ruby laser holographic technique (9). The resultant spray phenomena was reconstructed from holograms, making it possible to estimate maximum particle size. This information was compared with data on maximum particle size for the same nozzle during ambient testing. From this comparison we were able to translate the target Sauter mean diameter for scale-up to equivalent cold-flow conditions.

Additional droplet size work under flow conditions was not undertaken. The empirical expressions provided by Ingebo and Foster (10) were developed under conditions sufficiently similar to those present in the ACR to justify their use as a first approximation. Their data were derived from the injection of sprays into a transverse subsonic gas flow. They obtained the following correlation in Equations 5 and 6 between drop size parameters and force ratios by using dimensional analysis.

$$\frac{D_{\max}}{d_o} = 22.3 (\text{WeRe})^{-0.29} \quad (5)$$

$$\frac{\overline{D}_{30}}{d_o} = 3.9 (\text{WeRe})^{-0.25} \quad (6)$$

where D_{\max} = maximum droplet diameter, D_{30} = volume mean diameter, d_o = orifice diameter, We = Weber number $[(d_o V_\infty^2 \rho_\infty)/\sigma]$, Re = Reynolds number $[d_o V_\infty/\nu_1]$, ρ_∞ , V_∞ = free stream density and velocity, and σ , ν_1 = liquid surface tension and kinematic viscosity.

Oil-Particle Trajectory

The initial path or trajectory (termed "penetration") that the injected oil particles make in the steam flow has been found to be significant in determining the distribution of the ACR gas product yields and thus affects the ACR process economics. Since the injected oil trajectory can be controlled by adjustment of operating variables (i.e., injection pressure, injector orifice diameter, and number of injectors), the ability to predict the oil trajectory as a function of these parameters is a significant step forward in the ACR development.

Exact analytical solutions to the governing equations which produce the penetration trajectory are extremely difficult to obtain. For this reason, empirical penetration equations based on experimental data correlations are most often presented in the literature. These best-fit equations contain the dominant parameters which have been experimentally determined to significantly affect the penetration. To detail the specific ACR penetration phenomena, a series of cold-flow and hot-test experiments was conducted.

Cold-Flow Penetration Experiments

Flow visualization studies were first performed in a "plexiglas" mock-up of a small ACR. These studies revealed that the dynamic pressure ratio could significantly affect the liquid spray path. More importantly, it was discovered that large-scale testing would be necessary to examine ways to maintain kinematic similarity during scale-up. These initial conclusions were supported by previous work such as that carried out by Geery and Margetts (11) and Hojnacki (12) on the penetration of liquids into cross-flowing gases.

Partial reactor modeling was then used to shed light on the factors controlling penetration in the ACR. A full-scale, cold-flow simulation of the reactor throat region was performed. The tests were conducted in a trisonic wind tunnel at the McDonnell-Douglas Aerophysics Laboratory (13).

Injector nozzles of interest were secured to a plate mounted in the plenum chamber of the wind tunnel. The plate was positioned so that the interaction between the spray and the free stream could be observed through windows on opposite sides of the tunnel. For each run, after

steady-state liquid and gas flow had been confirmed, a spark of light was directed onto a parabolic mirror. The reflected parallel light was then passed through the spray scene via the viewing ports of the wind tunnel. A second parabolic mirror on the opposite side of the tunnel imaged the resulting spray shadow onto a film holder (see Figure 2). Penetration coordinates were taken from enlargements of negatives recorded with this back-lighted, spark-shadow photographic technique. The enlargements were scaled to actual size with the aid of a calibrated grid placed on the view window and recorded in each photograph.

The data collected during the test program consist of the fluid injection and wind tunnel parameters corresponding to the spark-shadow photographs. Water and air were used as the test fluids. Data were gathered for different sizes of injector nozzles at various levels of injection pressure and tunnel Mach number. Different injection angles also were examined.

Sets of penetration trajectory coordinates were extracted from each spark-shadow photograph. A stepwise multiple linear regression was performed using coordinates associated with the maximum penetration depth (top curve in Figure 3) and operating conditions. A generalized cold-flow penetration trajectory equation was obtained in this manner, having the following functional form of Equation 7.

$$X = f(Y, d_o, c_d, \alpha_e, \bar{q}) \quad (7)$$

where X = axial distance from the injector, Y = radial penetration depth ("maximum"), d_o = orifice diameter, c_d = injector discharge coefficient, α_e = injection angle (free stream basis), and q = liquid-to-gas dynamic pressure ratio. The resulting equation is similar to the models given by Dobrzynski (14), in that X rather than Y was chosen as the dependent variable. This was preferred because Y is not a continuous function of X

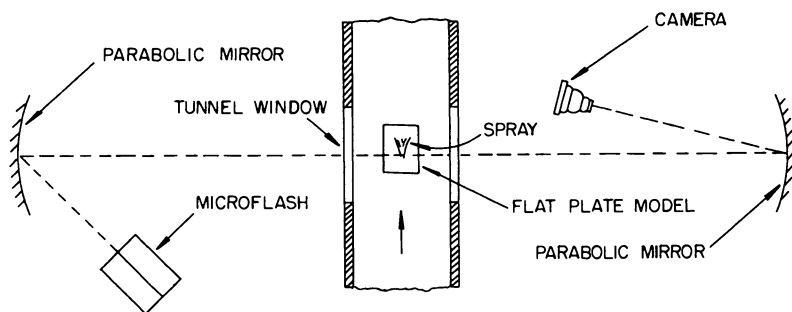


Figure 2. Schematic optical setup for spark photographs

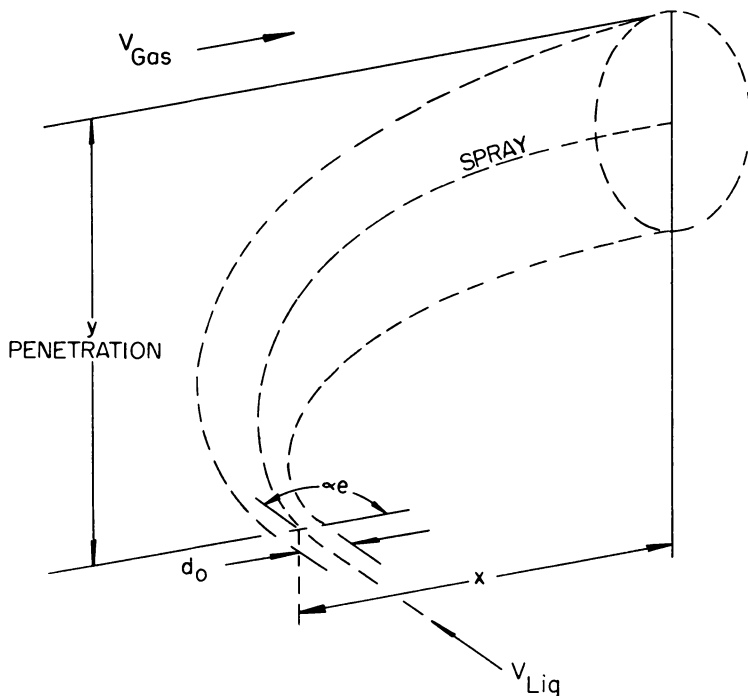


Figure 3. Spray penetration trajectory coordinates

over the entire trajectory path when the injection angle is greater than 90° . The rotated coordinate system proved to be a convenient way to handle upstream injection and to avoid more cumbersome expressions.

The equation derived from cold-flow simulation naturally cannot account for deviations in penetration when the spray enters the high temperature and varied geometry ACR environment. However, the results permitted the design of an injection system suitable for the full-scale ACR high temperature flow tests which refined the cold-flow penetration equation to assure kinematic similarity in a commercial ACR reactor.

Application of High Temperature, Short Duration Technology

The initial ACR experimental program proposed to test the scale-up criteria called for the construction of a 50 MM lb ethylene/year prototype reactor with its associated downstream gas processing facilities. This scale was originally thought to be the minimum size needed to assure the smooth start-up of a world-scale olefin plant. When the technology and economics of this proposed ACR plant were examined, the cost of the total facility was found to be extremely high.

The problem was reconsidered and was divided into two distinct parts: (1) verifying the reactor design criteria at full scale, and (2) obtaining long-term operating and ancillary scale-up data on the olefins process. It was estimated that the required operability data could be obtained from an intermediate scale unit. At the same time, a cost-effective breakthrough in the full-scale reactor testing program was proposed. The combination of the test programs allowed the required information to be obtained at a relatively low cost.

The full-scale reactor tests were conducted with high temperature experimental technology originally developed by the aerospace industry and currently in use for testing NASA rocket engines (15, 16, 17). These technologies make it possible to gather rocket engine data during test periods on the order of one second. A key factor in this technology is that fluid dynamic and chemical equilibrium can be achieved in small fractions of a second. The short duration of the tests allows for operation at temperatures above 2000°C in inexpensive equipment. As required, high-temperature mixing of flows can be examined with nondestructive techniques, and combustion product gases can be sampled.

Using this technology, it is possible to study the actual gas yields and fluid dynamics of a full-scale ACR at about 2% of the cost of a conventional chemical reactor prototype. One major factor contributing to this cost reduction is the use of standard construction materials, i.e., stainless steel rather than the high temperature ceramics which must be used in a continuously operating ACR plant. Also, the short-test duration avoids the extensive supporting facilities and high utility costs associated with long tests at full-scale.

Full-Scale High Temperature Tests

Two full-scale high temperature ACR experimental facilities were built at the Marquardt Co. (18). The first series of tests examined oil penetration in a two-dimensional version of the ACR operating at typical conditions. The experience gained from this facility was used to construct a second test facility that verified the full-scale ACR gas yields and confirmed the scale-up design methods. Both tests used similar equipment and experimental techniques.

The tests were run in multipurpose rocket test cells. An overall schematic of the ACR gas-yield test equipment is given in Figure 4. The full-scale equipment was manufactured from uncooled 304 stainless steel. A water-cooled burner was used to supply the cracking "steam" to the ACR test piece at commercial-scale flow rates, pressures, and temperature. The burner was mated to the ACR venturi test piece through a choked orifice and a diameter transition section. The reactor venturi consisted

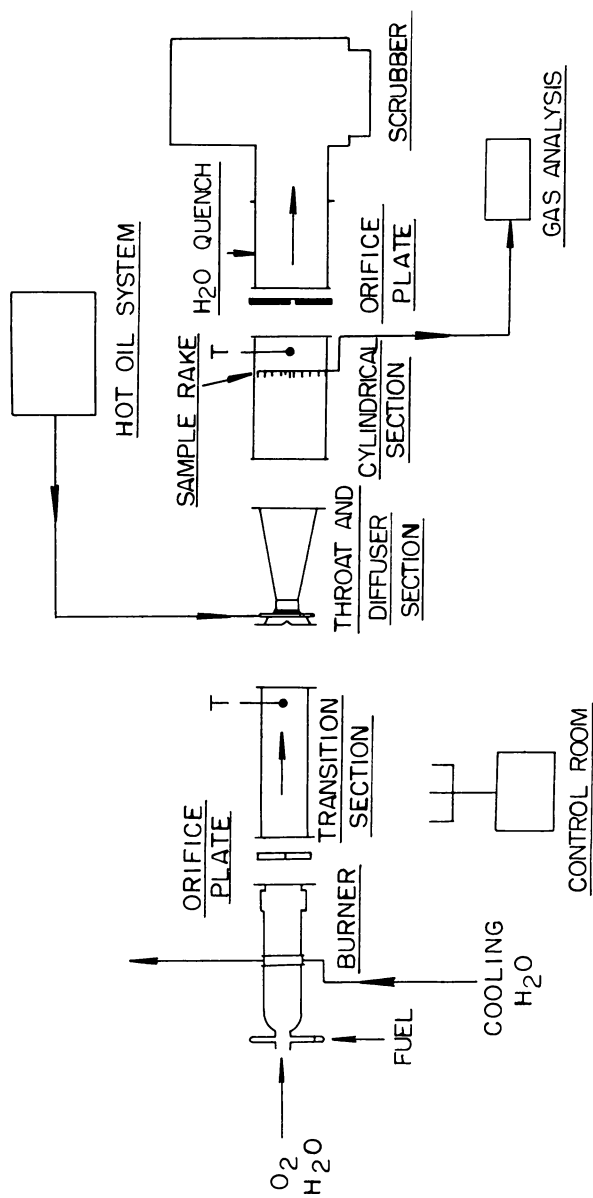


Figure 4. Full-scale ACR gas yield test equipment

of a converging region followed by the throat, diffuser, and reactor cylinder sections. A variable-area orifice at the end of the reactor was used to control the reactor pressure.

All of the experimental equipment was remotely controlled from inside a blockhouse. A bullet-proof window allowed the test equipment to be observed safely. During a test, the blockhouse was manned by several operators who controlled the flow and data systems. Flow data in the form of pressure and temperature readings from calibrated venturi flow systems were recorded automatically. Reactor and burner gas temperatures were measured with specially constructed thermocouples. The test piece was instrumented with a series of pressure transducers throughout its length.

During a test, the following general sequence of events occurred as the operators followed their checklists.

(1) Cooling water flows were initiated in the burner.

(2) Ignitor flows were brought up to a preset condition and the burner was ignited. This low-combustion gas flow was allowed to preheat the piece.

(3) Main burner flows were slowly (5–15 seconds) brought up to the desired set point combustion conditions.

(4) After operators indicated all systems were “on condition,” the data recording and oil injection systems were actuated.

(5) The data were recorded during the “on condition” time (5–20 seconds).

(6) The fuel, oxygen, and oil flows were then shut-off with fast acting valves.

In the test hardware, there are rather large heat losses and corresponding combustion-gas temperature drops which must be taken into account to generate the desired cracking temperatures at the oil injection location. For example, under typical ACR operating conditions, it is possible for the water-cooled burner to lose on the order of 100°C in gas temperature. An additional 100°C in gas temperature is lost to the uncooled stainless-steel transition ducting that connects to the test reactor. When running in the high temperature, short duration mode, this significant heat loss is controlled by increasing the burner temperature while constraining the total mass flow near the cracking S:F level.

To predict the heat losses and operate the facility, a storage heat exchanger analysis paralleling that of Becker (19) was first performed for each desired ACR condition. The analysis included the simple cooling heat loss in the burner and the more complex time- and position-dependent transfer of heat to the walls of the transition section. Accounting for this type of heat storage is fundamental to high temperature–short duration operation since it exists throughout the test assembly, including the reactor itself. For example, when the flows are at condition, the walls

of the transition section near the burner exit are initially at a relatively low temperature (i.e., position = 0, time = 0, $T_{\text{wall}} = 400^\circ\text{F}$). By the end of the test, the wall temperature has increased substantially (i.e., position = 0, time = 45 sec, $T_{\text{wall}} = 1500^\circ\text{F}$). This change in the transition section's average wall temperature is energy coupled with the gas temperature at the corresponding time and position.

During our short "on condition" test period, the heat loss associated with position rather than time is the dominating factor at the downstream oil injection location. The combustion gas temperature at this location is a prime process variable that was maintained nearly constant at the desired level. The temperature slightly upstream of the injection location was measured (20) at the 2000°C level, and an experimental graph of the "steam" temperature-time profile taken during the gas yield test is shown in Figure 5. This graph shows the burner ignition, operating changes in flows (ramps), and the constant level of "steam" temperature supplied during the "on condition" time.

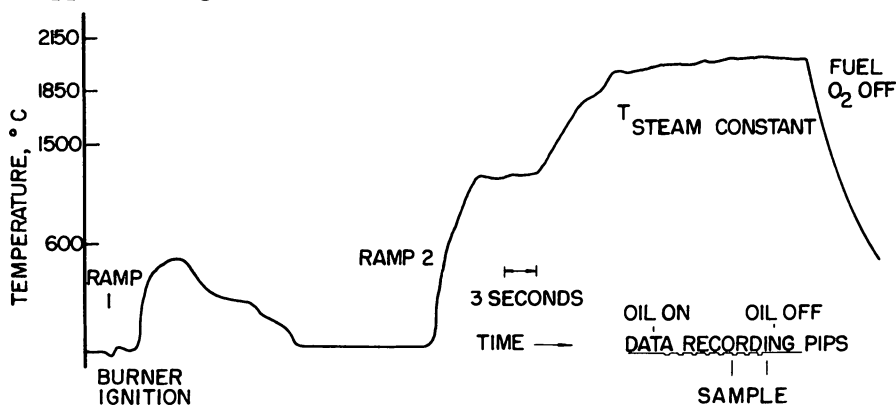


Figure 5. Venturi inlet "steam" temperature-time profile. Commercial test-run 13.

Hot-Flow Penetration Experiments

The full-scale ACR penetration test piece was equipped with large quartz windows in the throat region which permitted the use of various laser-camera photographic techniques for recording the desired oil penetration and atomization data. To allow the windows to survive the typical 2000°C test conditions, a nitrogen-film cooling technique was applied to the inner surface. The thin film of nitrogen was introduced into the combustion-gas flow through a manifold and specially constructed knife-edge slot positioned upstream from the windows in the test piece. Nitrogen film cooling was capable of protecting the entire exposed inner surface of the windows for up to 45 sec.

The window design required the penetration test piece to be constructed with a rectangular cross section rather than the typical circular ACR configuration. To duplicate expected ACR fluid-flow parameters, the rectangular dimensions were sized to produce the area ratios and Mach numbers consistent with the originally proposed prototype ACR. A reactor cylinder was not required since gas yields were not measured during this test.

In the test piece, the high temperature combustion gases converged into the venturi throat where oil was injected at high pressure from two opposing injectors located at the top and bottom. It was possible to observe the atomized oil vaporizing in the throat as it penetrates into the cracking gas stream. The resulting mixture then passes through the diffuser, exits into the atmosphere, undergoes combustion, and finally passes into a high capacity, vacuum exhaust manifold.

The initial phase of the hot penetration experiments was conducted using TRW (9) optical techniques. These techniques were based on firing a high intensity, ruby laser pulse (1/2 J) through one of the test piece windows. The 5–50 nsec duration of the pulse effectively stopped the motion of the injected oil particles. The particle shadows were recorded with a lens–camera assembly (shadowgraphy) that was mounted on the far window. A similar experimental assembly was built to obtain “Gabor” holograms. Most of the test pictures were recorded on holographic plates which were essentially grainless (~ 3000 line pairs/mm). After the experimental program was completed, photomicrographic analyses were performed with a helium–neon laser interference reconstruction technique. Minimum oil particle sizes on the order of 10–50 μm could be detected in the test piece throat.

Double pulsing of the laser recorded two sets of bulk particle images on the same photographic plate. The measured particle distance travelled (~ 1 cm) divided by the known time interval between pulses (20–400 μsec) was used to estimate the bulk particle velocity. The experimental velocities compare favorably with the theoretical velocities generated by the ACR computer model (*see* Tables II and III). The computer droplet size and velocity histories in the ACR throat were generated from the cold-flow test work, droplet distributions. In the calculations, resistance to mass transfer from the droplet surface is assumed to be negligible. Thus, the rate of vaporization is controlled by the rate of heat transfer to the droplet surface, which is at its boiling point. Also, it is assumed that the droplets are at a uniform temperature and that they vaporize as in true boiling point distillation. The vaporizing drop phenomenon is then modeled by a film theory approach (21, 22) in which the resistance to heat transfer is attributable to the film surrounding the droplet. The system conservation equations are then solved and the velocity of the

Table II. Particle Velocity Experimental Data

| <i>Laser Run</i> | <i>Injector^a</i> | Δt^b | ΔD^c | T^d | <i>Injection Pressure</i> | V^e |
|------------------|-----------------------------|--------------|--------------|-------|---------------------------|-------|
| 109 | 2 × KC5 | 20 | 0.8 | high | high | 1300 |
| 111 | 2 × KC5 | 20 | 0.5 | high | high | 800 |
| 113 | KC5 | 80 | 1.2 | high | low | 500 |
| 115 | 2 × KC5 | 80 | 1.25 | low | high | 500 |
| 116 | 2 × KC5 | 80 | 1.5 | high | high | 600 |
| 118 | KC5 | 420 | 3.3 | low | high | 250 |

^a KC5 = commercial scale injector × 2 (two injectors).

^b Δt = laser pulse separation (μsec ; 10^{-6} sec).

^c ΔD = particle distance traveled (cm).

^d T = combustion gas temperature.

^e V = particle velocity (ft/sec).

Table III. Computer Model Predicted Particle Velocity

| d_o^a | $d_{MT}^{b,d}$ | $PCVAP/MT^{c,d}$ | V^e |
|---------|----------------|------------------|-------|
| 81 | 23.7 | 97.5 | 970 |
| 94 | 37.9 | 93.4 | 900 |
| 113 | 56.5 | 87.4 | 830 |
| 138 | 79.3 | 81.0 | 770 |
| 188 | 122 | 72.6 | 680 |

^a d_o = assumed initial particle diameter at injector (μm) (the corresponding number frequency is based on cold flow distribution results).

^b d_{MT} = particle diameter in middle of throat (μm).

^c $PCVAP/MT$ = percent of mass vaporized in middle of throat for given initial particle size.

$$^d d_{MT} = \left[\left(\frac{100 - PCVAP}{100} \right) d_o^3 \right]^{0.333}$$

^e V = predicted velocity at middle of throat (ft/sec).

vaporizing droplet is changed as momentum is transferred between the droplet and the gas by both aerodynamic drag and mass transfer.

During some of the penetration tests, a high-speed movie camera (16 mm Fastex) was used to record the time-dependent spray stability in the ACR throat region. Film taken at 2,000 and 10,000 frames per second was then slowed down for data analysis. Also, conventional cameras (70 mm, Super 8) recorded the bulk oil spray by time integrating the overall oil penetration over relatively long exposure times (1/50 second). In this technique, the light from the oil-air combustion at the exit of the test piece diffuser illuminated the fine oil droplets in the throat. Color photographs showed the oil penetration as a well defined light region. A reference grid on the window allowed the appropriate penetration coordinates to be taken from the photographs. The hot-test penetration data was then compared with the cold-test predictions.

The experimental data permit the extension of cold-flow work resulting in the desired high temperature, oil penetration correlations. The additional information on particle sizes, velocities, and spray stability was used to confirm and revise our present understanding of the flashing/atomization/vaporization phenomena occurring in the ACR.

Full-Scale Gas Yield Test

The full-scale, ACR gas yield test equipment is illustrated in Figure 4. The appropriate ACR combustion gas temperature and mass flow rates ($T \sim 2000^\circ\text{C}$, $W < 25$ lb/sec) were generated in a manner similar to the hot penetration investigation. A hot oil system injected preheated oil at commercial flow rates (5–15 lb/sec).

A typical reactor cylinder temperature–time profile taken during the test is shown in Figure 6. This figure illustrates the general series of events controlled by a minicomputer. After the combustion gas temperature was brought “on condition,” the oil was injected, and the oil cracking rapidly lowered the reactor temperature. Constant flows were maintained, and the reactor temperature remained approximately constant with a slight upward drift. A number of vacuum, purge, and sampling valves were actuated, with the cracked gas sample being taken near the end of the oil injection period. Individual samples were simultaneously taken across the reactor cylinder diameter. Several hundred reactor volumes passed the sample probe during the sampling period. Pressure and temperature data were automatically recorded. The oil was then shut-off, causing the reactor temperature to rise because of the pure combustion gas flow condition.

The collected gas samples were analyzed batchwise with a gas chromatographic system. An argon-gas tracer technique was used to

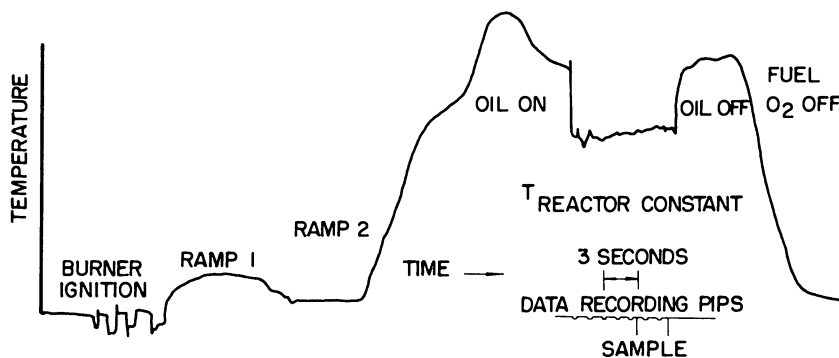


Figure 6. Reactor exit temperature–time profile. Commercial test–run 16.

determine the actual gas yield concentrations in the reactor. This technique was based on introducing a small but extremely well known flow of argon into the burner. The argon in the reactor was measured and ratioed to the hydrocarbon reactor products. These ratios were multiplied by the known argon mass flow to determine the absolute flow of reactor hydrocarbon products which was then converted to a gas yield basis (lb/100 lb oil).

Computer data analysis was conducted on site. The yields were then best-fit regressed as a function of operating variables. Yield-response contour maps around the base ACR operating case also were generated. This procedure was augmented by statistically designing the test around directly controllable operating variables. The general design allows one to obtain the maximum information from a minimum of data. This technique also avoids the necessity of exactly matching all the process variables simultaneously. The inherent control problems of the short duration method also are minimized.

Since the described short-duration technique was somewhat unique as a reactor-gas yield test method, a reference test of a well-known production oil cracking reactor was first run to calibrate the system. The reference reactor chosen was the crude oil cracker which is part of a production plant operated by one of our ACR partners, Kureha Chemical Ind., Ltd. The Kureha plant reactor operates at conditions approaching that of an ACR.

The reference test was conducted in a stainless steel reactor assembly which was sized to duplicate the Kureha reactor geometry. The experimental operating conditions compared favorably with the actual plant conditions. In particular, the steam temperature, S:F ratio, residence time, oil feed rate, and heat input were matched very closely. However, the reactor exit temperature was somewhat lower than that of the operating plant. The experimental gas yields for ethylene, ethane, propylene, and propadiene agreed very well with the plant. There were slightly lower experimental values for hydrogen, methane, acetylene, and total gas, which indicated a less severe crack.

In the reference test, the low reactor exit temperature at the constant plant-energy input conditions indicates the expected higher heat losses in a short-duration reactor. The corresponding lower overall temperature profile through the test-reactor length reduces the process kinetic time-at-temperature. The associated gas-phase chemical kinetics at the lower residence times are believed to be responsible for the slight discrepancies in the reference test gas yields. Also, the "true" enthalpy used for cracking is lower than that indicated by the measured reactor temperature.

The reference test work was used to calibrate and revise the operating procedures for the full-scale ACR test. The additional reactor heat

loss was accounted for by slightly increasing the process combustion gas flow (S:F) while keeping the combustion gas temperature at the oil-injection location constant. This added energy made up for the reactor heat loss resulting in a reactor exit temperature that experimentally matched the pilot scale data. However, this technique actually corresponds to a slight increase in the overall temperature profile through the short-duration reactor length. The temperature differential between the typical plant ACR case and the short duration reactor is greatest at the oil-injection control volume. This is also the region of the highest process temperatures which tend to generate high C_2H_2 yields.

Based on the temperature profile, a kinetic analysis of this short-duration heat loss adjustment technique predicts a slightly more severe cracking condition compared with the typical ACR operation. This effect is most pronounced near the oil-injection region and decreases through the reactor length. The combined result is to slightly increase the C_2H_2 yield and correspondingly lower the ethylene yield while keeping the total C_2s and total gas yield approximately constant. When the test is conducted without the heat-loss adjustment technique, the initial process temperature at the oil-injection control volume is equal in the short-duration and continuous-plant cases. However, as indicated by the Kureha reactor reference test, the final temperature at the reactor exit is too low. This tends to produce the same general quantities of C_2H_2 near the high temperature, oil-injection region while other yields fall off because of the lower overall temperature profile through the short-duration reactor. Since the short-duration test technique does not match both the oil-injection region and the reactor exit temperatures simultaneously, combinations of the heat-loss adjustment technique were run in the test design. The expected yield effects were observed experimentally and when they were accounted for, the full scale ACR yield distribution followed the pilot scale cracking pattern.

Thus, the ACR scale criteria has been verified under the extreme condition of directly scaling from a pilot to a full-scale reactor. This allows the smaller scale ACR demonstration unit to be designed with confidence. As required, the data from the demonstration unit will be used to further refine the scaling techniques before the commercial ACR process design is finalized.

Literature Cited

1. Hosoi, T.; Keister, R. G. *Chem. Eng. Prog.* 1975, 71, 63.
2. Ozaki, Kiyoji; et al. "Method of Recovering Heat from Hydrocarbon Thermal Cracking Products," Japan patent application Kokai 90302/1976, August 7, 1976. (See *Chem. Week* Sept. 28, 1977, p 39.)

3. Johnstone, R. E.; Thring, M. W. "Pilot Plants, Models, and Scale-up Methods in Chemical Engineering"; McGraw-Hill: New York, 1957.
4. Walas, S. M. "Scaling Test Results," In "Reaction Kinetics for Chemical Engineers"; McGraw-Hill: New York, 1959; Chapter 10.
5. Shapiro, A. H. "The Dynamics and Thermodynamics of Compressible Fluid Flow"; Ronald: New York, 1953.
6. Putnam, A. A.; et al. "Design of Atomizers," In "Injection and Combustion of Liquid Fuels"; 1957; Chapter 3 (WADC Technical Report 56-344).
7. Mugele, R. A.; Evans, H. D. *Ind. Eng. Chem.* **1951**, *43*, 1317.
8. Dombrowski, N.; Wolfsohn, D. L. *Trans. Inst. Chem. Eng.* **1972**, *50*, 259.
9. TRW Defense and Space Systems Group, Redondo Beach, CA
10. Ingebo, R. D.; Foster, H. H. "Drop-Size Distribution for Crosscurrent Breakup of Liquid Jets in Airstreams," NACA Technical Note 4087, 1957.
11. Geery, E. L.; Margetts, M. J. *J. Spacecr. Rockets* **1969**, *6*, 79.
12. Hojnacki, J. T. "Ramjet Engine Fuel Injection Studies," AFAPL Technical Report 72-76, 1972.
13. McDonnell-Douglas Aerophysics Laboratory, El Segundo, CA.
14. Dobrzynski, W. "Deutsche Luft-und Raumfahrt (German Aeronautics and Astronautics)," Research Report 72-19, 1972.
15. "Main Engine Test Program Accelerates," *Aviat. Week Space Technol.* **Nov. 8, 1976**, p 59.
16. Wuerker, R. F.; Matthews, B. J.; Briones, R. A. "Producing Holograms of Reacting Sprays in Liquid Propellant Rocket Engines," JPL Contract No. 952023 (NAS 7-100), 1968.
17. George, D. J.; Spaid, F. W. "Holography as Applied to Jet Breakup and an Analytical Method for Reducing Holographic Droplet Data," Technical Report AFRPL-TR-72-72, 1972.
18. The Marquardt Company, Van Nuys, CA.
19. Becker, J. R. "Analysis of Storage Type Heat Exchanger," The Marquardt Co., October 15, 1956; from Leitinger, H., "Research on the Design of Hypersonic Nozzles and Diffusers at High Stagnation Temperatures, Part 1," Appendix 4 (WADC 55-507).
20. "High Temperature Thermocouples," Manual 48125, probe T-1105, Aero Research Instrument, American Standard.
21. Priem, R. J.; Heidmann, M. F. "Propellant Vaporization as a Design Criterion for Rocket-Engine Combustion Chambers," Technical Report R-67, NASA, Lewis Research Center, Cleveland, Ohio, 1960.
22. Beér, J. M.; Chigier, N. A. "Combustion Aerodynamics"; Halstead: New York, 1972.

RECEIVED June 26, 1978.

Computer Modeling of Hydrocarbon Pyrolysis for Olefins Production

L. L. ROSS and W. R. SHU

C. F. Braun and Co., Alhambra, CA 91802

Computer modeling of hydrocarbon pyrolysis is discussed with respect to industrial applications. Pyrolysis models are classified into four groups: mechanistic, stoichiometric, semi-kinetic, and empirical. Selection of modeling schemes to meet minimum development cost must be consistent with constraints imposed by factors such as data quality, kinetic knowledge, and time limitations. Stoichiometric and semi-kinetic modelings are further illustrated by two examples, one for light hydrocarbon feedstocks and the other for naphthas. The applicability of these modeling schemes to olefins production is evidenced by successful prediction of commercial plant data.

Olefins constitute a basic building block of the petrochemical industry. Traditionally, light hydrocarbon pyrolysis has been a major source for olefins. Owing to present exploitation of North Sea and Middle East gas reserves, this should continue to be the case in the short term. Long-term demand, however, is accelerating a shift to petroleum-based feedstocks, such as naphthas, gas oils, and even whole crudes. The changing economics associated with the availability of these feedstocks have placed a premium on incorporating a high degree of flexibility into the design of a modern pyrolysis reactor. This, in turn, has provided the incentive for developing pyrolysis models applicable over a wide range of feedstocks—from light hydrocarbons to heavy gas oils. Fundamental to achieving this goal is the need for a self-consistent, computational framework for developing pyrolysis technology.

The system is illustrated in Figure 1. Inputs are a data base including pilot, commercial, and literature sources. The type and extent of data are compatible with plant design objectives. Although the contribution of all data sources is significant, the role of a pilot test facility is central to the development of sound technology.

The data form the basis of pyrolysis models consistent with both theoretical and practical considerations. The resulting models are integrated into a complete reactor simulation, which is then applied in design and optimization work. The simulation includes detailed models describing process-side heat and momentum transfer, thermophysical properties, and fired-side radiative heat transfer.

The reactor model is interfaced with a proved nonlinear optimization package. Its modular form ensures the flexibility needed to accommodate a wide range of problems, the bulk of which involve boundary-value specifications and constraints associated with well-defined objective func-

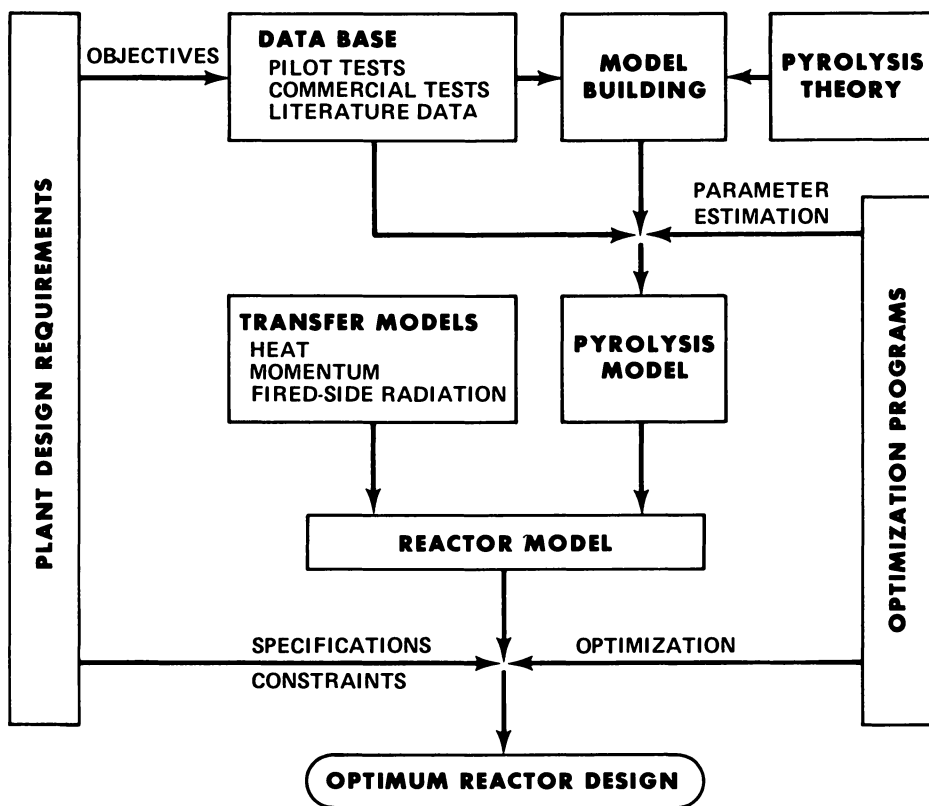


Figure 1. Pyrolysis technology development system

tions. Problems not amenable to direct solution, because of either incomplete definition or computational time limitations, are solved by case study.

The focus of this chapter is to provide an overview of pyrolysis-modeling techniques, with emphasis on industrial applications. Examples are outlined for the case light hydrocarbon and naphtha pyrolysis.

Reactor Model

All modern olefins plants now under design and construction use indirectly fired tubular pyrolysis reactors. Although this type of reactor is presently undergoing several challenges (1, 2), it should continue to hold a dominant position for many years to come. A tubular reactor may be simulated by a set of ordinary differential equations (3). Reaction

$$\text{Energy} \quad C_p G \frac{dT}{dZ} = - \sum_i H_i r_i + Q \quad (1)$$

$$\text{Momentum} \quad \frac{dP}{dZ} = - \frac{fG^2}{2g_c \rho D} + \frac{G^2}{\bar{a}g_c \rho^2} \frac{d\rho}{dZ} \quad (2)$$

$$\text{Kinetics} \quad G \frac{d\xi_i}{dZ} = r_i(\xi_1, \xi_2, \dots, \xi_m, T), i = 1, 2, \dots, m \quad (3)$$

extents, ξ , may be converted to experimentally accessible concentrations, Y_j , and fluid density, ρ , by means of the stoichiometric coefficients, S_{ij} , associated with the reaction network, r_i . The reactor description is com-

$$\text{Composition} \quad Y_j = Y_{j0} + \sum_i S_{ij} M_j \xi_i \quad (4)$$

$$\text{Density} \quad \rho = \rho_0 \frac{P}{P_0} \frac{T_0}{T} (1 + \bar{M}_0 \sum_i \bar{S}_i \xi_i)^{-1} \quad (5)$$

pleted by relating the tube and furnace side heat transfer processes via a radiative heat transfer model. (Refer to Nomenclature for symbol definitions.)

It should be noted that Equations 1, 2, 3, 4, and 5 imply a homogeneous kinetic system. Coking in tubular reactors results from a combination of homogeneous and heterogeneous processes. As the kinetics of these processes are not well understood and as the quantitative yield of coke is several orders of magnitude smaller than other pyrolysis products, it is more convenient to model coke formation separately based on commercial operating data.

Thermophysical and transfer properties needed to solve the heat and momentum transfer equations are available from the literature. Thus, reactor model is completed by the development of an appropriate kinetic model for pyrolysis.

Pyrolysis Model Development

Several factors must be considered in arriving at a level of sophistication of modeling consistent with industrial objectives. This is illustrated in Figure 2, where the cost of model development is expressed as a function of model sophistication. High level models require a smaller data base but are more expensive to develop and formulate. On the other hand, empirical models, although simpler to formulate and solve, rely heavily on an extensive data base which is costly to maintain.

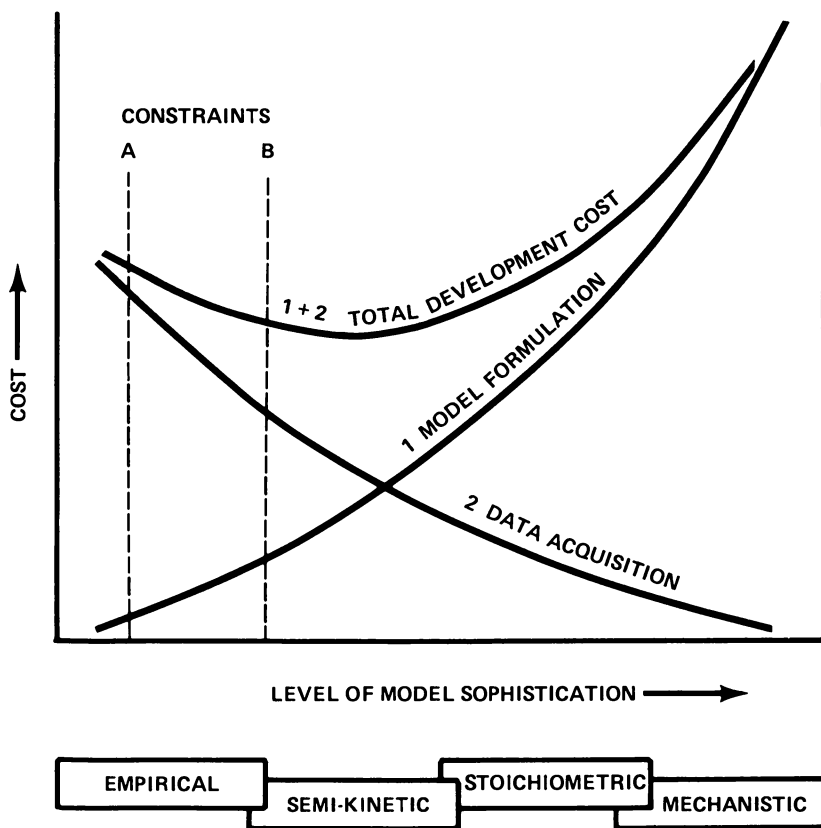


Figure 2. *Pyrolysis model development cost*

Although a global optimum modeling level may exist with respect to development cost, final selection must fall within the constraints imposed by the quality of data, the knowledge of kinetics, the ultimate use, and the computation and development time limitations. For example, although knowledge of kinetics may permit high-level modeling, the available development time might very well dictate a more empirical approach.

For convenience, computer modeling of hydrocarbon pyrolysis may be categorized into four types. In order of decreasing degree of sophistication, these are mechanistic, stoichiometric, semikinetic, and empirical. A brief description of each follows.

Mechanistic Modeling. In mechanistic modeling, an intrinsic reaction network is determined, based on the most probable mechanistic description. Rate constants are established individually for these elementary reactions through kinetic measurements. This type of model allows confident extrapolation outside the range of the data base used in its development.

Mechanistic modeling has been useful in studying pyrolysis kinetics at low conversion (4, 5, 6). Few attempts have been reported at the high conversion levels of commercial cracking (7). This stems from the large number of species and free radicals and of their associated reactions, which increases substantially with conversion and leads to excessive computation time. In addition, when one considers that precise pyrolysis mechanisms, for even a simple feedstock such as propane (8), are still subject to dispute, it is clear that more empirical models will continue to dominate commercial applications.

Stoichiometric Modeling. Here a series of reactions is postulated based on knowledge of gross stoichiometry, which may also include mechanistic knowledge. Sufficient reactions and stoichiometry are defined to enable the model to account for observed product distributions. No attempt is made to capture the fine details of pyrolysis. Rather, the model is simplified to incorporate the smallest number of rate equations. This minimizes the number of parameters that must be established from operating data.

Starting with the pioneering work of Myers and Watson (9) on propane pyrolysis, this approach has been successfully applied to virtually all light hydrocarbons (10, 11, 12, 13, 14) and extended up to C₈ normal and branched paraffins (15, 16). Fewer studies have been reported on mixture pyrolysis (17, 18, 19), especially for heavier feedstocks (20). This type of modeling will be illustrated later with an example.

Semikinetic Modeling. The kinetic framework used is relatively simple, often consisting of only one or two reactions. It is used to capture overall pyrolysis behavior. Solution of the kinetic framework provides the

system parameters needed for the development of empirical correlations for product spectra. Although their functional form may take into account theoretical considerations, the primary objective is to achieve a computational framework amenable to rapid linear regression methods.

This type of model is compatible with complex feedstocks (21, 22), where limited understanding of the mechanisms involved and the size of the reaction network preclude stoichiometric modeling. Its range of applicability depends not only on the extent of data base used to estimate model parameters, but on the degree to which its empirical framework reflects true kinetics. This approach will be illustrated later.

Empirical Modeling. Numerous yield data arrays are classified over many operating conditions and feedstock properties. The number and type of base feeds (and their yield arrays) are selected to approximate the specific application. Interpolation, using empirical and theoretical relationships, provides the means to the final prediction of reactor operating conditions and product slate.

Success in this type of modeling depends on the soundness of the interpolation methods used and the extensiveness of the data base. In addition, the data base must include substantial commercial data to confirm scale-up procedures, if needed. One example is a pyrolysis yield model for virgin gas oil and pretreated feedstocks (23). Feedstocks are classified by source and appropriate characterization parameters.

Light Hydrocarbon Pyrolysis Model

Stoichiometric modeling is illustrated by a pyrolysis model for light hydrocarbons and their mixtures. The reaction network is summarized in Table I. Details on the model development have been reported previously (24). The reactions can be categorized as primary reactions, R-1 through R-11, wherein reactants are decomposed, and secondary reactions, R-12 through R-19, which take into account degradation of primary products, including bimolecular reactions leading to heavy end products.

The model includes several reactions which account for cocracking effects. Examples of this type of reaction include the reverse reactions of R-1 and R-4 and the reaction R-17. R-17 predicts more ethylene and less heavier products from cocracking ethane and propane than from separate cracking.

Model Parameters. Model parameters to be estimated were reaction rate constants and the orders and stoichiometric coefficients of the secondary reactions. Stoichiometries of the primary reactions were directly accessible from free-radical mechanisms (4, 5). Secondary reac-

Table I. Light Hydrocarbon Pyrolysis Model^a

| <i>Reaction</i> | <i>Stoichiometry</i> | <i>Activation Energy (cal/g-mol)</i> |
|-----------------|--|--------------------------------------|
| R-1 | $C_2H_6 \rightleftharpoons H_2 + C_2H_4$ | 71,540 |
| R-2 | $C_2H_6 \rightarrow 0.3H_2 + 0.6CH_4 + 0.5C_2H_4 + 0.1C_4H_{10}$ | 60,000 |
| R-3 | $C_3H_8 \rightarrow CH_4 + C_2H_4$ | 65,700 |
| R-4 | $C_3H_8 \rightleftharpoons H_2 + C_3H_6$ | 63,000 |
| R-5 | $C_3H_8 \rightleftharpoons 0.5C_2H_6 + 0.5C_4H_{10}$ | 54,000 |
| R-6 | $C_4H_{10} \rightarrow CH_4 + C_3H_6$ | 47,500 |
| R-7 | $C_4H_{10} \rightarrow H_2 + 2C_2H_4$ | 68,100 |
| R-8 | $C_4H_{10} \rightarrow C_2H_4 + C_2H_6$ | 42,470 |
| R-9 | $C_4H_{10} \rightleftharpoons H_2 + C_4H_8$ | 63,000 |
| R-10 | $i-C_4H_{10} \rightarrow CH_4 + C_3H_6$ | 66,600 |
| R-11 | $i-C_4H_{10} \rightarrow H_2 + i-C_4H_8$ | 51,240 |
| R-12 | $C_2H_4 \rightleftharpoons H_2 + C_2H_2$ | 80,000 |
| R-13 | $1.5C_2H_4 \rightarrow CH_4, C_3H_6, C_4H_6, C_5^+$ | 60,800 |
| R-14 | $C_2H_4 + C_4H_6 \rightarrow H_2, CH_4, C_5^+$ | 52,000 |
| R-15 | $C_3H_6 \rightleftharpoons H_2 + C_3H_4$ | 82,600 |
| R-16 | $C_3H_6 \rightarrow H_2, CH_4, C_2H_4, C_4H_8, C_5^+$ | 64,000 |
| R-17 | $C_3H_6 + 0.5C_2H_6 \rightarrow C_2H_4, \dots$ | 54,720 |
| R-18 | $C_4H_8 \rightarrow CH_4, C_3H_6, C_4H_6, C_5^+$ | 50,000 |
| R-19 | $i-C_4H_8 \rightarrow CH_4, C_3H_4, C_3H_6, C_5^+$ | 50,700 |

^a Order of reaction is equal to the molecularity of the reaction, and the equilibrium constants of reversible reactions are calculated from thermodynamic data.

tions, on the other hand, proceed in a more complex kinetic environment. It was more convenient to calculate the parameters for these reactions by proportioning product distribution data.

Example Results. A demonstration of the fit of the model to commercial data is shown in Table II. The last column compares recent commercial test data for ethane-propane against model predictions. The close prediction of ethylene, ethane, and propylene yields provides confidence in the cocracking synergism mechanism built into the model. Figure 3 compares predicted and observed process-operating profiles for the case of the *n*-butane reactor. The firing level in the reactor simulation was adjusted to meet the observed conversion at the coil outlet. Agreement in the process, tubeskin, and firebox temperatures is well within the precision of the data.

Table II. Prediction of Commercial Plant

| | <i>Feed (wt %)</i> | |
|---------------------------------------|--------------------|------------------|
| | <i>1</i> | |
| Methane | 1.08 | |
| Ethylene | 0.02 | |
| Ethane | 97.20 | |
| Propylene | 1.35 | |
| Propane | 0.35 | |
| <i>n</i> -Butane | — | |
| <i>i</i> -Butane | — | |
| Operating Conditions | | |
| Res. Time > 650°C (sec) | 1.39 | |
| HC Partial Press. Out (atm) | 1.30 | |
| Obs/Pred Coil Outlet Temp (°C) | 829/830 | |
| Yields (wt % on feed) | <i>Observed</i> | <i>Predicted</i> |
| Hydrogen | 3.51 | 3.61 |
| Methane | 6.43 | 6.10 |
| Acetylene | 0.19 | 0.28 |
| Ethylene | 46.59 | 46.32 |
| Ethane | 37.50 | 37.53 |
| MA + Pd } Propylene } Propane } | } 1.70 0.09 | } 1.50 0.18 |
| Butadiene | 1.25 | 1.30 |
| Butenes | 0.32 | 0.20 |
| Butanes | 0.29 | 0.21 |
| C ₅ Plus | 2.13 | 2.77 |
| Total | 100.00 | 100.00 |

Naphtha Pyrolysis Model

Semikinetic modeling is illustrated by a generalized model for naphtha pyrolysis. The empiricism associated with the semikinetic model dictates the need for an extensive data base for parameter estimates. The naphtha data base consists of about 400 tests covering pure components and their mixtures and 17 naphthas (25). The pure components studied were normal and isopentanes, cyclohexane, and *n*-heptane. The wide range of naphtha feed properties is summarized in Table III.

Data—Light Hydrocarbon Pyrolysis

| <i>Feed (wt %)</i> | | | | | |
|--------------------|------------------|-----------------|------------------|-----------------|------------------|
| <i>2</i> | | <i>3</i> | | <i>4</i> | |
| 0.01 | | — | | 0.29 | |
| — | | — | | 0.02 | |
| 1.54 | | — | | 69.31 | |
| 0.70 | | — | | 0.46 | |
| 97.12 | | 1.57 | | 28.96 | |
| 0.63 | | 95.33 | | 0.96 | |
| — | | 3.10 | | — | |
| 1.35 | | 1.07 | | 0.85 | |
| 1.35 | | 1.51 | | 1.32 | |
| 834/834 | | 793/793 | | 849/846 | |
| <i>Observed</i> | <i>Predicted</i> | <i>Observed</i> | <i>Predicted</i> | <i>Observed</i> | <i>Predicted</i> |
| 1.50 | 1.45 | 0.63 | 0.61 | 2.90 | 3.05 |
| 23.74 | 23.35 | 18.94 | 19.05 | 11.92 | 11.20 |
| 0.50 | 0.63 | 0.19 | 0.26 | 0.53 | 0.41 |
| 33.49 | 33.36 | 27.02 | 26.18 | 46.21 | 45.50 |
| 4.94 | 5.02 | 6.92 | 7.02 | 27.45 | 27.43 |
| 0.20 | 0.54 | 0.30 | 0.34 | 0.14 | 0.20 |
| 15.05 | 14.86 | 21.96 | 23.64 | 4.09 | 4.03 |
| 9.72 | 9.71 | 0.91 | 1.41 | 1.74 | 1.85 |
| 1.92 | 2.64 | 2.19 | 2.35 | 2.10 | 1.72 |
| 0.90 | 1.04 | 2.54 | 2.87 | 0.59 | 0.38 |
| 0.11 | 0.29 | 11.18 | 11.41 | 0.06 | 0.24 |
| 7.93 | 7.11 | 7.22 | 4.86 | 2.27 | 3.99 |
| 100.00 | 100.00 | 100.00 | 100.00 | 100.00 | 100.00 |

Table III. Naphtha Feedstock Properties

| <i>Property</i> | <i>Low</i> | <i>High</i> |
|---------------------------|------------|-------------|
| API @ 60°F | 45 | 86 |
| Mol wt | 76 | 144 |
| Hydrogen (wt %) | 13.8 | 16.2 |
| Paraffin (wt %) | 27.0 | 89.0 |
| Iso/normal paraffin ratio | 0.7 | 3.9 |
| Naphthalene (wt %) | 8.5 | 69.7 |
| Aromatic (wt %) | 1.8 | 18.7 |

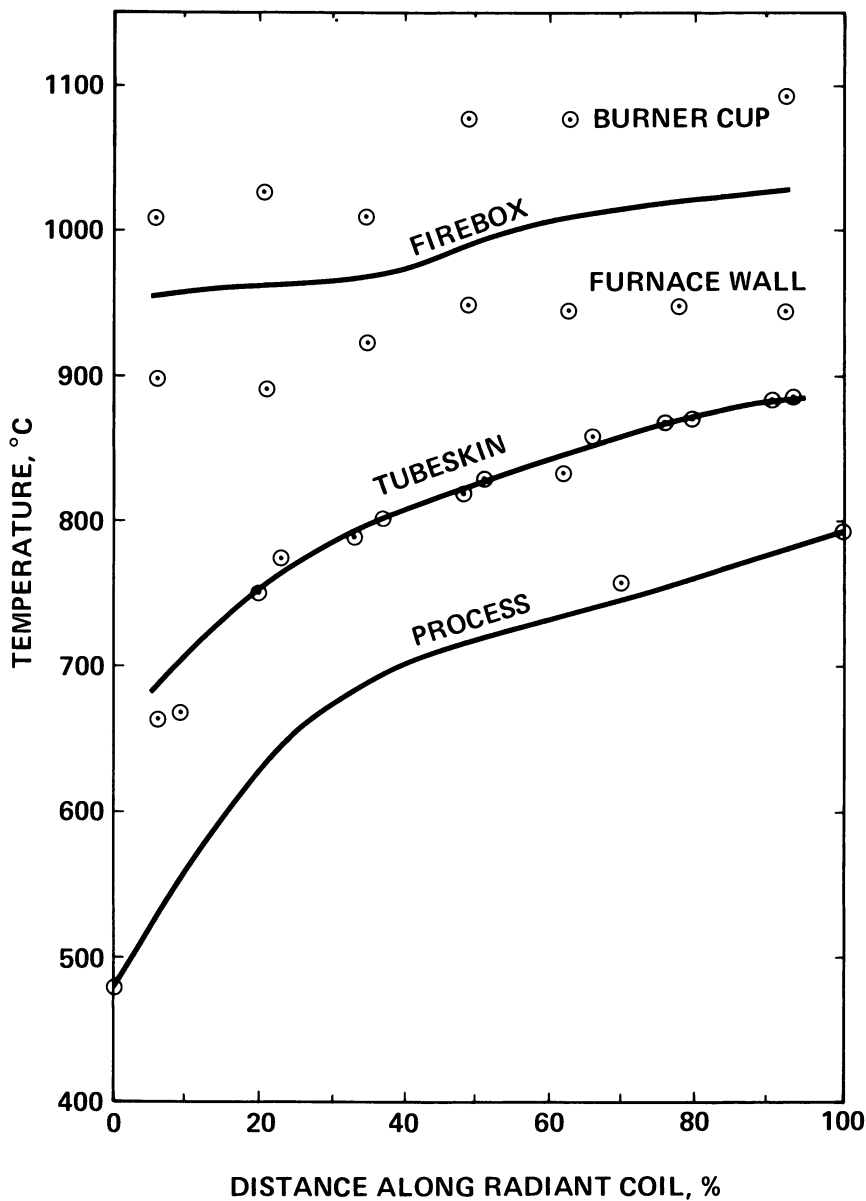


Figure 3. Temperature profiles of n-butane reactor. (—) Predicted, (○) measured.

Naphtha feed is treated as a single pseudo species. Naphthas, used as pyrolysis feedstocks, are mainly composed of paraffins and naphthenes, with lesser amounts of aromatics. Olefin content is usually very small. Consistent with observed pyrolytic behavior of paraffins and naphthenes (15, 16, 26, 27, 28), feed decomposition is assumed to follow first-order kinetics. Equation 3 of the reactor model can be simplified as follows.

$$G \frac{d\xi}{dZ} = k \frac{\rho Y_f}{M_f} \quad (6)$$

where

$$k = A e^{-E/RT} \quad (7)$$

and A and E are the Arrhenius constant and activation energy, respectively.

Likewise, the single reaction framework enables simplification of Equation 4:

$$Y_f = 1 - M_f \xi = 1 - X \quad (8)$$

$$Y_j = Y_{j0} + S_j M_j \xi = S_j \frac{M_j}{M_f} X \quad (9)$$

Substitution of Equations 7 and 8 into 6 yields, after integration:

$$\text{CSI} = -\ln(1 - X) = A \int_0^X e^{-E/RT} d\theta \quad (10)$$

CSI, defined as the Cracking Severity Index, is a direct measure of cracking severity (25).

As can be seen, the pyrolysis model consists of two parts—a kinetic-feed decomposition model (Equation 10) and an analytic-yield prediction model (Equation 9). The model parameters are the product stoichiometries, S_j , and the decomposition rate constant, k . In addition, estimation of the decomposition rate constant requires a knowledge of the feed conversion, X .

Feed Decomposition. In the case of naphtha pyrolysis, feed conversion is not generally known. Direct measurement is precluded by the large number of feed components and the difficulty of analyzing for them in the reactor effluent. To overcome this problem, a model was developed to relate the C_3 and lighter yield, an experimentally accessible variable, to feed conversion.

Both feed conversion and secondary reactions contribute in a complex manner to the net C_3 and lighter production. In spite of this, the C_3 and lighter yield (C) has been observed to increase in a simple relationship with feed conversion (X) over the range of cracking severities encountered in commercial operation. C_m is the ultimate C_3 and lighter

$$X = \frac{C}{C_m} \quad (11)$$

yield, i.e., C_3 and lighter yield per unit feed converted. It can be estimated from the C_3 and lighter yield and C_5+ hydrogen content data as in Equation 12 (25), where α and β are feed-dependent parameters

$$C_m = (\alpha + \beta \text{CSI}) \left(\frac{\text{CSI}}{\theta} \right)^{0.05} \quad (12)$$

and θ is reactor residence time above incipient cracking. It is clear that α is the initial C_3 and lighter yield per unit feed conversion which can be directly estimated from free-radical mechanism (25). Prediction of actual feed conversion using this approach is illustrated in Figure 4.

Equation 11 is now used to estimate feed conversion, which in turn is introduced into Equation 10 to generate the desired rate constant data. Modeling of the rate constant data centers on developing suitable functional forms for its parameters (A and E), followed by their estimation. It turns out that, for practical purposes, a single E -value of 55,000 cal/g-mol can be used for all naphthas (29). The Arrhenius constant requires further study.

Consistent with literature (12, 16, 27, 30), we observed that the decomposition rate constant of naphthas decreases with the increasing conversion. The overall effect of inhibition is taken into account by allowing the rate constant to vary with cracking severity index, CSI.

$$\ln k = \ln k_o + \sum_{i=1} a_i \text{CSI}^i \quad (13)$$

where

$$\ln k_o = a_o - \frac{55,000}{RT} \quad (14)$$

The inhibition effect is only weakly dependent on feed properties. It appears that heavier feeds, with higher carbon to hydrogen ratios, exhibit larger inhibition in their rate constants.

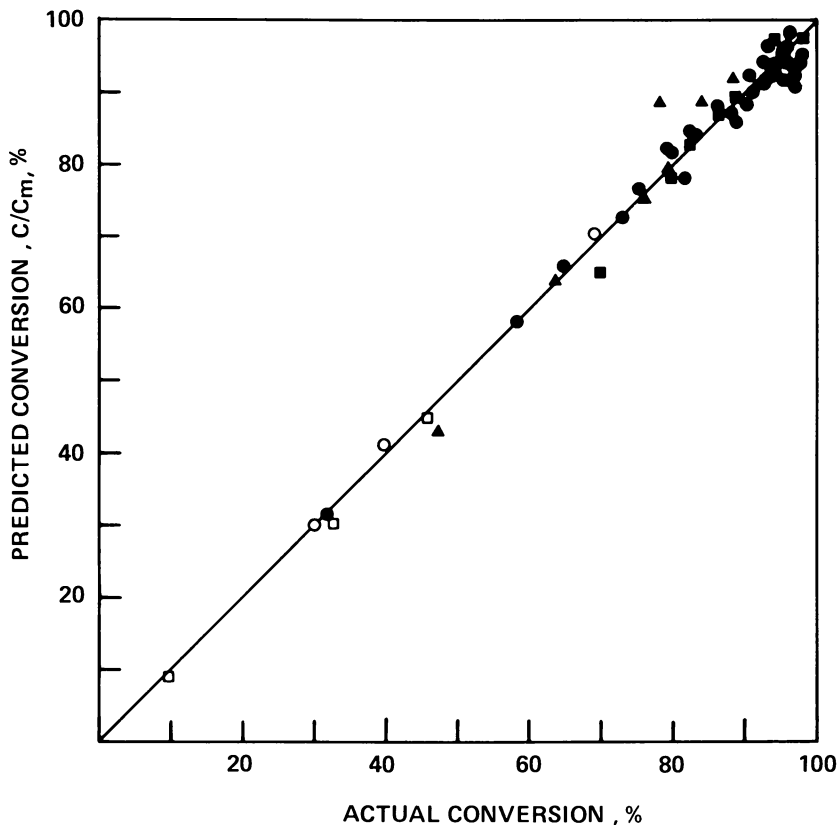


Figure 4. Predicted vs. actual feed conversion. Feed: (○●) *n*-heptane, (□■) *i*-pentane, (▲) cyclohexane (open symbols are literature data).

The zero-conversion rate constant (k_0) is correlated with feed properties. The dominant parameter is the average feed carbon number. Feed hydrogen content and *i/n* paraffin content also play an important role. These parameters are embodied in Equation 15 (29), where b_s are positive numbers.

$$\ln k_0 = b_0 + b_1 n + b_2 z - b_3 P_i - \frac{55,000}{RT} \quad (15)$$

Figure 5 shows predicted zero-conversion rate constants for C_5 through C_8 *n*-paraffins. Also shown are k -values extrapolated from low conversion literature data (15, 31–35). The correlation is seen to be in good agreement with literature data. The temperature dependence is well captured by the constant activation energy of 55,000 cal/g-mol. Figure 6

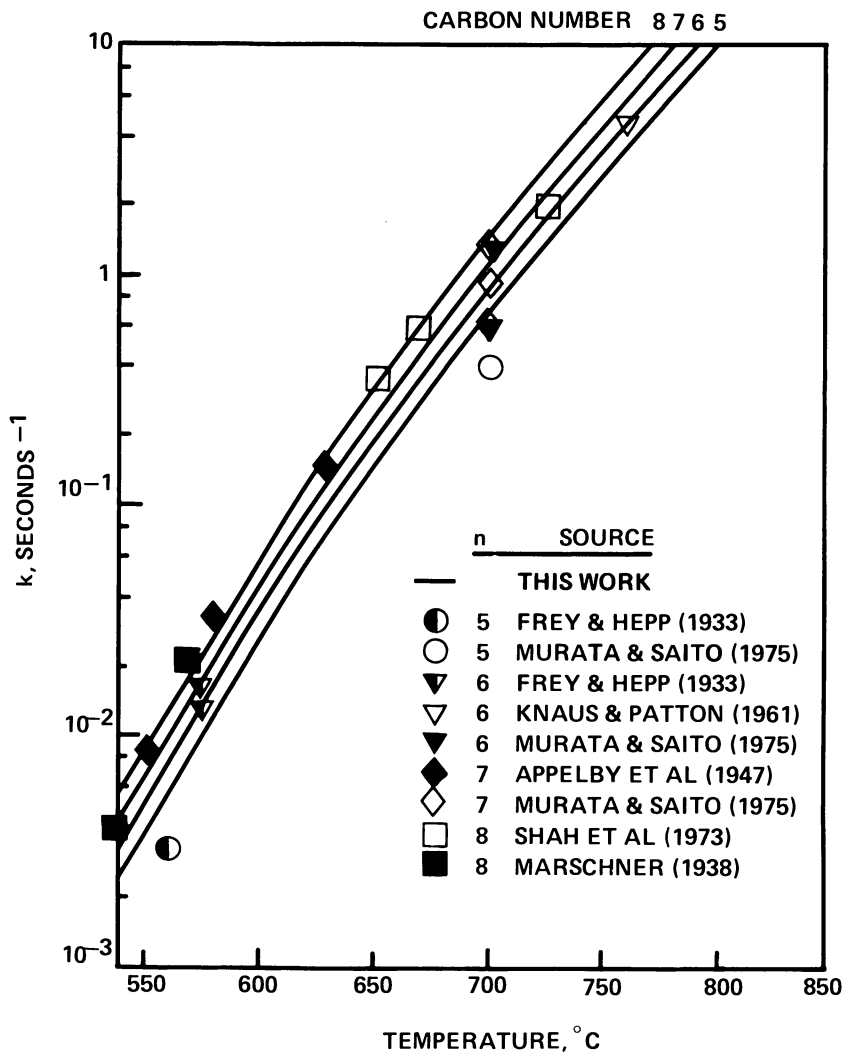


Figure 5. Decomposition rate constants for C_5 - C_8 n-paraffins at zero conversion

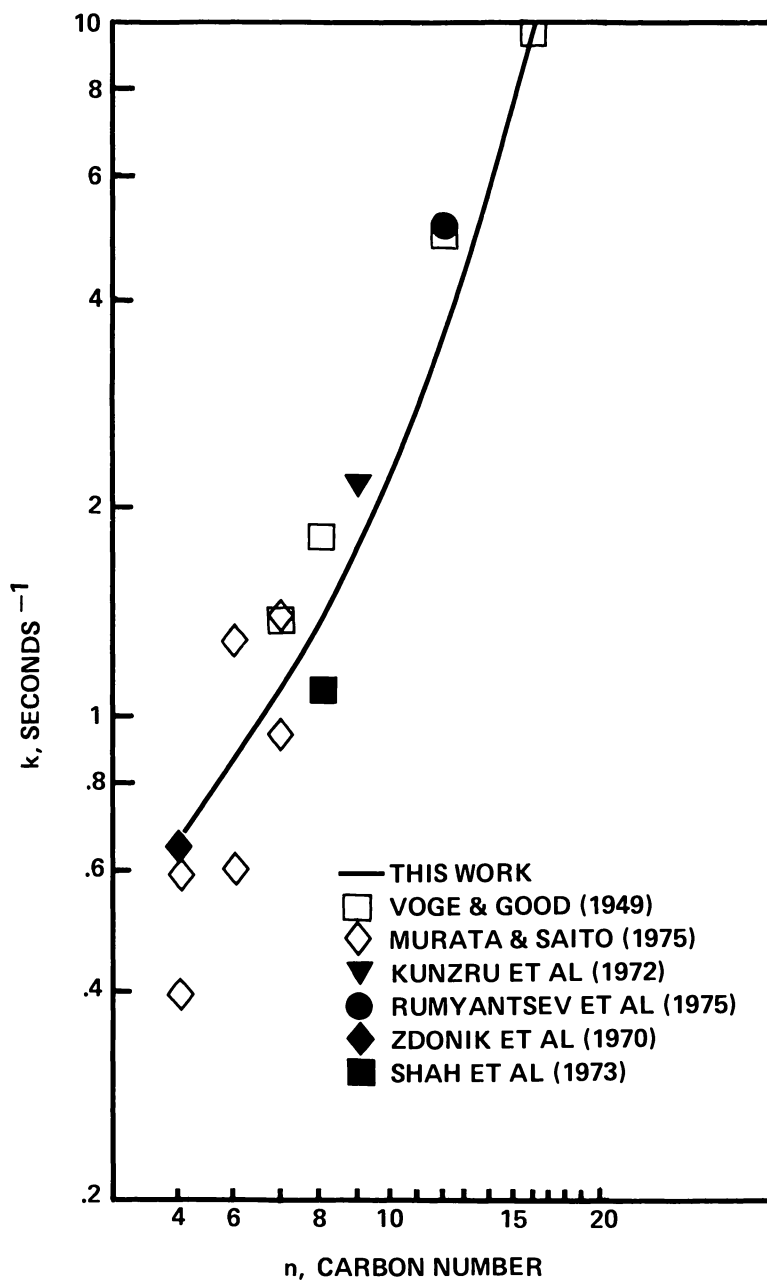


Figure 6. Decomposition rate constants for n-paraffins at zero conversion at 700°C

compares k_0 at 700°C for *n*-paraffins up to C₁₆. The predictions match very well with the data (15, 26, 28, 34, 36, 37). More significantly, the correlation takes into account the variation of feed carbon number.

It was pointed out earlier that Equations 11 and 12 do not apply at feed conversion outside the range of commercial operating conditions. In this regime, feed conversion must be calculated from the rate constant integrated via Equation 10. It remains to complete the overall model by developing a correlation to relate pyrolysis yields to process operating parameters and feed conversion.

Yield Correlation. Pyrolysis yields vary primarily with feed conversion and to a lesser degree with operating conditions. The latter is termed selectivity effect. Yield selectivity, for a given feedstock, can be defined as the effect of temperature and pressure profiles on yield structure at a fixed feed conversion or CSI. The present model uses two parameters based on integrated average operating conditions to account for nonisothermal and nonisobaric cracking profiles. These are residence time above incipient cracking (θ) and kinetic average hydrocarbon partial pressure (KAPP). The latter parameter is the reactor hydrocarbon partial pressure weighted with respect to cracking severity.

The cracking severity and selectivity parameters are used to correlate product yields. The stoichiometric coefficients in Equation 9 are modeled via a simple power series in CSI.

$$Y_j = \sum_i c_i \text{CSI}^i \quad (16)$$

where the polynomial coefficients c_i are functions of θ and KAPP. Equation 16 applies to all yields except the C₅-400°F, which is calculated by difference.

The resulting correlation gives an excellent fit to pyrolysis data. Typical examples for *n*-heptane pyrolysis are shown in Figures 7 and 8. Figure 7 compares model predictions with data for several components over a wide range of cracking severities. The ability of the model to reflect the different profile shapes is readily apparent. Figure 8 shows ethylene yield selectivities. As can be seen, the model accurately captures the temperature and pressure effects on yield selectivity.

At this point, the yield model can be used to represent the pyrolysis behavior of specific feedstocks. To generalize the model, the effect of feed properties must be incorporated. Naphthas are complex mixtures of hydrocarbons. Feed characterization is needed to condense a detailed naphtha description into a manageable set of parameters, which uniquely defines feed-dependent conversion and yield effects.

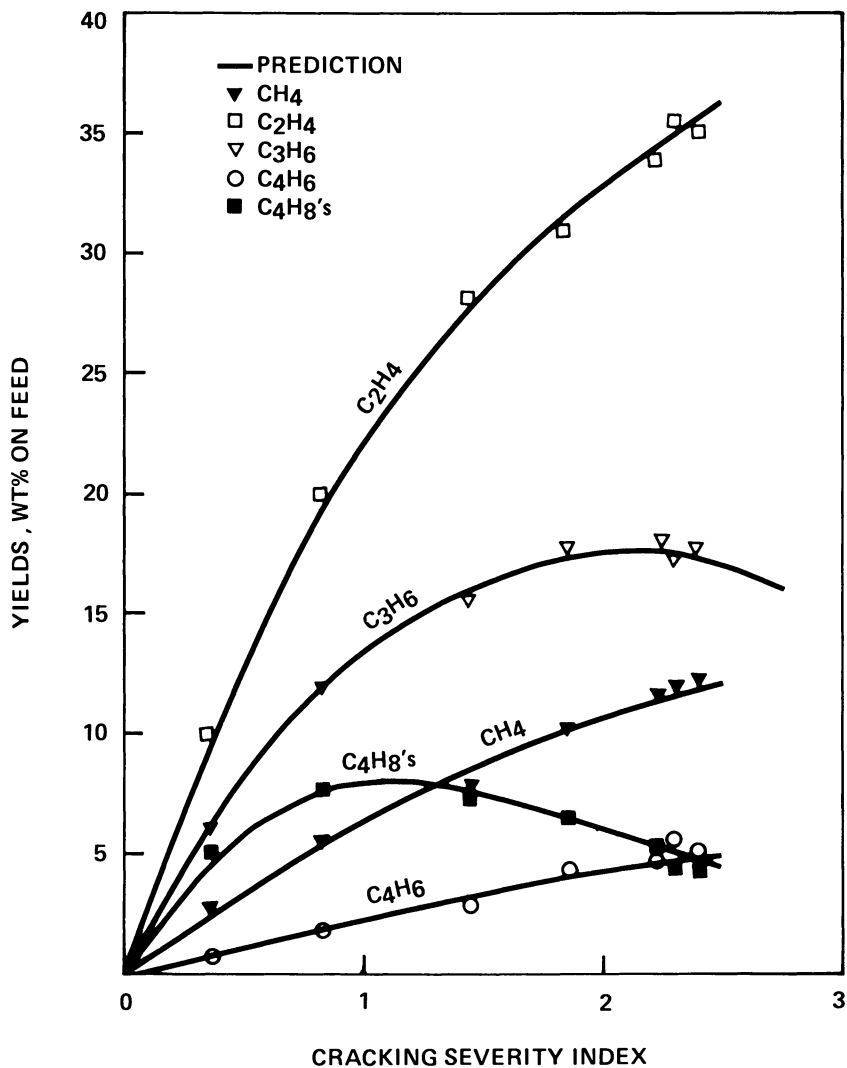


Figure 7. Yield profiles of n-heptane pyrolysis, $K_{APP} = 14.5$ psia, $\theta = 0.58$ sec

The following four feed parameters were found to be sufficient to characterize naphthas (25); hydrogen content (H_F); molecular weight (MW); isoparaffin content (P_I); normal-paraffin content (P_N). Other potential parameters were satisfactorily accounted for in the above set. For example, the inclusion of naphthenic and aromatic content as parameters did not significantly improve the yield correlation.

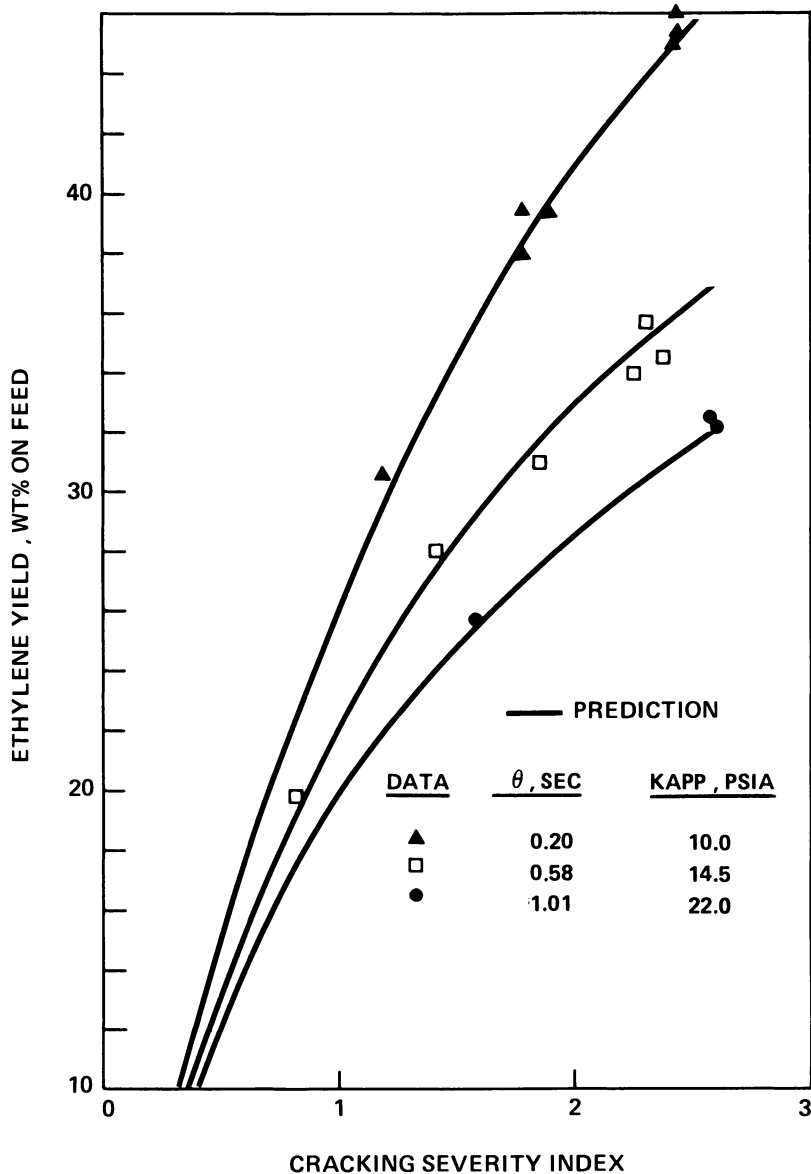


Figure 8. Ethylene yield selectivity, n-heptane pyrolysis

The conversion and yield models, Equations 12 and 16, were generalized via the feed characterization parameters.

$$c_i = c_i(H_F, MW, P_N, P_I, KAPP, \theta) \quad (17)$$

It is interesting to note that while feed carbon number is dominating for rate constant prediction, yield selectivity is influenced more by hydrogen content and iso- and normal-paraffin contents.

Predicted ethylene yields by the generalized correlation are illustrated in Figure 9. The data shown are from two light naphthas which differ only in their iso/normal paraffin ratios. The data illustrate not only the greater ethylene yield potential of the lower iso/normal paraffin ratio feed, but also the enhancement of ethylene production at shorter residence-time operation. As can be seen, the model quantitatively predicts the data.

Commercial Data. Table IV summarizes data from commercial reactors processing naphtha feeds. Temperature profiles for the reactor cracking the full-range naphtha are shown in Figure 10 (29). Agreement between predicted and observed reactor effluent compositions is excellent. Predicted and measured process and peak tubeskin temperatures also are in good agreement. Moreover, the predicted tubeskin temperature profile realistically simulates the dip exhibited by the data. (The dip was caused by an abnormal firing pattern during the data sampling period.)

Conclusion

Computer modeling of hydrocarbon pyrolysis is central to an optimum design of reactors for olefins production. Approaches to pyrolysis model development can be classified into four groups: mechanistic, stoichiometric, semikinetic, and empirical. Selection of approaches to meet minimum development cost must be consistent with constraints imposed by such factors as data quality, kinetic knowledge, and time limitations.

Successful stoichiometric modeling is demonstrated for industrial pyrolysis of light hydrocarbon and their mixtures. A semikinetic approach is more appropriate for naphtha pyrolysis. Although the final form of such a model is simple, its development generally requires more innovations. Applicability of the naphtha model to olefins production is evidenced by the successful prediction of commercial plant performances.

To meet the challenge of changing olefins technology, future pyrolysis modeling will move toward a more mechanistic framework. The rate of this development will be controlled by the advances made in kinetic theory and by the speed of computational tools.

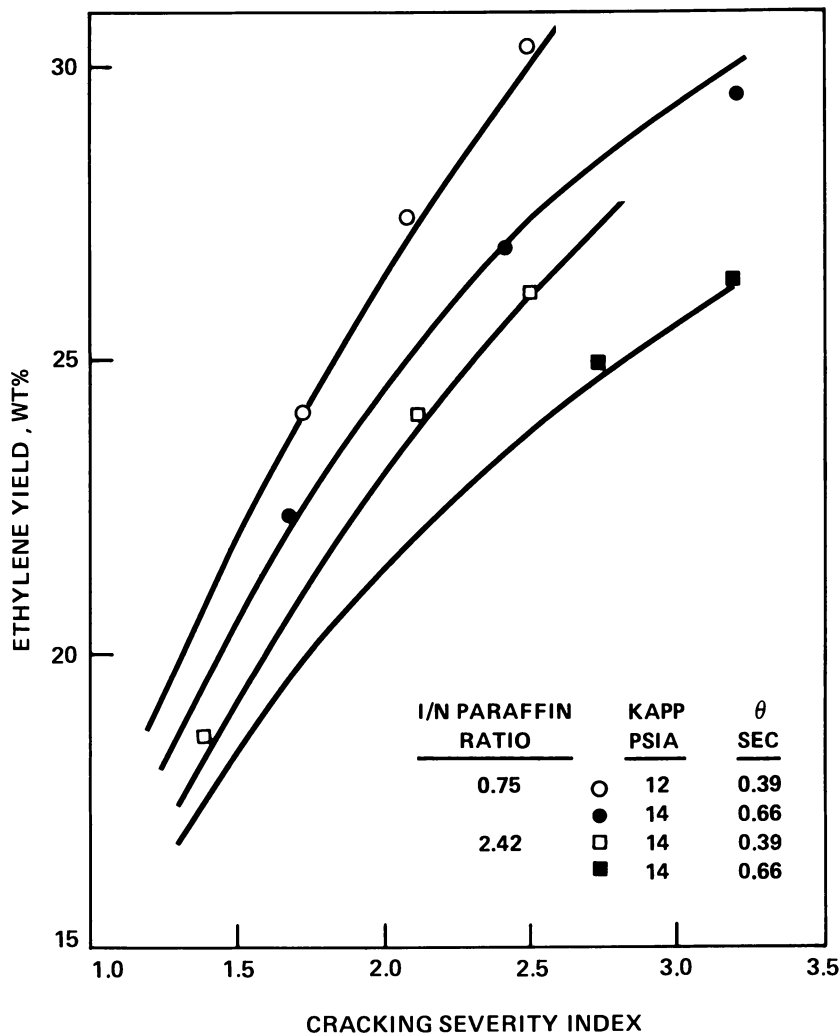


Figure 9. Ethylene yield selectivity, naphtha pyrolysis. (—) Prediction.

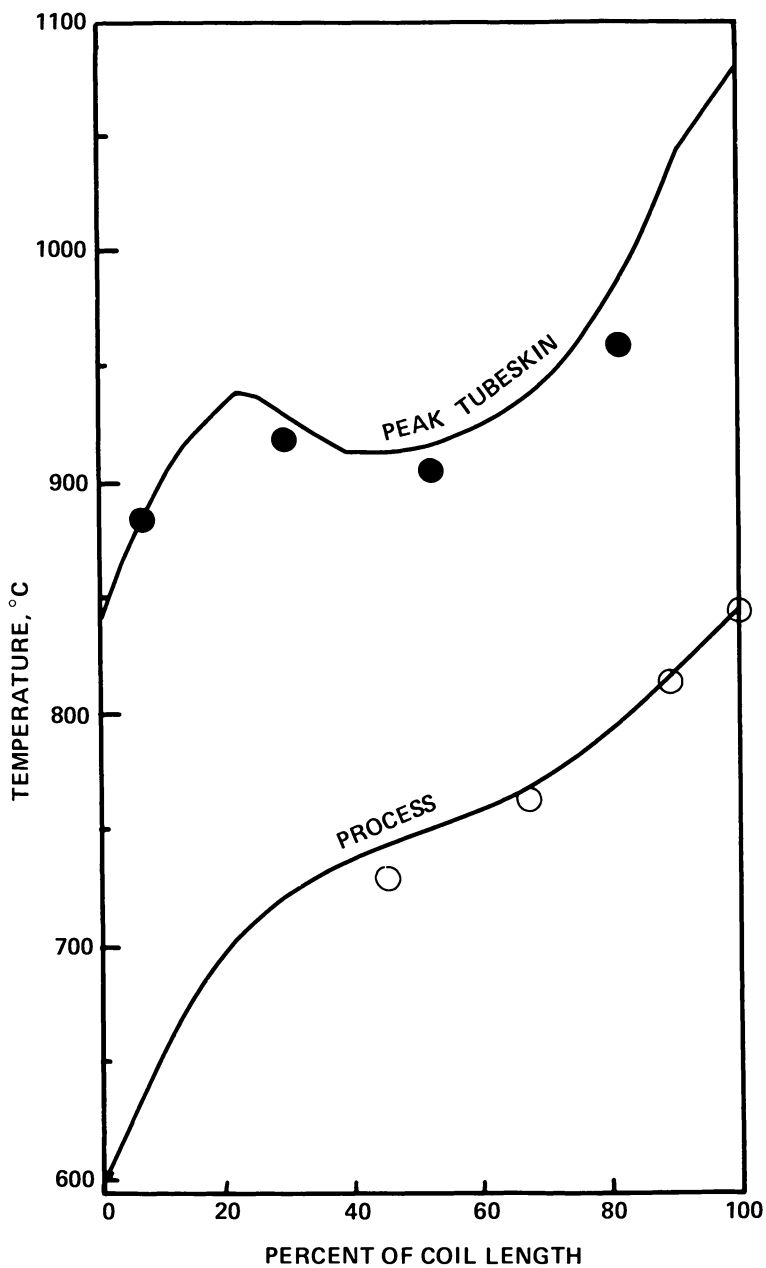


Figure 10. Temperature profiles of naphtha reactor. (○ ●) Data, (—) predictions.

Table IV. Prediction of Commercial Reactor Yields—Naphtha Pyrolysis

| <i>Feed Description</i> | <i>Light Naphtha</i> | | <i>Full Range Naphtha</i> | |
|--------------------------------|----------------------|------------------|---------------------------|------------------|
| API @ 60°F | 79.4 | | 67.4 | |
| ASTM D86 | | | | |
| IBP | 100 | | 102 | |
| 5% | 114 | | 138 | |
| 50% | 149 | | 210 | |
| 95% | 220 | | 310 | |
| EP | 246 | | 362 | |
| Hydrogen content (wt %) | 16.0 | | 15.2 | |
| Paraffin content (wt %) | 86 | | 67 | |
| <i>Operating Conditions</i> | | | | |
| CSI | 2.66 | | 2.81 | |
| θ (sec) | .70 | | .53 | |
| KAPP (psia) | 15.8 | | 14.8 | |
| <i>Yield Structure (wt %)</i> | <i>Observed</i> | <i>Predicted</i> | <i>Observed</i> | <i>Predicted</i> |
| H ₂ | 0.73 | 0.93 | 0.95 | 0.85 |
| CH ₄ | 16.11 | 16.27 | 14.80 | 14.90 |
| C ₂ H ₂ | 0.37 | 0.37 | 0.50 | 0.40 |
| C ₂ H ₄ | 28.71 | 28.04 | 26.60 | 26.09 |
| C ₂ H ₆ | 4.87 | 4.83 | 4.09 | 4.07 |
| C ₃ H ₄ | 0.48 | 0.87 | 1.07 | 0.81 |
| C ₃ H ₆ | 16.37 | 16.25 | 13.84 | 14.43 |
| C ₃ H ₈ | 0.47 | 0.54 | 0.16 | 0.46 |
| C ₄ H ₆ | 4.20 | 4.27 | 4.65 | 4.46 |
| C ₄ H ₈ | 5.19 | 4.54 | 3.78 | 4.03 |
| C ₄ H ₁₀ | 0.48 | 0.34 | 0.40 | 0.43 |
| C ₅ —400°F | 20.52 | 20.83 | 24.65 | 24.77 |
| Fuel oil | 1.50 | 2.02 | 4.51 | 4.31 |
| Total | 100.00 | 100.00 | 100.00 | 100.00 |

Nomenclature

The following is a list of nomenclature related to the reactor model, Equations 1, 2, 3, 4, and 5. Other letters and symbols are defined in the text.

| | |
|-------|---|
| C_p | Average heat capacity, J/kg · K |
| D | Tube diameter, m |
| f | Friction factor, dimensionless |
| G | Mass velocity, kg/m ² · sec |
| g_c | Gravitational constant, kg · m/N · sec ² |
| H | Heat of reaction, J/kg · mol reacted |

| | |
|----------------|---|
| M_j | Molecular weight of Component j |
| \bar{M} | Average molecular weight |
| P | Pressure, N/m^2 |
| Q | Heat transfer through reactor wall, $J/m^2 \cdot \text{sec}$ |
| r_i | Rate of Reaction i , $\text{kg mol reacted}/m^3 \cdot \text{sec}$ |
| S_{ij} | Stoichiometric coefficient for Component j in Reaction i |
| \bar{S}_i | $\sum_j S_{ij}$ |
| T | Temperature, K |
| Y_j | Yield of Component j , wt % on feed |
| Z | Axial distance, m |
| $\bar{\alpha}$ | Kinetic energy correction factor, dimensionless |
| ρ | Density, kg/m^3 |
| ξ | Reaction extent, $\text{kg-mol}/\text{kg}$ |

Literature Cited

1. *Chem. Week* 1975, 116(16), 35.
2. *Chem. Age (London)* 1978, April 14, 14.
3. Aris, R. "Elementary Chemical Reactor Analysis"; Prentice Hall: Englewood Cliffs, NJ, 1969.
4. Murata, M.; Saito, S.; Amano, A.; Maeda, S. *J. Chem. Eng. Jpn.* 1973, 6, 252.
5. Tanaka, S.; Arai, Y.; Saito, S. *J. Chem. Eng. Jpn.* 1975, 8, 305.
6. Powers, D. R.; Corcoran, W. H. *Ind. Eng. Chem., Fundam.* 1974, 13, 351.
7. Sundaram, K. M.; Froment, G. F. *Ind. Eng. Chem., Fundam.* 1978, 17, 174.
8. Volkan, A. G.; April, G. C. *Ind. Eng. Chem., Process Des. Dev.* 1977, 16, 429.
9. Myers, P. S.; Watson, K. M. *Nat. Pet. News* 1946, 38(18), R388.
10. Snow, R. H.; Schutt, H. C.; *Chem. Eng. Prog.* 1957, 53(3), 133-M.
11. Andrews, A. J.; Pollock, L. W. *Ind. Eng. Chem.* 1959, 51(2), 125.
12. Lichtenstein, I. *Chem. Eng. Prog.* 1964, 60(12), 64.
13. Shah, M. J. *Ind. Eng. Chem.* 1967, 59(5), 70.
14. Freedman, B. G., "Nonlinear Distributed Parameter Model of a Gaseous Feed Ethylene Furnace," presented at the 68th AIChE National Meeting Houston, 1971; Paper No. 61c.
15. Murata, M.; Saito, S.; *J. Chem. Eng. Jpn.* 1975, 8, 39.
16. Tanaka, S.; Arai, Y.; Saito, S.; *J. Chem. Eng. Jpn.* 1976, 9, 161.
17. Froment, G. F.; Van de Steene, B. O.; Van Damme, P. S.; Narayanan, S.; Goosens, A. G.; *Ind. Eng. Chem., Process Des. Dev.* 1976, 15, 495.
18. Sundaram, K. M.; Froment, G. F. *Chem. Eng. Sci.* 1977, 32, 601.
19. Sundaram, K. M.; Froment, G. F., *Chem. Eng. Sci.* 1977, 32, 609.
20. Hirato, M.; Yoshioka, S. *Int. Chem. Eng.* 1973, 13, 347.
21. White, L. R.; Davis, H. G.; Keller, G. E.; Rife, R. S. "A Model for Predicting Product Spectra from Naphtha Cracking Furnaces," presented at the 63rd Annual Meeting of AIChE, Chicago, November 1970; Paper No. 25d.
22. Illes, V.; Szalai, O.; Csermely, Z. "Industrial and Laboratory Pyrolyses"; Albright, L. F., Cyrnes, B. L.; Eds., *ACS Symp. Ser.*, 1976, 32, 423.
23. Zdonik, S. B.; Hayward, G. L.; Fishtine, S. H.; Feduska, J. C. *Hydrocarbon Process.* 1975, December, 111.

24. Ross, L. L.; Shu, W. R. *Oil Gas J.* **1977**, *October 17*, 58.
25. Shu, W. R.; Ross, L. L.; Pang, K. H. "A Naphtha Pyrolysis Model for Reactor Designs," presented at the 85th National Meeting of AIChE, Philadelphia, June 1978; Paper No. 27d.
26. Voge, H. H.; Good, G. M. *J. Am. Chem. Soc.* **1949**, *71*, 593.
27. Fabuss, B. M.; Kafesjian, R.; Smith, J. O.; Satterfield, C. N. *Ind. Eng. Chem., Process Des. Dev.* **1964**, *3*, 249.
28. Zdonik, S. B.; Green, E. J.; Halle, L. P. "Manufacturing Ethylene"; The Petroleum Publishing Company: Tulsa, OK, 1970.
29. Shu, W. R.; Ross, L. L. "A Feed Decomposition Model for Naphtha Pyrolysis," presented at the 71st Annual Meeting of AIChE, Miami Beach, November 1978; Paper No. 62c.
30. Davis, H. G.; Williamson, K. D. "Product Inhibition in the Pyrolysis of Paraffinic Hydrocarbons," *ACS Symp. Prepr.* **1978**, *23*, 737.
31. Frey, F. E.; Hepp, H. J. *Ind. Eng. Chem.* **1933**, *25*, 441.
32. Knaus, J. A.; Patton, J. L. *Chem. Eng. Prog.* **1961**, *57*(8), 51.
33. Appleby, W. G.; Avery, W. H.; Meerbott, W. K. *J. Am. Chem. Soc.* **1947**, *69*, 2279.
34. Shah, Y. T.; Stuart, E. B.; Kunzru, D. *Ind. Eng. Chem., Process Des. Dev.* **1973**, *12*, 344.
35. Marschner, R. F. *Ind. Eng. Chem.* **1938**, *30*, 554.
36. Kunzru, D.; Shah, Y. T.; Stuart, E. B. *Ind. Eng. Chem., Process Des. Dev.* **1972**, *11*, 605.
37. Rumyantsev, A. N.; Nametkin, N. S.; Lavrovsky, K. P.; Sanin, P. I.; Musae, I. A.; Vinnitsky, O. M.; Kurashova, E. Kh. *Proc. World Pet. Congr., 9th* **1975**, *5*, 155.

RECEIVED September 18, 1978.

Improvements in Cracking Technology and Furnace Design

BERNHARD LOHR and W. SCHWAB

Linde Ag, Werksgruppe TVT München, 8023 Hoellriegelskreuth,
Munich, West Germany

Recent design improvements with respect to yields, thermal efficiency, feed stock flexibility, and environmental protection are discussed. Also, it is shown that heavy feeds (such as hydrocracker residues) are good feed stocks for olefin production if they are cracked at the proper conditions. Furthermore, the economic application of design improvements to both the radiant and the convection sections in existing furnaces is shown.

Changes in the market situation caused a variety of technical improvements in cracking furnace design during recent years.

1. Increased feed stock costs require higher ethylene yields and better selectivity.
2. Increased energy costs require high thermal efficiency.
3. Changes in feed stock availability require feed stock flexibility and furnaces which are capable of processing new feed stocks for olefins production.
4. Higher environmental regulations require low emission of noise and NO_x .

Most of these design improvements are, of course, included in a new cracking furnace. However, as many of the existing older furnaces operate with lower thermal efficiency and lower yields, the application of these design improvements in existing furnaces also is discussed.

Cracking Technology

Cracking yields are highly influenced by cracking parameters; thus, better yields require better cracking conditions. Main cracking parameters are: hydrocarbon partial pressure, residence time, and temperature.

Hydrocarbon Partial Pressure. For naphtha, the influence of hydrocarbon partial pressure on different components is shown in Figure 1. For other feed stocks, this influence is similar. This is also shown in Figure 1 for the ethylene yields from kerosene and hydro-converter residue.

In general, with decreasing hydrocarbon partial pressure, unsaturated components such as acetylene, ethylene, propylene, and butadiene increase whereas BTX, pyrolysis fuel oil, and saturated components such as methane, ethane, and propane decrease. Low hydrocarbon partial pressure can be attained either by high steam dilution or by low absolute pressure in the cracking coil, which is determined by furnace outlet pressure and pressure drop in the cracking coil. For each specific case there is an optimum steam dilution. Reduction of steam dilution influences yields, utilities, running times and, in the case of a new ethylene plant, of course, investment costs—but in different ways, either positive or negative. Thus, an optimization has to be carried out to identify the most economic steam dilution.

For a constant ratio of propylene to ethylene, a reduction of the steam dilution decreases ethylene yields and, therefore, more feed stock is required. At the same time, however, production of byproducts increases so that, in most cases, net feed stock costs become lower for a smaller steam dilution. Utility costs including dilution steam, hp-steam, cooling water, and fired duty become lower with decreasing steam dilution. As steam production facilities become more compact, investment costs of the warm part of the ethylene plant also become smaller with decreasing steam dilution. Contrary to the aforementioned facts, the running time of furnace and TLX is influenced in a negative manner. This results in higher decoking costs, increased maintenance, and shorter life time of the cracking tubes. The result of such an optimization is shown in Figure 2. The curve shown was calculated for a full range naphtha and high severity cracking.

The location of the minimum indicates the most economic steam dilution. Higher cracking severity and heavier feed stock shifts the optimum steam dilution to higher values. Existing naphtha furnaces operate mostly with steam dilution between 0.5 and 0.6. An example of the reduction of steam dilution for existing furnaces is discussed at the end of this chapter.

It was found (1) that the optimum furnace outlet pressure depends very much on the different valuations of feed stock, products, and utilities. Depending on the type of feed stock, cracking severity, and valuation figures, the optimum furnace outlet pressure is in the range 1.6–2.0 bar absolute. Low pressure drop in the cracking coil can be achieved by proper coil design, which is discussed later.

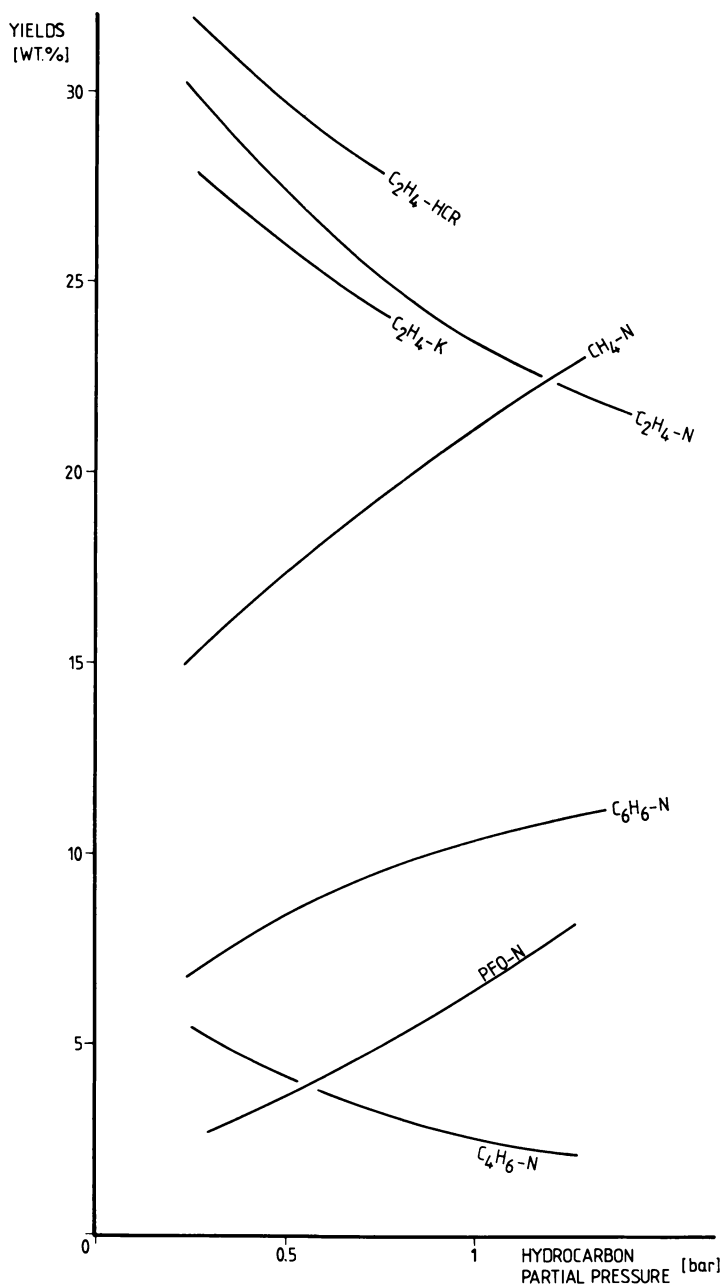


Figure 1. Yields as a function of hydrocarbon partial pressure; (N) naphtha, (K) kerosene, (HCR) hydroconverter residue.

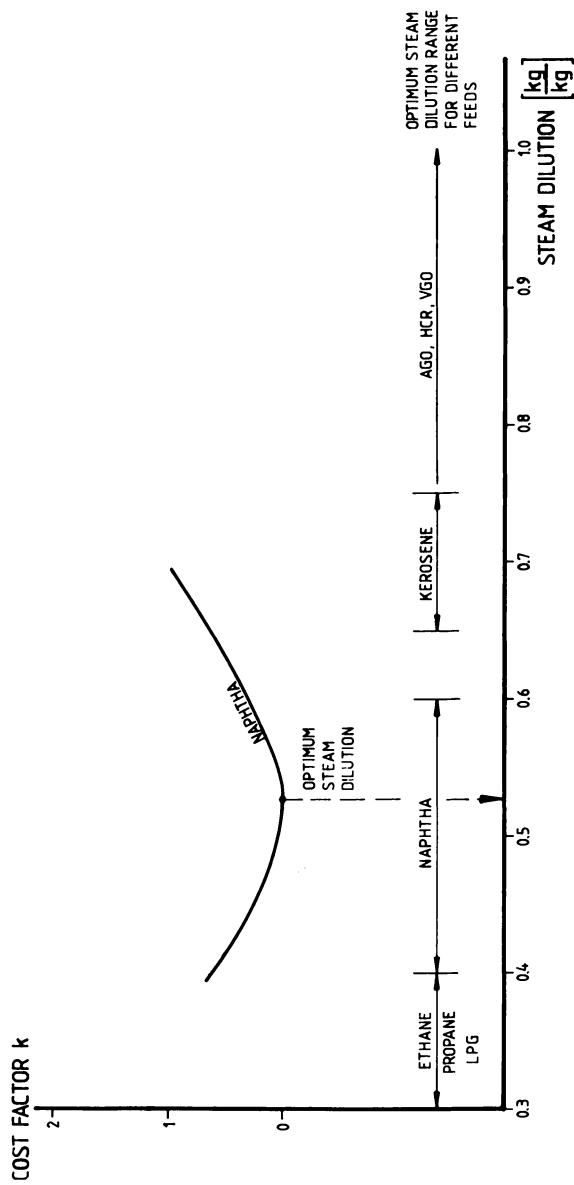


Figure 2. Optimization of steam dilution for naphtha. $k = f(\text{NFC, utility costs, investment costs and running time valuation})$.

Residence Time. The influence of residence time on yields is similar to that of hydrocarbon partial pressure, but smaller. In principle, unsaturated components increase slightly with shorter residence time, depending on the cracking severity. At the same time, saturated components and pyrolysis fuel oil (PFO) decrease. The quality of pyrolysis fuel oil also is influenced by residence time. For constant P:E, the ratio of carbon to hydrogen in PFO becomes smaller with decreasing residence time, which has a positive effect on coking tendency besides other parameters.

Molecular Collision Parameter. For high severity cracking, especially in the case of heavy feed stocks, hydrocarbon partial pressure and short residence time are necessary to get high yields and economic running times. Hydrocarbon partial pressure and residence time are interrelated for a fixed coil design. The molecular collision parameter combines these parameters to a single number (2) (*see* Equation 1),

$$\text{MCP} = \int_0^{\tau} \frac{\text{HCPP}^2}{T^{1.5}} d\tau \quad (1)$$

where MCP = molecular collision parameter, HCPP = hydrocarbon partial pressure, τ = residence time, and T = cracking temperature.

Equation 1 shows that the MCP is more strongly influenced by the HCPP than by the residence time. The MCP is a measure of the number of collisions between hydrocarbon molecules and is independent of coil geometry. Figures 3a–3d show methane, ethylene, butadiene, and PFO yields from naphtha as a function of MCP. For decreasing MCP, methane decreases, ethylene increases, butadiene increases, and PFO decreases at constant P/E.

Hydrocrack Residuum. Increasing crude oil prices raise the question of maximizing the olefin yields and minimizing the production of residue from crude oil. In this connection, atmospheric residue is used for olefins production. Vacuum gas oil or pretreated vacuum residue is processed in a special hydrocracker unit. In conventional hydrocrackers, light products show a high degree of isomerization, which is unfavorable for olefins production. However, processes exist (Linde MHC) which form products of good quality for steam cracker feed stock because of the low aromatic content, low sulfur, and an acceptable degree of isomerization. In particular, MHC residue (IBP 350°C) is a good feed stock for olefins production. Figure 4 shows ethylene and PFO yields from MHC residue as a function of hydrocracking conversion.

However, it should be pointed out that conventional cracking conditions are not suitable for such feed stocks. Conventional cracking conditions lead to lower ethylene yields and to increases in fuel oil

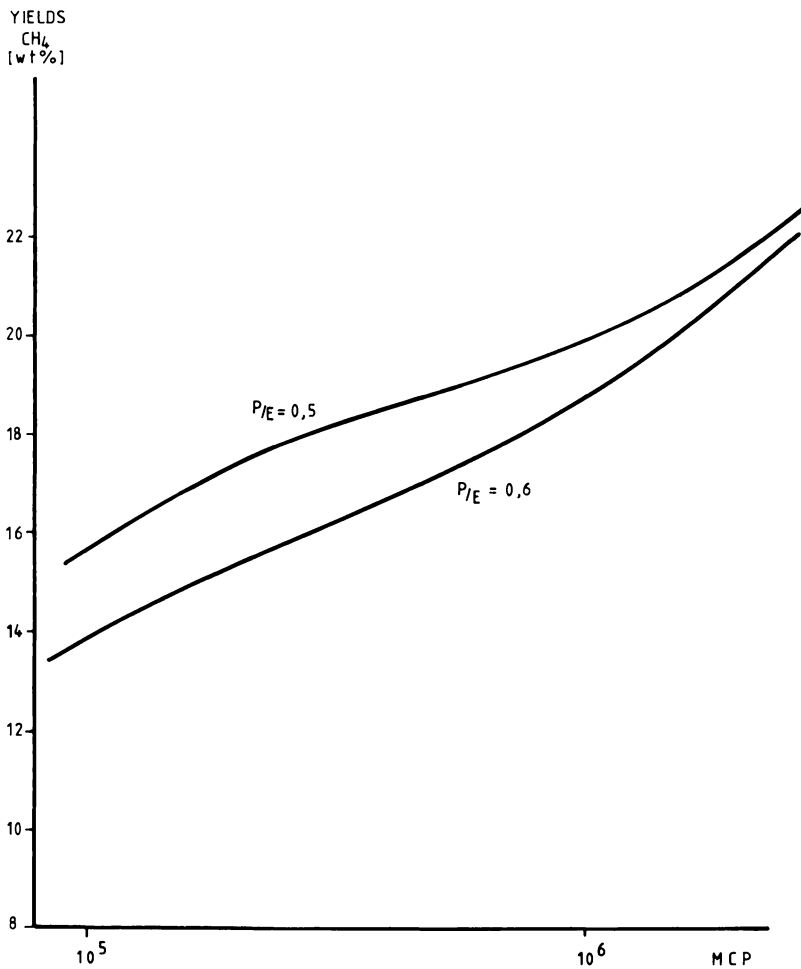


Figure 3a. Methane yields as a function of molecular collision parameter. Feedstock naphtha.

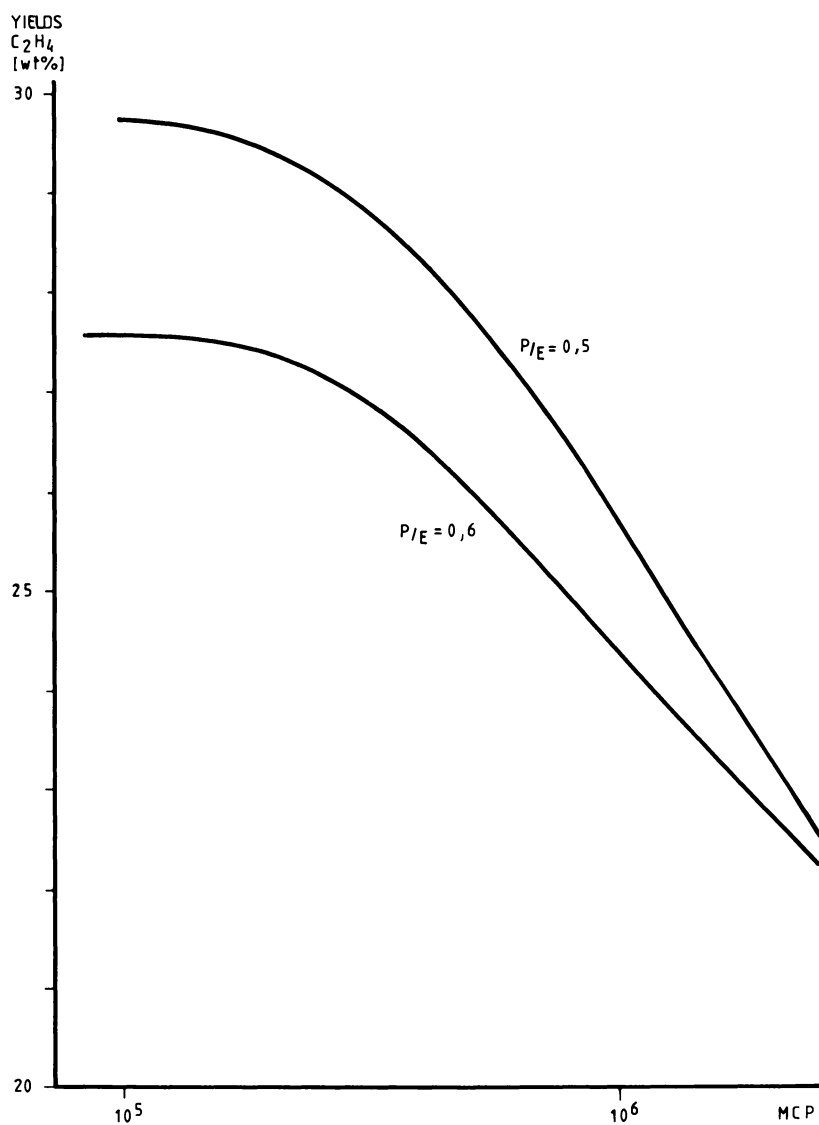


Figure 3b. Ethylene yields as a function of molecular collision parameter. Feedstock naphtha.

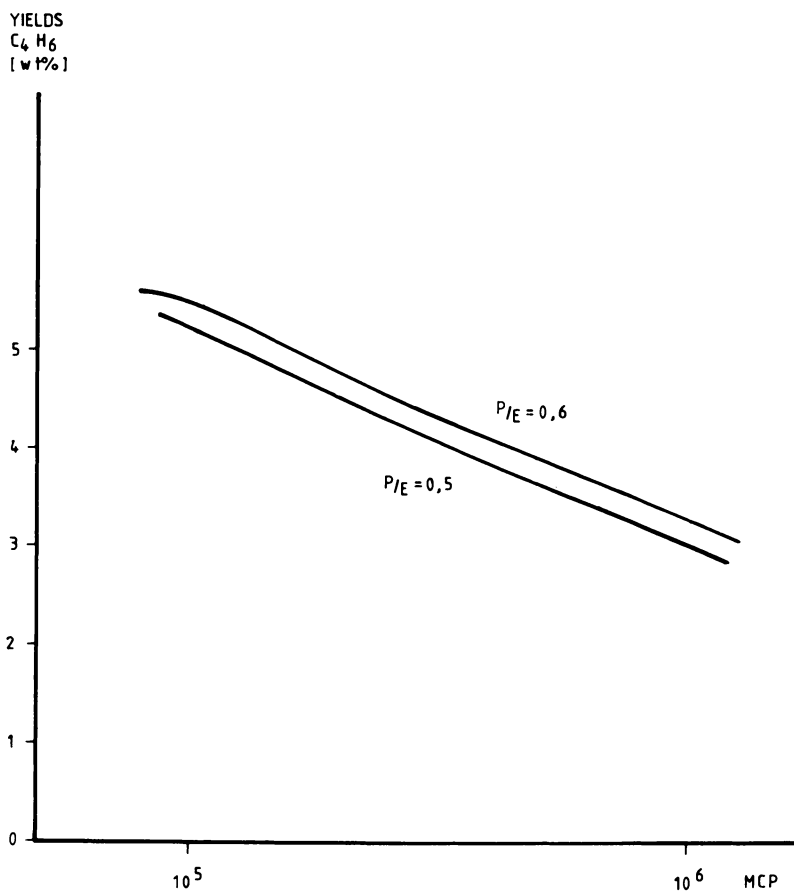


Figure 3c. Butadiene yields as a function of molecular collision parameter.
Feedstock naphtha.

YIELDS
PYROLYSIS
FUEL OIL
[wt%]

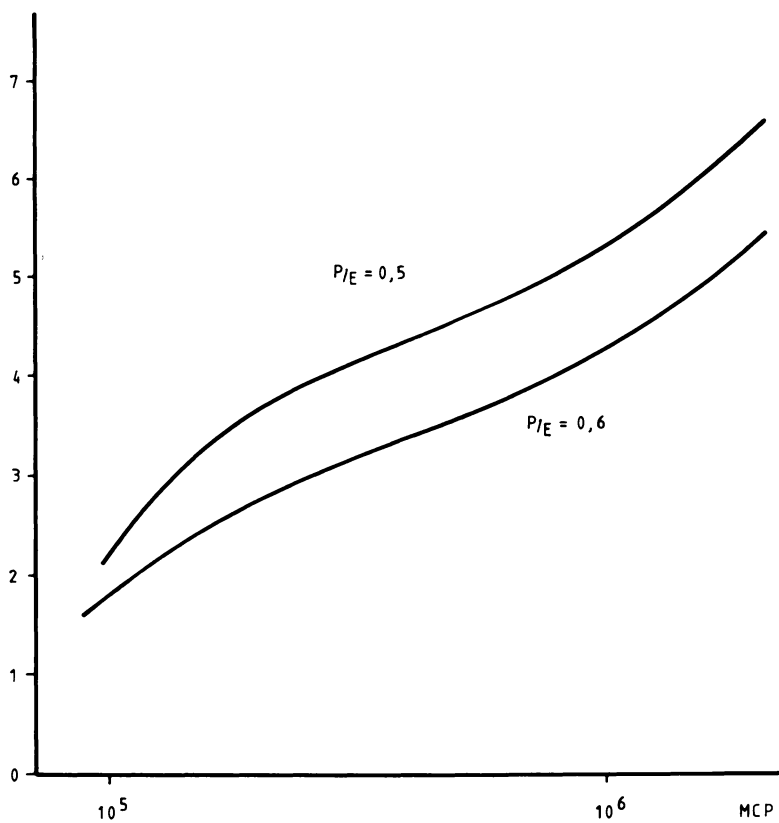
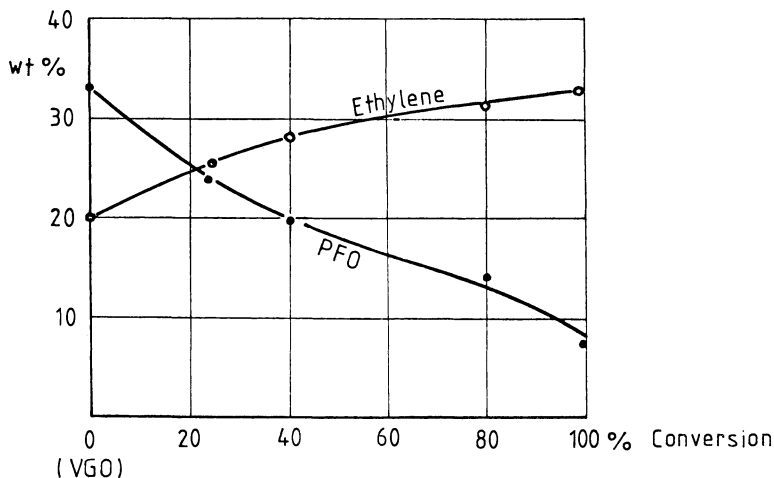


Figure 3d. Pyrolysis fuel oil yields as a function of molecular collision parameter. Feedstock naphtha.



LINDE Olefines Symposium

Figure 4. Ethylene and pyrolysis fuel oil yields from thermal, cracked hydroconverter residue (8).

production and the C:H ratio in fuel oil, which results in a high coking tendency and short running times. For successful cracking of heavy feeds such as hydrocrack residue or pretreated vacuum gas oil, low MCP has to be applied.

Radiant Section

Cracking Coil Design. Equation 1 shows that a fast increase in temperature, a low HCPP, and a short residence time lead to a small MCP. A low MCP can be attained either by uniform diameter design with small tubes of short length or with the so-called combined coil design. Two disadvantages of small size, uniform diameter tubes are a high sensitivity to coking and increased furnace costs attributable to small coil throughput.

A simplified Linde-Selas Combined Coil (LSCC) design is shown in Figure 5. Because of the small tubes at the beginning of the LSCC, the surface-to-volume ratio is high in this part of the coil, which permits a fast increase of temperature. After rapid heating, pairs of small tubes are combined to one large tube with a low pressure drop (3). Compared with a uniform diameter coil with the same hc-throughput and P:E ratio, HCPP is lower, residence time is shorter and, therefore, the MCP also is smaller. Thus the LSCC design improves the process parameters without paying any penalty for capacity.

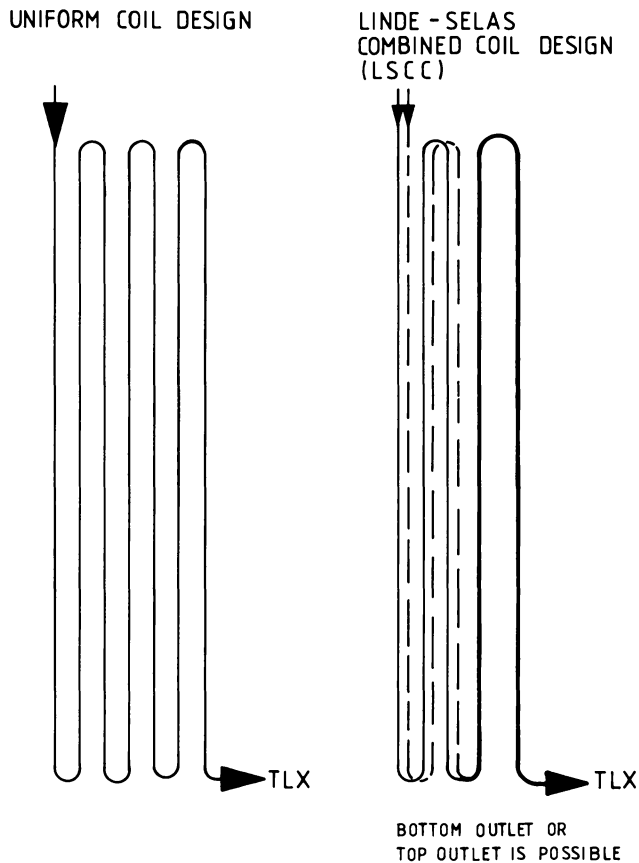


Figure 5. Coil designs

Coil Arrangement. Cracking coils are usually arranged in the radiant section in one or two rows. The advantage of the two-row, staggered arrangement is that the fire box becomes smaller as this arrangement is very compact. This results in lower investment costs. A disadvantage of this arrangement is the unsymmetric heat flux profile on the tube circumference. The advantage of the one-row arrangement is the symmetric heat flux distribution on the tube circumference, which results also in symmetric temperature distribution.

For an equal average heat flux, the local maximum tube skin temperature is somewhat lower for the one-row arrangement than for the two-row, staggered arrangement. This is of importance especially in the hot part (at the end) of the cracking coil.

The disadvantage of the one-row arrangement is the larger space requirement. This leads to a longer fire box, which results in higher

investment costs. Compared with the two-row, staggered arrangement, about 20% more space is necessary for the one-row arrangement.

The partial one-row (POR) arrangement combines the advantages of both the one-row and the two-row arrangement. In the first part of the coil, where the tube skin temperatures are low, the two-row arrangement is applied to make the coil more compact. In the second part of the coil, where the tube skin temperatures are high, the one-row arrangement is applied to get symmetric temperature distribution at the tube circumference and for equal average heat flux to get a lower maximum tube skin temperature. The POR arrangement, therefore, requires less space than the one-row arrangement.

In connection with the LSCC design, the POR arrangement requires approximately the same space as a uniform diameter coil with a two-row arrangement and is, therefore, also suitable for revamping of existing furnaces. An example of successful revamping of existing furnaces with LSCC design and POR arrangement is given at the end of this chapter.

Energy Saving

Energy consumption in the cracking section has a strong influence on the ethylene production costs. In principle, two types of energy savings in cracking furnaces are possible:

1. Reduction of fired duty; and
2. Reduction of flue-gas waste heat, which means lower flue-gas outlet temperature and, therefore, higher thermal efficiency of the cracking furnace.

Fired duty can be reduced by either reduction of dilution steam or combustion air preheating or to a lesser degree by reduction of excess air to the burners. The selection of the optimum steam dilution was discussed previously.

Air Preheating. The majority of the gas burners installed in cracking furnaces are natural draft burners. As combustion air is introduced at ambient conditions, a part of the heat released from the fuel has to be used to heat up the combustion air to the fire box temperature. Therefore, preheated air reduces the fired duty. Figure 6 shows the fuel consumption as a function of combustion air temperature. For example, preheating combustion air from 0° to 100°C reduces the fired duty from 100 to 95.5%, which means savings of 4.5% fuel.

Combustion air can be preheated either with flue gas, lp-steam, quench water, quench oil, or any other available waste heat stream. Air preheating is used in many industrial furnaces (such as reformers, refinery furnaces, steam boilers, etc.) but only in a very few cracking furnaces. The reason is the increased investment costs because of the large number of individual burners in cracking furnaces.

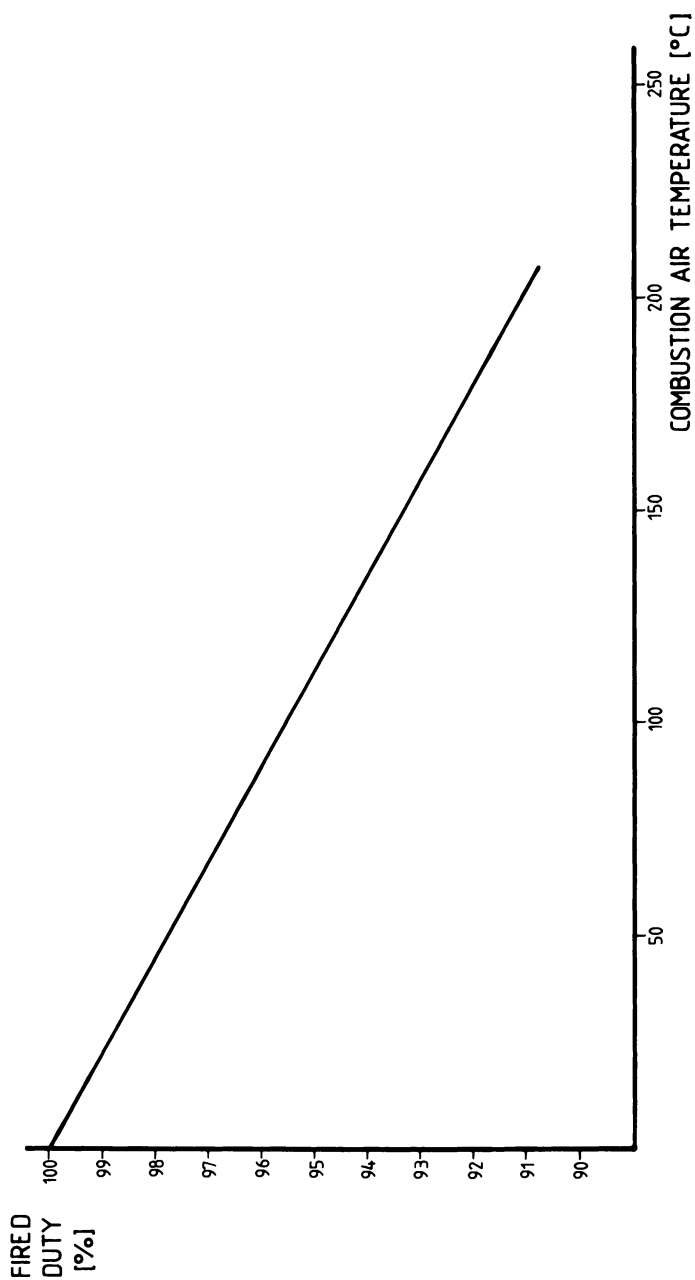


Figure 6. Fired duty as a function of combustion air temperature

In principle, two methods of preheated air supply to the burners are possible:

INDIVIDUAL AIR SUPPLY (IAS). Preheated air is fed by a header to the furnace side wall and then fed by single, small air ducts to each burner. In this case, forced draft burners are used. The advantage of this solution is that the air can be preheated to a high temperature. The disadvantage of IAS is the high investment cost.

COMMON AIR SUPPLY. In this case, the preheated air is not individually supplied to each burner but is fed into a plenum chamber which is formed by the furnace side wall and by additional mounted steel plates between two double-T beams. The burners are completely surrounded by the plenum chamber.

As the plenum chamber is approximately at atmospheric pressure, the burners are still natural draft burners. To control the air shutters, each burner has a lever which can be controlled from the outside. The additional mounted side-wall plates consist of different segments to ensure good maintenance.

The advantages of a common air supply system are the low investment cost, the fact that no complicated control system for air supply is necessary, it can be installed in existing furnaces, heat losses in the fire box are reduced, and, there is additional noise suppression.

The disadvantage of common air supply is the fact that the maximum preheated combustion air temperature is limited by the materials of the burner, the steel structure, and the side wall. An example of how common air supply can be applied in existing furnaces is given later.

Improved Flue-Gas Heat Recovery. The majority of the heat losses in cracking furnaces is contained in the flue gas which leaves the furnace. Today's cracking furnaces with integrated waste heat recovery are designed for thermal efficiencies between 90 and 93%, which correspond to flue-gas outlet temperatures of about 130° to 180°C. A further decrease of the flue-gas outlet temperature usually is not economic, as the heat-transfer surface of the upper bundles becomes too large because of the small mean logarithmic temperature difference.

With sulfur-containing fuels, attention has to be paid to the acid dew point of the flue gas. Acid dew point in flue gas is shown as a function of sulfur content in the fuel oil in Figure 7. To avoid corrosion in the upper bundles, it has to be ensured that the tube skin temperature is, in all cases, higher than the acid dew point.

Many of the older cracking furnaces, however, have flue-gas outlet temperatures of greater than 200°C. In such cases it is possible to revamp the furnace to lower the flue-gas outlet temperature, resulting in higher thermal efficiency.

Figure 8 shows the energy savings if flue gas is cooled down to a lower outlet temperature. In general, additional heat transfer surface has to be installed to transfer this additional flue-gas heat. However, in some cases it might be sufficient to replace bare tubes by finned or

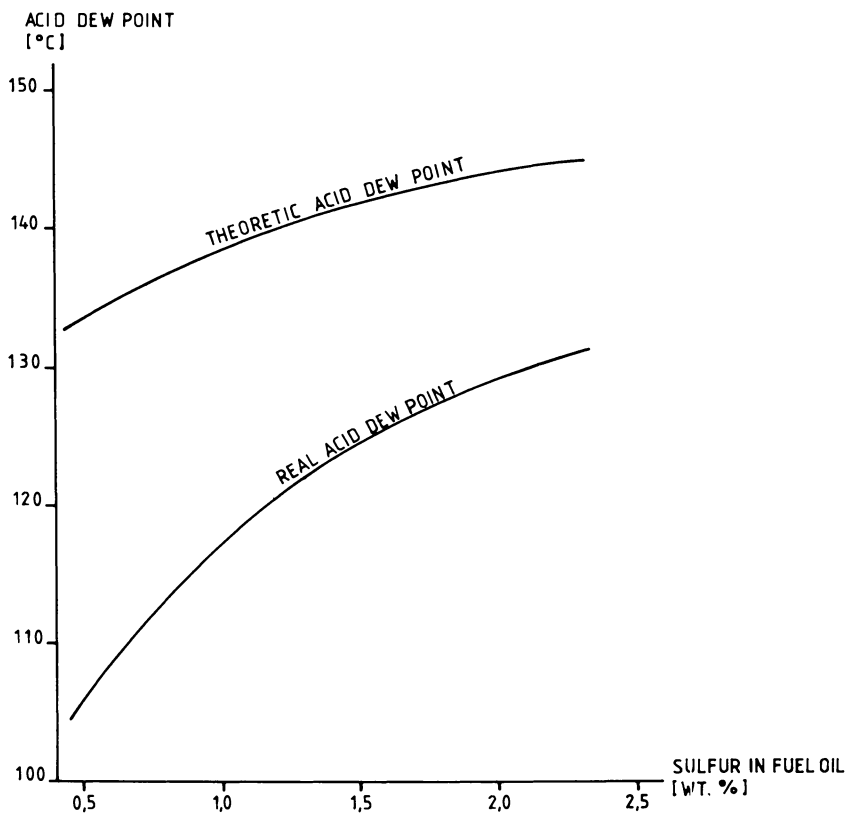


Figure 7. Acid dew point as a function of sulfur content in fuel oil

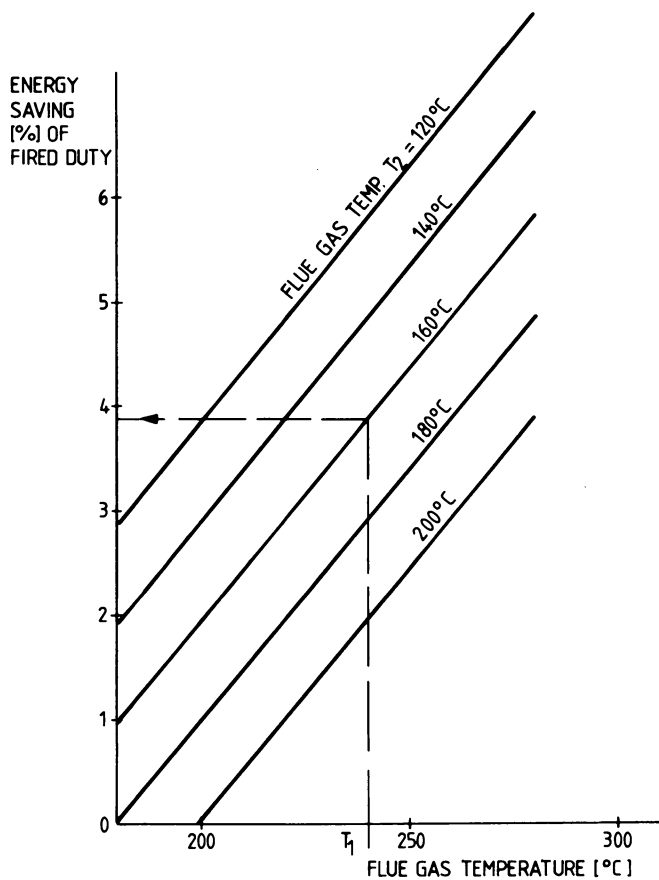


Figure 8. Energy savings by reduction of flue-gas outlet temperature

studded tubes. Additional surface might be either integrated in each convection section or installed in a centralized waste heat boiler. This additional heat removed from the flue gas can be used, for instance, for combustion air preheating or for boiler feed water preheating.

Feed Stock Flexibility

Many of today's cracking furnaces are designed for dual feed stock flexibility, e.g., ethane/LPG, LPG/naphtha, and naphtha/AGO. On the basis of a good knowledge of the kinetics of pyrolysis, cracking coils can be properly adapted to the requirements of the feed stock pairs mentioned above. Because of lower reaction velocity, light hydrocarbons operate at a lower throughput for the same cracking coil than do heavy feeds. Table I indicates approximate figures for maximum relative hydrocarbon throughput based on naphtha for the same coil.

Table I. Relative HC-Throughput of Cracking Coils

| | | |
|----------|---------------|------|
| Ethane | Approximately | 60% |
| Propane | " | 85% |
| Butane | " | 90% |
| Naphtha | " | 100% |
| Kerosene | " | 110% |
| AGO | " | 115% |

Great attention should be paid to the convection section. For each feed stock pair, different steam dilution, different initial cracking point, different physical properties, and different hp-steam production all result in different quantities of heat which have to be transferred in the convection section bundles. Table II shows typical heat transfer rates for a

Table II. Relative Heat Transfer Rates in a Naptha/AGO Flexible Cracking Furnace^a

| | <i>Naptha (%)</i> | <i>AGO (%)</i> |
|----------------------|-------------------|----------------|
| Radiant section | 100 | 111 |
| HT convection | 100 | 78 |
| HP steam superheater | 100 | 105 |
| Dil. steam | 100 | 137 |
| BFW-preheater | 100 | 89 |
| LT convection | 100 | 252 |
| | <i>Flows</i> | |
| HC-throughput | 100 | 112 |

^a The figures shown in this table are valid only for one specific design.

naphtha/AGO flexible furnace. Good adaptation to these different heat transfer rates and different temperature levels can be achieved by installing switchable heat exchange bundles.

Flexible naphtha/AGO furnaces can operate either on 100% naphtha, 100% gas oil, or on any mixture of the two feed stocks. However, yields from mixed cracking are not as good as yields from separate cracking. Table III shows yield distributions for mixed and separate cracking of 50% naphtha and 50% AGO for constant P:E. In separate cracking, yields of C4 and lighter components are higher, whereas in the case of mixed cracking, pyrolysis gasoline and pyrolysis fuel oil increase. Naphtha/AGO flexibility is discussed in more detail in Refs. 3 and 4 and naphtha/ethane flexibility is discussed in detail by Mikulla et al. (5).

Table III. Yields from Mixed and Separate Cracking^a

| | <i>Separate Cracking</i> (wt %) | <i>Mixed Cracking</i> (wt %) |
|-------------------------------|------------------------------------|---------------------------------|
| H ₂ | 0.76 | 0.70 |
| CH ₄ | 12.95 | 12.53 |
| C ₂ H ₄ | 24.12 | 22.34 |
| C ₃ H ₆ | 13.31 | 12.32 |
| C ₄ H ₆ | 4.20 | 4.20 |
| Gasoline | 23.19 | 23.68 |
| PFO | 12.70 | 15.59 |

^a Feedstock: 50 wt % naphtha; 50 wt % heavy AGO. All figures given are once through yields.

Environmental Protection

During recent years in many countries, tight environmental standards have been set. Therefore, the design of olefin plants and cracking furnaces was improved to meet those standards.

Burner noise is generated primarily by the combined effects of fuel gas pressure across the orifice, mixing of fuel with combustion air, and combustion intensity. Noise suppressors have been developed to produce a reduction of the sound pressure level for a single burner to as low as 67 dBA.

Emission of NO_x from cracking furnaces should be kept as low as possible. About 90% of the NO_x emitted from cracking furnaces is nitrogen monoxide, which is converted into NO₂ in the atmosphere.

In general, these types of NO formations are known (*see Ref. 6*):

1. "Thermal" NO which is formed by oxidation of the nitrogen contained in the combustion air:



2. "Prompt" NO which is formed by nitrogen-containing radicals, especially CN radicals, and

3. "Fuel" NO which is formed by the nitrogen-containing components of the fuel.

Whereas for fuel gas only Type 1 is of importance, fuel oil firing forms NO by all three types. Today's radiant cup burners are designed for minimum NO_x emission.

Application of Design Improvements in Existing Cracking Furnaces

Earlier, the LSCC design and the POR arrangement were introduced. It was shown that with LSCC design, better cracking parameters can be achieved and that the POR arrangement of LSCC does not need more space than conventional two-row arrangement. Therefore, a furnace with conventional cracking coils of uniform diameter and a two-row staggered arrangement can be easily replaced by LSCC design. This first example outlines a coil revamping to produce yield improvements, which was done recently.

Since investment costs had to be kept low, the convection section, the fire box, and the burners were left unchanged. To fulfill these requirements, the new LSCC design was calculated for the same naphtha, P/E, hc-throughput, steam dilution, and crossover temperature. The following improvements in cracking parameters were calculated for the LSCC design: pressure drop = 31% less, residence time = 28% less, and MCP = 43% less.

After start-up, the furnace effluent was analyzed and showed an increase in ethylene yield of 0.9 wt % whereas the PFO decreased by 1.2 wt %. These yield improvements resulted in a considerable decrease of net feed stock costs.

Fuel gas consumption increased slightly because of the higher heat of formation for the increased amount of light components. Hp-steam production is influenced positively because of the lower yields of PFO and the decreased C:H ratio in PFO (7). Dilution steam consumption remains unchanged. This results in approximately equal utility costs.

If the coil revamping is done instead of a scheduled cracking tube replacement, the effective investment costs become rather small. On this basis a payout time of 0.97 years was attained. But also in the case, where coil revamping is done without having a scheduled coil replacement, a

payout time of 1.73 years is attained. This example shows that, in any case, replacement of conventional vertical cracking coils with uniform diameter by an LSCC design leads to short payout times and is thus highly economical.

Many of the existing older cracking furnaces have horizontal cracking tubes. The revamping of such furnaces for vertical tubes and LSCC design is somewhat more complicated but is in many cases economical. Revamping of such a furnace was done recently.

The aforementioned example showed that good yield improvements can be obtained by an LSCC design because of better cracking parameters which means lower MCP. This example also shows that utility costs can be decreased considerably with LSCC revamping.

The original coil was a uniform diameter design and was operated with a steam dilution of 0.6. The old coils were replaced by LSCC with the same HC-throughput and the same P/E. For the same steam dilution this results in considerable improvements in cracking parameters (MCP) and yields (Figure 9). Reduction of steam dilution increases the MCP. If for the LSCC the same MCP is accepted as for the uniform diameter design, steam dilution can be reduced to less than 0.4 kg/kg, without paying any penalties for cracking parameters and yields. Reduction of steam dilution from 0.6 to 0.4 kg/kg results in overall utility savings of 9.6 DM/t ethylene.

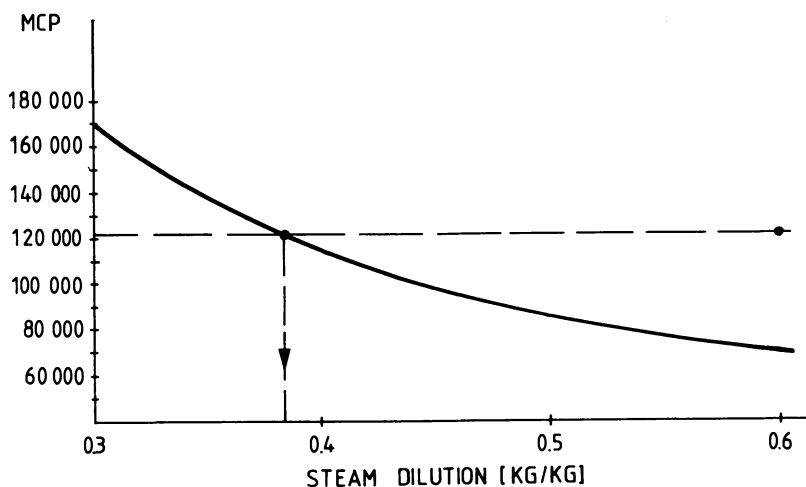


Figure 9. MCP for various steam dilutions. P/E = const; hc-throughput = const; (---) conventional uniform diameter design with steam dilution = 0.6; (—) LSCC design for various steam dilutions.

Table IV. Valuation Figures

| | | |
|---------------|-------|---|
| Naptha | 270.0 | DM/MT |
| Ethylene | 800.0 | DM/MT |
| Propylene | 510.0 | DM/MT |
| Butadiene | 820.0 | DM/MT |
| Butenes | 340.0 | DM/MT |
| Benzene | 645.0 | DM/MT |
| Gasoline | 270.0 | DM/MT |
| PFO | 190.0 | DM/MT |
| Fuel gas | 5.25 | DM/10 ⁶ kJ (22.0 DM/10 ⁶ kcal.) |
| HP-steam | 20.4 | DM/MT |
| MP-steam | 14.4 | DM/MT |
| Cooling water | 0.05 | DM/MT |

This includes reduced dilution steam generation, hp-steam generation by TLX and furnace, fuel consumption, and cooling water. For a 300,000 MTA ethylene plant, savings of 2.9 million DM per annum can be attained. This leads to a payout time of 1.08 years. Thus, cracking coil revamping by LSCC with respect to utility costs are calculated on the basis of valuation data given in Table IV. The utility reduction is also very economical. Because of the reduction of dilution steam, furnace operation also is affected. Crossover temperature increases by 5°–10°C whereas flue-gas outlet temperature decreases slightly.

Whereas the two aforementioned examples discussed improvements in the radiant section, this third example deals with the application of improvements in the convection section.

An existing naphtha furnace operates with a flue-gas outlet temperature of 240°C. If an additional preheater for combustion air is installed on top of each furnace to preheat the necessary combustion air up to 100°C, the flue gas can be cooled down to approximately 160°C. This results in energy savings of 3.9% of fired duty, which decreases ethylene production costs by about 5.3 DM/MT ethylene. Such a revamping, however, also influences furnace operation. The required draft for the burners increases because of the higher effective volume of preheated air. Because of the additional air preheater bundle, the flue-gas pressure drop increases slightly inspite of the reduced flue-gas pressure drop in the existing bundles caused by the smaller amount of flue gas. Thus, for the whole furnace a higher draft is necessary. Crossover temperature and hp-steam production decrease slightly whereas fire box efficiency increases.

In case of revamping, the necessary steps highly depend upon the specific individual design of each furnace; therefore, it is very difficult to give general figures on investment costs. Energy savings, including investment cost for air preheater bundle, flue-gas fan, combustion air fan, air ducts, material to install CAS, engineering and construction work, all

result in a payout time of 1.5–2 years, depending on the specific design of the furnaces. This calculation is based on the values given in Table IV. This example showed that a revamping of the convection section is economic at present energy costs. With ever increasing energy costs, payout times will become even shorter in the future.

These three examples showed that design improvements for either the radiant section or the convection can be applied economically to existing older furnaces.

Literature Cited

1. Schnetzler, H.; Slongo, R. Internal LINDE Report (June 1978) unpublished data.
2. Witt, R.; Wall, F. "Theoretical Analysis of Gas Oil Pyrolysis and Product Yield Correlation," AICHE Symposium on Energy Environment and Cost, November 1977.
3. Lohr, B.; Dittmann, H. "Design Matches Furnaces to Needs", *Oil Gas J.* October 17, 1977.
4. König, H. J.; Lohr, B.; Richter, H. "Feed Stock Flexibility in Ethylene Plants," *Chem. Ind.*, 1977, 11.
5. Mikulla, K.; Bölt, H.; Richter, H. "Feed Stock Flexibility in Olefines Plants," presented at LINDE Olefin Symposium, Munich, 1978.
6. Michelfelder, S.; Heap, M. P.; Lowes, T. M.; Smith, R. B., "Durch Vergrennungsvorgänge verursachte Schadstoffemission aus industriellen Feuerungen," 7. Deutsche Flammentag, Karlsruhe, September 1975.
7. Lohr, B.; Dittmann, H. "Steam Cracker Economy Keyed to Quenching," *Oil Gas J.* 1978, May 15.
8. Kreuter, W., "State of the Art with Reference to Olefines Production and Future Developments," presented at LINDE Olefines Symposium, Munich, 1978.

RECEIVED September 18, 1978.

Types of Coke Formed During the Pyrolysis of Light Hydrocarbons

LYLE F. ALBRIGHT, CHRISTOPHER F. McCONNELL¹
and KAROLY WELTHER²

School of Chemical Engineering, Purdue University, West Lafayette, IN 47907

Coke formed on solid surfaces during the pyrolyses of acetylene, ethylene, ethane, propylene, and butadiene were examined by using a scanning electron microscope. Seven types of coke have been identified: braided filament, uniform diameter filament, needle or spike, ribbon, fluffy or cotton-like fibers, knobby, and amorphous. The first four types contained metal (especially iron) and were magnetic. Magnetic cokes formed sometimes on Incoloy 800, stainless steel 304, stainless steel 410, and Hastelloy X surfaces, but never on Vycor glass or aluminized Incoloy 800 surfaces. Conditions at which each type of coke was formed are discussed.

During the pyrolysis of hydrocarbons, coke is unfortunately always formed in addition to ethylene, propylene, diolefins, aromatics, and other valuable hydrocarbons. Information available on coke formation up to 1965 has been reviewed by Pallmer and Cullis (1). Some (but not extensive) results obtained using an electron microscope have been reported.

Recently both Lobo and associates (2,3) and Baker and associates (4,5,6) have investigated the mechanism of coke formed from acetylene on nickel surfaces. Such investigations should be most helpful since acetylene is considered to be an important coke precursor in both pyrolysis tubes and in the transfer line exchanger connected to the tubes.

¹ Current address: Dow Chemical Co., Midland, MI 48640.

² Current address: Hungarian Oil and Gas Institute, Veszprem, Hungary.

Filament-type coke was produced from acetylene in the range 400°–600°C; this coke contained nickel atoms or particles. Apparently nickel granules were lifted from the surface as a result of the coke formation.

Metal granules also have been found in cokes formed or deposited on iron, cobalt, and nickel foils in experiments using methane, propane, propylene, and butadiene (7–10). Platelet-type coke, whose properties match those of graphite also was produced in some cases. Lahaye et al. (11) investigated the steam cracking of cyclohexane, toluene, and *n*-hexane over quartz, electrode graphite, and refractory steel. They report that heavy hydrocarbon species form in the gas phase, condense into liquid droplets which then strike the solid surface, and finally react on the solid surfaces to produce carbonaceous products. The liquid droplets wet and spread out on certain surfaces better than on others.

Essentially no known information is available, however, relative to the coking phenomena on stainless steels used commercially in pyrolysis furnaces. Incoloy 800 is one example of such a steel. Probably, the method of coking varies with the hydrocarbon molecules in the gas phase. Ethylene, propylene, butadiene, and benzene (or other aromatics) also are thought to be precursors for coke. Such information is, in part, based on the large amounts of coke that are formed when these hydrocarbons are heated to high temperatures. Also, Dunkleman and Albright (12) obtained experimental information that strongly suggests ethylene is the major precursor of coke during pyrolysis of ethane.

The purpose of the present investigation was to obtain scanning electron microscope pictures and to obtain metal analyses for the coke produced. Several types of surfaces were investigated and the results are analyzed.

Experimental Details

Ethane was pyrolyzed in several tubular reactors having internal diameters of about 0.47 cm and a heated length of 107 cm. The reactors used were constructed of Incoloy 800, stainless steel 304 (SS 304), stainless steel 410 (SS 410), Hastelloy X, and Vycor glass. Each reactor was maintained at almost isothermal conditions by suspending it in a fluidized sand bath. More details on the reactors are described by Dunkleman and Albright (12) and Herriott, Eckert, and Albright (13). After suitable pyrolysis, the reactor was cut to expose the coke on the inner surfaces.

Experiments with ethylene, acetylene, propylene, and butadiene were made using a 1.27 cm i.d. tubular reactor such as used by Tsai and Albright (14) or Brown and Albright (15). This reactor was inserted in a horizontal position in an electrical resistance furnace.

Metal coupons were inserted at various positions in the horizontal tubular reactor. The coupons had two types of surfaces: an Incoloy 800 surface and an aluminized Incoloy 800 surface. To prepare these coupons, flat pieces of Incoloy 800 were aluminized (or alonized) by the Alon Processing, Inc. of Tarentum, PA. In this process, gaseous aluminum was contacted with the Incoloy 800, and aluminum diffused into the surface. The alonized samples as received from Alon Processing were cut in small coupons so as to expose an Incoloy 800 surface which was cleaned and polished before use.

The metal coupons in the horizontal reactor were exposed at reactor temperature to either acetylene, ethylene, propylene, or butadiene for 120 minutes. The coupons were removed from the furnace, and pictures of the coke were taken using a JSM-U3 scanning electron microscope. Most pictures were taken using a magnification of 10,000. The type of metal in the coke was determined using EDAX Model 707, that was attached to the electron scanning microscope.

Experimental Results

Seven types of coke were identified from a relatively large number of pictures taken in the present investigation. Duplicate runs were made in several cases, and relatively good reproducibility of the photographic results was obtained. Surfaces on which each type of coke was found are reported in Table I. Photographs for some comparative runs are shown in Figures 1–10. Table I also reports the location of a photograph showing each type of coke. The seven types of coke were constant-diameter filament, braided filament, ribbon, needle or arrowhead, fluffy (or gas phase), knobby, and amorphous cokes. The first four types were always magnetic, containing metal particles which, based on EDAX analysis, were primarily iron with some nickel. However, the last three types of coke contained little or no metal particles.

Variables Affecting Type of Coke. The material of construction of the solid on which the coke formed, the temperature, and the space time all affected the type of coke formed. Cokes formed on Incoloy 800, SS 304, SS 410, and Hastelloy X were sometimes magnetic. Cokes formed in an alonized surface were always nonmagnetic, and no metals were detected by EDAX except for a trace of aluminum. Cokes formed in Vycor glass reactors were also nonmagnetic.

Figure 1 shows that the type of coke formed from acetylene in the range of about 410°–460°C depends on the metal surface. The coke on the Incoloy 800 surface appears to be braided or rope-like filaments. In another picture, as shown in Figure 2, two types of filaments were produced—both braided and constant-diameter filaments. Both types of filaments were relatively long compared with their diameters, which were approximately 0.25 μm . Each filament was firmly attached to the metal surface and could not be removed from it easily by mechanical means.

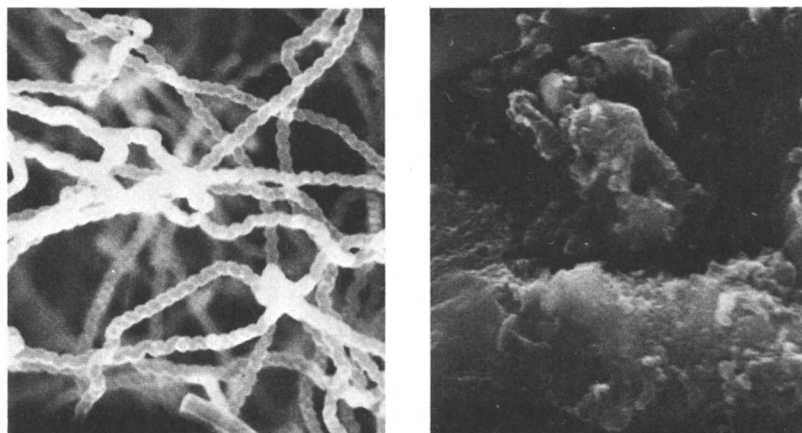
Table I. Surfaces on Which
Hydrocarbon Feedstock*

| Type of Coke | Ethane | Acetylene | Ethylene |
|---------------------|-----------|-----------|----------|
| Filament | | | |
| Constant diameter | A,C | A | — |
| Braided | A,B,C,D | A | A |
| Ribbon | B | — | — |
| Needle or arrowhead | — | — | A |
| Knobby | F | A,E | — |
| Fluffy (gas phase) | A,B,C,D,F | A,E | A,E |
| Amorphous | A,B,C | A,E | A,E |

* Reactor: (A) Incoloy 800; (B) SS 304; (C) SS 410; (D) Hastelloy X; (E) aluminized (or alonized) Incoloy 800; (F) Vycor glass.

The coke formed on the alonized Incoloy 800 surface was amorphous, and it could be scraped from the surface rather easily. Amorphous coke, as defined here, is sometimes referred to as polycrystalline coke. Other examples of amorphous coke are shown in Figure 6.

As shown in Figure 2, the types of coke formed on Incoloy 800 surfaces from acetylene varied significantly with temperature in at least the range 325°–770°C. At 325°C both braided and constant-diameter filaments occurred. In a photograph that is not shown here, part of a filament was apparently braided and the remainder had a constant



|—| = 1 micron

Figure 1. Coke formed from acetylene at about 410°–460°C. (Left) Incoloy 800; (right) alonized Incoloy 800.

Various Types of Coke Formed

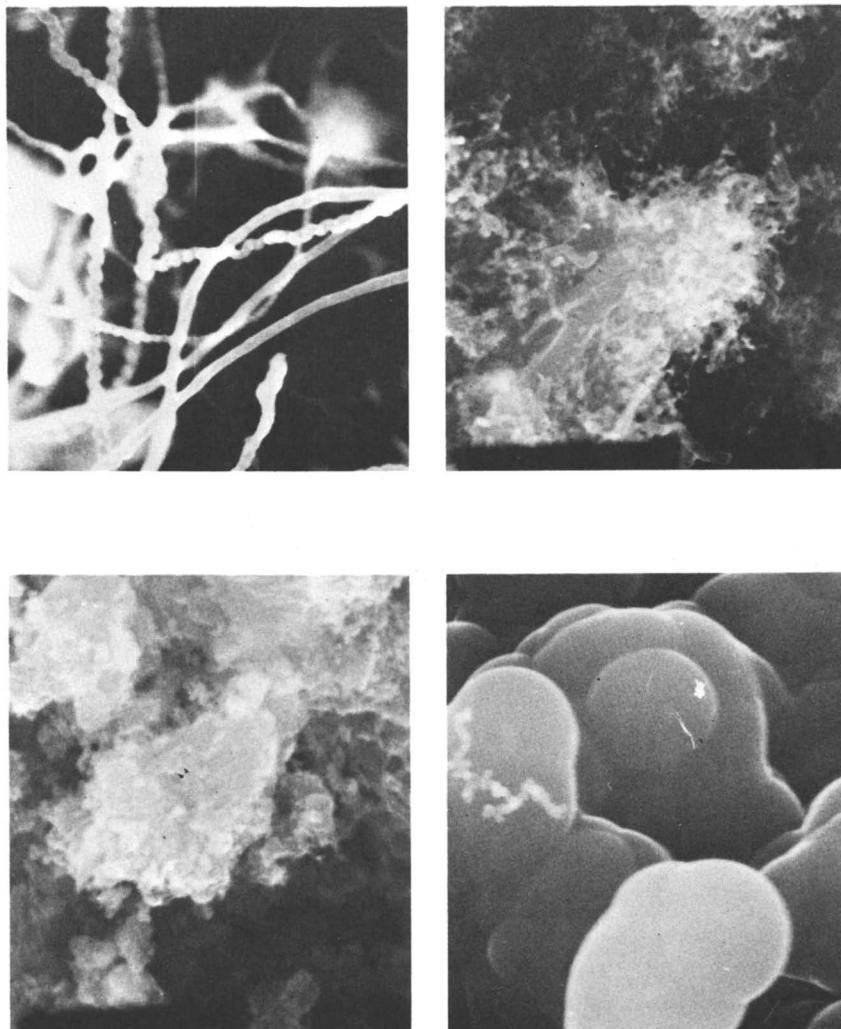
| <i>Hydrocarbon Feedstock*</i> | | <i>Magnetic Coke</i> | <i>Photographic Example</i> |
|-------------------------------|------------------|--------------------------|------------------------------------|
| <i>Propylene</i> | <i>Butadiene</i> | | |
| — | A | Yes | Figure 2, 325°C |
| A | A | Yes | Figure 1, Incoloy 800 |
| — | — | Yes | Figure 9, ethane |
| A | A | Yes | Figure 4, 460°, 560°, and 600°C |
| — | A | No | Figure 2, 770°C |
| A,E | A,E | No | Figure 2, 560°C |
| A,E | A,E | No | Figure 1, alonized Incoloy 800 |

diameter. As the temperature increased to 560°C, some coke filaments still formed, but they were smaller in diameter. A fluffy coke was apparently being deposited on the top of these filaments. Perhaps some amorphous coke also had formed on the metal surface. The fluffy coke is characterized as gas phase coke; it probably forms in the gas phase and then deposits (or precipitates) on the metal surface or on the coke already present.

At 600°C the coke no longer looks fluffy. It seems to be approaching an amorphous state and is less magnetic in nature. At 770°C the coke is rather knobby in appearance. Interestingly, a rather fluffy-appearing filament is present on one of the knobs. The knobs in general appear to be smooth and, in some cases, quite spherical.

Figure 3 shows an example of needle or arrowhead coke. This coke is produced from ethylene, propylene, and butadiene on Incoloy 800 surfaces in the temperature range from about 365°C up to at least 600°C. The size of needles as shown in Figure 3 was smaller than that observed in most other photographs; this coke was magnetic because of the iron present in it. The coke produced on alonized Incoloy 800 at comparable conditions was amorphous, however, as shown in Figure 3.

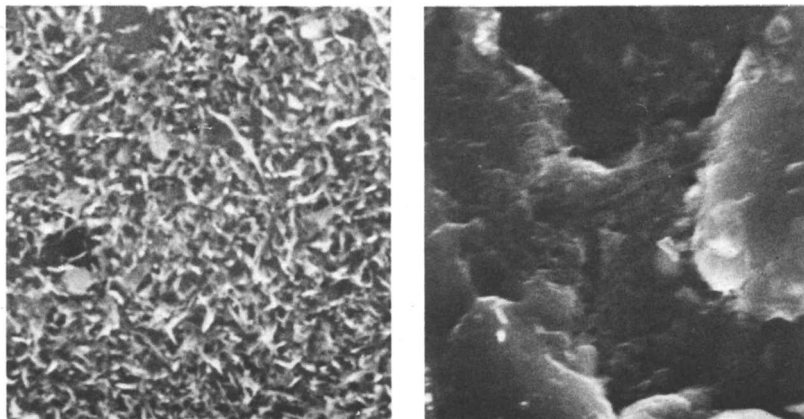
Figures 4 and 5 indicate that the types of coke formed on Incoloy 800 as ethylene and propylene, respectively, were contacted with an Incoloy 800 surface at various temperatures and at slightly different conversion levels. In these experiments, the Incoloy 800 coupons were positioned at different positions in the horizontal tubular reactor. The residence time of gases in the reactor was about 7, 10, 15, and 25 sec by the time the gases reached the coupon. The temperature of each location was about 460°, 560°, 600°, and 565°C, respectively. The cokes



|—| = 1 micron

Figure 2. Effect of temperature on coke formed from acetylene on Inco-loy 800. (Top left) 325°C, (top right) 560°C, (bottom left) 600°C, (bottom right) 770°C.

formed on the first three coupons were needle-like in character, but the cokes formed on the last coupons were rather amorphous or, in the case of ethylene, perhaps knobby. The differences in the coke formed at 10 and 25 seconds are thought to have been caused by slight differences in conversions and not to the small differences in temperatures; conversions after 25 seconds were approximately 2%. At 25 sec, more acetylene and



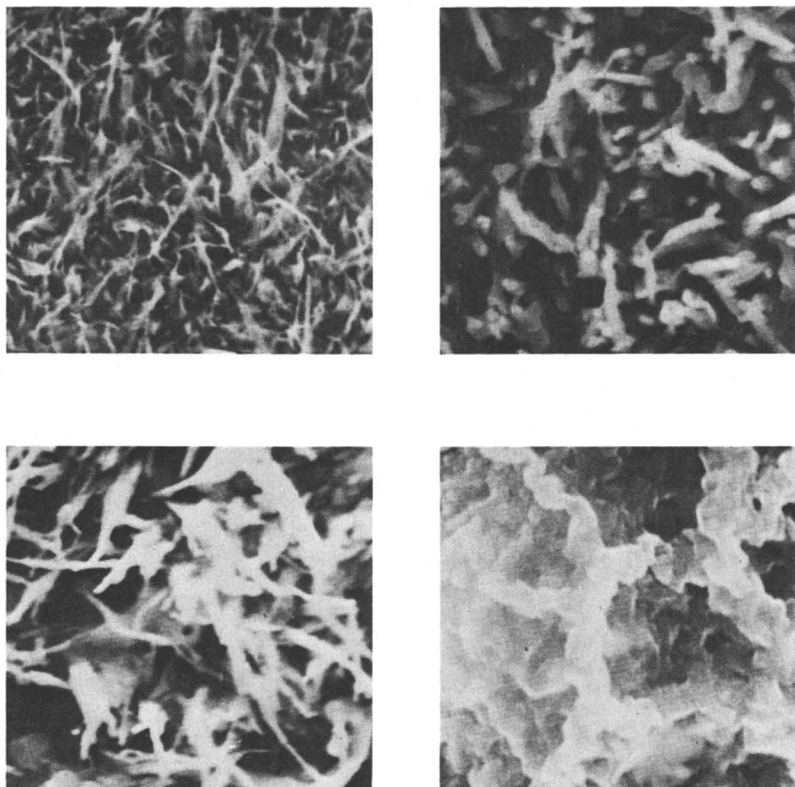
|—| = 1 micron

Figure 3. Cokes formed by butadiene at 465°C. (Left) Incoloy 800; (right) alonized Incoloy 800.

other coke precursors had probably formed than did at 10 sec. Also, perhaps some liquid droplets had condensed at longer residence times, as suggested by Lahaye et al. (11).

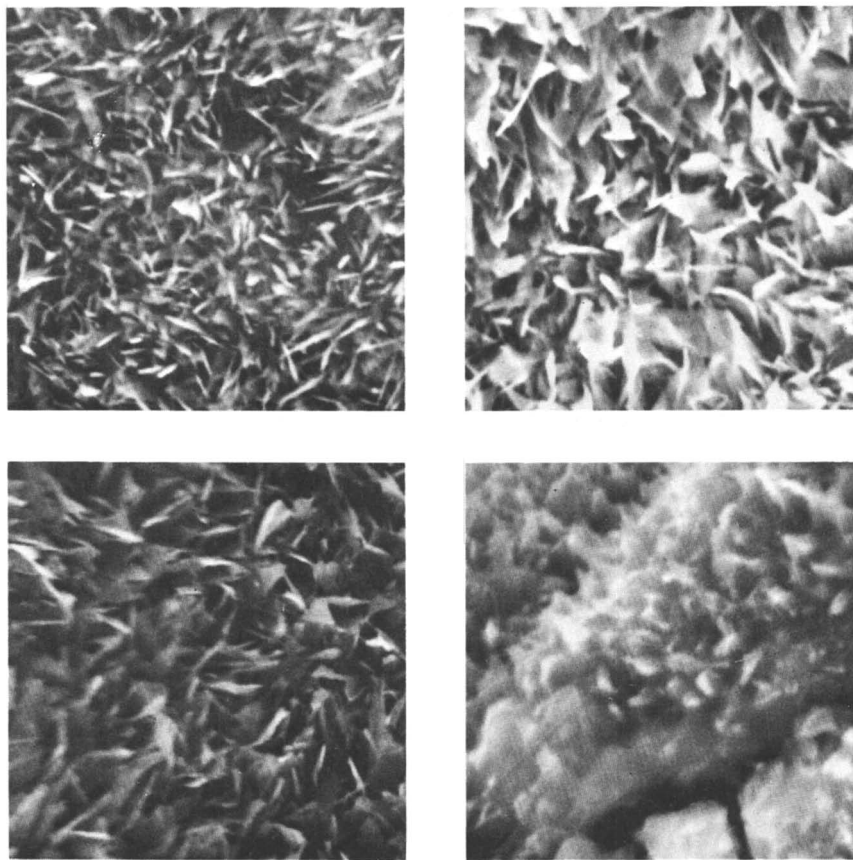
Figure 6 indicates that amorphous coke was formed from acetylene, ethylene, propylene, and butadiene at 600°C on alonized Incoloy 800 surfaces. These cokes were in all cases nonmagnetic in character and contained no detectable iron. They did contain a trace of aluminum, probably as alumina.

Surfaces Before and After Decoking. Photographic results are shown in Figures 7 and 8 for two series of runs using Incoloy 800 and alonized Incoloy 800 surfaces, respectively. In each figure, the top picture shows the original metal surface before coking with acetylene. The new Incoloy 800 surface (shown in Figure 7) indicated major differences in composition as measured by EDAX. The white area is attributable to high iron deposits on the surface. Two new and clean surfaces of Incoloy 800 and two surfaces of alonized Incoloy 800 were first contacted with acetylene at 700°C for about 120 min. The cokes on one Incoloy 800 surface and one alonized surface were then contacted with oxygen at 700°C for 80 min; most of the coke was removed, as indicated, by only a small amount of carbon oxides in the exit stream. The lower-left pictures of both Figures 7 and 8 show the resulting surfaces. The cokes on an Incoloy 800 and on an alonized surface also were contacted with steam at 700°C for 240 min until most of the coke had been gasified; a small amount of carbon monoxide and hydrogen was still being formed. The photographs of the resulting surfaces are shown



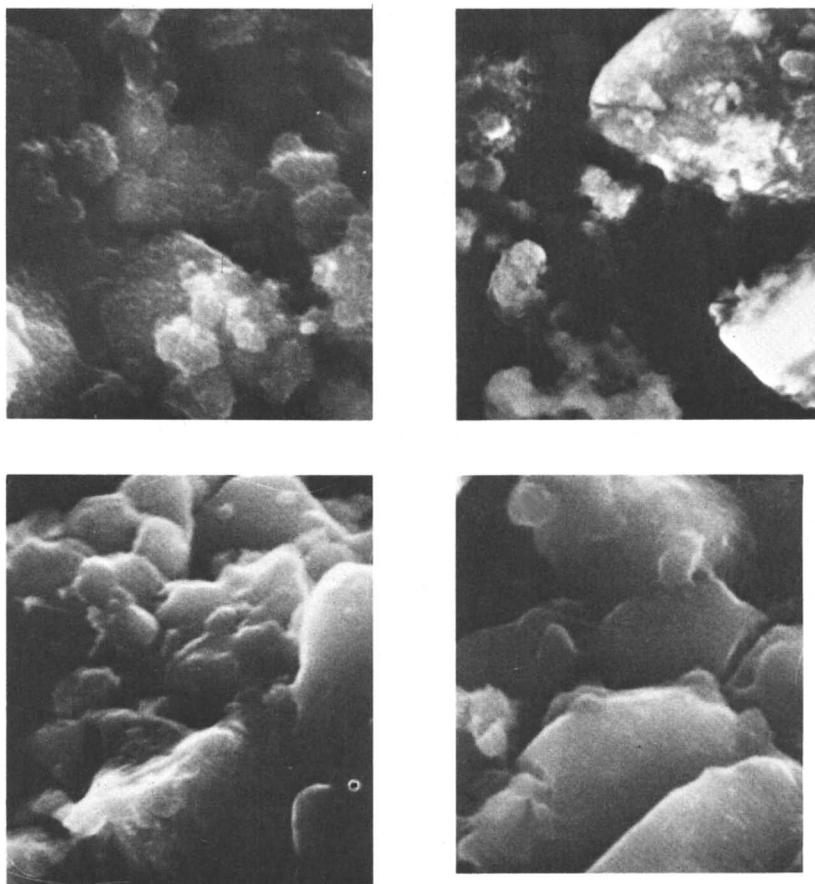
|—| = 1 micron

Figure 4. Effect of space time and temperature on coke formed from ethylene on Incoloy 800 surface. (Top left) 460°C, ~ 7 sec; (top right) 560°C, ~ 10 sec; (bottom left) 600°C, 15 sec; (bottom right) 565°C, 25 sec.



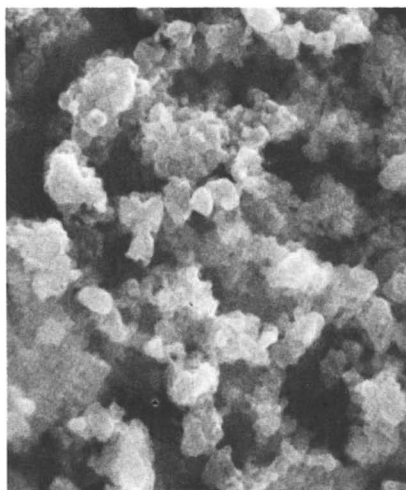
|—| = 1 micron

Figure 5. Coke formed at 600°C on Incoloy 800 with propylene. (Top left) 460°C, ~ 7 sec; (top right) 560°C, ~ 10 sec; (bottom left) 600°C, ~ 15 sec; (bottom right) 565°C, ~ 25 sec.



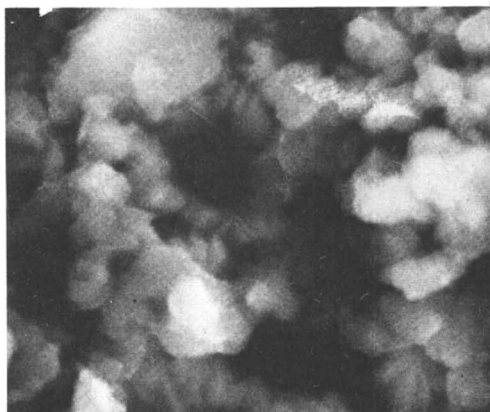
|—| = 1 micron

Figure 6. Coke formed at 600°C on alonized Incoloy 800 with four unsaturated hydrocarbons. (Top left) acetylene; (top right) ethylene; (bottom left) propylene; (bottom right) butadiene.



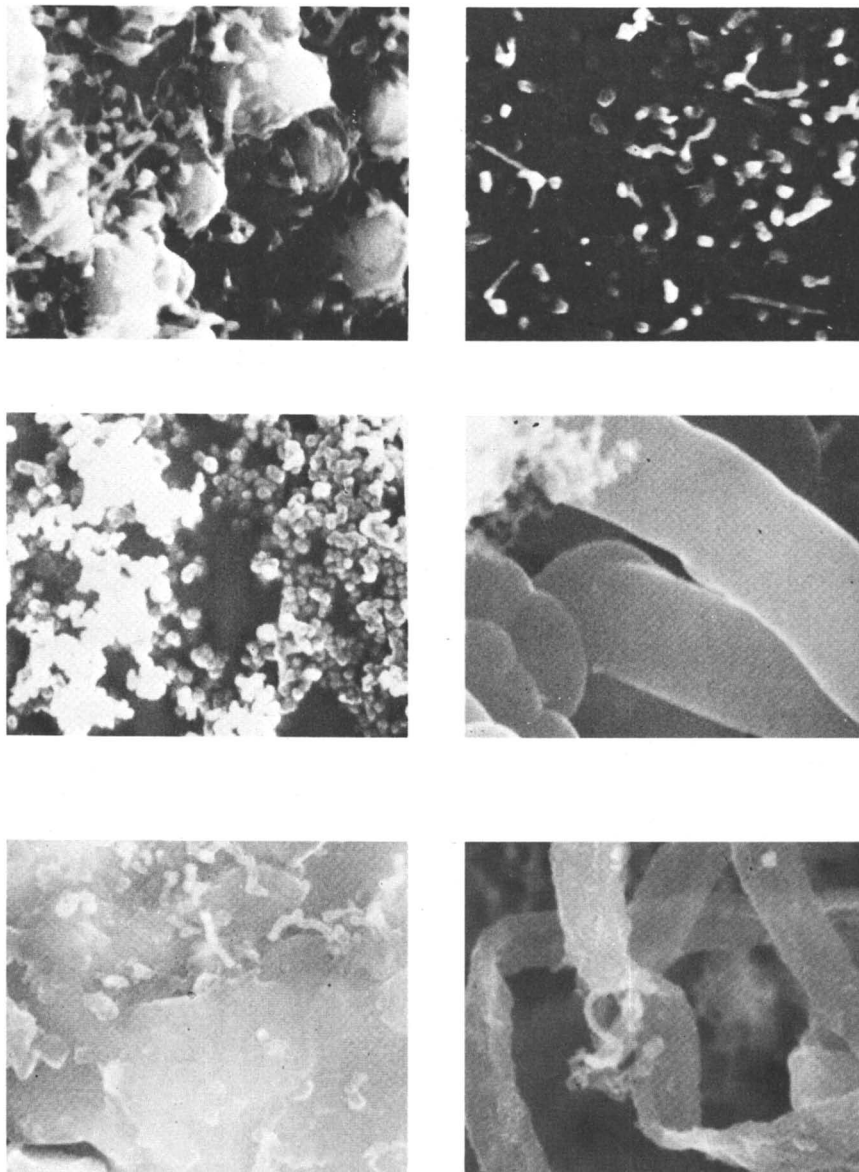
|—| = 1 micron

Figure 7. Various surface on Incoloy 800. (Top) new (or unused) surface; (bottom left) partially decoked (first acetylene and then oxygen treatment); (bottom right) partially decoked (first acetylene and then steam treatment).



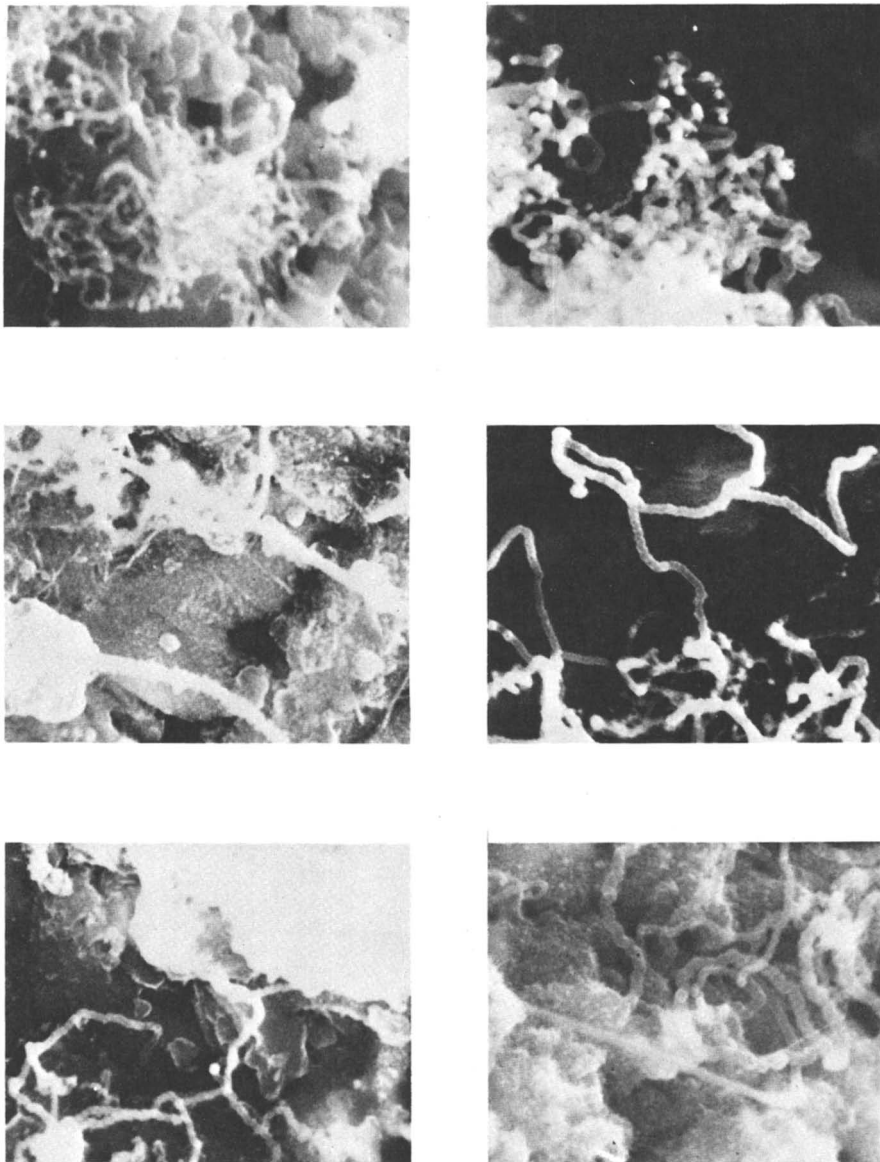
|—| = 1 micron

Figure 8. Various surface on alonized Incoloy 800. (Top) new (or unused) surface; (bottom left) partially decoked (first acetylene and then oxygen treatment); (bottom right) partially decoked (first acetylene and then steam treatment).



—| = 1 micron

Figure 9. Examples with more than one type of coke. (Top left) Butadiene—560°C (2nd position), incoloy coupon; (top right) ethylene—500°C (3rd position), incoloy coupon; (middle left) acetylene—800°C (alonized tube); (middle right) acetylene—780°C (4th position), alonized coupon; (bottom left) butadiene—460°C (1st position), alonized coupon; (bottom right) ethane pyrolysis—800°C, SS 304 tube.



—| = 1 micron

Figure 10. Coke at interface between alonized surface and Incoloy 800 base. (Top left) Butadiene—560°C (2nd position); (top right) butadiene—600°C (3rd position); (middle left) acetylene—380°C (1st position); (middle right) acetylene—440°C (2nd position); (bottom left) acetylene—450°C (3rd position); (bottom right) acetylene—440°C (4th position).

in the lower-right pictures. The large white spikes or sharp peaks noted in the Incoloy 800 picture were iron. Clearly, surface reactions involving iron were occurring in this case. Serious erosion or corrosion problems, such as experienced on the Incoloy 800 surface, were not noted for the alonized Incoloy 800 coupon.

Miscellaneous Coke Results. More than one type of coke was noted in many pictures. Figure 9 shows six cokes formed from various hydrocarbons:

1. Butadiene at 560°C on Incoloy 800 surface: both knobby and filament cokes.

2. Acetylene at 800°C on alonized surface: both knobby and amorphous cokes.

3. Butadiene at 460°C on alonized surfaces: both amorphous and a semiknobby, almost filament-type coke. The latter coke appears to be on top of the amorphous coke. The filaments, if they are filaments, are quite different in appearance to filaments shown in Figures 1 and 2.

4. Ethylene at 500°C on Incoloy 800 surface: both knobby and filament cokes.

5. Acetylene at 780°C on alonized surface: fluffy (or gas phase) and knobby (but almost filament-like) cokes.

6. Ethane pyrolysis at 800°C in SS 304 reactor: fluffy (or gas phase) and ribbon cokes.

The appearance of coke formed on the alonized and unalonized Incoloy 800 surfaces differed significantly, as was shown in both Figures 1 and 3. This fact was further demonstrated by taking a series of pictures at or very close to the boundary between the alonized and unalonized surfaces. Figure 10 shows six such photographs. On the alonized surface, aluminum atoms have penetrated into the Incoloy 800 matrix, but the concentration of aluminum decreases with depth. The length of filament coke is relatively long, and the filaments that had started on the unalonized surfaces apparently extended over alonized surfaces where amorphous coke was predominant. The upper-right picture of Figure 10 shows the sharpest change in the coke produced. In some cases, the filament coke apparently passed through or was later covered by amorphous coke; the lower two pictures show such examples.

Discussion of Results

Although several other investigators (1, 6-11) have obtained photographs of coke by using scanning electron or transmission electron microscopes, it is thought that the present results are more directly applicable to commercial units and also cover a wider variety of coke precursors in a single investigation. Clearly the scanning electron microscope with attached EDAX is a valuable tool for clarification of the

formation of coke in pyrolysis coils used for olefin production, in transfer line exchangers, and during dehydrochlorination of 1,2-dichloroethane in the production of vinyl chloride. A description of commercial equipment for production of both olefins and vinyl chloride is described by Albright (16). More details on coke formation during ethane pyrolyses are reported by Albright and McConnell (17).

The fact that seven types of coke were identified strongly supports the postulate that more than one coking mechanism is occurring. Evidence indicating that iron is often the predominant metal in the coke is considered especially important. The iron is apparently being removed (or extracted) rather selectively from stainless steel surfaces as the coke is produced.

Although the present results are considered most interesting, more questions are raised than are answered:

1. Why was iron the predominant metal in filament, ribbon, and needle cokes? Further information on the mechanism of coke formation is needed.

2. How does the composition of the metal surface change during pyrolysis? Surface reactions that have been identified on Incoloy 800 surfaces include oxidation, reduction, sulfidation, desulfidation, and coke formation (14). Do increased concentrations of nickel and chromium ever occur in the surface in view of the fact that iron is incorporated into the coke? Tsai and Albright (14) found increased iron concentrations on inner surfaces of tubes used for pyrolyses.

3. Does steaming always produce iron spikes on Incoloy 800 surfaces such as shown in the lower-right picture of Figure 8? This picture implies that steaming is a major factor contributing to corrosion of the inner surface. What happens to the chromium and nickel? Can improved methods of steaming be devised?

4. How do the amounts and types of coke deposited on the various metal surfaces vary as a function of time? In the present investigation, the resulting coke was obtained during 120-min runs. In the future, shorter and longer runs are needed to determine the kinetics of coke formation and to determine whether one type of coke is a precursor for another type. Possibly both filament and needle cokes act to some extent as a filter for gas phase coke to form eventually amorphous or knobby coke in which metal-containing coke is eventually covered with metal-free coke.

5. How does the type of coke vary with axial position in the pyrolysis tubes and in the transfer line exchanger? Conversions of the feed hydrocarbons vary with axial position.

6. Will alonized tubes retain their abilities to cause decreased amounts of coke formation even after long periods of use? Some aluminum is known to diffuse with time in the tubes. What fraction of aluminum reacts with steam to form alumina, and is diffusion of alumina in the metal of any importance?

7. Are there other metal treatments beside alonizing (or aluminizing) that are beneficial? Chromizing might be tested. Will any of these treatments minimize both the kinetics of coking and also the rate of surface corrosion?

8. How does sulfiding or oxidizing the metal surfaces affect the types of coke formed?

9. How rapidly does the surface roughen as coke formation occurs? Are there any ways to minimize this roughening?

10. Although coking is an undesired phenomenon during pyrolysis, what types of coke are less detrimental, and how could those types be promoted at the expense of other types?

11. Which types of coke are easiest to remove by steam or oxygen decoking? Can some mechanical means be developed to remove certain types of coke?

Investigations now in progress at Purdue University will hopefully provide answers to the above questions.

Acknowledgment

The United Nations and Purdue University provided some financial support for this project. Acknowledgment also goes to the donors of The Petroleum Research Fund, administered by the American Chemical Society, for partial support of this research.

Literature Cited

1. Palmer, H. B.; Cullis, C. F. "Chemistry and Physics of Carbon"; Walker, P. L., Ed.; Marcel Dekker, Inc.: New York, 1965; Vol. 1, p. 265-325.
2. Lobo, L. S.; Trimm, D. L. *J. Catal.* **1973**, *29*, 15.
3. Bernardo, C. A.; Lobo, L. S. *J. Catal.* **1975**, *37*, 267.
4. Baker, R. T. K.; Harris, P. S.; Thomas, R. B.; Waite, R. J. *J. Catal.* **1973**, *30*, 86.
5. Baker, R. T. K.; Waite, A. J. *J. Catal.* **1975**, *37*, 101.
6. Baker, R. T. K. *Chem. Eng. Prog.* **1977**, *73*(4), 97.
7. Robertson, S. D. *Carbon* **1970**, *8*, 365.
8. Robertson, S. D. *Carbon* **1972**, *10*, 221.
9. Baird, T.; Fryer, J. R.; Grant, B. *Carbon* **1974**, *12*, 591.
10. Baird, T. *Carbon* **1977**, *15*, 379.
11. Lahaye, J.; Badie, P.; Ducret, J. *Carbon* **1977**, *15*, 87.
12. Dunkelman, J. J.; Albright, L. F. In "Industrial and Laboratory Pyrolyses"; *ACS Symp. Ser.* **1976**, *32*, Chapter 14.
13. Herriott, G. E.; Eckert, R. E.; Albright, L. F. *AIChE J.* **1972**, *32*, 84.
14. Tsai, C. H.; Albright, L. F. In "Industrial and Laboratory Pyrolyses"; *ACS Symp. Ser.* **1976**, *32*, Chapter 16.
15. Brown, S. M.; Albright, L. F. In "Industrial and Laboratory Pyrolyses"; *ACS Symp. Ser.* **1976**, *32*, Chapter 17.
16. Albright, L. F. "Processes for Production of Major Addition-Type Plastics and Their Monomers"; McGraw-Hill: New York, 1974; Chapters 2 and 5.
17. Albright, L. F.; McConnell, C. F., Chapter 12 of this volume.

RECEIVED June 21, 1978.

Production of Coke and Other Pyrolysis Products From Acetylene, Butadiene, and Benzene in Various Tubular Reactors

LYLE F. ALBRIGHT and YU-HONG CAROL YU¹

School of Chemical Engineering, Purdue University,
West Lafayette, IN 47907

Thermal reactions of acetylene, butadiene, and benzene result in the production of coke, liquid products, and various gaseous products at temperatures varying from 450° to 800°C. The relative ratios of these products and the conversions of the feed hydrocarbon were significantly affected in many cases by the materials of construction and by the past history of the tubular reactor used. Higher conversions of acetylene and benzene occurred in the Incoloy 800 reactor than in either the aluminized Incoloy 800 or the Vycor glass reactor. Butadiene conversions were similar in all reactors. The coke that formed on Incoloy 800 from acetylene catalyzed additional coke formation. Methods are suggested for decreasing the rates of coke production in commercial pyrolysis furnaces.

This project is a continuation of the investigations of Tsai and Albright (1) and of Brown and Albright (2), who earlier studied surface reactions that occur during the pyrolysis of hydrocarbons. Such pyrolyses are used for commercial production of ethylene, other olefins, diolefins, and, to some extent, aromatics. Several important reactions occur on the inner surfaces of the high-alloy steel tubes used for pyrolyses. These surface reactions occur simultaneously and, to some extent, consecutively along with the gas-phase reactions that produce the desired products of

¹ Current address: Amoco Chemical Co., Naperville, IL 60540.

pyrolysis. The surface reactions are, for the most part, undesired and lead to production of significant amounts of coke, carbon oxides, hydrogen, and even methane. Surface reactions that occur along with coking and decoking including oxidation, reduction, sulfiding, and desulfiding of the inner surfaces of the high-alloy, stainless-steel reactors.

Brown and Albright (2) systematically investigated surface reactions when ethylene, ethane, propylene, and propane were pyrolyzed in Incoloy 800, stainless steel 304, and Vycor glass tubular reactors. The importance of surface reactions and of the amounts of coke produced often were significantly affected by the feed hydrocarbon, construction material of the reactor tube, oxidation and sulfiding of the metal reactors, and temperature. More coke was generally produced from ethylene or propylene than from ethane or propane. This finding is consistent with the general conclusion that the more unsaturated hydrocarbons are better coke producers. Stainless steel 304 reactors resulted in more coke than did Incoloy 800 reactors and much more than did Vycor glass reactors (2, 3). For the two metal reactors used, increased concentrations of metal oxides on the inner surface of the reactors often promoted coke formation. Metal oxides are produced when the metal surfaces react either with oxygen or steam at high temperatures. However, metal sulfides that were formed by reactions with hydrogen sulfide or sulfur-containing hydrocarbons, in general, act to suppress coke formation. Coke often contains metal granules, and coking and corrosion of the inner surfaces of the tubular reactors are at least sometimes related, being part of the same phenomena. In general, higher temperatures resulted in increased amounts of coke formation.

Acetylene, butadiene, and benzene are thought to be important coke precursors during pyrolysis reactions used to produce light olefins (especially ethylene) and during dehydrochlorination of 1,2-dichloroethane for production of vinyl chloride. Surface reactions involving these precursors were investigated in the present study. Also, an alonized (or aluminized) Incoloy 800 reactor was compared with a regular (or unalonized) Incoloy 800 reactor relative to both the production of coke and to surface reactions in general. The alonized reactor that was used frequently resulted in fewer surface reactions.

Experimental Details

The pyrolysis reactors were similar to those used earlier (1, 2); they were 1.1 to 1.26-cm i.d. tubes that were heated in an electrical resistance furnace over a length of about 48 cm. The materials of construction in the four reactors used in this investigation were as follows: Incoloy 800, stainless steel 304, Vycor glass, and alonized Incoloy 800. The latter reactor was prepared by Alon Processing, Inc. of Tarentum, Pennsylvania.

The inner surface of an Incoloy 800 tube had been exposed to aluminum vapors at high temperatures; aluminum diffused into the surface, resulting in an aluminized surface.

The temperatures reported in this investigation were those near the center point of the reactor that was positioned in the furnace. Maximum temperatures occurred at the center point. Temperatures near either end of the heated section of the tube were less than the maximum temperature by about 40°–90°C, depending to a considerable extent on the maximum temperature used. Temperatures at the center point were controlled at any desired value in the range from about 400° to 800°C. Temperatures in the lower portion of this range were tested since surface reactions at such temperatures are often significant even though gas-phase reactions are not. Hence the technique used provided valuable information relative to the role and importance of surface reactions.

Lighter hydrocarbons such as acetylene and 1,3-butadiene were metered at atmospheric pressure to the tubular reactors at a flowrate of about 30 mL/min. Benzene was introduced to the reactor in a mixture containing benzene and helium; helium was bubbled through liquid benzene maintained at approximately 25°C to produce a mixture containing about 12% benzene by volume. The flowrates of the inlet feed streams were such that the residence times of the hydrocarbons in the heated section of the tubular reactors varied from about 25 to 30 sec. The variations of residence times were caused primarily by the differences in the temperature levels used in the reactor and by the variations in the conversions.

The product gas stream from the tubular reactor was passed in each run through a glass condenser immersed in an ice bath. Part of the product stream condensed. Both the liquid product and the noncondensed gases were analyzed by using a Tracor dual-column, temperature-programmed gas chromatograph. The columns were constructed from about 180 cm of 6.35-mm stainless steel tubing that was packed with Porapak Q, 80/100 mesh. The chromatograph separated components from hydrogen to at least C₁₂ hydrocarbons.

Material balance calculations were made by using the inlet and exit streams from the tubular reactors to approximate the amounts of coke and other products that collected on or that coated the inner surfaces of the reactor. The amounts of coke or other heavy products left in the reactor also could be determined by a burnout procedure, using oxygen. In this procedure, the amounts of carbon oxides and water in the exit stream were measured at frequent intervals during the burnout. In general, reasonable agreement was noted in the values of coke and other heavy products, as calculated by these two methods. Oxygen burnouts generally resulted in mainly carbon oxides but in little water vapor; the products left in the reactor are hence thought to be primarily carbon.

Acetylene Results

Six runs were made using acetylene as the feedstock. Both the kinetics of acetylene conversions and the product composition frequently varied significantly depending on the reactor used, the immediate pre-

treatment of the reactor, and the temperature. Table I outlines the material of construction of the reactor, the pretreatment, and range of conditions investigated for each of the six runs. In these runs, significant amounts of gaseous, liquid, and solid (or coke) products were formed. The liquid product contained appreciable amounts of benzene; butadiene, C₅, other C₆, and C₇ hydrocarbons also were present. The noncondensed or gaseous products were, in each case, primarily hydrogen and methane. Trace amounts of ethane, propylene, and butadiene also were detected.

Table I. Runs with Acetylene

| <i>Run</i> | <i>Reactor</i> | <i>Immediate Pretreatment</i> | <i>Temperature Range Investigated (°C)</i> |
|------------|----------------------|--|--|
| 14 | Incoloy 800 | 1,3-butadiene runs to form coke on surface | 350–650 |
| 15 | Incoloy 800 | O ₂ at 700°C, 190 min H ₂ at 700°C, 1120 min | 350–550 |
| 18 | Incoloy 800 | O ₂ at 700°C, 150 min H ₂ at 700°C, 1020 min | 450–500 |
| 19 | Vycor Glass | C ₆ H ₆ at 25°C, 30 min | 400–650 |
| 21 | Alonized Incoloy 800 | O ₂ at 800°C, 570 min H ₂ at 700°C, 1050 min | 350–650 |
| 23 | Incoloy 800 | O ₂ at 700°C, 280 min H ₂ at 700°C, 1100 min H ₂ S at 700°C, 40 min | 450–600 |

Figure 1 indicates an example of how pretreatment of the Incoloy 800 reactor had a very large effect on the acetylene conversion (or on the kinetics of acetylene decomposition). The coke-coated Incoloy 800 reactor (the coke had been deposited on this reactor when butadiene reacted at 500°–700°C.) used in Run 14 resulted in much lower acetylene conversions in the range of 450° to 550°C compared with the same Incoloy 800 reactor after the coke had been burned off with oxygen and after the reactor had been contacted with hydrogen until nearly all surface oxides were eliminated. Most conversion results for the 11 gas samples collected during Run 15 are shown in Figure 1. Gas Samples 1 through 3 at 350°, 400°, and 450°C, respectively, indicated almost no acetylene conversions. A small amount of carbon dioxide was produced at 450°C, indicating some metal oxides had still been present on the surface after the hydrogen pretreatment. The temperature was then increased to 500°C, and the conversions then increased from 66% to 99% during the first 23 min (Samples 4 and 5). Some carbon oxide production was noted in Sample 4 but none in Sample 5 or in any later samples of the run; presumably

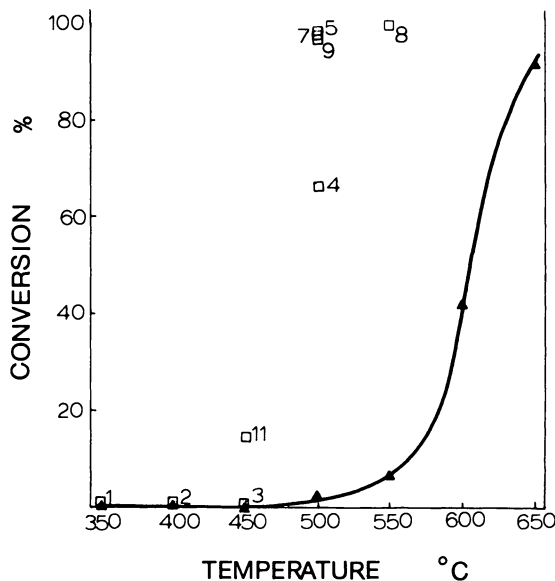


Figure 1. Acetylene conversions in coke-coated Incoloy 800 and clean Incoloy 800 reactors. Acetylene feed: (▲) Run 14, coke-coated Incoloy 800; (□) Run 15, clean Incoloy 800.

metal oxides on the surface had reacted and had been reduced before Sample 5 was taken. The conversion remained at about 99% for more than one hour as the temperature was maintained at 500°C, as indicated by Sample 7. At 500°C and higher, large amounts of hydrogen were produced. Obviously coke also was formed simultaneously. When the temperature was decreased to 450°C (Sample 11), a conversion of about 11% occurred. An earlier sample (Sample 3) taken at 450°C had indicated little or no conversion. Run 15 was terminated after about 4.7 hr.

The Incoloy reactor was pretreated prior to Run 18 similar to that before Run 15. For Run 18, substantial conversions were noted at 450°C, whereas none were detected in Run 15 until a temperature of 500°C was reached. Conversions of 85%–100% were noted in the range 475°–500°C in Run 18. After about 2.33 hr, the inlet pressure of the reactor began to rise, indicating a plug was starting. The run then was terminated. When the reactor was opened, it was found to be almost plugged with coke. This coke was magnetic in nature, and metal particles were visually observed in it. Analysis with a scanning electron microscope equipped with EDAX has confirmed the presence of metals in cokes formed from acetylene on Incoloy 800 surfaces (3). The mechanism that explains how metal granules are incorporated in the coke and how these

granules promote the formation of additional coke has been presented by both Lobo et al. (4, 5) and Baker et al. (6, 7, 8). Cokes formed, however, from acetylene on alonized Incoloy 800 surfaces are nonmagnetic and do not contain metals except for small amounts of aluminum (probably as alumina) (3). Cokes on Vycor glass surfaces also contain no metal.

An important finding of this investigation was that cokes formed from acetylene on Incoloy 800 surfaces caused what appears to be an ever increasing rate of coke formation, as indicated by the results of Run 15 and especially of Run 18. In other words, this coke resulted in an auto-acceleration phenomenon. Yet the coke formed from butadiene (as indicated by the results of Run 14) seemed to deactivate the surface so that a slow and rather steady rate of coke formation occurred. The reason for this difference in the rates of coke formation will be discussed later in this chapter.

Prior to Run 23, the reactor was contacted with hydrogen sulfide for about 15 min. Acetylene conversions of Run 23 increased from about 94% at 450°C to almost 98% at 600°C. The conversion results at a given temperature were quite reproducible during this run that totalled almost 3 hr in length. Yields of gaseous and coke products were significantly less than those of Runs 15 and 18 even though acetylene conversions were often similar. Yields of liquid products were much greater in Run 23 than in Runs 15 and 18. Liquid yields for Run 14 were, however, greater than those of Run 23.

The results for Run 19 (Vycor glass reactor), Run 21 (alonized Incoloy 800 reactor), and Run 14 (coke-covered Incoloy 800 reactor) were similar to both the kinetics and type of products obtained. Although neither oxygen or hydrogen pretreatments were tried in Vycor glass or alonized Incoloy 800 reactors prior to acetylene pyrolyses, it is thought that such pretreatments would have little or no effect on acetylene reactions. This conclusion is based on such pretreatments prior to pyrolysis with other hydrocarbons in these two reactors. It has been concluded that all increases in acetylene conversions above those of Runs 14, 19, and 21 were in some way caused by surface reactions. Based on this assumption, surface reactions were of major importance in Runs 15, 18, and 23.

Butadiene Results

1,3-Butadiene reacted in Incoloy 800, alonized Incoloy 800, and Vycor glass reactors to give quite similar results. Butadiene conversions increased from about 60%–80% at 500°C to about 94%–97% at 700°C. The main products formed were liquids (i.e., products that condensed

at 0°C) and were obviously condensation products. Analysis of the liquid products with the gas chromatograph indicated at least 25 peaks. The three peaks that were much larger than the others tentatively have been identified as benzene, toluene, and 4-vinylcyclohexene. Yields of liquid products decreased from about 65%–79% at 500°C to 57%–63% at 700°C. At 500°C, 4-vinylcyclohexene was by far the most important product, but significant amounts of benzene also were present. At 700°C, both benzene and toluene were more important, totaling about 75%–80% of the liquid product.

The results of this investigation are consistent with the findings of Sakai et al. (9). They had found 4-vinylcyclohexene to be the main product at low conversions of butadiene for temperatures ranging from 550° to 750°C. They also reported mechanisms to explain the production of benzene, cyclohexadiene, and cyclohexene.

The gaseous products for the butadiene reactions consisted mainly of hydrogen, methane, ethylene, ethane, and propylene. The first three mentioned were the major gaseous products at 500°C, but about 50% of the gaseous product was methane at 700°C. Yields of gaseous products increased from about 5%–7% at 500°C to 32%–35% at 700°C.

The "solid phase" retained in the reactor during butadiene reactions was probably a mixture of tar (or heavy hydrocarbons) and coke. This conclusion is based in part on material balance calculations. These calculations, although not considered highly accurate, suggest that heavy hydrocarbons or tar were formed in appreciable amounts at lower temperatures such as 500°C. Yields of surface-deposited products were about 16%–26% at 500°C but were only 5%–10% at 700°C. At the higher temperatures, calculations indicated the deposits were almost completely coke. Heavy hydrocarbons deposited at lower temperatures probably were decomposed rather completely to coke and hydrogen when the reaction temperature was increased to 700°C during the final stages of the run.

Visual observation of the Vycor glass reactor immediately following the butadiene run at 700°C resulted in important information. The reactor was cut to permit inspection of the black deposits thought to be primarily coke. The last two-thirds of the reactor and a short section of the unheated tube that extended beyond the furnace were covered on the inner surface with a smooth layer of coke. This deposit, when viewed from the outside of the reactor, appeared as a "black mirror." It is of special interest that the inlet section of the tubular reactor did not have any coke deposits. This section was the one that was subjected to increasing temperatures in the furnace. The start of the coke deposits occurred approximately in the section where maximum temperatures occurred during a run. Most of the deposits appeared to occur in the

exit section of the reactor, which was the portion of the reactor subjected to decreasing temperatures. The location of the coke deposits is consistent with the postulate that heavy condensation products were formed in the gas phase and that these heavy products were deposited or condensed in the cooler sections of the reactor. The smooth finish of the deposits on the inner walls can be explained by the postulate that initial deposits from the gas phase were liquid or semiliquid; the initial deposits then reacted (especially at higher temperatures) to yield the smooth coke deposits plus hydrogen. This proposed mechanism for coke production from butadiene would result in coke that contains little or no metal granules. This conclusion explains why the coke on the wall of the Incoloy 800 reactor in Run 14 resulted in a very inactive surface, whereas the metal-containing coke formed in Runs 15 and 18 was very active.

Benzene Results

Almost no reactions occurred when a mixture containing about 12% benzene and the remainder helium was passed through Vycor glass and alonized Incoloy 800 reactors in the 550°–700°C range. The concentration of hydrogen in the exit gas stream, which is related to the conversion of benzene, is reported as a function of temperature in Figure 2. Complete conversion of benzene to carbon and hydrogen would result in a hydrogen concentration of about 29%; such a line is shown in Figure 2. At 750° and 800°C, a small amount of benzene (up to about 0.4%) reacted in the alonized reactor. Hydrogen and coke were the main products. Traces of methane, ethylene, carbon dioxide, and water also were noted. The latter two compounds were apparently the result of trace amounts of metal oxides that had remained after pretreatment of the reactor, first with oxygen and then with hydrogen. Traces of carbon dioxide and water also were detected for runs in the Vycor glass reactor that was also pretreated first with oxygen and then with hydrogen.

Significant benzene conversions, however, occurred in the Incoloy 800 reactor at temperatures as low as 500°–550°C, as shown in Figure 2. Hydrogen, coke, and a heavy compound (probably diphenyl) were formed. The reactor had been pretreated prior to the run first with oxygen to remove coke deposits and then with hydrogen to reduce the metal oxides formed from oxygen. The results of the eight samples taken during the run are shown in Figure 2. Initial benzene conversions were high but as the run progressed, the conversions tended to decrease. Comparisons of the results of Samples 2 and 8 and of Samples 4 and 7 clearly show this trend. It also is of interest that a lower conversion occurred for Sample 7 at 700°C compared with Sample 5 at 650°C. Samples 4, 5, and 6 all indicate benzene conversions of 90% or greater.

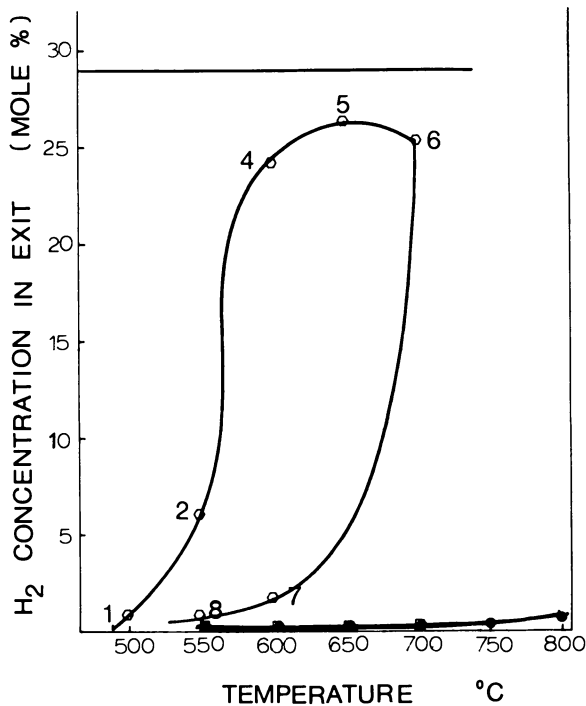


Figure 2. Hydrogen concentration in product gas stream during benzene pyrolysis in various reactors; 12% benzene feed: (\square) Vycor, (\square) Incoloy 800, (\bullet) Alon.

Methane was formed in significant amounts in such cases; it is thought that hydrogen reacts with the surface coke or metal carbides on the surface, such as has been shown earlier to occur (1). At the same temperatures (600°–700°C), little or no reactions occurred in the Vycor glass or in the alonized Incoloy 800 reactors. Clearly the Incoloy 800 surfaces were promoting significant coking reactions at these temperatures.

Based on the results of this run, the coke formed on the Incoloy 800 surface is quite inactive. Probably even lower conversions would have occurred if the run had continued longer and if more coke had been allowed to form on the surface. Unfortunately, no attempt was made to inspect or analyze the coke formed from benzene. It would be of special interest to determine how much metal was incorporated in the coke formed.

Additional Testing of Alonized Incoloy 800 Reactor

A series of runs was made in the alonized Incoloy 800 reactor by using ethylene, ethane, propylene, and propane. These runs were com-

parable with those of Brown and Albright (2) who had used Incoloy 800, stainless steel 304, and Vycor glass reactors. The conversion results of the runs using the alonized Incoloy 800 reactor were quite similar in all cases to the results obtained in this investigation for the same hydrocarbons in a reduced stainless steel 304 reactor and also to those results obtained earlier (2) in another reduced stainless steel reactor.

Several tests were made to compare the results obtained in the alonized reactor after pretreatment with oxygen, after pretreatment with hydrogen, and after no pretreatment. These runs, made with ethylene and propylene, indicated that pretreatments had little or no effect on the pyrolysis conversions. Tests reported earlier (2) with Incoloy 800 and stainless steel 304 reactors indicate that similar pretreatments had important effects on the conversion levels. In these latter two reactors, it is obvious that significant amounts of metal oxides are produced on the inner surfaces during oxygen pretreatments. Such surface oxides subsequently react with hydrocarbons to form both carbon oxides and water. In the case of the alonized Incoloy 800, apparently little or no metal oxides (except for alumina) were formed or destroyed as a result of oxygen and hydrogen pretreatments. It is probable that surface roughening occurs to at least some extent as a result of surface oxidation and then subsequent reduction of high-alloy steel reactors. Since alonizing minimizes this sequence of surface oxidation and reduction, surface roughening probably occurs to at least a reduced extent in alonized tubes; the results with the scanning electron microscope of Albright, McConnell, and Welther (3) support this conclusion.

Discussion of Results

The findings of this investigation help explain certain coking phenomena noted by Dunkleman and Albright (10) and also by Albright and McConnell (11). They had found, for ethane pyrolyses in laboratory tubular reactors, that relatively low rates of coke formation sometimes resulted after a short period of operation of a just-cleaned, Incoloy 800 tube but that high and essentially uncontrolled levels of coke formation occurred in other cases. The results of the present investigation suggest the cause of these two phenomena. In the former case, coke that deactivates the surface is probably initially formed and deposited on the surface. Such a coke is presumably similar to that formed from butadiene in the present investigation. This coke would likely have little or no metal granules incorporated in it. In the latter case, the initial coke formed in the just-cleaned reactor probably contains a large amount of metal granules that further catalyze coke formation. Coke such as was

formed in Run 15 and especially in Run 18 is an example of the latter (and undesired) coke. It would be preferred that during the start-up phases of a new or just-cleaned reactor an inactive coke be produced.

The results of this investigation and particularly of those with butadiene strongly suggest that at least portions of the inactive coke formed during pyrolyses involve the following sequence of events: (a) production in the gas phase of unsaturated hydrocarbons, (b) chemical condensation or polymerization of unsaturated hydrocarbons to produce rather heavy hydrocarbons, (c) physical condensation of these heavy hydrocarbons as liquids on the reactor walls or in the transfer line exchangers, and (d) decomposition of the liquids to coke (or tars) and hydrogen. This sequence of events is essentially identical to the one proposed by Lahaye et al. (12) for coke production from cyclohexane, toluene, or *n*-hexane.

Although more information is needed to determine details concerning factors that favor inactive coke formation, relatively high levels of surface sulfides probably promote formation of such coke. On the other hand, metal oxides on the surface likely favor production of active coke. Sulfiding the reactor tube immediately upon completion of the decoking step would form metal sulfides. An aluminized surface, such as provided by the alonized Incoloy 800 reactor, also has been found to be an effective way to prevent the production of active coke. Quite possibly, the initial type of coke formed on the just-cleaned tube would have an important effect on the length of time a reactor tube could be used in a commercial plant before decoking would be required.

Literature Cited

1. Tsai, C. H.; Albright, L. F. "Industrial and Laboratory Pyrolyses," ACS *Symp. Ser.* **1976**, *32*, chapter 16.
2. Brown, S. M.; Albright, L. F. "Industrial and Laboratory Pyrolyses," ACS *Symp. Ser.* **1976**, *32*, chapter 17.
3. Albright, L. F.; McConnell, C. F.; Welther, K. Chapter 10 in this book.
4. Lobo, L. S.; Trimm, D. L. *J. Catal.* **1973**, *29*, 15.
5. Bernardo, C. A.; Lobo, L. S. *J. Catal.* **1975**, *37*, 267.
6. Baker, R. T. K.; Harris, P. S.; Thomas, R. B.; Waite, R. J. *J. Catal.* **1975**, *30*, 86.
7. Baker, R. T. K.; Waite, R. J. *J. Catal.* **1975**, *37*, 101.
8. Baker, R. T. K. *Chem. Eng. Progr.* **1977**, *73*(4), 97.
9. Sakai, T.; Soma, K.; Sasaki, Y.; Tominga, H.; Kunugi, T. In "Refining Petroleum for Chemicals," *Adv. Chem. Ser.* **1970**, *97*, 68.
10. Dunkleman, J. J.; Albright, L. F. In "Industrial and Laboratory Pyrolyses," ACS *Symp. Ser.* **1976**, *32*, chapter 14.
11. Albright, L. F.; McConnell, C. F. Chapter 11 in this book.
12. Lahaye, J.; Badie, P.; Ducret, J. *Carbon* **1977**, *15*, 87.

RECEIVED June 21, 1978.

Deposition and Gasification of Coke During Ethane Pyrolysis

LYLE F. ALBRIGHT and CHRISTOPHER F. McCONNELL¹

School of Chemical Engineering, Purdue University,
West Lafayette, IN 47907

Considerable information was obtained for ethane pyrolysis relative to coke deposition on and to decoking from the inner walls of a tubular reactor. Both phenomena are affected significantly by the materials of construction (Incoloy 800, stainless steel 304, stainless steel 410, Hastelloy X, or Vycor glass) of the pyrolysis tube and often by their past history. Based on results with a scanning electron microscope, several types of coke were formed. Cokes that formed on metal tubes contained metal particles. The energy of activation for coke formation is about 65 kcal/g mol.

Although coke formation is always of importance during pyrolysis processes that are used for production of ethylene and other valuable olefins, diolefins, aromatics, etc., relatively little is known about the factors affecting such coke formation. It has been found that operating conditions, feedstock, pyrolysis equipment, and materials of construction and pretreatments of the inner walls of the pyrolysis tubes all affect the production of coke. General rules that have been devised empirically at one plant for minimizing coke formation are sometimes different than those for another plant. It can be concluded that there is relatively little understanding of, or at least little application of, fundamentals to commercial units.

Most coke investigations made to date have been at conditions that are related to, but not directly comparable with, those of commercial units. For example, acetylene has been investigated in considerable detail over nickel surfaces (1-5). Although acetylene is generally thought to be a

¹ Current address: Dow Chemical Co., Midland, MI 48640.

precursor for coke, the results would be more applicable if materials of construction such as those used commercially were applied. Investigations conducted at Purdue University (6-10) have resulted in considerable information pertaining to the importance of surface reactions in pyrolysis reactors. Such reactions, in general, result in decreased yields of ethylene and in increased yields of coke and carbon oxides. These results have been obtained in Incoloy 800, stainless steel 304, and stainless steel 410 reactors. The past history and pretreatments of the inner surface of the metal reactors often have a significant effect on both ethylene and coke yields. Such pretreatments include sulfiding or oxidizing the inner metal surfaces of reactors.

In the present investigation, ethane was pyrolyzed at conditions of commercial interest in several tubular reactors. Information has been obtained that provides further insights on the coke precursors, on the rate of formation of coke, on the rate of gasification as the coke reacts with steam, and on photographs of the coke and resulting metal surfaces as obtained by a scanning electron microscope.

Experimental

The system previously described by Herriott, Eckert, and Albright (6) and by Dunkleman and Albright (7) was used. Tubular reactors used were constructed from Incoloy 800, stainless steel 304, stainless steel 410, Hastelloy X, and Vycor glass. Most reactors were provided with two or three sample ports at intermediate distances along the coil. Reactors had internal diameters in the range of 0.40 to 0.49 cm, and about 107 cm of length was immersed in all cases in a fluidized sand bath that was controlled at 800°C. All pyrolyses were conducted at atmospheric pressure, using 0% to 50% dilution of the ethane with steam, and at residence times of 0.3-4.3 seconds to result in ethane conversions up to 80%. These residence times were obtained by varying the flowrate of the ethane-steam mixture and by sampling at various distances along the pyrolysis coil. A Jeolco scanning electron microscope (Model JSM-US) equipped with an EDAX analyzer (Model No. 707) was used for analysis of the coke and of the metal components in the coke or on the metal surface.

Analysis of the exit gas streams from the end of the tubular reactor and from sample ports at various positions on the tubular reactors were made by using a gas-phase chromatographic unit as described earlier (7). This unit was able to analyze routinely all components from hydrogen to C₄ hydrocarbons. By increasing the temperatures of the column, qualitative tests also could be made for C₅ and C₆ hydrocarbons. In the metal reactors, these latter two families of hydrocarbons were not detected. The amount of net coke (the amount of coke that formed and was left on the inner walls of the reactor) was calculated as the difference of the amounts of carbon atoms in the inlet and exit gas streams. Since sample ports in the reactors were used, the amounts of net coke formed for various path lengths also could be calculated.

Products Formed, Thermodynamic and Kinetic Results

Table I presents results for six comparable pyrolysis runs made by using five laboratory reactors; all runs were made with approximately 50% steam as diluent in the ethane feed. Conversions at the exit end of the reactor varied from 59% to 65%. Also, results reported for a commercial unit (11) are shown. Ethylene yields varied from about 78% to 89% in all cases except for run D44 made in the stainless steel 304 reactor. In that run, the ethylene yields were very low but production of CO, CO₂, and net coke were much higher. Ethylene yields were highest in the run made in the Vycor glass reactor. In this run, coke formation was least of all runs, and no CO or CO₂ was detected in the product stream.

For all metal reactors, the yields of ethylene and total coke were often found to vary significantly with the past history or pretreatment of the reactor. Pretreatments used were with either oxygen, steam, or hydrogen sulfide. Total coke is defined here as the sum of the CO, CO₂, and net coke; it is postulated that CO and CO₂ were formed by oxidation of part of the coke which formed and that net coke is the amount of coke left on the reactor walls at the end of the run. The results for runs M01 and D44 are one example of the large differences in yields that can be obtained in reactors of the same material of construction (*see* Table I). Run M01 was made after a stainless steel 304 reactor had been treated with hydrogen sulfide. Hydrogen sulfide results in the formation of metal sulfides (8) and acts in most cases to passivate the surface so that coke formation is minimized. D44 was made using a new stainless steel 304 reactor, whose surface became very active when it was treated with steam.

For a given ethane conversion, it was found that a plot of the total coke yield vs. ethylene yield resulted in a straight line and that the sum of ethylene and total coke yields was identical for a given ethane conversion, within experimental accuracy. Figure 1 shows a plot of these two yields at an ethane conversion of 65%; in this case, the sum of the yields was about 93%. At lower conversions the sum of yields was higher, approaching 100% at zero conversion.

The finding that the sum of ethylene and total coke yields was a constant at a given ethane conversion is, in a sense, another way of expressing the postulate reported earlier by Dunkleman and Albright (7). They had postulated that coke produced during ethane pyrolysis is primarily from ethylene or its precursor. Figure 2 shows a plot of the sum of ethylene and total coke yields as a function of ethane conversion. For runs using steam as a diluent, the sum of yields vs. ethane conversion is higher than that in runs without steam.

Table I. Comparison of Operating Conditions

| | | |
|--|-----------|------------|
| Run number | — | D40 |
| Reference | (11) | (7) |
| Tube material | — | Vycor |
| Outlet temp. (°C) | 824–829 | 799 |
| Outlet pres. (atm) | 0.2–2.1 | 0.96 |
| Mol % steam | 23–52 | 53 |
| % Conversion | 59–63 | 59 |
| Yields (% carbon) | | |
| CH ₄ | 4.5–12.0 | 3.6 |
| C ₂ H ₂ | 0.5 | — |
| C ₂ H ₄ | 77.9–83.9 | 89.0 |
| C ₃ H ₆ } C ₃ H ₈ } | 2.3–7.2 | 1.3 0.2 |
| C ₄ | 1.0–2.0 | 2.0 |
| C ₅ + | 0.6–8.0 | — |
| { CO | — | — |
| { CO ₂ | — | — |
| { Net coke | — | 3.9 |
| Subtotal (= Total coke) | — | 3.9 |
| Total | — | 100.0 |

* Run D44 exhibited unusually high activity for carbon deposition and gasification.

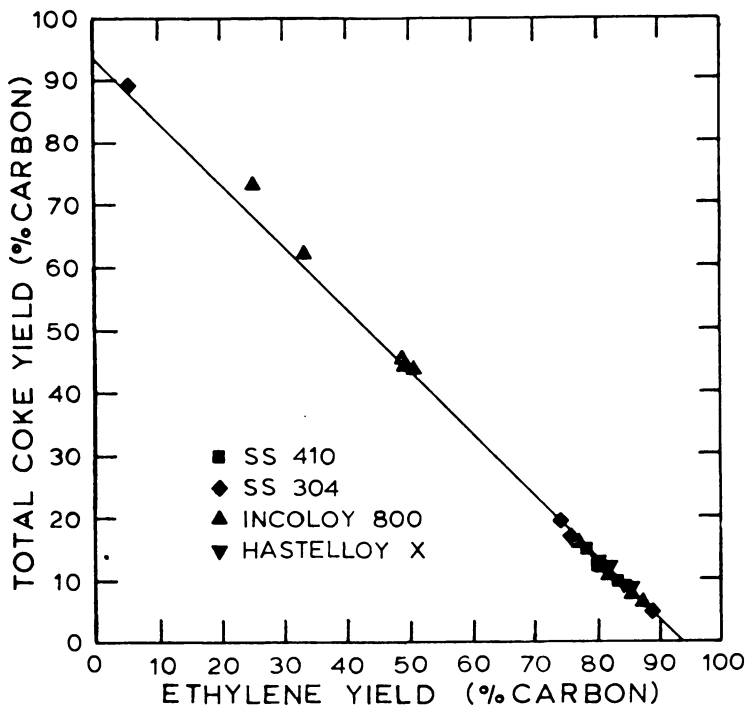
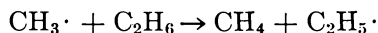
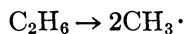


Figure 1. Total coke yield vs. ethylene yield at $65 \pm 2\%$ conversion. 800°C ; 1 atm; 50 mol % steam.

and Product Yields at 59–65% Conversion

| M04 This work SS410 799 | M01 This work SS304 800 | D30 (7) Incoloy 800 800 | M06 This work Hastelloy X 800 | D44 ^a (7) SS304 798 |
|----------------------------------|----------------------------------|----------------------------------|--|---|
| 0.98 | 0.98 | 0.98 | 0.98 | 0.99 |
| 50 | 51 | 52 | 51 | 47 |
| 63 | 59 | 65 | 65 | 65 |
| 4.0 | 4.8 | 5.4 | 4.3 | 5.0 |
| 81.3 | 79.1 | 79.6 | 80.2 | 6.0 |
| 1.6 | 1.1 | 1.5 | 1.2 | 0.2 |
| 0.2 | 0.1 | 0.1 | 0.1 | 0.1 |
| 1.6 | 1.2 | 1.3 | 1.8 | — |
| 1.3 | 1.1 | 2.3 | 2.1 | 60.3 |
| 0.2 | 0.1 | 0.6 | 0.1 | 0.7 |
| 9.8 | 12.5 | 9.2 | 10.2 | 27.7 |
| 11.3 | 13.7 | 12.1 | 12.4 | 88.7 |
| 100.0 | 100.0 | 100.0 | 100.0 | 100.0 |

Figure 2 also shows plots of methane yields vs. ethane conversion. Even though ethylene and coke yields often varied significantly, the methane yields were identical regardless of the reactor used or of its past history. Methane yields were lowered, however, when steam was added to the ethane feed. Dunkleman and Albright (7) also had made similar findings relative to methane yields in different reactors. This investigation, however, extends the finding to reactors constructed of additional materials of construction. The finding concerning methane yields is helpful relative to the reaction mechanism. Methane is generally considered to be formed primarily during the initiation steps in which ethyl radicals ($C_2H_5\cdot$) are formed by the following two reactions:



Based on the available results, the relative fraction of ethane that reacts by the above reactions is identical regardless of the reactor used. This conclusion is further supported by the findings of this investigation and also by those of Dunkleman and Albright (7) that the overall kinetics of ethane reactions are not affected by the material of construction or by the pretreatment of the reactor even though ethylene and total coke yields are. More discussion of the kinetics of pyrolysis will be reported later in this chapter.

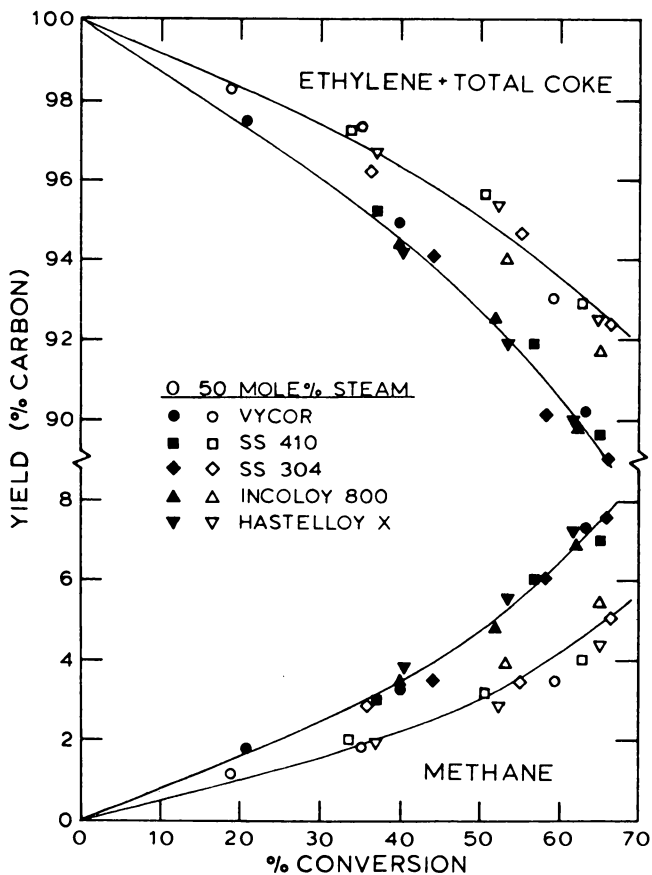


Figure 2. Ethylene + total coke yield and methane yield vs. conversion. 800°C; 1 atm.

The failure to find C_5 or C_6 hydrocarbons was somewhat surprising since significant amounts are found in commercial reactors (11). The much higher surface-to-volume ratios in the small laboratory reactor undoubtedly resulted in a greater importance of surface reactions compared with gas phase reactions. Possibly, C_5 and C_6 hydrocarbons were formed by gas phase reactions in the laboratory reactors but were destroyed by surface reactions either in the reactor tube or as the gases left the reactor and were cooled to moderate temperatures.

Equilibrium conversions were calculated for the following equation, which is reversible at 800°C: $C_2H_6 \rightleftharpoons C_2H_4 + H_2$. The equilibrium constant (K) for this equation is approximately 1.0 at 800°C:

$$K_{800} = \frac{\{C_2H_4\}\{H_2\}}{\{C_2H_6\}\{P\}} = 1.0$$

where the concentration of each component is expressed as the mole fraction and the pressure (P) is in atmospheres. At atmospheric pressure and 800°C , the equilibrium conversion of ethane is calculated as 78.1%. Production of coke and hydrogen from ethane is essentially irreversible and, hence, ethane conversions greater than 78.1% are possible when coke forms. Figure 3 shows the calculated equilibrium conversion curve, assuming variable coke formation vs. total ethane conversion.

The 45° line of Figure 3 would represent the conversions of ethane to ethylene, assuming 100% yields of ethylene. The line for predicted maximum yields of ethylene, however, lies slightly below the 45° line; this line was drawn with the assumption that no coke is formed; only methane, propylene, and other by-product hydrocarbons are produced. The slightly curved line was constructed by using the top curve of Figure 2. It is thought that the two curves drawn on Figure 3 define, with at least reasonable accuracy, the limits for ethane pyrolysis at 800°C , 50% steam in feed, and atmospheric pressure.

Data points for all runs of this investigation, including some up to four seconds residence time, all fell within the predicted limits, as shown in Figure 3. The results obtained when using the Vycor glass reactor were close to the zero coke line. With metal reactors, depending on the

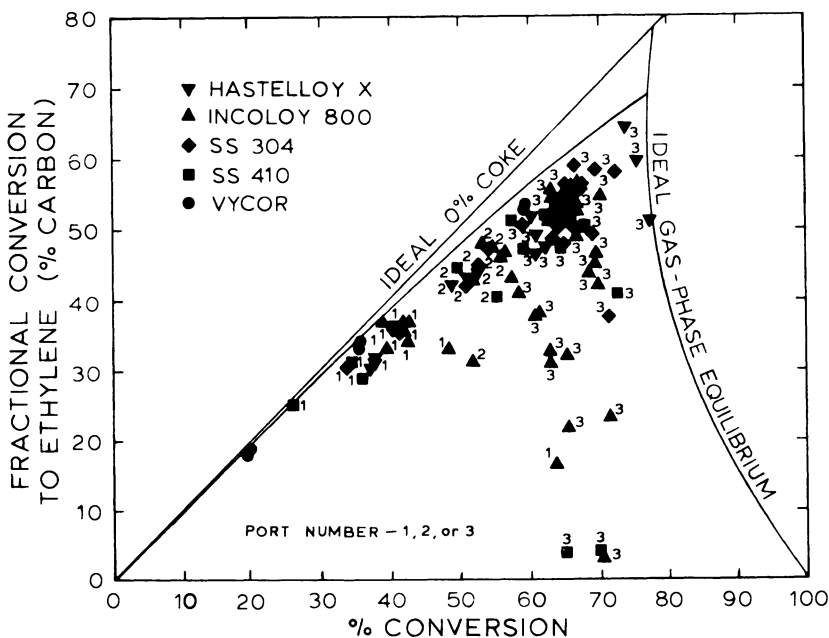


Figure 3. Fractional conversion to ethylene vs. conversion. 800°C ; 1 atm; 50 mol % steam.

past history of the reactor, there was sometimes a wide scatter in points; most points were near the zero coke line but others were rather far from it, indicating the formation of considerable amounts of coke.

Figures 4a and 4b for ethane pyrolyses with and without steam, respectively, indicate for runs at 800°C that equilibrium conversions were closely approached after about three seconds. Of interest, the kinetics at zero conversion could be predicted with good accuracy in the following manner. The change of the ethane concentration with time was expressed as a first-order kinetic expression (*see* Equation 1). The

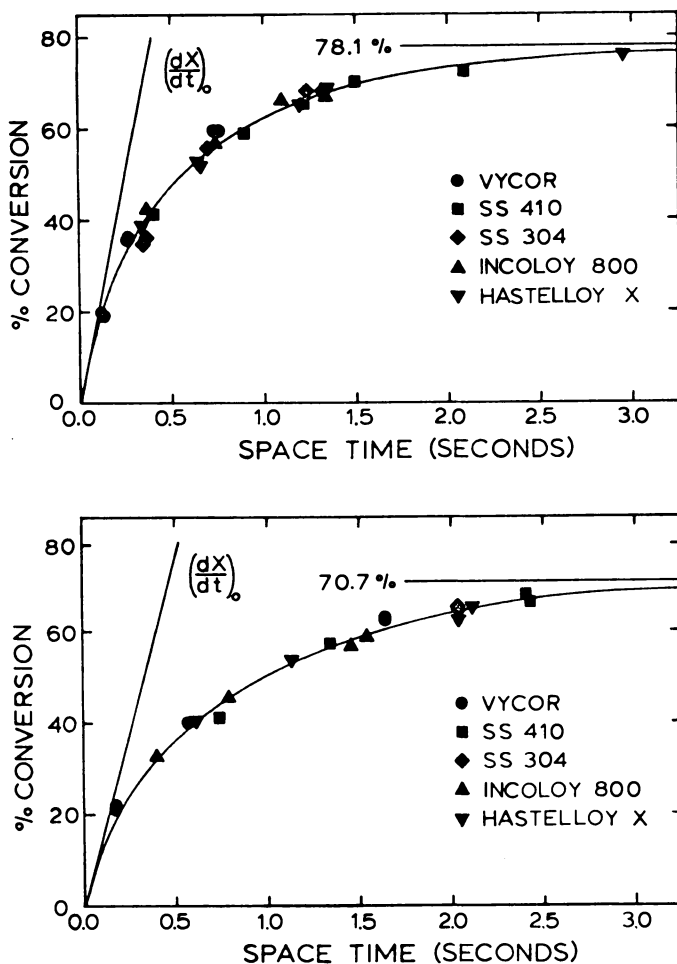


Figure 4. (a, top) Conversion with steam diluent vs. space time. 800°C; 1 atm; 50 mol % steam. (b, bottom) Conversion without steam diluent vs. space time. 800°C; 1 atm; 0 mol % steam.

ethane conversion (X) is expressed in terms of the ethane concentrations (Equation 2), where $(C_2H_6)_0$ is the concentration at zero time and where ϵ is the fractional change in the moles with conversion.

$$\frac{-d(C_2H_6)}{dt} = k(C_2H_6) \quad (1)$$

$$X = \frac{(C_2H_6)_0 - (C_2H_6)}{(C_2H_6)_0 + \epsilon(C_2H_6)} \quad (2)$$

$$\frac{dX}{dt} = \frac{(1 + \epsilon)(C_2H_6)_0}{\{(C_2H_6)_0 + \epsilon(C_2H_6)\}^2} \frac{d(C_2H_6)}{dt} \quad (3)$$

Substituting Equation 1 into Equation 3 and noting that at $t = 0$, $(C_2H_6) = (C_2H_6)_0$, Equation 4 is obtained. The rate constant (k) has

$$\frac{(dX)}{(dt)_0} = \frac{k}{1 + \epsilon} \quad (4)$$

reported to be about 3.0 sec^{-1} at 800°C (12). If the formation of by-products is low (such as normally occurs during the initial stages of pyrolysis), then the reaction is mainly the formation of ethylene and hydrogen. With 50 mol % steam dilution, the value of ϵ initially is 0.5 and $(dX/dt)_0 = 2.0 \text{ sec}^{-1}$. With dry ethane feed, ϵ initially is 1.0 and $(dX/dt)_0 = 1.5 \text{ sec}^{-1}$. The straight lines drawn from the origin are predicted values based on Equation 4. Clearly predicted and experimental rates of pyrolysis at zero conversions were in close agreement.

Coke forms to at least some extent along the entire length of the tubular reactor. The cumulative amount of total coke (or carbon) formed up to a sample port or to the end of the reactor was calculated by making material balances, as described earlier. The total amounts formed as a function of path area (directly proportional to the path area) are plotted for runs in four different reactors and for runs at several temperatures, as shown in Figure 5. For the preparation of Figure 5, considerable experimental data for runs exhibiting passive carbon deposition were used; these data were obtained during this investigation and investigations by Dunkleman (7, 13). The amounts of coke increased with temperature, and the rates of coke formation were determined by measuring the slopes of the curves shown in Figure 5. Table II reports the initial and final rates of coke formation in tubular reactors at temperatures from 750° to 850°C . Arrhenius-type plots of these rates yielded straight lines both with the same approximate activation energy, 65 ± 5

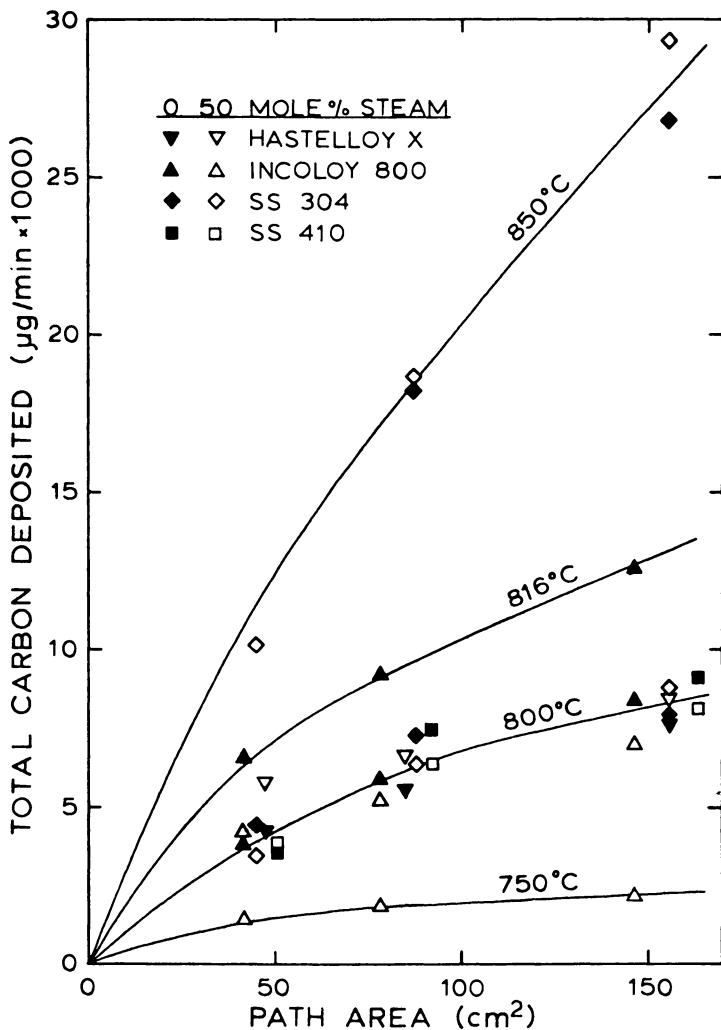


Figure 5. Total carbon deposition profile, 1 atm.

Table II. Total Carbon Deposition Kinetics

$$(r_{\text{dep}} = A \exp E_a/RT)$$

| Temperature (°C) | Initial Rate ($\mu\text{g}/\text{cm}^2/\text{min}$) | Final Rate ($\mu\text{g}/\text{cm}^2/\text{min}$) |
|--|--|--|
| 750 | 30 | 8 |
| 800 | 100 | 30 |
| 816 | 180 | 60 |
| 850 | 400 | 130 |
| E_a (kcal/mol) | 65 ± 5 | 65 ± 5 |
| A ($\mu\text{g}/\text{cm}^2/\text{min}$) | $10^{15.3}$ | $10^{14.8}$ |

kcal/g mol. Of interest, the overall activation energy for homogeneous ethane pyrolysis is also about 65 kcal/g mol (12). The types of coke formed, as will be discussed in more detail later in this chapter, were often quite different in the various reactors.

The finding based on Figure 5 and Table II that the rates of coke formation were higher in the front section of the tubular reactors compared with the end section was surprising. In the front section, there are fewer hydrocarbons such as olefins that are usually considered to be coke precursors. McConnell (14) has suggested that the main precursor for coke may be the ethyl radical. He based this postulate on the fact that the concentration of ethyl radicals is highest near the inlet of the reactor. Furthermore, the activation energy value of 65 kcal/g mol seems compatible with the postulate. An argument against the ethyl radical postulate is the failure to note significant differences in the rates of ethane disappearance for runs with widely differing rates of coke formation. The destruction of ethyl radicals might act to reduce the overall kinetics of the pyrolysis reactions since lower levels of radicals would likely occur. Furthermore, no increased production of methane was noted for runs in which coke production was high. Yet methane would presumably be produced during replenishment of ethyl radicals, assuming replenishment was by the technique reported earlier in this chapter.

It should be recognized that CO, CO₂, and solid coke are all included in the coke values reported in Figure 5. Some coke was probably formed in the gas phase and may have been transported appreciable distances in the tube before being deposited. A factor of possible importance concerns the levels of surface oxides on the inner reactor walls. Possibly, higher levels of surface oxides, which often promote coke deposition and gasification, occur at the inlet end of the tube. The reason for this may be that a higher concentration of steam and lower concentrations of hydrogen and olefins (which act to reduce the surface oxides) exist at the inlet end of the reactor.

Morphology of Coke Formed During Ethane Pyrolysis

The morphology of deposited coke was investigated with a scanning electron microscope. Several types of coke were identified, depending on the nature of surface. A summary of the findings, including metal incorporated in the coke, is presented in Table III.

The coke formed in the Vycor reactor had been produced in runs (13) conducted about one year prior to inspection. The detailed history of the reactor is reported in Table III. The inlet half of the reactor was clear, showing no signs of coke deposition. The outlet half was, however, covered with coke to make the reactor black and almost opaque. The exit end of the reactor outside the heated sand bath was covered with a

Table III. Summary

| | <i>Tube Material</i> | |
|-----------------------|----------------------------------|-----------------------------------|
| | <i>Vycor</i> | <i>SS 410</i> |
| Carbon Deposit | Figure 6 | Figure 7 |
| Gas side (surface A) | | Platelet |
| Tube side (surface B) | Globular | Platelet |
| Analysis | | Fe-Ni-Cr |
| Gas side (surface A) | — | 69-0-31 |
| Tube side (surface B) | Si | 97-0-3 |
| Tube wall (surface C) | — | 79-0-21 |
| Bulk (60) | Si | 87-0-13 |
| Sulfur | No | Yes |
| Tube History* | Ethane (-, +) 800°C, 167 min | Ethane (-, +) 800°C, 174 min |
| Time | Propane (-, +) 800°C, 115 min | Oxygen 800°C, 60 min |
| ↓ | Oxygen 750°C, 20 min | *Ethane (+, -) 800°C, 74 min |
| ↓ | Ethane (-) 750°C, 100 min | Oxygen 800°C, 15 min |
| ↓ | Oxygen 750°C, 20 min | Hydrogen Sulfide 800°C, 15 min |
| ↓ | Ethane (+) 570°C, 90 min | Ethane (-, +) 800°C, 130 min |
| ↓ | Propane (-, +) 750°C, 190 min | Ethane (+) 800°C, 275 min |

* (+) indicates pyrolysis with 50% steam diluent; (-) indicates pyrolysis without steam diluent; (*) indicates that high activity to carbon deposition and gasification occurred.

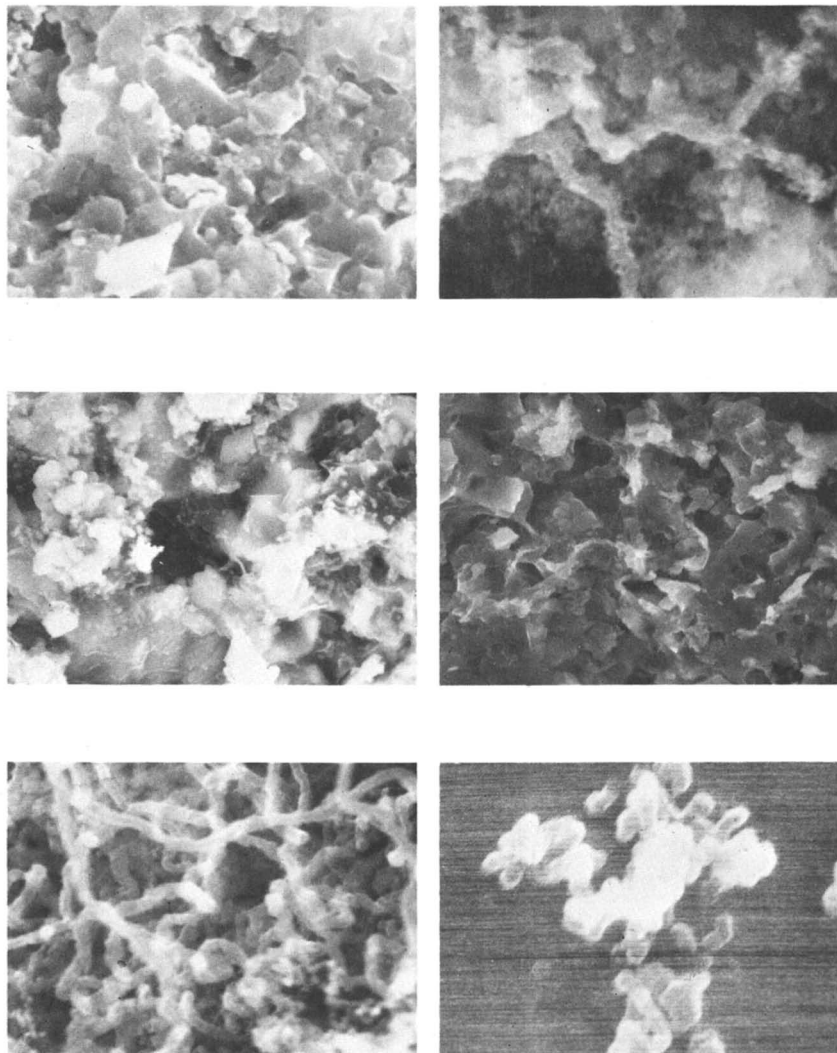
yellowish-brown material, probably condensation and polymerization products. A sample from the middle of the black section was examined under the electron microscope. The globular coke shown in Figure 6 was typical of the coke found, and the deposits were distributed sparsely on the surface. Larger agglomerates show signs of chain growth and are similar to the deposits observed by Johnson and Anderson (15). These investigators essentially proved that homogeneous polymerization in

of Experimental Findings

| <i>Tube Material</i> | | |
|--|--|--|
| <i>SS 304</i> | <i>Incoloy 800</i> | <i>Hastelloy X</i> |
| Figure 7 Filament Platelet | Figure 7 Polycrystalline Unidentified | Figure 6 Filament — |
| Fe–Ni–Cr — 66–3–31 71–5–24 71–10–19 Yes | Fe–Ni–Cr 43–35–22 40–42–18 32–58–10 46–33–21 No | Fe–Ni–Cr–Mo 28–32–21–19 — — 19–50–22–9 No |
| Ethane/Propane (–) 800°C, 131 min | *Ethane/Propane ~ 25 hr | Ethane (+) 800°C, 360 min |
| Hydrogen Sulfide 800°C, 15 min | Water/Air 25°C | Oxygen 800°C, 30 min |
| Ethane (–) 800°C, 56 min | *Ethane (–) 815°C, 22 min | Ethane (–) 800°C, 140 min |
| Ethane/Propane (+) 800°C, 206 min | Oxygen 815°C, 60 min | Ethane (+) 800°C, 145 min |
| Ethane (–, +) 850°C, 124 min | *Ethane (+) 815°C, 85 min | Ethane (–) 800°C, 285 min |
| Ethane (–, +) 900°C, 103 min | Oxygen 750°–800°C | } × 3 |
| Ethane (+) 800°C, 55 min | Hydrogen Sulfide 750°–800°C | |
| Hydrogen Sulfide 800°C, 65 min | Ethane (+, –) 750°–815°C | |
| Ethane (–, +) 800°C, 196 min | Oxygen 815°C, 110 min | |

acetylene pyrolyses was occurring, as they noted the evolution of small volatile droplets at 550°C to long dry chains at 1000°C. Presumably, a similar phenomena occurred here. EDAX analysis of this surface coke indicated only small amounts of silicon.

Metal reactors were inspected by breaking the tubes, which were often brittle from carburization. The ends were crimped longitudinally and often pieces of the deposited carbon layer broke loose. Normally,



1 μm = |——|

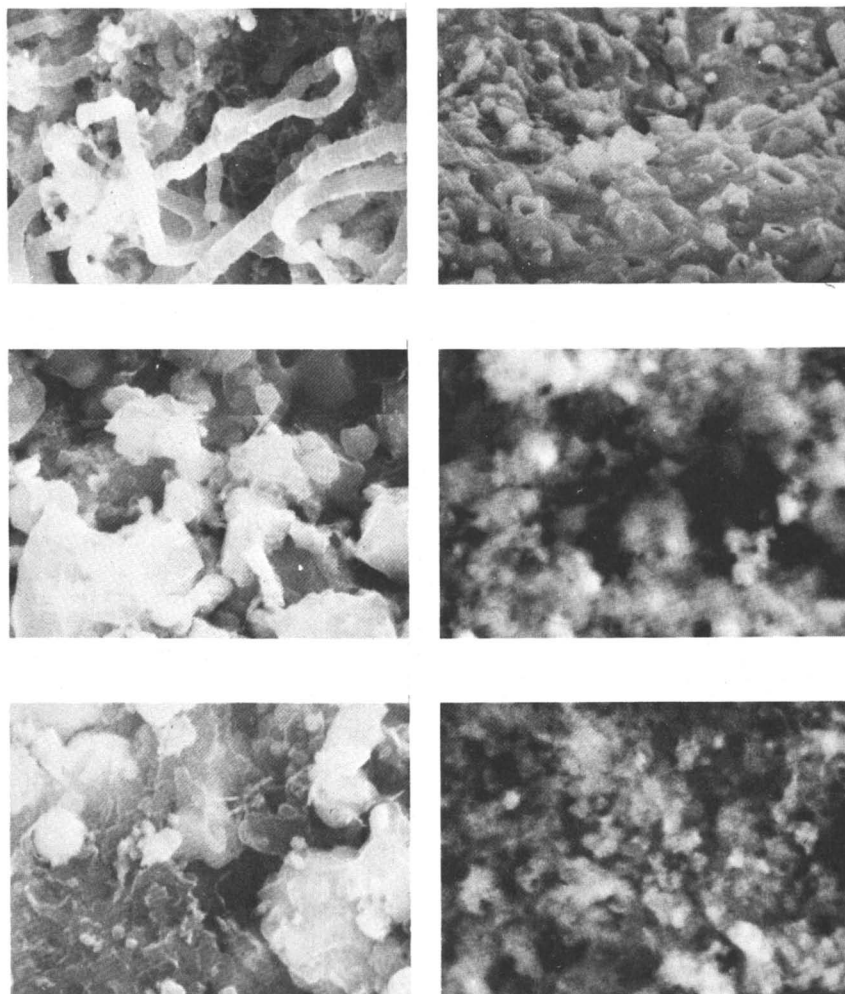
Figure 6. Surfaces formed on tubular reactors during pyrolysis of ethane at 800°C. (Top left) Stainless steel 410—Surface A, (predominant deposit); (top right) stainless steel 410—Surface A, (less frequent deposit); (middle left) stainless steel 410—Surface B; (middle right) stainless steel 410—Surface C; (bottom left) Hastelloy X—Surface A; (bottom right) coke on Vycor glass.

three surfaces were inspected: Surface A is the carbon layer which was exposed to the pyrolyzing gases, Surface B is the back side or tube side of this carbon layer, and Surface C was the exposed tube surface that had been next to the coke.

A reactor constructed of stainless steel 410 was used for pyrolysis since it contained no nickel. The coke layer formed during pyrolysis was usually thin and greyish. Less frequently, a piece of black coke was found on the surface. The metal surface (Surface C) was always grey. Figure 5 shows the two types of coke formed at Surface A in the stainless steel 410 reactor. The black (less frequent) coke appeared to be a floc of fine filaments, about $0.05\ \mu\text{m}$ in diameter, with occasional $0.4\text{-}\mu\text{m}$ filaments. The predominant deposit seems to be platelets of coke that include metal crystallite inclusions, the lighter area. The metal particles in the coke deposits, as detected by EDAX, were chromium rich compared with the bulk metal, as reported in Table III. Some sulfur also was present in the deposit; the sulfur was present, no doubt, because of the prior treatment of the surface with hydrogen sulfide. Surfaces B and C for the stainless steel 410 reactor are also shown in Figure 6. Surface B indicated porous coke platelets. Surface C was covered mostly with coke platelets, and cavities existed on the surface. Metal crystallites rich in iron apparently were pulled from the metal surface and were now rather firmly bound to Surface B. Surface C was richer in chromium than the bulk metal.

The coke deposit obtained in the Hastelloy X reactor was black, thin, and adherent to the metal wall. Hence only Surface A was inspected in the reactor. Rather large diameter (about $0.3\ \mu\text{m}$) filaments predominate, as shown in Figure 6. Some smaller diameter filaments also were observed. Table III indicates the analysis of the metal in the coke filaments. The signals generated were so low in magnitude that the results should only be considered as approximate. Apparently iron and molybdenum were being extracted preferentially by the coke.

Morphology of the coke formed in the stainless steel 304 reactor was quite different than that in the stainless steel 410 reactor. In the stainless steel 304 reactor, several pyrolysis runs, including ones at 850° and 900°C , had been made without burning out the coke. Furthermore, two treatments with hydrogen sulfide were made. The coke found on the stainless steel 304 surfaces was relatively thick compared with the reactors already discussed. Under an optical microscope the coke was black and granular. The coke was also magnetic. Surface A was found to be a profuse growth of filaments, including ones of approximately $0.4\ \mu\text{m}$ plus others of about $0.05\ \mu\text{m}$ in diameter, as shown in Figure 7. Baker et al. (3) earlier reported iron particles sometimes fragment into smaller particles that continue to produce small-diameter filaments. Numerous attempts were made with the EDAX analyzer to analyze the smallest observable specks



1 μm = |——|

Figure 7. Surfaces formed on tubular reactors during or after pyrolysis of ethane at 800°C. (Top left) stainless steel 304—Surface A; (top right) Incoloy 800—Surface A, (magnification 20% of other pictures); (middle left) stainless steel 304—Surface B; (middle right) Incoloy 800—Surface B; (bottom left) stainless steel 304—Surface C; (bottom right) Incoloy 800—Surface C.

in the filaments. The EDAX analyzer always indicated a small amount of metal but no localized concentrations could be found. Presumably the metal was highly dispersed throughout the filaments.

Both platelet coke and metal crystallites were detected at Surfaces B and C of the stainless steel 304 reactor, as shown in Figure 7. The disruption of the stainless steel 304 surfaces is more pronounced compared

with stainless steel 410 surfaces. The crystallites in the stainless steel 304 coke deposits were larger and their edges were more clearly defined, as shown in the photographs of Surface A. Tsai and Albright (8) also had found serious roughening and corrosion of stainless steel 304 surfaces. The platelet deposits on Surface C of the stainless steel 304 surfaces were found to be chromium rich compared with the bulk stainless steel 304 metal.

The Incoloy 800 reactor used for preparation of Surfaces A, B, and C (shown in Figure 7) had been subjected to severe pretreatments. The reactor was oxidized three times to burn out coke and also was treated three times with hydrogen sulfide. In spite of these treatments, low yields of ethylene and high yields of coke were generally obtained in the reactor. Eventually during a pyrolysis run, the reactor plugged at the bottom of a U-bend between the inlet of the reactor and the first sample port. After the pyrolysis run was terminated, the reactor was filled with water to measure the available gas volume in the tube and was then dried. The water possibly washed away or destroyed carbon filaments (if they had been present). Such a wash was found to destroy filaments in a stainless steel 304 reactor. The gas side (Surface A) of the plug material was massive and rough. Protuberent growths and holes were visible on the surface. Perhaps the deposit had been nearly molten at the reaction temperatures, and gas had forced its way to the surface, creating the holes. This hypothesis is consistent with the finding that partial plugs had formed at the bottom of other U-bends in the reactor. Nickel sulfides that were likely formed during hydrogen sulfide treatments melt at temperatures below 800°C.

Surfaces B and C for the Incoloy 800 reactor were quite different from the platelets and crystallites formed in the stainless steel 304 and 410 reactors. The metal concentrations for Surfaces A, B, and C varied rather erratically compared with the bulk metal (*see* Table III). Clearly, further investigations are needed to learn about coke deposits formed during ethane pyrolysis in Incoloy 800 reactors.

Coke Gasification

CO and CO₂ were always present in the product gas steam from pyrolysis whenever steam was used as diluent in the feedstream to metal reactors. Calculations indicated that, in general, approximately 1%–5% of the steam reacted with coke to form carbon oxides and hydrogen. These values are significantly higher than the values obtained in commercial reactors that have much smaller surface-to-volume ratios than do the tubes used in the present investigation. Based on the results of the present investigation there were, however, some cases in which the metal surfaces

were highly active, resulting in high ratios of steam reactivity. In some cases, 90% or more steam reacted. In contrast for runs in the Vycor reactor, no steam reacted and no carbon oxides were detected.

Decoking (or carbon gasification involving steam) is a heterogeneous reaction because the coke is a solid and the carbon oxide products are gaseous. Analogously, carbon deposition is also heterogeneous. Both reactions apparently exhibit similar dependencies based on the available surface area. Gasification also is, however, strongly influenced by the surface concentration of active sites occupied by oxygen. These sites may be surface carbon atoms dissolved in the metal atomic matrix. Ergun and Mentser (16) have suggested that when the number of active sites occupied by oxygen is constant, the rate of gasification is directly proportional to the available surface area. When the oxygen exchange reactions are in equilibrium, then this concentration of occupied sites will be at steady-state and the shift reaction will be at equilibrium.

$$K_{\text{shift}} = \frac{(\text{H}_2)(\text{CO}_2)}{(\text{H}_2\text{O})(\text{CO})}$$

At 800°C with excess carbon, K_{shift} is approximately 1.0. Invariably the oxygen exchange reactions never reached equilibrium. The apparent or pseudo values for K_{shift} were generally less than 0.2. Ergun and Menster found similar low values when steam conversion was low.

Pseudo values for K_{shift} , designated as K_{pseudo} , were found to be useful for characterization of coke gasification. In four runs, K_{pseudo} was relatively constant (± 0.01) during the entire run. Figure 8 shows for these runs the straight-line correlations between the gasification rates and coke deposition rates. In these runs, the ratios between the gasification and deposition rates (G:D) were between 0.08 and 0.18, depending on the reactor material. The ratios were highest for both Incoloy 800 and Hastelloy X reactors and lowest for the stainless steel 304 reactor. The ratio for the stainless steel 410 reactor was intermediate. Ideally G:D would be 1.0 so that there would be no net build-up of coke on the metal surface. When K_{pseudo} varied, as it often did, the G:D ratio was not constant; in such cases, the gasification and deposition rates varied independently.

G:D ratios greater than 1.0 sometimes occurred with Incoloy 800, and stainless steel 410 and 304 reactors. Initially, dry ethane was pyrolyzed in a new reactor and then wet ethane was used, resulting in high G:D ratios. In such cases, 90% or more steam reacted, but the deposition rate did not appear to change markedly. After a short period of time, the gasification rate dropped to produce G:D ratios less than 1.0. As this occurred, the deposition rates increased to large values.

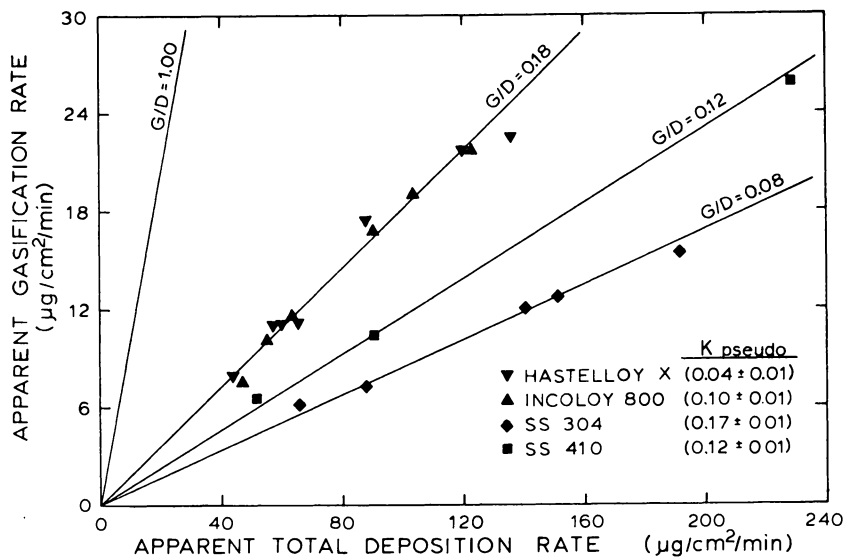


Figure 8. Gasification rate vs. deposition rate at surface steady state (K_{pseudo} constant). 800°C; 1 atm; 50 mol % steam.

Activated deposition and gasification never occurred after a reactor was treated with hydrogen sulfide. An Incoloy 800 reactor becomes highly active after being treated with hydrogen at 800°C for 24 hours and then being cleaned with water and air at room temperature. Plugging occurred in this reactor shortly after pyrolysis was started. The reactor was then cleaned of carbon by using oxygen. In the subsequent run where wet ethane feed was used, both the gasification and deposition rates increased rapidly to large values. Hydrogen sulfide treatment returned the activity of the reactors to normal. The surface concentrations of metal atoms, metal oxides, and metal sulfides appears to be of critical importance. Considerable more information certainly is needed to clarify the phenomenon of activated coke deposition and gasification.

Conclusions

The results of this investigation have indicated the importance of several variables relative to rates of coke deposition and of coke gasification. Both deposition and gasification depend, in some complex manner, on the surface composition. The present investigation indicates that important information can be obtained with the scanning electron microscope.

Literature Cited

1. Lobo, L. S.; Trimm, D. L. *J. Catal.* **1973**, *29*, 15.
2. Bernardo, C. A.; Lobo, L. S. *J. Catal.* **1975**, *37*, 267.
3. Baker, R. T. K.; Harris, P. S.; Thomas, R. B.; Waite, R. J. *J. Catal.* **1975**, *30*, 86.
4. Baker, R. T. K.; Waite, R. J. *J. Catal.* **1975**, *37*, 101.
5. Baker, R. T. K. *Chem. Eng. Prog.* **1977**, *73*(4), 97.
6. Herriott, G. E.; Eckert, R. E.; Albright, L. F. *AIChE J.* **1972**, *18*, 84.
7. Dunkleman, J. J.; Albright, L. F. "Industrial and Laboratory Pyrolyses," *ACS Symp. Ser.* **1976**, *32*, chap. 14.
8. Tsai, C. H.; Albright, L. F. "Industrial and Laboratory Pyrolyses," *ACS Symp. Ser.* **1976**, *32*, chap. 16.
9. Brown, S. M.; Albright, L. F. "Industrial and Laboratory Pyrolyses," *ACS Sym. Ser.* **1976**, *32*, chap. 17.
10. Albright, L. F.; McConnell, C. F.; Welther, K., Chapter 11 in this book.
11. Nelson, W. L. "Petroleum Refining Engineering," 4th ed.; McGraw-Hill: New York, 1958; p. 648.
12. Kramer, L.; Happel, J. "Chemistry of Petroleum Hydrocarbons"; Brooks, B. T., Kurtz, S. S., Boord, C. E., Schmerling, L., Eds.; Reinhold: New York, 1955; Vol. II.
13. Dunkleman, J. J. "Kinetics and Surface Effects of Pyrolyses of Ethane and Propane," Ph.D. dissertation, Purdue University, West Lafayette, IN, 1976.
14. McConnell, C. F. "Catalytic Carbon Deposition and Gasification during Ethane Pyrolysis," MS dissertation, Purdue University, West Lafayette, IN, 1976.
15. Johnson, G. C.; Anderson, R. C. *Proc. Conf. Carbon*, **5th**, **1962**, *1*, 395.
16. Ergun, S.; Menster, M. "Chemistry and Physics of Carbon," Walker, P. L. Jr., Ed.; Marcel Dekker: New York, 1965; Vol. I.

RECEIVED June 21, 1978.

Mild Hydrocarbonization of Western Coal

H. D. COCHRAN, JR. and J. M. HOLMES

Chemical Technology Division, Oak Ridge National Laboratory,
Oak Ridge, TN 37830

Experiments with mild hydrocarbonization of Wyodak western coal at ORNL have led to a proposed process for the production of oil, gas, and low-sulfur char with a very low overall consumption of hydrogen. The process yields: (a) high-Btu pipeline gas, (b) a light oil that requires only mild hydrotreating, and (c) a high-quality char that can fuel a pressurized, fluidized-bed combustor (PFBC) without adding limestone for SO_x control or using high-pressure solid feeders. Preliminary heat and mass balances have been prepared for a commercial-scale facility which includes a PFBC for power generation. An economic analysis of this facility indicates that the oil product can be marketed at a very attractive price by using current published estimates for the prices of the product pipeline gas and electricity. Further development and technical evaluation of this promising coal conversion process are recommended.

One way to reduce the overall costs of coal conversion is to reduce capital costs. This can be achieved by simplifying the process, using mild process conditions, and sharing part of the capital costs with a complementary facility such as a utility power plant. Experiments with Wyodak coal at ORNL have suggested such a process based on mild hydrocarbonization to produce oil, gas, and a low-sulfur char with a very low overall consumption of hydrogen. Preliminary economic evaluation of this process is highly encouraging. The experimental results will be presented, and a process flowsheet will be described. Product price estimates have been derived which are very attractive when compared with product prices from other coal conversion technologies.

Carbonization of coal at atmospheric pressure results in a net evolution of molecular hydrogen—up to 2–3 wt % [based on moisture- and ash-free (MAF) coal]. The use of elevated hydrogen pressure, on the other hand, results in a net consumption of hydrogen that increases substantially with increasing temperature and hydrogen partial pressure. Under milder, intermediate conditions it is possible to hydrocarbonize coal so the consumption of hydrogen is just offset by the small evolution of hydrogen; that is, mild hydrocarbonization with no net consumption of hydrogen. The elimination of hydrogen consumption permits the gasifier to be removed from the process flowsheet and, with it, the oxygen plant.

Experimental

A complete description of the experimental equipment, procedures, materials, run conditions, and results is available elsewhere (1); therefore, only minimal information on the experimental work is presented here.

The 10 lb/hr bench-scale hydrocarbonization facility at ORNL is shown in Figure 1; the equipment flowsheet is presented in Figure 2. With this apparatus, yield data have been generated for the mild hydrocarbonization of Wyodak subbituminous coal. Table I summarizes the proximate and ultimate analyses of this coal. When Wyodak coal is hydrocarbonized at 1040°F under a hydrogen pressure of 300 psi (315 psia total pressure), the yields obtained (expressed as wt % of MAF coal fed) were as follows: oil, 20; gas, 21; water, 13; and char, 46. Figure 3 shows the variation of oil yield with temperature at a hydrogen pressure of 300 psi; as observed, a gentle maximum occurs at about 1040°F. The steady-state, make gas composition under these conditions is presented in Table II.

The process to be described is based on four significant attributes of mild hydrocarbonization of western coal: (a) subbituminous coals are noncaking and do not agglomerate in the fluidized-bed hydrocarbonizer; (b) significant yields of oil and gas can be obtained with a very low overall consumption of hydrogen; (c) the residual solid char is a clean, efficient boiler fuel; and (d) the quality of the oil produced is such that only light hydrotreating is required. These attributes are illustrated in the next few figures.

Figure 4 is a plot of hydrogen consumption vs. hydrogen partial pressure with temperature as a parameter. The solid lines are taken from a correlation (2) of published data (3); the point shown is our recent experimental verification of the zero net hydrogen consumption at a temperature of about 550°C (1040°F) and a hydrogen pressure of 300 psi. Table III summarizes the proximate and ultimate analyses of the char produced during this mild hydrocarbonization process. Figure 5 shows the distillation curve (simulated by the ASTM chromatographic procedure) for the oil produced by mild hydrocarbonization of Wyodak coal. Note that, in contrast to many other coal-derived liquids, more than 90% of this oil can be distilled at 900°F. Other properties of the raw product are presented in Table IV.

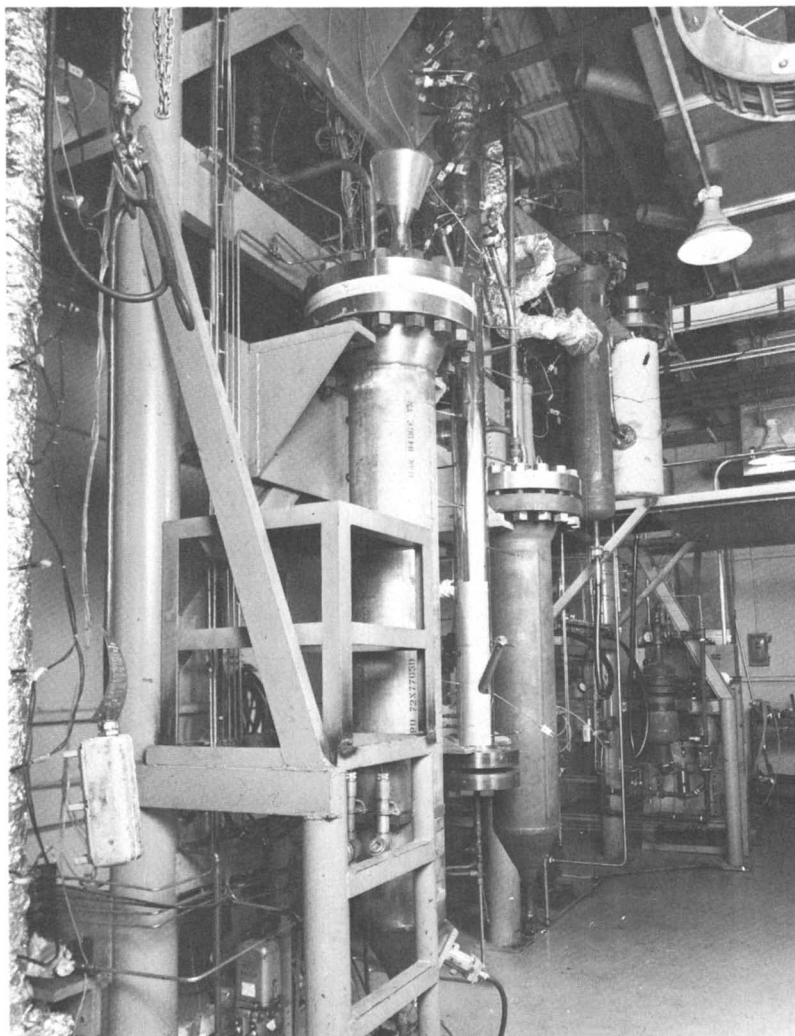


Figure 1. Hydrocarbonization apparatus

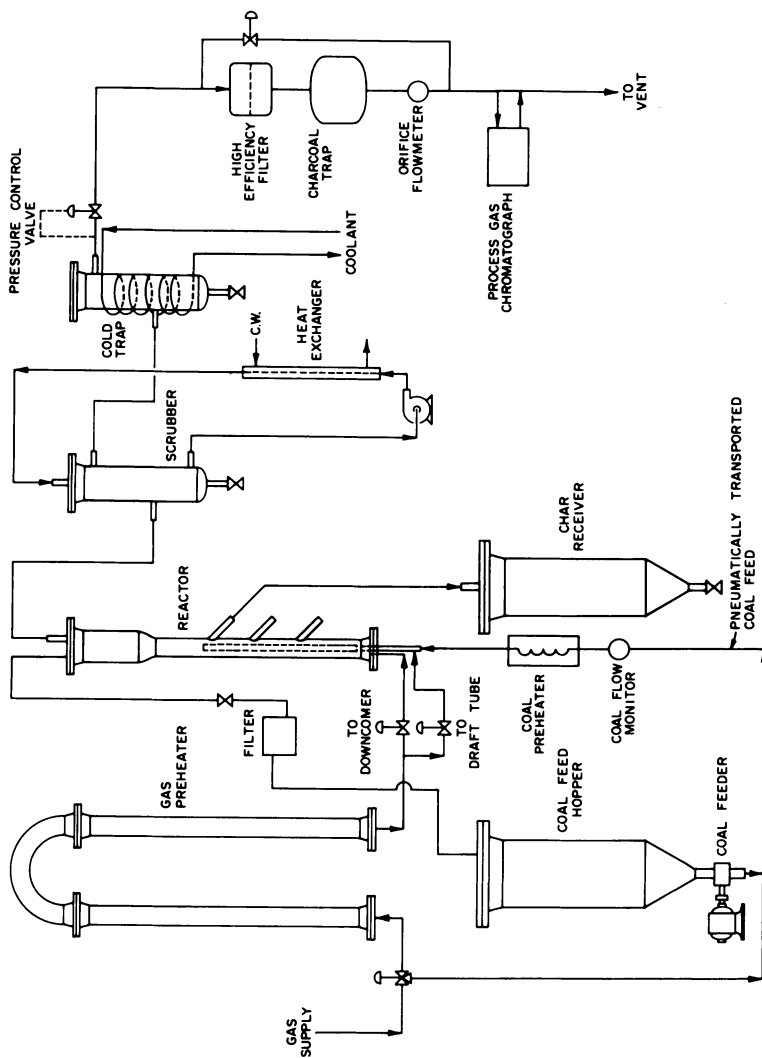
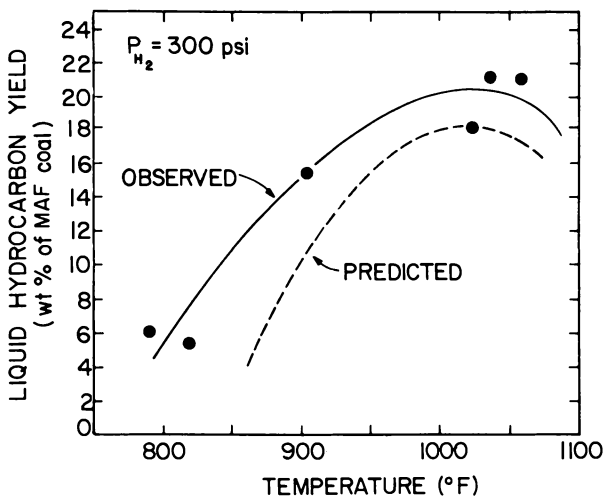


Figure 2. Bench-scale hydrocarbonization flowsheet

Table I. Proximate and Ultimate Analyses of Wyodak Coal (%)

| <i>Proximate Analysis</i> | |
|--------------------------------|---------------|
| Moisture | 30.9 |
| Ash | 5.0 |
| Volatile matter | 32.3 |
| Fixed carbon | 31.8 |
| <i>Ultimate Analysis (MAF)</i> | |
| Carbon | 72.40 |
| Hydrogen | 5.63 |
| Nitrogen | 1.04 |
| Sulfur | 0.85 |
| Oxygen | 20.08 |
| Calorific content: | 12,500 Btu/lb |

*Figure 3. Liquid hydrocarbon yield vs. temperature for hydrocarbonization of subbituminous C coals at a hydrogen pressure of 300 psi***Table II. Carbon Distribution in Make Gas from Wyodak Coal Hydrocarbonized at 300 psi and 1040°F**

| <i>Component</i> | <i>Concentration (vol %)</i> |
|---|------------------------------|
| CH ₄ | 51 |
| C ₂ H ₆ + C ₂ H ₄ | 13 |
| C ₃ H ₈ + C ₃ H ₆ | 4 |
| C ₄ ⁺ | nil |
| CO | 23 |
| CO ₂ | 9 |

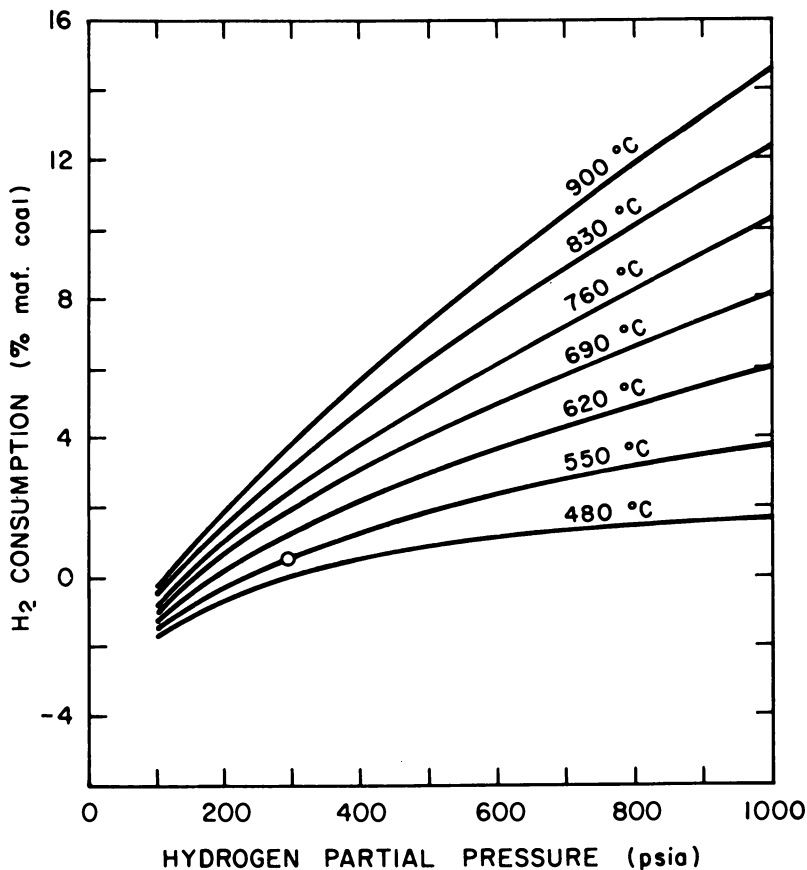


Figure 4. Hydrogen consumption during hydrocarbonization of sub-bituminous C coals

Table III. Proximate and Ultimate Analyses of Wyodak Hydrocarbonization Char (%)

| <i>Proximate Analysis</i> | |
|--------------------------------|---------------|
| Moisture | < 0.1 |
| Ash | 11.6 |
| Volatile matter | 10.6 |
| Fixed carbon | 77.8 |
| <i>Ultimate Analysis (MAF)</i> | |
| Carbon | 91.10 |
| Hydrogen | 3.75 |
| Nitrogen | 1.23 |
| Sulfur | 0.31 |
| Oxygen | 3.61 |
| Calorific content: | 15,100 Btu/lb |

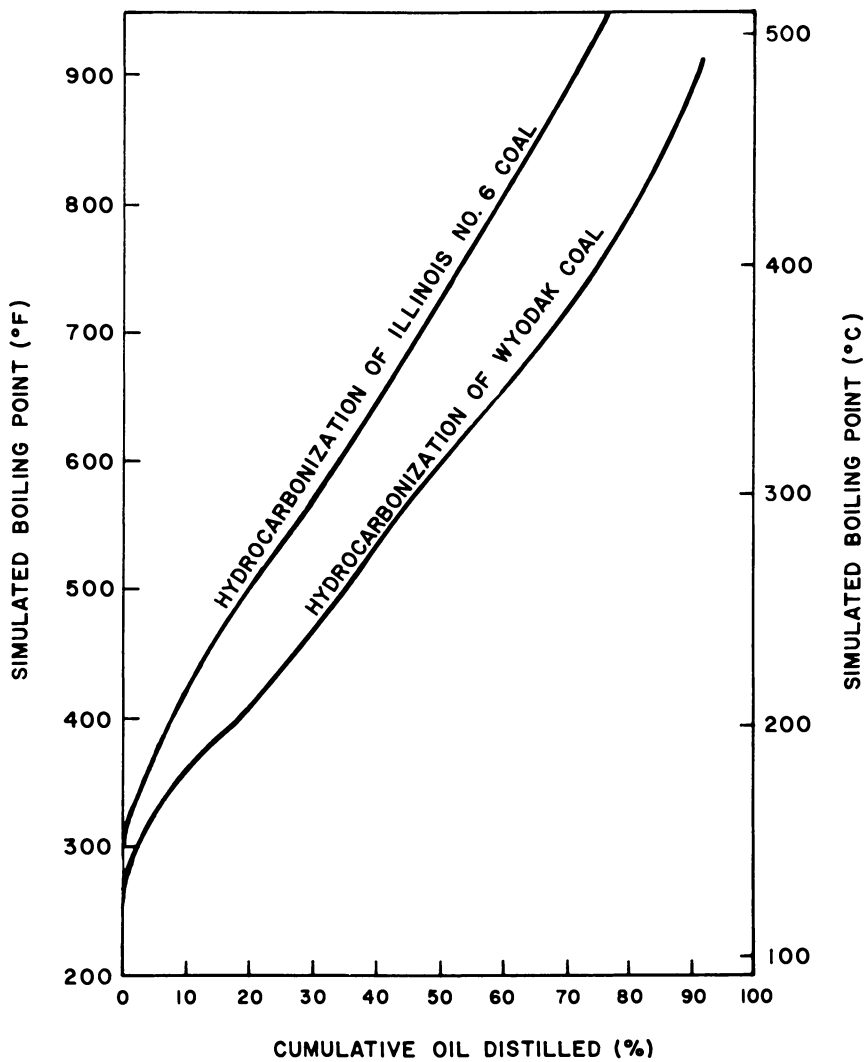


Figure 5. Distillation curve for raw oil product

Table IV. Properties of Raw Oil Product

(Specific gravity, 1,074)

Viscosity (cS)

| | |
|-------|------|
| 100°F | 18.4 |
| 210°F | 2.6 |

Composition (%)

| | |
|---------------------------------------|--------|
| Moisture ($\leq 105^\circ\text{C}$) | 0.68 |
| Ash | < 0.01 |
| Carbon | 84.76 |
| Hydrogen | 7.35 |
| Nitrogen | 1.02 |
| Sulfur | 0.28 |
| Oxygen (difference) | 5.9 |

Process Concept

These experimental results suggest several attractive applications for this mild hydrocarbonization process. For purposes of illustration, one such application (represented schematically in Figure 6) will be analyzed in some detail. Based on the attributes just discussed, this flowsheet has several notable features. The SNG (substitute natural gas) and LPG (liquefied natural gas) are direct products of hydrocarbonization that are separated cryogenically from the recycle gas; thus, no methanator is required. Because the net hydrogen consumption during mild hydrocarbonization is near zero, no char gasifier or oxygen plant is included. Mild hydrotreating of the product oil is all that is required to meet EPA standards, and the hydrogen needed for this operation can be obtained from the hydrocarbonizer make gas by shifting the carbon monoxide product and steam-reforming part of the LPG produced during hydrocarbonization, if necessary. Although the experimental results suggest that hydrogen consumption in the hydrocarbonizer is near zero, they are not sufficiently precise to provide an exact hydrogen balance. The hydrogen required for the hydrotreater was estimated to be about 3000 scf per barrel of oil feed to the unit. This is equivalent to less than 1 lb of hydrogen per 100 lb of MAF coal feed to the system.

Finally, the low-sulfur char is used as a clean boiler fuel for electric power generation. The hot char can be used directly, at pressure, with obvious advantages in thermal efficiency by using a pressurized, fluidized-bed combustion system (PFBC). The size consist of the char should ensure good performance when fluidized in the PFBC. Because the char has been partially desulfurized, the flue gas can easily meet a SO_2 emission specification of less than 0.8 lb per 10^6 Btu without the need to add limestone. This is in contrast to burning the Wyodak feed coal in a

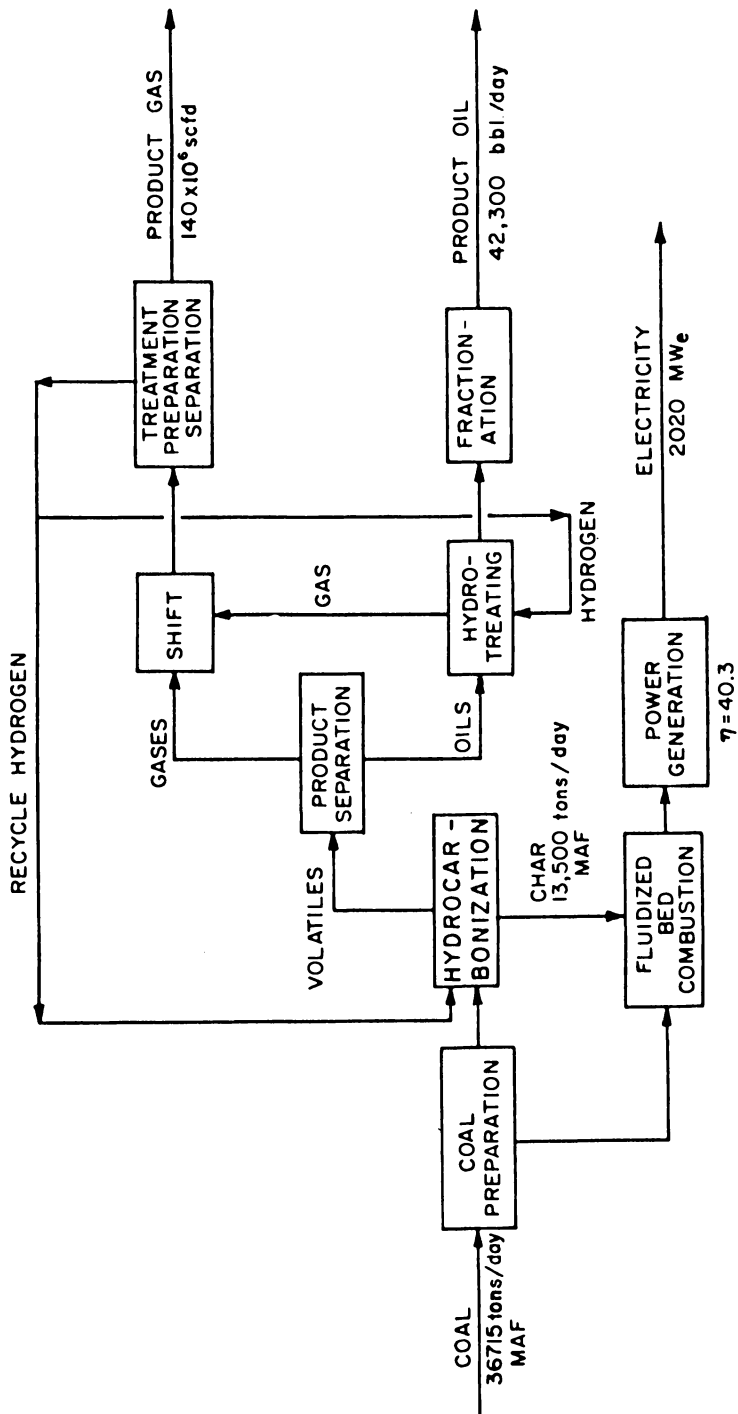


Figure 6. Flowsheet for commercial process concept

PFBC, which would require the addition of limestone in order to satisfy the current SO_2 emission requirement of no more than 1.2 lb per 10^6 Btu. Therefore, the capital cost of limestone handling and disposal would be avoided by using a char-fired PFBC. Of course, other attractive flowsheets are possible, based largely on alternatives for the use of the clean char product. Among several that we have considered are transporting the char (instead of coal) in a slurry pipeline; gasifying the char to produce a synthesis gas for Fischer-Tropsch or methanol synthesis; and gasifying the char for ammonia synthesis. In the balance of this chapter, we shall focus attention on the flowsheet in which the char is burned for power generation.

We have prepared preliminary heat and mass balances for a commercial-sized plant, with a feed rate of 36,715 tons of MAF coal per day, by using the flowsheet in Figure 6 and the experimental data presented here. The significant conclusions from these rough balances are as follows: (a) process heat requirements can be satisfied by the combustion of not more than 21% of the char produced; (b) the remaining char can be used to produce a net power output of 2020 MW (electric); (c) hydrogen for hydrotreating [estimated from COED (4) hydrotreating data] can be supplied from the make gas, largely through shift reaction of the carbon monoxide product; (d) the net gas product will exceed 140×10^6 scf per day; and (e) the net oil product will be more than 42,000 bbl per day of 27° API oil with nitrogen and sulfur contents of less than 0.2% and 0.01%, respectively.

Some uncertainty does remain regarding the hydrotreating step; however, recent hydrotreating tests performed at Oklahoma State University (5) on hydrocarbonization oils produced from Illinois No. 6 coal have shown that our estimates are quite conservative. Application of these results to Wyodak coal is probably conservative because the liquids produced during this investigation have been shown to be considerably lighter than those obtained from Illinois No. 6 bituminous coal (see Figure 6) under similar processing conditions.

Preliminary Economic Analysis

Information from the heat and mass balances allowed us to generate preliminary capital cost estimates (mid-1977 dollars) for the conceptual commercial plant by using the Dravo (6) analysis of the Coalcon hydrocarbonization plant. As noted above, significant capital savings are realized by the elimination of the gasifier, the oxygen plant, and the methanator. The cost for the hydrotreater was added, based on the scaled cost of the hydrotreater from a detailed engineering evaluation of a hydrocarbonization process published recently by ORNL (7). The

capital cost for the hydrocarbonization plant was then determined by appropriate scaling from Dravo's detailed equipment list. This cost amounts to approximately \$830 million, including working capital. The capital cost of the PFBC system and power-generating equipment was determined by eliminating the coal preparation and limestone-handling equipment and then scaling appropriately from the Energy Conversion Applications Study (ECAS) (8). The PFBC cost amounts to approximately \$867 million, including working capital. Details of the capital cost for the individual processing areas within the plant are presented in Table V. The total capital cost (excluding interest during construction) is about \$1697 million. Interest during construction is included as an integral part of the discounted cash-flow analysis performed on the system. Annual operating costs, exclusive of coal cost, for hydrocarbonization and for the power plant were estimated to be \$55.8 million and \$28.0 million, respectively.

A discounted cash-flow analysis of the system was made using conservative financing assumptions. These included 100% equity, 12% return on investment, and a plant life of 20 years plus a construction time of five years. Strip-mined western coal was priced conservatively at \$15 per ton. This is a reasonable price, for example, for coal delivered from Gillette, Wyoming by unit train to a plant serving the Chicago area (mid-1977 prices); alternatively, a mine-mouth plant site would obtain coal at lower prices, but product transportation costs would be higher.

Table V. Capital Cost of Hydrocarbonization-Pressurized, Fluid-Bed Combustion Plant (1977 Dollars)

| <i>Area</i> | <i>Capital Cost (\$ million)</i> |
|---|--------------------------------------|
| Coal handling and preparation | 72 |
| Hydrocarbonization, fractionation, and gas purification | 245 |
| Hydrotreating | 62 |
| Hydrogen plant | 35 |
| Sulfur recovery plant | 15 |
| Utilities | 210 |
| Hydrocarbonization power plant | 43 |
| Pressurized fluid-bed power plant | 788 |
| Offsites, storage, and buildings | 55 |
| total fixed capital: | 1525 |
| working capital: | 172 |
| total capital investment: | 1697 |

Conclusions

Although this economic analysis is preliminary and only approximate, we believe that it is conservative and quite realistic. The market price for each of the three main products from this process is sensitive to the prices set for the other two. Figure 7 shows the sensitivity of the oil price to SNG and power prices (in mid-1977 dollars). For example, we might first set the SNG price at $\$3.88/10^6$ Btu, which was the price determined by C. F. Braun (9) for SNG from the Hygas process under equivalent financing assumptions and the lowest among the six processes they evaluated. (This price is essentially unchanged when capital costs are escalated and coal costs are adjusted.) We believe that this price is very competitive for SNG from coal gasification and, indeed, would be competitive with imported LNG. We might then set the price of power

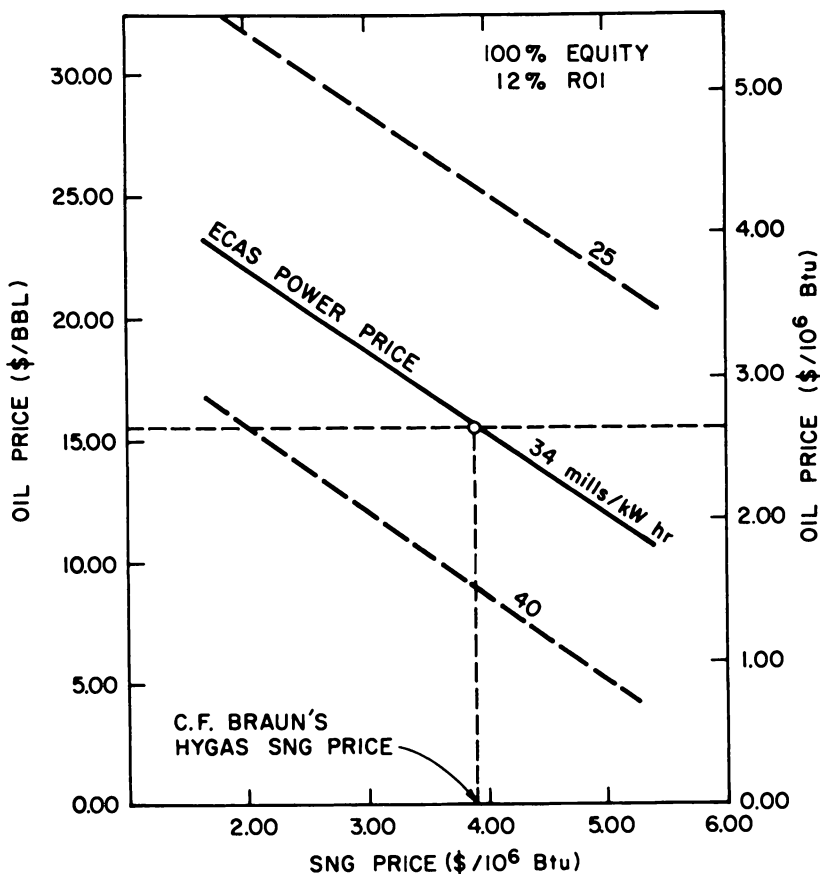


Figure 7. Oil price sensitivity to SNG and power prices

at 34 mils/kW hr. This is within the range determined by the General Electric Company in the ECAS study (8) for the new coal-fired power plants—either conventional pulverized-coal plants with scrubbers or PFBC plants. With these two product prices set on a reasonable basis, the resulting oil price is \$15.50/bbl. This is an attractive price, considering the conservative financing assumptions used. Of course, other price structures can be set.

At present, this conceptual coal conversion process is limited in its application to western coals because of their noncaking character and lower sulfur content compared with eastern bituminous coals. It is of interest to note, however, that certain chemical pretreatment processes (10, 11) have been shown to eliminate the caking tendency of the coal and reduce its sulfur content. Recent experiments at ORNL (12) have confirmed the suitability of several chemically treated coals to mild hydrocarbonization. In fact, there is evidence to suggest that some of these pretreated coals are actually more reactive under hydrocarbonization conditions than untreated coal, thereby enhancing the yield of oil or gas.

We conclude from this preliminary study that processes based on the mild hydrocarbonization of western coal appear to be technically and economically feasible, and we have proposed to DOE that a more thorough evaluation of the process concept be undertaken. Although we recognize the institutional problems that might be associated with a process producing power, gas, and oil for sale, we believe they are minor compared with the problems associated with other processes that appear to be less likely to yield profits attractive to industry.

Literature Cited

1. Cochran, H. D.; Youngblood, E. L. "Hydrocarbonization Research: Completion Report," *Oak Ridge Natl. Lab. U.S. ORNL-TM-6693*, in preparation.
2. Holmes, J. M.; Cochran, H. D.; Edwards, M. S.; Joy, D. S.; Lantz, P. M. "Evaluation of Coal Carbonization Processes," In "Coal Processing Technology"; *AICHE*: New York, 1977; Vol. 3.
3. Albright, C. W.; Davis, H. G. "A Process for Dry Hydrogenation of Low Rank Coals with High Yields of Phenolics," *Am. Chem. Soc., Div. Fuel Chem., Prepr.* 1970, *14*(4), 99–114.
4. Jones, J. F.; Schoemann, F. H.; Hamshar, J. A.; Eddinger, R. T., "Char Oil Energy Development, R&D Report No. 56—Final Report"; prepared for the Office of Coal Research, Department of the Interior, 1971.
5. Crynes, B. L. "Catalysts for Upgrading Coal-Derived Liquids," FE-2011-10, Quarterly Report for Period Sept. 9–Dec. 8, 1977, School of Chemical Engineering, Oklahoma State University, Stillwater, OK.
6. "Conceptual Commercial Design and Commercial Feasibility Analysis for Clean Boiler Fuel Facility," Dravo Corporation, ERDA/FE-1772-13, 1978, Vols. I and III.

7. Holmes, J. M.; Dyslin, D. A.; Edwards, M. S.; Joy, D. S.; Peterson, G. R.; Smith, C. B.; Lantz, P. M. "Hydrocarbonization Process Evaluation Report," *Oak Ridge Natl. Lab. U.S. ORNL-5212 and -5213* 1977, I and II.
8. "Study of Advanced Energy Conversion Techniques for Utility Applications Using Coal or Coal Derived Fuels," General Electric Company, NAS-19406, 1976.
9. Detman, R. "Preliminary Economic Comparison of Six Processes for Pipeline Gas from Coal," *Proc. Synth. Pipeline Gas Symp., 8th* 1976, 515-527.
10. Stambaugh, E. P.; Miller, J. F.; Tam, S. S.; Chauhan, S. P.; Feldmann, H. F.; Nack, H. E.; Oxley, J. H. "Environmentally Acceptable Solid Fuels by the Battelle Hydrothermal Process," *Pap. Symp. Coal Util. 2nd* 1975, 250-255.
11. Van Nice, L. J.; Santy, M. J.; Kousoukos, E. P.; Orsini, R. A.; Meyers, R. A., "Coal Desulfurization Test Plant Status," presented at the Fourth Annual International Conference on Coal, Pittsburgh, PA, August 1977.
12. Cochran, H. D., Jr. "Coal Conversion Process Development," In "Coal Technology Program Quarterly Progress Report for the Period Ending September 30, 1977," J. P. Nichols, Ed., *Oak Ridge Natl. Lab. U.S. ORNL-5357*, January 1978.

RECEIVED July 5, 1978. Research sponsored by the Fossil Energy Office, U.S. Department of Energy under contract W-7405-eng-26 with the Union Carbide Corporation.

A Comparison of the Rapid Pyrolysis of a Lignite and a Bituminous Coal

ERIC M. SUUBERG¹, WILLIAM A. PETERS, and JACK B. HOWARD

Department of Chemical Engineering and Energy Laboratory,
Massachusetts Institute of Technology, Cambridge, MA 02139

The rapid pyrolysis behavior of a Pittsburgh Seam bituminous coal has been compared with that of a Montana lignite for systematic variations in reaction temperature, heating rate, total pressure, and particle diameter. The dominant volatile products from the bituminous coal are hydrocarbons while those from the lignite are carbon oxides and pyrolytic water. The different species evolve from both coals in distinct but overlapping temperature intervals. Pressure and particle size exert little effect on product yields from the lignite but for the bituminous coal under rapid heating conditions and above 800°C, increases in either of these parameters decrease the yields of tar and hydrocarbon liquids and increase the yields of methane, hydrocarbon gases, and char. The data suggest direct correlations between certain products and chemical structures in coal.

Effective use of the vast coal reserves of the United States requires quantitative information on their conversion behavior in commercially important reactions. Studies using small-scale equipment and aimed at determining the effects of temperature, pressure, particle size, and heating rate on the rapid thermal decomposition of coal in atmospheres of both helium (pyrolysis) and hydrogen (hydrolypyrolysis) have been in

¹ Current address: Department of Chemical Engineering, Carnegie-Mellon University, Pittsburgh, PA 15213.

Table I. Characteristics

| | <i>Proximate Analysis</i> (wt %) (as-received) | | <i>Ultimate Analysis</i> (wt %) (as-received) |
|----------|---|--------------------------------|--|
| | <i>Lignite</i> ^a | <i>Bituminous</i> ^b | |
| Moisture | 6.8 | 1.4 | carbon |
| V.M. | 36.9 | 38.9 | hydrogen |
| F.C. | 46.4 | 48.4 | nitrogen |
| Ash | 9.9 | 11.3 | sulfur |
| | | | oxygen ^c |
| | | | moisture |
| | | | ash |
| Total | 100.0 | 100.0 | |

^a The Lignite is a partially dried Montana Lignite from the Savage Mine of the Knife River Coal Mining Company.

^b The Pittsburgh Seam (No. 8) Bituminous coal is from the Ireland Mine of the Consolidation Coal Company.

^c By difference.

progress in this laboratory for some time (1-8). This chapter summarizes recent findings on pyrolysis of a partially dried Montana lignite and a Pittsburgh No. 8 Seam bituminous coal. Proximate, ultimate, and petrographic analyses for each coal are given in Table I. Significant differences in product yields, compositions, and formation kinetics, and in the effects of reaction conditions have been found for both coals, with some of the variations appearing to be consistent with differences in chemical structures hypothesized for the starting materials.

Experimental

The experimental system has been described previously (1, 2, 7, 8) and is shown schematically in Figure 1. It consists of a 325-mesh stainless steel screen on which a thin layer of coal particles and a thermocouple are heated at rates of between 100° and 10,000°C/sec to temperatures as high as 1100°C, and held there for times up to 30 sec. The sample is contained within a pressure vacuum vessel of large volume such that the dispersion of evolving volatiles is great. Only the screen and sample are heated, and the volatiles are rapidly quenched as they mix with cold gas or condense on cold surfaces.

All products are collected at the conclusion of an experiment. Char remains on the screen while products that condense at room temperature (tars and oils, hereafter defined as tars) are collected primarily on foil liners within the reactor and on a paper filter at the exit of the reactor. Any condensate on nonlined reactor surfaces is collected by washing, using filter paper soaked in methylene chloride. Products in the vapor phase at room temperature are collected by purging the reactor vapors

of the Coals Examined

| <i>Ultimate Analysis (wt %) (as-received)</i> | | <i>Petrographic Analysis (wt %) (mineral-matter-free)</i> | | |
|---|-------------------|---|----------------|-------------------|
| <i>Lignite</i> | <i>Bituminous</i> | | <i>Lignite</i> | <i>Bituminous</i> |
| 59.3 | 67.8 | vitrinites | 69.7 | 84.5 |
| 3.8 | 4.8 | semifusinite | 15.2 | 4.5 |
| 0.9 | 1.3 | fusinite | 7.9 | 3.3 |
| 1.1 | 5.3 | micrinite | 5.2 | 4.4 |
| 18.2 | 8.1 | exinite + resinite | 2.0 | 3.3 |
| 6.8 | 1.4 | | | |
| 9.9 | 11.3 | | | |
| 100.0 | 100.0 | | 100.0 | 100.0 |

through two lipophilic traps containing 50/80 mesh Porapak Q chromatographic packing. The first trap is operated at room temperature and collects oils such as benzene, toluene, and xylene. The second trap is operated at -196°C and collects all fixed gases produced by pyrolysis with the exception of hydrogen, which is determined by direct vapor phase sampling with a precision syringe.

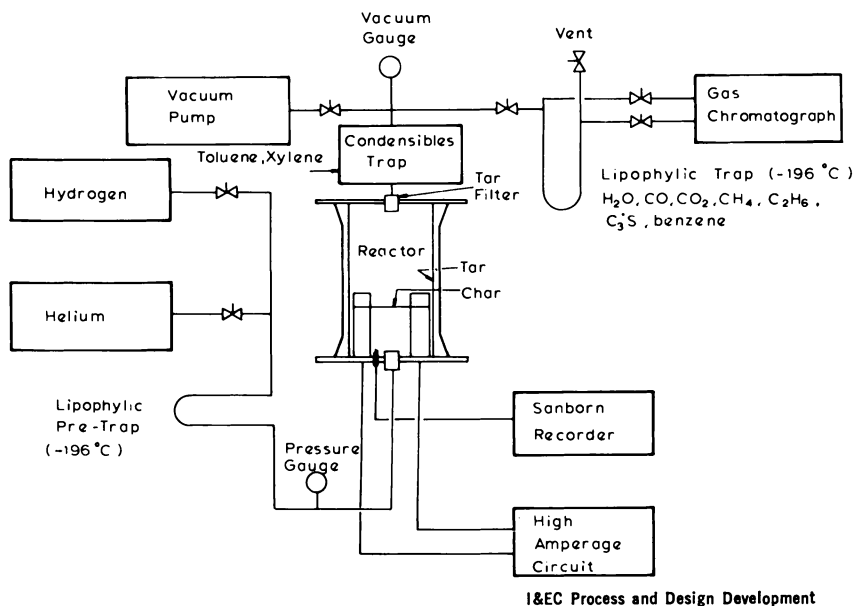


Figure 1. Captive sample apparatus and analysis system (8)

The gases and light liquids are analyzed by gas chromatography while the tar and char are determined gravimetrically and are characterized by elemental analysis. Total mass balances are typically excellent, with maximum deviations of no more than 5% from complete closure. Carbon balances are almost as good, showing maximum deviations of about 10%; hydrogen and oxygen balances are usually comparable, but in a few cases show higher deviations partly because of the uncertainty in the calculation of oxygen by difference in coal and char. The entire temperature-time history of the sample is measured with an error less than $\pm 8^\circ\text{C}$.

Base Case Data

The overall pyrolysis behavior of the bituminous coal and lignite under 1 atm helium is summarized in Figures 2 and 3. These data were obtained by heating 53 to 88- μm diameter particles at a nominal rate of $1000^\circ\text{C}/\text{sec}$ to the peak temperature indicated on the abscissa and then immediately permitting the sample to cool at a rate of about $200^\circ\text{C}/\text{sec}$. The ordinate of each data point represents the integral yield over the actual experimental time-temperature history. The data are plotted cumulatively up to the total weight loss of the sample, with the vertical separation between successive curves representing the contribution of the indicated products.

Tar Formation

Comparison of Figures 2 and 3 identifies a number of differences in the behavior of the lignite and the bituminous coal. The lignite, having a high oxygen content, produces large quantities of oxygenated volatiles while the bituminous coal volatiles are dominated by hydrocarbons, especially tar. The yield of tar from the bituminous coal in the temperature range $850^\circ\text{--}1000^\circ\text{C}$ under the conditions stated above or when the coal is held in this temperature range from 2-10 sec before quenching, approaches 23 wt % of the coal (as-received) or approximately four times the tar yield from the lignite under comparable conditions (~ 5 wt %).

The composition of the tars from the lignite and bituminous coal also differs as indicated by the respective empirical formulae $\text{CH}_{1.5}\text{O}_{0.1}\text{N}_{0.01}$ and $\text{CH}_{1.1}\text{O}_{0.08}\text{N}_{0.01}$. The H:C ratio of the lignite tar is higher even though this ratio for the starting materials (moisture-free basis) is somewhat lower for the lignite than for the bituminous coal (0.76 vs. 0.84). This finding is consistent with the much larger tar yields from the bituminous coal and the roughly comparable amounts of hydrogen available in the starting materials (Table I). Furthermore, the sequence in which this hydrogen is consumed differs for the two coals. Pyrolytic water

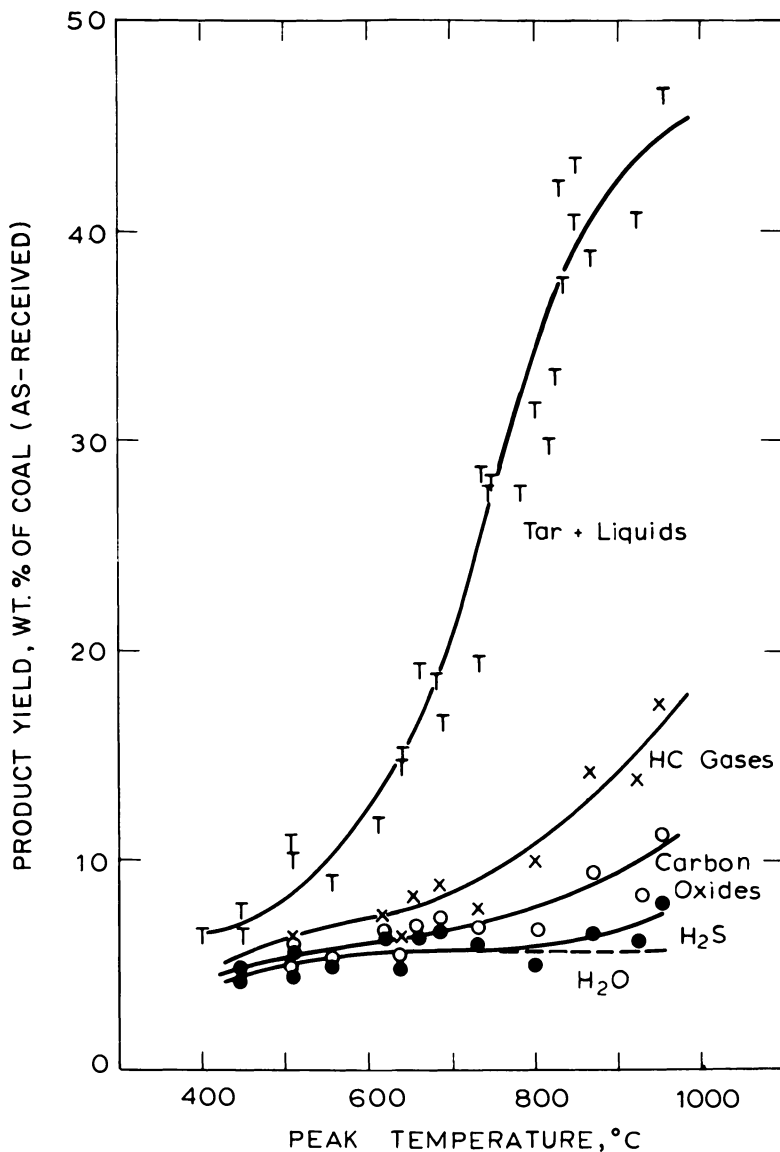
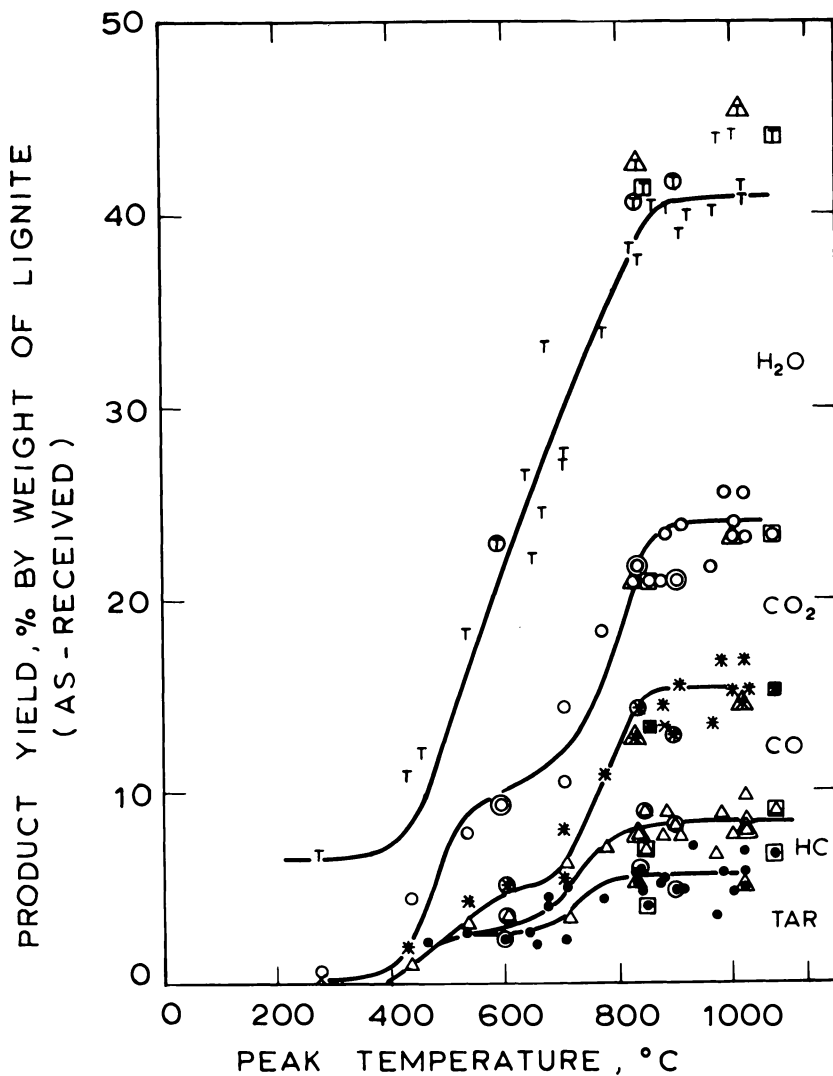


Figure 2. Pyrolysis product distributions from bituminous coal heated to different peak temperatures. (●) H_2O and H_2S ; (○) H_2O , H_2S , CO , and CO_2 ; (x) H_2O , H_2S , CO , CO_2 , and all hydrocarbon gases; (T) total weight loss, i.e., H_2O , H_2S , CO , CO_2 , all HC gases, tar, and liquids. Pressure = 1 atm (helium). Heating rate = $1000^\circ C/sec.$ (14)



I&EC Process and Design Development

Figure 3. Pyrolysis product distributions from lignite heated to different peak temperatures. (●) tar; (△) tar and other hydrocarbons (HC); (*) tar, HC, and CO; (○) tar, HC, CO, and CO₂; (T) total, i.e., tar, HC, CO, CO₂, and H₂O. Pressure = 1 atm (helium). Heating rate: (single points) 1000°C/sec; (points inside ○) 7100°C/sec; (points inside △) 270 to 470°C/sec; (points inside □) 1000°C/sec, but two-step heating; (curves) first-order model. (8)

formation from the bituminous coal under the stated reaction conditions occurs prior to tar production and accounts for 11% of the parent organic hydrogen whereas for the lignite an initial stage of tar evolution precedes pyrolytic water formation. Pyrolytic water is defined as the amount of water evolved beyond that amount attributable to moisture, as measured by the ASTM technique. The ASTM moisture is generally evolved at temperatures below those necessary for pyrolysis, even at these high heating rates. Thus, per unit mass of product there is more hydrogen available at the initiation of tar formation in the case of the lignite. Determination of molecular structures of these tars might suggest possible chemical mechanisms responsible for their formation.

Recent studies of the rapid pyrolysis of the same Montana lignite under vacuum over the temperature range 300°–1000°C (9) also found the resulting tar to be enriched in hydrogen (H:C ratio ≤ 1.2) compared with the starting material, but not to the extent observed here. Otherwise, the vacuum tar exhibited an elemental composition and IR and NMR spectra very similar to the lignite sample. In comparison with the vacuum results of Ref. 9, it is possible that the present 1-atm data reflect a greater influence of intraparticle secondary reactions that furnish hydrogen-enriched cracking products, including light and intermediate oils which would be counted here as tar. This explanation would be in line with selected vacuum pyrolysis experiments performed in the present study which showed tar yields for the lignite and bituminous coal to increase by about 28% and 39%, respectively, of their corresponding values at 1 atm (6, 7, 8). Further, tar from coal pyrolysis in a packed bed where secondary reactions would be enhanced has been found to contain a higher fraction of light oil than that resulting from rapid heating in a stirred bed where secondary cracking should be diminished (10).

Temperature Dependence of Volatiles Production

For both coals, thermal decomposition occurs in several overlapping phases, each of which is dominated by a single product or class of products. Four such regimes for the bituminous coal can be recognized from Figure 2: (i) low temperature ($\sim 100^\circ\text{C}$) removal of moisture; (ii) liberation of pyrolytic water at peak temperatures below 400°C; (iii) a broad phase occurring between 400° and 900°C, during which the coal softens and hydrocarbons are evolved; and (iv) a phase occurring above 900°C in which CO and H₂ are the principal products. Pyrolysis of the lignite occurs in five phases (Figure 3): (i) the low temperature removal of moisture; (ii) low temperature CO₂ and hydrocarbon evolution (about 450°–600°C); (iii) evolution of pyrolytic water (about 600°–700°C); (iv) evolution of hydrocarbons, hydrogen, and carbon oxides (700°–900°C);

and (v) the evolution of carbon oxides ($> 1000^{\circ}\text{C}$) (8). The above temperature intervals are observed with a heating rate of $1000^{\circ}\text{C}/\text{sec}$. For other heating rates, the limits as well as the widths of the temperature intervals decrease with decreasing heating rate in accordance with the increasing amount of time available for reaction during heat up (6, 11).

Most of these phases are much more distinct for the lignite, which exhibits almost a step-like behavior believed to reflect formation of individual volatiles by one, two, or possibly three specific primary decomposition reactions or reaction pathways. In fact, the volatiles product spectrum for the lignite pyrolysis is dominated by just three compounds (CO_2 , CO , and H_2O), allowing the essential features of the decomposition to be described quite well by a small number of product formation steps. Also, these compounds are relatively stable to further (secondary) reaction at the residence times and temperatures prevailing in this work. Thus these three products are far from water gas shift equilibrium (except at temperatures above 1000°C), and from equilibrium with solid carbon unless a total pressure of 1000 atm is postulated to occur inside the decomposing lignite particles (8).

In contrast, as noted above, tar dominates volatiles production from the bituminous coal. This material is undoubtedly a complex mixture of aliphatic and aromatic hydrocarbons varying in molecular weight from less than 200 to greater than 1200 g/mol (12, 13). Even if only one or two chemical reactions or reaction pathways led to the formation of each compound in this composite sample, the evolution of the overall tar product would reflect the occurrence of many reactions. Also, as discussed below, this bituminous coal tar undergoes significant secondary cracking reactions during its transport through or away from the coal particles. Thus, the measured tar yield is probably the result of a complex interaction among chemical and transport processes that include primary decomposition and secondary cracking reactions and coupled diffusive and convective flows within and away from the decomposing coal particles. A stepwise evolution of tar would seem unlikely under these circumstances, and indeed such behavior is not seen (*see* Figure 2). Results of our research on the simplification and modeling of tar evolution will be reported elsewhere (14, 15).

Influence of Chemical Structure on Pyrolysis Behavior

Examination of the data on CO_2 and pyrolytic water evolution may provide some insight into the thermal decomposition behavior of specific organic and inorganic structures in the parent coals. Some CO_2 may arise from the decomposition of inorganic matter within the coal. It also has been suggested (16) that decomposition of carboxyl groups in the

coal may lead to the CO₂ evolution, especially at lower temperatures. To assess the possible importance of these two sources in the present work, thermodynamic equilibrium and kinetic calculations using literature data were performed to determine the maximum amount of CO₂ that could be attributed to inorganic matter in the starting materials. For the thermodynamic computations, it was assumed that (a) all inorganic-matter CO₂ was produced by decomposition of calcium and magnesium carbonates, and (b) CaO and MgO determined previously (17) in ash from other samples of these two coals correspond on a molar basis to the quantities of the respective carbonates in the present coal samples. It is recognized that, in the case of subbituminous coals and lignites, some of the carbonates that ultimately decompose to yield CO₂ may themselves only be formed during lower temperature stages of pyrolysis from reactions involving ion-exchanged calcium or magnesium. The results show that up to 3.5 and 0.6 wt % (as received) of the lignite and bituminous coal, respectively, could be evolved as CO₂ by complete decomposition of these carbonates. Since the dissociation pressure of CO₂ over pure MgCO₃ and over pure CaCO₃ reaches 1 atm at 400° and 870°C, respectively, and since small quantities of coal (10 mg) were used in a rather large reactor volume (> ½ L), total decomposition of the pure carbonates or of carbonate minerals such as calcite and dolomite would indeed be expected if equilibrium were attained in the temperature regime studied.

The possible influence of chemical kinetic limitations on the attainment of these equilibria under the conditions of the present study was assessed by computing extents of conversion of pure MgCO₃ and CaCO₃ by using literature data. For estimation purposes, the kinetic parameters and model of Britton et al. (18) were extended to the nonisothermal conditions and wider temperature ranges of the present work. According to the results thus found for a heating rate of 1000°C/sec and a peak temperature of 1100°C, with no time spent at the peak temperature, less than 2% of the CaCO₃ and greater than 63% of the MgCO₃ should decompose. However, heating at 1000°C/sec to 1000°C and there holding for 10 sec gave predicted conversions of 9.1% for the CaCO₃ and total decomposition of the MgCO₃, corresponding to CO₂ yields of 1.3 and 0.13 wt % (as received) of the lignite and the bituminous coal, respectively.

The present lignite data revealed a high temperature stage of CO₂ evolution (Phase v) as described above, which occurs at peak temperatures above 1100°C or at around 1000°C for 5 to 10 seconds holding times. The maximum CO₂ yield from this phase was 1.1 wt %, in good agreement with the 1.3 wt % predicted above and lending support to our earlier suggestion that this stage of CO₂ formation could be associated with high temperature decomposition of mineral carbonates (7, 8).

Analysis of the kinetics of the high temperature stage of CO_2 evolution by fitting a single-reaction, first-order decomposition model to the present data gave an activation energy of 42.0 kcal/mol and a preexponential factor of $5.5 \times 10^6 \text{ sec}^{-1}$ (7, 8). The corresponding literature values used in the above calculation are $1.88 \times 10^4 \text{ sec}^{-1}$ and 40.0 kcal/mol for CaCO_3 and $2.56 \times 10^5 \text{ sec}^{-1}$ and 35.6 kcal/mol for MgCO_3 (18). Other workers (19) found values of $1.18 \times 10^4 \text{ g/cm}^2\text{-sec}$ and 40.6 kcal/mol for the respective parameters for the thermal decomposition of precipitated CaCO_3 pelletized into various shapes. The similarity of parameter values is intriguing although the bases of the literature values include fractional order (18) rather than first-order kinetic formalism and a topochemical kinetic analysis (19).

Blom et al. (20) presented a correlation between the amount of oxygen estimated to be present in coal as carboxyl groups and rank as defined by carbon content (daf). Figure 4 compares their correlation with the amount of oxygen evolved as CO_2 during pyrolysis of some 19 different coals of varying rank and represents results from this and from four other laboratories (7, 21–25). Final temperatures ranged from

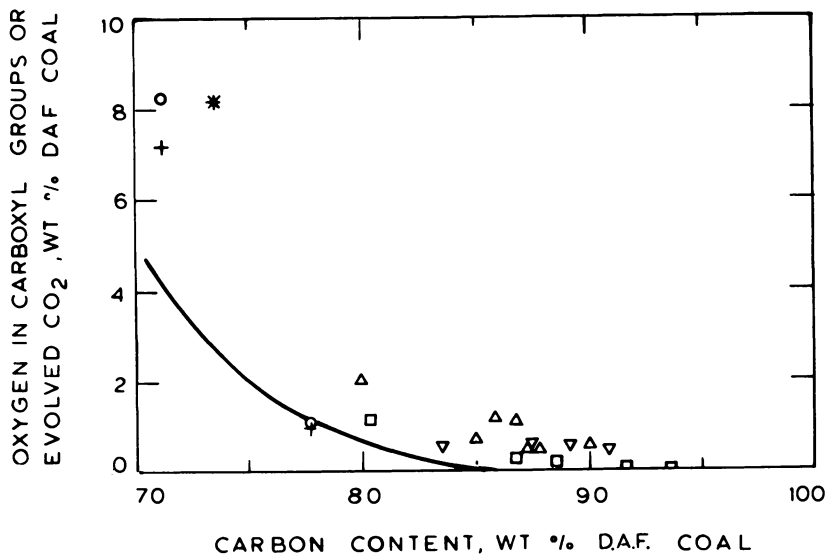


Figure 4. Comparison of pyrolysis yields of oxygen in carbon dioxide with estimated content of oxygen in carboxyl groups in raw coal. (—) Correlation of percent oxygen in carboxyl groups in coal, Blom et al. (20); (O) this study (7); (+) this study corrected for decomposition of carbonates; (*) Campbell and Stevens (21); (Δ) Loison and Chauvin (22); (□) Fitzgerald and Van Krevelen (23); (▽) Jüütgen and Van Heek (24) after Hanbaba et al. (25).

approximately 600° (24) to 1050°C (7, 22) and heating rates ranged from 4×10^{-5} (24, 25) to 1500°C/sec (22). The present data are represented by open circles that show oxygen yield based on the total CO₂ production up to 1100°C, including for the lignite the contribution of the high temperature step beginning at 1000°C, and crosses that incorporate the stated totals less the maximum kinetically allowed carbonate contributions calculated above. The correlation of pyrolytically formed CO₂ with the estimate of carboxyl group content is seen to be fair for the higher rank coals, including the present bituminous coal with or without the indicated correction, and no dependence on heating rate or final temperature is apparent. However, for the lower rank coals (including the present lignite), agreement based on total measured CO₂ evolution is not particularly good. The stated correction of the present lignite data for carbonate decomposition modestly improves the agreement. Similar corrections could not be made for the other coals of Figure 4 since mineral matter analyses were not reported. All of the data points except those for the present bituminous coal fall above the correlation. Assuming the carboxyl oxygen measurements to be accurate, this behavior implies that other sources such as additional organic functional groups, mineral matter, and secondary reactions (such as the water-gas shift) may contribute to CO₂ production during pyrolysis. A similar type of correlation of CO₂ data from the vacuum pyrolysis of 13 different coals at temperatures and heating rates similar to those of this work was reported recently (26).

These findings suggest that it may be possible to estimate lower bounds for the amount of CO₂ attainable from organic sources during pyrolysis, based on a knowledge of the carboxyl group content of the coal. Combination of this information with a determination of the carbonate content and appropriate thermodynamic equilibrium and kinetic calculations would allow estimates of the total amount of CO₂ evolution expected from pyrolysis.

Another possible correlation between coal structure and pyrolysis behavior is indicated by the temperature dependence of the evolution of pyrolytic water being strikingly different for the two coals. Figure 5 shows pyrolytic water evolution data for experiments in which the sample was heated at 1000°C/sec to the peak temperature indicated on the abscissa and then immediately allowed to cool at around 200°C/sec. The smooth curves are based on a single reaction, first-order decomposition model (7, 8) and on the stated temperature-time history. Parameters used for the lignite have been published (8) while for the bituminous coal the Arrhenius frequency factor and activation energy were taken as 10^{13} sec^{-1} and 35 kcal/mol, respectively, with the yield of pyrolytic water ultimately attainable estimated from experimental measurements as 4.6 wt % of the coal (as-received).

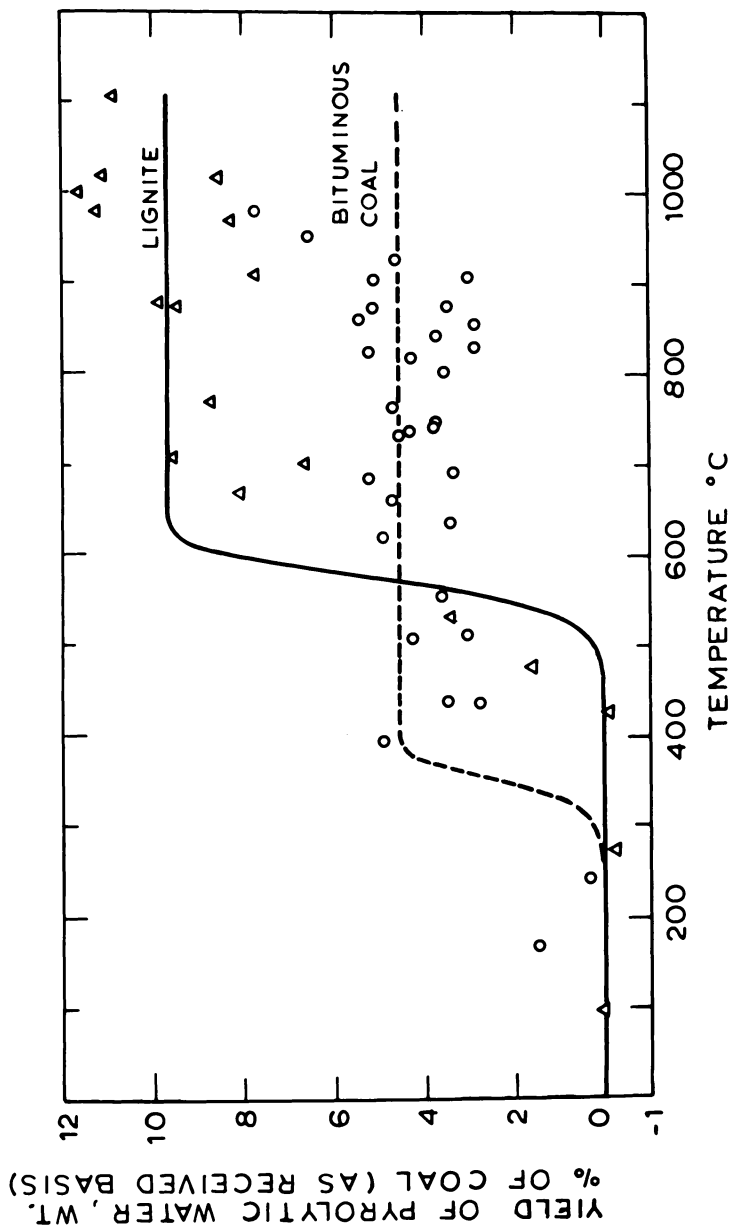


Figure 5. Evolution of chemical water during pyrolysis. (Curves) nonisothermal single reaction, first-order decomposition model; (—) parameters from Suuberg *et al.* (8); (---) parameters from text; (○) data points from this study (7); (Δ) lignite; (○) bituminous coal. Pressure = 1 atm (helium). Heating rate = 1000°C/sec.

For the bituminous coal, most of this water is formed at temperatures below 400°C before any other products are observed. For the lignite, neither pyrolytic water nor more than a small amount of hydrocarbons (Figure 3) (7, 8) is evolved until temperatures of around 600°–700°C are attained. This behavior supports the view, based on work with coal model substances (27), that water production from phenolic hydroxyl groups deprives the pyrolyzing coal of hydrogen which could otherwise stabilize hydrocarbon species (e.g., tar).

This mechanistic picture is further explored in Figure 6, where the amount of oxygen produced as pyrolytic water in several experiments covering the ranges of temperature and heating rate specified for Figure 4 (7, 22–25) is compared with a correlation (dashed line) of phenolic hydroxyl oxygen with coal rank originally presented by Given (28). (The comparison here of daf values with a correlation based on dmmf values is, of course, not strictly consistent, but data for conversion to the same basis

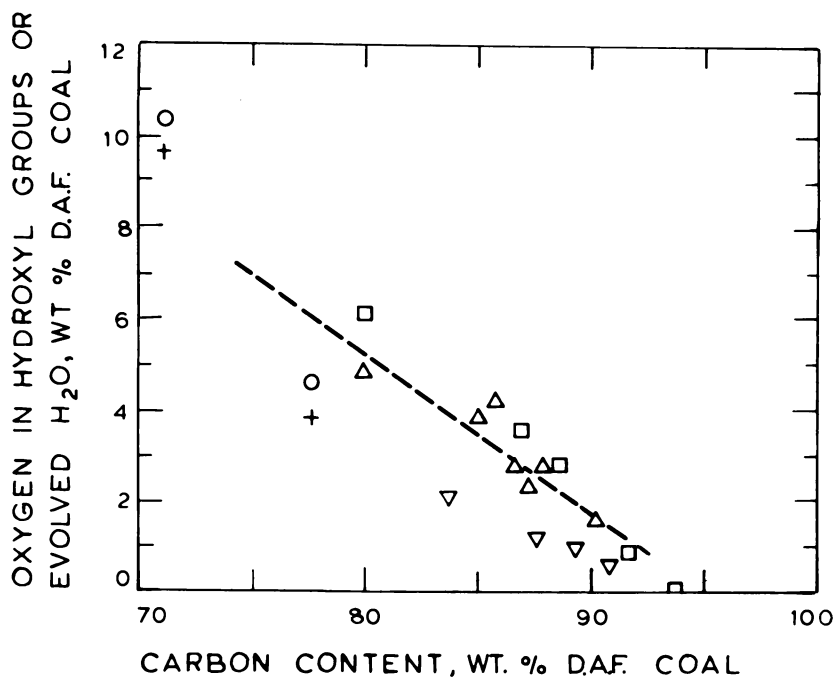
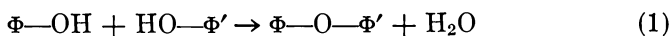


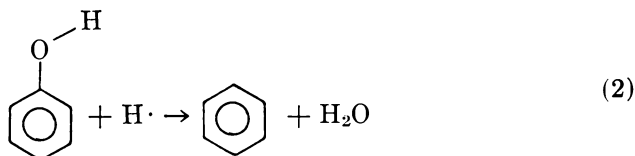
Figure 6. Comparison of yields of oxygen in pyrolytic water with estimated content of oxygen in phenolic hydroxyl groups in raw coal. (---) Correlation of percent oxygen in phenolic hydroxyl groups in coal, Given (28); (O) this study (7); (+) this study corrected for decomposition of kaolinite; (Δ) Loison and Chauwin (22); (□) Fitzgerald and Van Krevelen (23); (∇) Jüntgen and Van Heek (24) after Hanbaba et al. (25).

were not available.) The agreement appears to be fair and independent of heating rate and final temperature. No rigorous statistical comparison of the two sets of data was possible, again because of lack of necessary data, but the correlation for percent oxygen in phenolic hydroxyls was %O as OH = 33.2 - 0.35 (%C) while the yield of oxygen in pyrolytic water gave %O as H₂O = 37.8 - 0.41 (%C).

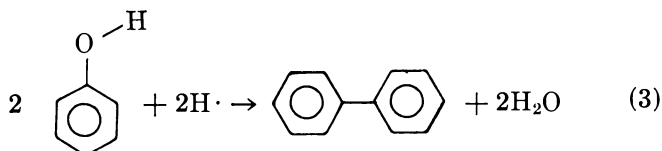
A similar comparison recently has been made using data on the vacuum pyrolysis of 13 different coals over ranges of temperature and heating rate comparable with those of this study (26). Fair agreement was found between correlations with rank of hydroxyl oxygen and of oxygen evolved as pyrolytic water although the water yields from 12 of the 13 coals fell below the hydroxyl correlation curve, in line with the behavior observed here for bituminous coal. The agreement was improved when oxygen evolved as low temperature CO was added to that evolved as pyrolytic water. The CO formation was attributed to scission of weak ether linkages formed from two phenolic groups via Reaction 1



(26). Some theoretical basis for a correlation between pyrolytic water and phenolic hydroxyls in the coal is provided by thermochemical calculations for hypothesized reactions of relevant model compounds. Thus the formation of water by Reaction 2 is calculated to be exothermic and



hence energetically favored at room temperature by from 14 to 18 kcal/mol, depending on whether the heat of formation of the phenyl radical is taken respectively as + 73 kcal/mol, a value calculated from thermochemical cycles by using standard data tabulations (29-32), or as the literature value of + 69 kcal/mol (32, 33). Also, the overall sequence involving Reaction 2 plus recombination of two phenyl radicals to give biphenyl and water (i.e., Reaction 3) is highly favored thermodynamically,



having a $\log_{10} K_p$ value that varies from + 91 at 25°C to + 17 at 1000°C. Hydrogen atoms would be expected to be present during coal pyrolysis because of scission of labile coal structures. However, thermodynamic calculations show that Reaction 3 would still be favored strongly even if molecular hydrogen were the reactant. Calculations also show that a variation on Reaction 2 in which the hydrogen atom replaces the hydroxyl group to give benzene and a free hydroxyl radical is essentially thermo-neutral from 25° to 1000°C with $\log_{10} K_p$ values ranging from about + 1.0 to + 0.5.

It is emphasized that calculated thermochemical favorability does not prove that a given reaction actually occurs during coal pyrolysis. Thus these findings are presented not to advocate the specific reactions but rather to indicate that a radical-based dehydroxylation pathway is plausible.

The distinctly different temperature dependences of pyrolytic water evolution from the two coals of this study, despite the fair agreement with the correlation of Figure 6, is not completely understood. It may be that the phenolic hydroxyl groups exist in sufficiently different chemical environments, (e.g., they may be bound to sufficiently distinct parent structures) so that reactions analogous to Reactions 2 and 3 become kinetically allowed at different temperatures. It also should be acknowledged, however, that other totally or partly different reaction pathways may contribute to the formation of pyrolytic water. For example, using the ash analyses of Ref. 17, it is estimated that above 600°C, pyrolytic water from kaolinite decomposition could be up to 0.57 and 0.76 wt % (as-received) of the lignite and bituminous coal, respectively. Values of oxygen in pyrolytic water less this mineral matter contribution were plotted as crosses in Figure 6. While the result for the lignite is brought into somewhat better agreement with the correlation of Ref. 28, that for the bituminous coal moves slightly further away.

In summary, some qualitative inferences on the possible role of mineral matter and selected organic functional groups in determining product compositions in coal pyrolysis can be made from the present data. More quantitative information could be obtained by detailed spectroscopic and elemental analyses of the organic material and mineral matter in chars from coals allowed to proceed to varying extents of pyrolytic decomposition under well-defined reaction conditions. Some work to this end is currently in progress at CMU and MIT.

Modeling

A semiempirical model of lignite pyrolysis has been developed in which the rate of formation of each of the key components (e.g., H₂O,

CO₂, CO, and CH₄) or classes of components (e.g., other hydrocarbons and tar) has been described successfully by use of one, two, or three first-order reactions (7, 8):

$$\frac{dV_{ij}}{dt} = \sum_j k_{ij}(V^*_{ij} - V_{ij}) \quad j = 1, 2, \text{ or } 3 \quad (4)$$

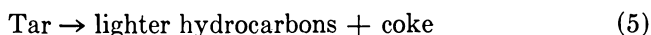
where V_{ij} = total yield of product i up to time t attributable to reaction j

V^*_{ij} = value of V_{ij} at $t = \infty$

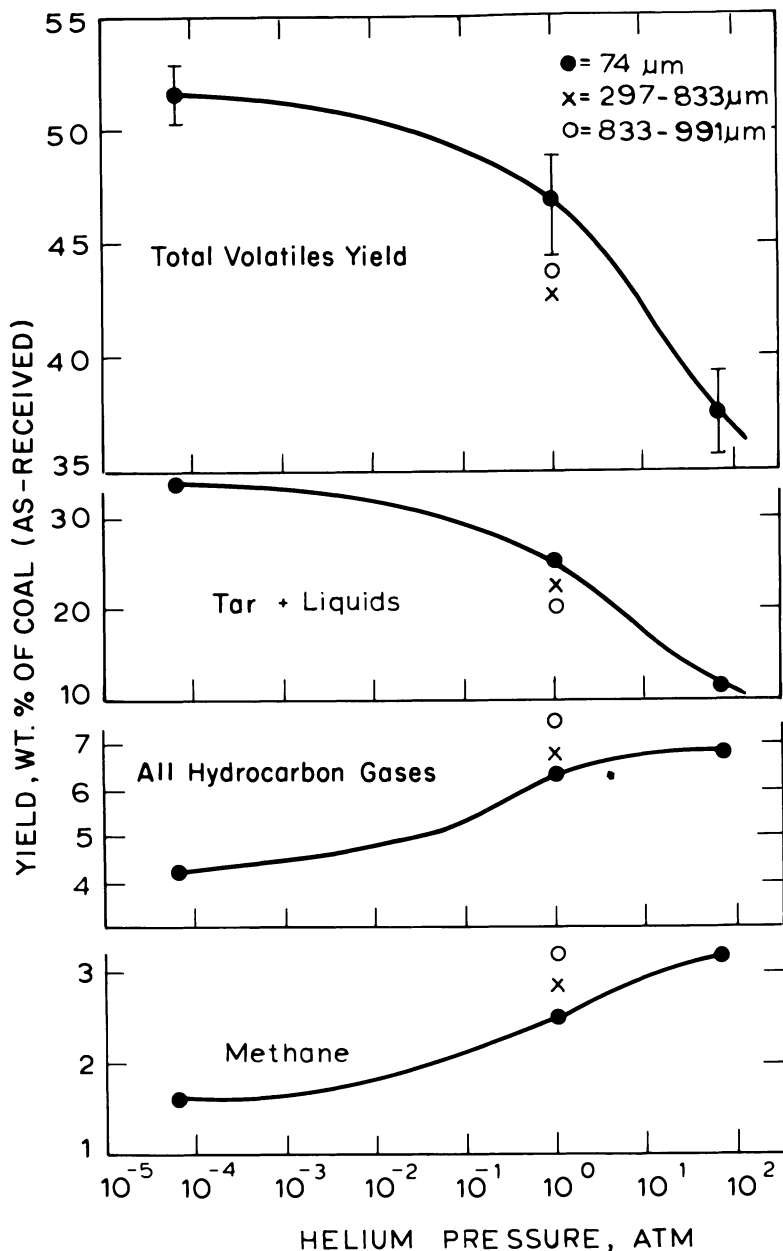
k_{ij} = the Arrhenius rate constant = $k_{0ij}e^{-E_{ij}/RT}$ for production of product i by reaction j

Key features of the lignite pyrolysis which suggest use of this relatively simple model are (1) the insensitivity of total product yields to time-temperature history and (2) the relative insensitivity of total yields to large variations in external gas pressure and hence in resistance to mass transport out of the particle. Figure 3 addresses the first of these points. Data obtained at heating rates one order of magnitude higher and lower than the base case (1000°C/sec) gave an essentially unchanged product spectrum. Similarly, experimentally separating the pyrolysis into two steps (a low temperature step followed by cooling and a subsequent high temperature step to the indicated peak temperature) failed to alter significantly the total product spectrum. This behavior is consistent with thermal decomposition by a set of parallel, independent reactions (7, 8).

The data on volatile yields from the bituminous coal also were found to show little effect of heating rate over the range studied. However, as shown in Figure 7, they did exhibit a strong dependence on both external helium pressure and on particle diameter. The changes in product distributions observed with shifts to higher pressure imply that secondary cracking reactions of the type in Reaction 5 are being affected. These phenomena are discussed in greater detail elsewhere (14).



If data were available from experiments in which mass transport limitations could be shown to be small (as might occur with very small particle sizes and high vacua), some success might be expected from the lignite-type model. Its general application to bituminous coal pyrolysis for the range of conditions depicted in Figure 7 is inappropriate, however, because it does not account for mass transport effects. Nevertheless, because of its relative simplicity and, hence, appeal for engineering



The Combustion Institute

Figure 7. Effects of pressure and coal particle size on yields of total volatiles, tar plus hydrocarbon liquids, all hydrocarbon gases, and methane, from bituminous coal pyrolysis. Heating rate = $1000^\circ\text{C}/\text{sec}$. Temperature = 1000°C . Isothermal holding time = 2–10 sec. Particle diameters, μm : (●) 74; (×) 297–833; (○) 833–991 (14).

calculations, a version of the above model based on one first-order decomposition reaction for each product was fitted to data on the pyrolysis of the bituminous coal at 1-atm helium and 53 to 88- μm diameter particles. Quite good best fit correlations were obtained but the resulting rate parameters were unrealistic for activated chemical processes. These findings were not surprising considering the somewhat broad temperature interval over which products evolve (as opposed to the distinct stepwise behavior exhibited by lignite products). The findings suggest that mass-transport effects can influence the kinetics of product evolution and, as discussed above, that the products are formed by many more than one or two dominant first-order processes. The latter behavior could probably be much more effectively modeled by a distributed activation energies model of the form described in Ref. 3, applied to the individual products, as it has been previously for the formation of hydrocarbon gases in coal pyrolysis (25). Results of modeling investigations by using this approach, as well as formulations which account for transport-kinetics coupling effects, will be presented elsewhere (14, 15).

Acknowledgment

We are grateful to R. N. Caron for laboratory work; to S. T. Free, M. W. Zacharias, and J. M. Lopez for modeling calculations; and to Inland Steel Research Laboratories for petrographic analyses. We are also grateful for financial support provided by the National Science Foundation, Research Applied to National Needs (RANN), under Contract AER 75-13673; by the United States Department of Energy, University Affairs Section of the Division of Materials and Exploratory Research, under Contract No. EX-76-A-01-2295, T.O. No. 26; by the Mobil Research Foundation, Inc.; and by the National Science Foundation, through an Energy Traineeship to E.M.S.

Literature Cited

1. Anthony, D. B. "Rapid Devolatilization and Hydrogasification of Coal," Sc.D. Thesis, Massachusetts Institute of Technology, Cambridge, MA, 1974.
2. Anthony, D. B.; Howard, J. B.; Meissner, H. P.; Hottel, H. C. *Rev. Sci. Instrum.* 1974, 45, 992.
3. Anthony, D. B.; Howard, J. B.; Hottel, H. C.; Meissner, H. P. *Symp. (Int.) Comb. (Proc.)*, 15th 1975, 1303.
4. Anthony, D. B.; Howard, J. B.; Hottel, H. C.; Meissner, H. P. *Fuel* 1976, 55, 121.
5. Anthony, D. B.; Howard, J. B. *AIChE J.* 1976, 22, 625.
6. Howard, J. B. "Fundamentals of Coal Pyrolysis and Hydrolysis," In "Chemistry of Coal Utilization"; Elliott, M. A., Ed.; Wiley: New York; Second Supplementary Vol., in press.

7. Suuberg, E. M. "Rapid Pyrolysis and Hydropyrolysis of Coal," Sc.D. Thesis, Massachusetts Institute of Technology, Cambridge, MA, 1977.
8. Suuberg, E. M.; Peters, W. A.; Howard, J. B. *Ind. Eng. Chem. Process Des. Dev.* 1978, 17, 37.
9. Solomon, P. R. *Symp. (Int.) Comb. (Proc.)*, 17th, in press.
10. Peters, W.; Bertling, H. *Fuel* 1965, 44, 317.
11. Jüntgen, H.; Van Heek, K. H. *Brennst.-Chem.* 1969, 50, 172.
12. Gavalas, G. R.; Oka, M. *Fuel* 1978, 57, 285.
13. Weiler, J. F. "High Temperature Tar," In "Chemistry of Coal Utilization"; Lowry, H. H., Ed.; Wiley: New York, 1963; Supplementary Vol., pp. 580-628.
14. Suuberg, E. M.; Peters, W. A.; Howard, J. B. *Symp. (Int.) Comb. (Proc.)*, 17th, in press.
15. Suuberg, E. M.; Peters, W. A.; Howard, J. B. "Product Compositions in Rapid Hydropyrolysis of Coal," to be published.
16. Howard, H. C. "Pyrolytic Reactions of Coal," In "Chemistry of Coal Utilization"; Lowry, H. H., Ed.; Wiley: New York, 1963; Supplementary Vol., pp. 340-394.
17. Padia, A. S. "The Behavior of Ash in Pulverized Coal Under Simulated Combustion Conditions," Sc.D. Thesis, Massachusetts Institute of Technology, Cambridge, MA, 1976.
18. Britton, H. T. S.; Gregg, S. J.; Winsor, G. W. *Trans. Faraday Soc.* 1952, 48, 63.
19. Ingraham, T. R.; Marier, P. *Can. J. Chem. Eng.* 1963, 41, 170.
20. Blom, L.; Edelhause, L.; Van Krevelen, D. W. *Fuel* 1957, 36, 135.
21. Campbell, J. H.; Stevens, D. R. *Am. Chem. Soc., Div. Fuel Chem., Prepr.* 1976, 21 (7), 94.
22. Loison, R.; Chauvin, F. *Chem. Ind. (Paris)* 1964, 91, 269.
23. Fitzgerald, D.; Van Krevelen, D. W. *Fuel* 1959, 38, 17.
24. Jüntgen, H.; Van Heek, K. H. "Research in the Field of Pyrolysis at Bergbau Forschung during the Last Fifteen Years," paper presented at the meeting on Coal Fundamentals, Stoke Orchard, England, January, 1977.
25. Hanbaba, P.; Jüntgen, H.; Peters, W. *Brennst.-Chem.* 1968, 49, 368.
26. Solomon, P. R. "The Evolution of Pollutants During the Rapid Devolatilization of Coal," Report of Research, United Technologies Research Center, to the National Science Foundation, November, 1977.
27. Wolfs, P. M. J.; Van Krevelen, D. W.; Waterman, H. I. *Fuel* 1960, 39, 25.
28. Given, P. H. "The Organic Chemistry of Coal Macerals," Penn State Short Course on Coal, The Pennsylvania State University, June, 1976.
29. Cottrell, T. L. "The Strengths of Chemical Bonds"; Academic: New York, 1954.
30. Stull, D. R.; Prophet, H. "JANAF Thermochemical Tables"; National Bureau of Standards, U. S. Dept. of Commerce: Washington, DC, 1971.
31. Stull, D. R.; Westrum, E. F., Jr.; Sinke, G. C. "The Chemical Thermodynamics of Organic Compounds"; Wiley: New York, 1969.
32. Gray, P.; Williams, A. *Chem. Rev.* 1959, 59, 239.
33. Steacie, E. W. R. "Atomic and Free Radical Reactions"; Reinhold: New York, 1954.

RECEIVED September 22, 1978.

Thermogravimetric Studies on Catalytic and Noncatalytic Pyrolysis of Pitch Derived from Hydrocracked Athabasca Bitumen

M. V. C. SEKHAR and M. TERNAN

Catalysis Section, Synthetic Fuels Research Laboratory, Energy Research Laboratories, Canada Centre for Mineral and Energy Technology (CANMET), Department of Energy, Mines and Resources. Ottawa, Canada

The pyrolytic behavior of a hydrocracked vacuum residuum was studied in an inert atmosphere in the presence and absence of an alumina catalyst by using thermogravimetric techniques. The noncatalyzed pyrolysis proceeded in two stages. The first half of the pyrolysis obeyed overall first-order kinetics while in the second half the kinetics became complex. When the gamma alumina catalyst was used, the total yield of distillate products increased. Also, the catalyzed reaction was first order with respect to the reactant throughout the entire pyrolysis. In the first-order regime of both the catalytic and noncatalytic pyrolysis, the activation energy and the preexponential factor increased with increasing extent of reaction. This was explained in terms of a compensation effect between the two Arrhenius parameters.

The increasing demand for oil and gas, coupled with the predicted decline in their supply, recently has stimulated researchers into developing means and techniques for better using the raw materials already available. For a number of years our laboratories (1) have been engaged in developing processes for upgrading the bitumen recoverable from the large oil-sands deposits of the Athabasca basin in northeastern Alberta, Canada. The main objective of the upgrading process is to effect molecular weight reduction and thereby convert the (50%) nondistillable residue to distillate hydrocarbons. Studies on hydrocracking processes

(2) have shown that it offers a significant improvement over conventional coking processes for upgrading the bitumen, with 10–15% higher yields of usable liquid products. However, the hydrocracking process also produces 5–10% of nondistillable pitch, boiling above 525°C. Optimum use of the oil-sands resource requires using this pitch by-product, in accordance with environmental constraints.

The pitch material contains sulfur, finely divided minerals, and organometallic vanadium and nickel. Combustion of the pitch is one method of using its energy content. Unfortunately combustion processes will produce large quantities of sulfur dioxide which are environmentally unacceptable. One alternate option for using the pitch may be to gasify it to either a low-Btu gas or to hydrogen to supplement the energy and hydrogen requirements of the upgrading process, respectively.

When considering gasification processes, it became apparent that at low temperatures pyrolysis of the pitch would occur. The pyrolytic reactions would take place prior to or concurrent with other reactions in a gasifier. Therefore we felt it desirable to study and establish the behavior of pyrolysis before attempting to understand the gasification characteristics.

Experimental

A diagram of the equipment is shown in Figure 1. Samples of pitch with or without added catalyst were placed in a cylindrical quartz basket (15 x 40 mm) which was suspended from one arm of a Cahn RG electrobalance. A stream of helium or nitrogen flowed through the reactor, sweeping away the products formed during the pyrolysis. The volatile products carried by the inert carrier were condensed in traps maintained at dry-ice temperatures while the noncondensable gases were collected in sampling bulbs for gas chromatographic analysis. The reactor was surrounded by a tubular furnace which could be operated either isothermally or in a temperature programmed mode. The sample temperature was monitored using a thermocouple (Type K) positioned in close proximity to the sample basket. Both the weight of the sample and its temperature were continuously monitored and recorded as a function of time.

The pitch used in these experiments was the portion of the liquid product boiling above 525°C, obtained by thermally hydrocracking Athabasca bitumen in a pilot plant reactor. The Athabasca bitumen was obtained from Great Canadian Oil Sands Ltd., Fort McMurray, Alberta. The properties of the pitch used in this study are shown in Table I. In the case of the noncatalytic experiments, the pitch sample was used in lumps, and the sample sizes were in the 20–100 mg range. For the catalytic case, the catalyst pellet ($L = D = 1.25$ mm) was dipped in hot pitch (250°C), resulting in a thin coating of the pitch around the pellet. The catalyst:pitch weight ratio in these experiments varied from one to four. The gamma alumina catalyst used in this study has been described previously (3).

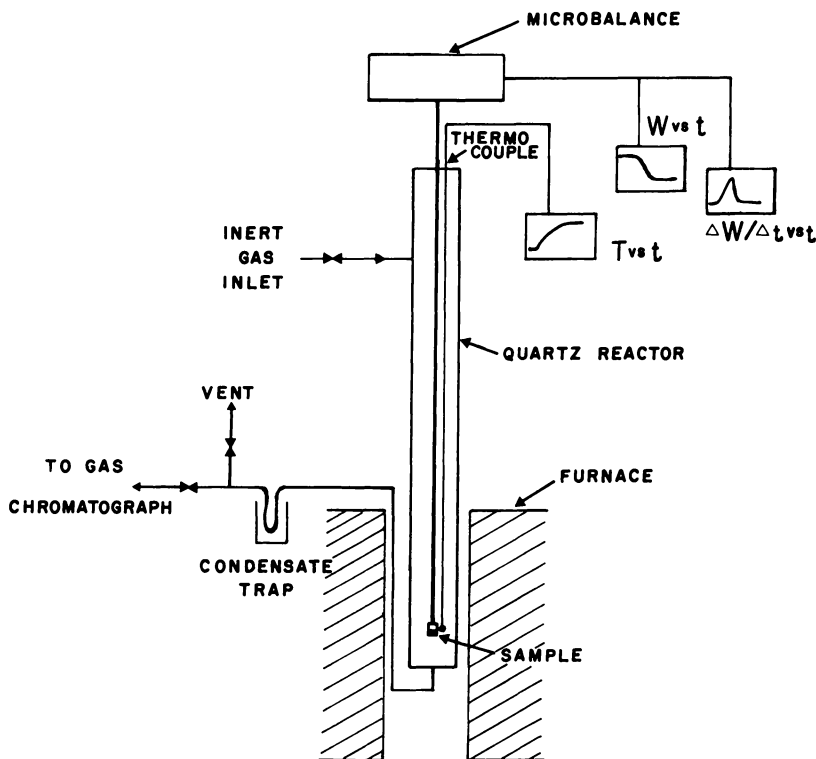


Figure 1. Diagram of the microbalance reactor

Several experiments were performed with heating rates of 1°, 2.5°, 5°, 10°, and 20°C per minute. Each experiment began at room temperature, and the furnace was heated at the desired rate to a final temperature of 850°C. In the majority of cases, the run was terminated 10–15 minutes after reaching the final temperature. Some experiments also were performed with nonlinear heating rates. The furnace temperature was set at the desired final level, and the furnace was allowed to reach this temperature. The heating rate in these experiments varied from a maximum of 50°C/min to essentially zero as the final temperature was reached. In all of the experiments, the inert carrier gas flow was maintained at 150 mL/min.

To obtain product samples required for all the analyses, some experiments were performed with approximately 5 g of pitch. These experiments were carried out under isothermal conditions without the electrobalance attached to the sample basket.

The pyrolysis products were analyzed by using several techniques. The gas samples collected were analyzed by using gas chromatography and mass spectrometry. Elemental analysis and proton NMR and ¹³C NMR analysis were performed on the initial reactant and the final distillable liquid products.

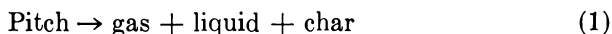
Table I. Feedstock Properties

| | |
|------------------------------------|------|
| Proximate Analysis (wt %) | |
| Moisture | Nil |
| Ash | 5.2 |
| Volatile matter | 42.4 |
| Fixed carbon (by diff.) | 52.4 |
| Ultimate Analysis (wt %) | |
| Carbon | 79.6 |
| Hydrogen | 6.8 |
| Sulfur | 5.4 |
| Nitrogen | 1.5 |
| Ash | 5.2 |
| Oxygen (by diff.) | 1.5 |
| *Pentane Insolubles (wt %) | 70.1 |
| *Benzene Insolubles (wt %) | 27.1 |
| *Tetrahydrofuran Insolubles (wt %) | 10.4 |
| Conradson Carbon Residue (wt %) | 63.5 |
| Percent Aromatic Carbon | 67 |
| Ash Analysis (wt %) | |
| SiO ₂ | 43.3 |
| Al ₂ O ₃ | 24.7 |
| Fe ₂ O ₃ | 11.4 |
| Mn ₃ O ₄ | 0.3 |
| TiO ₂ | 6.6 |
| P ₂ O ₅ | 0.3 |
| CaO | 2.8 |
| MgO | 1.6 |
| SO ₃ | 1.2 |
| Na ₂ O | 0.2 |
| K ₂ O | 1.7 |
| V ₂ O ₅ | 3.1 |
| NiO | 0.8 |

* On ash-included basis.

Results

Since pitch is a multicomponent material, it is difficult to identify and study the various pyrolytic reactions separately. One simple representation of the overall pyrolysis process is:



The products of the pyrolysis are grouped under three categories: a gas phase material, a distillable liquid, and a nondistillable char, all at ambient conditions. At any time during the course of the reaction, the material in the microbalance reactor would be a combination of the incompletely reacted pitch and the char reaction product, which will be referred to as the residue.

Typical experimental data from the microbalance reactor are shown in Figures 2 and 3. As is evident from Figure 2, very little reaction resulting in weight loss occurred up to approximately 400°C. Above 500°C, the rate of weight loss is small but relatively constant. In Figure 3, the weight of the residue is shown as a function of time for both the catalyzed and noncatalyzed cases. The furnace temperature in both of these two cases increased nonlinearly, reaching 500°C in about 20 minutes and 850°C in about 120 minutes and remaining constant thereafter. The difference in the shape between the curves in Figure 2a and 3 are attributable to the widely different heating rates. As can be seen from Figure 3, the weight-loss pattern with and without added catalyst is identical up to about 28% total weight loss. The catalytic effects come

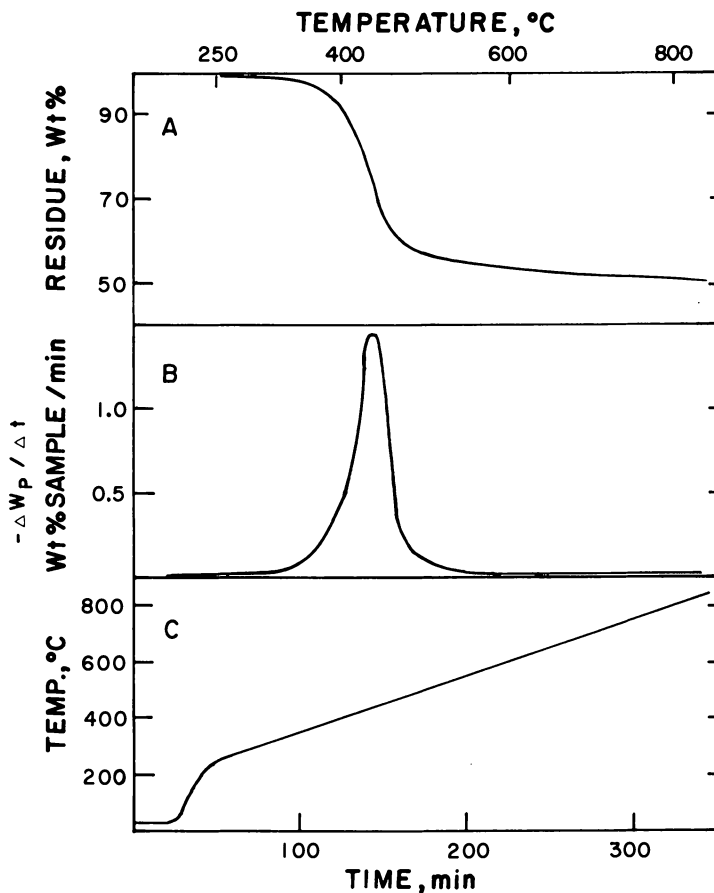


Figure 2. Amount of residue (wt %), time derivative of the amount of pitch, $-\Delta w_p / \Delta t$ (wt %/min), and temperature (°C) vs. time (min)

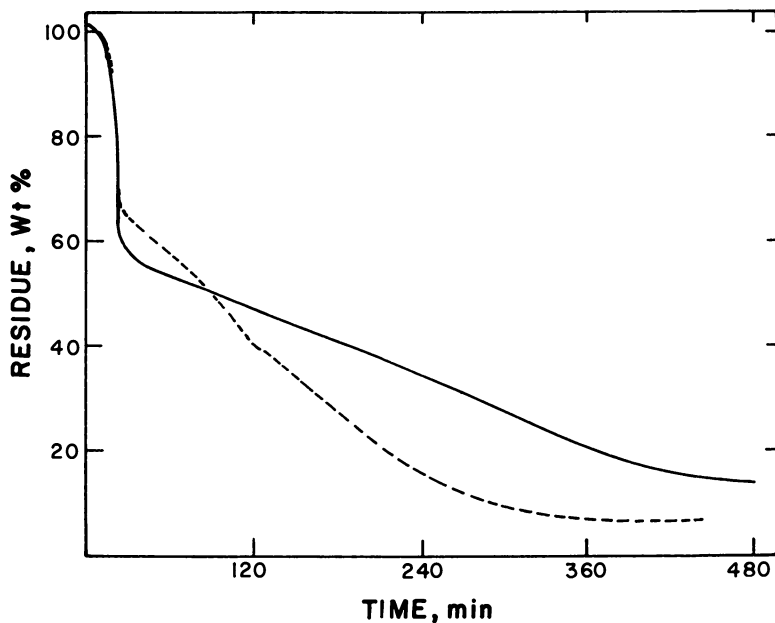


Figure 3. Amount of residue (wt %) vs. time (min). Final temperature, 850°C in 120 minutes; (—) no catalyst, (---) $\gamma\text{Al}_2\text{O}_3$ catalyst; catalyst: pitch = 3.5.

into force after that point, and the rate of weight loss in the presence of the catalyst is significantly higher than in the case when no catalyst was present.

Values illustrating product yields and gas compositions from isothermal experiments are shown in Table II. The yield data shown were obtained after a reaction period of two hours at a reaction temperature of 450°C. The gas and liquid yields are higher and the residue yield is lower when a catalyst is present. The gas compositions with and without catalyst are fairly similar. However ^{13}C NMR analyses showed that the liquid products obtained in the catalyzed experiment have a higher aromatic content than those formed in the absence of the catalyst.

The effect of the heating rate on the cumulative weight loss with and without added catalyst is shown in Table III. The weight loss in both cases increases with decreasing rate of heating. Similar behavior has been observed with decompositions of petroleum residuum. Other workers (4) have concluded that the decreasing extent of reaction with increasing rate of heating is characteristic of decomposition reactions, which are the type occurring in this system.

Table II. Product Distribution and Gas and Liquid Analysis^a

| | <i>Uncatalyzed</i> | <i>Catalyzed</i> $\left(\frac{\text{catalyst}}{\text{pitch}} = 0.6\right)$ |
|-------------------------|--------------------|---|
| Residue (wt %) | 70.8 | 61.2 |
| Liquid (wt %) | 22.0 | 25.8 |
| Gas (wt %) | 6.0 | 12.0 |
| Unaccounted (wt %) | 1.2 | 1.0 |
| Percent Reacted | 29.2 | 38.8 |
| Gas Analysis (Vol %) | | |
| H ₂ | 60 | 66 |
| H ₂ S | 16 | 12 |
| C ₁ | 10 | 12 |
| C ₂ | 7 | 5 |
| C ₃ | 4 | 4 |
| Liquid Product Analysis | | |
| Hydrogen (wt %) | 8.84 | 9.18 |
| Carbon (wt %) | 84.0 | 84.9 |
| Percent Saturate Carbon | 62 | 52 |
| Percent Aromatic Carbon | 38 | 48 |
| Olefins | trace | trace |

^a Reaction temperature, 450°C; reaction time, 2 hr.

Table III. Effect of Heating Rates on the Cumulative Weight Loss (Final Temperature 500°C)

| <i>Heating Rate</i> (°C/min) | <i>Uncatalyzed</i> (Percent weight of original sample) | <i>Catalyzed</i> |
|---------------------------------|---|------------------|
| 1 | — | 39 |
| 2.5 | 43 | — |
| 5 | 43 | 39.5 |
| 10 | 40 | — |
| 15 | — | 35.5 |
| 20 | 32 | 36 |

Discussion

The results can be interpreted in terms of standard kinetic expressions. A simple *n*th-order equation which describes the rate of loss of pitch would be given by Equation 2, where W_p refers to the weight of

$$-\frac{dW_p}{dt} = kW_p^n \quad (2)$$

the reactive portion of the residue expressed as a percentage of the original sample, and k is the rate constant. The Arrhenius equation (Equation 3) can be substituted in Equation 2 after taking logarithms to

$$\ln k = \ln A - E_a/RT \quad (3)$$

give Equation 4. In the Equation 4, A is the Arrhenius constant, E_a is

$$\ln (-dW_P/dt) = \ln A + n \ln W_P - E_a/RT \quad (4)$$

the overall activation energy for the pyrolysis process, and R is the gas constant.

A method of relating the extent of reaction to the amount of residue remaining in a microbalance reactor was described previously (5). An important part of that method involved the calculation of W_P from W_R , the weight of the residue expressed as a percentage of the original sample. Briefly, it involved relating the magnitude of W_P to the hydrogen content of the residue, assigning the char a hydrogen content of zero and performing material balance calculations.

By using the procedure described above, W_P and W_R were related by the expression in Equation 5, where W_R refers to the weight of the

$$W_P = 0.0146_4 W_R^2 - 0.464 W_R \quad (5)$$

residue expressed as a percentage of the initial sample weight and W_P refers to the weight of the reactive portion of the residue expressed as a percentage of the initial sample weight. Differentiation of Equation 5 with respect to t gives Equation 6. The experimentally measured rate

$$\frac{dW_P}{dt} = (0.0293 W_R - 0.464) \frac{dW_R}{dt} \quad (6)$$

(dW_R/dt) can then be related to the rate of loss of pitch (dW_P/dt) by using the Equation 6.

Figure 4 shows the rates of change in W_P as a function of the total residue weight (W_R) for three different heating rates. The faster heating rates produced higher temperatures and greater reaction rates for any given amount of residue. With this representation it is easy to compare reaction rates at constant amount of residue. Each unique value of the amount of residue has been equated to a unique reactant composition. A comparison at a specific value of the amount of residue is then equivalent to a comparison at a specific reactant composition. An inspection of Equation 4 shows that the first two terms on the right-hand side would be

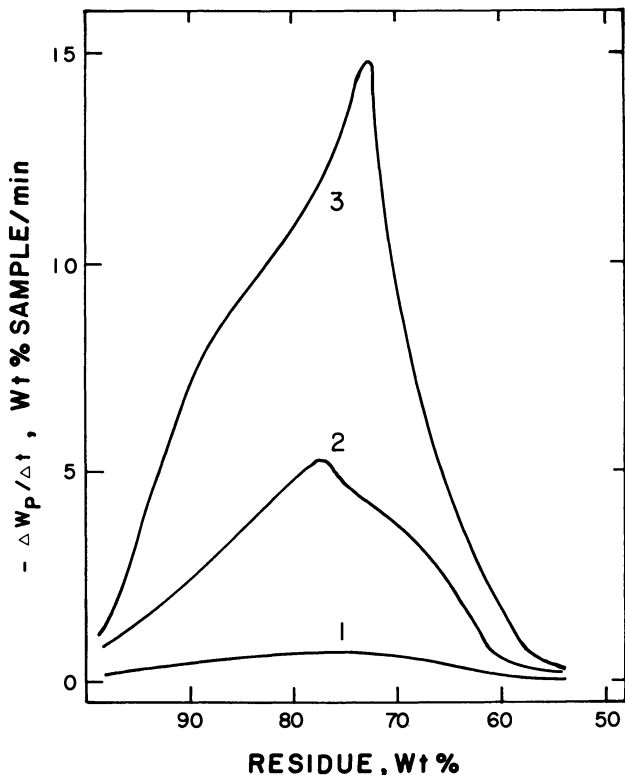


Figure 4. Rate of change of amount of pitch, $-\Delta W_p/\Delta t$ (wt %/min), vs. amount of residue, W_R (wt %), for catalytic pyrolysis. Heating rates were 1°, 5°, 20°C per minute for Curves 1, 2, and 3, respectively.

a constant for a specific reactant composition. Therefore a plot of the logarithm of the rate of weight loss $\ln(-dW_p/dt)$ vs. the inverse of the corresponding temperature ($1/T$) should result in a straight line whose slope is related to the activation energy (E_a).

Figure 5 shows four such straight lines corresponding to two different reactant compositions with and without added catalyst. It is immediately apparent from Figure 5 that the activation energy varies as a function of the reactant composition.

Figure 6 shows the variation in activation energy with extent of reaction. In the case of the noncatalyzed experiment, the activation energy increases initially as the extent of reaction increases and approaches a maximum when about 20% of the sample has decomposed. During the course of the remainder of the pyrolysis, the activation energy was found to decrease with increasing reaction. In the presence of the catalyst, on the other hand, the activation energy continually increases

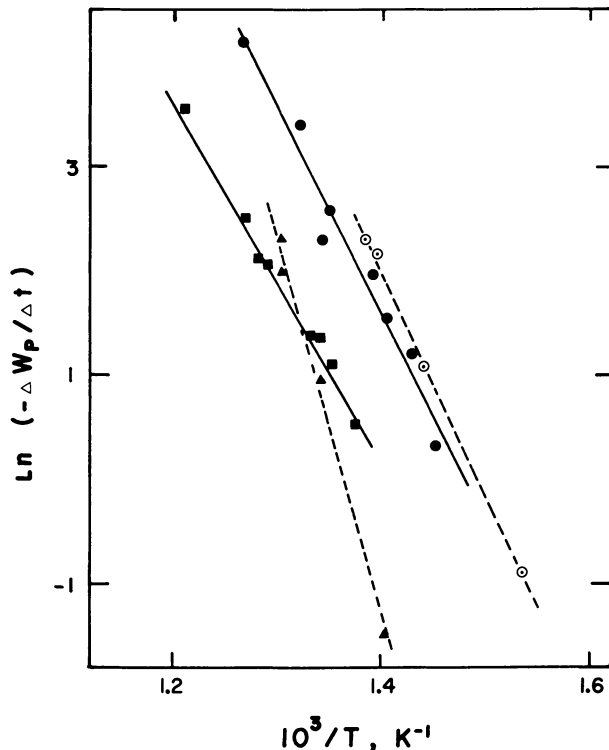


Figure 5. Natural logarithm of $-\Delta W_p/\Delta t$ vs. inverse temperature (K^{-1}); (—) no catalyst, (---) γAl_2O_3 catalyst, (\blacksquare , \blacktriangle) $W_R = 66.5$ wt %, (\bullet , \circ) $W_p = 87.5$ wt %.

with increasing extent of reaction. The apparent activation energies from the temperature-programmed data shown in Figure 6 varied from 80 to 170 kJ/mol for the uncatalyzed experiments and from 120 to 300 kJ/mol for the catalyzed experiments.

According to Equation 4, the intercept (I) from Figure 5 is given by Equation 7. It was found that the intercept (I) also varied with the

$$I = \ln A + n \ln W_p \quad (7)$$

extent of reaction in an analogous manner to the activation energy. Both the catalytic and noncatalytic results formed curves for I which were similar in shape to those curves for E_a shown in Figure 6.

Since the intercept (I) which includes the Arrhenius constant (A) and the apparent activation energy (E_a) exhibit a similar pattern of variation as a function of the extent of reaction, it was decided to explore

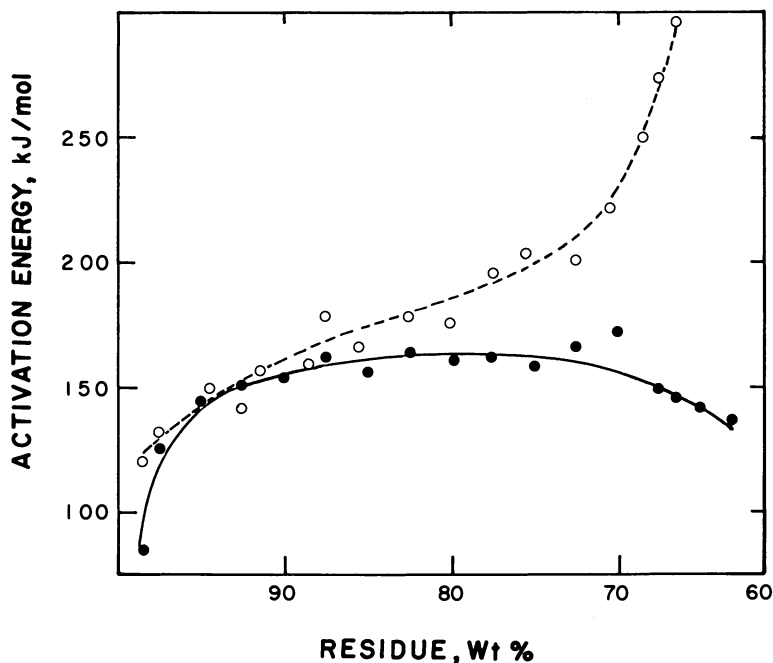


Figure 6. Activation energy as a function of weight of residue; (●, ○) noncatalytic and catalytic data, respectively.

the existence of a compensation effect between A and E_a . Such compensation effects have been observed with many solid-state decomposition reactions (6, 7, 8).

The compensation effect is usually expressed as Equation 8, where

$$\ln A = \ln k_{1so} + \frac{E_a}{RT_{1so}} \quad (8)$$

k_{1so} is the isokinetic rate constant, and T_{1so} is the isokinetic temperature. Introduction of Equation 8 into Equation 7, followed by rearrangement gives Equation 9. A multiple linear regression was performed on Equa-

$$I - \ln k_{1so} - \frac{E_a}{RT_{1so}} = n \ln W_P \quad (9)$$

tion 9 to obtain values of k_{1so} , T_{1so} , and n .

Pyrolysis in the presence of catalyst produced a value of n close to 1.0, indicating a first-order reaction. No variation in the order of reaction was apparent as a function of W_R . Noncatalytic pyrolysis produced a

value of n close to 1.0 for $100\% < W_R < 80\%$. For smaller values of W_R , a value of 4.1 for n fitted the data. The values for k_{180} and T_{180} corresponding to a first-order reaction are shown in Table IV.

The above value of n does not represent any imaginable kinetic process. Furthermore, no satisfactory relationships could be obtained when the data were analyzed in terms of a variety of diffusion models. A satisfactory explanation may involve a more complex reaction sequence than that of Equation 1, perhaps including some intermediate reaction steps.

Figure 7 shows the relationship between the left-hand side of Equation 9 and $\ln W_P$. The straight lines in this figure have been drawn with a slope of $n = 1$. It is apparent that the data can be represented by first-order kinetics although there is some scatter.

The compensation effect is normally observed when different catalysts are used. The reaction data for a single catalyst are usually plotted in the form of the Arrhenius equation (Equation 3) to obtain a value for E_a and a value for A . When a number of catalysts with widely varying properties are tested, they can produce different activation energies E_a (9, 10, 11) which lead to the compensation effect.

If the expression for $\ln A$ in Equation 8 is substituted into Equation 3, the expression in Equation 10 is obtained. Equation 10 is a modified

$$\ln k = \ln k_{180} + \frac{E_a}{RT_{180}} - \frac{E_a}{RT} \quad (10)$$

Arrhenius equation with two variables E_a and T . E_a is a variable which will only be constant for a specific catalyst and a specific reactant molecule.

In the present study, the compensation effects were observed both with a single catalyst and without a catalyst. These compensation effects may be attributed to differences in E_a associated with different reactant molecules. As W_R (the residue weight) changed, the reactant composition also changed. Initial pyrolysis of the reactive species was followed by the pyrolysis of less reactive species with increasing reaction temperature. The less reactive species have higher activation energies, as may

Table IV. Kinetic Parameters from Equation 7

| Parameter | Catalytic Pyrolysis | Noncatalytic Pyrolysis | |
|--------------------------------|------------------------|---------------------------|----------------------|
| | $W_R > 66$ | $W_R > 80$ | $W_R < 72$ |
| n | 1.05 | 1.05 | 4.10 |
| k_{180} (sec ⁻¹) | 3.2×10^{-2} | 2.9×10^{-4} | 2.0×10^{-7} |
| T_{180} (K) | 805 | 679 | 805 |

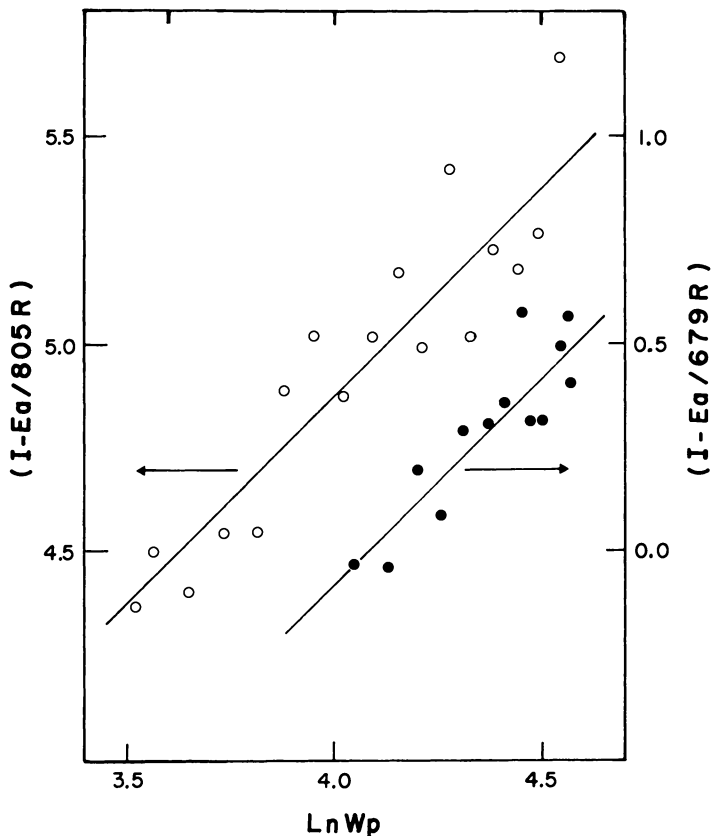


Figure 7. $(I - E_a/RT_{iso})$ vs. $\ln W_p$. The straight lines have a slope of $n = 1$; (\bullet , \circ) noncatalytic and catalytic data, respectively.

be seen from the data in Figure 6, for all of the catalytic results and for the noncatalytic results at values of W_R greater than 80%. These changes in E_a , when considered in conjunction with Equation 8, completely explain the observed compensation effect.

Conclusion

In summary, it was observed that the alumina catalyst increased the extent of pitch pyrolysis at long reaction times, accompanied by some changes in the product distribution. The pyrolysis reaction was found to be first order with respect to the pitch reactant. A compensation effect was observed in which the Arrhenius parameters E_a and A were found to vary with the residue weight, W_R . This effect was explained in terms of a modified Arrhenius equation and of the increasing activation energy E_a associated with the less reactive molecular species.

Acknowledgment

The authors wish to thank E. C. McColgan and M. Channing for performing the pyrolysis experiments and R. Ozubko for NMR analyses.

Literature Cited

1. Pruden, B. B. *Can. J. Chem. Eng.* **1978**, *56*, 277.
2. Pruden, B. B.; Denis, J. M. *Can. Chem. Proc.* **1977**, *61* (6), 37.
3. Parsons, B. I.; Ternan, M. *Proc. Int. Congr. Catal.*, *6th* **1977**, *2*, 965.
4. Primak, R. G.; Bogdanov, M. V.; Bodan, A. N. *Kinet. Catal.* **1976**, *12*, 920.
5. Sekhar, M. V. C.; Ternan, M. *Fuel* **1979**, *58*, 92.
6. Dollimore, D.; Heal, G. R.; Krupay, B. W. *Thermochim Acta* **1978**, *24*, 293.
7. Garn, P. D. "Thermal Analysis, Vol. 1," *Proc. Int. Conf. Therm. Anal.*, *4th* **1974**, 25.
8. Zmijewski, T.; Pyriak, J. *Proc. Int. Conf. Therm. Anal.* **1974**, *1*, 205.
9. Ranganathan, R.; Bakhshi, N. N.; Mathews, J. F. *Can. J. Chem. Eng.* **1977**, *55*, 544.
10. Walker, P. L., Jr.; Shelef, M.; Anderson, R. A. "Chemistry and Physics of Carbon," Walker, P. L., Jr., Ed.; Marcel Dekker: New York, 1968; Vol. 4, p. 287.
11. Bond, G. C. "Catalysis by Metals"; Academic: London, 1962; pp. 248-249.

RECEIVED October 27, 1978.

Production of Electrode Binder Pitch from Petroleum-Based Materials

E. C. PEASE and A. LOGAN

Gulf Canada Limited, Research and Development Department,
Sheridan Park, Ontario, Canada

A patented process has been developed for the production of electrode binder pitch from petroleum-based materials. Carbon anodes produced from the petroleum-based pitch and coke have been used successfully on a commercial scale by the aluminum industry. One stage of the process involves the pyrolysis of a highly aromatic petroleum feedstock. To study the pyrolysis stage of the process a small, sealed tube reactor was used to pyrolyze samples of feedstock. The progress of the reaction is discussed in terms of the formation of condensed aromatic structures, defined by selective solvent extraction of the reaction product. The pyrolysis of the feedstock exhibits a temperature-dependent induction period followed by reaction sequences that can be described by first-order kinetics. Rate constants and activation energies are derived for the formation of condensed aromatic structures and coke.

The carbon electrodes used in the production of aluminum by the Hall-Heroult process normally are produced from a combination of calcined coke and a pitch binder. While coal tar pitch traditionally has been used as the binder in electrode fabrication, variations in methods of production and the diversity of sources of supply result in variations in pitch quality. In addition, some locations in North America import pitch from areas such as Europe and Japan. With the desire for a more consistent quality product and more accessible sources of supply, alternative methods of producing binder pitch have been sought. This has led to a number of studies in the production of binder pitch from petroleum-derived materials (1-5). In these developments, the preferred feedstock

for producing pitch has been the heavy aromatic residues produced from the catalytic cracking of heavy petroleum distillates. These residues are generally referred to as clarified slurry oil or decant oil. A review by Stokes (6) of petroleum raw materials used in the manufacture of industrial carbons indicates a steady increase in the production of pitch from decant oil.

Gulf Canada has been active in this area for sometime and recently has developed a process that produces a high quality electrode binder pitch from a petroleum-based feedstock (7). This pitch has been used on a commercial scale by the aluminum industry in both vertical stud Soderberg and prebaked electrodes.

Although the pitch used in the fabrication of carbon anodes is referred to as a binder, it is worth emphasizing that the function of the pitch is much more than simply acting as a glue to hold the coke aggregate together during the carbonization process. Studies have shown that the binder pitch plays a major role in determining the performance of the finished electrode (8, 9, 10). However, it may be noted that the nature of many of the relationships between pitch properties and electrode performance still remains obscure.

One stage of the Gulf Canada process for producing pitch involves the pyrolysis of the highly aromatic petroleum residue, decant oil. This chapter describes a laboratory study of this pyrolysis step.

Experimental

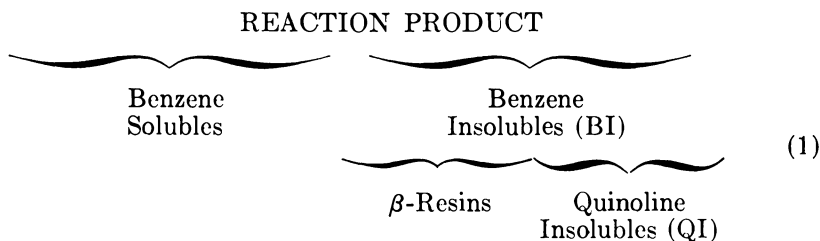
Pyrolysis Equipment and Procedure. The decant oil samples were pyrolyzed using a horizontal tube furnace equipped with an electronic temperature controller. The samples (1–2 g) were weighed into stainless steel tubes (6 mm o.d., 200 mm long), which were then flushed with nitrogen and sealed with Swagelok end caps. It was important that the sample holder be capable of complete disassembly to facilitate the recovery of the products of pyrolysis, which were largely viscous tars and coke. It had been found previously with a more elaborate flow-through reactor system, that not all the carbonaceous reaction products could be recovered readily.

Prior to placing the sample tube in the furnace at the desired temperature, the sample was preheated at 700°F (370°C) for 5 minutes. This step reduced the time required for the furnace to restabilize at the preset temperature. It was determined that no measurable degree of reaction occurred during the preheating step. After the required reaction time had elapsed, the sample tube was removed from the furnace, allowed to cool for a few minutes, and immersed in liquid nitrogen.

Recovery and Analysis of Pyrolysis Products. Frequently the quality of electrode binder pitches is assessed partially on the basis of how much material they contain that is insoluble in benzene (BI) and quinoline (QI) (8, 9, 10). In addition, the pyrolysis and coking of

petroleum residues have been followed using these insoluble components as a measure of the degree of reaction (11, 12). In effect, the determination of these insolubles provides a broad classification of the types of condensed aromatic compounds present in the pitch, or reaction product. Also, the rather intractable nature of some of the pyrolysis reaction products does not permit the use of more definitive analytical techniques such as NMR and mass spectrometry. We therefore found it more fruitful to follow the course of the pyrolysis reaction in terms of the formation of these insoluble components, rather than try to follow detailed changes in the concentration of specific components in a compositionally complex material.

The subdivision of the sample by selective solvent extraction is illustrated in the following scheme.



That portion of the BI that is soluble in quinoline is usually referred to as β -resins.

The sample tube, still at liquid nitrogen temperature, was opened and any uncondensed gases vented off. The tube was then heated to about 150°F (66°C) and the contents washed out with benzene. Any solid material remaining in the tube was dislodged mechanically. The benzene was evaporated off on a steam bath and the amount of residue determined. The residue was redissolved in boiling benzene and the BI separated by filtering off the undissolved material. A portion of the BI was taken up in hot quinoline and the QI separated by filtering off the insoluble residue. The gases and light hydrocarbons (up to C₇) produced during the pyrolysis were not recovered from the sealed tube runs. However, data on these by-products were obtained from a small pilot scale operation of the pitch process.

Feedstock. Analytical data for the sample of decant oil used in all the pyrolysis runs are given in Table I. The compositional data were obtained by a combination of liquid chromatography and high resolution mass spectrometry. In the liquid-chromatographic procedure, the decant oil was first absorbed onto silica gel (Davidson grade 923). The aromatic component of the decant oil then was desorbed with benzene, and the polar component desorbed with a 50:50 v/v blend of ethanol and chloroform. The aromatic component of the decant oil was analyzed on an AEI Model MS9 high resolution mass spectrometer. The decant oil was also separated into eight fractions by vacuum distillation, using a Wheeler spinning band column. Fractions 1, 3, 5, 7, and 8 were also analyzed by high resolution mass spectrometry, *see* Table IV. Each of

Table I. Decant Oil Analysis

| Aromatic Rings Per Molecule | Wt % |
|-------------------------------|--------|
| 1 | 7.4 |
| 2 | 22.5 |
| 3 | 20.7 |
| 4 | 20.2 |
| 5 | 8.1 |
| ≥ 6 | 5.2 |
| Polar compounds | 2.3 |
| Specific gravity, 60°F (16°C) | 1.1092 |
| API gravity, 60°F (16°C) | -3.9 |
| Sulfur, wt % | 2.4 |
| Quinoline insolubles, wt % | 0.0 |

these distillate fractions represented 10 wt % of the decant oil with the distillation residue making up the remaining 20%. The boiling ranges of the selected fractions are also shown in Table IV.

X-Ray Diffraction Studies. A Phillips x-ray diffractometer was used to obtain powder diffraction patterns for samples of QI, β -resins and carbon. The latter sample was obtained from a test carbon electrode that had been carbonized at about 1800°F (1000°C).

Results and Discussion

X-Ray Diffraction Data. The QI components found in the products of hydrocarbon pyrolysis are generally brittle, infusible solids. Because of this appearance the QI are usually classified under the general heading of coke. However, to more clearly define the nature of the QI produced in this work, x-ray diffraction patterns were obtained. The crystallite parameters for a graphitic matrix, as defined in Table II, were calculated for the QI and are compared in Table II with the same parameters determined for a sample of β -resins and for a sample of coke obtained from a test carbon anode. The x-ray diffraction pattern for the sample of β -resins was not well defined, so the value of L_c could not be determined reliably. The values of the other β -resin parameters are

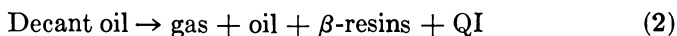
Table II. Crystallite Parameters* from X-ray Diffraction Patterns

| | L_a (nm) | L_c (nm) | a (nm) | C (nm) |
|------------------|---------------|---------------|-------------|-------------|
| QI's | 3.4 | 2.1 | 0.249 | 0.692 |
| β -resins | 1.8 | — | 0.254 | 0.756 |
| Electrode carbon | 3.4 | 2.3 | 0.246 | 0.692 |

* Crystallite parameters: L_a , crystallite diameter in the plane of the a axis; L_c , crystallite thickness in the C axis; a , graphite unit cell dimension in the plane of the layers; C , twice the interlayer spacing in the graphite matrix.

approximate only. However, there is clearly a significant difference between the QI and β -resins, while the QI and electrode carbon have very similar values for the four parameters. Carbon crystallites with dimensions of those shown for the carbon in Table II are referred to as turbostratic crystallites. This term distinguishes graphitic structures having short-range order, such as are formed at low carbonizing temperatures, from the graphitic structure that is produced at temperatures in excess of 2700°F (1500°C). Although the sheets of aromatic rings in turbostratic crystallites are parallel, the rotational orientation about the C axis departs significantly from that found in highly graphitized carbon. Although the x-ray diffraction data are not unequivocal evidence, these findings are reasonable grounds for using the QI formed during the pyrolysis of the decant oil to measure the extent of the coking reaction.

Pyrolysis Products. By mass spectrometry the compounds present in decant oil can be broadly classified into group types, which represent a range of isomeric condensed polynuclear aromatics. In Table I the group-type classification has been translated into the number of aromatic rings per molecule. A few of the isomeric structures in decant oil can be isolated and identified. For example, it is known (5, 13) that the three-ring condensed aromatic in decant oil is essentially all phenanthrene, with and without alkyl substituents; the structural isomer anthracene only exists in trace amounts. Among the four-ring condensed aromatics, pyrenes, benzphenanthrenes, benzanthracenes, and chrysenes have been identified. The five- and six-ring aromatics are poorly defined but probably contain benz- and dibenzchrysenes, dibenzanthracenes, perylenes, and dibenzpyrenes. As the number of aromatic rings per molecule increases, so does the number of possible isomers; additional complexity is caused by alkyl substituents. Decant oil is produced at temperatures in excess of 900°F (480°C) and in the presence of a cracking catalyst. These are vigorous reaction conditions and the large alkyl groups attached to the aromatic molecules in the heavy petroleum distillates are reduced to only a few carbon atoms in size. The complex nature of decant oil, combined with the wide variety of possible reactions, makes it essentially impossible to completely define the chemical processes occurring during pyrolysis. However, based on the readily determined products of pyrolysis, the overall conversion of decant oil may be represented by Equation 2.



While we are concerned primarily with the formation of β -resins and coke, the composition of the gases and light products provides qualitative information about the reaction sequences that lead to the formation of

these high molecular weight components. Table III contains compositional data obtained by mass spectrometry on the gases and light products.

The oil component is the benzene soluble material and contains unreacted decant oil. In addition, as proposed later in the discussion, the oil component probably contains the β -resin precursors, which are entities distinct from the original decant oil components.

Table III. Gases and Light Hydrocarbon Pyrolysis Products^a

| <i>Component</i> | <i>Mol %</i> |
|--|--------------|
| Hydrogen | 3.6 |
| Methane | 65.7 |
| Ethane | 14.5 |
| Propane | 5.9 |
| C ₂ -C ₇ olefins | 1.6 |
| C ₄ -C ₇ paraffins | 7.6 |

^a Analysis obtained by mass spectrometry. The above sample of pyrolysis product was obtained at 835°F, 300 psig, in a continuous-flow coil reactor, residence time 45 min.

Kinetics of β -Resin Formation. Pyrolysis experiments were performed on the decant oil at 800°, 825°, 850°, and 980°F (430°, 440°, 450°, and 530°C, respectively) in a closed vessel under an inert atmosphere and under the pressure generated by the pyrolytic reactions. It has been established in a number of studies that for temperatures below about 1000°F (540°C) the pyrolysis of petroleum and related hydrocarbons can be described by first-order rate equations (14, 15, 16). An integrated form of the first-order rate equation is shown in Equation 3:

$$\log_{10} (A_0 - X) = \frac{-kt}{2.303} + \text{constant} \quad (3)$$

where t = reaction time, x = weight percent of product formed in time t , A_0 = initial weight percent of starting material, and k = specific rate or velocity constant.

Using this form of the rate equation, with $A_0 = 100$, the β -resin data obtained at 800°, 825°, and 850°F (430°, 440°, and 450°C, respectively) are plotted in Figure 1. The first-order rate equation produces a series of reasonably straight lines, but only after the reaction has passed through what appears to be some form of induction period. The data obtained at 980°F (530°C) (not shown in Figure 1 because of the much smaller time interval involved) produces a plot with similar character-

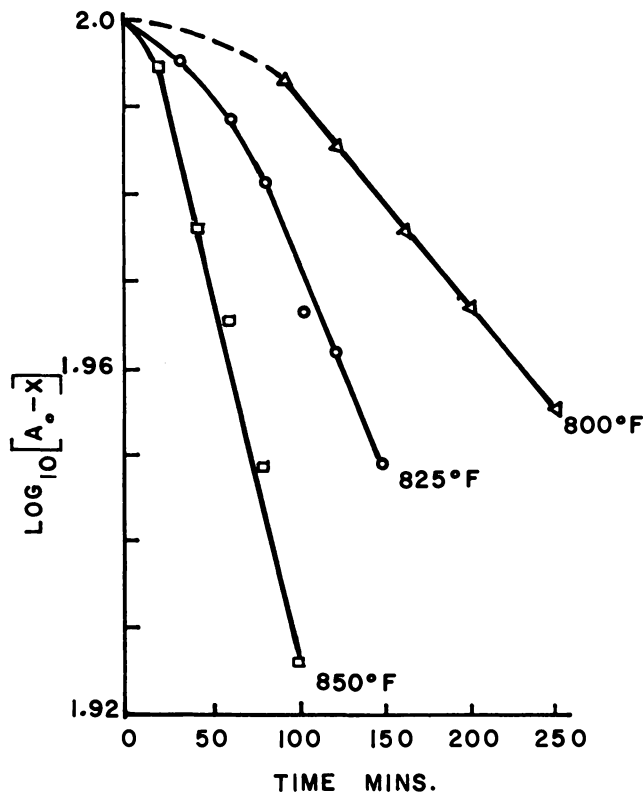


Figure 1. First-order kinetic plot for β -resins

istics. This pseudo-induction period is clearly temperature dependent. To eliminate the possibility that it was due to slow temperature recovery in the furnace, the sample always was preheated. Subsequent to the nonlinear portion of the curve, the reaction shows apparent first order kinetics. This is true at least to the extent to which the reaction was followed for most of the temperatures employed. However, as discussed later, at levels of β -resin formation greater than about 16%, the first-order rate equation no longer produces a straight line.

The rate constant was calculated from the linear portion of each plot for the four temperatures used. The temperatures and rate constants are plotted in the Arrhenius equation in Figure 2. A reasonably straight-line relationship is obtained and an activation energy for β -resin formation of 49 kcal is obtained from the slope of the plot.

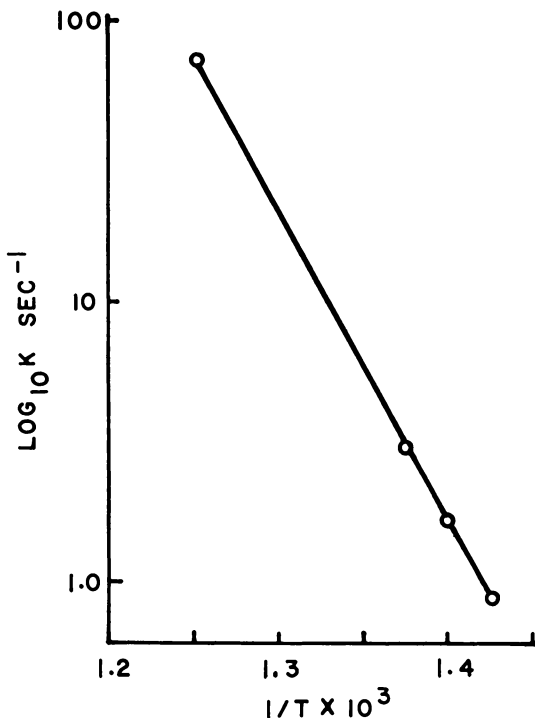


Figure 2. Arrhenius plot for β -resins

Kinetics of Coke Formation. On the basis of the x-ray diffraction data, the QI can be considered equivalent to coke and for the remainder of the discussion the term coke will be used in place of QI. The first-order rate equation was applied to the data for coke formation. The plots of these data in Figure 3 are similar to the curves produced with the β -resin results. A temperature-dependent induction period is obtained, followed by a reaction sequence that shows a reasonable fit with the first-order kinetic equation. Rate constants calculated from the linear portion of each curve are plotted in the Arrhenius equation in Figure 4. From the slope of the best straight line for the data points in Figure 4, the activation energy for coke formation is found to be 61 kcal.

The temperature-dependent induction period exhibited for the formation of coke bears a superficial resemblance to the characteristics of an autocatalytic reaction. Though it is not suggested that the formation of coke is necessarily autocatalytic, the presence of an induction period indicates that the coke is not being formed directly from the decant oil components, but rather from some intermediate product or products.

Thus, before the rate of coke formation can build up to a steady level, the coke precursors must reach some suitable concentration. At this point, the most logical candidates for coke precursors are the β -resins. Plotting the amount of coke formed as a simple function of the quantity of β -resins produces the curve shown in Figure 5. The β -resins/coke data obtained at 800°, 825°, and 850°F (430°, 440°, and 450°C, respectively) lie approximately on the same curve, while the data obtained at 980°F (530°C) follow a separate curve. At relatively low levels of β -resin formation the coke concentration increases only slowly, but as the β -resin concentration approaches 14–16%, the amount of coke formed rises rapidly and the two curves converge. In the pyrolysis runs where the reactions were terminated before the β -resin concentration had risen much above 10–12%, a substantial portion of the β -resin producing reaction follows first-order kinetics. However, if the pyrolysis reaction is allowed to continue, the concentration of β -resins levels off at about 16–17%, regardless of any further reaction, and the first-order relationship no longer

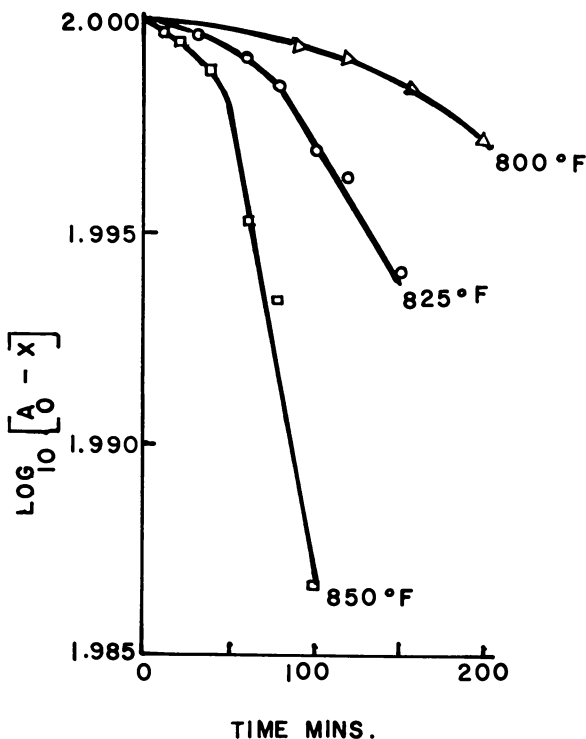


Figure 3. First-order kinetic plot for QI

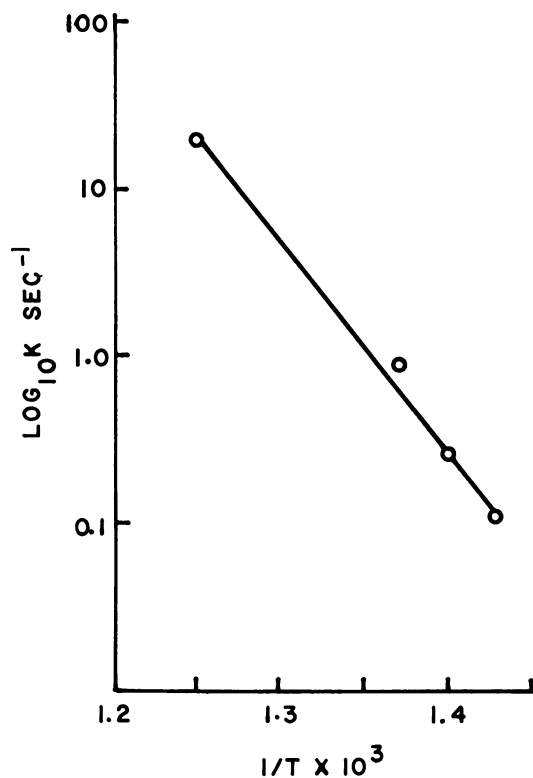
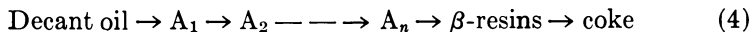


Figure 4. Arrhenius plot for QI

holds. At this point the concentration of coke rises rapidly, as indicated in Figure 5. Therefore, the β -resins reach an equilibrium concentration that is determined by the rate of coke formation from the β -resins and by the rate of the β -resins producing reaction.

In view of the induction period exhibited in the formation of β -resins and by analogy with the reaction sequence β -resins \rightarrow coke, it is reasonable to infer that the formation of β -resins is also dependent on a precursor species, which is distinct from the original components of the starting material. Therefore, it is possible to visualize the formation of β -resins and coke as two stages in a chain of reactions in which the end product is the coke. This sequence of reactions is illustrated by Equation 4.



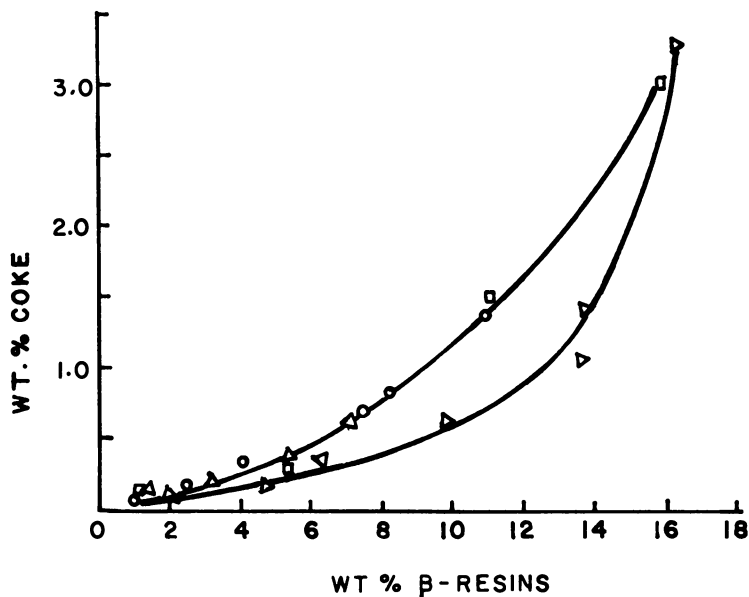
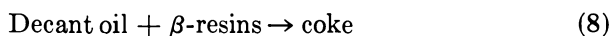
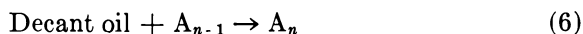


Figure 5. Coke formed vs. β -resins. (Δ), 800°F; (\circ) 825°F; (\square) 850°F; (∇), 900°F.

This concept is an oversimplification of the complexity of the reaction system; it is unlikely that the intermediate products are formed exclusively in sequential fashion, as suggested in Equation 4. The number of intermediate products in the sequence leading to coke is uncertain, but there are at least two—the β -resin precursors and the β -resins. As indicated earlier in the discussion, the β -resin precursors are probably found in the benzene soluble fraction. In work that will not be discussed in detail here, some evidence has been found for the existence of the β -resin precursors. When these are preformed in the decant oil and that material pyrolyzed, the induction period shown for β -resins in Figure 1 is absent. In speculating on the number of distinct intermediate products in the reaction chain, we emphasize that the technique of selective solvent extraction can be a poor discriminator between the different sizes of condensed aromatic systems. We are therefore limited in our interpretation of the reaction sequences by not being able to identify the products of each stage. Thus, the reactions shown in Equations 5, 6, and 7 may represent the main sequence of reactions, but it is virtually impossible to isolate the products formed by stepwise addition of the decant oil aromatics.



Considering the apparent molecular size differences between the β -resins and coke, it is unlikely that the coke is produced by the simple stepwise addition of decant oil aromatics to β -resins as shown in Equation 8.

The x-ray diffraction data for the β -resins and QI show these materials to be much larger condensed aromatic systems than the three, four, and five ring aromatics that predominate in the decant oil. Attempting to classify those aromatic components that undergo condensation most readily, a sample of decant oil was fractionated by high vacuum distillation into a number of narrower cuts. These cuts were then pyrolyzed at 825°F (440°C) for 100 min and the BI determined. Table IV shows the distribution of aromatics in each fraction according to ring number, as determined by mass spectrometry, and the amount of BI formed at 825°F (440°C). Although the range of aromatic types in these fractions is somewhat narrower than in the decant oil, the fractions are compositionally very complex. Therefore it is not possible to identify the role of each type of multiring aromatic in the formation of BI. A more general relationship can be examined by plotting the average number of aromatic rings per molecule for each of the cuts against the amount of BI formed. (see Figure 6). The curve is not very well defined because of insufficient data points, but there is a pronounced increase in the amount of BI formed as the number of aromatic rings per molecule increases from about four

**Table IV. Analysis of Decant Oil Fractions
Wt % Aromatics by Ring Number**

| Cut Num- ber | Boiling Range (°F) ^a | Aromatic Rings per Molecule | | | | | | Wt % BI ^b |
|--------------------|---------------------------------------|-----------------------------|------|------|------|------|------|-------------------------|
| | | 1 | 2 | 3 | 4 | 5 | ≥ 6 | |
| 1 | 457-597 | 13.5 | 56.4 | 15.1 | 1.1 | 0.0 | 0.0 | 0.25 |
| 3 | 660-729 | 2.6 | 5.1 | 41.8 | 31.9 | 4.2 | 0.0 | 2.30 |
| 5 | 777-787 | 0.0 | 1.0 | 18.0 | 54.8 | 8.9 | 0.0 | 4.50 |
| 7 | 810-854 | 0.0 | 0.7 | 6.5 | 53.7 | 16.2 | 0.0 | 7.6 |
| 8 | 854-957 | 0.0 | 0.0 | 0.9 | 17.0 | 49.6 | 18.0 | 13.6 |

^a Vacuum distillation data corrected to 760 mm Hg.

^b After sample was heated 100 min at 825°F.

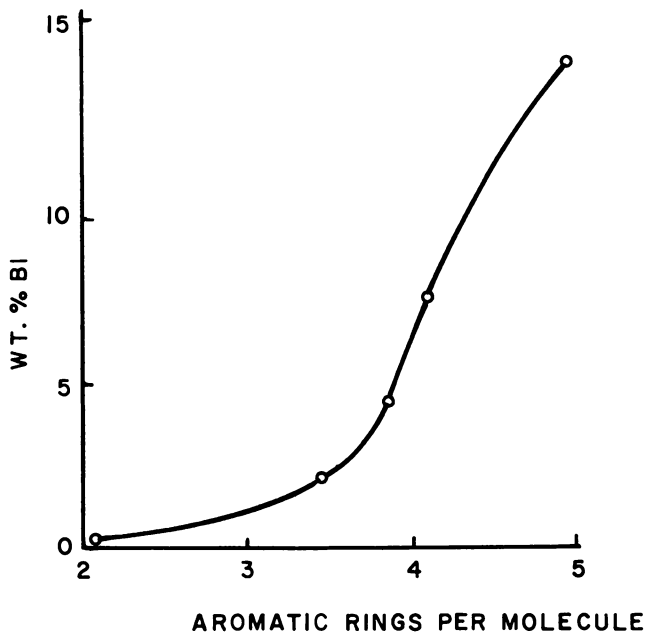


Figure 6. Average number aromatic rings per molecule vs. wt % BI formed

to five. King and Robertson (1) obtained a similar curve for the coking value vs. aromatic ring number of aromatic fractions obtained from both coal tar pitch and petroleum-derived pitch. These workers noted that the coking value rises sharply as the number of aromatic rings per molecule increases from four to five, then rises less rapidly for molecules containing more than five rings.

Polynuclear aromatic hydrocarbons can undergo a variety of thermally induced reactions. These include polymerization, dehydrogenation, and rearrangement, all reactions which can lead to the formation of higher molecular weight compounds. Unsubstituted polynuclear aromatics can polymerize via an aromatic free radical intermediate that is formed by the abstraction of a ring hydrogen atom. However, this is a relatively high energy reaction and many unsubstituted aromatics fail to show significant thermal reactivity below about 1000°F (540°C). With the reaction temperatures employed with the decant oil it is unlikely that such hydrogen abstraction occurs to any great extent. The small amount of hydrogen found in the pyrolysis gases (3.6 mol %, see Table III) may be indicative of the extent of this reaction, however, hydrogen could also have been derived from the alkyl substituents.

The thermal reactivity of polynuclear aromatics is influenced by their chemical structures and by the presence of substituent groups. The introduction of one methyl group into an aromatic compound can increase the compounds thermal reactivity quite markedly and reduce by about 100°F (38°C) the threshold temperature at which significant reaction will occur (17). The gaseous products formed during the pyrolysis of alkyl-substituted polynuclear aromatics depend on the degree and type of alkyl substitution. Madison and Roberts (17) have shown that methane is the primary gaseous product from the thermal condensation of methyl substituted multiring aromatics. With larger alkyl substituents, such as ethyl and propyl groups, the thermal reactivity increases and ethane and propane appear in the produced gases. The primary component of the decant oil pyrolysis gases at the temperatures investigated is methane, with lesser amounts of ethane and propane. These findings are consistent with the alkyl substituents in decant oil aromatics, which are predominantly methyl groups with some ethyl groups and possibly small amounts of propyl groups. In the early stages of the pyrolysis free radical formation probably takes place with the more readily broken alkyl C-C bonds of the larger alkyl substituents. These reactions produce ethane and propane and initiate the formation of larger aromatic structures. As the concentration of the initial condensation products increases, molecular rearrangements and additional free radical interactions with the decant oil aromatics lead to larger intermediate structures. However, as the more thermally reactive compounds and alkyl groupings become depleted it becomes progressively more difficult for the aromatic structures to increase in size. Consequently, there is a tendency for higher activation energies to be required for the formation of succeeding intermediate products.

The formation of coke and coke precursors has been discussed in the context of decant oil pyrolysis. However, it should be noted that coking reactions and the compounds in binder pitch that produce coke, also play a critical part in the formation of the finished carbon anode.

Literature Cited

1. King, L. F.; Robertson, W. D. *Fuel* 1968, 47, 197.
2. Alexander, C. D.; Bullough, V. L.; Pendley, J. W. 100th Annual Meeting of AIME and WAAIME, New York, March 1971; AIME Paper No. A71-29.
3. Reid, J. M.; Linden, H. R. *Prepr., Div. Pet. Chem., Am. Chem. Soc.* 1965, 11, B39.
4. King, L. F.; Robertson, W. D. *Am. Chem. Soc., Div. Fuel Chem., Prepr.* 1973, 138, 145.
5. Ball, G. L.; Cannon, C. R.; Newman, J. W. 101st Annual Meeting of AIME, San Francisco, Feb. 1972; AIME Paper No. A72-26.
6. Stokes, C. A. *Prepr., Div. Pet. Chem., Am. Chem. Soc.* 1975, 20, 690.

7. Moyle, M.; Galvez, B. B.; Pease, E. C.; Logan, A., U.S. Patent 4 039 423, 1977.
8. Charette, L. P.; Bischofberger, G. T. *Ind. Eng. Chem.* **1955**, 1412.
9. Darney, A. Industrial Carbon and Graphite Conference, Society of Chemical Industry, London, 1958, 152.
10. Mason, C. R. *Fuel* **1970**, *49*, 165.
11. Huettinger, K. J. *Bitumen, Teere, Asphalte, Peche* **1973**, *24*, 255.
12. Ozaki, H.; Yamane, M.; Takainin, T. *Bull. Jpn. Pet. Inst.* **1975**, *17*(2), 188.
13. Dietz, W. A.; King, W. H.; Priestly, W.; Rehner, J. *Ind. Eng. Chem.* **1952**, 1818.
14. Henderson, J. H.; Weber, L. *J. Can. Pet. Tech.* **1965**, 206.
15. Magaril, R. Z.; Aksenova, E. I. *Chem. Technol. Fuels Oils* **1970**, 509.
16. Barbour, R. V.; Dorrence, S. M.; Vollmer, T. L.; Harris, J. D. *Am. Chem. Soc., Div. Fuel Chem., Prepr.* **1976**, *21*(6), 278.
17. Madison, J. J.; Roberts, R. M. *Ind. Eng. Chem.* **1958**, 237.

RECEIVED October 2, 1978.

Modification of Thermal Alkylation with HCl

RICHARD K. LYON and JAMES E. MITCHELL

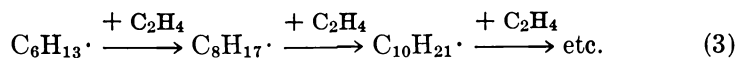
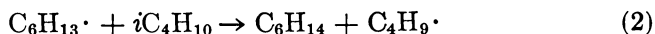
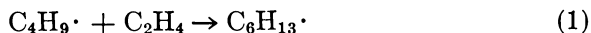
Corporate Research Laboratory, Exxon Research and Engineering Co.,
P.O. Box 45, Linden, NJ 07036

The thermal alkylation of ethylene-isobutane mixtures at high pressures in the gas phase has been studied in the presence and absence of HCl, and it has been found that HCl can (a) dramatically increase the total yield of alkylate, (b) increase the fraction of the alkylate which is C₆ rather than C₈, and (c) both increase and decrease the ratio of 2-methyl pentane to 2,2-dimethylbutane in the C₆ fraction of the alkylate, this latter depending on the amount of HCl used. All of these effects can be explained readily in terms of the generally accepted free radical mechanism of thermal alkylation, provided one assumes that HCl acts as a catalyst for those reaction steps that involve transfer of a hydrogen atom between a free radical and a hydrocarbon.

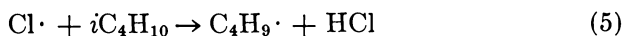
It is well known that HCl can serve as a catalyst in free radical reactions, for example, the thermal decomposition of neopentane (2) and ditertiary butyl peroxide (3). In these reactions the slow and rate-controlling step is a reaction of the type $R + R'H \rightarrow RH + R'$ where both R and R' are polyatomic radicals. The addition of HCl causes the rapid chain process, $R + HCl \rightarrow RH + Cl$ and $R'H + Cl \rightarrow R' + HCl$ to occur and to accelerate the overall reaction.

While it has been less generally recognized, there are free radical reaction systems in which hydrogen atom transfer between radicals is not rate controlling but does control the selectivity with which the various possible reaction products are formed. This chapter is a study of the effect of HCl on such a reaction system, the thermal alkylation of ethylene. (The effect of HCl upon this reaction was first disclosed in one of the author's patents (4). Several years after this disclosure, Schmerling (6) published a paper which, though differing in many details, showed

substantially the same effect.) Thermal alkylation of ethylene, especially with isobutane, has been repeatedly studied (5 and references cited therein). Since the ethylene-isobutane thermal alkylation was used commercially during World War II to produce aviation gasoline (1), many of these studies were conducted from a commercial viewpoint. It is generally accepted that the desired C₆ product is produced by a two-step nonbranching chain reaction (*see* Reactions 1 and 2). However, Reaction 2 is in competition with Reaction 3 sequence; which together with other similar reactions leads to the formation of low molecular weight, low quality polyethylene.



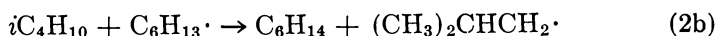
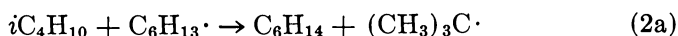
In past commercial practice this difficulty was solved by operating at high isobutane-to-ethylene ratios (typically 10 to 1) and at high total pressure (4500 psi in Ref. 4), thereby favoring Reaction 2 over Reaction 3 by mass action. This approach, while workable, has obvious practical disadvantages. Moreover, another and more elegant solution to the problem appears possible. If one adds HCl, then Reactions 4 and 5 may occur.



By analogy with reactions of known rate constants, one would expect both Reactions 4 and 5 to be rapid compared with Reaction 2. Since the sum of Reactions 4 and 5 is equivalent to Reaction 2, the effect of adding HCl is to catalyze Reaction 2 at the expense of reactions such as Reaction 3.

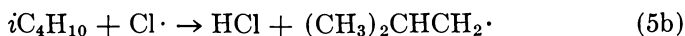
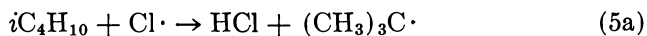
Thus, it would appear that catalyzing the thermal alkylation with HCl might achieve the same result as operation at high isobutane-to-ethylene ratio.

One also would expect that HCl catalysis would influence the nature of the C₆H₁₄ product formed. In the absence of HCl, Reaction 2 occurs by two different pathways (*see* Reactions 2a and 2b). Since Reaction 2a



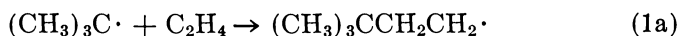
leads to the formation of 2,2-dimethyl butane (the desired isomer) and Reaction 2b leads to 2-methyl pentane (a much less useful isomer), the ratio of these two isomers will be k_{2a}/k_{2b} .

The first small additions of HCl will cause Reactions 5a and 5b to occur concurrently with Reactions 2a and 2b (*see* Reactions 5a and 5b).



The ratio of 2,2-dimethyl butane to 2-methyl pentane produced by these reactions will be k_{5a}/k_{5b} . In general, chlorine atom is less selective in hydrogen abstraction reactions than are hydrocarbon free radicals and hence $k_{2a}/k_{2b} \gg k_{5a}/k_{5b}$. Consequently, one would expect that the first increment of HCl would decrease the ratio of 2,2-dimethyl butane to 2-methyl pentane in the C_6 alkylation product.

However, as the HCl concentration is further increased, one would expect that the reverse reactions of Reactions 5a and 5b would become rapid compared with Reaction 1 and that the ratio of *tert*-butyl and *iso*-butyl radicals would tend toward its equilibrium value, $K_{t/i}$. In this equilibrium limit, the ratio of 2,2-dimethyl butane to 2-methyl pentane will be $K_{t/i}(k_{1a}/k_{1b})$, where 1a and 1b refer to the reactions:



The above arguments suggest that HCl may be used to alter significantly the reactions occurring during thermal alkylation and based on this interesting possibility, the experiments reported in the experimental section were carried out.

Experimental

Alkylation reactions were conducted in a 20-mL monel vessel. Measured amounts of the reactants were condensed into the vessel by cooling it to liquid nitrogen temperature. Thereafter, the vessel was heated to a temperature above the critical point of isobutane and was allowed to stand for 16 hr to assure complete mixing of the reactant gases. To carry out the reaction, the vessel was then rapidly heated in a sand bath for a measured time, and the reaction was terminated by depressurizing.

Light hydrocarbon products were analyzed with a P&E F-11 gas chromatograph with a benzyl cyanide-silver nitrate column and flame ionization detector. No effort was made to recover and analyze heavy hydrocarbons.

The bulk of these experiments was done using methane as an internal standard. Preliminary experiments showed that the ethylene isobutane

alkylation reaction did not produce observable product methane. Further, if one made the reasonable assumption that the percent of the methane internal standard which might be lost via alkylation to propane would be less than the percent of isobutane alkylated to 2-methyl pentane, the data showed that this source of error was trivial.

Results

Using a hydrocarbon mixture of 9.97 mol % CH_4 , 29.7 mol % C_2H_4 , and 60.3 mol % $i\text{C}_4\text{H}_{10}$, and various amounts of HCl , a series of runs was carried out at a reaction time of 30 min and reaction temperature of 399°C . During these runs the initial pressure of the hydrocarbons was held constant at 109 atm, and the total pressure varied slightly, depending on how much HCl was added.

As one would expect, the major products of the reaction were found to be C_6 paraffins (consisting solely of 2-methyl pentane and 2,2-dimethyl butane) and C_8 paraffins (predominantly 2,2-dimethyl hexane). The effect of varying amounts of HCl upon the yield of the alkylation reaction, the ratio of C_8H_{18} to C_6H_{14} in the alkylation product, and the ratio of 2-methyl pentane to 2,2-dimethyl butane within the C_6 product are shown in Figures 1, 2, and 3, respectively.

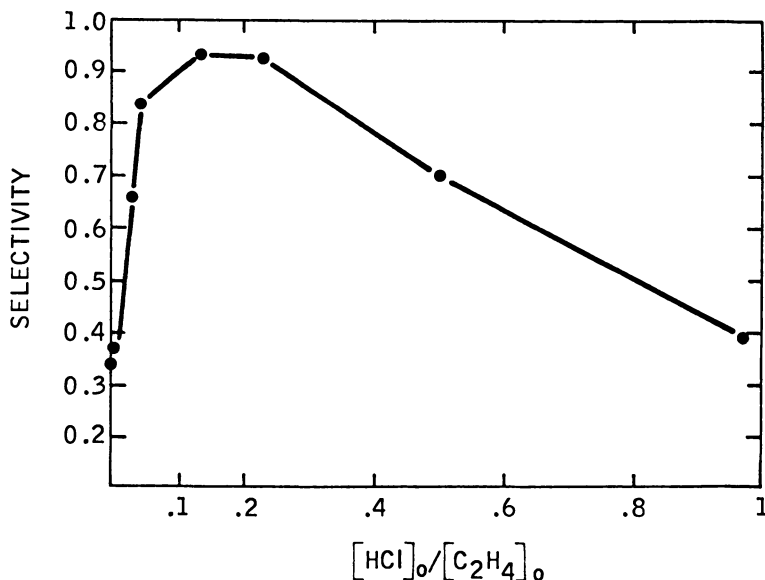


Figure 1. Effect of HCl upon the selectivity of the alkylation reaction. Selectivity based on ethylene consumption and defined as $([\text{C}_6\text{H}_{14}] + 2[\text{C}_8\text{H}_{18}])/\Delta[\text{C}_2\text{H}_4]$.

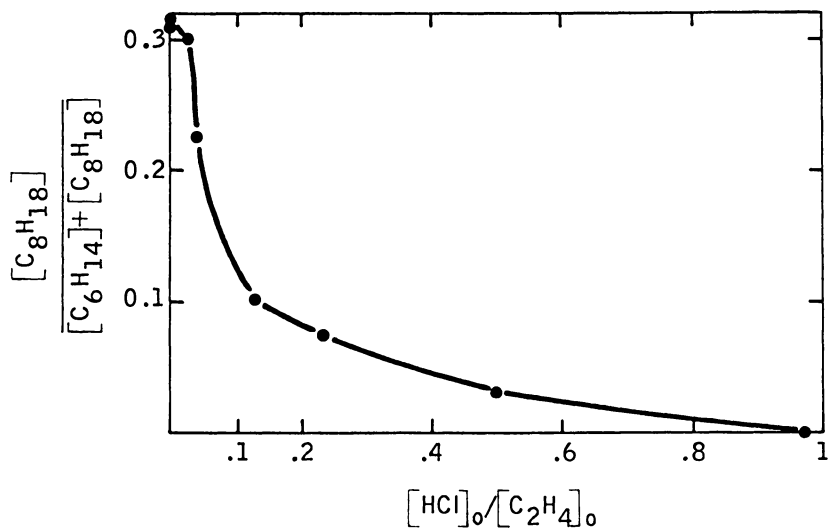


Figure 2. Effect of HCl on the fraction of C_8H_{18} within the $C_6 + C_8$ alkylate

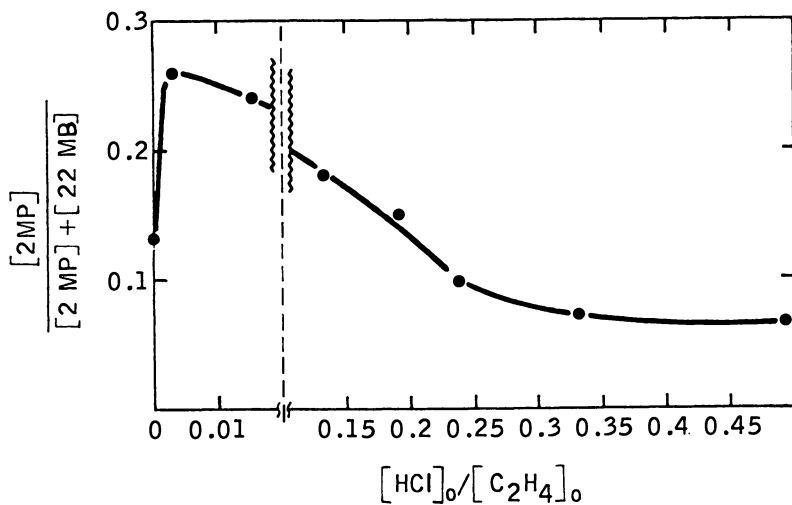


Figure 3. Effect of HCl on the fraction of 2-methyl pentane within the C_6 alkylate

Ethane and propane also were observed, propane being a minor product under all conditions and ethane being minor initially and increasing with increasing HCl:C₂H₄ ratio to be about 10% of the reacted ethylene at HCl:C₂H₄ = 0.5. Ethylene consumption averaged 60% ± 4% with no systematic dependence on HCl. Reaction times greater than 30 min showed increase ethylene consumption but no significant change in product distribution.

To study the relative ease with which various hydrocarbons undergo thermal alkylation with ethylene, a mixture of propane, normal butane, isobutane, and neopentane (9.2 mol % each), 4.6 mol % C₂H₄, and 17 mol % HCl were reacted at 399°C and at an initial pressure of 177 atm for 1 hr. The yields of the alkylation products (*n*C₅H₁₀ and *i*C₅H₁₀ from C₃H₈; *n*C₆H₁₄ and 3-methyl pentane from *n*C₄H₁₀; 2-methyl pentane and 2,2-dimethyl butane from isobutane; and 2,2-dimethyl pentane from neopentane) were measured and are shown in Table I on a relative basis.

Table I. Relative Yields During HCl-Catalyzed C₂H₄ Alkylation^a

| Reaction | Relative Yield |
|---|----------------|
| C ₃ H ₈ + C ₂ H ₄ → <i>i</i> C ₅ H ₁₂ | 0.077 |
| C ₃ H ₈ + C ₂ H ₄ → <i>n</i> C ₅ H ₁₂ | 0.24 |
| <i>n</i> C ₄ H ₁₀ + C ₂ H ₄ → <i>n</i> C ₆ H ₁₄ | 0.105 |
| <i>n</i> C ₄ H ₁₀ + C ₂ H ₄ → 3MP | 0.38 |
| C(CH ₃) ₄ + C ₂ H ₄ → 22DMP | 0.043 |
| <i>i</i> C ₄ H ₁₀ + C ₂ H ₄ → 2MP | 0.052 |
| <i>i</i> C ₄ H ₁₀ + C ₂ H ₄ → 22DMB | 1 |

^a By an equimolar mixture of C₃H₈, *n*C₄H₁₀, *i*C₄H₁₀, and C(CH₃)₄.

Discussion

Although the effect of HCl upon the alkylation reaction is dramatic, it is largely what one would expect based on the mechanistic considerations given in the introduction. Thus, the initial extreme improvement in selectivity shown in Figure 1 for addition of small amounts of HCl is in approximate accord with what one would expect based on estimates of the rate constants for hydrogen atom transfer among isobutane and primary free radicals directly and via HCl catalysis. The gradual decline in selectivity occurring at high [HCl]/[C₂H₄]₀ ratios may be attributable to formation of ethyl chloride which then decomposes largely to materials that are not recovered.

Defining the products of the alkylation reaction so as to include C₈H₁₈ and to exclude C₁₀H₂₂ and higher, is, of course, arbitrary and merely based on the fact that the former was convenient to recover and

analyze while the latter was not. The continuous decline in the C_8H_{18} portion of the alkylate with increasing $[HCl]/[C_2H_4]_0$ shown in Figure 2 is obviously consistent with the proposed mechanism.

Figure 3 shows that quantities of HCl which are too small to influence significantly the yield of $C_6 + C_8$ alkylate or the ratio of C_8 to C_6 can change substantially the product distribution within the C_6 fraction. While this may be surprising at first glance, it is to be remembered that both of the former relate to the competition between ethylene and HCl, the ethylene adding to the free radicals and the HCl transferring hydrogen atom to them, whereas the latter relates to the competition between isobutane and HCl at transferring hydrogen atoms to the free radicals. Since the latter competition is less stringent, it is understandable that less HCl is required to produce a significant effect.

The fact that the C_6 product distribution appears in Figure 3 to asymptotically approach a limiting value at high $[HCl]/[C_2H_4]_0$ is consistent with an equilibrium between *tert*-butyl and *iso*-butyl radicals. One then would expect that the relative yields in Table I also represent mutual equilibrium among the free radicals. In that case, the yield of each product relative to 2,2-dimethyl butane should be $K_{RH + t-Bu} = R \cdot + iC_4H_{10} (k_{R \cdot + C_2H_4}/k_{t-Bu \cdot + C_2H_4})$. Although the available thermodynamic data do not have sufficient precision to permit accurate calculation of relative rate constants from data such as those shown in Table I, such calculations were carried out and the results were sufficiently self consistent to warrant reporting them in qualitative terms. Of the four primary free radicals studied, the neopentyl radical had the lowest rate of addition to ethylene. In general, the rate of radical addition to ethylene and radical thermodynamic stability were inversely correlated, the more stable radicals being less reactive. Under conditions where radicals tend toward mutual equilibrium, the thermodynamic factor is dominant and the stable radicals produce most of the product despite their lack of reactivity.

Acknowledgment

The authors wish to thank David Benn for his skillful assistance in carrying out the experiments described.

Literature Cited

1. Alden, R. C. *Nat. Pet. News* 1940, 32(26R), 234.
2. Benson, S. W. "Thermochemical Kinetics," 2nd ed.; Wiley: New York, 1976; p. 253.
3. Benson, S. W. "Foundations of Chemical Kinetics"; McGraw-Hill: New York, 1960; p. 368.
4. Lyon, R. K. U.S. Patent 3 764 637, 1973.
5. Ridgway, J. A. *Ind. Eng. Chem.* 1958, 50, 1531.

6. Schmerling, L. "Free Radical-Induced Monoethylation with Ethylene," In "Industrial and Laboratory Alkylation," *ACS Symp. Ser.* 1977, 55, 147-166.

RECEIVED June 26, 1978.

Hydropyrolysis of Model Compounds

J. SHABTAI, R. RAMAKRISHNAN, and A. G. OBLAD

Department of Mining and Fuels Engineering, University of Utah,
Salt Lake City, UT 84112

Hydropyrolysis of representative C₁₀-C₁₆ n-paraffins and bicyclic naphthenes, e.g., n-hexadecane (1) and decalin (2), in the range of 500-600°C and hydrogen pressures of 500-2250 psi, is a faster and more selective process than conventional thermal cracking of such compounds under nitrogen pressure. Selectivity is reflected in the practical absence of any condensation reactions or coking. By coordination of operating variables hydropyrolysis of 1 can be directed to yield preferentially liquid (C₅-C₁₅) products. Paraffin:olefin and internal olefin:1-olefin ratios in the latter are controllable. Hydropyrolysis of 2 in the indicated range yields predominantly (55%-90%) liquid products, consisting of C₅-C₈ branched paraffins and olefins, C₆-C₁₀ cyclohexenes and cyclohexanes, and some C₆-C₈ arenes. Mechanistic schemes for hydropyrolysis of 1 and 2 are outlined.

Conventional thermal processes, e.g., coking, gas-oil cracking, and vis-breaking, are applied mainly for upgrading heavy oils and residues into lighter liquid fuels (1, 2). Hydropyrolysis, viz. thermal cracking under hydrogen pressure, is being used primarily in processes involving hydrodealkylation of alkylbenzenes (3, 4) and hydrogasification (5). Recent reports on a process for production of ethylene by hydropyrolysis of heavy petroleum cuts indicates that hydrogen promotes the cracking reaction, suppresses the formation of condensation products, and sharply decreases coking tendencies (6).

Conventional thermal cracking of pure hydrocarbons has been studied extensively in the past, and well-substantiated mechanistic proposals have been outlined (7-19). In contrast, hydropyrolysis of pure model compounds has been studied to a lesser extent and has been confined mostly to low (C₁-C₅) paraffins, and simple alkylbenzenes and naphthenoaro-

matics (20–25). To provide additional fundamental data on this process and contribute to a better evaluation of its scope and potential, systematic hydropyrolysis studies with model compounds, e.g., long-chain paraffins, polycyclic naphthenes, and multiring naphthoaromatics and heterocyclics have been undertaken. Results obtained with C_{10} – C_{16} *n*-paraffins and with a representative bicyclic naphthene, i.e., decalin, are presented in this chapter.

Hydropyrolysis of n-Paraffins

The hydropyrolysis of representative *n*-alkanes, and in particular of *n*-hexadecane (1), was investigated as a function of reaction temperature, hydrogen pressure, liquid hourly space velocity (LHSV), and contact time. In addition, a comparison with conventional thermal cracking of 1 was made by doing a parallel study with this compound under nitrogen pressure, using otherwise identical experimental conditions. The effect of chain length in the starting compound also was studied by comparative hydropyrolysis of *n*-alkanes having different carbon numbers (C_{10} – C_{16}). Experiments were carried out in a continuous flow reactor system described in the experimental section of this chapter. Products obtained were identified and quantitatively analyzed by a combination of gas chromatography (GC), ^1H NMR, and mass spectral methods (*see* Experimental section).

Results and Discussion. Table I summarizes a comparison of products obtained by hydropyrolysis and by thermal cracking of 1 at 525° and 575°C, under a pressure of 1,000 psig. The conversion of 1 in Experiment 1 is higher than that in Experiment 2 by a factor of about 1.8, reflecting a markedly higher reaction rate in hydropyrolysis than in ordinary thermal cracking. The C_{10} – C_{15} fraction in Experiment 1 is smaller, while the C_5 – C_9 fraction is larger, than the corresponding fractions in Experiment 2, indicating that the gradual cleavage of higher liquid-product components into lower ones is markedly faster in hydropyrolysis. At 525°C (Experiment 1) the gaseous product from hydropyrolysis is characterized by higher relative concentrations of C_3 – C_4 components and lower concentrations of methane and C_2 products than those of the corresponding fractions in Experiment 2. Differences in the depth and mode of decomposition are also found by comparing the results of Experiments 3 and 4 (575°C). However, the most important observation in these and other experiments is that hydropyrolysis is a versatile and easily controllable process, which by proper selection of temperature, pressure, and contact time can be operated for preferential formation of cracking products in any desired molecular weight range. The process is very clean even at high conversion and is essentially free of any sec-

Table I. Comparison of Product Distribution from Hydropyrolysis (HP) and Thermal Cracking (TC) of *n*-Hexadecane (1)^{a-c}

| | <i>Experiment Number</i> | | | |
|--|--------------------------|----------|----------|-------------------|
| | <i>1</i> | <i>2</i> | <i>3</i> | <i>4</i> |
| Reaction temperature (°C) | 525 | 525 | 575 | 575 |
| Type of reaction | HP | TC | HP | TC |
| Conversion of 1 (mol %) | 43.1 | 24.0 | ~ 100 | 75.2 ^d |
| Product distribution (wt %) | | | | |
| gas | 45.4 | 42.8 | 79.7 | 66.5 |
| liquid | 54.6 | 57.2 | 20.3 | 33.5 |
| Product component (mol %) ^e | | | | |
| CH ₄ | 32.2 | 43.9 | 76.3 | 81.0 |
| C ₂ H ₄ | 28.2 | 77.6 | 26.3 | 105.7 |
| C ₂ H ₆ | 83.2 | 64.3 | 174.1 | 83.8 |
| | 111.4 | 141.9 | 200.4 | 189.5 |
| C ₃ H ₆ | 37.4 | 47.7 | 36.6 | 80.8 |
| C ₃ H ₈ | 67.3 | 40.4 | 135.0 | 41.0 |
| | 104.7 | 88.1 | 171.6 | 121.8 |
| C ₄ H ₆ | 3.5 | 3.0 | 6.8 | 7.5 |
| 1-C ₄ H ₈ | 11.6 | 7.0 | 3.9 | 26.9 |
| 2-C ₄ H ₈ | 4.5 | — | 5.2 | — |
| C ₄ H ₁₀ | 17.2 | 9.3 | 26.8 | 11.6 |
| | 36.8 | 19.30 | 42.7 | 46.0 |
| C ₅ | 28.8 | 5.9 | 21.1 | 12.6 |
| C ₆ | 15.8 | 13.7 | 11.9 | 14.6 |
| C ₇ | 14.6 | 11.3 | 10.7 | 17.4 |
| C ₈ | 11.1 | 10.3 | 6.6 | 11.6 |
| C ₉ | 7.8 | 8.7 | 3.0 | 8.3 |
| | 78.1 | 49.9 | 53.3 | 64.5 |
| C ₁₀ | 7.1 | 10.8 | 2.3 | 3.6 |
| C ₁₁ | 5.8 | 10.6 | 1.4 | 2.3 |
| C ₁₂ | 5.2 | 9.1 | 1.0 | 1.8 |
| C ₁₃ | 5.6 | 7.7 | 0.6 | 1.5 |
| C ₁₄ | 4.8 | 6.0 | 0.3 | 1.1 |
| C ₁₅ | 1.7 | 3.0 | 0.1 | 0.3 |
| | 30.2 | 47.2 | 5.7 | 10.6 |

^a Pressure: 1000 psig.^b LHSV: 3.13 hr⁻¹.^c Experiments 1 and 3 were performed under hydrogen; Experiments 2 and 4 under nitrogen pressure; hydrogen (nitrogen) flow rate = 0.13 L/min at 1000 psig and 20°C (calculated contact time = 16 sec).^d Including 21.0% of high-boiling condensation products.^e Mol/100 mol of converted 1; for the purpose of comparison, condensation products in Experiment 4 were neglected.

Table II. Change in Product Composition from Hydropyrolysis of *n*-Hexadecane (1) as a Function of Reacted Temperature^{a-d}

| | <i>Experiment Number</i> | | | |
|---|--------------------------|----------|----------|----------|
| | <i>5</i> | <i>6</i> | <i>7</i> | <i>8</i> |
| Reaction temperature (°C) | 525 | 550 | 575 | 600 |
| Conversion of 1 (mol %) | 33.8 | 73.0 | 88.5 | ~ 100 |
| Product distribution (wt %) | | | | |
| gas | 40.1 | 51.6 | 66.3 | 83.4 |
| liquid | 59.9 | 48.4 | 33.7 | 16.6 |
| Product component (mol %) ^e | | | | |
| CH ₄ | 24.5 | 45.2 | 77.2 | 138.7 |
| C ₂ H ₄ | 39.5 | 48.2 | 63.2 | 50.0 |
| C ₂ H ₆ | 54.6 | 82.8 | 115.9 | 171.7 |
| C ₃ H ₆ | 41.0 | 52.2 | 69.5 | 62.8 |
| C ₃ H ₈ | 44.0 | 57.9 | 75.1 | 101.0 |
| C ₄ H ₆ | 6.7 | 5.2 | 1.5 | 5.1 |
| 1-C ₄ H ₈ | 12.6 | 6.6 | 5.2 | 3.5 |
| 2-C ₄ H ₈ | 5.2 | 14.7 | 13.2 | 18.1 |
| C ₄ H ₁₀ | 12.5 | 13.7 | 14.7 | 19.8 |
| <i>n</i> -C ₅ H ₁₂ | 1.3 | 6.0 | 16.2 | 2.6 |
| 1-C ₅ H ₁₀ | 4.7 | 3.2 | 1.2 | 0.2 |
| (i.o.)' C ₅ H ₁₀ | 0.1 | 6.1 | 7.0 | 1.4 |
| <i>n</i> -C ₆ H ₁₄ | 4.2 | 6.2 | 10.3 | 2.7 |
| 1-C ₆ H ₁₂ | 15.0 | 9.6 | 5.3 | 1.6 |
| (i.o.)' C ₆ H ₁₂ | 0.2 | 7.1 | 5.1 | 2.8 |
| <i>n</i> -C ₇ H ₁₆ | 2.6 | 5.1 | 4.7 | 2.9 |
| 1-C ₇ H ₁₄ | 9.6 | 7.9 | 4.8 | 1.6 |
| (i.o.)' C ₇ H ₁₄ | 0.1 | 5.8 | 5.1 | 5.4 |
| <i>n</i> -C ₈ H ₁₈ | 2.1 | 3.8 | 3.5 | .9 |
| 1-C ₈ H ₁₆ | 7.3 | 5.8 | 3.1 | 1.3 |
| (i.o.)' C ₈ H ₁₆ | 0.1 | 3.1 | 2.6 | 4.2 |
| <i>n</i> -C ₉ H ₂₀ | 2.5 | 3.1 | 2.4 | .6 |
| 1-C ₉ H ₁₈ | 9.5 | 4.7 | 1.2 | .6 |
| (i.o.)' C ₉ H ₁₈ | 1.1 | 1.9 | 1.0 | 1.7 |
| <i>n</i> -C ₁₀ H ₂₂ | 2.4 | 2.3 | .8 | .7 |
| 1-C ₁₀ H ₂₀ | 8.6 | 3.4 | 1.0 | .5 |
| (i.o.)' C ₁₀ H ₂₀ | .8 | 1.0 | 0.6 | .7 |
| <i>n</i> -C ₁₁ H ₂₄ | 2.0 | 1.6 | .6 | .4 |
| 1-C ₁₁ H ₂₂ | 7.2 | 2.3 | .2 | .2 |
| (i.o.)' C ₁₁ H ₂₂ | .5 | .6 | .1 | .6 |
| <i>n</i> -C ₁₂ H ₂₆ | 1.7 | 1.3 | .5 | .5 |
| 1-C ₁₂ H ₂₄ | 6.2 | 1.9 | .8 | .1 |
| (i.o.)' C ₁₂ H ₂₄ | .1 | .5 | .6 | .2 |

Table II. Continued

| | Experiment Number | | | |
|---|-------------------|-----|-----|-----|
| | 5 | 6 | 7 | 8 |
| <i>n</i> -C ₁₃ H ₂₈ | 1.5 | 1.0 | .3 | .3 |
| 1-C ₁₃ H ₂₆ | 5.6 | 1.5 | .5 | .2 |
| (i.o.) ^f C ₁₃ H ₂₆ | .1 | .6 | .2 | .3 |
| <i>n</i> -C ₁₄ H ₃₀ | 1.5 | .9 | .2 | .3 |
| 1-C ₁₄ H ₂₈ | 5.5 | 1.3 | .3 | .1 |
| (i.o.) ^f C ₁₄ H ₂₈ | — | .1 | .2 | .1 |
| <i>n</i> -C ₁₅ H ₃₂ | .5 | .2 | .02 | .02 |
| 1-C ₁₅ H ₃₀ | 1.9 | .4 | .03 | .02 |
| (i.o.) ^f C ₁₅ H ₃₀ | — | .05 | .02 | .02 |

^a Hydrogen pressure: 500 psig.

^b LHSV = 3.13 hr⁻¹.

^c In each experiment, **1** was pumped at the rate of 5 mL/min for 10 min.

^d Hydrogen flow rate = 0.12 L/min at 500 psi and 20°C (calculated contact time = 17.3 sec).

^e Mol/100 mol of converted **1**.

^f For each fraction i.o. stands for the total yield of internal (nonterminal) olefinic isomers.

ondary condensation reactions and/or coke formation. In contrast, ordinary thermal cracking at high conversion is accompanied to a considerable extent by secondary condensation and aromatization reactions, as well as coking (*see* Footnote d, Table I).

Table II and Figures 1–4 summarize the change in product composition from hydropyrolysis of **1** as a function of temperature (between 525°–600°C), keeping a constant hydrogen pressure (500 psig). As seen from Table II, the conversion of **1** increases from 33.8% at 525°C to about 100% at 600°C. Further, the relative yield of gas products increases while that of liquid products decreases with an increase in temperature.

The yield of methane increases with temperature (*see* Figure 1). The yield of ethane and propane increases while that of the corresponding C₂–C₃ olefins remains within a narrow range with increasing temperature. This is in contrast with composition patterns in steam cracking, in which the yield of olefinic products markedly increases with an increase in temperature. As seen in Figure 2, the yields of C₅–C₈ components in the liquid fraction tend toward a maximum around 550°–570°C and then decrease with further increase in temperature, *viz.* with further progress of the hydropyrolysis process. Also (*see* Table II), the yield of higher (C₉–C₁₅) products passes through a maximum at temperatures below 525°C.

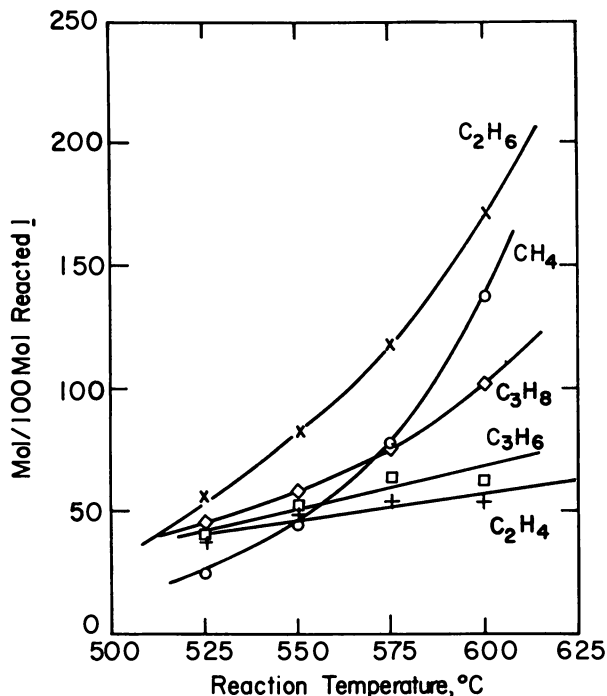


Figure 1. Change in concentration of C_1 - C_3 products from hydropyrolysis of 1 as a function of reaction temperature; pressure: 500 psig; LHSV: 3.1 hr^{-1} .

Figure 3 shows the change in relative yields of 1-olefins, internal olefins, and paraffins in the liquid product from hydropyrolysis of 1 as a function of reaction temperature. The relative concentration of 1-olefins decreases, whereas that of internal olefins and paraffins increases (and ultimately tends towards a stable level) with an increase in temperature. Figure 4 shows a similar change in type distribution for a particular liquid fraction (C_7 components). The observed trends indicate that C_5 - C_{15} 1-olefins are less stable at higher temperature, viz. more susceptible to reactions such as cracking, isomerization, or hydrogenation, than corresponding internal olefins. The Rice-Kossiakoff hypothesis of thermal cracking (10) indicates 1-olefins as the only type of anticipated monounsaturated products, viz. the observed formation of internal alkenes was not predicted.

An accurate determination of the activation energy for hydropyrolysis of *n*-hexadecane (1) was not possible since the conversions in the temperature range studied were too high for this purpose. However, the activation energy is estimated to be approximately 50 kcal/mol,

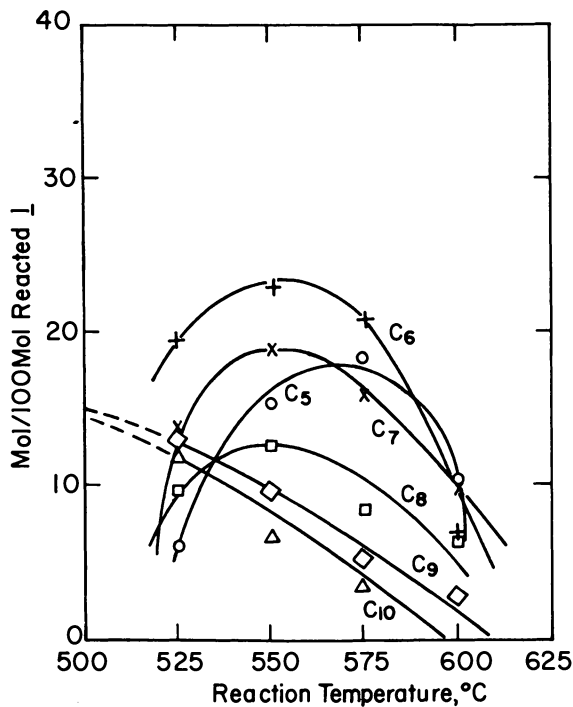


Figure 2. Change in liquid product composition (C_5 - C_{10} fraction) from hydro-pyrolysis of 1 as a function of reaction temperature; pressure: 500 psig; LHSV: 3.1 hr^{-1} .

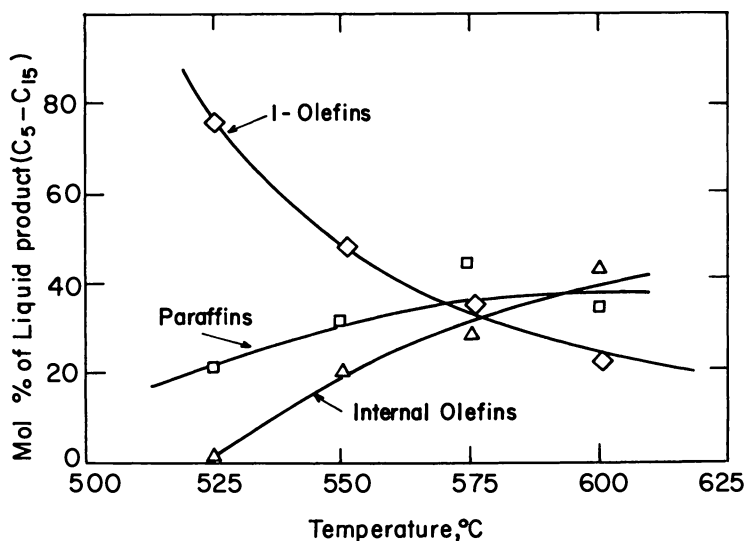


Figure 3. Change in composition of liquid product (C_5 - C_{15}) from hydro-pyrolysis of 1 as a function of reaction temperature; pressure: 500 psig; LHSV: 3.1 hr^{-1} .

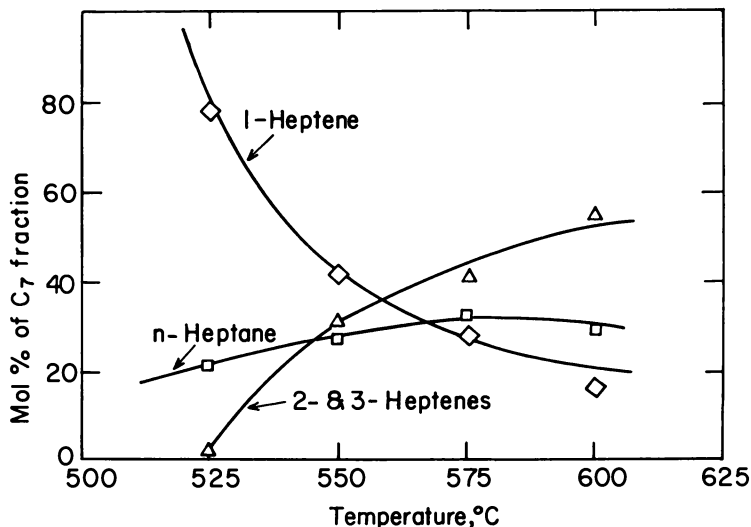


Figure 4. Change in composition of C_7 fraction from hydropyrolysis of 1 as a function of reaction temperature; pressure: 500 psig; LHSV: 3.1 hr^{-1} .

which is lower than the value of about 60 kcal/mol found for thermal cracking of 1. This indication is in agreement with the lower activation energy found for hydropyrolysis than for thermal cracking of decalin.

Table III and Figures 5–8 summarize the change in product composition from hydropyrolysis of 1 as a function of hydrogen pressure (500–2250 psig), keeping a constant reaction temperature of 575°C. The conversion of 1 increases with increase in pressure (*see* Table III). Further, the yield of gas products increases while that of liquid products decreases with an increase in pressure.

Examination of the change in composition of C_1 – C_4 gaseous products reveals that the relative yields of C_2 – C_4 olefins decrease and those of the corresponding C_2 – C_4 paraffins increase with hydrogen pressure up to about 1500 psig (*see* also Figure 5). However, the concentrations of all individual C_1 – C_4 components reach a stable level at higher hydrogen pressures (1500–2250 psig). Methane is formed in lower yields than ethane and propane in the entire pressure range examined.

Figure 6 shows that for a given temperature the yield of C_5 – C_{10} liquid products decreases with increasing hydrogen pressure, reflecting an increase in the depth of the cracking process. The same trend with increasing pressure is observed for C_{11} – C_{15} liquid products (*see* Table

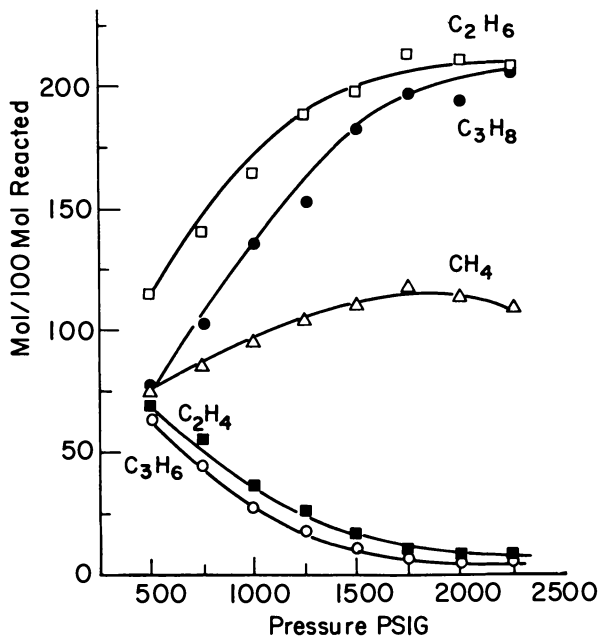


Figure 5. Change in concentration of C_1 - C_3 products from hydropyrolysis of 1 as a function of reaction pressure; temperature: 575°C ; LHSV: 3.1 hr^{-1} .

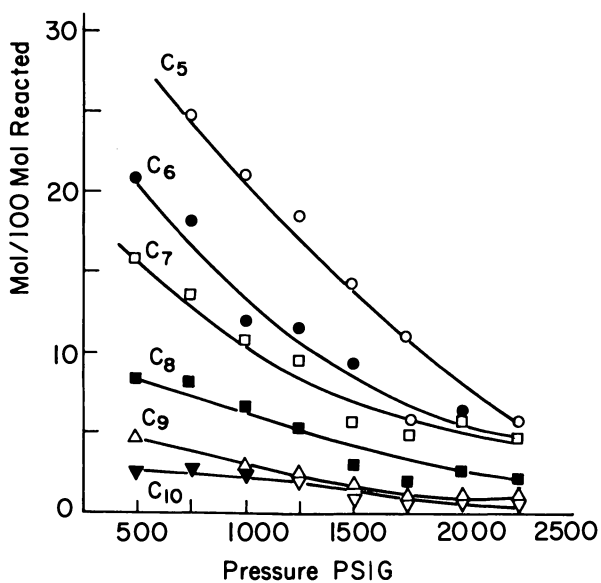


Figure 6. Change in product composition (C_5 - C_{10}) from hydropyrolysis of 1 as a function of hydrogen pressure; temperature: 575°C ; LHSV: 3.1 hr^{-1} .

Table III. Change in Product Composition from Hydropyrolysis

| | Experiment Number | | |
|---|-------------------|-------|-------|
| | 9 | 10 | 11 |
| Hydrogen pressure (psig) | 500 | 750 | 1,000 |
| Conversion of 1 (mol %) | 88.5 | 92.6 | 97.3 |
| Product distribution (wt %) | | | |
| gas | 66.3 | 68.2 | 79.7 |
| liquid | 33.7 | 31.8 | 20.3 |
| Product component (mol %) ^a | | | |
| CH ₄ | 77.2 | 85.5 | 96.3 |
| C ₂ H ₄ | 63.0 | 44.7 | 24.3 |
| C ₂ H ₆ | 116.0 | 141.2 | 166.1 |
| C ₃ H ₆ | 70.0 | 55.2 | 36.6 |
| C ₃ H ₈ | 75.0 | 102.7 | 135.0 |
| C ₄ H ₆ | 1.5 | 2.9 | 3.8 |
| 1-C ₄ H ₈ | 5.2 | 2.7 | 3.9 |
| 2-C ₄ H ₈ | 13.2 | 7.8 | 5.2 |
| C ₄ H ₁₀ | 14.7 | 17.8 | 26.8 |
| <i>n</i> -C ₅ H ₁₂ | 16.2 | 14.9 | 16.2 |
| 1-C ₅ H ₁₀ | } 8.2 | 9.5 | 4.9 |
| (i.o.) ^b C ₅ H ₁₀ | | | |
| <i>n</i> -C ₆ H ₁₄ | 10.3 | 7.7 | 5.9 |
| 1-C ₆ H ₁₂ | 5.3 | 5.5 | 2.3 |
| (i.o.) ^b C ₆ H ₁₂ | 5.1 | 5.2 | 3.8 |
| <i>n</i> -C ₇ H ₁₆ | 4.7 | 5.2 | 5.4 |
| 1-C ₇ H ₁₄ | 4.8 | 4.7 | 1.9 |
| (i.o.) ^b C ₇ H ₁₄ | 6.1 | 4.5 | 3.4 |
| <i>n</i> -C ₈ H ₁₈ | 3.5 | 2.9 | 3.3 |
| 1-C ₈ H ₁₆ | 3.1 | 3.2 | 1.2 |
| (i.o.) ^b C ₈ H ₁₆ | 2.6 | 2.7 | 2.3 |
| <i>n</i> -C ₉ H ₂₀ | 2.4 | 1.2 | 1.5 |
| 1-C ₉ H ₁₈ | 2.2 | 2.1 | .7 |
| (i.o.) ^b C ₉ H ₁₈ | — | 1.0 | 0.9 |
| <i>n</i> -C ₁₀ H ₂₂ | .8 | 1.2 | 1.1 |
| 1-C ₁₀ H ₂₀ | 1.6 | 1.4 | .7 |
| (i.o.) ^b C ₁₀ H ₂₀ | .1 | .5 | .5 |
| <i>n</i> -C ₁₁ H ₂₄ | .6 | .5 | .8 |
| 1-C ₁₁ H ₂₂ | .4 | .3 | .03 |
| (i.o.) ^b C ₁₁ H ₂₂ | .1 | .1 | .3 |
| <i>n</i> -C ₁₂ H ₂₆ | .5 | .4 | .6 |
| 1-C ₁₂ H ₂₄ | .8 | .5 | .2 |
| (i.o.) ^b C ₁₂ H ₂₄ | .6 | .3 | .2 |

of *n*-Hexadecane (1) as a Function of Hydrogen Pressure^{a-d}

| <i>Experiment Number</i> | | | | |
|--------------------------|-----------|-----------|-----------|-----------|
| <i>12</i> | <i>13</i> | <i>14</i> | <i>15</i> | <i>16</i> |
| 1,250 | 1,500 | 1,750 | 2,000 | 2,250 |
| 97.9 | > 99 | 100 | 100 | 100 |
| 80.0 | 87.7 | 88.7 | 88.9 | 91.6 |
| 20.0 | 12.3 | 11.3 | 11.1 | 8.4 |
| 105.0 | 111.0 | 114.6 | 115.0 | 110.3 |
| 17.07 | 10.5 | 7.0 | 5.6 | 4.9 |
| 189.5 | 199.4 | 210.6 | 211.6 | 209.5 |
| 26.2 | 17.2 | 10.5 | 8.3 | 7.4 |
| 153.2 | 183.0 | 192.8 | 195.4 | 206.7 |
| 3.9 | 2.4 | 3.7 | 3.1 | 3.4 |
| 2.7 | — | — | — | — |
| 2.9 | 1.8 | — | — | — |
| 26.5 | 40.8 | 42.9 | 38.5 | 43.1 |
| 15.8 | 14.7 | 10.2 | 9.3 | 6.0 |
| 2.4 | .4 | — | — | — |
| 6.9 | 4.8 | 4.2 | 5.2 | 3.6 |
| .8 | .2 | — | — | — |
| 4.2 | 3.3 | 2.9 | 2.2 | 2.1 |
| 5.6 | 4.2 | 3.7 | 3.8 | 3.1 |
| .7 | .2 | — | — | — |
| 1.8 | 2.3 | 1.6 | 2.0 | 1.7 |
| 3.3 | 2.0 | 1.3 | 1.9 | 1.6 |
| 0.4 | 0.1 | — | — | — |
| 1.6 | 2.3 | .6 | .7 | .6 |
| 1.6 | 1.0 | .8 | .9 | .8 |
| .3 | .1 | — | — | — |
| .5 | .4 | .2 | .1 | .2 |
| 1.4 | .9 | .6 | .8 | .4 |
| .2 | .1 | — | — | — |
| .3 | .1 | .1 | .1 | — |
| .9 | .5 | .4 | .3 | .1 |
| .1 | .03 | — | — | — |
| .2 | .1 | .03 | — | — |
| .6 | .4 | .2 | .1 | .1 |
| .1 | .02 | — | — | — |
| .2 | .1 | .02 | .01 | — |

Table III.

| | <i>Experiment Number</i> | | |
|---|--------------------------|-----------|-----------|
| | <i>9</i> | <i>10</i> | <i>11</i> |
| <i>n</i> -C ₁₃ H ₂₈ | .3 | .2 | .4 |
| 1-C ₁₃ H ₂₆ | .6 | .2 | .1 |
| (i.o.)' C ₁₃ H ₂₆ | .1 | .1 | .1 |
| <i>n</i> -C ₁₄ H ₃₀ | .21 | .18 | .16 |
| 1-C ₁₄ H ₂₈ | .36 | .18 | .07 |
| (i.o.)' C ₁₄ H ₂₈ | .04 | .06 | .07 |
| <i>n</i> -C ₁₅ H ₃₂ | .02 | .04 | .04 |
| 1-C ₁₅ H ₃₀ | .03 | .05 | .02 |
| (i.o.)' C ₁₅ H ₃₀ | .01 | .02 | .02 |

^a Temperature: 575°C.

^b LHSV: 3.13 hr⁻¹.

^c In each experiment 1 was pumped at the rate of 5 mL/min for 10 min.

^d The hydrogen flow rate was adjusted to give a contact time of 16 sec.

III). Maximal yields of C₅–C₁₅ products from 1 at 575°C should be reached at lower hydrogen pressures (< 500 psig) and/or shorter contact times (< 16 sec) than those used in the present study.

Figure 7 indicates the change in relative yields of 1-olefins, internal olefins, and paraffins in the C₅–C₁₅ liquid products as a function of hydrogen pressure. For a selected temperature (575°C) the concentration of paraffins increases with increasing pressure until it reaches a stable level between 1500–2250 psig. On the other hand, the concentration of 1-olefins decreases sharply, while that of internal olefins increases and then remains at a stable level, with increase in pressure. Figure 8 shows a similar change in type distribution for a particular liquid fraction (C₇ components).

The change in product composition from hydropyrolysis of 1 was also investigated as a function of LHSV in the range of 1.6–9.4 hr⁻¹ (reaction temperature, 575°C; hydrogen pressure, 500 psi). An increase in LHSV in this range corresponds to a decrease in the H₂:1 molar ratio from 17.2 to 2.0. There is only a slight decrease (from 90 mol % to 82 mol %) in the overall conversion of 1 with an increase in LHSV in the above indicated range. Also, the yield of gaseous products decreases while that of liquid products increases with an increase in LHSV, reflecting a decrease in the depth of hydropyrolysis with a decrease in the H₂:1 molar ratio. The changes in product composition were consistent with the patterns observed in the study of the temperature and pressure effects.

Continued

| <i>Experiment Number</i> | | | | |
|--------------------------|------|------|-----|-----|
| 12 | 13 | 14 | 15 | 16 |
| .4 | .2 | .7 | .7 | .1 |
| .1 | .03 | — | — | — |
| .1 | — | — | — | — |
| .18 | .08 | .04 | .04 | .07 |
| .03 | .01 | — | — | — |
| .05 | .03 | .01 | — | — |
| .04 | 0.03 | 0.02 | .01 | .02 |
| .01 | — | — | — | — |
| .02 | .01 | — | — | — |

* Mol/100 mol of reacted 1.

† For each fraction i.o. stands for the total yield of internal (nonterminal) olefinic isomers.

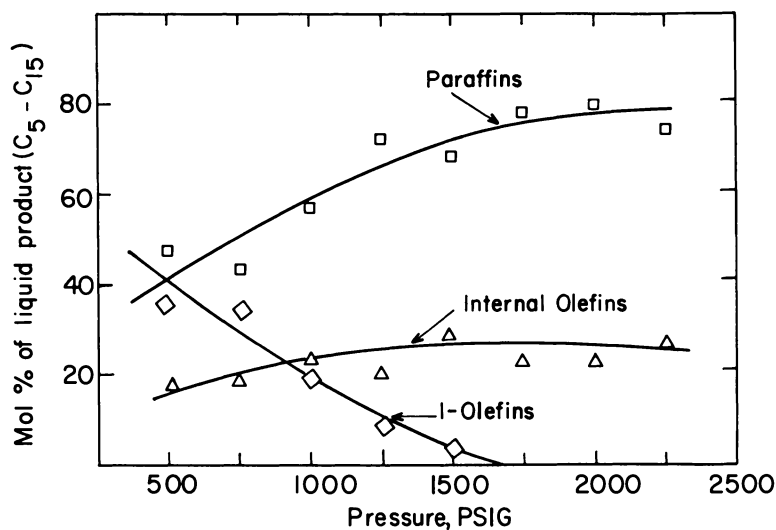


Figure 7. Change in composition of liquid product (C_5-C_{15}) from hydro-pyrolysis of 1 as a function of hydrogen pressure; temperature: 575°C ; LHSV: 3.1 hr^{-1} .

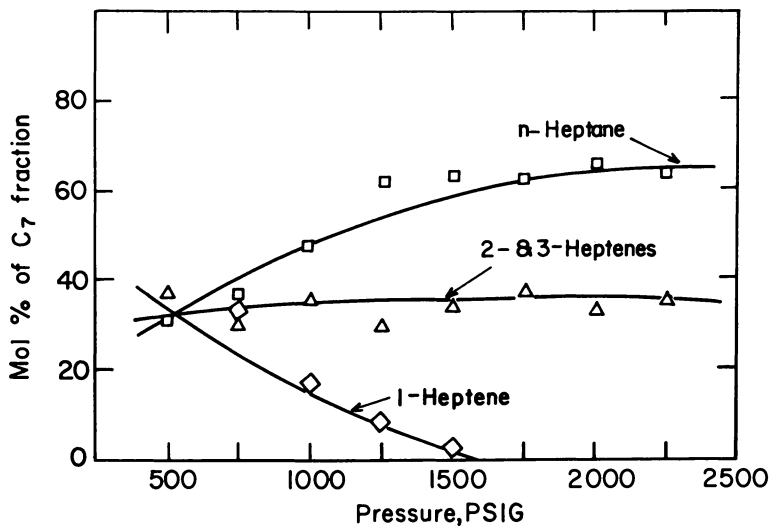


Figure 8. Change in composition of C_7 fraction from hydropyrolysis of 1 as a function of pressure; temperature: 575°C ; LHSV: 3.1 hr^{-1} .

The effect of paraffinic chain length upon product composition was also examined by performing comparative hydropyrolysis studies of C_{10} – C_{16} *n*-paraffins. Results obtained are summarized in Table IV. The contact time in Experiments 17, 18, and 19 was 3 sec; that in Experiments 20, 21, and 22 was 16 sec.

In the series of Experiments 17, 18, and 19, the conversion of the starting paraffin decreases markedly with decreasing chain length. Formation of gaseous products increases while that of liquid products decreases with decreasing chain length. Examination of the product composition data reveals close similarities in the concentrations of C_1 – C_3 gaseous products from the examined C_{10} – C_{16} *n*-paraffins. On the other hand, there are significant differences in the distribution of higher products, as the concentrations of all individual product components with more than four carbon atoms decrease as the chain length in the starting *n*-paraffin decreases from C_{16} to C_{10} . This is understandable because the hydropyrolysis sequence leading to lower products becomes shorter with decreasing chain length. The same general dependence upon chain length is observed at the higher contact time (Experiments 20, 21, and 22), although in this case the differences found are less pronounced because of the very high feed conversions.

Table IV. Change in Product Composition from Hydropyrolysis of *n*-Paraffins as a Function of Chain Length^{a-e}

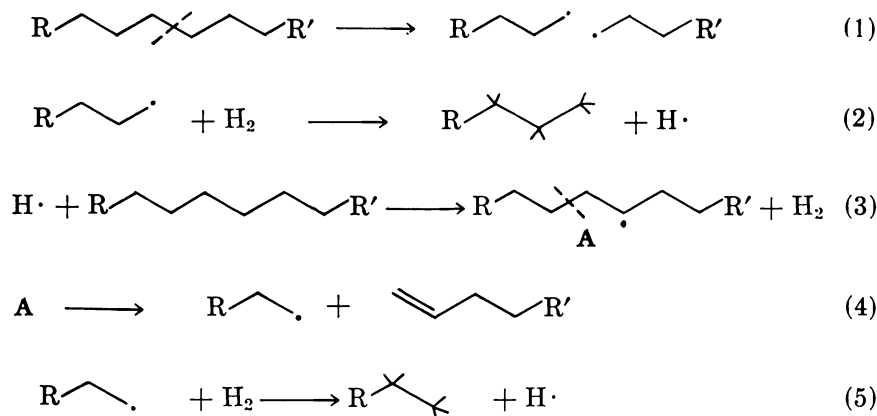
| | <i>Experiment Number</i> | | | | | |
|---|--------------------------|-----------------|-----------------|-----------------|-----------------|-----------------|
| | 17 | 18 | 19 | 20 | 21 | 22 |
| <i>n</i> -Paraffin | C ₁₀ | C ₁₂ | C ₁₆ | C ₁₀ | C ₁₂ | C ₁₄ |
| Conversion (mol %) | 39.8 | 45.9 | 64.5 | 82.15 | 87.2 | 89.4 |
| Product distribution (wt %) | | | | | | |
| gas | 88.1 | 78.1 | 59.4 | 72.6 | 66.7 | 59.3 |
| liquid | 11.9 | 21.9 | 40.6 | 27.4 | 33.3 | 40.7 |
| Product components (mol %) ^f | | | | | | |
| CH ₄ | 61.7 | 63.7 | 61.4 | 58.6 | 69.2 | 69.2 |
| C ₂ H ₄ | 68.5 | 77.6 | 65.6 | 39.3 | 46.7 | 50.0 |
| C ₂ H ₆ | 116.6 | 111.3 | 110.0 | 100.0 | 105.8 | 106.2 |
| C ₃ H ₆ | 57.1 | 58.1 | 54.0 | 42.2 | 46.5 | 50.4 |
| C ₃ H ₈ | 62.8 | 56.6 | 63.3 | 57.1 | 57.4 | 60.3 |
| C ₄ H ₆ | 1.6 | 2.4 | 5.5 | 1.3 | 1.6 | 1.8 |
| 1-C ₄ H ₈ | 0.8 | 2.1 | 7.9 | 3.3 | 3.7 | 3.7 |
| 2-C ₄ H ₈ | 1.0 | 2.8 | 15.4 | 6.1 | 7.4 | 7.9 |
| C ₄ H ₁₀ | 4.8 | 5.5 | 12.5 | 8.7 | 7.0 | 7.4 |
| C ₅ | — | 4.4 | 9.6 | 13.3 | 20.1 | 26.8 |
| C ₆ | 6.2 | 5.9 | 15.2 | 11.1 | 15.8 | 20.6 |
| C ₇ | 4.0 | 6.5 | 12.6 | 9.0 | 11.7 | 16.7 |
| C ₈ | 3.7 | 6.6 | 9.6 | 5.1 | 7.1 | 9.1 |
| C ₉ | 2.6 | 5.9 | 8.0 | 2.0 | 4.1 | 4.5 |
| C ₁₀ | — | 5.3 | 6.7 | — | 2.3 | 3.7 |
| C ₁₁ | — | 1.6 | 6.7 | — | 0.8 | 2.7 |
| C ₁₂ | — | — | 4.3 | — | — | 1.1 |
| C ₁₃ | — | — | 3.6 | — | — | 0.3 |
| C ₁₄ | — | — | 2.7 | — | — | — |
| C ₁₅ | — | — | 1.2 | — | — | — |

^a Temperature: 575°C.^b Hydrogen pressure: 500 psig.^c In Experiments 17–19, hydrogen flow rate = 0.78 L/min (calculated contact time = 3 sec).^d In Experiments 20–22, hydrogen flow rate = 0.118 L/min (calculated contact time = 16 sec).^e In each experiment the feed was pumped at the rate of 5 mL/min for 10 min.^f Mol/100 mol of converted *n*-paraffin.

Mechanism of Hydropyrolysis of *n*-Paraffins. The hydrogen:carbon ratio in the total hydropyrolysis product from **1** is higher (H:C > 2.2) than that in **1** itself (H:C = 2.12) in all experiments performed (Tables II and III). This clearly indicates participation of hydrogen in the process. To account for the observed differences between hydropyrolysis and conventional thermal cracking (Table I), and to rationalize the variations in product composition as a function of reaction conditions,

the following mechanism for hydropyrolysis of *n*-paraffins could be considered (Scheme 1):

Scheme 1. Proposed mechanism for hydropyrolysis of n-paraffins



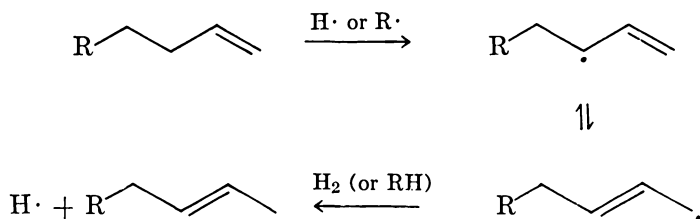
The initiation step in hydropyrolysis is probably the same as in thermal cracking, i.e., homolytic cleavage of a C-C bond to produce two lower-molecular weight primary radicals (Step 1). The radicals formed could undergo to some extent β -scission, but would be stabilized preferentially by interaction with molecular hydrogen (Step 2), which is present in large excess in the system. Hydrogen atoms thus produced can propagate the radical chain by abstracting hydrogen from other hydrocarbon molecules (Step 3). Such abstraction would yield preferably secondary radicals (A), which upon splitting (Step 4) give an 1-olefin and a lower primary radical. The latter is then saturated by interaction with hydrogen (or hydrocarbon molecules) to give a product paraffin with regeneration of the reaction chain (Step 5). The higher relative reaction rate in hydropyrolysis than in thermal cracking of 1 is in agreement with the reported catalytic effect of hydrogen on the pyrolysis of dimethyl ether (26). This effect has been attributed to replacement of the normal chain step (in the noncatalyzed reaction) by fast propagation steps involving formation of H atoms by H abstraction from molecular hydrogen, followed by metathesis between the H atoms and dimethyl ether molecules (compare with Steps 2 and 3, Scheme 1).

The fate of 1-olefins formed in the cracking process was not treated in the original Rice-Kossiakoff hypothesis (7-10) and such compounds were apparently considered stable products at low conversion. It was

found recently, however, that higher 1-olefins are unstable under cracking conditions (27), and therefore could undergo decomposition or isomerization reactions, which contribute to the final composition of the hydro-pyrolysis product.

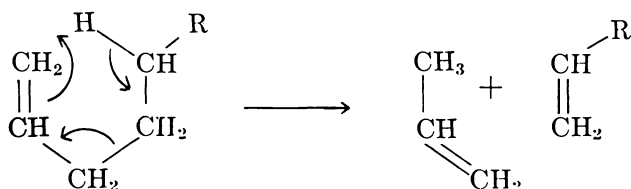
The activation energies for metathesis reactions involving H-atom abstraction from alkane molecules by alkyl radicals are only about 9 ± 2 kcal/mol (26). Likewise, the activation energies for metathesis reactions involving H-atom abstraction from molecular hydrogen by alkyl radicals (e.g., Steps 2 and 5, Scheme 1) are estimated on the basis of thermochemical data (26, 28) to be in the vicinity of 14–15 kcal/mol. This is considerably lower than the activation energy for competing β -scission of an alkyl radical (about 26 kcal/mol). It should be taken into account, however, that the bimolecular abstraction of an H atom from a hydrogen molecule could have a significantly lower pre-exponential factor than that of unimolecular β -cracking. Suppression of β -cracking by saturation of intermediate radicals should lead to a decrease in the formation of ethylene and methane. Further, it should result in paraffin:olefin ratios greater than those in ordinary cracking. An increase in the collision frequency between intermediate radicals and hydrogen molecules, by increasing hydrogen pressure, should augment the rate of radical saturation.

The occurrence of double bond isomerization under the conditions of hydropyrolysis is clearly indicated by the decrease in concentration of 1-olefins and a parallel increase in the concentration of the thermodynamically more stable internal olefins with increase in temperature (Figure 3) or contact time. Such a reaction could proceed by abstraction of an allylic H atom from the 1-olefin, followed by double bond migration:

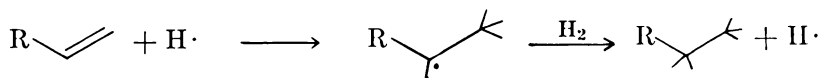


Evidence for another possible reaction, viz. cleavage of an 1-olefin into propylene and a lower 1-olefin, is found in a recent study on the

thermal cracking of C_{10} – C_{16} 1-olefins (27). Splitting of the allylic bond in the olefin may proceed by a concerted coiling mechanism:



Noncatalytic hydrogenation of olefins under the conditions of hydrolysis is a definite possibility. Such a reaction could proceed by a chain mechanism involving addition of a hydrogen atom to a double bond, followed by metathesis between the radical produced and molecular hydrogen:



An activation energy of only about 2.0 kcal/mol has been reported (26) for the addition of a hydrogen atom to ethylene to form an ethyl radical.

Hydrolysis of Decalin

The hydrolysis of a representative polycyclic naphthene, i.e., decalin (2), was investigated as a function of reaction temperature (525°–625°C) and hydrogen pressure 500–2000 psig). In addition, a comparison between hydrolysis and thermal cracking of 2 was made by doing a parallel study with this compound under nitrogen pressure, using otherwise identical experimental conditions. The apparatus and experimental methods were the same as in the study of *n*-hexadecane (see Experimental section).

Results and Discussion. Table V summarizes the composition of products obtained by hydrolysis and by thermal cracking of 2 at two different temperatures (550° and 600°C). Conversion of 2 is markedly higher in hydrolysis than in thermal cracking at both temperatures. At 550°C, the conversion in the hydrolysis run (Experiment 23) is higher by a factor of about 3 compared with that in the thermal-cracking run (Experiment 24). Further, a major difference is observed between the two types of reaction at 550°C, viz. hydrolysis of 2 yields mainly (76.6%) liquid products, whereas thermal cracking produces mostly (56.3%) gaseous products. However, the difference becomes less pronounced at 600°C. C_1 – C_3 hydrocarbons are the major constituents of the

Table V. Comparison of Product Composition from Hydropyrolysis (HP) and Thermal Cracking (TC) of Decalin (2)^{a-d}

| | <i>Experiment Number</i> | | | |
|---|--------------------------|-----------|-----------|-------------------|
| | <i>23</i> | <i>24</i> | <i>25</i> | <i>26</i> |
| Temperature (°C) | 550 | 550 | 600 | 600 |
| Type of reaction | HP | TC | HP | TC |
| Conversion of 2 (mol %) | 26.3 | 8.9 | ~ 100 | 51.7 ^e |
| Product distribution (wt %) | | | | |
| gas | 23.4 | 56.3 | 44.1 | 57.9 |
| liquid | 76.6 | 43.7 | 55.9 | 42.1 |
| Product components (mol %) ^f | | | | |
| CH ₄ | 26.8 | 82.7 | 76.6 | 92.1 |
| C ₂ H ₄ | 10.4 | 61.0 | 12.3 | 52.5 |
| C ₂ H ₆ | 23.3 | 46.6 | 68.7 | 46.0 |
| C ₃ H ₆ | 14.7 | 43.0 | 10.0 | 29.7 |
| C ₃ H ₈ | 24.2 | 30.0 | 38.9 | 25.7 |
| C ₄ H ₈ | 1.0 | 2.6 | 3.1 | 3.7 |
| <i>i</i> -C ₄ H ₁₀ | 1.4 | 0.1 | 3.8 | 0.5 |
| <i>n</i> -C ₄ H ₁₀ | 1.2 | 1.7 | 2.3 | 2.9 |
| C ₅ -C ₈ open-chain components ^g | 15.3 | 0.1 | 25.2 | 8.7 |
| C ₆ -C ₁₀ cyclohexenes and cyclohexanes | 60.2 | 10.3 | 27.6 | 12.5 |
| C ₆ -C ₈ benzenes | 3.8 | 5.7 | 23.9 | 47.9 |
| octahydro <i>N</i> | 7.9 | 32.8 | 1.5 | 2.2 |
| tetrahydro <i>N</i> | 0.1 | 0.7 | 1.2 | 2.1 |
| naphthalene (<i>N</i>) | 0.6 | 1.7 | 1.2 | 1.9 |

^a Pressure: 1,000 psig.^b LHSV: 3.1 hr⁻¹.^c Experiments 23 and 25 were performed under hydrogen, Experiments 24 and 26 under nitrogen pressure; hydrogen (nitrogen) flow rate = 0.12 L/min at 20°C.^d In each experiment **2** was pumped at the rate of 5 mL/min for 10 min.^e Including some high-boiling condensation products.^f Mol/100 mol converted **2**.^g Mostly branched paraffins and olefins.

gas products from both reactions, although the yield of methane is markedly lower in hydropyrolysis, especially at 550°C. Further, paraffin:olefin ratios in the C₂-C₄ fractions are consistently higher in hydropyrolysis than in thermal cracking.

The differences in liquid product composition from the two types of processes are even more pronounced. The major liquid products (*see* Table V) from hydropyrolysis of **2** at 550°C are C₆-C₁₀ cyclohexenes and cyclohexanes, and C₅-C₈ open-chain hydrocarbons, while in thermal cracking the main liquid product at this temperature is 1,2,3,4,5,6,7,8-octahydronaphthalene. At 600°C a much higher conversion of **2** into C₅-C₁₀ aliphatic products is observed in the hydropyrolysis Experiment 25, whereas in the thermal cracking Experiment 26 there is much higher formation of aromatic products, i.e., benzene, toluene, ethylbenzene, and

xylenes. Thus, suppression of excessive thermal aromatization is characteristic for hydropyrolysis even under drastic temperature conditions, e.g., 600°C.

Table VI and Figures 9 and 10 summarize the change in product composition from hydropyrolysis of **2** as a function of reaction temperature in the range of 525°–625°C. Conversion of **2** increases with an

Table VI. Change in Product Composition from Hydropyrolysis of Decalin (2**) as a Function of Reaction Temperature^{a-c}**

| | <i>Experiment Number</i> | | | | |
|---|--------------------------|-----------|-----------|-----------|-----------|
| | <i>29</i> | <i>25</i> | <i>30</i> | <i>27</i> | <i>31</i> |
| Temperature (°C) | 525 | 550 | 575 | 600 | 625 |
| Conversion of 2 (mol %) | 8.1 | 26.3 | 57.4 | 93.5 | 100 |
| Product distribution (wt %) | | | | | |
| gas | 10.0 | 23.4 | 33.7 | 43.7 | 66.9 |
| liquid | 90.0 | 76.6 | 66.3 | 56.3 | 33.1 |
| Product components (mol %) ^d | | | | | |
| CH ₄ | 5.5 | 26.8 | 50.9 | 83.5 | 136.5 |
| C ₂ H ₄ | 4.2 | 10.4 | 11.9 | 12.1 | 8.5 |
| C ₂ H ₆ | 6.5 | 23.3 | 40.3 | 69.0 | 122.9 |
| C ₃ H ₆ | 10.6 | 14.7 | 11.7 | 10.0 | 5.4 |
| C ₃ H ₈ | 11.1 | 24.2 | 30.9 | 38.7 | 52.8 |
| C ₄ H ₈ | 0.1 | 1.0 | 2.9 | 3.1 | 3.3 |
| <i>i</i> -C ₄ H ₁₀ | — | 1.4 | 1.8 | 3.8 | 9.7 |
| <i>n</i> -C ₄ H ₁₀ | 0.1 | .7 | 2.0 | 2.3 | 2.4 |
| C ₅ open-chain ^e | — | .2 | 4.8 | 7.9 | 3.6 |
| C ₆ open-chain | — | .2 | 4.7 | 5.5 | 1.8 |
| C ₇ open-chain | — | .1 | 4.5 | 4.4 | .8 |
| C ₈ open-chain | — | 15.3 | 9.7 | 7.3 | .9 |
| cyclohexane | — | .2 | 4.1 | 2.8 | .8 |
| methylcyclohexane | — | 5.9 | 6.2 | 6.0 | — |
| ethylcyclohexane | — | 10.9 | 7.2 | 4.4 | — |
| methylcyclohexenes | — | 8.4 | 13.2 | 7.3 | .2 |
| C ₈ cyclohexenes | — | 30.1 | 7.4 | 5.5 | .2 |
| C ₁₀ cyclohexenes and cyclohexanes | 56.6 ^f | 9.4 | 7.9 | 5.4 | .6 |
| benzene | — | — | .1 | 9.7 | 15.7 |
| toluene | — | — | 4.0 | 9.0 | 12.3 |
| ethylbenzene + xylenes | — | 3.3 | 5.7 | 5.1 | 5.2 |
| octahydro <i>N</i> ^g | 30.1 | 7.9 | 2.6 | 1.5 | .7 |
| tetrahydro <i>N</i> | 3.2 | 1.8 | 3.3 | 1.2 | .9 |
| naphthalene (<i>N</i>) | — | .2 | .3 | 1.6 | 2.0 |

^a Hydrogen pressure: 1000 psig.

^b LHSV = 3.1 hr⁻¹.

^c Hydrogen flow rate = 0.14 L/min.

^d Mol/100 mol converted **2**.

^e Paraffins plus olefins.

^f Mostly 1-butylcyclohexene and 1-methyl-2-propylcyclohexene.

^g 1,2,3,4,5,6,7,8-Octahydronaphthalene.

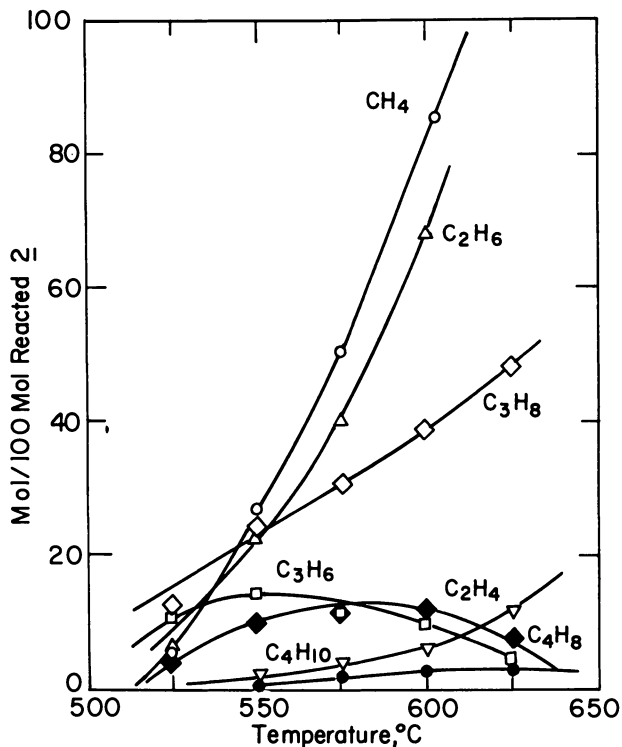


Figure 9. Change in composition of the gas product (C_1 - C_4) from hydro-pyrolysis of 2 as a function of reaction temperature; pressure: 500 psig; LHSV: 3.1 hr^{-1} .

increase in temperature and is essentially complete at 600°C . Further, formation of liquid products predominates at 525°C - 575°C , but then gradually decreases at higher temperature. Examination of the gaseous product composition (Figure 9) shows that formation of methane increases with an increase in temperature. The yield of C_2 - C_3 paraffins increases rapidly with temperature, while the change in the concentration of C_2 - C_3 olefins is relatively minor. Some increase in the yield of isobutane with temperature is also observed.

The following changes are observed in the composition of the liquid product from 2 as a function of temperature (Figure 10). At 525°C the main products are C_{10} cyclohexenes and cyclohexanes, and 1,2,3,4,5,6,7,8-octahydronaphthalene. With increasing temperature these primary products evolve into lower (C_6 - C_8) cyclohexenes and cyclohexanes, and C_5 - C_8 open-chain paraffins and olefins. Finally, a steady increase in the yield

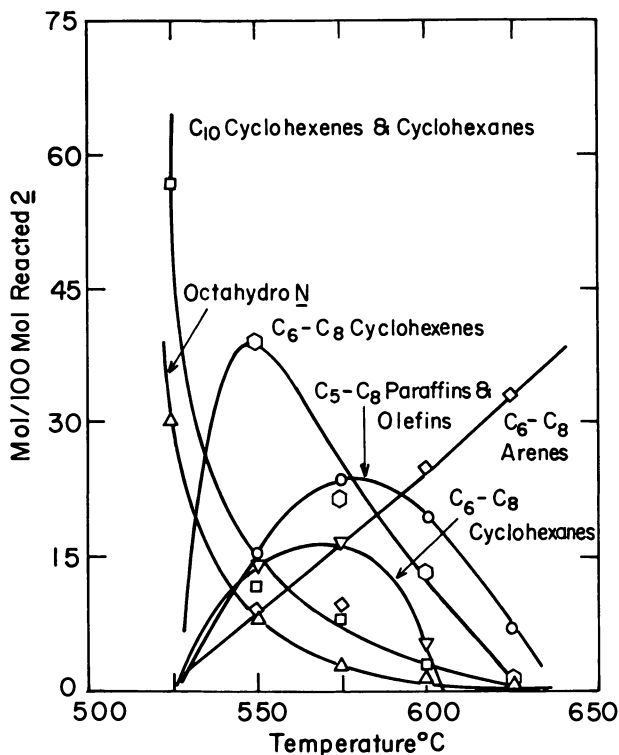


Figure 10. Change in composition of the liquid product from hydropyrolysis of **2** as a function of reaction temperature; pressure: 500 psig; LHSV: 3.1 hr^{-1} .

of C₆-C₈ arenes is observed with further increase in temperature. Essentially no condensation products boiling higher than the feed were found in any of the experiments.

Rate constants for the hydropyrolysis of **2** were calculated assuming first-order dependence, as reported in the literature for thermal cracking. An Arrhenius plot for the hydropyrolysis of **2** is given in Figure 11. The last point (corresponding to 625°C) was not included in the calculation of the activation energy, since the conversion is complete at this temperature. The rest of the points fall on a fairly good straight line, giving an activation energy of 59.0 kcal/mol for the hydropyrolysis of **2**. This is lower than the reported values of 64.3–72 kcal/mol for thermal cracking of decalin (29).

Table VII and Figures 12 and 13 summarize the change in product composition from hydropyrolysis of **2** as a function of hydrogen pressure. As seen from Table VII, conversion of **2** gradually increases with an increase in pressure from 500 to 2000 psig. However, the distribution of

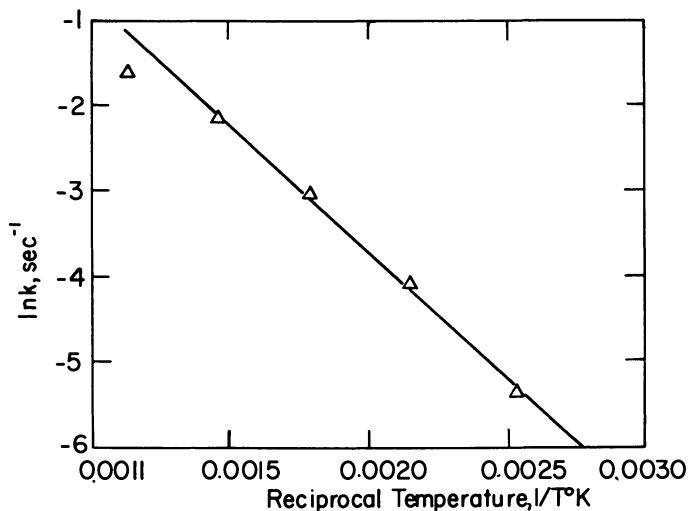


Figure 11. Arrhenius plot for hydro-pyrolysis of 2

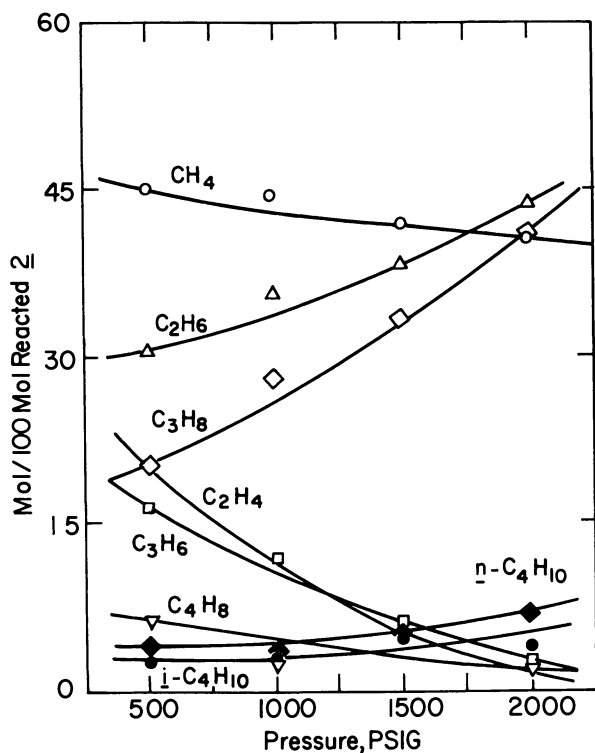


Figure 12. Change in composition of gas products (C_1 - C_4) from hydro-pyrolysis of 2 as a function of hydrogen pressure; temperature: 575°C ; LHSV: 3.1 hr^{-1} .

Table VII. Change in Product Composition from Hydropyrolysis of Decalin (2) as a Function of Pressure^{a-d}

| | Experiment Number | | | |
|--|-------------------|-------|-------|-------|
| | 32 | 33 | 34 | 35 |
| Hydrogen pressure (psig) | 500 | 1,000 | 1,500 | 2,000 |
| Conversion of 2 (mol %) | 48.6 | 57.4 | 61.0 | 68.0 |
| Product distribution (wt %) | | | | |
| gas | 33.1 | 33.8 | 33.3 | 34.0 |
| liquid | 66.9 | 66.2 | 66.7 | 66.0 |
| Product components (mol %) ^e | | | | |
| CH ₄ | 44.8 | 45.5 | 41.8 | 40.4 |
| C ₂ H ₄ | 19.9 | 11.9 | 5.3 | 1.5 |
| C ₂ H ₆ | 30.3 | 40.3 | 38.2 | 43.8 |
| C ₃ H ₆ | 16.4 | 11.7 | 6.4 | 2.6 |
| C ₃ H ₈ | 20.2 | 30.9 | 33.4 | 41.1 |
| C ₄ H ₈ | 6.2 | 2.9 | 6.3 | 2.0 |
| <i>i</i> -C ₄ H ₁₀ | 2.5 | 1.8 | 4.8 | 4.1 |
| <i>n</i> -C ₄ H ₁₀ | 3.9 | 2.0 | 5.0 | 7.0 |
| C ₅ open-chain ^f | 4.0 | 4.8 | 3.8 | 3.5 |
| C ₆ open-chain | 2.7 | 4.7 | 7.5 | 8.2 |
| C ₇ open-chain | 3.1 | 4.5 | 4.9 | 5.8 |
| C ₈ open-chain | 10.4 | 9.7 | 9.5 | 9.3 |
| cyclohexane | 3.4 | 4.1 | 5.2 | 4.5 |
| methylcyclohexane | 3.9 | 10.2 | 11.8 | 15.4 |
| ethylcyclohexane | 4.9 | 7.2 | 9.7 | 11.7 |
| methylcyclohexenes | 15.1 | 13.2 | 9.7 | 4.7 |
| ethylcyclohexenes | 9.3 | 3.4 | 3.2 | 2.0 |
| C ₁₀ -cyclohexenes and cyclohexanes | 8.7 | 7.9 | 9.5 | 10.6 |
| benzene | 1.5 | — | — | — |
| toluene | 7.3 | 4.0 | 1.0 | — |
| ethylbenzene + isomers | 6.7 | 5.7 | 3.6 | 5.7 |
| octahydro <i>N</i> | 4.7 | 2.6 | 2.8 | 3.3 |
| tetrahydro <i>N</i> | 3.9 | 3.3 | 4.5 | 2.0 |
| naphthalene (<i>N</i>) | .5 | .3 | 1.7 | 1.8 |
| residues | .4 | .3 | 1.2 | 0.8 |

^a Temperature: 575°C.

^b LHSV: 3.1 hr⁻¹.

^c In each experiment 2 was pumped at the rate of 5 mL/min for 10 minutes.

^d The hydrogen flow rate was adjusted to give a contact time of 16 sec.

^e Mol/100 mol of converted 2.

^f Paraffins plus olefins.

the gas and liquid products remains essentially constant in this pressure range. On the other hand, although the yield of gas products remains unchanged, there is a marked increase in the paraffin:olefin ratio in each of the C₂-C₄ fractions with increasing pressure (*see* also Figure 12).

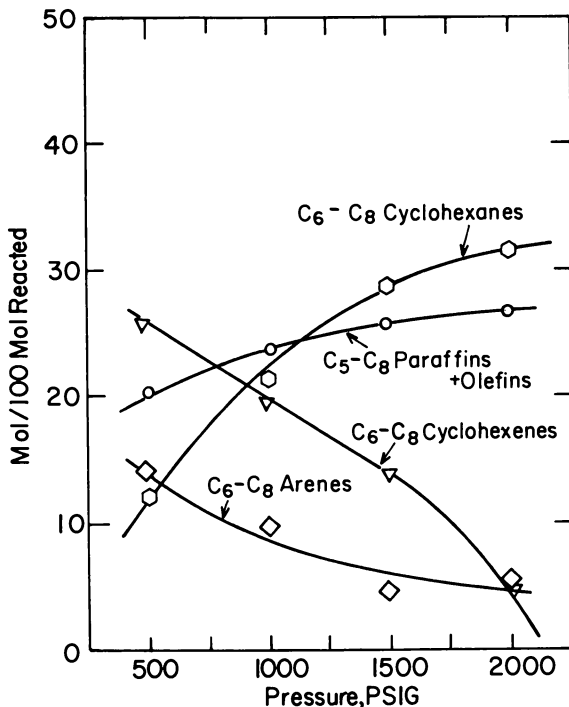


Figure 13. Change in composition of the liquid product from hydropyrolysis of **2** as a function of hydrogen pressure; temperature: 575°C; LHSV: 3.1 hr⁻¹.

Also, this ratio decreases in value with increasing carbon number of the fraction. Significantly, the concentration of methane does not change to an appreciable extent with increasing pressure.

As seen in Figure 13, C₆-C₈ cyclohexenes decrease in concentration, while corresponding C₆-C₈ cyclohexenes increase in concentration with an increase in hydrogen pressure. Similar behavior is observed for C₁₀ cyclohexenes and cyclohexanes (not shown in Figure 13). C₁₀ cyclohexenes, which are precursors of the C₅-C₈ liquid products, reach a maximum concentration at a lower contact time and/or lower temperature. Further, concentrations of C₅-C₈ open chain paraffins and olefins slightly increase (*see* Figure 13), while C₆-C₈ arenes steadily decrease with increasing hydrogen pressure. Dehydrogenation products such as tetralin and naphthalene are produced in small amounts only.

The observed constancy in the relative yields of liquid and gas products from hydropyrolysis of **2** as a function of pressure (Table VII) shows that hydropyrolysis of polycyclic naphthenes can be carried out

essentially to completion without excessive gasification. This is significantly different from the behavior of *n*-paraffins, which show increased tendency for gasification with increasing hydrogen pressure.

Mechanism of Decalin Hydropyrolysis. On the basis of some principles of the Rice-Kossiakoff free-radical theory (7-10), the compositional changes summarized in Table VI and Figure 10 can be rationalized in terms of the following suggested mechanism for hydropyrolysis of 2 (Scheme 2):

1. The reaction is initiated by preferential abstraction of a tertiary hydrogen in 2 by an initiator such as $R\cdot$ or $H\cdot$ (alternative abstraction at secondary carbon positions also occurs).

2. The resulting tertiary radical undergoes β -splitting to form unsaturated C_{10} radicals that by hydrogen abstraction yield C_{10} cyclohexenes, in particular 1-butylcyclohexene and 1-methyl-3-propylcyclohexene (and double bond isomers).

3. Alternatively, the intermediate C_{10} radicals undergo C_2H_4 -eliminating, β -scission steps to yield C_6 - C_8 cyclohexenes.

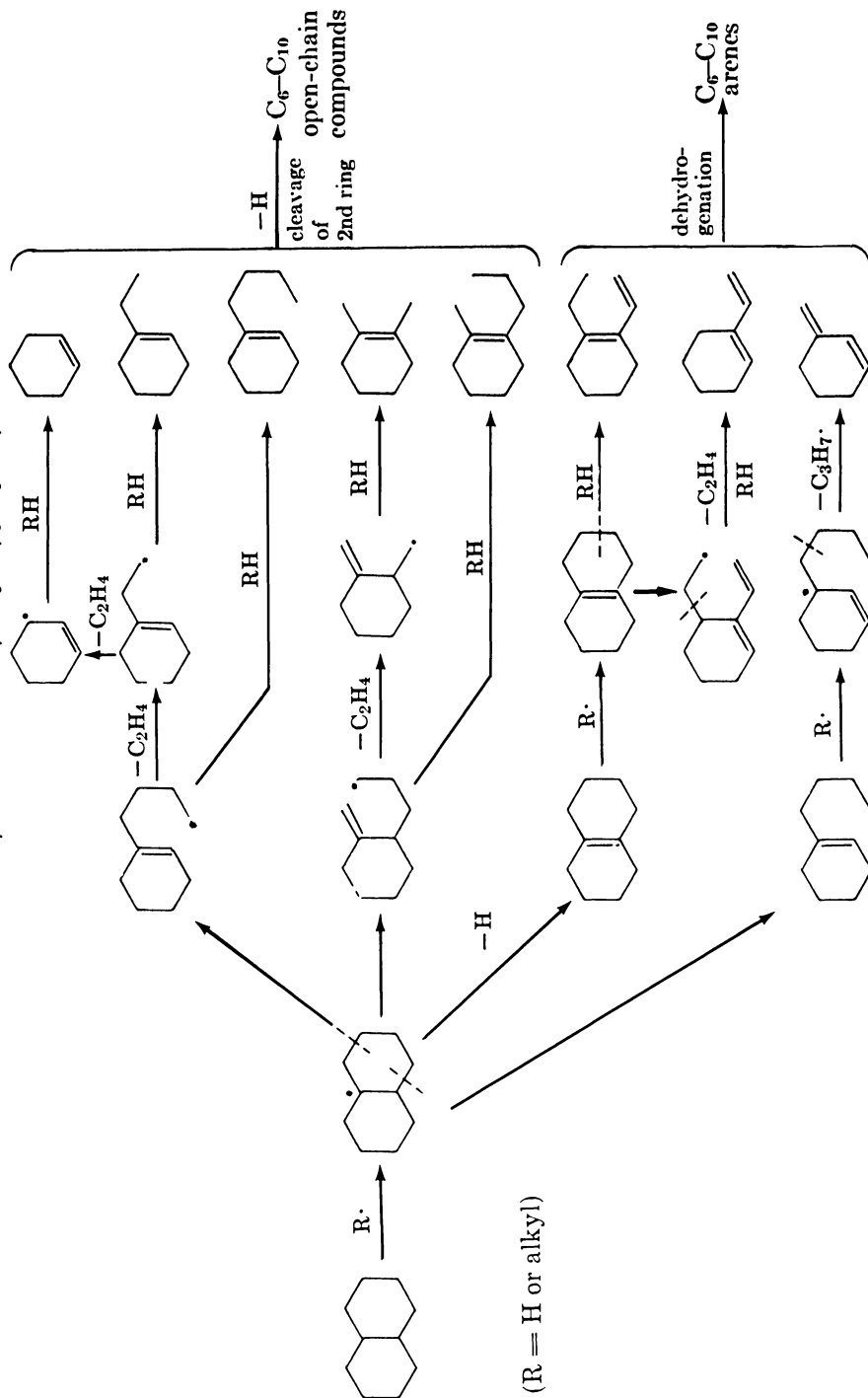
4. Additional β -splitting reactions of alkylcyclohexene products result in cleavage of the residual naphthenic ring to yield C_5 - C_8 open-chain paraffins and olefins.

5. A reaction competing with Step 2 above is the removal of the second tertiary hydrogen in 2 to form 1,2,3,4,5,6,7,8-octahydronaphthalene, which upon splitting yields cyclic dienes serving as precursors of C_6 - C_{10} alkylbenenes. Alternatively, the octahydronaphthalene may undergo dehydrogenation to tetrahydronaphthalene, which yields C_6 - C_{10} arenes upon splitting.

Similar decomposition patterns can be proposed for secondary radicals derived from 2 in the initiating hydrogen abstraction Step 1. Thermal aromatization of 6-ring cyclic dienes containing one exocyclic and one endocyclic double bonds is a facile process at 550°-600°C. The reaction involves fast double bond isomerization to a conjugated cyclohexadiene, followed by dehydrogenation (30, 31, 32).

On the basis of the above described studies, as well as of some ongoing investigations with naphthenoaromatic and heterocyclic model compounds, it was possible to establish specific optimal ranges for hydropyrolysis of different types of feedstocks. This allowed for the development of a versatile and highly efficient noncatalytic hydropyrolysis process for conversion of coal liquids and other heavy oils or solids into light, lower boiling liquids, without noticeable coking and without any major extent of gasification. Hydrogen consumption under proper operating conditions is found to be very low (e.g., 0.5-2% by weight), and therefore the process seems to have considerable industrial potential (33).

Scheme 2. Proposed mechanism for hydropyrolysis of 2



Experimental

Hydropyrolysis Apparatus and Experimental Procedure. A diagram of the bench-scale, pressure flow system used in this study is shown in Figure 14. It includes a specially designed hydropyrolysis reactor in which strictly isothermal conditions can be maintained and has numerous advantages over previously used molten-lead bath or fluidized-bed reactors (29). An important feature of the reactor is a cylindrical copper block, cast and machined to a length of 9 in. and an i.d. of 10 in. (o.d., 11 in.). This block is sandwiched between two stainless steel cylinders and closed at the top and bottom with stainless steel rings to prevent oxidation. A good contact between the copper cylinder and the outer stainless steel cylinder is secured to provide for good heat transfer. Some holes (caused by gas pockets) are formed in the copper cylinder during moulding, but their estimated volume does not exceed more than 5% of the total volume of the mold.

Two semicircular, parallel, helical grooves were machined in the outer stainless steel cylinder to accommodate the reactor tube and the tubular heater. The latter is 5/16 in. in diameter and 144 in. long, and has a heating capacity of 4000 W. The reactor consists of a 316 stainless steel tube 236 in. long \times 3/8 in. o.d. (3/16 in. i.d.). The first 18 in.-section of the tube is used as a preheater. Reactor and heater are held in place by mechanical means. The machining and fitting are done so as to avoid any gap between the solid block and the reactor, or between the block and the heater. Details on the reactor block are given in Figure 15. The block temperature is controlled by measuring the temperature of the heater, this allows for maintenance of an essentially isothermal condition along the entire length of the reactor. The preheater is equipped with two separate semicircular heaters, each having a capacity of 600 W. The temperatures of the inflow and exit streams are measured by thermocouples placed inside the reactor inlet and exit. By properly adjusting the heating rate of the reactor heater and of the preheater the temperature of the inlet and exit streams of the reactants can be controlled within 1°C.

The inner surface of the stainless steel reactor was deactivated by the following procedure. The tube was cleared by passing air at the rate of 1–2 L/min. for 30 min while maintaining a temperature of 575°C. Hydrogen sulfide was then passed for 30 min at the rate of 250 mL/min. Finally, hydrogen was passed for 30 min at the rate of 3 L/min. To equilibrate the surface a small amount of the liquid hydrocarbon was pumped before starting the experiment. This treatment apparently eliminates any major catalytic effects of the reactor surface, as indicated by the lack of carbon deposits in all runs.

A Milton Roy pump was used for introduction of liquid feeds into the reactor. In runs with such feeds, the storage burette, the pump head, and the feed lines were heated to maintain appropriately low viscosity for pumping. The selected pressure of the system was maintained by a pressure regulator attached to the hydrogen cylinder. The hydrogen flow rate was controlled by a Brook's high pressure rotameter, and by two needle valves at the outlet (Figure 14).

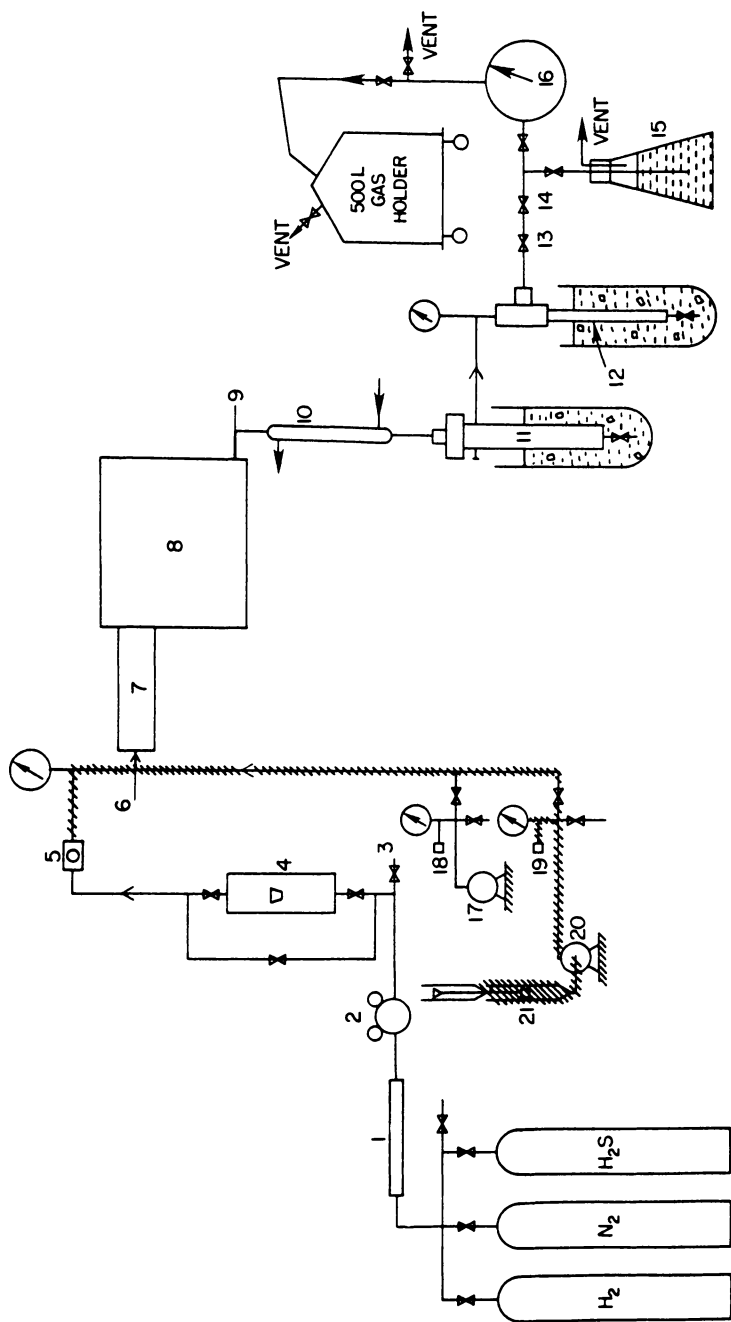


Figure 14. Flow diagram of bench-scale hydropyrolysis unit, 1. drier, 2. pressure regulator, 3. air inlet, 4. rotameter, 5. check valve, 6. 9. thermocouples, 7. preheater, 8. reactor, 10. condenser, 11, 12. collectors, 13, 14. flow control valves, 15. CdCl_2 scrubber, 16. wet test meter, 17. piston pump, 18, 19. rupture discs, 20. reciprocating pump, 21. oil reservoir, heated.

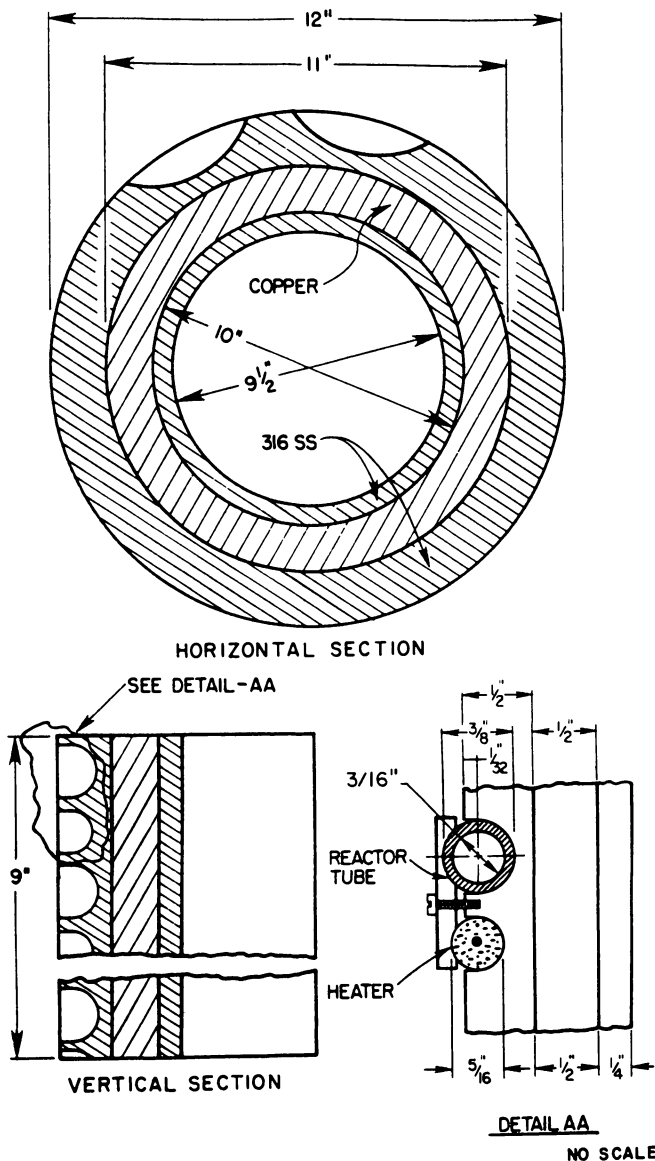


Figure 15. Reactor isothermal block

The reactor was brought to the desired temperature and stabilized for at least 30 min. Then the system was pressurized to the desired pressure and the flow of hydrogen adjusted to the selected level. The liquid hydrocarbon feed and the hydrogen were preheated to about 200–250°C before being introduced in the preheater. Upon entering the preheater the reactants were heated quickly to reaction temperature.

During the experiment the temperature at different points of the reactor system was measured by a Honeywell 10-point recorder. Liquid products leaving the reactor were cooled and collected by a water condenser and a series of ice-water traps. Gaseous products were collected in a 500-L gasholder to obtain a reliable material balance. At the end of each run, the system was brought to atmospheric pressure and the liquid receivers were warmed slowly to room temperature under a stream of hydrogen. By this procedure any condensed C₃ and C₄ gases were chased and quantitatively collected in the gasholder, together with the other gas products.

High purity ($\geq 99\%$) *n*-paraffins and decalin were used as starting materials in all runs.

Analysis of Products. Gas products were analyzed by GC with activated alumina and molecular-sieve columns.

Identification of liquid products was carried out mainly by combined high resolution GC/mass spectrometry. Identity of products in most cases was confirmed by comparison of their retention volumes and ¹H NMR spectra with those of reference compounds. Differentiation between the *n*-paraffin, α -olefin, and internal olefins in each fraction of the product from **1** was likewise based on comparison with available reference samples. Gas chromatographic columns used for quantitative analysis of liquid products included packed columns, e.g., 6% OV-17 on 100–120 mesh Chromosorb W, as well as capillary columns (29).

Acknowledgment

The financial assistance of the United States Department of Energy is gratefully acknowledged.

Literature Cited

1. Cantrell, A. *Oil Gas J.* **1977**, 75(13), 97.
2. Rossi, W. G.; Deighton, B. S.; MacDonald, A. G. *Hydrocarbon Process.* **1977**, 56(5), 105.
3. Feigelman, S.; Lehman, L. M.; Arisotoff, E.; Pitts, P. M. *Hydrocarbon Process.* **1965**, 44(12), 147.
4. Lehman, L. M.; Vergara, M. *Hydrocarbon Process.* **1977**, 56(7), 126.
5. Pelofsky, A. H. "Heavy Oil Gasification"; Marcel Dekker: New York, 1977.
6. Barre, C.; Chahlvekilian, E.; Dumon, R. *Hydrocarbon Process.* **1976**, 55(11), 176.
7. Rice, F. O. *J. Am. Chem. Soc.* **1931**, 53, 1959.
8. Rice, F. O. *J. Am. Chem. Soc.* **1933**, 55, 3035.
9. Rice, F. O.; Herzfeld, K. F. *J. Am. Chem. Soc.* **1934**, 56, 284.
10. Kossiakoff, A.; Rice, F. O. *J. Am. Chem. Soc.* **1943**, 65, 590.
11. Voge, H. H.; Good, G. M. *J. Am. Chem. Soc.* **1949**, 71, 593.
12. Appleby, W. G.; Avery, W. H.; Meerbott, W. K. *J. Am. Chem. Soc.* **1947**, 69, 2279.
13. Doue, F.; Guiochon, G. *J. Chim. Phys. Phys.-Chim. Biol.* **1968**, 64, 395.
14. Fabuss, B. M.; Smith, J. O.; Lait, R. E.; Borsanyi, S. A.; Satterfield, C. N. *Ind. Eng. Chem., Process Des. Dev.* **1962**, 1, 293.

15. Murata, M.; Saito, S.; Amano, A.; Maeda, S. *J. Chem. Eng. Jpn.* 1973, 6(3), 252.
16. Murata, M.; Saito, S. *J. Chem. Eng. Jpn.* 1974, 7(5), 389.
17. Szabo, A. G. *Catal. Rev. Sci. Eng.* 1968, 2, 221.
18. Fabuss, B. M.; Smith, J. O.; Satterfield, C. N. In "Advances in Petroleum Chemistry and Refining"; Interscience: New York, 1964; Vol. 9, p. 157.
19. Fabuss, B. M.; Kafesjian, R.; Smith, J. O.; Satterfield, C. N. *Ind. Eng. Chem., Process Des. Dev.* 1964, 3, 248.
20. Brooks, C. T. *Trans. Faraday Soc.* 1966, 62, 935.
21. Brooks, C. T. *Ind. Eng. Chem., Prod. Res. Dev.* 1967, 6, 236.
22. Shultz, E. B.; Linden, H. R. *Ind. Eng. Chem., Process Des. Dev.* 1962, 1, 111.
23. Penninger, J. M. L.; Slotboom, H. W. *Recl. Trav. Chim. Pays-Bas* 1973, 92, 513.
24. Tominaga, H.; Arai, H.; Kunugi, T.; Amano, A.; Uchiama, M.; Sato, Y. *Bull. Chem. Soc. Jpn.* 1970, 43, 3658.
25. Burr, J. G.; Meyer, R. A.; Strong, J. D. *J. Am. Chem. Soc.* 1964, 86, 3846.
26. Bensen, S. W. "Thermochemical Kinetics"; Wiley: New York, 1976.
27. Rebick, C. *Prepr., Div. Pet. Chem., Am. Chem. Soc.* 1978, 23, 142.
28. Rosenstock, H. M.; Draxl, K.; Steiner, B. W.; Herron, J. T. *J. Phys. Chem. Ref. Data* 1977, 6 (Suppl. 1), pp. I-774-I-783.
29. Ramakrishnan, R., Ph.D. Thesis, University of Utah, 1978.
30. Gil-Av, E.; Shabtai, J.; Steckel, F. *Ind. Eng. Chem.* 1960, 52, 31.
31. Gil-Av, E.; Shabtai, J.; Steckel, F. *J. Chem. Eng. Data* 1960, 5, 98.
32. Shabtai, J.; Gil-Av, E. *Tetrahedron* 1962, 18, 87.
33. Oblad, A. G.; Shabtai, J.; Ramakrishnan, R., pending patents.

RECEIVED December 14, 1978.

Retorting Oil Shale by Microwave Power

E. T. WALL, R. DAMRAUER, W. LUTZ, R. BIES, and M. CRANNEY

University of Colorado at Denver, 1100 14th St., Denver, CO 80202

Shale oil and a fuel gas have been produced by microwave-heating oil shale in a standard microwave oven in conjunction with experimentation to develop an in situ microwave retorting process. Various grades of oil shale have been subjected to high microwave fields. The derived oil has been submitted to various physical and chemical testing methods, and the chemical composition of the evolved gas has been evaluated. The specific gravity; pour point; yields of oil, water, gas, and losses; and spent shale are compared with parallel data obtained with the Fischer assay procedure. Important differences in oil flow properties and gas composition are discussed in view of microwave interactive theory.

Oil shale represents an enormous reserve of fossil fuel for domestic and foreign needs (1,2). Shale oil production can be divided into direct and indirect heating processes (2). In direct heating, some of the products or some other fuel is combusted to raise the oil shale to the necessary temperature for conversion to gas and oil while an indirect process transfers heat from an outside source. Although high yields have been demonstrated in some indirect procedures (3), the application to in situ retorting has been limited. Direct processes developed for in situ recovery of shale oil have not demonstrated sufficient control of the underground combustion for reliable operation.

Electromagnetic radiation in the microwave frequency spectrum is absorbed most strongly by molecules with permanent dipole moments (4). The relaxation phenomenon of this absorbed power manifests itself in a heatlike reaction. The University of Colorado Oil Shale Project has studied the degradation of the liquid-fuel precursor (kerogen) by microwave interaction. Kerogen is a moderately strong absorber of this radia-

tion because of its large percentage of polarized bonds and entrapped polar molecules (5). Microwave retorting represents a controllable underground application of energy without combustion.

It is well known that important differences do occur with different methods of thermal retorting, and microwave interactive theory indicates even greater differences may be possible. We examined the products of this novel retorting system by using product quality as feedback control to gain some insight into the basic microwave interaction with fuel precursors.

Experimental

Equipment. A commercial microwave unit (rated at 2450 MHz and 650 W) was modified to fit a beaker-shaped quartz retort of approximately 500-mL capacity in which the oil shale was placed. Much effort was expended with this original design in obtaining materials, both of low microwave loss and high thermal stability. The apparatus was required to be gas tight. The oil and gas produced were fed through glass tubing to a series of condensers, a mercury manostat, stainless-steel bellows diaphragm pump, a gas test meter, and various gas collection apparatus (*see* Figure 1).

The literature has virtually no references for using a commercial microwave oven unit for high temperature applications on a closed system. Each observation and parameter that changed gave important data and direction in designing a possible microwave interactive process. A quartz vessel was required because of its lower microwave energy absorption (7) and low reflectivity, a quality not well understood but well documented in our experiments. A newer apparatus, essentially a new cavity with greater loading and better reproducibility, is nearing completion. The experiment can be varied by changing the manner of collection of products, the atmosphere in the retort, and the sample size.

A modified Fischer assay apparatus was obtained from the Colorado School of Mines Research Institute with the temperature program controlled manually with a chromel-alumel thermocouple readout. The signal from the thermocouple was monitored by a Radiometer pH/mV meter and outputted to a calibrated laboratory recorder. Gas collection was either metered or collected over water by using a mercury manostat instead of solenoids (6).

Crude oil analysis techniques, developed by the Bureau of Mines (9), was used initially to describe the overall quality of the product. Spent shale samples were ashed using a two-day, low temperature procedure. The covered samples were placed in a room temperature furnace, and the temperature was increased to 700°C (370°C) in a near-reductive atmosphere. The sample was uncovered and the temperature was increased to 750°F (300°C) for one more day with air forced over the sample. This method has been suggested to cause the least changes to heat-sensitive mineral components of the shale (17). Actual experience has shown that the time for this procedure can be halved because of the porous nature of the spent shale and the small sample size. Results are presented as weight percent of the pre-retorted sample.

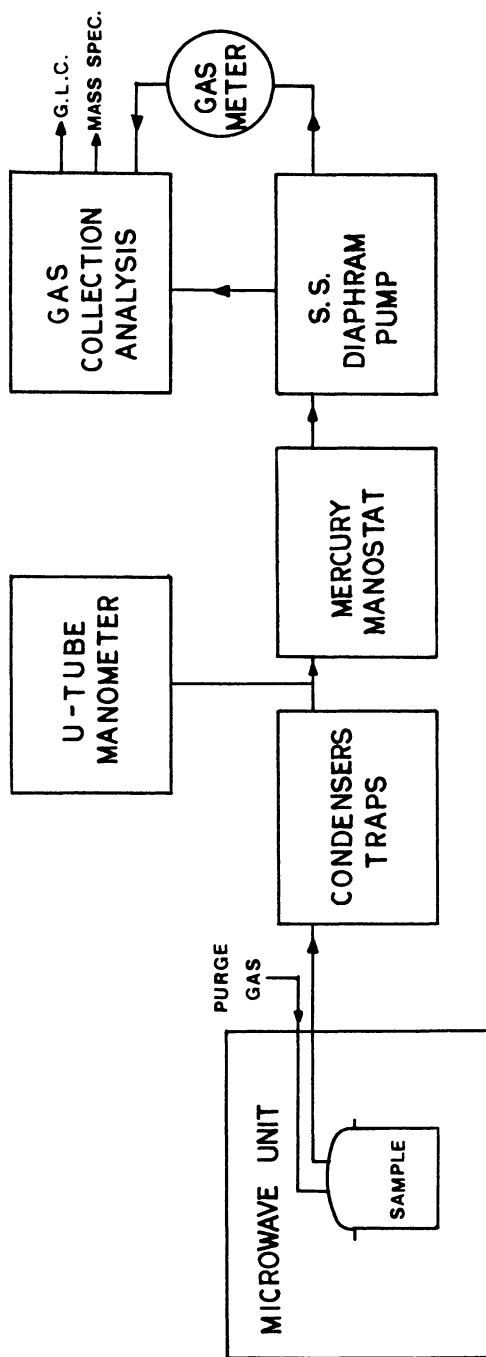


Figure 1. Schematic of microwave retorting operation

The gaseous product was examined using a Perkin-Elmer 3920B programmed temperature chromatograph. Oxygen and nitrogen content were used as a leakage indicator, and the gas outputs were adjusted as to volume and energy content. Crude absorption measurements were made by measuring the temperature rise of known quantities of water and shale in a standard microwave oven. Although by no means an exhaustive study, this method allowed us to confirm the level of power consumption and its variation with kerogen content.

Shale Samples. Initial experimentation was carried out on samples graciously supplied by TOSCO from their grounds located in Golden, Colorado. These samples assayed at 35 gal/ton by modified Fischer assay. These samples had been exposed to weathering for approximately 10 years. Results from these samples are examined in Tables I and VII. Samples of various grades were obtained from the vicinity of the large retort facility of the Laramie Energy Research Center and represented a loose collection of uncharacterized pieces of oil shale. Fischer assays were performed in this laboratory. Sample size ranged from 100 to 200 g, depending on specific gravity.

Retorting Procedure. Oil shale of a block configuration with sides parallel to the bedding plane was halved with one piece retorted and the other ground for Fischer analysis of maximal oil content. Sharp projections of rock were removed, and the retort was centered in the cavity and sealed. The entire system is purged initially with nitrogen or helium to remove oxygen. Results reported here used no other atmosphere except that generated by the product evolution of the shale. A moderate vacuum of 60–80 mm Hg was maintained to prevent loss of product although samples run without vacuum were found not to differ significantly. As many as four traps were used for sample collection, with two circulating ice-water condensers, a high surface-area dry ice/acetone trap, and a 32°F (0°C) condenser packed with glass wool being the final configuration. The unit is activated and the experiments are clocked with a built-in timer.

Results and Discussion

Microwave Power. Microwave heating has been examined with renewed interest since the development of ovens for the home and of high power, high efficiency industrial equipment. Microwave interaction has long been used to probe structural details of polymers (10) and rotational/vibrational spectra of small molecules. Higher power applications have become more prominent.

In considering the mechanism of interaction of microwave energy and materials, a simplified model of a capacitor with the material between charged plates can illustrate the more important aspects of heating (4). The ability of the material to maintain the charge separation (that is, resist current flow) is closely related to the inverse of the dielectric constant (ϵ'). When materials are subjected to the electric field between the plates, those with permanent dipoles (polar molecules) will orient

their partial positive charges toward the negative capacitor plate. This phenomenon is known as polarization.

Polarization can be classified as electronic (electron cloud distortion), atomic, molecular, ionic, and crystalline. The point of maximum polarization in a system would occur when all dipoles reacted to the applied field and aligned. This is difficult to obtain even in a static situation. In an alternating field situation, the dielectric remains the same or decreases as the frequency increases past the microwave region (11). In the microwave region, attainment of equilibrium is more difficult, and there is an observable lag in the dipole orientation which is commonly called relaxation. The polarization then acquires a component out of phase with the field thermal dissipation of some of the energy of the field. This dissipation and its relation to the normal charging current can be related by Equation 1 where ϵ' is the measured dielectric constant of the material and ϵ''

$$\tan \delta = \frac{\text{loss current}}{\text{charging current}} = \frac{\epsilon''}{\epsilon'} \quad (1)$$

is its loss factor. As the frequency approaches zero, ϵ'' approaches zero and ϵ' approaches the static dielectric constant (12). At very high frequencies most of the polarization disappears. Small molecular polarizations in a low viscosity medium would give a maximum near the microwave frequencies; large molecules with restricted orientation freedom would have maxima at frequencies lower than microwave. However, true resonance effects are not seen in impure or mixed materials. The behaviors of the dielectric constant and loss factor are often considered separately for a given material because usually only the loss constant changes dramatically in the microwave region (*see* Equation 2.) Hence the $\tan \delta$ can approximate the loss behavior of similar materials (4, 13).

$$\epsilon'' = \epsilon' \tan \delta \quad (2)$$

Microwave heating has been called volume heating because of its frequent independence of thermal conduction. Penetration is inversely proportional to frequency and will be greatest with those materials of low loss (e.g., saturated hydrocarbons, some ceramics, glasses, etc.). Radiated heat from the surfaces of materials heated in microwave cavities can reach high internal temperatures. Low thermal conductivity samples can retain heat build-up until increased rotational freedom can be obtained and then can absorb power at a more rapid rate. Some materials heat so slowly by thermal conduction that only either size reduction or volume heating would be practical (14). Application to the fracturing of concrete by using broadcast microwave power takes advantage of the low thermal conductivity to concentrate heating interaction (4).

High polymers always have atomic and electronic polarization contributing to the dielectric constant. In heterogeneous materials, an additional type of polarization arises from an accumulation of charge between regions with differing loss characteristics. High polymers containing polar groups can show orientation polarization attributable to change in orientation of molecular segments in an externally applied field without changing the entire molecular orientation (10). Crosslinking of the polymer segments can reduce this freedom considerably. Pure rubber is a hydrocarbon with little polarity. When it is vulcanized, the reaction with sulfur gives crosslinking with a corresponding increase in dielectric constant attributable to polar carbon-sulfur bonds. However, as crosslinking increases, the rotational freedom is restricted and the dielectric constant decreases. Here also, interfacial polarization contributes to the overall loss (10).

Results from Microwave Shale. From the preceding discussion, oil shale would offer an interesting substrate for microwave power interaction. Kerogen is chemically composed of many segments with permanent dipoles and contains entrapped polar compounds (5, 15). Although a solid, its heterogeneity would be expected to and did display a liquidlike dielectric constant and suitable loss tangent. Also, its layered structure in the shale would have a high interfacial polarization contributing to power absorption. Early experimentation showed that the rock strata, devoid of organic matter, had very little power absorption properties (14), and a sequential heating situation was envisioned and demonstrated. That is, the initial fixed water is heated, the fracturing of the shale is followed by kerogen pyrolysis, and lastly, the spent ore absorbs power. This selective interaction indicated lower power requirements than a strictly thermal process.

After a period of time (depending on sample load), water vapor condenses in the first traps, accompanied by major cracks appearing parallel to the bedding plane. After the majority of the water vapor condenses, sulfurous gases appear, followed by oil vapor and mist, all continuing to completion. The spent shale remains solid but with much less structural integrity and with serious fracturing along planes parallel to the bedding plane, together with many small cracks greatly increasing the shale porosity. Gas output was copious, often overloading condensing and separating systems. Also, loading of the solid shale indicated a minimum weight below which coupling with the microwave energy was ineffective. Mist formation exceeds the nominal 3%–5% reported in the literature for many processes (8). Nucleation methods have not been attempted. Since gas evolution was quite copious, it was assumed that it contained a large proportion of the overall heating value of the products. This was later confirmed. Also, because of the closed system, no

dilution of the gas occurred, and the calorific heating value should be higher than most direct heating processes.

Table I lists some results of microwaving oil shale (35 gal/ton) from TOSCO. These initial experiments indicated a need for comparative studies with thermally produced liquid and gaseous products. Flow property indicators (API gravity, pour point), showed conflicting trends. The gas output was very high. Studies of oil generation and degradation with thermal heating have led to a simplified mechanism for the estimation of retort products of blocks of shale (15). Experimental data showed that the highest oil yields were obtained by removing intraparticle oil [(Oil)_{IP}, Figure 2] very quickly either by increased heating rate, as in Fischer assay, or by using a sweep gas; i.e. $k_d \gg k_c$, the rate constants for intraparticle oil production and degradation by coking, respectively. Since coking has been described as the main degradation mechanism of shale oil by thermal heating, and since microwave retorting under these conditions produces low residual carbon, cracking reactions would more easily describe the increased gas production by microwave retorting. The effective gas and oil production rate in microwave retorting is so rapid that cracking reactions must occur inside the shale as soon as oil liquid is produced (microwave interaction is greatly decreased in gas phase reactions). Frequently the inside of the blocks of spent shale are devoid of visual carbon.

Table I. Initial Results on Retorting Oil Shale by Microwave Power

| <i>Parameter</i> | <i>Results</i> |
|-------------------------------|-------------------------------|
| Gas and losses | 21.0 (%) |
| Carbon in semicoke | 4.5 (% of spent shale weight) |
| Oil yield | 71.0 (% of Fischer Assay) |
| Heat of combustion | 16,744 (Btu/lb) |
| API gravity (pour point 30°F) | 17.2 |
| Nitrogen | 1.9 (%) |
| Sulfur | 0.93 (%) |
| Conradson coke | 5.5 (%) |
| Ash | 0.3 (%) |

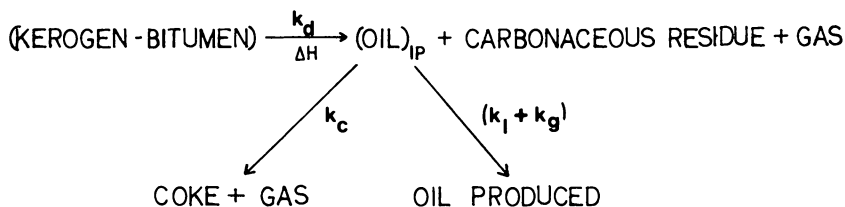


Figure 2. Simplified mechanism for oil production (15)

Results from a series of experiments performed under maximal energy absorption conditions are shown in Table II. These samples were subjected to a microwave field until gas and vapor evolution returned to near background. These conditions are not those of maximal efficiency either in power used or in yield obtained, but do show a direct comparison with a thermal retorting system, the modified Fischer assay being an "indirect process" reference. The microwave run was complete within 30 min since dependence on heat transfer, as in the thermal retort, is unnecessary. Comparing some characteristics of the oils obtained, significant differences in the overall specific gravity and in the pour points were observed. The Fischer assay specific gravity decrease correlated well with increasing yield, as is often the case in the literature. In all cases, the specific gravity of the microwaved oil is higher than the Fischer assay oil; this held true for every sample tested. Yet, the microwave oils show excellent flow properties which were later confirmed by kinematic viscosity measurements. The trend for greatest pour-point depression seems to be in the area of middle grade of Colorado oil shale.

It has been noted that shale oil properties can vary with the percentage yield of a thermal process. The percentage of oil recovery compared with the Fischer assay is presented in Table III, which shows some more characteristics of the retorting runs of Table II. The data

Table II. Characteristics of Microwave-Produced Oil and Oil from the Modified Fischer Assay of Divided Oil Shale Samples

| Number of Experiments | Grade (gal/ton) | Fischer Assay Oil | | Microwave Oil | |
|-----------------------|-----------------|-------------------|-----------------|------------------|-----------------|
| | | Specific Gravity | Pour Point (°F) | Specific Gravity | Pour Point (°F) |
| 3 | 68.8 | 0.896 | 53 | 0.956 | 45 |
| 2 | 40.6 | 0.917 | 69 | 0.934 | < 10 |
| 2 | 23.0 | 0.926 | 53 | 0.937 | 19 |
| 2 | 12.5 | 0.950 | 60 | 0.940 | 37 |

Table III. Residues from Microwave- and Fischer-Assay Processed Shales

| Average Grade (gal/ton) | Fischer Assay | | Microwave | |
|-------------------------|--|----------------------------------|--|----------------------------------|
| | Spent Shale (% of initial sample weight) | Ash (% of initial sample weight) | Spent Shale (% of initial sample weight) | Ash (% of initial sample weight) |
| 68.8 | 67.8 | 60.8 | 60.2 | 57.9 |
| 40.6 | 79.3 | 75.8 | 65.8 | 62.8 |
| 23.0 | 87.8 | 85.5 | 76.5 | 75.6 |
| 12.5 | 91.6 | 89.5 | 75.3 | 74.9 |

indicate a decrease in the amount of nonretorted volatiles remaining in the high yield shales after microwave retorting. In the lower grades when comparing ash figures for the two models, the microwave interaction with the shale residue has volatilized some of the spent shale not normally volatilized during low temperature ashing. This interaction can be verified in Table IV in examining the gas percentages of the two processes. Mineral analysis was not performed. Changes in the solid structure could represent variables in the amounts of gases evolved and volatiles remaining in the shale. X-ray analysis and inorganic and organic carbon balances are presently being examined. The enormous percentage of gas evolved cannot be accounted for by just the decrease in the yield of oil or by even the total loss of organic carbon of oil and coke.

Averaged overall properties of the crude oil obtained by microwave interaction are summarized in Table V. Although these published figures are not the best for some of the processes listed (2), they are presented for an approximate comparison. From these data, microwave-produced oil is shown to be a suitable liquid fuel precursor although differing from that produced from a variety of thermal processes. The recoveries from this prototype, multimode, cavity-retorting system are promising.

Table IV. Yields of Oil and Gaseous Products

| Grade | <i>Fischer Assay</i> | | <i>Microwave</i> | | |
|-------|----------------------|---------------------------|------------------|---------------------|---------------------------|
| | <i>Oil (%)</i> | <i>Gas and Losses (%)</i> | <i>Oil (%)</i> | <i>(Recovery %)</i> | <i>Gas and Losses (%)</i> |
| 68.8 | 25.7 | 5.3 | 17.2 | (67) | 20.9 |
| 40.6 | 15.5 | 4.1 | 8.1 | (52) | 17.6 |
| 23.0 | 8.9 | 2.6 | 6.4 | (72) | 19.6 |
| 12.5 | 5.0 | 2.0 | 3.4 | (68) | 18.9 |

Table V. Properties of Crude Shale Oils from Microwave Process and ex situ Processes

| <i>Process</i> | <i>Micro-wave</i> | <i>NTU^a</i> | <i>Gas^a Com-bustion</i> | <i>TOSCO II^a</i> | <i>Union^a</i> |
|---------------------|-------------------|------------------------|------------------------------------|-----------------------------|--------------------------|
| Gravity (API) | 19 | 25.2 | 19.7 | 28 | 20.7 |
| Sulfur (%) | 0.85 | 0.76 | 0.74 | 0.8 | 0.77 |
| Nitrogen (%) | 1.80 | 1.77 | 2.18 | 1.70 | 2.01 |
| Pour Point (°F) | 35 | 70 | 80 | 75 | 90 |
| Viscosity (SUS 100) | 60 | 79 | 256 | 120 | 223 |
| % of Fischer Assay | (60-70) | 62 | 85 | 106 | 86 |

^a Data from Ref. 2.

Gas Analysis. The gas output from initial experimentation was copious. Table VI lists chemical reactions possible with thermal processes in shale particles. The release of fixed water together with the decomposition of kerogen and oil degradation are the results of a reaction apparently occurring during the generation of products by microwave interaction with the shale blocks. The molar composition of the gas (*see* Table VII) is examined in reference to the remaining chemical reactions in Table VI. The results would coincide with a mechanism of increasing tendency for bond rupture in areas of permanent dipoles of the kerogen macrostructure.

HIGH CO. The retorting had been performed in a closed system initially flushed with nitrogen. Since the CO content of the gas remained fairly constant throughout the retorting process, high temperature (*i.e.*, high temperature throughout the shale) reactions are not likely; for example, $\text{CO}_2 + \text{C} \rightarrow 2 \text{CO}$. An altered mechanism of pyrolysis in the

Table VI. Chemical Reactions in Shale Particles (16)

Decomposition of kerogen
 Decomposition of carbonate minerals
 Reaction of carbon with CO_2
 Reaction of carbon with O_2
 Thermal degradation of oil
 Release of fixed water

10th Oil Shale Symposium Proceedings

Table VII. Gaseous Products Composition from Microwaved Oil Shale

| | |
|--|------------------|
| Gaseous product | |
| Heat of combustion, net | 500–700 Btu/scf |
| Heat of combustion, net (CO_2 and H_2S removed) | 700–900 Btu/scf |
| Yield | 2–3 scf/lb shale |

Composition (mol %) (sample 35 gal/ton)^a

| | |
|------------------|------|
| Carbon monoxide | 17.7 |
| Carbon dioxide | 14.5 |
| Hydrogen | 15 |
| Hydrogen sulfide | 3.0 |
| Methane | 35.9 |
| Ethanes | 12.4 |
| Propanes | 3.3 |
| Butanes | 1.0 |
| Pentanes | 0.2 |
| Hexanes + | 0.2 |

^a Heating Value (calculated): approx. 744 Btu/ft³, CO_2 H_2S 902 Btu/ft³ removed.

presence of the intense microwave field is suspected for those compounds with a tendency for coke to produce CO and liquid fuels. Low coke values in the solid residue might add further evidence.

MODERATE TO LOW CO₂. The value in the table represented the overall percentage composition. Sequential analysis showed a fairly linear increase in the CO₂ content with time. Since low temperature ashing studies did show some degradation of the carbonate matrix under intensive microwave heating for prolonged periods, it is surprising that this value was not higher. Reports in the literature on gas composition from TOSCO-modified Fischer assay apparatus suggested that half of the CO₂ in the product gas was of inorganic origin (6). This would leave very little CO₂ gas to be produced by kerogen pyrolysis, indicating possible altered kinetics of degradation.

LOW HYDROGEN LEVELS. These levels would be consistent with the rapid degradation of the kerogen and the low coking levels observed. The possibility exists for active reforming of compounds with hydrogen at the reaction sites.

HIGH METHANE CONTENT. High methane content together with the high CO levels indicate a predominantly gasification process and fits a hydrogen-conserving interaction.

LOW ETHYLENE:ETHANE RATIO. Examination of the C₂ fraction indicated an ethylene:ethane ratio of 0.5 for the total gas, projected retorting indices would suggest a longer residence time, or an effective temperature slightly higher than Fischer assay (18).

LOW PENTANE + FRACTIONS. During the product collection, all gases and vapors were required to flow past silanized glass wool for mist reduction. Also, extensive dry ice cooling was used. These factors may account for the lower values seen. Debutylation of the liquid product was not performed, and these dissolved gases were probably lost in the water separation procedure. These losses would further upgrade the Btu output of the gas.

In these studies, the possibility exists that the kinetics of gas formation have been modified or that they require a different mechanism of localized interaction within the macrostructure. The larger, more amorphous the structure, the greater the opportunity for product ratio inversion by the localized "high temperature" power input to specific bond types. Presently, gas output and composition are being studied as a function of shale grade, time, and power. Tentative results indicate the individual hydrocarbon components maintain a consistent relationship to each other but the CO₂ and CO content vary with grade of shale and time.

Conclusions

The data presented suggest the possibility of selecting feedstock or raw materials for a specific product mix. The quality of both the liquid and gaseous products indicates the advantages of indirect reactions with applied microwave power.

The unique nature of microwave power, as applied through matter to some reactant absorber, has increased the scope of our investigations to encompass more basic studies of the chemical-microwave interaction. The matrix component (shale, sand, etc.) of this interaction is being examined presently by electrical experiments and calculations (dielectric components, permativity, thermal capacity, and conduction).

Acknowledgment

This work was supported by NSF Grant AER75-17453 "A Study of the Use of Microwave Heating for the Release of Oil from Oil Shale." Portions of this paper were presented at the Annual Oil Shale Conversion Symposium, September 1977, University of Wyoming, Laramie, Wyoming and at the Symposium on Thermal Hydrocarbon Chemistry presented before the Division of Petroleum Chemistry, American Chemical Society.

Literature Cited

1. Rattien, S.; Eaton, D. "Oil Shale: The Prospects and Problems of an Emerging Energy Industry," In "Annual Review of Energy"; Annual Reviews, Inc.: Palo Alto, CA, 1976; Vol. I.
2. Yen, T. F. "Oil Shales of United States—A Review," In "Science and Technology of Oil Shale"; Ann Arbor Science Publishers, Inc.: Ann Arbor, MI, 1976.
3. Whitcombe, J. A.; Vawter, R. Glenn. "The TOSCO-II Oil Shale Process," In "Science and Technology of Oil Shale"; Ann Arbor Science Publishers, Inc.: Ann Arbor, MI, 1976.
4. Okress, E. C., Ed.; "Microwave Power Engineering"; Academic: New York, 1968; Vol. 2.
5. Schmidt-Collerus, J. J.; Prien, C. H. "Investigations of the Hydrocarbon Structure of Kerogen from Oil Shale of the Green River Formation," In "Science and Technology of Oil Shale"; Ann Arbor Science Publishers, Inc.: Ann Arbor, MI, 1976.
6. Goodfellow, L.; Atwood, M. T. "Fischer Assay of Oil Shale—Procedures of the Oil Shale Corporation," In "Proc. Seventh Oil Shale Symposium," *Colo. Sch. Mines Mag.* 1974, 69(2).
7. Weast, R. C., Ed.; "Handbook of Chemistry and Physics," 56th ed.; CRC Press: Cleveland, OH, 1975; p. E-60.
8. Perrini, E. M. "Oil from Shale and Tar Sands"; Noyes Data Corporation: Park Ridge, NJ, 1975.
9. McKinney, C. M. "Evaluation of Crude Oils," In "Petroleum Processing Handbook"; Bland, W. F.; Davidson, R. L., Eds.; McGraw-Hill: New York, 1967.
10. McCrum, N. G.; Read, B. E.; Williams, G. "Anelastic and Dielectric Effects in Polymeric Solids"; Wiley: London, 1967.
11. Smyth, C. P. "Dielectric Behavior and Structure"; McGraw-Hill: New York, 1955.
12. Von Hippel, A. R. "Dielectrics and Waves"; M.I.T. Press: Cambridge, MA, 1954.
13. Johnk, C. T. A. "Engineering Electromagnetic Fields and Waves"; Wiley: New York, 1975; p. 179.

14. Stuckey, W. D. "A Study of the Pyrolysis of Oil Shale by Microwave Heating," M.S. Thesis, University of Colorado, Boulder, CO, 1977.
15. Campbell, J. H., et al. "Dynamics of Oil Generation and Degradation During Retorting of Oil Shale Blocks and Powders," In "Tenth Oil Shale Symposium Proceedings"; Colorado School of Mines, 1977.
16. Braun, R. L.; Chin, R. C. Y. "Computer Model for In Situ Oil Shale Retorting: Effects of Gas Introduced into the Retort," In "Tenth Oil Shale Symposium Proceedings"; Colorado School of Mines, 1977.
17. Tisot, P. R.; Murphy, W. I. R. "Physical Structure of Green River Oil Shale," *Chem. Eng. Prog., Symp. Ser.* 1965, 61 (54), 25-32.

RECEIVED October 6, 1978.

A Comparison Between the Properties of Devonian Shale and Green River Oil Shale via Thermal Analysis

C. S. WEN¹ and T. F. YEN²

University of Southern California, Los Angeles, CA 90007

Differential scanning calorimetry (DSC) and thermal gravimetric analysis (TGA) have been used for the investigation of Devonian shale. Activation energy values of both raw shale and kerogen concentrate were obtained, and the values are considerably higher than those of the Green River oil shale. The same is true for the heats of pyrolysis. Specific heats of Devonian shale are lower than those of Green River oil shale. Heat absorbed above 550°C is attributable to the presence of pyrite in Devonian shale. In a pyrite-free Devonian shale kerogen, the peak near 550°C had disappeared. Removal of pyrite will have a thermal decomposition peak at 450°C, which is lower than that of the Green River oil shale kerogen.

Oil shales offer a potential crude oil resource for the United States. These oil shales represent two trillion barrels of oil in Colorado, Utah, and Wyoming, and an additional one trillion barrels of oil of Devonian shale formation in the eastern United States. Eastern Devonian shale is quite different from western Green River shale. The noticeable differences are in geological age, kerogen structure, oil content, pyrite, and other mineral compositions. In the past, little effort has been focused on Devonian shales. However, the increasing role of eastern shales has now

¹ Current address: Gulf Science and Technology Co., P.O. Drawer 2038, Pittsburgh, PA 15230.

² To whom correspondence should be addressed.

been recognized (1) because of their proximity to the industrial center of the United States and their unique character, and because of the shortage of oil and gas supplies.

Thermal decomposition of oil shales is essential to obtain shale oil from the insoluble organic matter (kerogen) and to release gas from the gas-bearing shale. The use of the thermogravimetric analysis (TGA) to investigate the thermal properties of Green River oil shales has been studied extensively in the past few decades (2, 3, 4, 5). However, only a few workers (6, 7, 8) have studied Devonian shales by this technique. Recently there is considerable interest in the production of gas from eastern Devonian shale. This chapter presents the results of a comparison between Green River oil shale and Devonian shale by using differential scanning calorimetry (DSC) and TGA. The effect of demineralization of shales upon heat of reaction also is reported.

Experimental

Ground shale samples (150-200 mesh) from the Green River Formation (Anvil Point, Colorado) as well as those of Devonian shale (Cottageville, West Virginia) were used. From these samples kerogen concentrates were prepared by an acid leaching method (9) in which the soluble organic matter (bitumen) had been extracted in advance. The elemental analyses of samples are listed in Table I. In the case of Devonian shale kerogen, pyrite had been removed by the electrolytic treatment (10).

The DSC data were obtained with a Du Pont cell base and a Model 990 thermal analyzer. An aluminum pan containing the sample was placed on the raised platform in the DSC cell, and an empty pan was placed on the reference platform. DSC scans for the samples were obtained from 150° to 600°C at a linear heating rate of 20°C/min. During the run, a slight flow of nitrogen was maintained. The TGA data was taken with a Du Pont 951 TGA balance in conjunction with a Model 990 thermal analyzer. A platinum boat containing the sample was suspended from the quartz beam of the balance. Samples were heated to 900°C at 20°C/min with a constant nitrogen flow.

Results and Discussion

The thermogravimetric analysis curves of kerogen concentrates from both Green River oil shale and Devonian shale are shown in Figure 1. A sharp peak at 500°C for each sample represents the decomposition of kerogen concentrate. Although the geological age of Devonian shale (Devonian, 300 x 10⁶ years) is much older than Green River shale (Eocene, 60 x 10⁶ years), their transition temperatures for kerogen decomposition are identical. In the case of raw shales, their transition temperatures of organic decomposition are 490°C for Green River shale

Table I. Elemental Analysis of Green River Oil Shale and Devonian Shale

| <i>Substance</i> | <i>Org. C</i> (wt %) | <i>H</i> (wt %) | <i>N</i> (wt %) | <i>S</i> (wt %) | <i>Ash</i> (wt %) |
|---|-------------------------|--------------------|--------------------|--------------------|----------------------|
| Green River oil shale | 16.5 | 2.2 | 0.5 | 0.8 | 62.2 |
| Green River shale kerogen | 68.6 | 8.4 | 3.5 | 2.4 | 9.8 |
| Devonian shale-8 ^{a, b} | 5.0 | 1.2 | 0.1 | 2.6 | 89.0 |
| Devonian shale-43 ^{a, c} | 7.4 | 1.4 | 0.02 | 1.9 | 87.1 |
| Devonian shale kerogen-8 ^{a, b} | 43.1 | 3.9 | 0.5 | 19.5 | 32.5 |
| Devonian shale kerogen-43 ^{a, c} | 59.3 | 6.4 | 0.6 | 14.6 | 21.0 |
| Pyrite-reduced Devonian ^d shale kerogen | 69.7 | 7.4 | 0.6 | 1.2 | 3.3 |

^a Cottageville Devonian shale, core No. 11940.

^b 3445.10–3445.60 ft.

^c 3713.78–3714.43 ft.

^d Pyrite removed from Devonian shale kerogen-43 by electrolytic method (8).

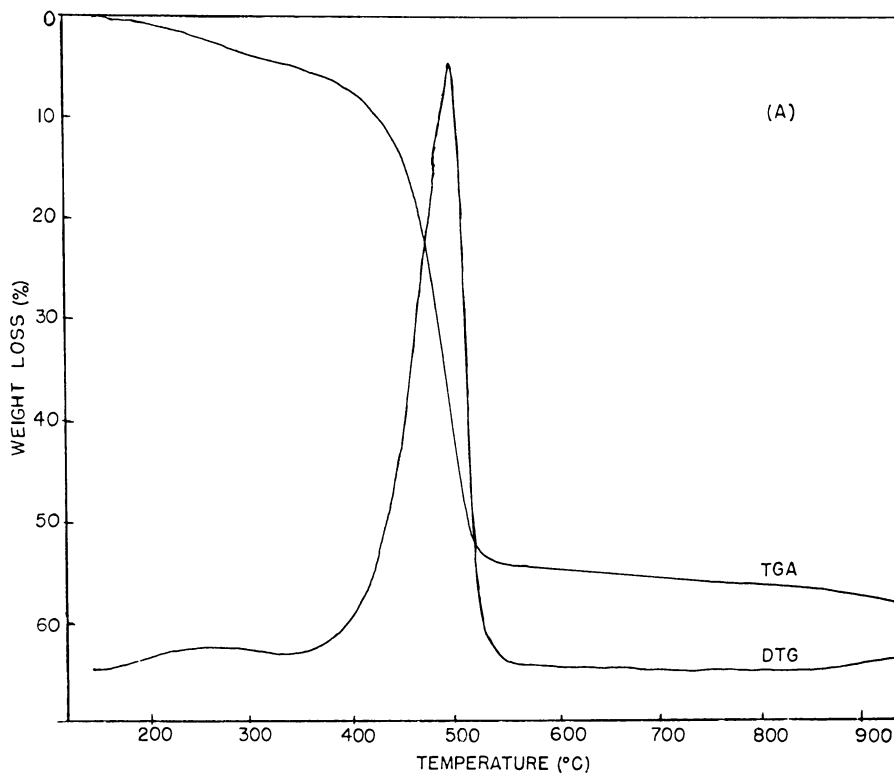


Figure 1. TGA and DTG thermal analyses for (A) Green River shale kerogen and (B) Devonian shale kerogen (No. 43)

and 490°C for Devonian shale, respectively. The minor trailing peak at 556°C (Figure 1b) is attributable to the pyrite decomposition from Devonian shale kerogen. The wide peak around 200°–330°C (Figure 1a) is probably attributable to the volatile hydrocarbons contained in the Green River shale kerogen. The peak is not present in Devonian shale kerogen. The initial temperature of thermal decomposition occurs slowly at around 400°C for both kerogen samples.

In applying the kinetic analysis of Freeman and Carroll (11, 12) to the TGA data (Table II), it was found that the activation energies for thermal decomposition of Devonian shale are higher than those of Green River oil shale for both raw shale and kerogen samples. Similar data on activation energies of Green River shales, presented previously (3, 4, 13), ranged from 40 to 48 kcal/mol for the same grade of oil shale (~ 26 gallons per ton, Fischer Assay).

DSC output curves for raw shales and kerogen concentrates of the two shale samples are shown in Figure 2. It was observed that the thermal effects of the samples are mainly endothermic in nature. Values of heats of pyrolysis can be expressed as calories per unit weight of starting shale sample, as given in Table III. The results of the values concerning heats of pyrolysis are compared in Table III with the experimental work of Sohns et al. (14), Wise et al. (15), and Cook (16) at retorting temperatures. There is a close agreement with the results of those workers. The minor differences are not surprising when one realizes that the mechanism of oil shale pyrolysis is highly complex (17, 18)—it is probably that the observed thermal behavior is the result of several competing reactions. In the case of Green River shale kerogen, the first wide endothermic peak (temperatures ranging from 160° to 330°C) in the DSC curve (Figure 2a) could be attributable to the combined heat of temperature sensation, decomposition, and product volatilization. The second section of the DSC curve (temperature ranging from 330° to 400°C) shows a small constant endothermic region which may be

Table II. Activation Energy for Thermal Decomposition of Raw Shale and Kerogen Concentrate from Green River Oil Shale and Devonian Shale^a

| <i>Raw Shale</i> | | <i>Kerogen Concentrate</i> | |
|------------------------------|---------------------------|----------------------------|------------------------|
| <i>Green River</i> | <i>Devonian</i> | <i>Green River</i> | <i>Devonian</i> |
| 46.2 (40–48) ^o | 74.6 57.1 ^d | 50.0 — | 64.9 ^b — |

^a Average activation energy (kcal/g-mol).

^b Shale No. 43.

^c Data collected from Refs. 3, 4, and 13.

^d Ref. 8 Chattanooga black shale, Oak Ridge, Tennessee.

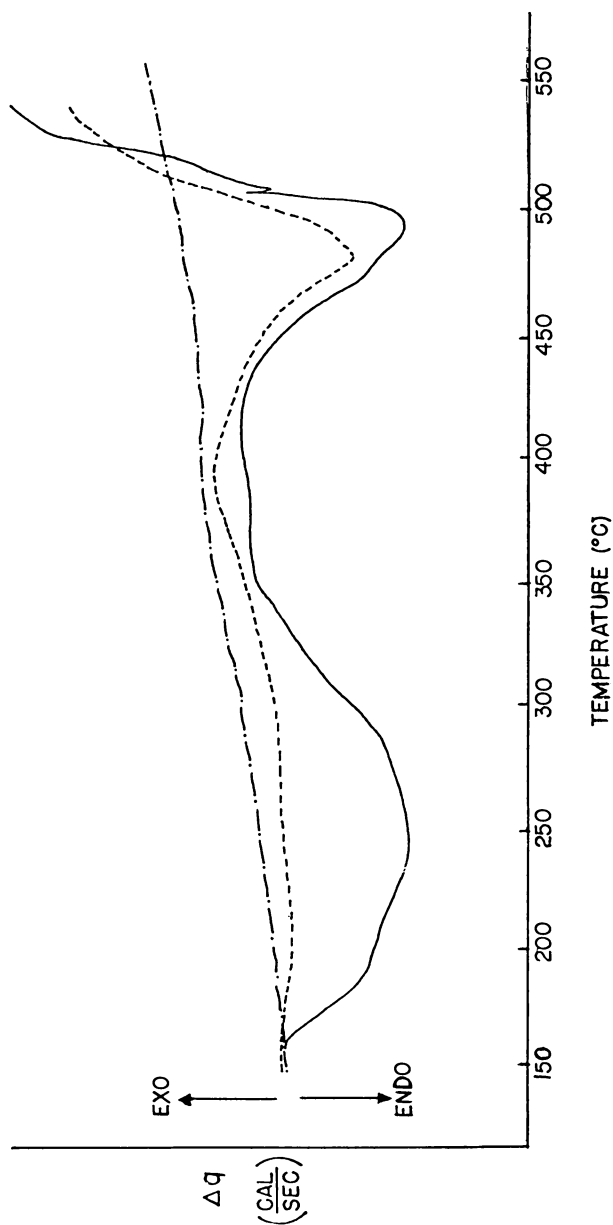


Figure 2. DSC thermal analysis for (A) Green River oil shale and (B) Devonian shale (No. 43). (Both raw shale and kerogen concentrate.) (---) Raw shale, (—) kerogen concentrate, (- · - ·) baseline.

Table III. Heats of Pyrolysis for Green River Oil Shale and Devonian Shale (Unit: cal/g)

| Raw Shale | | | | Kerogen | | | | |
|---------------------------|--------------------------|--------------------------|------------------|------------------|--------------------------|------------------|--------------|---------------|
| Green River | | | Devo- | Devo- | Green River | | Devonian | |
| <i>Sohns</i> ^a | <i>Wise</i> ^b | <i>Cook</i> ^c | <i>This Work</i> | | <i>Cook</i> ^c | <i>This Work</i> | <i>No. 8</i> | <i>No. 43</i> |
| 143 | 163 | 158 | 164 | 186 ^d | 293 | 283 | 330 | 314 |

^a From Ref. 13.

^b From Ref. 14.

^c From Ref. 15.

^d Average value for No. 8 and No. 43.

attributable to the thermal cancellations from some endothermic and exothermic reactions. Though the overall pyrolysis of oil shale has always been reported as an endothermic reaction, several exothermic reactions (e.g., carbon residue formation and hydrogen transfer within pyro-bitumen) might occur during the pyrolysis. The sharp peak (temperature above 400°C) in the DSC curve of kerogen (Figure 2) is attributed mainly to the thermal decomposition of the kerogen matrix.

The specific heats of raw shales and kerogen for both samples (Table IV) are calculated from the relation with the DSC data (Equation 1),

$$C_p = \frac{E\Delta_{qs}\Delta_y}{H_r m} \quad (1)$$

where C_p = specific heat of the sample (cal/g·°C), E = cell calibration coefficient at a given temperature (dimensionless), Δ_{qs} = y-axis sensitivity (mcal/min-in.), Δ_y = difference in y-axis deflection between sample and blank baselines at temperature of interest (in.), H_r = heating rate (°C/min), m = sample mass (mg). Values of C_p for Devonian shale are lower than those of Green River shale. Most of the heat absorbed in Devonian shale above 550°C (Figure 2b and Table III) was attributable to the pyrite present in Devonian shale.

Devonian raw shale contains 2–3% (by weight) of pyrite (19). Pyrite is strongly associated with kerogen matrices in Devonian shales. It is extremely difficult to separate it from the shale organic material. The DSC curves of Devonian shale kerogen, pyrite mineral, and pyrite-reduced kerogen are compared in Figure 3. The major DSC peak of pyrite centered around 550°–560°C had been eliminated in the pyrite-reduced kerogen. The heat of pyrite decomposition from Devonian shale

Table IV. Specific Heats for Green River Oil Shale and Devonian Shale

| T (°C) | C_p (cal/g-°C) | | | | |
|--------|-----------------------|---------------------------|-----------------|---------------------------|----------------------------|
| | Green River Raw Shale | Green River Shale Kerogen | Devonian Shale* | Devonian Shale Kero-gen-8 | Devonian Shale Kero-gen-43 |
| 160 | 0.067 | 0.486 | 0.005 | 0.218 | 0.167 |
| 180 | 0.106 | 0.615 | 0.012 | 0.242 | 0.158 |
| 200 | 0.143 | 0.706 | 0.019 | 0.297 | 0.206 |
| 220 | 0.197 | 0.833 | 0.027 | 0.320 | 0.306 |
| 240 | 0.185 | 0.860 | 0.032 | 0.365 | 0.506 |
| 260 | 0.203 | 0.836 | 0.063 | 0.586 | 0.669 |
| 280 | 0.258 | 0.681 | 0.078 | 0.554 | 0.614 |
| 300 | 0.320 | 0.492 | 0.105 | 0.457 | 0.515 |
| 320 | 0.346 | 0.341 | 0.104 | 0.334 | 0.408 |
| 340 | 0.345 | 0.262 | 0.106 | 0.189 | 0.328 |
| 360 | 0.334 | 0.303 | 0.111 | 0.148 | 0.317 |
| 380 | 0.304 | 0.283 | 0.105 | 0.258 | 0.438 |
| 400 | 0.413 | 0.308 | 0.105 | 0.818 | 0.793 |
| 420 | 0.525 | 0.493 | 0.121 | 1.359 | 1.343 |
| 440 | 0.768 | 0.987 | 0.239 | 2.303 | 2.190 |
| 460 | 1.068 | 1.674 | 0.455 | 2.287 | 2.645 |
| 480 | 1.669 | 2.148 | 0.657 | 1.595 | 3.061 |
| 500 | 1.194 | 1.011 | 0.814 | 0.863 | 2.074 |

* Average value for Devonian shale No. 8 and No. 43.

kerogen was estimated to be 67.6 cal/g. This value agrees with the enthalpy of pyrite (64.5 cal/g) reported by the U.S. Geological Survey (20).

Though transition temperatures of decomposition for both kerogen concentrates are identical (at 500°C), Devonian shale kerogen is much older in geological age and has higher aromaticity than does Green River shale kerogen (19). The higher activation energy obtained from Devonian shale kerogen (64.9 kcal/g-mol vs. 50 kcal/g-mol *see* Table II) may be attributable to the difference of aromatic bond breaking rather than a rupture of the saturated aliphatic bonds. This may provide some information on the internal structural difference between the two types of kerogen.

The thermal properties of Devonian shale are quite different from those of Green River oil shale. The associated pyrite in kerogen concentrate may contribute greatly to the effect on thermal degradation of Devonian gas-bearing shale. For the first time DSC was applied to determining thermal properties of Devonian shale as well as Green River oil shale.

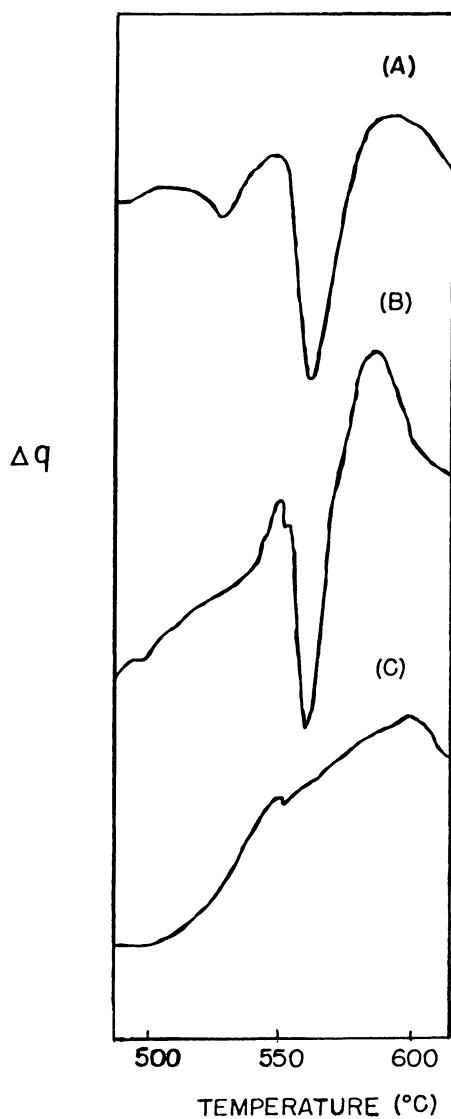


Figure 3. DSC thermal analysis of pyrite in (A) pyrite mineral (Rico, Colorado), (B) Devonian shale kerogen, and (C) pyrite-reduced kerogen of Devonian shale

Acknowledgment

This work was supported by the U.S. Department of Energy under contracts MERC EY-77-G-21-8104, LERC E(29-2)-3619, A.G.A. BR-48-21, and GRI 5010-362-0035.

Literature Cited

1. "Enhanced Recovery of Unconventional Gas, The Program, Vol. II"; DOE, 1978.
2. Heady, H. *Am. Mineral.* 1952, 37, 804.
3. Allred, V. D. *Chem. Eng. Prog.* 1966, 62, 55.
4. Arnold, C., Jr. In "Industrial and Laboratory Pyrolyses"; Albright, L. F., Crynes, B. L., Eds.; ACS Symp. Ser. 1976, 32, 492.
5. Weitkamp, A. W.; Gutberlet, L. C. *Ind. Eng. Chem., Proc. Des. Dev.* 1970, 9, 386.
6. Scrima, D. A.; Meyer, W. C.; Yen, T. F. "Chemistry of Marine Sediments"; Yen, T. F., Ed.; Ann Arbor Science, 1977; Chapter 14.
7. Claypool, G. E.; Threlkeld, C. N. Preprints, First Eastern Gas Shale Symposium, 1977, 438-449.
8. Herrell, A. Y.; Arnold, C., Jr. *Thermochim. Acta*, 1976, 17, 165.
9. Robinson, W. E. "Organic Geochemistry"; Eglinton, G., Murphy, M. T. J., Eds.; Springer-Verlag: New York, 1969, Chapter 6.
10. Wen, C. S.; Kwan, J.; Yen, T. F. *Fuel*, 1976, 55, 75.
11. Freeman, E. S.; Carroll, B. *J. Phys. Chem.* 1958, 62, 394.
12. Daniels, T. "Thermal Analysis"; John Wiley and Sons: New York, 1973; 60-82.
13. Hill, G. R.; Dougan, P. *Q. Colo. Sch. Mines* 1967, 62, 75.
14. Sohns, H. W.; Mitchell, L. E.; Cox, R. J.; Barnett, W. I.; Murphy, W. I. R. *Ind. Eng. Chem.* 1951, 43, 33.
15. Wise, R. L.; Miller, R. C.; Sohns, H. W. *U.S. Bureau of Mines*, 1971, RI 7482.
16. Cook, E. W. *Q. Colo. Sch. Mines* 1970, 65, 133.
17. Wen, C. S.; Yen, T. F. *Chem. Eng. Sci.* 1977, 32, 346.
18. Fausett, D. W.; George, J. H.; Carpenter, H. C. *U.S. Bureau of Mines*, 1974, RI 7889.
19. Yen, T. F.; Wen, C. S.; Tang, J. I. S.; Kwan, J. T.; Young, D. K.; Chow, E. Preprints, First Eastern Gas Shale Symposium, 1977, 414-430.
20. Robie, R. A.; Waldbaum, D. R. *U.S., Geol. Surv. Bull.* 1968, 1259.

RECEIVED June 30, 1978.

INDEX

A

- Acetylene ... 71, 154, 189, 195, 205–206
 butadiene, and benzene, pyrolysis products from 193–203
 coke formed from 178*f*, 184*f*, 187*f*–188*f*
 effect of temperature on coke from 180*f*
 as pyrolysis feedstock 195–198
- Acid
 dew point of flue gas 166, 167*f*
 gas removal 110
 leaching 344
- Activation energy (ies) of
 alkyl radical β -scission 313
 bituminous coal pyrolysis 249
n-butenes pyrolysis 37–40
 carbon dioxide evolution 248
 coke formation 280
 dodecene cracking 5, 10*f*
 ester decomposition 2
 ethane pyrolysis 215
 hydrogen abstraction 313
 hydrogen addition to ethylene .. 314
 hydropyrolysis of decalin 318
 hydropyrolysis of *n*-hexadecane 302, 304
n-paraffins conversion 141
 pyrolysis 266–271
 β -resin formation 279
 thermal decomposition of shale . 346
- Adiabatic cracking 108
- Advanced Cracking Reactor (ACR) technology 107–127
- Alkyl radical(s) 34, 42
 β -scission, activation energy for . 313
- Alkylation, modification of thermal 289–295
- Alkylation reaction conditions . 291–292
- Alkylbenzenes 80, 297
- Alkyl-naphthalenes 80
- Alonization 177
- γ Alumina catalyst 259–271
- Ammonia synthesis 234
- Amorphous coke(s) 178, 181, 189
- Analysis
 crude oil 95, 330
 storage heat exchanger 121–122
- Aromatics reduction, gas oil 86*t*
- Arrhenius
 constant 140
 equation 266–271, 279–280
 frequency factor for bituminous coal pyrolysis 249

Arrhenius (continued)

- plot(s) of
n-butenes pyrolysis 38*f*, 39*f*
 decalin hydropyrolysis 319*f*
 quinoline insoluble pyrolysis products 282*f*
 β -resins 280*f*
 retro-ene reaction 15*f*, 16
 rate constant for lignite pyrolysis production 254
- Arrowhead coke 179

B

- Back hydrogenation of ethylene .. 59
- Back-mixed flow 56–58
- Benzanthracenes 277
- Benzchrysenes 277
- Benzene 70, 82, 195, 199, 241, 253
 insoluble pyrolysis products (BI) 275
 as pyrolysis feedstock 200–201
 pyrolysis products from acetylene, butadiene, and 193–203
- Benzphenanthrenes 277
- Bitumen 344
 pyrolysis of pitch from hydrocracked 259–271
- Bituminous coal, pyrolysis product distributions from 242, 243*f*
- Bituminous coal, rapid pyrolysis of 239–256
- Black coke 214*f*, 219
- Black mirror 199–200
- Brown-Ladner treatment 78
- n*-Butene pyrolysis 21–40, 58–65
 Arrhenius plot of 38*f*
 products of 25
 selectivity diagrams for 31*f*
- 1-Butene, thermal decomposition of 21–40
- 2-Butenes pyrolysis
 Arrhenius plot of 39*f*
 products of 25
 selectivity diagram for 32*f*
 thermal decomposition of 21–40
- Burner noise 170
- Butadiene 24, 30, 154, 179, 189
 benzene, and acetylene pyrolysis products from 193–203
 coke(s) formed from 181*f*, 184*f*, 187*f*–188*f*
 as pyrolysis feedstock 198–200
 yields 160*f*
- 1,3-Butadiene 70, 73, 195
- Butane, 2,2-dimethyl 291

- n*-Butane reactor, temperature profiles of 138f
 Butyl peroxide, thermal decomposition of ditertiary 289
 By-products, cracking 108

C

- Calcite 247
 Calorimetry, differential scanning 343-350
 Capital cost of hydrocarbonization combustion plant 235t
 Captive sample apparatus and analysis system 241f
 Carbon
 deposition 222
 kinetics 213-215
 dioxide 200, 339
 evolution, activation energy of 248
 pyrolysis yields of oxygen in 248f
 distribution in make gas from
 Wyodak coal 229t
 monoxide 338
 Carboxyl oxygen measurements 249
 Carburization 217
 Catalysts, cracking 96t
 Catalytic cracking residues 274
 Catalytic hydrogenation 80
 Catalyzed pyrolysis, rate of 267f
 Chain length effect on hydro-pyrolysis of *n*-paraffins 310-311
 Char, low-sulfur 232, 234
 Chemical
 feedstocks, shale oil conversion to 96f
 feedstocks yield from shale oil 104-105
 kinetics, gas-phase 126
 pyrolysis in ACR, rate of 111
 structure, effect on pyrolysis
 behavior 246-253
 Chrysenes 277
 Coal(s)
 analysis of 240t-241t
 -derived liquids 226
 hydrocarbonization of western 225-237
 liquefaction processes 68
 particle size, effect on volatiles
 yields 255f
 Coalcon hydrocarbonization plant 234
 Coke
 formation
 factors affecting 205
 kinetics of 280-286
 during pyrolysis 175-191
 gasification 221-223
 precursor(s) 176, 181, 189, 194, 206, 215, 281
 types of 177
 variables affecting 177-181
 yield vs. ethylene yield 208f
 Cold-flow ACR penetration experiments 116-118
 Cold flow conditions 115
 Colorado oil shale 336

- Combustion air preheating 164-166, 173
 Commercial
 carbonization process, flowsheet for 233f
 hydrocarbonization process 232-235
 pyrolysis plant data, prediction of 136t-137t
 reactor yields, naphtha
 pyrolysis 147, 150t
 Compensation effect 268-270
 Computer modeling of hydro-carbon pyrolysis 129-151
 Computer simulation of ACR 111
 Condensation products 318
 Conversion dependence of product ratios 30-35
 Cracking (*see also* Pyrolysis)
 coil(s)
 arrangement 163-164
 design 162, 163f
 hydrocarbon throughput of 169t
 energy consumption in 164-169
 furnace(s)
 design 153-175
 heat transfer rates in 169t
 updating 171-175
 parameters 153, 171
 profiles, nonisobaric 144
 profiles, nonisothermal 144
 Severity Index 139-140, 144
 technology 153-175
 test techniques, short duration 107-127
 yields 170t
 Crude(s)
 oil analysis 95, 330
 oil cracking reactor, scaling
 methods for 107-127
 shale oils, properties of 337t
 Crystallite parameters for a
 graphitic matrix 276
 Crystallites, turbostratic 277
 Cycloalkanes pyrolysis experiments 69-71
 Cycloalkanes pyrolysis product spectra 69, 70t
 Cyclohexane
 pyrolysis of 67-76
 pyrolysis pathways 71f
 toluene, and *n*-hexane, steam
 cracking of 176
 Cyclohexyl radical 71

D

- Damköhler number 111-112
 Debutylation 339
 Decahydronaphthalene, pyrolysis of 67-76
 Decahydroanaphthalene pyrolysis pathways 71-73
 Decalin, activation energy of
 hydropyrolysis of 318
 Decalin, hydropyrolysis of 314-323
 Decalyl radicals 73

- Decant oil274-276
 fractions, analysis of 284*t*
 pyrolysis products277-278
 Decoking 222
 reactor surfaces before and
 after181-189
 Decomposition
 of 1-butene, thermal 21-40
 of 2-butenes, thermal 21-40
 first-order 256
 kaolinite 253
 model, first-order 248
 of petroleum residuum 264
 rate of propane 45*t*
 rates of α -olefins 4, 9*f*
 reactions, solid-state 269
 thermal245-253
 Degree of reaction, determina-
 tion of 275
 Dehydrogenation products 321
 Dehydroxylation pathway, radical-
 based 253
 Deposition of coke during
 pyrolysis205-224
 Deposition rate, gasification
 rate vs. 223*f*
 Development system, pyrolysis
 technology 130*f*
 Devonian shale, thermal
 analysis of343-350
 Dibenzanthracenes 277
 Dibenzchrysenes 277
 Dibenzpyrenes 277
 Dicycloalkanes, pyrolysis of 67-76
 Dielectric constant 332-334
 Differential scanning calorime-
 try343-350
 Differential yields of pyrolysis
 products 85-88
 1,4-Dihydronaphthalene 73
 Dipole orientation 333
 Dispersion criterion 56
 Distillation curve226, 231*f*
 Distillation of whole crudes 95
 Dodecene
 cracking
 activation energy of 5, 10*f*
 reaction paths in 14*t*
 relative contributions of
 reaction paths in17-19
 product distributions for radical
 addition to 13*t*
 pyrolysis, reaction order of 8*t*, 12
 Dolomite 247
 Double bond shift 24, 313
 Droplet-size experiments, ACR .114-116
 Dynamic similarity 112

E

- Electrode(s)
 binder pitch from petroleum-
 based materials273-286
 fabrication273-286

- Electrode(s) (*continued*)
 graphite, quartz, and refractory
 steel, steam cracking over . 176
 prebaked 274
 vertical stud Soderberg 274
 Elemental analysis of shale 345*t*
 Energy consumption in cracking 164-169
 Enthalpy of formation of feedstock 88
 Environmental protection170-171
 Equilibrium constant for ethane
 pyrolysis 210
 Equilibrium, water gas shift 246
 Ester decomposition 2
 Ethane199, 201, 286, 294, 339
 coke formed from 187*f*
 pyrolysis, deposition, and gasi-
 fication of coke during .205-224
 Ether linkages, scission of 252
 Ether, pyrolysis of dimethyl 312
 Ethylene30, 73, 82, 154,179,
 199, 201, 339
 activation energy of hydrogen
 addition to 314
 back hydrogenation of 59
 coke from184*f*, 187*f*
 effect of space time and tem-
 perature on coke formed
 from 182*f*
 production 147
 thermal alkylation of289-295
 and total coke yield vs.
 conversion 210*f*
 yield(s)159*f*, 162*f*, 207
 vs. coke yield 208*f*
 vs. conversion 211*f*
 from crude oil 108*t*
 effect of pyrolysis
 severity on 82-84, 83*f*
 selectivity, *n*-heptane pyrolysis 146*f*
 selectivity, naphtha pyrolysis .148*f*
 Ethyl radical(s) 41, 215
 Experimental facilities, ACR ...119-122
 Experimental pyrolysis rate con-
 stants, predicted and 57
 Extent of pyrolysis reaction ...266-271
 Extraction, selective solvent ... 275, 283

F

- Feed conversion, predicted vs.
 actual 141*f*
 Feed decomposition 139-140
 Feedstock
 acetylene as pyrolysis195-198
 analysis275-276
 benzene as pyrolysis200-201
 butadiene as pyrolysis 198-200
 characterization78-80
 enthalpy of formation of 88
 flexibility169-170
 fouling propensity of 88
 hydrogenation effect on
 pyrolysis yields 78

- Feedback (*continued*)
 from Paraho shale oil 91-105
 properties, naphtha 137*t*, 139
 properties, pitch 262*t*
- Filament
 coke 176-177, 219-220
 cokes, knobby 189
- Fired duty 165*f*
- First-order
 decomposition 256
 model 248
 kinetic plot for pyrolysis
 products 281*f*
 kinetic plot for β -resins 279*f*
 kinetics 139, 212-213
 rate
 constants 55-56
 equations 278
 law 35
 reaction(s) 254, 269
- Fischer-assay
 apparatus 330
 characteristics of micro-
 wave-produced oil 336*t*
 intraparticle oil 335-337
 processed shales, residues from . 336*t*
- Fischer-Tropsch synthesis 234
- Flame cracking of crude oil ... 107-127
- Flow property indicators 335
- Flow systems, venturi 121
- Flowsheet for commercial car-
 bonization process 233*f*
- Flue-gas heat recovery 166-169
- Fluffy coke 179
- Fluid-flow parameters, ACR 123
- Fouling propensity of feedstock .. 88
- Fraction yields from carboni-
 zation of coal 226
- Fraction yields, effect of hydro-
 carbon partial pressure ... 154, 155*f*
- Free radical
 inhibition 9
 mechanism(s) 134, 140
 of *n*-butenes decomposition .. 32-35
 of α -olefin 9-16
 reactions 71, 289-295
 theory, Rice-Kossiakoff 322
- Fuel
 gas consumption 171
 oil
 differential yields of pyrolysis .84-88
 pyrolysis 69, 71, 82, 154, 170
 yields, effect of pyrolysis
 severity on 82-84, 83*f*
 yields, pyrolysis 161*f*-162*f*

G

- Gas
 analysis, retorting 338-339
 chromatographic analyses of
 off-gas 97, 99
 chromatographic analysis con-
 ditions 3*t*

- Gas (*continued*)
 chromatography ... 23-24, 195, 206,
 242, 260, 291, 298, 327, 332
 differential yields of 84-88
 evolution during retorting ... 334-339
 oil(s)
 atmospheric 78
 petroleum-derived 99
 pyrolysis of virgin and
 hydrogenated 77-88
 phase coke 179, 189
 yield test, ACR 125-127
 yield test equipment, ACR ... 119-121
- Gasification
 coke 221-223
 of coke during pyrolysis ... 205-224
 rate vs. deposition rate 233*f*
- Gasoline
 aviation 290
 differential pyrolysis yields ... 84-88
 pyrolysis 170
- Geometrical isomerization 35
- Globular coke 216, 218*f*
- Graphitic matrix, crystallite
 parameters for 276
- Gravimetric analysis of char
 and tar 242
- Green River oil shale 93
 thermal analysis of 343-350

H

- Hall-Heroult process 273-286
- Heat(s)
 loss adjustment, kinetic
 analysis of 127
 recovery, flue-gas 166
 of shale pyrolysis 346-348
 transfer rates in cracking
 furnace 169*t*
- Heating rates, effect on pitch
 pyrolysis 265*t*
- n*-Heptane pyrolysis, ethylene
 yield selectivity 146*f*
- n*-Heptane pyrolysis, yield
 profiles of 145*f*
- Heteroatom poisoning 100
- Heteroatom removal during
 hydrocracking 100*t*-101*t*
- Heterocyclics, hydropyrolysis of .. 298
- n*-Hexadecane, hydropyrolysis of 298-314
- Hexane, 2,2-dimethyl 292
- n*-Hexane pyrolysis 60*f*, 62*f*-63*f*
- n*-Hexane, steam cracking of
 cyclohexane, toluene, and ... 176
- 1,3,5-Hexatriene 73
- Hot-flow penetration experi-
 ments, ACR 122-125
- Hydrocarbon(s)
 partial pressure effect on
 fraction yields 154, 155*f*
 polynuclear aromatic 285-286
 pyrolysis products 278*t*

Hydrocarbons (*continued*)
 throughput of cracking coils . . . 169*t*
 yield vs. hydrocarbonization
 temperature 229*f*
 Hydrocarbonization
 apparatus 227*f*
 flowsheet 228*f*
 temperature vs. hydrocarbon
 yield 229*f*
 of western coal 225–237
 Hydroconverter residue yields . . . 155*f*
 Hydrocrack residuum 157, 162
 Hydrocracking of shale oil 96–100
 Hydrogen 199–200, 339
 abstraction 33–35, 59, 71–76,
 285, 322
 activation energies for 313
 addition 33–35
 to ethylene, activation
 energy of 314
 from benzene pyrolysis 201*f*
 -chloride catalyzed alkylation,
 yields from 294*t*
 chloride on alkylation selec-
 tivity, effect of 292–294
 consumption 232
 vs. hydrogen partial
 pressure 226, 230*f*
 content of residue 266
 elimination 15
 pressure effect on hydrocracking 98*f*
 pressure effect on hydropropylo-
 sis products . . . 304–310, 318–322
 sulfide 207, 219, 223, 324
 transfer 348
 Hydrogenated gas oils, pyrolysis
 of 77–88
 Hydropropyloysis
 apparatus 324–327
 of model compounds 297–327
 and thermal cracking, product
 distribution from 299*t*, 315*t*
 Hydrotreating of shale oil 100
 Hydroxyl radical 253

I

Interfacial polarization 334
 Internal standard, methane as an . 291
 Intraparticle oil, Fischer-assay
 produced 335–337
 Iron deposits 181, 185*f*
 Isobutane 290–295
 Isobutyl radicals 291
 Isomerization, geometrical 24
 Isothermal block, hydropropyloysis
 reactor 326*f*

K

Kaolinite decomposition 253
 Kerogen 343–350
 degradation 329–330, 338
 pyrolysis 334, 339
 specific heats of shales and . . 348–349

Kerosene 78
 yields 155*f*
 Kinematic similarity 112, 116
 Kinetic(s)
 analysis of heat loss adjustment 127
 analysis of thermal gravimetric
 analysis data 346
 of *n*-butenes pyrolysis 35–37
 calculations of coal pyrolysis . 347–249
 carbon deposition 213–215
 coke formation 280–286
 first-order 139
 limitations, chemical 247
 model of higher paraffins
 pyrolysis 58–65
 model of pyrolysis 50–51
 of pitch pyrolysis 265–271
 of β -resin formation 278–280
 system, homogeneous 131
 zero conversion 212
 Knobby filament cokes 189
 Kureha reactor reference test . . . 127

L

Laser
 helium–neon 123
 pulsed ruby 115
 pulsed UV- 114
 Lignite, pyrolysis product distri-
 butions from 242, 244*f*
 Lignite, rapid pyrolysis of 239–256
 Linde–Selas Combined Coil . . . 162, 163*f*
 Linear regression 117
 Lipophilic traps 241
 Liquid
 chromatographic separation of
 whole crudes 95
 chromatography 275
 hourly space velocity (LHSV) . . 298
 effect on hydropropyloysis
 products 308
 Loss tangent 333–334

M

Mach number(s) 113, 123
 wind tunnel 117
 Make gas from Wyodak coal,
 carbon distribution in 229*t*
 Mass
 spectrometry . . . 23, 80, 261*f*, 277, 327
 high resolution 275
 transport limitations 254
 Mechanism of decalin hydro-
 pyrolysis 322–323
 Mechanism of *n*-paraffins hydro-
 pyrolysis 311–314
 Mechanistic modeling 133
 Metallic coke 177–181, 189, 197, 219–221
 Methane 24, 30, 199, 211, 286, 301,
 304, 315, 317, 339
 as an internal standard 291
 production 215
 yield(s) 158*f*, 209
 vs. conversion 210*f*

- Methanol synthesis 234
 Methyl allyl radical 33
 Methyl radical(s) 34, 41-42
 Methylacetylene + propadiene
 (MAP) 25, 30, 35
 Methylene chloride 240
 Methylvinyl radical 35
 Microbalance reactor 261*f*
 Microwave
 energy 332-334
 power, retorting oil shale by .. 329-340
 processed shales, residues from . 336*t*
 produced oil, characteristics of . 336*t*
 Mineral carbonates 247
 Model
 compounds hydrolysis 297-327
 of lignite pyrolysis 253-256
 parameters 134-135
 Molecular collision parame-
 ter 157-161, 172*f*
 Monocycloalkanes, pyrolysis of .. 67-76
 Montana lignite 239-256
 Morphology of coke formed during
 ethane pyrolysis 215-221

N

- Naphtha(s)
 conversion from gas oils 97*f*-98*f*
 optimization of steam dilution .. 156*f*
 pyrolysis
 commercial reactor yields .147, 150*t*
 ethylene yield selectivity 148*f*
 model 136-147
 reactor, temperature profiles of . 149*f*
 reforming of hydrotreated ... 100-103
 steam pyrolysis of 101-104
 yields 155*f*
 Naphthalene 321
 Naphthenes, hydrolysis of
 polycyclic 298
 Naphthoaromatics 297
 hydrolysis of multiring 298
 Natural gas, liquefied 232
 Natural gas, substitute 232
 Needle coke 179
 Neopentane, thermal decomposition 289
 Neopentyl radical 295
 Nickel sulfides 221
 Nitrogen oxides emission 170-171
 Nonisobaric cracking profiles 144
 Nonisothermal cracking profiles ... 144
 Nozzle reaction chamber, venturi . 108
 Nozzles, swirl-spray pressure 114

O

- Octahydrophenanthrene 68-69, 315,
 317, 322
 Oil
 characteristics of Fischer-assay
 produced 336*t*
 characteristics of microwave-
 produced 336*t*

- Oil (*continued*)
 degradation 338
 -particle trajectory, ACR 116
 price sensitivity to synthetic
 natural gas and power prices 236*f*
 shale
 gaseous products from micro-
 waved 338*t*
 retorting by microwave
 power 329-340
 thermal analysis of Devonian
 and Green River 343-350
 Olefin(s)
 conversion to 104
 cracking 4
 α -Olefins, pyrolysis of 1-19
 production, computer modeling
 of 129-151
 Optical setup for spark photo-
 graphs 117*f*
 Optical techniques, TRW 123
 Ottawa sand 43-44
 Outlet pressure, furnace 154
 Outlet temperatures,
 flue-gas 166, 168*f*, 173
 Oxygen exchange reactions 222

P

- Paraffin(s)
 cracking 4
 isothermal pyrolysis 41-66
 pyrolysis 1-2
 n-Paraffins
 conversion, activation energy of 141
 decomposition rate con-
 stants 142*f*-143*f*
 hydrolysis 298-314
 Paraho process 93*f*
 Paraho shale oil, properties of 94*t*
 Parameters for propane cracking .. 52
 Partial pressure effect on
 paraffin pyrolysis 64-65
 Particle velocity 123, 124*t*
 Penetration experiments, ACR
 cold-flow 116-118
 hot-flow 122-125
 Penetration trajectory coordi-
 nates, spray 118*f*
 Pentane 339
 2-methyl 291
 Pentyl radical 34
 Perhydrophenanthrene pyrolysis .. 67-76
 pathways 73, 74*f*
 Pericyclic reactions 71
 Perylenes 277
 Petroleum-based materials, pro-
 duction of pitch from 273-286
 Phenanthrene 277
 Phenolic hydroxyl groups 253
 Phenolic hydroxyl oxygen 251
 Phenyl radical 252
 Photographic technique,
 spark-shadow 117

- Pilot plant, ACR 110
 Pilot plant reactor 260
 Pitch
 feedstock properties 262*t*
 from hydrocracked bitumen . . .259–271
 production from petroleum-based
 materials273–286
 pyrolysis of259–271
 pyrolysis thermogravimetric
 studies259–271
 Pittsburgh Seam bituminous coal 239–256
 Platelet-type coke176, 219–220
 Plenum chamber 166
 Plug flow56–58
 Polarization 333
 interfacial 334
 orientation 334
 Polycrystalline coke 178
 Polyethylene 290
 Polymer crosslinking 334
 Polynuclear aromatic hydro-
 carbons68, 285–286
 Power prices, oil price sensi-
 tivity to 236*f*
 Pressure effect on paraffin
 pyrolysis64–65
 Pressure effect on volatiles yields .. 255*f*
 Processed naphthas, compositions
 of102*t*–103*t*
 Processing shale oil95–96
 Product(s)
 of *n*-butenes pyrolysis, primary .30–35
 distribution
 analysis, pitch pyrolysis 265*t*
 in *n*-butene pyrolysis25–30
 from entrained-solids retort
 crudes 93*f*
 from hydropyrolysis and
 thermal cracking299*t*, 315*t*
 of α -olefin pyrolysis4–7, 12–14
 inhibition in pyrolysis41–66
 inhibition model of propane
 cracking 49
 ratios, conversion dependence of 30–35
 spectra, cycloalkanes pyrolysis .69, 70*t*
 yield(s)
 of 1-butene pyrolysis 26*t*–28*t*
 of 2-butenes pyrolysis26*t*–28*t*
 gas oil pyrolysis 81*t*
 pyrolysis conditions and .208*t*–209*t*
 Propadiene 71
 + methylacetylene
 (MAP)25, 30, 35
 Propane 201, 286, 294
 conversion 64*f*
 cracking models49–51
 cracking parameters 52
 decomposition 42
 decomposition rate 45*t*
 pyrolysis46*f*, 48*f*, 52–58
 Propyl radicals 42
 Propylene24, 30, 42, 82, 154,
 179, 199, 201, 211
 coke formed from183*f*–184*f*
 Pyrenes 277
 Pyrite decomposition346, 348–349
 Pyrite, thermal analysis of 350*f*
 Pyrolysis (*see also* Cracking)
 behavior, effect of chemical
 structure on246–253
 of *n*-butenes 21–40
 coke formation during175–191
 computer modeling of129–151
 conditions194–195, 206,
 240, 260–261
 and product yields208*t*–209*t*
 deposition and gasification of
 coke during205–224
 of dicycloalkanes67–76
 equipment and procedure 274
 ethane205–224
 experiments, gas oil81–84
 flow apparatus 3*f*
 of gas oils77–88
 kerogen334, 339
 of lignite and bituminous
 coal, rapid239–256
 model
 development132–134
 light hydrocarbon134–137
 naphtha136–147
 of monocycloalkanes67–76
 of α -olefins1–19
 for olefins production129–151
 of paraffins41–66
 of pitch from hydrocracked
 bitumen, thermogravimetric
 studies of259–271
 product(s)
 from acetylene, butadiene,
 and benzene193–203
 distributions from bituminous
 coal242, 243*f*
 distributions from lignites 242, 244*f*
 inhibition41–66
 in tubular reactors193–203
 recovery and analysis274–275
 rate constants 57
 tetradecene 9
 of tricycloalkanes67–76
 yields of oxygen in carbon
 dioxide 248*f*
 Pyrolytic water242, 245
 evolution, temperature de-
 pendence of249–253
 oxygen yields 251*f*
- ## Q
- Quartz
 electrode graphite, and refrac-
 tory steel, steam cracking
 over 176
 reactor 2, 43
 retort 330
 Quinoline insoluble pyrolysis prod-
 ucts (QI)275–277, 280–286

R

| | |
|---|------------------------|
| Radical addition reactions | 11-19 |
| Radical-based dehydroxylation pathway | 253 |
| Rate | |
| of catalyzed pyrolysis | 267f |
| constant (s) | 134 |
| of Arrhenius lignite pyrolysis production | 254 |
| of <i>n</i> -butenes pyrolysis | 35-37 |
| of ethane pyrolysis | 213 |
| first-order | 55-56 |
| of hydropyrolysis | 318 |
| of <i>n</i> -paraffins, decomposition | 142f-143f |
| zero-conversion | 141 |
| equations, first-order | 278 |
| of gasification | 222 |
| law, first-order | 35 |
| law, second-order | 36 |
| Raw oil product, distillation curve for | 231f |
| Raw oil product, properties of | 232f |
| Reaction order | |
| of dodecene pyrolysis | 8f |
| of α -olefin pyrolysis | 4, 8f, 12 |
| paths in dodecene cracking | 14f |
| relative contributions of | 17-19 |
| Reactor (s) | |
| alonized | 201-202 |
| continuous flow | 298 |
| exit temperature-time profile | 125f |
| fluid-bed | 44, 56-59 |
| Hastelloy | 183-224 |
| high-alloy steel | 202 |
| horizontal tubular | 176-177, 179, 274 |
| hydropyrolysis | 324-327 |
| Incoloy 800 | 183-224 |
| Kureha, reference test | 127 |
| metal | 221 |
| microbalance | 261f |
| pilot plant | 260 |
| pretreating | 196, 200-202, 207, 221 |
| quartz | 2, 43 |
| stainless steel | 126, 183-224 |
| surfaces before and after decoking | 181-189 |
| temperature profiles of <i>n</i> -butane tubular flow | 138f |
| flow | 206 |
| model | 69, 81 |
| pyrolysis products in | 131-132 |
| two-phase flow | 193-203 |
| Vyclor glass | 111 |
| Vyclor glass | 183-224 |
| Recycle hydrocracking | 98-101 |
| Reforming of hydrotreated naphthas | 100-103 |
| Refractory steel, steam cracking over quartz, electrode graphite, and | 176 |
| Residence time | 157 |

| | |
|---|------------------|
| Residue (s) | |
| catalytic cracking | 274 |
| from Fischer-assay processed shales | 336f |
| formation | 348 |
| hydrogen content of | 266 |
| from microwave-processed shales | 336f |
| weight, effect on activation energy | 269f |
| yield during pitch pyrolysis | 263f-264f |
| Residuum, decomposition of petroleum | 264 |
| β -Resin (s) | 275-278, 281-284 |
| formation, kinetics of | 278-280 |
| precursors | 283 |
| Retort crudes, product distribution from entrained-solids | 93f |
| Retorting | |
| microwave | 331, 331f |
| oil shale, yields from | 335f |
| procedure | 332 |
| Retro-ene reaction | 2, 9, 17-19 |
| Arrhenius plot of | 15f, 16 |
| Ribbon coke | 189 |
| Rice-Herzfeld pathway | 73 |
| Rice-Kossiakoff | |
| free-radical theory | 322 |
| hypothesis | 302, 312 |
| isomerizations | 73 |
| mechanism | 12, 15 |
| Ring opening | 80 |

S

| | |
|--|-----------------|
| Sauter mean diameter | 112, 114-115 |
| Scale-up, ACR | 110-114 |
| Scaling methods for crude oil cracking reactor | 107-127 |
| Scanning electron microscope | 189, 197, 215 |
| Scission of ether linkages | 252 |
| β -Scission | 71-76, 312, 322 |
| activation energy for alkyl radical | 313 |
| paths in dodecene cracking | 17 |
| Secondary decomposition | 25 |
| Second-order rate law | 36 |
| Selectivity | |
| diagrams, zero conversion extrapolation of | 30-32 |
| effect | 144-147 |
| hydrogen chloride effect on alkylation | 292-294 |
| Semikinetetic modeling | 133-134 |
| Severity, cracking | 144 |
| Severity function | 82, 84 |
| Shale (s) | |
| activation energies for thermal decomposition | 346 |
| elemental analysis of | 345f |
| heats of pyrolysis | 346-348 |
| and kerogen, specific heats | 348-349 |

Shale(s) (*continued*)

- oil(s)
 - characterization92-95
 - crude, properties of 337*t*
 - feedstocks from Paraho ...91-105
 - particles, chemical reactions in . 338*t*
 - residues from Fischer-assay
 - processed 336*t*
 - residues from microwave
 - processed 336*t*
 - thermal analyses for344-350
- 1,3-Sigmatropic-alkyl migration .. 73
- Similarity groups, scale-up111-114
- Single-pass hydrocracking 98
- Skeletal isomerization 24
- Space
 - time effect on coke from ethylene 182*f*
 - time vs. steam diluent 212*f*
 - velocity112-113
- Specific gravity of oil 336
- Specific heats of shales and
 - kerogen348-349
- Spray penetration trajectory
 - coordinates 118*f*
- Steam
 - cracking 301
 - commercial operations69, 81
 - of cyclohexane, toluene, and
 - n*-hexane 176
 - over quartz, electrode graph-
 - ite, and refractory steel . 176
 - diluent vs. space time 212*f*
 - dilution154, 207
 - for naphtha, optimization of . 156*f*
 - pyrolysis of
 - gas oils101-104
 - naphtha101-104
 - shale oil 95
- Stoichiometric modeling 133
- Storage heat exchanger analysis .121-122
- Subbituminous coals226, 247
- Substrate
 - characterization68-69, 70*t*
 - graphs 75*f*
 - topology 73
- Surface-deposited products 199
- Surface reactions during pyroly-
 - sis193-203
- Synthetic natural gas prices, oil
 - price sensitivity to 236*f*

T

- Tar formation242, 245
- Temperature
 - dependence of
 - paraffins pyrolysis45-49
 - pyrolytic water evolution ..249-253
 - volatiles production245-246
 - effect on coke from acetylene .. 180*f*
 - effect on coke from ethylene ... 182*f*
 - effect on hydrolypyrolysis
 - products300-304, 314, 318

Temperature (*continued*)

- profiles of *n*-butane reactor 138*f*
- profiles of naphtha reactor 149*f*
- time profile, reactor exit 125*f*
- time profile, venturi inlet 122*f*
- Tetradecene pyrolysis 9
- Tetralin 321
- Thermal
 - alkylation, modification of ...289-295
 - analyses of shale343-350
 - aromatization of dienes 322
 - cracking, product distribution
 - from hydrolypyrolysis
 - and299*t*, 315*t*
 - decomposition245-253
 - of neopentane and ditertiary
 - butyl peroxide 289
 - of shale, activation energies .. 346
 - dissipation 333
 - efficiency164, 166, 232
 - similarity 113
- Thermodynamic equilibrium of
 - coal pyrolysis247-249
- Thermogravimetric analysis ...343-350
- Time dependence of paraffins
 - pyrolysis45-49
- Toluene70, 82, 199, 241
- cyclohexane, and *n*-hexane,
 - steam cracking of 176
- Tricycloalkanes, pyrolysis of67-76

V

- Vacuum distillation 275
- Vacuum pyrolysis coals 252
- Vapor evolution during retort-
 - ing334-339
- Venturi
 - inlet temperature-time profile .. 122*f*
 - nozzle reaction chamber 108
 - reactor11, 119-121
 - throat 123
- 4-Vinylcyclohexene 199
- Virgin gas oils, pyrolysis of77-88
- Volatile(s)
 - effect of pressure and coal par-
 - ticle size on 255*f*
 - production, temperature de-
 - pendence of245-246
 - yields from bituminous coal 254

W

- Water gas shift equilibrium 246
- Wind tunnel, trisonic 116
- Wyodak
 - coal225-237
 - analyses of 229*t*
 - carbon distribution in make
 - gas from 229*t*
 - hydrocarbonization char,
 - analyses of 230*t*

| X | | Z | |
|---|-------|----------|------------------------------|
| X-ray diffraction studies | | 276-277 | |
| Xylene | | 82, 241 | |
| Y | | | |
| Yield correlation, pyrolysis | | 144 | |
| Yields from hydrogen-chloride catalyzed alkylation | | 294t | |
| | | | Zero conversion |
| | | | extrapolation |
| | | | |
| | | | 36, 42, 49 |
| | | | extrapolation of selectivity |
| | | | diagrams |
| | | | |
| | | | 30-32 |
| | | | kinetics at |
| | | | |
| | | | 212 |
| | | | rate constant |
| | | | |
| | | | 141 |

*Jacket design by Carol Conway.
Editing and production by Robin Allison.*

*The book was composed by Service Composition Co., Baltimore, MD,
printed and bound by The Maple Press Co., York, PA.*